Zhidong Deng
Hongbo Li

Editors

Proceedings of the 2015 Chinese Intelligent Automation Conference

Intelligent Technology and Systems

Springer

Lecture Notes in Electrical Engineering

Volume 338

About this Series

"Lecture Notes in Electrical Engineering (LNEE)" is a book series which reports the latest research and developments in Electrical Engineering, namely:

- Communication, Networks, and Information Theory
- Computer Engineering
- Signal, Image, Speech and Information Processing
- Circuits and Systems
- Bioengineering

LNEE publishes authored monographs and contributed volumes which present cutting edge research information as well as new perspectives on classical fields, while maintaining Springer's high standards of academic excellence. Also considered for publication are lecture materials, proceedings, and other related materials of exceptionally high quality and interest. The subject matter should be original and timely, reporting the latest research and developments in all areas of electrical engineering.

The audience for the books in LNEE consists of advanced level students, researchers, and industry professionals working at the forefront of their fields. Much like Springer's other Lecture Notes series, LNEE will be distributed through Springer's print and electronic publishing channels.

More information about this series at http://www.springer.com/series/7818

Zhidong Deng · Hongbo Li
Editors

Proceedings of the 2015 Chinese Intelligent Automation Conference

Intelligent Technology and Systems

Editors
Zhidong Deng
Tsinghua University
Beijing
China

Hongbo Li
Department of Computer Science
  and Technology
Tsinghua University
Beijing
China

Printed on acid-free paper

Contents

Chapter 1
Two-Level Robust Weighted Measurement Fusion Kalman Filter over Clustering Sensor Network with Uncertain Noise Variances

Guihuan Nie, Peng Zhang, Wenjuan Qi and Zili Deng

Abstract Applying the Lyapunov equation method, this paper presents a robust weighted measurement fusion Kalman filter over clustering sensor network with uncertain noise variances, which can significantly reduce the communicational load and save energy when the number of sensors is very large. Its robust accuracy is equal to that of the global centralized robust Kalman fuser or the two-level centralized Kalman fuser, and is higher than those of each local robust Kalman filter and each local robust weighted measurement Kalman fuser. One simulation example is given to verify its effectiveness and correctness.

Keywords Clustering sensor network · Weighted measurement fusion · Robust Kalman filter · Uncertain noise variance · Robust accuracy

1.1 Introduction

The estimation and fusion in sensor networks have been widely applied in many fields, including signal processing, target tracking, robotics, guidance, GPS position, and environmental monitoring [1]. In practice, the uncertainties inevitably exist, so that it has motivated many studies on designing robust Kalman filters. An important class of the robust Kalman filtering problems is to design a Kalman filter such that its actual filtering error variances are guaranteed to have minimal upper bound for all admissible uncertainties [2].

The robust Kalman filtering for sensor networks with uncertainty of model parameters was presented in [3], where the robustness of the fused filter was not proved and the robust accuracy of the fused filter was not given. Two-level robust

G. Nie · P. Zhang · W. Qi · Z. Deng (✉)
Department of Automation, Heilongjiang University, Harbin 150080, China
e-mail: dzl@hlju.edu.cn

Fig. 1.1 The two-level
clustering sensor network

Level 1

Base station   Level 2

▫ Cluster heads   ● Sensor nodes
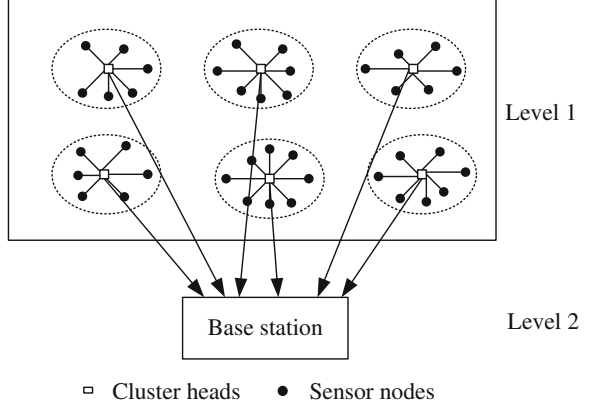
sequential covariance intersection (SCI) fusion steady-state Kalman predictors over time-invariant clustering sensor networks with uncertain noise variances were presented in [4].

A sensor network system consists of a number of sensor nodes distributed over a spatial region. Using the nearest neighbor rules [5], each cluster consists of a cluster head and a number of sensor nodes. Each member node sends its measurement data or local estimator to the corresponding cluster heads, and each cluster head sends its measurement data or local fusion estimator to the base station to give the global fused estimator, as shown in Fig. 1.1.

In this paper, we consider a clustering sensor network system with uncertain noise variances. We shall present the two-level weighted measurement fusion Kalman filter. Not only can it significantly reduce the communicational load and save energy, but also it has higher robust accuracy.

1.2 Local Robust Steady-State Kalman Filter

Consider the clustering sensor network system with the L clusters and uncertain noise variances

$$x(t+1) = \Phi x(t) + \Gamma w(t) \tag{1.1}$$

$$y_i^{(l)}(t) = H_i^{(l)} x(t) + v_i^{(l)}(t), i = 1, \ldots, n_l, l = 1, \ldots, L \tag{1.2}$$

where t is discrete time, $x(t) \in R^n$ is the state, $y_i^{(l)}(t) \in R^{m_i^{(l)}}$ is the measurement of the ith node for the l cluster shown in Fig. 1.2, $w(t) \in R^r$ is the input noise, $v_i^{(l)}(t) \in R^{m_i^{(l)}}$ are the measurement noises of the ith subsystem for the l cluster, Φ, Γ and H_i are known constant matrices with appropriate dimensions.
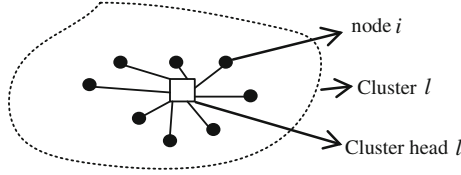
Fig. 1.2 The structure of cluster l

Assumption 1.1 $w(t)$ and $v_i^{(l)}(t)$ are uncorrelated white noises with zero means and uncertain true variances $\bar{Q}$ and $\bar{R}_i^{(l)}$, respectively, satisfying

$$\bar{Q} \leq Q, \bar{R}_i^{(l)} \leq R_i^{(l)}, \ i = 1, \ldots, n_l, l = 1, \ldots, L \qquad (1.3)$$

where Q and $R_i^{(l)}$ are known conservative upper bounds, respectively.

Assumption 1.2 Each sensor subsystem is completely observable and completely controllable.

Assumption 1.3

$$m_1^{(l)} + \cdots + m_{n_l}^{(l)} = m_c^{(l)} \geq n.$$

In the lth cluster, based on the worst-case conservative subsystems (1.1) and (1.2) with conservative upper bounds Q and $R_i^{(l)}$ of noise variances satisfying (1.3), the local steady-state robust Kalman filters are given by [6]

$$\hat{x}_i^{(l)}(t|t) = \Psi_i^{(l)}\hat{x}_i^{(l)}(t-1|t-1) + K_i^{(l)}y_i^{(l)}(t), \quad i = 1, \ldots, n_l, l = 1, \ldots, L \qquad (1.4)$$

$$\Psi_i^{(l)} = \left[I_n - K_i^{(l)}H_i^{(l)}\right]\Phi, \ K_i^{(l)}(t) = \Sigma_i^{(l)}H_i^{(l)\mathrm{T}}\left[H_i^{(l)}\Sigma_i^{(l)}H_i^{(l)\mathrm{T}} + R_i^{(l)}\right]^{-1} \qquad (1.5)$$

where I_n is the $n \times n$ identity matrix, T denotes the transpose, and the measurements $y_i^{(l)}(t)$ are the actual measurements.

The conservative prediction error variances $\Sigma_i^{(l)}$ satisfy the Riccati equations

$$\Sigma_i^{(l)} = \Phi\left[\Sigma_i^{(l)} - \Sigma_i^{(l)}H_i^{(l)\mathrm{T}}\left(H_i^{(l)}\Sigma_i^{(l)}H_i^{(l)\mathrm{T}} + R_i^{(l)}\right)^{-1}H_i^{(l)}\Sigma_i^{(l)}\right]\Phi^{\mathrm{T}} + \Gamma Q\Gamma^{\mathrm{T}} \qquad (1.6)$$

The conservative filtering error variances $P_i^{(l)}$ satisfy the Lyapunov equations

$$\bar{P}_i^{(l)} = \Psi_i^{(l)}P_i^{(l)}\Psi_i^{(l)\mathrm{T}} + \left[I_n - K_i^{(l)}H_i^{(l)}\right]\Gamma Q\Gamma^{\mathrm{T}}\left[I_n - K_i^{(l)}H_i^{(l)}\right]^{\mathrm{T}} + K_i^{(l)}R_i^{(l)}K_i^{(l)\mathrm{T}} \qquad (1.7)$$

The actual filtering error variances $\bar{P}_i^{(l)}$ satisfy the Lyapunov equations as

$$\bar{P}_i^{(l)} = \Psi_i^{(l)} \bar{P}_i^{(l)} \Psi_i^{(l)\mathrm{T}} + \left[I_n - K_i^{(l)} H_i^{(l)}\right] \Gamma \bar{Q} \Gamma^{\mathrm{T}} \left[I_n - K_i^{(l)} H_i^{(l)}\right]^{\mathrm{T}} + K_i^{(l)} \bar{R}_i^{(l)} K_i^{(l)\mathrm{T}} \quad (1.8)$$

Lemma 1.1 [6] *For the clustering sensor network system* (1.1) *and* (1.2) *with Assumptions* 1.1–1.3, *the robust local steady-state Kalman filters* (1.4) *are robust in the sense that for all admissible uncertain noise variances* $\bar{Q}$ *and* $\bar{R}_i^{(l)}$ *satisfying* (1.3), *the corresponding actual variances* $\bar{P}_i^{(l)}$ *satisfy*

$$\bar{P}_i^{(l)} \leq P_i^{(l)}, \, i = 1, \ldots, n_l, l = 1, \ldots, L \quad (1.9)$$

and $P_i^{(l)}$ *is a minimal upper bound of all admissible* $\bar{P}_i^{(l)}$.

Remark 1.1 From (1.9), we have $\mathrm{tr}\bar{P}_i^{(l)} \leq \mathrm{tr}P_i^{(l)}$, where the symbol tr denotes the trace of matrix. The trace $\mathrm{tr}P_i^{(l)}$ is called as its robust accuracy, and the trace $\mathrm{tr}\bar{P}_i^{(l)}$ is called as its actual accuracy. This shows that the actual accuracy of a robust Kalman filter is higher than its robust accuracy. The smaller trace means the higher robustness or actual accuracy.

1.3 Two-Level Weighted Measurement Robust Kalman Filter

The first level local centralized fusion equations for the *l*th cluster are

$$y_c^{(l)}(t) = H_c^{(l)} x(t) + v_c^{(l)}(t), \, l = 1, \ldots, L, \, H_c^{(l)} = \left[H_1^{(l)\mathrm{T}}, \ldots, H_{n_l}^{(l)\mathrm{T}}\right]^{\mathrm{T}} \quad (1.10)$$

and $v_c^{(l)}(t) = \left[v_1^{(l)\mathrm{T}}(t), \ldots, v_{n_l}^{(l)\mathrm{T}}(t)\right]^{\mathrm{T}}$ have the conservative and actual variances

$$R_c^{(l)} = \mathrm{diag}\left(R_1^{(l)}, \ldots, R_{n_l}^{(l)}\right), \, \bar{R}_c^{(l)} = \mathrm{diag}\left(\bar{R}_1^{(l)}, \ldots, \bar{R}_{n_l}^{(l)}\right) \quad (1.11)$$

According to Assumption 1.3, introducing the full-rank decomposition [7]

$$H_c^{(l)} = M^{(l)} H_M^{(l)} \quad (1.12)$$

where $M^{(l)}$ are the $m_c^{(l)} \times m_l$ full-column rank matrices, and $H_M^{(l)}$ are the $m_l \times n$ full-row rank matrices.

Substituting (1.12) into (1.10) and applying the weighted least square (WLS) method [8] yields the first level local weighted measurement fusion equations

$$y_M^{(l)}(t) = H_M^{(l)} x(t) + v_M^{(l)}(t), \quad l = 1, \ldots, L \tag{1.13}$$

where $y_M^{(l)}(t)$ are the fused measurements and $v_M^{(l)}(t)$ are fused measurements white noise with conservative and actual variances $R_M^{(l)}$ and $\bar{R}_M^{(l)}$, respectively,

$$y_M^{(l)}(t) = \left[M^{(l)\mathrm{T}} R_c^{(l)-1} M^{(l)} \right]^{-1} M^{(l)\mathrm{T}} R_c^{(l)-1} y_c^{(l)}(t) \tag{1.14}$$

$$R_M^{(l)} = \left[M^{(l)\mathrm{T}} R_c^{(l)-1} M^{(l)} \right]^{-1} \tag{1.15}$$

$$\bar{R}_M^{(l)} = \left[M^{(l)\mathrm{T}} R_c^{(l)-1} M^{(l)} \right]^{-1} M^{(l)\mathrm{T}} R_c^{(l)-1} \bar{R}_c^{(l)} R_c^{(l)-1} M^{(l)} \left[M^{(l)\mathrm{T}} R_c^{(l)-1} M^{(l)} \right]^{-1} \tag{1.16}$$

For the lth measurement fusion subsystem (1.1) and (1.13) with conservative upper bounds Q and $R_i^{(l)}$ of noise variances satisfying (1.3), applying the standard Kalman filter algorithm (1.4)–(1.8), the first level weighted measurement fusion steady-state robust Kalman filters $\hat{x}_M^{(l)}(t|t)$ and their conservative and actual variances $P_M^{(l)}$ and $\bar{P}_M^{(l)}$ can be obtained.

From (1.13), we have the second level centralized fusion measurement equation (indirect centralized fusion)

$$y_c^{(M)}(t) = H_c^{(M)} x(t) + v_c^{(M)}(t), \; H_c^{(M)} = \left[H_M^{(1)\mathrm{T}}, \ldots, H_M^{(L)\mathrm{T}} \right]^{\mathrm{T}} \tag{1.17}$$

$$y_c^{(M)}(t) = \left[y_M^{(1)\mathrm{T}}(t), \ldots, y_M^{(L)\mathrm{T}}(t) \right]^{\mathrm{T}}, \; v_c^{(M)}(t) = \left[v_M^{(1)\mathrm{T}}(t), \ldots, v_M^{(L)\mathrm{T}}(t) \right]^{\mathrm{T}} \tag{1.18}$$

and $v_c^{(M)}(t)$ has the conservative and actual variances

$$R_c^{(M)} = \mathrm{diag}\left(R_M^{(1)}, \ldots, R_M^{(L)} \right), \; \bar{R}_c^{(M)} = \mathrm{diag}\left(\bar{R}_M^{(1)}, \ldots, \bar{R}_M^{(L)} \right) \tag{1.19}$$

Assumption 1.4

$$m_1^{(c)} + \cdots + m_L^{(c)} = m^{(c)} \geq n.$$

According to Assumption 1.4, introducing the full-rank decomposition [7]

$$H_c^{(M)} = M H_M \tag{1.20}$$

where M is the $m^{(c)} \times m$ full-column rank matrix, and H_M is the $m \times n$ full-row rank matrix.

Substituting (1.20) into (1.17), applying the WLS method, yields the second level weighted measurement fusion equation

$$y_M(t) = H_M x(t) + v_M(t) \tag{1.21}$$

where $y_M(t)$ is the fused measurement and $v_M(t)$ is the fused measurement white noise with conservative and actual variance R_M and $\bar{R}_M$, respectively,

$$y_M(t) = \left[M^T R_c^{(M)-1} M\right]^{-1} M^T R_c^{(M)-1} y_c^{(M)}(t), \ R_M = \left[M^T R_c^{(M)-1} M\right]^{-1} \tag{1.22}$$

$$\bar{R}_M = \left[M^T R_c^{(M)-1} M\right]^{-1} M^T R_c^{(M)-1} \bar{R}_c^{(M)} R_c^{(M)-1} M \left[M^T R_c^{(M)-1} M\right]^{-1} \tag{1.23}$$

For the weighted measurement fusion system (1.1) and (1.21) with conservative upper bounds Q and $R_i^{(l)}$ satisfying (1.3), applying the standard Kalman filter algorithm (1.4)–(1.8), the second level weighted measurement fusion steady-state robust Kalman filter $\hat{x}_M(t|t)$ and their conservative and actual variance P_M and $\bar{P}_M$ can be obtained.

From (1.10) to (1.11), we have the global centralized fusion equation (direct centralized fusion)

$$y_c(t) = H_c x(t) + v_c(t), \ H_c = \left[H_c^{(1)T}, \ldots, H_c^{(L)T}\right]^T \tag{1.24}$$

$$y_c(t) = \left[y_c^{(1)T}(t), \ldots, y_c^{(L)T}(t)\right]^T, \ v_c(t) = \left[v_c^{(1)T}(t), \ldots, v_c^{(L)T}(t)\right]^T \tag{1.25}$$

and $v_c(t)$ has conservative and actual variance R_c and $\bar{R}_c$, such that

$$R_c(t) = \mathrm{diag}\left(R_c^{(1)}(t), \ldots, R_c^{(L)}(t)\right), \ \bar{R}_c(t) = \mathrm{diag}\left(\bar{R}_c^{(1)}(t), \ldots, \bar{R}_c^{(L)}(t)\right) \tag{1.26}$$

From (1.1) and (1.10), applying the standard Kalman filter algorithm (1.4)–(1.8), we can obtain the first level centralized fusion robust Kalman filter $\hat{x}_c^{(l)}(t|t)$ with the upper bound $P_c^{(l)}$ and actual variance $\bar{P}_c^{(l)}$. From (1.1) and (1.17), applying the standard Kalman filter algorithm (1.4)–(1.8), we can obtain the second level centralized fusion (indirect centralized fusion) robust Kalman filter $\hat{x}_c^{(M)}(t|t)$ with the upper bound $P_c^{(M)}$ and actual variance $\bar{P}_c^{(M)}$.

From (1.1) and (1.24), similar to (1.4)–(1.8), we can obtain the global centralized fusion (direct centralized fusion) robust Kalman filter $\hat{x}_c(t|t)$ with the upper bound P_c and actual variance $\bar{P}_c$.

Theorem 1.1 *For the clustering sensor network system* (1.1) *and* (1.2) *with Assumptions* 1.1–1.4, *the two-level weighted measurement robust steady-state Kalman filters, centralized fusion Kalman filters (direct and indirect) are robust in*

the sense that for all admissible uncertain noise variances $\bar{Q}$ and $\bar{R}_i^{(l)}$ satisfying (1.3), it follows that

$$\bar{P}_M^{(l)} \leq P_M^{(l)}, \bar{P}_M \leq P_M, \operatorname{tr}\bar{P}_M^{(l)} \leq \operatorname{tr}P_M^{(l)}, \operatorname{tr}\bar{P}_M \leq \operatorname{tr}P_M \quad (1.27)$$

$$\bar{P}_c^{(l)} \leq P_c^{(l)}, \bar{P}_c^{(M)} \leq P_c^{(M)}, \bar{P}_c \leq P_c, \operatorname{tr}\bar{P}_c^{(l)} \leq \operatorname{tr}P_c^{(l)}, \operatorname{tr}\bar{P}_c^{(M)} \leq \operatorname{tr}P_c^{(M)}, \operatorname{tr}\bar{P}_c \leq \operatorname{tr}P_c \quad (1.28)$$

and $P_M^{(l)}, P_M, P_c^{(l)}, P_c^{(M)}$ or P_c is a minimal upper bound of $\bar{P}_M^{(l)}, \bar{P}_M, \bar{P}_c^{(l)}, \bar{P}_c^{(M)}$ or $\bar{P}_c$, respectively.

Proof The proof is similar to that of Ref. [6]. The detail is omitted.

1.4 Accuracy Analysis

Theorem 1.2 *For the clustering sensor network system* (1.1) *and* (1.2), *the two-level weighted measurement fusion steady-state robust Kalman filters, centralized fusion robust Kalman filters and local robust Kalman filters have robust and actual accuracy relations*

$$\hat{x}_M^{(l)}(t|t) = \hat{x}_c^{(l)}(t|t), P_M^{(l)} = P_c^{(l)}, \bar{P}_M^{(l)} = \bar{P}_c^{(l)}, \operatorname{tr}P_M^{(l)} = \operatorname{tr}P_c^{(l)}, \operatorname{tr}\bar{P}_M^{(l)} = \operatorname{tr}\bar{P}_c^{(l)} \quad (1.29)$$

$$\hat{x}_M(t|t) = \hat{x}_c(t|t) = \hat{x}_c^{(M)}(t|t), P_M = P_c = P_c^{(M)}, \bar{P}_M = \bar{P}_c = \bar{P}_c^{(M)}$$
$$\operatorname{tr}P_M = \operatorname{tr}P_c = \operatorname{tr}P_c^{(M)}, \operatorname{tr}\bar{P}_M = \operatorname{tr}\bar{P}_c = \operatorname{tr}\bar{P}_c^{(M)} \quad (1.30)$$

$$P_M \leq P_M^{(l)} \leq P_i^{(l)}, \operatorname{tr}P_M \leq \operatorname{tr}P_M^{(l)} \leq \operatorname{tr}P_i^{(l)} \quad (1.31)$$

Proof The proof is similar to that of Ref. [6]. The detail is omitted.

1.5 Simulation Examples

Consider the clustering sensor network system for target tracking with 29 sensors and with uncertain noise variances

$$x(t+1) = \begin{bmatrix} 1 & T_0 \\ 0 & 1 \end{bmatrix} x(t) + \begin{bmatrix} 0.5T_0^2 \\ T_0 \end{bmatrix} w(t) \quad (1.32)$$

$$y_i^{(l)}(t) = H_i^{(l)} x(t) + v_i^{(l)}(t), \quad i = 1, \ldots, n_l, l = 1, \ldots, L \quad (1.33)$$

where we take $H_1^{(1)} = [1 \quad 0]$, $H_2^{(1)} = I_2$, $H_3^{(1)} = [1 \quad 0]$, $H_4^{(1)} = I_2$, $H_5^{(1)} = I_2$, $H_6^{(1)} = I_2$, $H_1^{(2)} = [1 \quad 0]$, $H_2^{(2)} = I_2$, $H_3^{(2)} = [1 \quad 0]$, $H_4^{(2)} = I_2$, $H_5^{(2)} = I_2$, $H_1^{(3)} = [1 \quad 0]$, $H_2^{(3)} = I_2$, $H_3^{(3)} = [1 \quad 0]$, $H_4^{(3)} = I_2$, $H_5^{(3)} = I_2$, $H_6^{(3)} = I_2$, $H_7^{(3)} = I_2$, $H_1^{(4)} = [1 \quad 0]$, $H_2^{(4)} = I_2$, $H_3^{(4)} = [1 \quad 0]$, $H_4^{(4)} = I_2$, $H_5^{(4)} = I_2$, $H_1^{(5)} = [1 \quad 0]$, $H_2^{(5)} = I_2$, $H_3^{(5)} = [1 \quad 0]$, $H_4^{(5)} = I_2$, $H_5^{(5)} = I_2$, $H_6^{(5)} = I_2$, T_0 is the sample period, $x(t) = [x_1(t), x_2(t)]^{\mathrm{T}}$ is the state, $x_1(t)$, and $x_2(t)$ are the position and velocity of target at time tT_0, $y_i^{(l)}(t)$ are the measurements for sensor i in the lth cluster, $w(t)$ and $v_i^{(l)}(t)$ are white noises with zero means and uncertain variances $\bar{Q}$ and $\bar{R}_i^{(l)}$, respectively. Assume that Q and $R_i^{(l)}$ are conservative upper bounds of $\bar{Q}$ and $\bar{R}_i^{(l)}$, respectively. In the simulation, we take $T_0 = 0.5$, $t = 1, \ldots, 300$, $Q = 1$, $\bar{Q} = 0.8$, $R_1^{(1)} = 0.3$, $\bar{R}_1^{(1)} = 0.2$, $R_2^{(1)} = 1.3 I_2$, $\bar{R}_2^{(1)} = I_2$, $R_3^{(1)} = 2.3$, $\bar{R}_3^{(1)} = 2$ $R_4^{(1)} = 3.3 I_2$, $\bar{R}_4^{(1)} = 3 I_2$, $R_5^{(1)} = 4.3 I_2$, $\bar{R}_5^{(1)} = 3.6 I_2$, $R_6^{(1)} = 5.3 I_2$, $\bar{R}_6^{(1)} = 4.9 I_2$, $R_1^{(2)} = 1.4$, $\bar{R}_1^{(2)} = 1$, $R_2^{(2)} = 3.5 I_2$, $\bar{R}_2^{(2)} = 3 I_2$, $R_3^{(2)} = 2.5$, $\bar{R}_3^{(2)} = 2$, $R_4^{(2)} = 6.9 I_2$, $\bar{R}_4^{(2)} = 6 I_2$, $R_5^{(2)} = 9 I_2$, $\bar{R}_5^{(2)} = 8 I_2$, $R_1^{(3)} = 1$, $\bar{R}_1^{(3)} = 0.81$, $R_2^{(3)} = 5 I_2$, $\bar{R}_2^{(3)} = 4 I_2$, $R_3^{(3)} = 7$, $\bar{R}_3^{(3)} = 6$, $R_4^{(3)} = 9 I_2$, $\bar{R}_4^{(3)} = 8 I_2$, $R_5^{(3)} = 12 I_2$, $\bar{R}_5^{(3)} = 10 I_2$, $R_6^{(3)} = 2 I_2$, $\bar{R}_6^{(3)} = 1.8 I_2$, $R_7^{(3)} = 20 I_2$, $\bar{R}_7^{(3)} = 16 I_2$, $R_1^{(4)} = 0.9$, $\bar{R}_1^{(4)} = 0.6$, $R_2^{(4)} = 6 I_2$, $\bar{R}_2^{(4)} = 4 I_2$, $R_3^{(4)} = 9$, $\bar{R}_3^{(4)} = 8$, $R_4^{(4)} = 11 I_2$, $\bar{R}_4^{(4)} = 9 I_2$, $R_5^{(4)} = 12 I_2$, $\bar{R}_5^{(4)} = 10 I_2$, $R_1^{(5)} = 20$, $\bar{R}_1^{(5)} = 16$, $R_2^{(5)} = 29 I_2$, $\bar{R}_2^{(5)} = 25 I_2$, $R_3^{(5)} = 16$, $\bar{R}_3^{(5)} = 12$, $R_4^{(5)} = 40 I_2$, $\bar{R}_4^{(5)} = 36 I_2$, $R_5^{(5)} = 55 I_2$, $\bar{R}_5^{(5)} = 50 I_2$, $R_6^{(5)} = 65 I_2$, $\bar{R}_6^{(5)} = 60 I_2$.

The robust and actual accuracy comparisons of local and fused Kalman filters are shown in Tables 1.1, 1.2, 1.3, and 1.4, which verify the accuracy relations (1.27)–(1.31).

Table 1.1 The accuracy comparison of $\mathrm{tr} P_i^{(l)}$ and $\mathrm{tr} \bar{P}_i^{(l)}$, $i = 1, \ldots, n_l, l = 1$

$\mathrm{tr} P_1^{(1)}$	$\mathrm{tr} P_2^{(1)}$	$\mathrm{tr} P_3^{(1)}$	$\mathrm{tr} P_4^{(1)}$	$\mathrm{tr} P_5^{(1)}$	$\mathrm{tr} P_6^{(1)}$
0.5966	0.7974	1.7569	1.5901	1.9349	2.26
$\mathrm{tr} \bar{P}_1^{(1)}$	$\mathrm{tr} \bar{P}_2^{(1)}$	$\mathrm{tr} \bar{P}_3^{(1)}$	$\mathrm{tr} \bar{P}_4^{(1)}$	$\mathrm{tr} \bar{P}_5^{(1)}$	$\mathrm{tr} \bar{P}_6^{(1)}$
0.4395	0.6197	1.4774	1.4006	1.6014	2.0173

Table 1.2 The accuracy comparison of $\mathrm{tr} P_\theta^{(l)}$ and $\mathrm{tr} \bar{P}_\theta^{(l)}$, $l = 1, \ldots, 5$, $\theta = c, M$

$\mathrm{tr} P_\theta^{(1)}$	$\mathrm{tr} P_\theta^{(2)}$	$\mathrm{tr} P_\theta^{(3)}$	$\mathrm{tr} P_\theta^{(4)}$	$\mathrm{tr} P_\theta^{(5)}$
0.3143	0.6387	0.5032	0.7169	2.4198
$\mathrm{tr} \bar{P}_\theta^{(1)}$	$\mathrm{tr} \bar{P}_\theta^{(2)}$	$\mathrm{tr} \bar{P}_\theta^{(3)}$	$\mathrm{tr} \bar{P}_\theta^{(4)}$	$\mathrm{tr} \bar{P}_\theta^{(5)}$
0.2468	0.5193	0.42	0.5355	1.999

Table 1.3 The accuracy comparison of $\mathrm{tr}P_\theta$ and $\mathrm{tr}\bar{P}_\theta$, $\mathrm{tr}P_c^{(M)}$ and $\mathrm{tr}\bar{P}_c^{(M)}$, $\theta = c, M$

$\mathrm{tr}P_\theta$	$\mathrm{tr}\bar{P}_\theta$	$\mathrm{tr}P_c^{(M)}$	$\mathrm{tr}\bar{P}_c^{(M)}$
0.1846	0.1487	0.1846	0.1487

Table 1.4 The comparison of $\hat{x}_\theta^{(1)}(t|t)$, $\hat{x}_\theta(t|t)$ and $\hat{x}_c^{(M)}(t|t)$, $\theta = c, M$

t	$\hat{x}_M^{(1)}(t|t)$	$\hat{x}_c^{(1)}(t|t)$	$\hat{x}_M(t|t)$	$\hat{x}_c(t|t)$	$\hat{x}_c^{(M)}(t|t)$
50	$\begin{bmatrix} -8.4551 \\ 1.0050 \end{bmatrix}$	$\begin{bmatrix} -8.4551 \\ 1.0050 \end{bmatrix}$	$\begin{bmatrix} -8.3078 \\ 1.4051 \end{bmatrix}$	$\begin{bmatrix} -8.3078 \\ 1.4051 \end{bmatrix}$	$\begin{bmatrix} -8.3078 \\ 1.4051 \end{bmatrix}$
100	$\begin{bmatrix} 68.1176 \\ 2.6390 \end{bmatrix}$	$\begin{bmatrix} 68.1176 \\ 2.6390 \end{bmatrix}$	$\begin{bmatrix} 68.2486 \\ 2.8064 \end{bmatrix}$	$\begin{bmatrix} 68.2486 \\ 2.8064 \end{bmatrix}$	$\begin{bmatrix} 68.2486 \\ 2.8064 \end{bmatrix}$

1.6 Conclusion

For the clustering network system with uncertain noise variances, according to the minimax robust estimation principle, the two-level weighted measurement fusion steady-state Kalman filter is presented, which can significantly reduce the communicational burden and save energy. It is proved that its robust accuracy is equal to that of the two-level centralized fuser (indirect centralized fuser) or the global centralized fuser (direct centralized fuser), and is higher than those of every local robust Kalman filter and every local weighted measurement fuser.

References

1. Liggins ME, Hall DL, Llinas J (2009) Handbook of multisensory data fusion, 2nd edn. Theory and practice. CRC Press. Boca Raton, Taylor & Francis Group
2. Petersen I, Savkin AV (1999) Robust Kalman filtering for signals and systems with large uncertainties. Control engineering. Birkhauser, Boston
3. Ahmad A, Gani M, Yang FW (2008) Decentralized robust Kalman filtering for uncertain stochastic systems over heterogeneous sensor networks. Signal Process 88(8):1919–1928
4. Qi WJ, Zhang P, Deng ZL (2013) Two-level robust sequential covariance intersection fusion Kalman predictors over clustering sensor networks with uncertain noise variances. Int J Sens Netw 14(4):251–261

5. Jadbabaie A, Lin J, Morse AS (2003) Coordination of groups of mobile autonomous agents using nearest neighbor rules. IEEE Trans Autom Control 48(6):988–1001
6. Qi WJ, Zhang P, Deng ZL (2014) Robust weighted fusion Kalman smoothers for multisensory time-varying systems with uncertain noise variances. Signal Process 282:15–37
7. Fang BR, Zhou JD, Li YM (2004) Matrix theory. Tsinghai University Press, Springer, New York
8. Kailath T, Sayed AH, Hassibi B (2000) Linear estimation. Prentice Hall, New York

Chapter 2
Multi-population and Self-adaptive Genetic Algorithm Based on Simulated Annealing for Permutation Flow Shop Scheduling Problem

Huimin Sun, Jingwei Yu and Hailong Wang

Abstract In order to solve the permutation flow shop scheduling problem, a multi-population and self-adaptive genetic algorithm based on simulated annealing is proposed in this paper. For the precocity problem of traditional genetic algorithm, the multi-population coevolution strategy is adopted. We introduce a squared term to improve traditional self-adaptive genetic operators, which can increase the searching efficiency and avoid getting into local optimum. A new cooling strategy is proposed to reinforce the ability of overall searching optimal solution. The algorithm is used to solve a series of typical Benchmark problems. Moreover, the results are compared with SGA, IGA, and GASA. The comparison demonstrates the effectiveness of the algorithm.

Keywords Permutation flow shop scheduling problem · Multi-population · Self-adaptive · Simulated annealing · Genetic algorithm

2.1 Introduction

Flow Shop Scheduling Problem (FSSP) aims at minimizing the completion time/makespan (or other criterion) for cases where n jobs are executed through m machines. It is the simplified model of many modern factory pipeline production scheduling problems and has extensive application both in the integrated manufacturing industry and in the processing industry. The FSSP has been extensively investigated in the last several decades [1], since first proposed by Johnson [2].

H. Sun (✉) · J. Yu · H. Wang
School of Astronautics Institution, Harbin Institute of Technology,
Aviation University of Air Force, Changchun, 92 West Dazhi Street,
Nan Gang District, Harbin 150001, China
e-mail: sunminggehuimin@163.com

Permutation Flow Shop Scheduling Problem (PFSSP), with all machines processing their jobs following an identical route, is a special case of FSSP. It also belongs to an extremely complex and difficult combinational optimization problem. In the existing literature [3], the PFSSP has proved to be an NP-hard problem and is quite difficult to be solved. Therefore, it has important theoretical and practical significance to develop and study efficient algorithm.

A lot of algorithms have been proposed to solve the PFSSP with some certain optimum criterion (e.g., makespan). The computational intelligence algorithms have become a hot research topic such as ant colony algorithm [4], genetic algorithm (GA) [5], etc. All of them have better performance than traditional algorithms (e.g., dynamic programming, etc.).

In this paper, we propose multi-population and self-adaptive genetic algorithm based on simulated annealing (MSGASA). We adopt multi-population coevolution strategy to solve the precocity problem. We introduce a squared term to improve traditional self-adaptive genetic operators in order to increase the searching efficiency and avoid getting into local optimum. We proposed a new cooling strategy to reinforce the ability of overall searching optimal solution. A series of typical benchmark problems have been solved using the proposed algorithm and the results have been compared with simple GA (SGA), an improved GA (IGA) [6] and GA based on simulated annealing (GASA) [7]. The comparisons show the effectiveness of proposed algorithm.

2.2 Description of Permutation Flow Shop Scheduling Problem

2.2.1 Assumptions

In order to establish the mathematical model for PFFSP, the following assumptions are given at first.

- All jobs are processed by all machines in the same order.
- Each job is processed by each machine once.
- Each machine can process one job and each job can be processed by one machine at the same time.
- The processing time for each job in each machine is known in advance.
- There is no breakdown or interruption in the process.

2.2.2 Mathematical Model

There is a set of n jobs $(1, 2, \ldots n)$ to process in a set of m machines $(1, 2, \ldots m)$ in the same order. Let t_{ij} $(i = 1, 2, 3, \ldots n; j = 1, 2, 3, \ldots m)$ donates the processing time of job i on machine j. $T(i, j)$ $(i = 1, 2, 3, \ldots n; j = 1, 2, 3, \ldots m)$ is the completion

time of job i on machine j. Therefore, the mathematical model of PFSSP can be written as

$$
\begin{aligned}
&T(1,1) = t_{11}; \\
&T(1,j) = T(1,j-1) + t_{1j};\ (j = 2,3,\ldots m) \\
&T(i,1) = T(i-1,1) + t_{i1};\ (i = 2,3,\ldots n) \\
&T(i,j) = \max\{T(i-1,j), T(i,j-1) + t_{ij}\};\ (i = 2,3,\ldots n; j = 2,3,\ldots m)
\end{aligned}
\tag{2.1}
$$

The total completion time/makespan is $C_{\max}$

$$
C_{\max} = T(n,m)
\tag{2.2}
$$

In this paper, the optimization goal is to minimize the makespan $C_{\max}$.

2.3 Multi-population and Self-adaptive Genetic Algorithm Based on Simulated Annealing

In this section, we will introduce the multi-population coevolution strategy, improved self-adaptive genetic operators, and simulated annealing cooling strategy.

2.3.1 Multi-population Coevolution Algorithm

The traditional GA has a single population searching through the whole search space. Research shows that multi-population GA has excellent performance with solving the precocity problem of the GA [8]. In this paper, we adopt the multi-population coevolution algorithm to take the place of the single population. The process of multi-population coevolution strategy is shown in Fig. 2.1.

Suppose there are P independent subpopulations and each subpopulation evolves Q generations independently. Then populations migrate once with the effect of immigration operator, namely the worst individuals in a population will be replaced by the best individual in another population. The order of migration can be expressed as: $1 \rightarrow 2$, $2 \rightarrow 3$, …, $P \rightarrow 1$. After migration, we select the best individual from each subpopulation artificially as the quintessence population.

2.3.2 Self-adaptive Crossover and Mutation Operators

In this paper, the linear order crossover method and multi-point exchange mutation are adopted respectively. The population crossover and mutate according to their
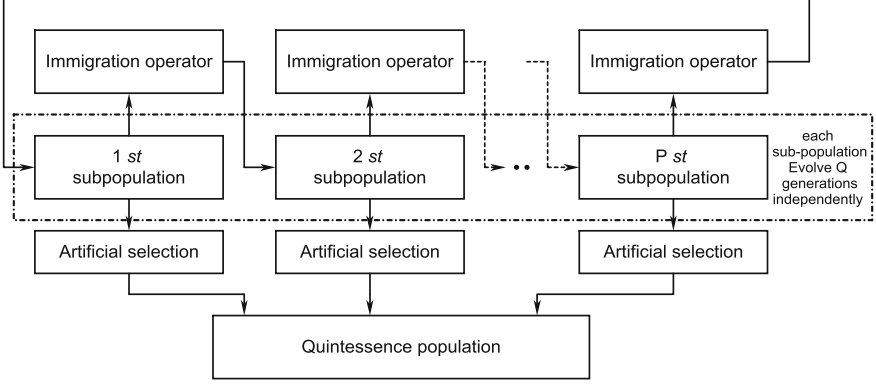
Fig. 2.1 Process of multi-population coevolution strategy

corresponding probability P_c and P_m. The selected values of crossover and mutation probabilities will greatly affect the quality of solution of the algorithm and the convergence rate. In order to improve the searching efficiency and avoid getting into local optimum, the cosine self-adaptive GA algorithm [9] adopts the following crossover probability P_c and mutation probability P_m.

$$P_c = \begin{cases} \frac{P_{c\max}+P_{c\min}}{2} + \left(\frac{P_{c\max}-P_{c\min}}{2}\right)\cos\left(\left(\frac{\bar{f}-f_{avg}}{f_{max}-f_{avg}}\right)\pi\right) & \bar{f} \geq f_{avg} \\ P_{c\max} & \bar{f} < f_{avg} \end{cases} \quad (2.3)$$

$$P_m = \begin{cases} \frac{P_{m\max}+P_{m\min}}{2} + \left(\frac{P_{m\max}-P_{m\min}}{2}\right)\cos\left(\left(\frac{f-f_{avg}}{f_{max}-f_{avg}}\right)\pi\right) & f \geq f_{avg} \\ P_{m\max} & f < f_{avg} \end{cases} \quad (2.4)$$

Inspired by the idea of Shi Shan, we introduce a squared term to improve self-adaptive genetic operators in genetic algorithms as shown in Eqs. (2.5) and (2.6).

$$P_c = \begin{cases} \frac{P_{c\max}+P_{c\min}}{2} - (P_{c\max}-P_{c\min})\left(\frac{Max\_gen}{Count\_opt+k1}\right)^2\cos\left(\left(\frac{\bar{f}-f_{avg}}{f_{max}-f_{avg}}\right)\pi\right) & \bar{f} \geq f_{avg} \\ P_{c\max} - (P_{c\max}-P_{c\min}) \times \left(\frac{Count\_opt+k1}{Max\_gen}\right)^2 & \bar{f} > f_{avg} \end{cases} \quad (2.5)$$

$$P_m = \begin{cases} \frac{P_{m\max}+P_{m\min}}{2} - (P_{m\max}-P_{m\min})\left(\frac{Max\_gen}{Count\_opt+k2}\right)^2\cos\left(\left(\frac{f-f_{avg}}{f_{max}-f_{avg}}\right)\pi\right) & f \geq f_{avg} \\ P_{m\max} - (P_{m\max}-P_{m\min}) \times \left(\frac{Count\_opt+k2}{Max\_gen}\right)^2 & f < f_{avg} \end{cases} \quad (2.6)$$

where $P_{c\,\min}$ and $P_{c\,\max}$ are the lower and upper limits of crossover probability respectively; $\bar{f}$ is the larger fitness of two crossover individuals; $\bar{f}$ donates the fitness of mutating individuals. f_{avg} is the average fitness of population; f_{max} is the maximum fitness of population; $P_{m\,\min}$ and $P_{m\,\max}$ are the lower and upper limits of mutation probability; Max_gen donates the generation number of optimal value keeping on;

Count_opt is the optimal value counter; $k1$ and $k2$ are constant which are less than Max_gen, which is used to adjust the P_c and P_m.

In the initial phase of algorithm, the value of Count_opt is very small. In this condition: Max_gen > Count_opt + $k1(k2)$. It can be obtained that:

$$\begin{cases} H_1 = \left(\frac{\text{Max\_gen}}{\text{Count\_opt}+k1(k2)} \right)^2 > 1 \\ H_2 = \left(\frac{\text{Count\_opt}+k1(k2)}{\text{Max\_gen}} \right)^2 < 1 \end{cases} \tag{2.7}$$

The H_1 is strengthening factor and H_2 is weakening factor. For those individuals $(\bar{f}, f < f_{av})$, the value of P_c and P_m will be larger, and more poor individuals will involve in crossover and mutation. That will increase the diversity of population.

In the late period of algorithm, the value of Count_opt will increase gradually. In this case: Max_gen < Count_opt + $k1(k2)$. We can obtain that:

$$\begin{cases} H_1 = \left(\frac{\text{Max\_gen}}{\text{Count\_opt}+k1(k2)} \right)^2 < 1 \\ H_2 = \left(\frac{\text{Count\_opt}+k1(k2)}{\text{Max\_gen}} \right)^2 > 1 \end{cases} \tag{2.8}$$

The H_1 is weakening factor and H_2 is strengthening factor. For those individuals $(\bar{f}, f > f_{av})$, the P_c and P_m will be larger, more good individuals will involve in crossover and mutation. That will increase the probability of the best individuals.

2.3.3 Simulated Annealing Cooling Strategy

Simulated Annealing (SA) was proposed by Metropolis et al. [10] and Scott Kirkpatrick et al. in 1983 [11]. Combined with simulated annealing mechanism, the genetic algorithm will reinforce the ability of overall searching optimal solution. In order to improve the ability of the sudden jump, we adopt formula (2.9) as cooling strategy.

$$T_{\text{start}} = \left(\frac{\text{Count\_opt}+p}{\text{Max\_gen}} \right)^q \times T_{\text{start}} \tag{2.9}$$

Selecting the appropriate p value, we can get that: when (Count_opt + p < Max_gen), it is a cooling process. When (Count_opt + p<Max_gen), it is heating process. Formula (2.9) has the ability to dynamically adjust the temperature changing. To some extent, it improves traditional monotony of sudden jump probability.
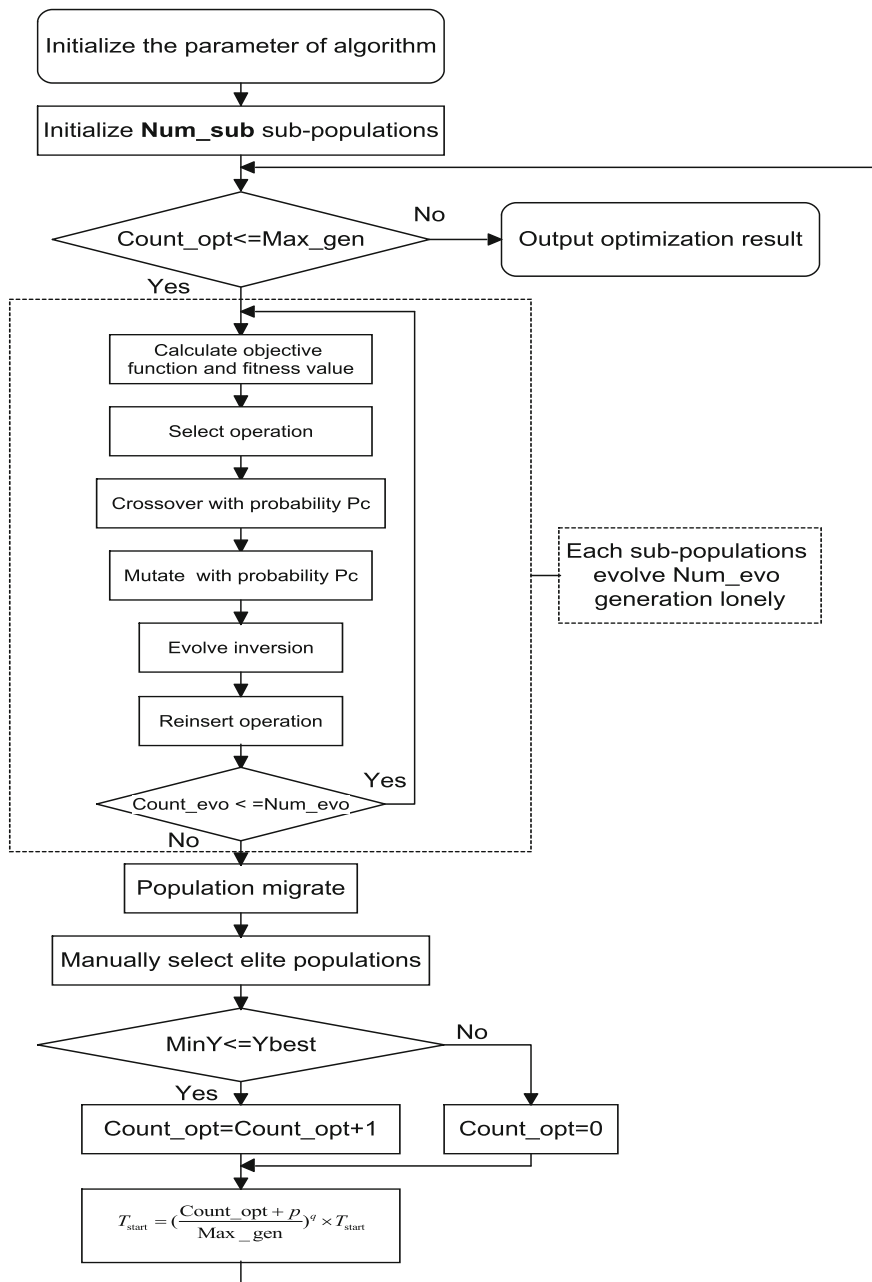
Fig. 2.2 Flowchart of algorithm

2.3.4 Realization of Algorithm

The procedure of the MSGASA for PFFSP is as follows:

Step 1. Initialize the parameter of algorithm.
Step 2. Generate subpopulations; initialize the generation number of optimal values keeping on; set the optimal value counter.
Step 3. Set the independent evolution generation counter.
Step 4. For each subpopulations, make the following operation (1–7), until generate Num_sub new population.

   (1) Calculate objective function value;
   (2) Select L individuals according to Roulette rule;
   (3) For L individuals selected in (2.2), make crossover with self-adaptive crossover probability P_c (calculated in formula (2.5));
   (4) Make mutate with self-adaptive mutation probability P_m.
   (5) Evolve inversion: keep the high fitness value individuals;
   (6) Reinsert: choose the optimum individuals from offspring and parent populations;
   (7) If Count_evo < Num_evo, turn to Step 4; if not, turn to Step 5;

Step 5. Populations migrate.
Step 6. Artificially select the quintessence population.
Step 7. Change the annealing temperature in accordance with the formula (2.9).
Step 8. If Count_opt <=Max_gen, return to Step 3; if not, output the optimization result.

The flowchart of algorithm is shown in Fig. 2.2.

2.4 Experimental Results and Comparisons

To test the performance of MAGASA, some benchmark problems [12] have been solved. The parameters of MAGASA are set as in Table 2.1.

In order to evaluate the performance of the performance of the MAGASA, the best relative error (BRE) and average relative error (ARE) are adopted. They are calculated using the following formulae:

$$\begin{cases} \text{BRE}(\%) = \frac{C_{\text{best}} - C^*}{C^*} \times 100\,\% \\ \text{ARE}(\%) = \frac{C_{\text{avg}} - C^*}{C^*} \times 100\,\% \end{cases} \tag{2.10}$$

where C^* = Lower bound makespan; C_{best} = Makespan obtained using algorithm; C_{avg} = Average makespan obtained (20 times experiments)

The comparisons of SGA, IGA, GASA, and MAGASA are listed in Table 2.2.

Table 2.1 Parameters of MAGASA

Parameter	Value	Parameter	Value
$P_{c\ max}$	0.9	Num_ind	100
$P_{c\ min}$	0.6	$k1$	10
$P_{m\ max}$	0.2	$k2$	10
$P_{m\ min}$	0.05	p	12
Num_sub	4	T_{start}	1000
Max_gen	30	q	0.8
Num_evo	20		

Table 2.2 Comparisons of SGA, IGA, GASA, and MAGASA

Problem $_{n*m}$		SGA		IGA		GASA		MAGASA	
		BRE	ARE	BRE	ARE	BRE	ARE	BRE	ARE
Car1	11*5	0	0	0	0	0	0	0	0
Car2	13*4	0	0	0	0	0	0	0	0
Car3	12*5	0	0	0	0	0	0	0	0
Car4	14*4	0	0	0	0	0	0	0	0
Car5	10*6	0	0	0	0	0	0	0	0
Car6	8*9	0	0	0	0	0	0	0	0
Car7	7*7	0	0	0	0	0	0	0	0
Car8	8*8	0	0	0	0	0	0	0	0
Rec3	20*5	0	0.01	0	0	0	0.1	0	0
Rec7	20*10	0	0.4	0	0.34	0	0.27	0	0.06
Rec13	20*15	0.52	1.39	0.41	0.87	0.31	0.67	0	0.16
Rec19	30*10	0.91	1.7	0.67	1.09	0.38	1.07	0.14	0.34
Rec25	30*15	1.91	3.45	1.03	2.28	0.84	1.28	0.4	0.57

It can be observed that: with the problem of Car class (Car1–Car8), all the four algorithms have excellent performance in global searching and stability. With the problem of Rec class (Rec01–Rec25), the BRE and ARE obtained by MAGASA are less than those obtained by SGA, IGA, and GASA.

2.5 Conclusions

In this work, for the permutation flow shop scheduling problem, we proposed a multi-population and self-adaptive genetic algorithm based on simulated annealing. We improve traditional self-adaptive genetic operators by introducing the squared term. We propose a new cooling strategy to reinforce the ability of overall searching optimal solution. Experimental results show that the proposed algorithm has better performance compared with other existing heuristics.

References

1. Ribas I, Leisten R, Framiñan JM (2010) Review and classification of hybrid flow shop scheduling problems from a production system and a solutions procedure perspective. Comput Oper Res 37(8):1439–1454
2. Johnson SM (1954) Optimal two-and three-stage production schedules with set up times included. Naval Res Logist Q 1:61–68
3. Brucker P (2007) Scheduling algorithm, 5th edn. Springer, Berlin
4. Fardin A (2012) A new ant colony algorithm for makespan minimization in permutation flow shops. Comput Ind Eng 63(2):355–361
5. Zhang Y, Liao XP, Wang Q (2009) Hybrid genetic algorithm for permutation flowshop scheduling problems with total flowtime minimization. Eur J Oper Res 196(3):869–876
6. Rajkumar R, Shahabudeen P (2009) An improved genetic algorithm for the flowshop scheduling problem. Int J Prod Res 47(1):233–249
7. Wang L (2003) Intelligent optimization algorithm and application. Tsinghua University Press, Beijing
8. Huang M, Liu P, Xu L (2010) An improved multi-population genetic algorithm for job shop scheduling problem. In: Proceedings of the 2010 IEEE international conference on progress in informatics and computing, PIC 2010, vol 1, pp 272–275
9. Shi S, Li Q, Wang X (2002) Design optimization of brushless direct current motor based on adaptive genetic algorithm. J Xi'an Jiaotong Univ 36(12):1215–1218
10. Metropolis N, Rosenbluth A et al (1953) Equation of state calculations by fast computing machines. J Chem Phys 56(21):1087–1092
11. Kirkpatrick S, Gelatt CD, Vecchi MP (1983) Optimization by simulated annealing. Science 220(11):650–671
12. Taillard E (1993) Benchmarks for basic scheduling problems. Eur J Oper Res 64(N.2):278–285

Chapter 3
Adaptive Cluster Synchronization for Weighted Cellular Neural Networks with Time-Varying Delays

Yuxiu Li and Guoliang Cai

Abstract In this paper, the adaptive cluster synchronization for weighted cellular neural networks with multiple time-varying delays is investigated. The weighted configuration matrix in the networks under consideration is time-varying, which does not need to satisfy the diffusive coupling conditions or be symmetric. Based on Lyapunov stability theory, Kronecker product, and adaptive control method an adaptive strategy is derived to ensure each node in the networks achieves the asymptotical cluster mean square synchronization. The numerical simulations are performed to verify the effectiveness of the theoretical results.

Keywords Adaptive cluster synchronization · Weighted cellular neural networks · Multiple time delays · Lyapunov stability theorem

3.1 Introduction

In the past decade, there has been a great interest in neural networks due to their wide range of applications, such as associative memory, pattern recognition, signal processing, image processing, fault diagnosis, automatic control engineering, combined imitation, and so on. Papers [1–4] introduced the stability and synchronization of cellular neural networks with different controllers. Paper [5] presented topology identification of weighted complex dynamical networks with non-delayed and time-varying delayed coupling. Papers [6] investigated adaptive synchronization of several kinds of neural networks and chaotic systems. Paper [7] showed that adaptive synchronization in an array of asymmetric neural networks.

Y. Li (✉)
School of Mechanical Engineering, Jiangsu University, Zhenjiang 212013, China
e-mail: jxdw@ujs.edu.cn

G. Cai
Nonlinear Scientific Research Center, Jiangsu University, Zhenjiang 212013, China
e-mail: glcai@ujs.edu.cn

Recently, some works for the cluster synchronization in complex networks have been published. Belykh et al. [8] studied the effect of cluster partitioning in the networks of coupled oscillators, and the conditions for the existences of the unconditional and the conditional clusters are given. Li et al. [9] investigated the cluster synchronization in hybrid coupled discrete-time delayed complex networks with nonidentical delayed dynamical systems using the pinning control method. Wu and Lu [10] investigated the cluster synchronization in adaptive complex dynamical networks with nonidentical nodes using a local control method and a novel adaptive strategy for the coupling strengths of networks. Furthermore, most studies of cluster synchronization focus on the undirected inaction topology, i.e., the coupling matrix should be symmetric. Such as in [11], the coupling matrix should be symmetric, irreducible, and should satisfy the diffusive coupling conditions. In fact, networks with time-varying coupling matrix are widely seen in the real world, such as communication networks and signal transmission networks. Therefore, in practical applications, time-varying weight configuration matrix in the networks is worth much more consideration.

Based on the above discussion, this paper investigates the global cluster mean square synchronization in weighted cellular neural networks with multiple time-varying delays. The main contribution can be summarized as the following two cases: (1) The proposed new kind of weighted cellular neural networks with non-identical nodes and multiple time-varying delays is more general. (2) The weighted configuration matrix is time-varying, and does not need to satisfy the diffusive coupling conditions or be symmetric or irreducible.

This paper is organized as follows: In Sect. 3.2, the cellular neural networks which is made up of n identical nodes with coupling multiple delays is considered. At the same time, assumption and lemma are stated. In order to reach the cluster mean synchronization, a sufficient criterion is presented in Sect. 3.3. In Sect. 3.4, several simulations are illustrated to verify the effectiveness of the theory proposed. Finally, conclusions are drawn in Sect. 3.5.

3.2 Problem Formulation and Preliminaries

In this section, based on the paper [1], one adds an inner-coupling matrix $H(t)$. The modified cellular neural networks made up of n identical nodes with multiple coupling delays is considered, described as follows:

$$\dot{x}_i(t) = -d_i \dot{x}_i + \sum_{j=1}^{n} a_{ij} f_j(x_j(t)) + \sum_{j=1}^{n} b_{ij} H(t) f_j(x_j(t - \tau_{ij}(t))), \quad i = 1, 2, \ldots, n. \quad (3.1)$$

where $x_i(t) = (x_{i1}(t), x_{i2}(t), \ldots, x_{in}(t))^{\mathrm{T}} \in R^n$ is the state variable of the ith neuron, $d_i > 0$ is a constant, a_{ij} and b_{ij} are connection weight and delayed connection weight coefficients, respectively, $f(x_i) = 0.5(|x_i+1|-|x_i-1|)$ is the activation

function, $\tau_{ij} > 0$ is the time-varying coupling delay, $i = 1, 2,…,n$. $H(t)$ is inner-coupling matrix.

In order to realize the cluster synchronization of networks (1), an adaptive controller to be designed for networks (1) is considered. Therefore, the networks (1) with a controller are described as follows:

$$\dot{x}_i(t) = -d_i x_i + \sum_{j=1}^{n} a_{ij} f_j(x_j(t)) + \sum_{j=1}^{n} b_{ij} H(t) f_j(x_j(t - \tau_{ij}(t))) + u_i,$$

$$i = 1, 2, \ldots, n. \tag{3.2}$$

where u_i ($i = 1, 2,…,n$) are nonlinear controllers to be designed.

First, we will introduce the definition of cluster mean square synchronization in the cellular neural networks with time-varying delays.

Definition 3.1 The cellular neural networks (1) is said to be cluster mean square synchronized with networks (2), if, for a suitably design controller, the trivial solution of the error system is stable in the square, i.e.,

$$\lim_{t \to \infty} E\left\{ \|e_i(t)\|^2 \right\} = 0 \tag{3.3}$$

where $e_i(t) = x_i(t) - s_{C_i}(t)$ ($i = 1, 2,…, n$) and satisfy:

$$\lim_{t \to \infty} E\left\{ \|x_i(t) - x_j(t)\|^2 \right\} = 0, \ C_i \neq C_j \tag{3.4}$$

Assumption 3.1 The time delay $\tau_{ij}(t)$ is a differential function which satisfies $0 \le \dot{\tau}_{ij} \le 1$ and $\sigma \in \left[2\dot{\tau}_{ij}(t)-1, 1\right]$, σ is a constant to be determined.

Assumption 3.2 Suppose there exists a positive constant L such that:

$$\|f(t, x(t)) - f(t, y(t))\| \le L\|x(t) - y(t)\|.$$

It holds for any distributed vectors $x(t)$, $y(t)$, where norm $\|x\| = (x^T x)^{\frac{1}{2}}$.

Lemma 3.1 [12] *Function Class Quad (P, Δ, δ) (see* [9]). *Suppose that P is a positive definition matrix and Δ is a diagonal matrix i.e. $P = \text{diag}(p_1, p_2, \ldots, p_n)$, δ is a positive constant. For any x, $y \in R_n$ and $t \ge 0$, if continuous functions $f_i(x)$ satisfy:*

$$(x - y)^T P(f_i(x) - f_i(t) - \Delta\Gamma(x - y)) \le -\delta(x - y)^T(x - y)$$

We denote the class $f_i(x) \subset$ Quad (P, Δ, δ).

Lemma 3.2 [13] *For any vectors x, $y \in R_n$, there exists a positive definite matrix $Q \in R_{n \times n}$ such that the following inequality holds:*

$$2x^{\mathrm{T}}y \leq x^{\mathrm{T}}Qx + y^{\mathrm{T}}Q^{-1}y.$$

3.3 Main Results

In this section, we consider the global adaptive cluster synchronization of the networks (1) with networks (2). Some elegant results on cluster synchronization criteria are derived. The results are obtained based on Lyapunov functional method combined with adaptive control technique as well as Kronecker product.

The error dynamical networks of the networks (1) and (2) are as follows:

$$\begin{aligned}
\dot{e}_i(t) &= -d_i(x_i(t) - s_{C_i}(t)) + \sum_{j=1}^{n} a_{ij}f_j(x_j(t)) - \sum_{j=1}^{n} a_{ij}f_j(s_{C_j}(t)) \\
&\quad + \sum_{j=1}^{n} b_{ij}H(t)f_j(x_j(t - \tau_{ij}(t))) - \sum_{j=1}^{n} b_{ij}H(t)f_j(s_{C_j}(t - \tau_{ij}(t))) \\
&\quad - f_{C_i}(s_{C_i}(t)) + f_{C_i}(x_i(t))
\end{aligned} \tag{3.5}$$

where $e_i(t) = x_i(t) - s_{C_i}(t)$.

Theorem 3.1 *Suppose Lemmas* 3.1 *and* 3.2 *hold, if there exists a positive definite matrix $p^* = \max(p_1, p_2, \ldots, p_n)$ and a diagonal matrix $\Delta = \max(q_1, q_2, \ldots, q_n)$ such that $f_i(x_i(t)) \subset \mathrm{Quad}(P, \Delta, \eta)$ and the following inequality holds:*

$$-\mathrm{d}I + AL - \frac{\delta}{p^*} + \frac{1}{1 - \sigma}I + \frac{1}{2}LKK^T + \lambda_{\max}(\Delta\eta) < 0$$

where $K = B \otimes H(t)$, $d = \max(d_1, d_2, \ldots, d_n)$, $A = (a_{ij})_{n \times n}$, I is the identity maximal.

The networks (1) with networks (2) reach cluster synchronization under the controllers:

$$\begin{aligned}
u_i(t) &= -d_i s_{C_i}(t) - \sum_{j=1}^{n} a_{ij}f_j(s_{C_j}(t)) \\
&\quad - \sum_{j=1}^{n} b_{ij}H(t)f_j(s_{C_j}(t - \tau_{ij}(t))) + f_{C_i}(x_i(t))
\end{aligned}$$

Proof Let $p^* = \max(p_1, p_2, \ldots, p_n)$ and consider the following Lyapunov function:

$$V(t) = \frac{1}{2} \sum_{i=1}^{n} e_i^T p e_i(t) + \frac{1}{1-\sigma} p \int_{t-\tau_{ij}(t)}^{t} e_i^T(t) e_i(t) \mathrm{d}t. \qquad (3.6)$$

Calculating the derivative of (3.6) along the trajectories of 3.5), we get:

$$
\begin{aligned}
\dot{V}(t) = {} & \sum_{i=1}^{n} e_i^T(t) p \dot{e}_i(t) + \frac{1}{1-\sigma} p \sum_{i=1}^{n} e_i^T(t) e_i(t) \\
& - \frac{1 - \dot{\tau}_{ij}}{1 - \sigma} p \sum_{i=1}^{n} e_i^T(t - \tau_{ij}(t)) e_i(t - \tau_{ij}(t)) \\
\leq {} & - \sum_{i=1}^{n} \sum_{j=1}^{n} e_i^T p^* d_i e_i(t) + p^* \sum_{i=1}^{n} \sum_{j=1}^{n} a_{ij} l_i e_i^T(t) e_i(t) \\
& + p^* \sum_{i=1}^{n} \sum_{j=1}^{n} e_i^T b_{ij} H(t) l_i e_j(t - \tau_{ij}(t)) \\
& - \delta \sum_{i=1}^{n} e_i^T(t) e_i(t) + p^* \lambda_{\max}(\Delta\eta) e_i^T(t) e_i(t) \\
\leq {} & E^T(t) p^* \Big[-\mathrm{d}I + AL - \frac{\delta}{p^*} + \frac{1}{1-\sigma} I \\
& + \frac{1}{2} L K K^T + \lambda_{\max}(\Delta\eta) \Big] E(t)
\end{aligned}
$$

According to the condition of Theorem 3.1, when

$$-\mathrm{d}I + AL - \frac{\delta}{p^*} + \frac{1}{1-\sigma} I + \frac{1}{2} L K K^T + \lambda_{\max}(\Delta\eta) < 0$$

We have $\dot{V}(t) < 0$. Therefore, based on Lyapunov stability theory, the neural cellular networks (1) with networks (2) achieve adaptive cluster synchronization. Then Theorem 3.1 has been proved.

Theorem 3.1 shows that the suitable controllers and the right adaptive strategies can guarantee each node of networks (1) with networks (2) reaching the adaptive cluster synchronization. At the same time, the conditions of Theorem 3.1 are easy to obtain with Matlab.

3.4 Numerical Simulations

Now let us consider the Lü system as follows:

$$\dot{x} = f(z) = \begin{pmatrix} a(z_2 - z_1) \\ cz_2 - z_1 z_3 \\ -bz_3 + z_1 z_2 \end{pmatrix},$$

where $a = 36$, $b = 3$, $c = 20$. $L = 1$, $H(t) = \text{diag}(1, 1)$.

Let $L^* = (l_{ij}^*)_{2 \times 2} = \begin{bmatrix} 0.4 & 1.5 \\ 1 & 0.3 \end{bmatrix}$ and $\sigma = \frac{1}{4}$, for simplicity, we assume that matrix $\Gamma = \text{diag}(1, 1)$. We analyze the networks with 15 nodes, namely $N = 15$. We choose the coupling matrices as

$$A = \begin{pmatrix} -6 & 1 & 1 & 1 & 1 & 2 \\ 1 & -2 & 1 & 0 & 0 & 0 \\ 1 & 1 & -3 & 1 & 0 & 0 \\ 1 & 0 & 1 & -3 & 0 & 1 \\ 1 & 0 & 0 & 0 & -1 & 0 \\ 2 & 0 & 0 & 1 & 0 & -3 \end{pmatrix}, \quad B = \begin{pmatrix} -4 & 1 & 1 & 2 \\ 1 & -1 & 0 & 0 \\ 1 & 0 & -1 & 0 \\ 2 & 0 & 0 & -2 \end{pmatrix},$$

$$C = \begin{pmatrix} -2 & 1 & 0 & 0 & 1 \\ 1 & -2 & 1 & 0 & 0 \\ 0 & 1 & -3 & 2 & 0 \\ 0 & 0 & 2 & -2 & 0 \\ 1 & 0 & 0 & 0 & -1 \end{pmatrix}, \quad D = \begin{pmatrix} A & 0 & 0 \\ 0 & B & 0 \\ 0 & 0 & C \end{pmatrix}.$$

According to LMI toolbox, there exists a positive definite matrix $P = \text{diag}(1, 1)$, $\Delta = \text{diag}(50, 50)$, and $\delta = 6.656 \times 10^5$ satisfying Theorem 3.1. We choose

$$x_i(0) = (0.3 + 0.1i, 0.3 + 0.1i, 0.3 + 0.1i)^T,$$
$$s_i(0) = (2.0 + 0.7i, 2.0 + 0.7i, 2.0 + 0.7i)^T.$$

The simulation results given in Figs. 3.1, 3.2, and 3.3 correspond with community I, II and III. Obviously, different initial values of error are stable at the origin within two seconds, that is, $\lim_{t \to \infty} \|e_i(t)\| = 0$, so $\lim_{t \to \infty} \|x_i(t) - s_{C_i}(t)\| = 0$, $i = 1, 2 \ldots, n$.

The weighted neural cellular networks (1) with networks (2) achieve global stability of cluster mean square synchronization. Then Theorem 3.1 has been proved.

Fig. 3.1 The cluster
synchronization error
in community I
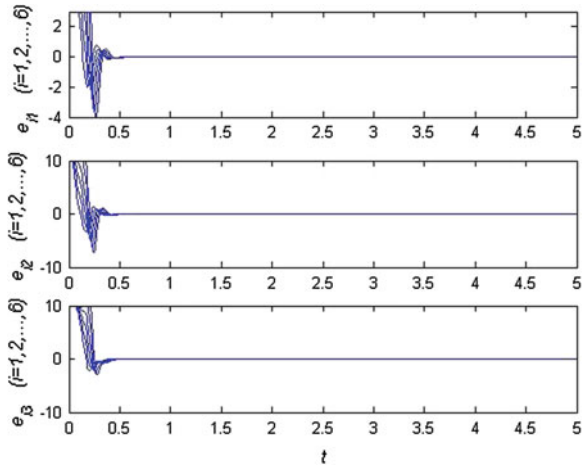
Fig. 3.2 The cluster
synchronization error
in community II
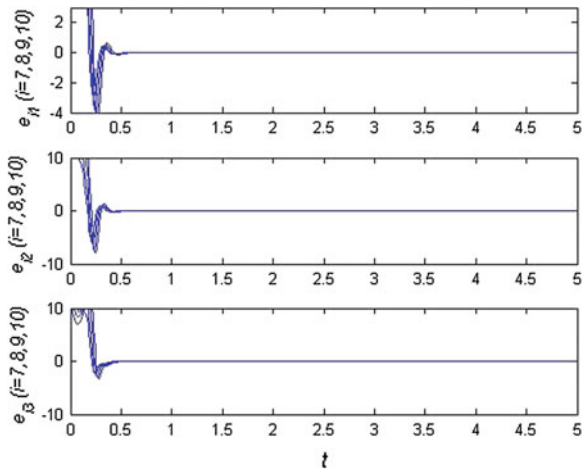
Fig. 3.3 The cluster
synchronization error
in community III
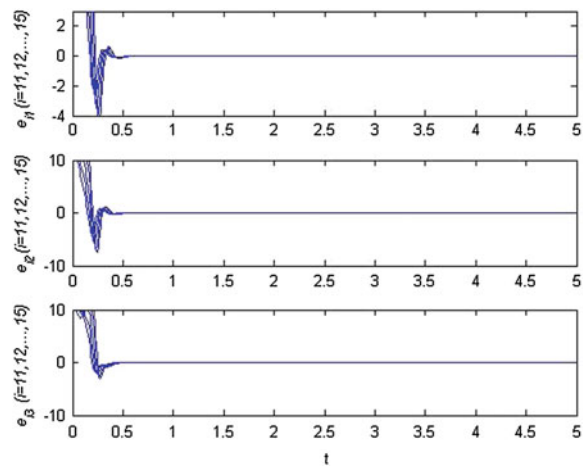
3.5 Conclusions

The global cluster synchronization in cellular neural networks with multi time-varying has been studied. By using an adaptive control method, we ensure each node in cellular neural networks achieves cluster synchronization. Particularly, the weighted configuration matrix of the networks is time-varying and does not need to satisfy the diffusive coupling conditions or be symmetric. Besides, compared to previous works, one adds an inner-coupling matrix $H(t)$. Finally, the numerical simulations are performed to verify the effectiveness of the theoretical results.

References

1. Zhang HG, Wang ZS, Liu D (2007) Global asymptotic stability of delayed cellular neural networks. IEEE Trans Neural Netw 18(3):947–950
2. Cai GL, Yao Q, Shao HJ (2012) Global synchronization of weighted cellular neural network with time-varying coupling delays. Commun Nonlinear Sci Numer Simul 17(10):3843–3847
3. Cai GL, Ma H, Gao XQ (2013) Function projective synchronization in drive-response neural networks with multi-delayed and non-delayed coupling. Lect Note Comp Sci 7951:125–132
4. Ding W (2009) Synchronization of delayed fuzzy cellular neural networks with impulsive effects. Commun Nonlinear Sci Numer Simul 14:3945–3952
5. Xu J, Zheng S, Cai GL (2010) Topology identification of weighted complex dynamical networks with non-delayed and time-varying delayed coupling. Chin J Phys 48(4):481–492
6. Zhu QX, Cao JD (2010) Adaptive synchronization of chaotic Cohen-Crossberg neural networks with mixed time delays. Nonlinear Dyn 61(3):517–534
7. Cai GL, Yao Q, Fan XH, Ding J (2012) Adaptive projective synchronization in an array of asymmetric neural networks. J Comput 7(8):2024–2030
8. Belykh VN, Osipov GV, Petrov VS et al (2008) Cluster synchronization in oscillatory networks. Chaos 18:037106
9. Li T, Wang T, Yang X et al (2012) Cluster synchronization in hybrid coupled discrete-time delayed complex networks. Commun Theor Phys 56(5):686–696
10. Wu XJ, Lu HT (2011) Cluster anti-synchronization of complex networks with nonidentical dynamical nodes. Phys Lett A 375(14):1559–1565
11. Lu X, Qin B (2009) New approach to cluster synchronization in complex dynamical networks. Commun Theor Phys 51:485–489
12. Lu W, Chen T, Chen G (2006) New approach to synchronization analysis of linearly coupled ordinary differential systems. Phys D 213:214–230
13. Lu J, Cao J (2007) Synchronization-based approach for parameters identification in delayed chaotic neural networks. Phys A 382(2):672–682

Chapter 4
Equivalent Model and Parameter Identification of Lithium-Ion Battery

Rui Li, Jialing Yu, Jingnan Li and Fuguang Chen

Abstract Lithium-ion batteries have been widely used on account of their properties such as high voltage grade, high specific energy, low self-discharge rate, long cycle life, pollution free, and no memory effect. Lithium-ion battery equivalent model plays an important role in studying charging, discharging, and capacity of lithium-ion battery. Reasonable battery model can fully characterize its external features, and the model parameters can reflect its performance state through system identification method. This article adopted the improved second-order dynamic battery model to simulated battery charging and discharging performance in three different working conditions, used the recursive least squares algorithm to identify model parameters, verified the identification result through simulation experiments. The results indicate that the second-order dynamic lithium-ion battery model parameters can effectively simulate charging and discharging process, contribute to reflect the battery performance status, provide support for the efficient management and application of lithium-ion battery.

Keywords Lithium-ion battery · Battery equivalent model · Parameter identification · The least square method

4.1 Introduction

Since the successful development of lithium-ion battery, it has been widely used with the characters of high voltage grade, high specific energy, low self-discharge rate, long cycle life, pollution free, and no memory effect [1, 2]. It requires battery management for efficient use of lithium-ion batteries. Battery management system is not only to real-time monitor the battery state such as temperature, voltage and

R. Li · J. Yu (✉) · J. Li · F. Chen
Department of Electric Power Engineering, Chongqing Institute of Communications,
Chongqing, China
e-mail: 317117592@qq.com

current, but also to estimate the battery SOC and health status. However, due to the complexity of battery electrochemical process and the influence of various factors in actual application, the state variables are difficult to be directly measured by sensor, only can be acquired through the estimate. The commonly used methods of battery state estimation are the ampere-hour integral method, the open circuit voltage measurement, AC impedance method, and so on [3, 4]. Based on the battery characteristics shown in charging and discharging process, it contributes to predict the capacity characteristics in charging and discharging process to improve the battery use efficiency that adopt equivalent circuit to simulate the battery input and output.

The model accuracy depends on the model applicability and the model parameter identification method. For the selected battery model, its parameters are affected by many factors such as SOC, OCV, charge and discharge rate, temperature, cycle index, self-discharge, and so on. It is necessary to do rapid identification of model that the battery model can reflect the actual working status of the battery.

4.2 Lithium-Ion Battery Equivalent Model

Equivalent battery model composed of ordinary circuit element is simple, easy to analyze and simulate. This paper chooses traditional second-order Thevenin equivalent circuit model [5–7] as research object, the model is shown in Fig. 4.1.

Second-order Thevenin equivalent circuit model is composed of several resistors and capacitors. R_0 is the ohm internal resistance of lithium-ion battery which indicates battery ohm polarization process. R_1 is the electrochemical polarization internal resistance, C_1 is shunt capacitor in parallel with R_1, the RC circuit composed of them represents electrochemical polarization reaction of battery, and define the branch voltage as U_1, call it U_1 branch for short. R_2 is the concentration polarization internal resistance, C_2 is shunt capacitor in parallel with R_2, the RC circuit composed of them represents concentration polarization reaction of battery, and define the branch voltage as U_2, call it U_2 branch for short. R_s is the self-discharge internal resistance, $i(t)$ is the battery charge or discharge current, V_t is

Fig. 4.1 The second-order Thevenin equivalent circuit model
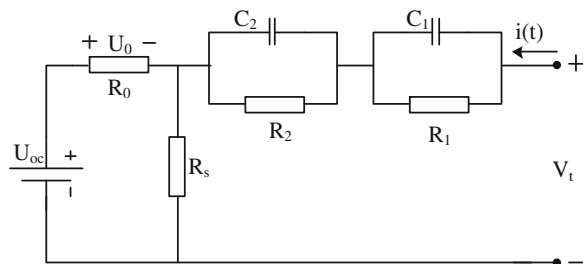
Fig. 4.2 Battery
experimental system
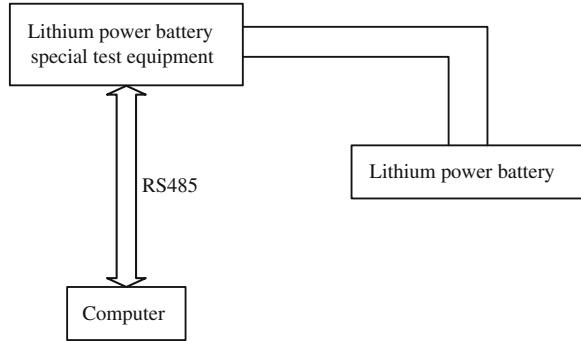
terminal voltage, U_{oc} is the ideal voltage source which represents battery open circuit voltage. This model considers the battery ohm polarization, electrochemical polarization, concentration polarization, and the self-discharge phenomenon. Considering the self-discharge phenomenon only be placed for a long time, so self-discharge resistance R_s can be neglected in charge and discharge process and in short time rest.

The traditional second-order Thevenin equivalent circuit model considering the charge and discharge process separately leads to model parameter cannot respond to charge and discharge characteristics accurately at the same time, especially in dynamic condition that charge and discharge state exist at the same time. Single charge or discharge model has large error. In order to make the battery model analog battery dynamic process more real and more intuitively, improved traditional equivalent circuit model, analyzed model parameters in two work conditions. The improved equivalent circuit model is dynamic model, considering the battery charge and discharge component values vary with the voltage and current, calculating the battery terminal voltage in each work condition through the index formula.

The improved second-order Thevenin equivalent circuit model is shown in Fig. 4.2. When the battery is in charge, $i(t) > 0$, D_1 closed and D_2 open, C_3, R_3, C_4, R_4 worked. Similarly, when the battery is in discharge, $i(t) < 0$, D_2 closed and D_1 open, C_1, R_1, C_2, R_2 worked. D_1 and D_2 control battery charge and discharge state, and each state uses two RC branch to keep load balance.

4.3 Parameter Identification of Equivalent Circuit Model

4.3.1 Parameter Identification Method

It is necessary to motivate the battery with dynamic current to get the battery-related experimental data of dynamic process. The most widely used method is Hybrid Pulse Power Characterization Test (HPPC Test). The improved second-order
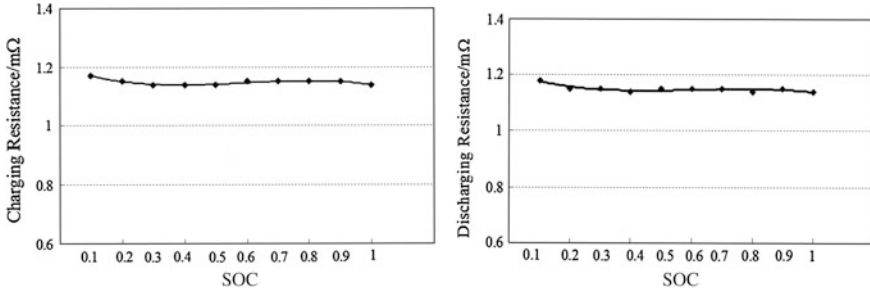
Fig. 4.3 The graph of ohm resistance and SOC in charge–discharge model

Thevenin equivalent circuit model needs to identify the ohm internal resistance, the concentration polarization resistance and capacitance, the electrochemical polarization resistance and capacitance. Considering the battery model parameters in measurement equation have the relationship with SOC, identified the model parameters at two working conditions. The test lithium-ion battery is a new power lithium iron phosphate battery, so ignore the cycle effect in model parameters.

This article selects 60 Ah/3.2 V lithium iron phosphate (LiFePO$_4$) power monomer battery. The experiment is carried out under the normal temperature 25 °C. The experimental system consists of lithium power battery special test equipment, computer, lithium iron phosphate power monomer battery, as shown in Fig. 4.3.

Specific experimental scheme is as follows:

Step 1: Do HPPC test in charge and discharge condition separately;
Step 2: Analysis of two parameter identification results to get the charge model parameter and discharge model parameters;
Step 3: Establish the relationship between model parameters and SOC, analyze the influence on SOC estimation by different parameters.

4.3.2 Process of Parameter Identification Experiment

Do constant current and constant voltage charge to make the battery in full charge state (SOC = 1), then discharge it until SOC = 0.9. HPPC test starts after battery resting 30 min, records its battery parameters, then discharges it until SOC = 0.8. In the same way, after resting 30 min starts the next HPPC test cycle, a total of 10 times. HPPC charge test on lithium iron phosphate power battery starts with SOC = 0, every charge process increases 0.1 SOC, rests 30 min, 10 circulations. Between every two stop discharge 10 s, rest 40 s, and charge 10 s. Supposing charge current is positive, the complex dynamic chemical reaction process inside the battery can be

Table 4.1 Internal resistance identification results

SOC	0.1	0.2	0.3	0.4	0.5	0.6	0.7	0.8	0.9	1.0
$R_0'(m\Omega)$	1.18	1.15	1.15	1.14	1.14	1.15	1.15	1.14	1.15	1.14
$R_0''(m\Omega)$	1.17	1.15	1.14	1.14	1.14	1.15	1.15	1.15	1.15	1.14

reflected by the external characteristic. In order to make the model parameters more rational, this paper does the same charge and discharge identification at different SOC.

4.3.3 The Charge and Discharge Model Parameters

4.3.3.1 Battery Ohm Internal Resistance

Due to battery internal resistance characteristics, the battery voltage will drop for a moment after stopping charge and battery voltage will appear as a temporary rise process at the end of discharge. Use it to calculate the discharge internal resistance R_0' and charge internal resistance R_0'', the identification results are shown in Table 4.1. Battery ohm resistance curve is shown in Fig. 4.4. It can be seen that difference among lithium power battery ohm resistances corresponding to different SOC is small, the charge and discharge resistance is approximate.

Fig. 4.4 Simulation result of HPPC cycling experiment
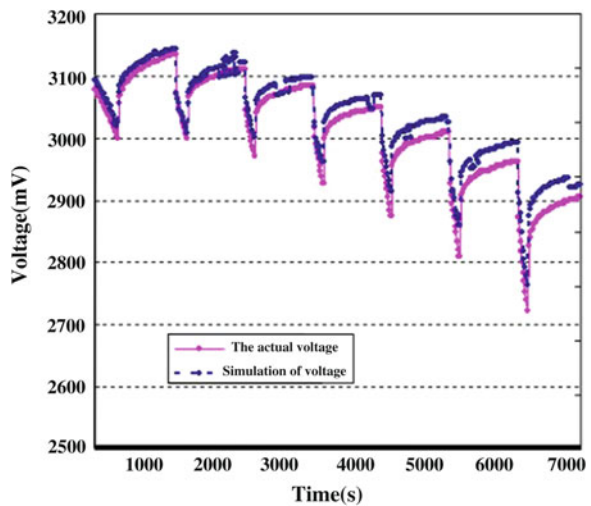
4.3.3.2 The Polarization Resistance and Capacitance

Time constant τ: In HPPC charge and discharge experiment, while battery stand 40 s after charge and discharge each time, current is zero, could regard circuit response of branch U_1 and branch U_2 as zero input response, and use the least squares fitting method calculate the charge and discharge time constant.

Polarization resistance: Calculate concentration polarization resistance and electrochemical polarization resistance through HPPC discharge experiment. In HPPC cycle experiment, battery stand for a long time, could neglect the polarization phenomenon. According to the model parameters such as capacitor voltage at the end of discharge process and discharge time constant τ, calculate the zero input response in charge process, and calculate charge resistance R_3, R_4, through the least square method.

Polarization capacity: According to equation $\tau = RC$, polarization capacitance equals to time constant divided by the corresponding polarization resistance. The polarization resistance and capacitance of discharge model and charge model are shown in Tables 4.2 and 4.3, respectively.

Seen from the table, the concentration polarization resistance changes little at every stage of SOC. Electrochemical polarization resistance changes with the SOC in saddle shape on the whole. The reason is that the active of active material on electrode is strongest in the middle value of SOC in the process. Equation (4.1) is fitting relation between discharge model parameters and SOC, Eq. (4.2) is fitting relation between discharge model parameters and SOC. It can be seen that the battery model parameters are not only related to battery charge or discharge state, but also related to the SOC.

$$\begin{cases} R_0' = 1.14 \\ C_1 = 2000 \\ C_2 = 200 \\ R_1 = 140.86 \times SOC^3 - 141.81 \times SOC^2 + 8.0605 \times SOC + 82.1 \\ R_2 = 2.11 \end{cases} \tag{4.1}$$

$$\begin{cases} R_0'' = 1.15 \\ C_3 = 2000 \\ C_4 = 190 \\ R_3 = (-239.33) \times SOC^3 + 462.48 \times SOC^2 - 240.99 \times SOC + 93.179 \\ R_4 = 3.02 \end{cases} \tag{4.2}$$

Table 4.2 The polarization resistance and capacitor of discharge model

SOC	0.1	0.2	0.3	0.4	0.5	0.6	0.7	0.8	0.9	1.0
R_1 (mΩ)	78.35	83.91	78.30	68.50	66.34	60.44	62.70	75.69	78.12	87.23
C_1 (F)	1984	1987	1989	1990	1989	1995	2000	2002	2000	2001
R_2 (mΩ)	4.12	3.58	2.02	2.11	2.05	2.10	2.10	2.11	2.11	2.11
C_2 (F)	188	186	189	192	192	194	200	201	201	202

Table 4.3 The polarization resistance and capacitor of charge model

SOC	0.1	0.2	0.3	0.4	0.5	0.6	0.7	0.8	0.9	1.0
$R_3\,(m\Omega)$	71.28	63.26	62.11	49.32	60.04	48.98	69.35	78.73	75.51	74.36
$C_3\,(F)$	1985	1986	1988	1991	1989	1993	2000	2001	2001	2000
$R_4\,(m\Omega)$	3.07	3.04	3.02	2.76	3.02	3.03	3.02	3.04	3.01	3.02
$C_4\,(F)$	182	181	187	190	192	194	190	191	193	192

4.4 Model Validation

Model validation is to input the battery module and battery model the same current, record its voltage response curve, determine the model accuracy by calculating the error between measured voltage and simulated voltage. According to the identification of model parameters at different SOC and battery state space model, establish corresponding simulation model in Matlab/Simulink. The input of simulation model is the SOC and the load current $i(t)$, the output is the battery voltage. This paper adopts HPPC cycle experiment, 0.3 C (18 A) constant current discharge experiment and variable current dynamic working condition experiment to analyze the precision of battery model.

4.4.1 HPPC Cycle Experiment

As shown in Fig. 4.5, the lithium power battery polarization characteristics differ between the standing after charge and discharge. It shows that this paper divided the battery model parameter identification into charge and discharge is feasible, which is consistent with the characteristics of the battery itself.

4.4.2 Constant Current Discharge Experiment

The experiment process is as follows. After the battery is full charged, discharge it at 0.3 C (18 A) to SOC = 0.9, stand for 5 min, then begin the second cycle, to SOC = 0.8, repeat the process above until SOC = 0. Figure 4.6 is the simulation result of constant current discharge experiment.

Fig. 4.5 Simulation result of constant current discharge experiment
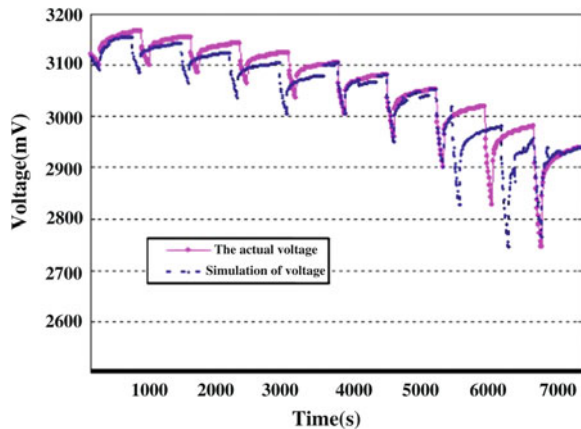
Fig. 4.6 Simulation result of variable current experiment
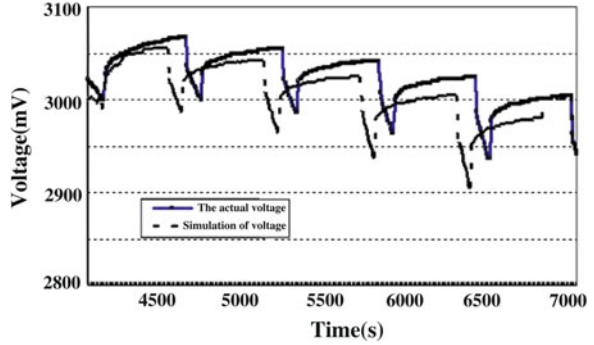
4.4.3 Variable Current Experiment

Variable current experiment is a typical method to simulate the power battery, the specific steps are as follows. Charge battery to SOC = 0.8, stand for 30 min. Then discharge 30 s at 90 A, charge 120 s at 30 A, discharge 60 s at 60 A, charge 60 s at 20 A, stand for 2 min, repeat these four steps 15 times. Simulation result of variable current experiment is shown in Fig. 4.6.

Table 4.4 lists, respectively, battery model average error and maximum error in HPPC cycle experiment, constant discharging experiment, experiment of variable current dynamic working condition. The maximum error is under variable current dynamic operating conditions. It has to do with highly nonlinear characteristics of battery itself. This shows that the change of the internal resistance of battery has certain relationships with the change of SOC and the change of charging and discharging rate. In this paper, set up internal resistance is constant in order to be simplified. Although there is an error, but small, we can still consider the model conforms to the characteristics of the battery. In this paper, the model as the foundation, carries on the research of estimation algorithm.

Table 4.4 The error of improved battery equivalent model

Experiment	Average error (V)	Maximum error (V)
HPPC cycle experiment	0.0797	0.00437
Constant current discharge experiment	0.0870	0.02568
Variable current experiment	0.1023	0.03145

4.5 Conclusion

This paper improved the traditional second-order Thevenin equivalent circuit model, established the dynamic model of battery, adopted the nonlinear least squares curve fitting method to identify OCV and SOC, analyzed parameter identification method, process and result in detail. Finally, set up Matlab/Simulink simulation model to improve the accuracy of model. As it turns out, parameters identification can reflect lithium-ion battery internal complex electrochemical reaction process, laid a foundation for lithium-ion battery management.

References

1. Burke AF (2007) Batteries and ultra capacitors for electric hybrid and fuel cell vehicles. Proc IEEE Trans Energy Convers 95(4):806–820
2. Xie X, Wang P, An H (2010) Auto power lithium-ion battery development present situation. New Energy Veh 35(1):21–25 (in Chinese)
3. Qi G, Li J, Jia H (1997) Research on the measuring technology of battery capacity for electric vehicles. J Tsinghua Univ (Sci Tech) 34(3):16–23 (in Chinese)
4. Wei S, Jiuchun J, Suoyu C (2010) Research on SOC estimation for LiFePO$_4$ Li-ion batteries. J Electr Meas Instrum 24(8):769–773 (in Chinese)
5. Hu S, Sun F, Zou Y (2011) Modeling the dynamic behavior of a lithium-ion battey for electric vehicles using numerical optimization. J Beijing Inst Technol 20(1):60–64 (in Chinese)
6. He H, Xiong R, Guo Hongqiang (2011) Online estimation of model parameters and state of charge of LiFePO$_4$ batteries in electric vehicles. Appl Energy 89(4):413–420 (in Chinese)
7. Hu X, Li S, Peng H (2012) A comparative study of equivalent circuit models for lithium-ion batteries. J Power Sources 198(8):359–367 (in Chinese)

Chapter 5
Dual Scheduling and Quantized Control for Networked Control Systems Based on Dynamic Dwell Time

Hui Lu, Chuan Zhou and Qingwei Chen

Abstract A novel integrated design scheme of dynamic dwell time scheduling strategy, dynamic bandwidth allocation policy, and quantized control for networked control systems (NCS) with time delay and communication constraints is proposed in this paper. A scheduling policy is raised to accommodate a limited number of node-controller connections which depend on the periodic communication sequences and dynamic dwell time. Then, the neural network technique is employed to dynamically allocate bit rate for the scheduling nodes. The networked control systems are modeled as discrete-time switched systems with bounded disturbances. Finally, a design procedure for the state feedback controller is presented to guarantee asymptotic stability of the NCS. A simulation example is given to illustrate effectiveness of the proposed method.

Keywords Networked control systems · Dynamic dwell time · Neural network

5.1 Introduction

Networked control systems (NCS) have attracted increasing attention in the recent years. However, the communication constraints of network make the analysis of NCS more complex than before. There are two main approaches to modeling band-limited communication channels in control loops: (i) media access constraints in which only a subset of sensors and/or actuators can transmit their data over the channel at each transmission instant. (ii) Bit rate constraints, i.e., a finite number of bits can be transmitted over the channel at any transmission instant due to limited bandwidth.

H. Lu · C. Zhou (✉) · Q. Chen
School of Automation, Nanjing University of Science and Technology,
Nanjing 210094, China
e-mail: njust_zc@126.com

For the problem of the media access constraints, much research effort has been devoted to investigate the scheduling policy to determine the nodes which can be allowed to access the network. In [1, 2], the medium access order of different sensors and actuators is determined offline in terms of a periodic "Communication sequence". In [3], a scheduling-and-feedback-control co-design procedure was proposed to deal with communication constraints for a collection of NCSs by using the average dwell time. A novel dynamic dwell time technique [4] is adopted in the scheduling strategy to choose switching instant which depends on the system performance function. On the other hand, for the problem of limited bit rate, current researches mainly focus on quantized feedback control method. Several quantizers have been designed to achieve different control objectives [5, 6]. In NCS, another significant issue is the bit rate allocation problem for limited bandwidth networks. Increasing the transmission rate will always lead to higher cost of bandwidth while spending fewer bits on quantization will increase the quantization distortion. This raised a fundamental problem: how much bit rate needs to be assigned to the quantizer in order to achieve a desired control performance? A significant amount of research has been devoted to the problem of determining the minimum bit rate that is required to stabilize a system through feedback over a rate-limited communication channel [6, 7]. Then, the rate allocation [8, 9] is used to improve the system performance by exploiting the additional degree of freedom offered by communication resources. Therefore, it is meaningful to investigate the co-design scheme of nodes scheduling and bit rate assignment in order to optimize overall performance.

5.2 System Description

The structure of networked control system is shown in Fig. 5.1, and the plant to be controlled is described by the following state variable model:

$$\dot{x}(t) = A_p x(t) + B_p u(t) \tag{5.1}$$

where $x(t) \in R^n$, $u(t) \in R^m$ are the state variables and control input vectors. A_p, B_p are constant matrices with appropriate dimensions.

Assumption 5.1 The sensors are time driven with sampling period h_i, and controllers, actuators and bandwidth scheduler are event driven.

Assumption 5.2 Networked-induced delay is constant, and $0 < \tau_i < h_i$.

Assumption 5.3 Because of the limitation of communication capacities, only R_{max} bit can be transmitted over the channel, and only $C_{max} < n$ nodes can access the network communication channel at each transmission instant.
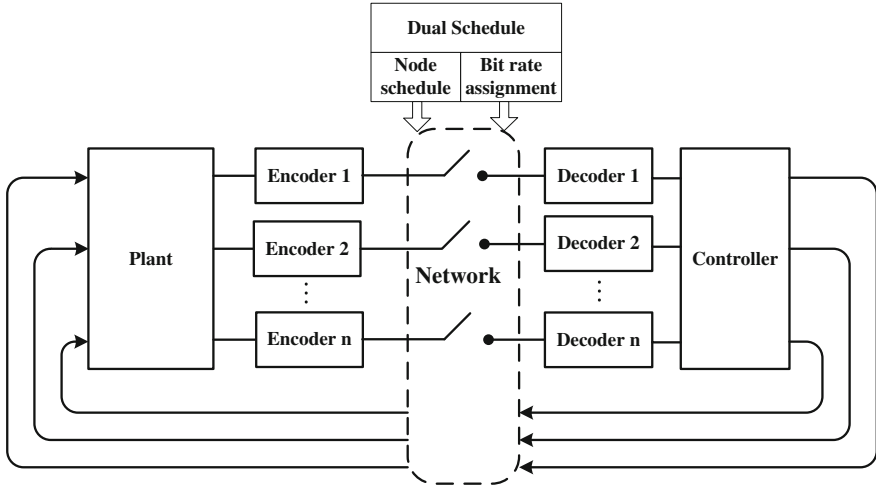
Fig. 5.1 The structure of networked control systems

The discrete time model of system (5.1) is as follows:

$$x(k+1) = Ax(k) + B_1 u(k) + B_2 u(k-1) \tag{5.2}$$

where $A = e^{A_p h}$, $B_1 = \int_0^{h-\tau} e^{A_p s} B_p \mathrm{d}s$, $B_2 = \int_{h-\tau}^{\tau} e^{A_p s} B_p \mathrm{d}s$.

In this paper, the mid-tread uniform quantizers are as follows:

$$Q(x_i(k)) = \begin{cases} L_i & \text{if} & x_i(k) > L_i \\ -L_i & \text{if} & x_i(k) < -L_i \\ [x_i(k)/d_i + 1/2] \times d_i & \text{other} \end{cases} \tag{5.3}$$

where L_i is quantization range, $d_i = L_i/(2^{R_i-1} - 1)$ is sensitivity, R_i is the number of bit determined by the bandwidth allocation strategy.

To deal with the saturation problem of quantizer, we introduce the following definition of saturation:

$$Q_{ki}(x_i(k)) = \mathrm{Sat}(x_i(k)) + w_i(k) \tag{5.4}$$

where $\|w_i(k)\| \leq (L_i/(2^{R_i} - 2))$. Define $\mathrm{Sat}(x_i(k)) = g_i x_i(k)$, where $0 < g_i \leq 1$.

In this paper, we use periodic communication sequences and dynamic dwell time to determine the nodes which and when can be allowed to access the network. Then we allocate bit rate to the scheduling nodes using neural network techniques so as to realize the dual scheduling policy formed by the combination of multi-node scheduling and bit rate assignment. We introduce the communication sequences in this paper and define the scheduling vector $\alpha(k)$

$$\alpha_i(k) = \begin{cases} 1 & \text{if } x_i(k) \text{ is transmitted} \\ 0 & \text{otherwise} \end{cases} \quad i \in \{1, 2, \ldots, n\} \tag{5.5}$$

At the kth instant, the nodes that can access the network are decided by the scheduling vector $\alpha(k) = [\alpha_1(k), \ldots, \alpha_n(k)]$. Define diagonal matrix $M(k) = \text{diag}\{\alpha_1(k), \ldots, \alpha_n(k)\}$, then the input vector of controller is:

$$\hat{x}(k) = MQ_x(x(k)) + (I - M)\hat{x}(k - 1) \tag{5.6}$$

There are $L = C_n^{C\max}$ modes in the system. The $j(j = 0, 1, 2, \ldots, L - 1)$ modes correspond to a set of M_j, $\sigma(k) \in \{0, 1, \ldots, L - 1\}$.

Definition 5.1 [4] $\tau(k_l)$ is called the dwell time of switching law $\sigma(k)$ for the kth switching instant, which stands for the time between switching instants l_k and l_{k-1}, i.e. $\tau(k_l) = k_l - k_{l-1}$.

In this paper, we present a scheduling algorithm based on dynamic dwell time, the switching sequence is determined offline by the periodic sequence while switching instant is determined online by the system performance function. The scheduling sequence by the periodic sequence is predetermined as follows:

$$\Sigma : \{(M_0, k_0), (M_1, k_1), \ldots, (M_{L-1}, k_{L-1}), (M_0, k_0), \ldots\} \tag{5.7}$$

For the closed loop NCS (5.2), we adopt the following state feedback control law:

$$u(k) = K_{\sigma(k)}\hat{x}(k) \tag{5.8}$$

where $K_{\sigma(k)}$ is the controller gain corresponding to different switching mode. Under the designed controller (5.8), the closed NCS (5.2) can be expressed as

$$\begin{cases} x(k + 1) = Ax(k) + B_1u(k) + B_2u(k - 1) \\ \hat{x}(k) = M_{\sigma(k)}Q(x(k)) + (I - M_{\sigma(k)})\hat{x}(k - 1) \\ Q(x(k)) = gx(k) + w(k) \\ u(k) = K_{\sigma(k)}\hat{x}(k) \end{cases} \tag{5.9}$$

We use the integral of the absolute error (IAE) performance criterion defined in (5.10). The IAE for the ith plant is as follows:

$$IAE_i = \int_0^\infty e(t)\mathrm{d}t \tag{5.10}$$

In fact, the relationship between control performance (IAE) and bandwidth can be approximated by a nonlinear relationship [8]. The function is approximated as

$$J(R_i) = \alpha_i + \beta_i / R_i \tag{5.11}$$

Give $C_{\max}$ control notes with allocated bandwidth vector $R_1, \ldots, R_{c_{\max}}$, the optimal overall performance can be summarized as the following multi-objective optimization problem with constraints

$$\min_{R} \left\{ J_1 = \sum_{i=1}^{c_{\max}} (\alpha_i + \beta_i / R_i) \right\} \tag{5.12}$$

$$\min_{R} \left\{ J_2 = \sum_{i=1}^{c_{\max}} R_i \right\} \tag{5.13}$$

$$\text{s.t.} \quad \sum_{i=1}^{c_{\max}} R_i \leq R_{\max} \tag{5.14}$$

$$\text{s.t.} \quad R_i^{\min} \leq R_i \leq R_i^{\max} \tag{5.15}$$

$$\text{s.t.} \quad R_i = R_i^{\min}, \quad e_i \leq e_i^h \tag{5.16}$$

where (5.12–5.16) refer to [8] in detail. In [6] it is shown that the quantized system is asymptotically stable if and only if $R_i \geq \sum_{\lambda(A_i)} \max\{0, \lceil \log_2 |\lambda(A_i)| \rceil\}$, where the minimum bit rate determined by (5.17), and the maximum $R_i^{\max}$ determined by (5.18) according to the constraint conditions of network resources.

$$R_i^{\min} = \sum_{\lambda(A_i)} \max\{0, \lceil \log_2 |\lambda(A_i)| \rceil\} \tag{5.17}$$

$$R_i^{\max} = R_{\max} - \sum_{j=1, j \neq i}^{C_{\max}} R_j^{\min} \tag{5.18}$$

We weight (5.12) and (5.13) to the following single-objective function for the problem solving of multi objective optimization:

$$\min_{R} \left\{ J = \sum_{i=1}^{c_{\max}} (\alpha_i + \beta_i / R_i) + \gamma_i \sum_{i=1}^{c_{\max}} R_i \right\} \tag{5.19}$$

where γ_i is weight coefficient, which balances the objective functions J_1 and J_2.

To address the above problems, we intend to exploit a simple and effective structure that uses a feed-forward NN for dynamic bandwidth allocation. For this case, a three-layer feed-forward NN is selected as the bandwidth scheduling optimizer. The input vector $P = [e_1, \ldots, e_{c_{\max}}]$ is chosen as the network inputs, whereas network output vector $R^* = [R_1^*, \ldots, R_{c_{\max}}^*]$ is the bandwidth.

The relationship between input and output of neural network is

$$R^* = f_2(W_2 f_1(W_1 P + B_1) + B_2) \tag{5.20}$$

For this work, the NN is trained offline using the Levenberg-Marquardt (LM) algorithm which combines the filled function method [8]. The training for NN can be seen in [10] in detail.

5.3 Main Results

Theorem 5.1 For the closed-loop NCS (5.9) with dual scheduling strategy and quantized control, if there exist positive symmetry matrices P_j, Q_j, S_j, scalar $\lambda_j > 0 (j = 0, 1, \ldots, L - 1)$ and g, such that

$$\begin{bmatrix} -P_j^{-1} & 0 & \Omega_j & \Xi_j & \Lambda_j & 0 \\ * & -Q_j^{-1} & gM_j & I - M_j & M_j & 0 \\ * & * & -\lambda_j P_j & 0 & 0 & 0 \\ * & * & * & -\lambda_j Q_j & 0 & 0 \\ * & * & * & * & S_j & 0 \\ * & * & * & * & * & -\lambda_j S_j \end{bmatrix} < 0 \tag{5.21}$$

$$\rho_1 \|x(k)\|^2 \leq V(k) \leq \rho_2 \|x(k)\|^2 \tag{5.22}$$

hold, and the system switches from subsystem i to subsystem j at the switching instant K_j, if the dwell time satisfies

$$\tau(k_j) > \tau^*(k_j) = \begin{cases} \frac{\ln V_j(k_j) - \ln V_{j-1}(k_j)}{\ln \lambda_j^{-1}} & \text{if } \ln V_j(k_j) > \ln V_{j-1}(k_j) \\ 0 & \text{other} \end{cases} \tag{5.23}$$

where

$\Omega_j = A + gB_1 K_j M_j, \Xi_j = B_1 K_j (I - M_j) + B_2 K_j, \Lambda_j = B_1 K_j M_j,$
$\rho_1 = \min\{\lambda_{\min}(P_0), \ldots, \lambda_{\min}(P_{L-1})\}, \rho_2 = \min\{\lambda_{\max}(P_0), \ldots, \lambda_{\max}(P_{L-1})\}.$

Then system (5.9) is asymptotically stable.

Proof The Lyapunov functional is constructed as

$$V_j(k) = x^T(k)P_jx(k) + \hat{x}^T(k-1)Q_j\hat{x}(k-1) + w^T(k-1)S_jw_i(k-1)$$
$$V_j(k+1) - \lambda_jV_j(k) = \eta_j^T(k)\Theta_j\eta_j(k) < 0 \quad j \in \{0, 1, \ldots, L-1\} \tag{5.24}$$

where $\eta_j(k) = \begin{bmatrix} x_j^T(k) & \hat{x}_j^T(k-1) & w_j^T(k) & w_j^T(k-1) \end{bmatrix}^T$

By using Schur complement, we can obtain $V_j(k+1) \leq \lambda_jV_j(k)$, hence the closed-loop system (5.9) is asymptotically stable.

Assuming that the subsystem j is active in the interval (k_j, k) and the subsystem $j-1$ is active in the interval (k_{j-1}, k_j), we can obtain that

$$V(k) < \lambda_j^{k-k_j}V_j(k_j) = \lambda_j^{k-k_j}\frac{V_j(k_j)}{V_{j-1}(k_j)}V_{j-1}(k_j) = e^{(k-k_j)\ln\lambda_j + \ln V_j(k_j) - \ln V_{j-1}(k_j)}V_{j-1}(k_j) \tag{5.25}$$

Let $k = k_{j+1}$, we have

$$V_j(k_{j+1}) < e^{\tau(k_j)\ln\lambda_j + \ln V_j(k_j) - \ln V_{j-1}(k_j)}V_{j-1}(k_j) \tag{5.26}$$

Therefore we have $V_j(k_{j+1}) < V_{j-1}(k_j)$, hence system (5.9) is stable.

Theorem 5.2 Considering the closed-loop networked control system, given positive scalar $\lambda_j > 0$ and quantitative processing parameter g, if there exist $P_j > 0, Q_j > 0, S_j > 0, \tilde{K}_j, \varepsilon_j > 0$, such that the following inequalities hold, there exist a feedback controller $K_j = \tilde{K}_j/\varepsilon_j$ such that the overall NCS is asymptotically stable under the above dual scheduling policy.

$$\begin{bmatrix} -\varepsilon_jI & 0 & 0 & 0 & gB_1\tilde{K}_jM_j & \tilde{\Xi}_j & \tilde{\Lambda}_j & 0 \\ * & -\varepsilon_jI & P_j & 0 & 0 & 0 & 0 & 0 \\ * & * & -P_j & 0 & P_jA & 0 & 0 & 0 \\ * & * & * & -Q_j & gQ_jM_j & Q_j(I-M_j) & Q_jM_j & 0 \\ * & * & * & * & -\lambda_jP_j & 0 & 0 & 0 \\ * & * & * & * & * & -\lambda_jQ_j & 0 & 0 \\ * & * & * & * & * & * & S_j & 0 \\ * & * & * & * & * & * & * & -\lambda_jS_j \end{bmatrix} < 0. \tag{5.27}$$

where $\tilde{\Xi}_j = B_1\tilde{K}_j(I-M_j) + B_2\tilde{K}_j, \tilde{\Lambda}_j = B_1\tilde{K}_jM_j$.

Fig. 5.2 The response of
states
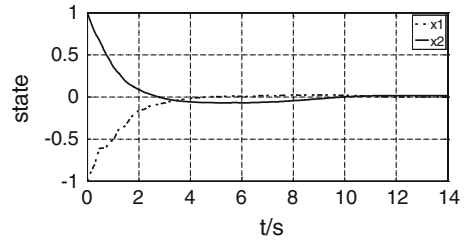
Fig. 5.3 The response of
switched mode
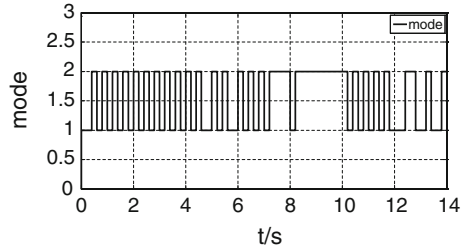
5.4 Illustrative Example

Considering the plant to be controlled in NCSs as follows:

$$\dot{x}(t) = \begin{bmatrix} -0.8 & -0.01 \\ 1 & 0.1 \end{bmatrix} x(t) + \begin{bmatrix} 0.4 \\ 0.1 \end{bmatrix} u(t)$$

where the sampling period is $h = 0.2$ s, time delay $\tau(k) = 0.004$ s. Using Theorem
5.2, we can obtain the matrices of controller

$$K_1 = \begin{bmatrix} -1.2145 & 0.16376 \end{bmatrix}, K_2 = \begin{bmatrix} -0.02143 & -1.4237 \end{bmatrix}$$

The simulation results through True time is shown in Figs. 5.2 and 5.3. The state
responses of the NCS with dual scheduling are illustrated in Fig. 5.2, and the
response of each mode is shown in Fig. 5.3. It can be seen that the networked
control system is asymptotically stable under dual scheduling.

5.5 Conclusions

In this paper, we proposed a co-design scheme of dual scheduling and quantized
control for NCS with communication constraints and time delay. We use periodic
communication sequences and dynamic dwell time to determine the nodes which
and when can be allowed to access the network. Then we allocate bit rate to the

scheduling nodes by using neural network techniques. The future work includes the extension of our scheduling policy to deal with the communication constraints in NCS by the combination of multi-node scheduling and bit rate assignment.

References

1. Brockett R (1995) Stabilization of motor networks. In: Proceedings of the 34th TEEE conference on decision and control. New Orleans, USA, IEEE, pp 1484–1488
2. Zhang L, Hristu VD (2006) Communication and control co-design for networked control systems. Automatica 42(6):953–958
3. Dai SL, Lin H, Ge SZS (2010) Scheduling-and-control co-design for a collection of networked control systems with uncertain delays. IEEE Trans Control Syst Technol 18(1):66–78
4. Xiang ZR, Xiang WM (2009) Stability analysis of switched systems under dynamical dwell time control approach. Int J Syst Sci 19(5):59–70
5. Brockett RW, Liberzon D (2004) Quantized feedback stabilization of linear systems. IEEE Trans Autom Control 45(7):1279–1289
6. Tatikonda S, Mitter S (2004) Control under communication constrains. IEEE Trans Autom Control 49(7):1056–1068
7. Ling Q, Lemmon MD (2005) Stability of quantized control systems under dynamic bit assignment. IEEE Trans Automatic Control 50(5):734–740
8. Ji K (2008) Optimal Bandwidth allocation and QoS-adaptive control co-design for networked control systems. Inte J Control Autom Syst 6(4):596–606
9. Li Z, Wang W, Jiang Y (2010) Intelligent scheduling and optimisation for resource-constrained networks. IET Control Theor Appl 12(4):2982–2992
10. Hagan MT, Menhaj M (1994) Training feed-forward networks with the marquardt algorithm. IEEE Trans Neural Networks 5(6):989–993

Chapter 6
Modeling and Identification of the Human-Exoskeleton Interaction Dynamics for Upper Limb Rehabilitation

Xiaofeng Wang, Xing Li and Jianhui Wang

Abstract A number of machines have been developed for the upper limb rehabilitation to meet patients' needs for upper limb rehabilitation exercises. As active exercise has proven to be effective and necessary for neural rehabilitation and motor recovery, it is suggested to be implemented to the rehabilitation machines. Toward this goal, the human motion desire should have been recognized exactly first. Because the muscle strength of the patient's upper limb may not be able to supply the gravity of the arm and the rehabilitation machines, some torques coming from the rehabilitation machines will be needed to supply the exercise. This paper is focused on modeling and identifying the human-exoskeleton interaction (HEI) dynamics, so that the motion desire is able to be recognized exactly based on it. First, the human arm can be taken as two links with three degrees of freedom (two DOF in shoulder, one in elbow). By combining the dynamics model of the human arm and the exoskeleton, the HEI dynamic model was formed. Meanwhile, the joint angles and torques of human arm can be measured indirectly by using the position and torque sensors mounted on the joints of the exoskeleton. In this way, a 19-parameter HEI dynamic model has been established using the Lagrange method based on the pseudo inertia matrix. The model can be used to estimate the torques during rehabilitation exercises after identifying the underdetermining dynamic parameters. The motion desire can be recognized by comparing the measured joint torques to the estimated ones. Finally, the feasibility of the HEI dynamic model is validated by simulation experiments.

Keywords Human-exoskeleton interaction · Dynamic modeling · Identification online · Active rehabilitation exercise · Motion desire

X. Wang · J. Wang
Northeast University, Shenyang 110004, Liaoning Province, China
e-mail: wxflamy@yeah.net

X. Li (✉)
State Key Laboratory of Synthetical Automation for Process Industries,
Northeast University, Shenyang 110004, Liaoning Province, China
e-mail: lixing8245@163.com

6.1 Introduction

Stroke is one of the higher incidences of disease in the elderly. The motor dysfunction caused by stroke has serious impacts on the health of older people. The traditional methods for upper limb rehabilitation required physicians to treat patients on a one-to-one and a one-by-one basis. However, this is inefficient and imposes a heavy burden on the family and society. Proper rehabilitation exercise training can promote the recovery of the physical activity function of patients. The exercise training of upper limb rehabilitation assisted by robots is targeted at, which is longer lasting and repeatable. Several studies have shown that robot-aided rehabilitation has better significance than the traditional method [1, 2]. Therefore, increasing attention is now paid to the upper limb rehabilitation robot [3], which is supposed to be able to ease physicians out of heavy manual work, improve the efficiency of rehabilitation, and meanwhile reduce the burden of the associated people. As shown in Fig. 6.1, the training system of the five-DOF exoskeleton robots [4] for upper limb rehabilitation is a medical device used to serve patients with hemiplegic upper limb and assist the physician to complete the rehabilitation. This system can accomplish large-scale single joint movement or multi-joint compound movement and realize the patient's mobility in daily activities. It consists of two parts: the exoskeleton mechanical structure and the control system. The mechanical structure has five degrees of freedom, which are shoulder elevation, shoulder roll, elbow flexion/extension, wrist roll, and wrist flexion/extension. The base part and five irregular rigid links are connected together by movable joints; each joint is driven by a motor. The orientation of each joint between two parts is inconsistent in the triaxial *X-Y-Z* coordinates system. The rotation angle of each joint also has certain limitations considering the security of rehabilitation.

In the exercises provided by the exoskeleton, the angular range of the wrist joint is relatively small and has little effect on the dynamics; therefore the wrist joint is neglected in modeling [5] and is kept unchanged during the simulation experiment. Then the exoskeleton for upper limb rehabilitation can be regarded as an irregular exoskeleton machine which has 3 DOFs. The inertia properties should be described by pseudo inertia matrix in the dynamic model [6]. To ensure the range of exercises and match the motion of the exoskeleton, the wrist's motion of human arm were neglected similarly. The human arm can be seen as a manipulator with two links and 3 DOFs in the modeling of dynamics.

Fig. 6.1 The training system of the five-DOF exoskeleton robot for upper limb rehabilitation

For the measurement of the joint torques, there was a method [7] of using torque sensors mounted on the end effector of the exoskeleton to measure some values, and then converting them to the joint torques by Jacobian matrix. This method will not only impose additional constraints on the patient's hand but will also get a converted data that cannot reflect the real joint torques. In fact, if the human upper limb (HUL) is bound on the exoskeleton, the rotation centers of the exoskeleton's joints can be consistent with HUL by adjusting the length of the links. The angle change on each joint of HUL and the exoskeleton will be the same and they can all be measured directly by the sensors mounted on the exoskeleton. The joint torques of HUL can be obtained indirectly from the joint torque sensors mounted on the joints of the exoskeleton.

Active exercise is considered more effective than the passive one for motor recovery of the upper limb [8]. In order to realize active rehabilitation exercise, the voluntary motion desire of the patients should be recognized. It has been carried out using electromyography (EMG) in the literature [9, 10]. However, each patient is in a different situation, the EMG signals are different from person to person, and the accuracy of EMG is affected by a number of factors. So it would take a complex and repeated debugging before it is used on the patient.

In this paper, the dynamic parameters are identified based on the sensors mounted on every joint of the exoskeleton, and are used to recognize the human motion desire [11]. This method reduces the use of the external device and avoids the interference of external factors. The measured data is more stable and reliable, and the result of identification and recognition is accurate. Figure 6.2 depicts the structure of recognizing the human motion desire by HEI dynamics in active rehabilitation exercise. The angles and torques in Fig. 6.2 are measured by the sensors mounted on the joints of the exoskeleton.

It can be seen from Fig. 6.2 that Tm is the measured torque and Tc is calculated from HEI dynamics. dT represents the human motion desire. When d$T < 0$, it shows that HUL has imposed a torque in the direction of movement, and the motion desire is toward the positive orientation. Otherwise if d$T > 0$, it means HUL has imposed a torque against the direction of movement, and the motion desire is toward the negative orientation. If d$T = 0$, there is no additional torque and no motion desire. A threshold value of dT can adjust the sensitivity. The control commands can be derived from dT.

Fig. 6.2 The structure of recognizing the human motion desire in active rehabilitation exercise
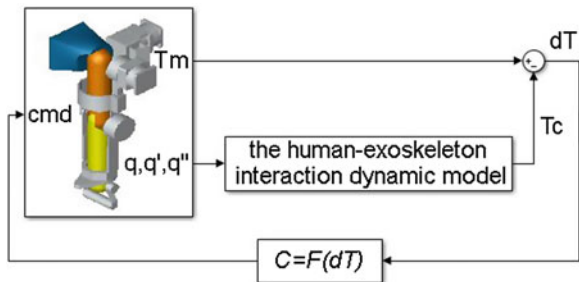
The remainder of this paper is organized as follows: Sect. 6.1 describes HEI dynamic model and identifies the dynamic parameters; Sect. 6.2 gives the experiments, the results, and the feasibility; the paper is concluded in Sect. 6.3.

6.2 Modeling and Identifying of HEI Dynamics

The schematic of HEI model is shown in Fig. 6.3. It can be seen that the exoskeleton is worn on the upper limb, and supports the upper limb. Both the exoskeleton and the human upper limb can be regarded as a robot with three degrees of freedom as the wrist joints have been neglected. The length of the exoskeleton can be adjusted, so the joint rotation centers can be in the same axis. As a result, they have the same kinematics and Jacobian matrix, the structures of the dynamics are the same but the parameters are different. The HEI dynamic model is established by combining the dynamics of HUL and the exoskeleton.

6.2.1 Modeling of the Exoskeleton Dynamics

As shown in Fig. 6.4, the D-H method is used in the kinematics modeling of the exoskeleton, and the D-H parameters are given in Table 6.1. The Lagrange method is used to model the dynamics of the exoskeleton, which is defined by Eq. 6.1 neglecting the frictions.

$$\tau = M(q)\,\ddot{q} + C(q,\dot{q}) + G(q) \tag{6.1}$$

where q is the joint angle of the exoskeleton; M is a 3×3 inertia matrix. C is a 3×3 vector of Coriolis and Centripetal forces; G is a 3×1 vector of gravity. τ is a 3×1 vector of control input torques. The elements in the M, C and G consist of the inertia parameters of each link, which is a vector of ten constant values (mass of link, moment of inertia, product of inertia, and center of gravity to the coordinate).

Fig. 6.3 The schematic of HEI
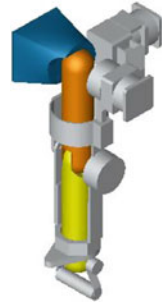
Fig. 6.4 Coordinate relations
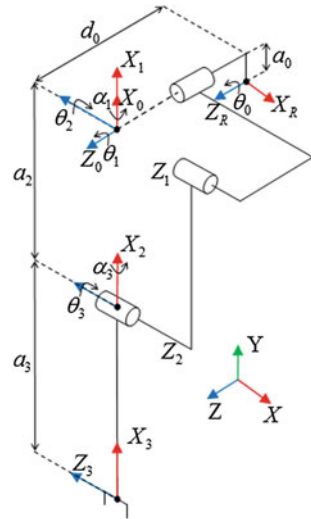
Table 6.1 D-H parameters

i	θ_i	d_i	a_i	α_i
0	90°	0.235	0.047	0
1	q_1	0	0	−90°
2	q_2	0	−0.277	0
3	q_3	0	−0.299	0

Putting the inertia constant values into the exoskeleton dynamics defined in Eq. 6.1, the linear form is derived as shown in Eq. 6.2.

$$\Phi_{\mathrm{exo}}(q_{\mathrm{exo}}, \dot{q}_{\mathrm{exo}}, \ddot{q}_{\mathrm{exo}})P_{\mathrm{exo}} = \tau_{\mathrm{exo}} \tag{6.2}$$

where τ_{exo} is a 3 × 1 joint torques; Φ_{exo} is a 3 × 19 regressed variable matrix; P_{exo} is a 19 × 1 unknown inertia parameter vector of the exoskeleton dynamic model.

6.2.2 Modeling of the Upper Limb Dynamics

The dynamic model of HUL is derived using the same method as in Sect. 6.1.1:

$$\Phi_u(q_u, \dot{q}_u, \ddot{q}_u)P_u = \tau_u \tag{6.3}$$

The dynamics of HUL and the exoskeleton have the same structure but different parameters. As the shoulder elevation degree of freedom has no links, the inertia parameter of link 1 is zero.

6.2.3 Modeling of HEI Dynamics

Combining Eqs. 6.2 and 6.3, the HEI dynamic model is derived as Eq. 6.4:

$$J_{\text{exo}}^T J_u^{-T} \Phi_u(q_u, \dot{q}_u, \ddot{q}_u) P_u + \Phi_{\text{exo}}(q_{\text{exo}}, \dot{q}_{\text{exo}}, \ddot{q}_{\text{exo}}) P_{\text{exo}} = \tau_m \qquad (6.4)$$

where τ_m is measured by the torque sensors mounted on the exoskeleton; J_{exo} and J_u are the Jacobian matrix. As mentioned above, because of the adjusted links, the exoskeleton and HUL have the same kinematics. $J_{\text{exo}} = J_u$ and $\Phi_u = \Phi_{\text{exo}}$ in this paper. Equation 6.4 can be arranged as follows:

$$\Phi(q, \dot{q}, \ddot{q}) P = \tau_m \qquad (6.5)$$

6.2.4 Identification of HEI Dynamic Model

It can be seen from Eq. 6.5 that HEI dynamic model is nonlinear for the motion states but linear for the inertia parameters. Therefore, the inertia parameters can be identified.

The joint space trajectories implemented on the exoskeleton during the identification experiment can be calculated. The quintic polynomial was used to represent the joint angle. Set the boundary conditions in Eq. 6.6 and let $q(0) = q_s$, $q(T) = q_e$ and $\dot{q}(0) = \dot{q}(T) = \ddot{q}(0) = \ddot{q}(T) = 0$, the joint space trajectories are obtained.

$$\begin{cases} q(t) = at^5 + bt^4 + ct^3 + dt^2 + et + f \\ \dot{q}(t) = 5at^4 + 4bt^3 + 3ct^2 + 2dt + e \\ \ddot{q}(t) = 20at^3 + 12bt^2 + 6ct + d \end{cases} \qquad (6.6)$$

Implement the trajectories on the exoskeleton using the position control method. The angle and torque data measured by the sensors mounted on the exoskeleton joints will help us identify the inertia parameters through the MIMO recursive least square online method which is shown in Eq. 6.7.

$$\begin{cases} \hat{P}(k) = \hat{P}(k-1) + K(k)[\tau(k) - \Phi(k)\hat{P}(k-1)] \\ K(k) = Q(k-1)\Phi^T(k)[I_m + \Phi(k)Q(k-1)\Phi^T(k)]^{-1} \\ Q(k) = [I - K(k)\Phi(k)]Q(k-1) \end{cases} \qquad (6.7)$$

6.3 Simulation Experiment and Results

The simulation model of the exoskeleton and HUL can be established, respectively, by combining the SolidWorks and the SimMechanics in the Simulink environment. The measured joint torques is the result of adding the two models' joint torques. Then we get HEI Simulink model after the input and output are set. Implementing the calculated joint space trajectories on the Simulink model, the inertia parameters of HEI dynamic model will be recognized by using the MIMO recursive least square online method, based on the measured state data of each joint. The feasibility will be validated by comparing the joint torques estimated by HEI dynamic model to the measured one on the new trajectories.

6.3.1 Experiments for Identification of HEI Dynamic Model

Figure 6.5 depicts the identification trajectories, the left one shows the joint angles' change, and the right is the route of the end effecter. The parameter P of HEI dynamic model is identified by using the recursive least square method based on the measured joint angles and torques. The results are shown in Table 6.2.

6.3.2 Experiment for Validation of HEI Dynamic Model

Different trajectories in the opposite direction are designed in the experiment for validation of HEI dynamic model. The trajectories are depicted in Fig. 6.6.

The left one shows the joint angles' change, and the right is the route of the end effector. Implement the trajectories on the Simulink model and estimate the joint torques change based on the measured joint angles, angular velocities, and angular
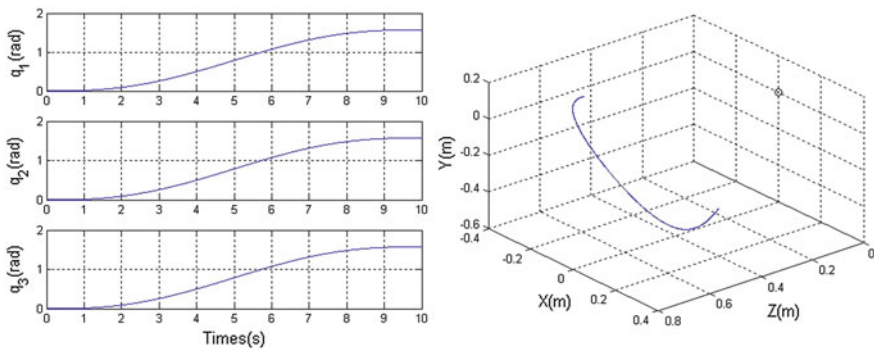
Fig. 6.5 Trajectories for identification

Table 6.2 Parameters identified by the recursive least square method

P	P_1	P_2	P_3	P_4	P_5	P_6	P_7	P_8	P_9
Value (kg m²)	0.3905	0.1933	0.2002	−0.0029	0.0001	0.0893	−0.0028	0.0013	−0.0000
P_{10}	P_{11}	P_{12}	P_{13}	P_{14}	P_{15}	P_{16}	P_{17}	P_{18}	P_{19}
−0.0514	0.0288	0.5894	0.1835	6.1451	−0.0003	15.3275	0.0026	6.8448	−0.0514
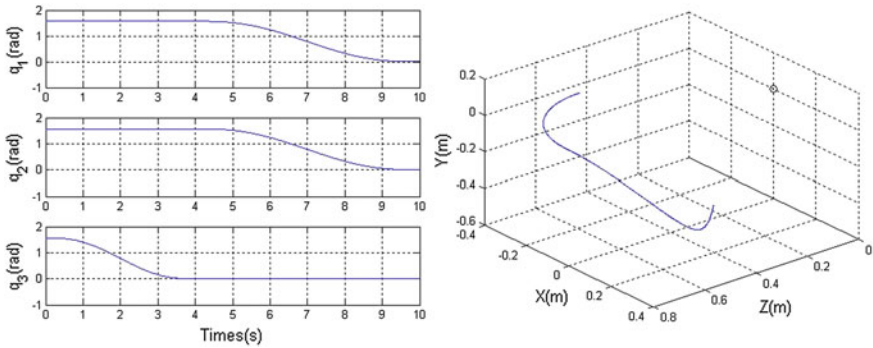
Fig. 6.6 Trajectories for validation
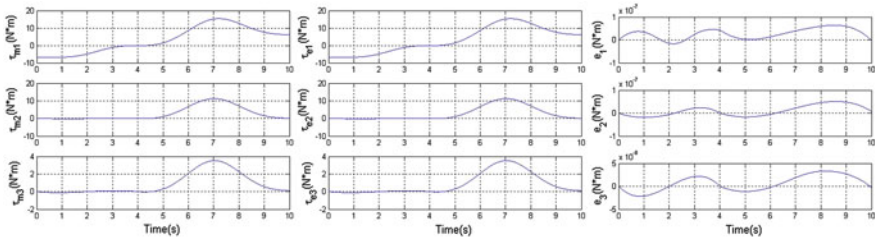
Fig. 6.7 Measured and estimated joint torques and their errors in the experiment for validation

accelerations. The feasibility of HEI dynamic model can be validated by comparing the measured joint torques to the estimated joint torques. The measured and estimated joint torques and their errors are depicted in Fig. 6.7.

It can be seen from Fig. 6.7 that the three joint errors of comparing the measured joint torques to the estimated ones are all very small. It can be validated that the joint torques in the motion estimated by HEI dynamic model.

6.4 Conclusion

The dynamics of HEI are modeled and identified to recognize the human motion desire in time for the purpose of active rehabilitation exercises which have been proven effective on patients with upper limb dysfunction.

In the exercises provided by the exoskeleton, the angular range of the wrist's two degrees of freedom are relatively small and have little effect on the dynamics, therefore the wrist's two joints are neglected in the modeling. The Lagrange method based on the pseudo inertia matrix was used to describe the dynamics in the triaxial coordinate. The HEI dynamic model with 19 parameters was derived based on Lagrange equations. The dynamic models of the exoskeleton, HUL and HEI, have the same structure but different parameters, and they show an additive property relationship. The joint torques of HUL can be measured indirectly by the torque sensors mounted on the exoskeleton. The trajectories for identification and validation are designed by the quintic polynomial. The recursive least square online method was used to identify the dynamic parameters of HEI based on the measured data of the sensors mounted on the exoskeleton. The identified parameters were used to estimate the joint torques. The human motion desire could be recognized by the errors by comparing the measured joint torques with the estimated ones. The future work will focus on the application of HEI dynamic model obtained in this paper.

References

1. Liang T, Xiaoping W, Mingyu M (2012) Effect of upper limb rehabilitation robot on upper extremity function of hemiplegic patients. Chin J Rehabil Med 27(3):254–256 (in Chinese)
2. Yao-bin L (2012) Effect of rehabilitation robot on upper extremity function of hemiplegic patients. Chin J Rehabil 27(3):171–173 (in Chinese)
3. Lo HS, Xie SQ (2012) Exoskeleton robots for upper-limb rehabilitation: state of the art and future prospects. Med Eng Phys 34(3):261–268
4. Li Q, Wang D, Du Z et al (2005) A novel rehabilitation system for upper limbs[C]. In: IEEE-embs 2005 27th annual international conference of the engineering in medicine and biology society, 2005: IEEE, pp 6840–6843
5. Li Q (2009) Study on sEMG based Exoskeletal robot for upper limbs rehabilitation[D]. Harbin Institute of Technology, Harbin (in Chinese)
6. Niku SB (2001) Introduction to robotics: analysis, systems, applications: Prentice Hall, New Jersey
7. Rahman MH, Ochoa–luna C, Rahman MJ et al (2014) Force–position control of a robotic exoskeleton to provide upper extremity movement assistance. Int J Model Ident Control 21 (4):390–400
8. Qizhi Y, Dianfeng C, Jinhai Z (2013) Analysis on state of the art of upper limb rehabilitation robots. Robot 35(5):630–640 (in Chinese)

9. Amsuss S, Gobel P, Jiang N et al (2014) Self-correcting pattern recognition system of surface emg signals for upper limb prosthesis control. IEEE Trans Biomed Eng 61(4):1167–1174
10. Li Z, Wang B, Sun F et al (2014) Semg-based joint force controls for an upper-limb power-assist exoskeleton robot. IEEE J Biomed Health Inform 18(3):1043–1050
11. Wang W, Hou Z, Tong L et al (2014) Dynamics modeling and identification of the human-robot interface based on a lower limb rehabilitation robot. 2014 IEEE international conference on robotics and automation: IEEE, pp 6012–6017

Chapter 7
Mobile Robot Self-localization System Based on Multi-sensor Information Fusion in Indoor Environment

Linhai Xie and Xiaohong Xu

Abstract Robot self-localization is a fundamental problem for mobile robots and various kinds of algorithms and sensors are used for indoor robot self-localization. However, a single kind of sensor or algorithm usually cannot reach the ideal performance in different environments. Thus this paper proposes a robot self-localization algorithm based on multi-sensor information fusion (MSIF) and realizes the corresponding indoor robot self-localization system. To realize the whole system, two subsystems are constructed which are the gyro and encoder-based subsystem and the laser rangefinder and gyro-based subsystem. In these two subsystems, dead reckoning algorithm is used in the former one, and ranging self-localization, together with map matching algorithm, is used in the latter one. With the information acquired by the two subsystems, Kalman filter algorithm is used to obtain the optimal estimation of the robot localization. The experimental results show that the system and the algorithms work well in indoor environments.

Keywords Self-localization · Information fusion · Kalman filter

7.1 Introduction

A main problem we know in robotics is the robot self-localization. To date, there are numerous kinds of sensors and algorithms which are used to solve this problem. Many of these technologies have been mature and practical. Sensors used in robot localization are quite varied, such as encoder, gyro, accelerometer, camera, sonar, laser rangefinder and optical mouse. But there are some drawbacks in each of them. There are also many kinds of self-localization algorithm, for instance, dead reckoning [1], ranging self-localization, map-matching [2], and sensor self-localization. Thus, the paper is mainly to propose a robot self-localization algorithm and build

L. Xie (✉) · X. Xu
College of Mechatronics and Automation, National University
of Defense Technology, No 109 DeYa Road, Changsha, China
e-mail: xxhac311@126.com

the corresponding real system, using several kinds of sensors and algorithms to achieve good performance by combining the advantages of these sensors and algorithms and compensate their disadvantages for each other with the utilization of multi-sensor information fusion (MSIF) [3, 4].

7.2 The Realization of the System

7.2.1 The Robot Mechatronic System

As shown in Fig. 7.1, the robot chassis is equipped with three omnidirectional wheels together with two driven wheels with encoders which are perpendicular to each other in horizontal panel. Gyro is fixed on the chassis surface, the same as other things like DSP and its peripheral circuits, battery, wireless communication module and three EPOSEs controlling three DC motors which are under the chassis. There is a bracket in the middle of the chassis which is used to fix eight laser rangefinders. These laser rangefinders are on and under the top circle panel of the bracket and the angle between the one and the adjacent one on the opposite side is 45°.

7.2.2 Hardware Architecture

DSP is used as the main controller of the robot. It communicates with three EPOSEs through CAN bus and communicates with gyro through SPI. The data of
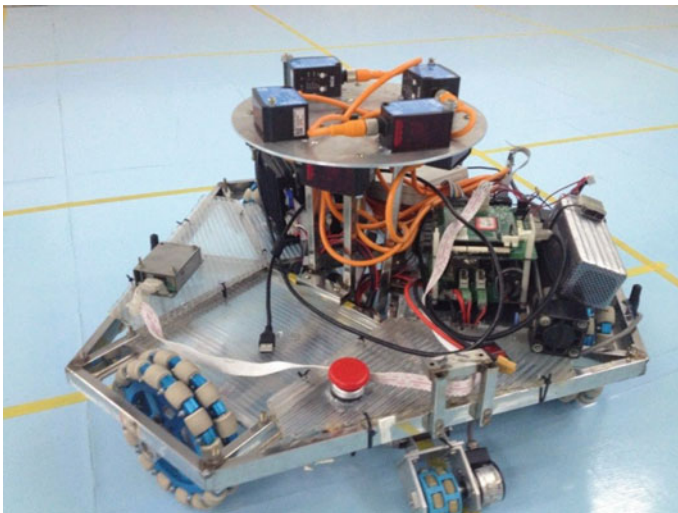
Fig. 7.1 The photo of the robot

encoders are sent to the EQEP counters of the DSP. And the data of eight laser rangefinders are collected by an A/D converter and then sent to the DSP through SCI. DSP is also connected with a wireless communication module through SCI.

7.2.3 The Design of the Algorithm

As shown in Fig. 7.2, there are two subsystems. The first one called rangefinder subsystem uses eight laser rangefinders as self-localization sensors and adopts the combination of ranging self-localization and map-matching algorithm to compute the robot pose. Thus it can acquire the self-localization result with moderate amount computation and effectively make full use of the environment information. Furthermore, if environment information is enough it can calibrate gyro which is used in the other subsystem, solving the problem of gyro drift. The second subsystem named encoder and gyro subsystem utilizes two encoders and a gyro, adopting dead reckoning algorithm to calculate the robot pose. This is a subsystem which needs little environment information, owning the obvious self-localization advantage when the environment information is too little or extremely complicated. With the self-localization information obtained by these two subsystems, Kalman filter is used to fuse the information and compute the final and optimal robot self-localization estimation.
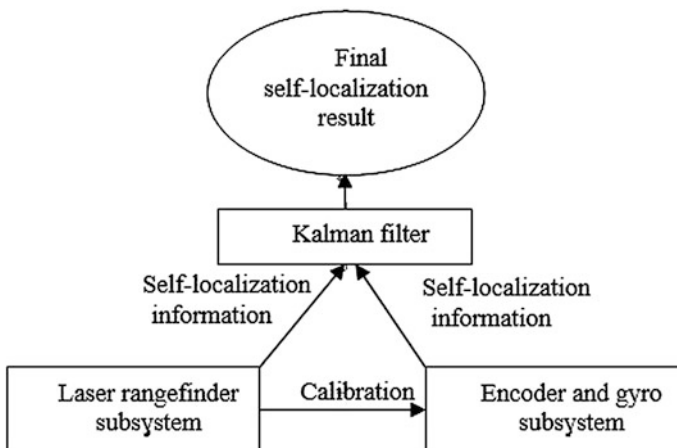
Fig. 7.2 System organization

7.2.4 The Realization of Self-localization Algorithm

7.2.4.1 Establishment of Coordinate System

Three coordinate systems are mentioned in the paper. The first one is the body coordinate system which is a dynamic coordinate system. The second one is the field coordinate system which is a static coordinate system. And the last one is the intermediate coordinate system which shares the same origin point with body coordinate system but its axes are parallel and in the same direction with the ones of field coordinate system.

As shown in Fig. 7.4, the coordinate system $X_bO_bY_b$ and $X_gO_gY_g$ are body coordinate system and field coordinate system, respectively. And θ is the orientation angle of body coordinate system for field coordinate system. Figure 7.3 shows the definition of field coordinate system. The field is designed as a rectangular field surrounded by wooden walls with the height of 60 cm. Edge a, b, c, and d represent the edges of the field. The origin point O is also the center of the rectangular field. In Fig. 7.5, coordinate system $X_iO_iY_i$ is the intermediate coordinate system.

Fig. 7.3 Field coordinate system
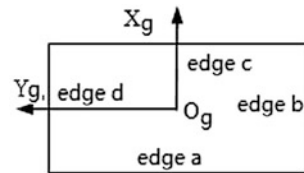
Fig. 7.4 Body coordinate system
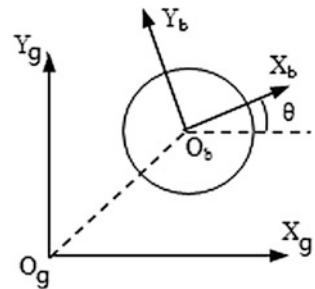
Fig. 7.5 Intermediate coordinate system
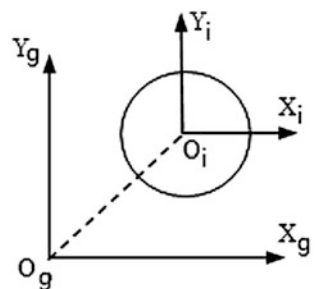
7.2.4.2 The Self-localization Algorithm of Encoder and Gyro Subsystem [5]

This subsystem adopts traditional dead reckoning algorithm. Gyro can measure the rotating speed of the robot, and by accumulating it, robot can acquire the orientation angle θ. And encoder can know the distance that robot move within unit time in the body coordinate system. Then, projecting the distance in body coordinate system into field coordinate system by using robot rotation angle and accumulating it, the robot can compute the total distance that it moves in the field coordinate system. At last, with the awareness of its origin position, the robot can know where it is in the field.

7.2.4.3 The Self-localization Algorithm of Laser Rangefinder Subsystem

This subsystem adopts an original self-localization algorithm with the data of eight laser rangefinders and gyro by using the algorithm combining ranging self-localization and map matching. The algorithm is divided into two periods, the first one is ranging self-localization period. In this period, the robot collects the data of laser rangefinders and gyro to calculate the coordinates of the eight detecting points. Then with the information of the field edges, the robot can deduce its position if the information is enough.

However, if there is no sufficient information, the second period called map-matching period will be needed to complete the robot self-localization. In this period, the field map which has been inputted in the system before the robot self-localization is necessary.

The main step of the algorithm can be generalized as follows:

Step 1:   Calculating the coordinate of eight points in body coordinate system.
Step 2:   Transferring the points into intermediate coordinate system with robot orientation angle θ.
Step 3:   Obtaining eight lines.
Step 4:   Checking whether there are lines belonging to field edges. If "yes", renew the data of points and lines. If "no", the algorithm ends.
Step 5:   Checking and recording lines belonging to field edges.
Step 6:   Checking whether there are lines belonging to both long edges and short edges. If "yes", calculating the robot coordinates in yield coordinate system. If "no", calculating a part of the coordinate, then going to the next step.
Step 7:   Using map matching to calculate the rest part of the coordinate.

7.2.4.4 The Fusion Process of Kalman Filter

The five main formulas of Kalman filter [6, 7] will not be introduced here since they are quite classical. And what will be talked about here is how Kalman filter is used

to fuse the sensors information in the system. Two Kalman filters are applied separately in X axis and Y axis.

We assume that the predicted values of robot coordinates are X_p and Y_p which are the self-localization results of *encoder and gyro subsystem*, the measured values are X_o and Y_o which are the self-localization results of *laser rangefinder subsystem*, and the errors are e_x and e_y which are related to the distance the robot move within unite time.

First, the self-localization results obtained by encoder and gyro subsystem are regarded as the predicted values, namely X_p and Y_p, and the errors of these predicted values are calculated as (7.1).

$$\begin{cases} e_x = \sqrt{e_x^2 + w_x^2} \\ e_y = \sqrt{e_y^2 + w_y^2} \end{cases} \tag{7.1}$$

In (7.1), w_x and w_y are the noise of prediction process which is composed with two parts. The first part is the basic noise which is a constant, and the other part is proportional to the distance that the robot moves within unit time.

Then we need to calculate Kalman gains with (7.2).

$$\begin{cases} Kg_x = e_x^2/[e_x^2 + v_x^2] \\ Kg_y = e_y^2/[e_y^2 + v_y^2] \end{cases} \tag{7.2}$$

Kg_x and Kg_y are Kalman gains and v_x and v_y are the noise of measurement which is a constant.

With Kalman gains, the predicted values and measured values, the optimal estimation of robot coordinates X and Y can be acquired by (7.3):

$$\begin{cases} X = X_p + Kg_x(X_o - X_p) \\ Y = Y_p + Kg_y(Y_o - Y_p) \end{cases}. \tag{7.3}$$

Finally, the errors should also be renewed to calculate Kalman gains for the next time with (7.4).

$$\begin{cases} e_x = \sqrt{e_x^2(1 - Kg_x)} \\ e_y = \sqrt{e_y^2(1 - Kg_y)} \end{cases}. \tag{7.4}$$

7.3 Experiments and Results

Three experiments are performed to test the proposed self-localization system and the algorithms. In all of these, robot is controlled to move randomly in the field for 5 min and for each half minutes, the real position of robot is recorded to compare

with the self-localization results sent from robot to test the accuracy of robot self-localization.

7.3.1 The First Experiment

The performances between individual subsystems and the whole self-localization system are compared.

The average self-localization error of encoder and gyro subsystem is 125.648 mm, and the line chart is shown in Fig. 7.6, in which the abscissa represents the time (unit: s) and the ordinate represents the error of the robot self-localization (unit: mm).

The average self-localization error of laser rangefinder subsystem is 444.783 mm, and the line chart is shown in Fig. 7.7, in which the abscissa represents the time (unit: s) and the ordinate represents the error of the robot self-localization (unit: mm).

The average error of the whole self-localization system is 20.243 mm, and the line chart is shown in Fig. 7.8, in which the abscissa represents the time (unit: s) and the ordinate represents the error of the robot self-localization (unit: mm).

As can be known from the data above that by using Kalman filter, the performance of self-localization system is improved obviously.
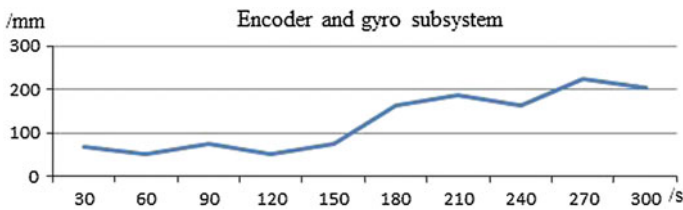
Fig. 7.6   Self-localization error of encoder and gyro system
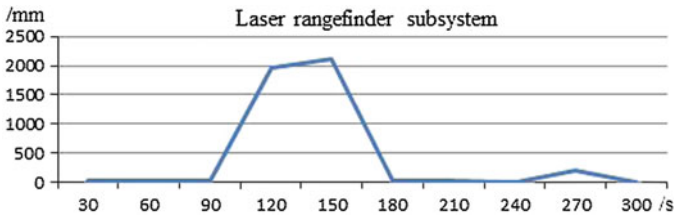
Fig. 7.7   Self-localization error of laser rangefinder subsystem
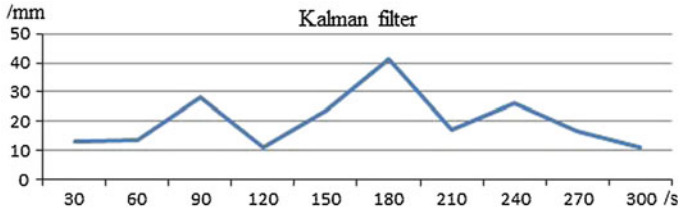
Fig. 7.8 The error of the whole self-localization system

7.3.2 The Second Experiment

The sensitivity of the self-localization system to the parameters of Kalman filter is tested in this experiment. And the parameter is the basic parts of w_x and w_y in Eqs. 7.3 and 7.4. They can affect the Kalman gains, in other words, the weights of the predicted value and the measured value, influencing whose self-localization result is more believable and accurate between subsystems.

When the parameter is 50, the average self-localization error is 38.365 mm.

When the parameter is 100, the average self-localization error is 20.243 mm.

When the parameter is 150, the average self-localization error is 36.98 mm.

As can be seen from the data, when the parameter is 100, the robot can achieve the best performance. However, this conclusion is in the base of the certain environment in this experiment. Thus, we also need to test the effects of varying environment.

7.3.3 The Third Experiment

In this experiment, the sensitivity to obstructions in the field of robot is tested. And after changing the amount and the position of obstructs twice, we find that the average of self-localization error of robot rises from 20.243 to 29.371 and 44.944 mm, respectively.

From the conclusion in the second experiment, it is known that in a certain environment, the robot achieves different performances by adjusting parameter in Kalman filter, and there is certain one for the robot to obtain the best performance. In the third experiment, the data show that with the constant parameters in Kalman filter, the robot performs with different self-localization accuracies in distinct environments.

Thus, by combining the results in two experiments, it obvious that the parameters and the environments need to be matched. It is mainly because in different environments, the performances of two subsystems vary, and the Kalman filter has to judge which subsystem owns the more believable and accurate self-location result, and adjusting the parameters in Kalman filter is to decide the tendency of the final self-localization result. So, if the environment is changed, the parameters should be adjusted to make the robot acquire the best performance.

7.4 Conclusions

The paper proposes a robot self-localization algorithm based on multi-sensor information fusion (MSIF) and realizes the corresponding indoor robot self-localization system. The robot self-localization algorithm solves the problem of robot self-localization in different environment effectively. First, a robot self-localization algorithm based on multi-sensor information fusion is proposed. It combines dead reckoning, range self-localization, and map-matching algorithm. Then, two self-localization subsystems are constructed whose self-localization information is fused by Kalman filter to obtain the optimal estimation. The good performance is tested in three experiments with the real system.

References

1. Yu J, Cai Z, Duan Z (2006) Design of dead reckoning system for mobile robot. J Central S Univ Technol 13(5):542–547
2. Xi LX, Liu Q, Li M, Liu Z (2007) Advances in intelligent systems research: ISKE 2007: map matching algorithm and its application
3. Groves PD (2013) Principles of GNSS, inertial, and multi-sensor integrated navigation system. Artech House, Boston, pp 78–82
4. Kam M, Zhu X, Kalata P (1997) Sensor fusion for mobile robot navigation. Proc IEEE 85(1):108–119
5. Ziaie-Rad S, Janabi-Sharifi F, Danesh-Panah MM et al (2005) A practical approach to control and self-localization of Persia omni directional mobile robot. (IROS 2005). 2005 IEEE/RSJ international conference on intelligent robots and systems, IEEE, pp 3473–3479
6. Sun SL, Deng ZL (2004) Multi-sensor optimal information fusion Kalman filter. Automatica 40(6):1017–1023
7. Welch G, Bishop G (1995) An introduction to the Kalman filter, pp 19–29

Chapter 8
Robust Control Using Self Recurrent Wavelet Neural Network for a Coaxial Eight-Rotor UAV with Uncertainties

Cheng Peng, Yue Bai, Xun Gong and Yantao Tian

Abstract This paper focuses on the robust control of a coaxial eight-rotor UAV in the presence of model uncertainties and external disturbances. The dynamical and kinematical model of the eight-rotor with high drive capability is established. On account of the uncertainties, a robust back-stepping sliding mode control (BSMC) with self-recurrent wavelet neural network (SRWNN) method is proposed as the attitude controller of the eight-rotor. SRWNN as the uncertainty observer can effectively estimate the lumped uncertainties. All weights of SRWNN can be trained online by the adaptation laws based on Lyapunov stability theorem. Then the uniformly ultimate stability of the eight-rotor system is proved. Finally, simulation results demonstrate the validity of the proposed robust control method adopted in the eight-rotor under model uncertainties and external disturbances.

Keywords Coaxial eight-rotor UAV · Self-recurrent wavelet neural network · Uncertainties · External disturbances

8.1 Introduction

A quad-rotor UAV has been extensively studied in the automatic control community due to its simple mechanical structure and VTOL capability [1]. Nevertheless, in practical situations, there are many difficult problems in controlling quad-rotor UAV because of the inevitable uncertainties. Thus, the robust control problem has been

C. Peng · Y. Tian (✉)
Department of Control Science and Engineering, Jilin University, Changchun, China
e-mail: tianyt@jlu.edu.cn

C. Peng
e-mail: litianjinorc@126.com

Y. Bai · X. Gong
Chinese Academy of Sciences, Changchun Institute of Optics Fine Mechanics and Physics, Changchun, China

increasingly considered for quad-rotor with model uncertainties and external disturbances, such as [2–4]. However, those robust methods are based on the inherent structure of quad-rotor that has the poor drive capability and weak robustness. This paper therefore proposes an eight-rotor UAV with a coaxial configuration. It is designed with eight rotors that are arranged as four counterrotating offset pairs mounted at the ends of four arms in a cruciform configuration. The four sets of matched counter rotating rotor blades provide differential thrust from four equally spaced points, which allows the eight-rotor to maneuver with higher agility. It offers markedly increased drive capability, stronger robustness against disturbances and greater payload capacity owing to its added four rotors than quad-rotor in condition of using the same type of motors and rotors. Furthermore, the eight-rotor has stronger damage tolerance to remain stable flight when some of rotors broken.

Considering model uncertainties of the eight-rotor and external disturbances, a robust BSMC with self-recurrent wavelet neural network (SRWNN) is proposed to control the attitude of the eight-rotor. The combination between back-stepping technique and sliding mode control has the advantages with inherent insensitivity and robustness against disturbances [5]. Then, SRWNN which combines the properties of attractor dynamics of recurrent neural network [6] and the good convergence of wavelet neural network [7] is employed to estimate uncertainties. SRWNN can store the past information of the network and adapt rapidly to sudden changes of the control environment because it has a mother wavelet layer composed of self-feedback neurons [8]. Then, the eight-rotor control system using SRWNN is proved uniformly ultimately bounded with Lyapunov stability theory. Finally, the satisfactory robustness and attitude control performance of BSMC with SRWNN method are demonstrated via simulation tasks in the case where the inertia matrix uncertainties as model uncertainties of the eight-rotor and external disturbance are taken into account.

8.2 Dynamic Model of Coaxial Eight-Rotor UAV

The eight-rotor UAV in cruciform configuration consists of four pairs of coaxial double rotors, as shown in Fig. 8.1, where Ω_i, $i = 1, 2, \ldots, 8$ is the speed of eight rotors, respectively. The pitch movement is obtained by increasing (reducing) the speed of the rear pair of rotors and reducing (increasing) the speed of the front pair of rotors, the roll angle can be obtained similarly using the remaining two pairs of rotors. The yaw movement is provided by speeding up or slowing down the speed of rotary counterclockwise rotors and changing the same speed of rotary clockwise rotors in the opposite direction.

Two reference frames defined to express the dynamics of eight-rotor are the earth-fixed inertial frame $E = \{O_g x_g y_g z_g\}$ and the body-fixed frame $B = \{O_b x_b y_b z_b\}$. The attitude is expressed by three Euler angles $\eta = [\phi, \theta, \psi]^T$.
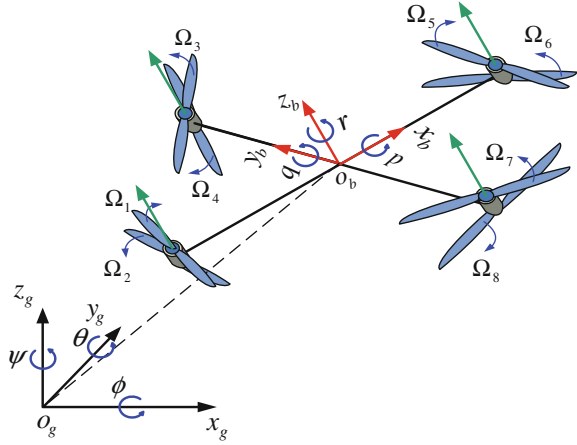
Owing to the eight-rotor treated as a symmetrical rigid body with six degrees of freedom, the rotational kinematic equations of the eight-rotor with unmodeled dynamics can be derived as follows

$$(J + \Delta J) \cdot \dot{\omega} = -sk(\omega) \cdot (J + \Delta J) \cdot \omega + M \tag{8.1}$$

with $J = \mathrm{diag}(I_x, I_y, I_z)$ as the moment of inertia and $\Delta J = \mathrm{diag}\left(\Delta I_x, \Delta I_y, \Delta I_z\right)$ considered as the inertia matrix uncertainty that is caused by the change in mass properties. $\omega = [p, q, r]^T$ denotes the angle velocity on B. $sk(\omega)$ is called as skew-symmetric matrix [9]. The torque provided by the rotors thrust is expressed as

$$M = \begin{bmatrix} M_x \\ M_y \\ M_z \end{bmatrix} = \begin{bmatrix} lk_1\left(\Omega_3^2 + \Omega_4^2 - \Omega_7^2 - \Omega_8^2\right) \\ lk_1\left(\Omega_1^2 + \Omega_2^2 - \Omega_5^2 - \Omega_6^2\right) \\ k_2\left(\Omega_1^2 + \Omega_4^2 + \Omega_5^2 + \Omega_8^2 - \Omega_2^2 - \Omega_3^2 - \Omega_6^2 - \Omega_7^2\right) \end{bmatrix} \tag{8.2}$$

where the thrust factor k_1 and the drag factor k_2 are positive coefficient, l is the distance between the rotor and the center of the aircraft. Due to external disturbances, in the general case of small attitude, the rotational kinematics equation can be facilitated as follows:

$$\begin{bmatrix} \ddot{\phi} \\ \ddot{\theta} \\ \ddot{\psi} \end{bmatrix} = \begin{bmatrix} M_x/(I_x + \Delta I_x) + \tau_{\mathrm{dx}} \\ M_y/(I_y + \Delta I_y) + \tau_{\mathrm{dy}} \\ M_z/(I_z + \Delta I_z) + \tau_{\mathrm{dz}} \end{bmatrix} \tag{8.3}$$

where $\tau_d = [\tau_{\mathrm{dx}}, \tau_{\mathrm{dy}}, \tau_{\mathrm{dz}}]^T$ denotes external disturbances.

8.3 Robust Attitude Control of the Eight-Rotor

On account of inevitable model uncertainties and external disturbances, BSMC with SRWNN method is exploited to control the attitude of the eight rotor. The attitude control block diagram is depicted in Fig. 8.2, which is divided into three channels: roll channel, pitch channel, and yaw channel. Each attitude channel is separately controlled by the proposed algorithm.

Take the roll channel of the eight-rotor as an example, which is described as

$$
\begin{aligned}
\dot{x}_1 &= x_2 \\
\dot{x}_2 &= M_x/I_x + D_x
\end{aligned}
\tag{8.4}
$$

where x_1 denotes the state of roll angle, x_2 is the state of roll angle velocity. $D_x = \tau_{dx} + f_x$ termed the lumped uncertainties in the roll channel, where τ_{dx} treated as the external disturbance is bound, $f_x = -\Delta I_x M_x/[(I_x + \Delta I_x) \cdot I_x]$ is the model uncertainty.

Define the roll angle tracking error as $z_1 = x_{1d} - x_1$, where x_{1d} is the desired roll angle. Define $c_1 = \alpha z_1$, where α is a positive constant. The roll angle velocity tracking error is $z_2 = x_2 - \dot{x}_{1d} - c_1$. Then, the first Lyapunov function is taken as $V_1 = z_1^2/2 + s^2/2$ with the sliding surface designed as $s = kz_1 + z_2$, where k is a positive constant.
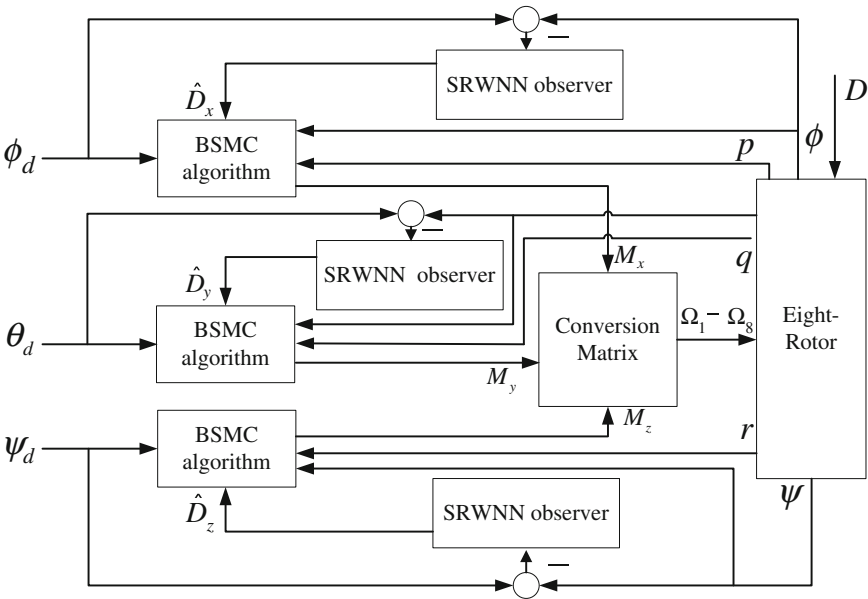
Fig. 8.2 The attitude control block diagram using BSMC with SRWNN method
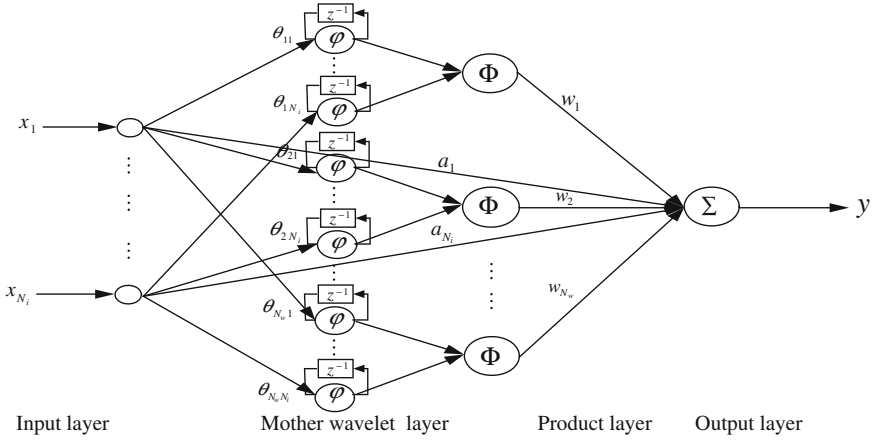
Fig. 8.3 The structure of SRWNN

Since the lumped uncertainty D_x is unknown in practical application, an SRWNN observer is proposed to adapt the estimated value of $\hat{D}_x$. SRWNN consists of four layers: an input layer, a mother wavelet layer, a product layer, and an output layer, as shown in Fig. 8.3. The mother wavelets are chosen as the first derivative of a Gaussian function [10]. The weights $a_k, m_{jk}, d_{jk}, \theta_{jk}, w_j$ of the SRWNN will be trained online by the adaptation laws based on Lyapunov stability analysis.

The SRWNN uncertainty observer is defined as

$$\hat{D}_x = \hat{W}^T \hat{\Phi}(x, \hat{M}, \hat{D}, \hat{\Theta}) + \hat{A}^T X \tag{8.5}$$

with the input of SRWNN as $X = [z_1, \dot{z}_1]^T$. $\hat{W}, \hat{M}, \hat{D}, \hat{\Theta}, \hat{A}$ are the estimation vector of $m_{jk}, d_{jk}, \theta_{jk}, a_k$, respectively. The product layer is $\hat{\Phi} = \hat{\Phi}(x, \hat{M}, \hat{D}, \hat{\Theta})$. Based on the universal approximation theorem, the estimated error $\tilde{D}_x = D_x - \hat{D}_x$ can be rewritten by

$$\tilde{D}_x = \tilde{W}^T \hat{\Phi} + \tilde{M}^T E \hat{W} + \tilde{D}^T C \hat{W} + \tilde{\Theta}^T G \hat{W} + \tilde{A}^T X + \Delta \tag{8.6}$$

with the expansion of $\tilde{\Phi}$ in Taylor series. $E = [\partial \Phi_1/\partial M, \partial \Phi_2/\partial M, \ldots, \partial \Phi_{N_w}/\partial M]\big|_{M=\hat{M}}$, $C = [\partial \Phi_1/\partial D, \partial \Phi_2/\partial D, \ldots, \partial \Phi_{N_w}/\partial D]\big|_{D=\hat{D}}$, $G = [\partial \Phi_1/\partial \Theta, \partial \Phi_2/\partial \Theta, \ldots, \partial \Phi_{N_w}/\partial \Theta]\big|_{\Theta=\hat{\Theta}}$ $\tilde{W} = W^* - \hat{W}$, $\tilde{\Phi} = \Phi^* - \hat{\Phi}$ and $\tilde{A} = A^* - \hat{A}$. H is the higher order terms. Δ is an approximation error term and assumed to be bounded by $|\Delta| \leq P$.

Then, the following Lyapunov candidate is chosen as

$$V_2 = V_1 + \frac{1}{2\eta_1}\tilde{W}^T\tilde{W} + \frac{1}{2\eta_2}\tilde{M}^T\tilde{M} + \frac{1}{2\eta_3}\tilde{D}^T\tilde{D} + \frac{1}{2\eta_4}\tilde{\Theta}^T\tilde{\Theta} + \frac{1}{2\eta_5}\tilde{P}^T\tilde{P} + \frac{1}{2\eta_6}\tilde{A}^T\tilde{A}$$
(8.7)

where $\eta_1, \eta_2, \eta_3, \eta_4, \eta_5$ and η_6 are positive constants. Therefore, the BSMC with SRWNN control law U_x that is equivalent to M_x of the eight-rotor is designed as

$$U_x = M_x = I_x[-(k-\alpha)\dot{z}_1 + \ddot{x}_{1d} - \gamma s - h\,\mathrm{sgn}(s) - \hat{D}_x - \hat{P}\,\mathrm{sgn}(s)]$$
(8.8)

where γ, h are positive constants. The adaptive laws for the SRWNN observer and the approximation error bound are given as follows:

$$\dot{\hat{W}} = -\dot{\tilde{W}} = \eta_1 s\hat{\Phi} \quad \dot{\hat{M}} = -\dot{\tilde{M}} = \eta_2 sE\hat{W} \quad \dot{\hat{D}} = -\dot{\tilde{D}} = \eta_3 sC\hat{W}$$
$$\dot{\hat{\Theta}} = -\dot{\tilde{\Theta}} = \eta_4 sG\hat{W} \quad \dot{\hat{A}} = -\dot{\tilde{A}} = \eta_6 sX \qquad \dot{\hat{P}} = -\dot{\tilde{P}} = \eta_5|s|$$
(8.9)

Then, the derivative of V_2 can be written as

$$\dot{V}_2 = -z_1 z_2 - \alpha z_1^2 - \gamma s^2 - h|s| + s\Delta - P|s|$$
$$\leq -z_1 z_2 - \alpha z_1^2 - \gamma s^2 - h|s|$$
(8.10)

According to Barbalat's lemma [11], it is noted that $\dot{V}_2 \leq 0$ in the case where $\gamma(\alpha - k) - \frac{1}{4} > 0$. Thereby, the eight-rotor control system in the roll channel is asymptotically stable in the case of the above condition under model uncertainties and external disturbances. Furthermore, the attitude control in pitch channel and yaw channel with the proposed method have the same design procedure, which is no longer described for the sake of simplicity.

8.4 Numerical Simulations Results

Comparison simulations for the attitude control of the eight-rotor between BSMC with SRWNN method and BSMC method are performed to demonstrate the validity and robustness of the proposed method under model uncertainties and external disturbances. The parameters of dynamic model in the simulations are taken from the eight-rotor prototype, as listed in Table 8.1.

Assume the initial attitude angles as $\eta_0 = [0, 0, 0]^T$ degree, and the desired attitude angles as $\eta_d = [12\cos(t), 12\cos(t), 30\cos(t)]^T$ degree. An uncertainty of $-30\,\%$ in the inertia matrix is assumed as the model uncertainties. The time-varying external disturbance is given by $\tau_d = 0.2\sin(0.5t)$ act on the pitch, roll as well as

Table 8.1 The parameters of the eight-rotor prototype

Parameters	Values
Mass m	2.5 kg
Distance between rotor and the center l	0.5 m
Moment of inertia to x-axis I_x	8.1×10^{-3} N m s^{-2}
Moment of inertia to y-axis I_y	8.1×10^{-3} N m s^{-2}
Moment of inertia to z-axis I_z	14.2×10^{-3} N m s^{-2}
Thrust factor k_1	54.2×10^{-6} N s^2
Drag factor k_2	1.1×10^{-6} N m s^{-2}

yaw control, respectively. To achieve the favorable control performance along with the stability condition, the parameters of BSMC are tuned as $\alpha_x = 10, k_x = 0.5, \gamma_x = 17, h_x = 1, \alpha_y = 15, k_y = 0.5, \gamma_y = 23, h_y = 3, \alpha_z = 13, k_z = 0.5, h_z = 1$ in roll, pitch, and yaw channels. The learning rates of the SRWNN are taken as $\eta_1 = \eta_2 = \eta_3 = \eta_4 = \eta_6 = 10$ and $\eta_5 = 0.3$ by the trial and error.

The attitude control compared simulations results between BSMC with SRWNN method and BSMC method are carried out in the case of model uncertainties and time-varying external disturbance, as shown in Figs. 8.4, 8.5, and 8.6. It can be seen that the proposed method provides dominant advantage about control performance against disturbances over BMSC method, which is more obvious under external
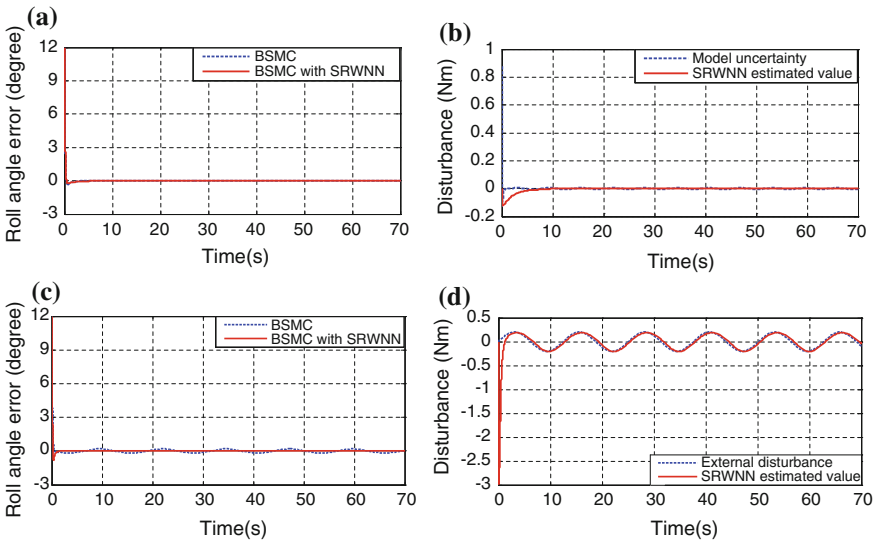
Fig. 8.4 The roll control comparison result under uncertainties. **a** Roll angle error under model uncertainties. **b** SRWNN result under model uncertainties. **c** Roll angle error under external disturbance. **d** SRWNN result under external disturbance
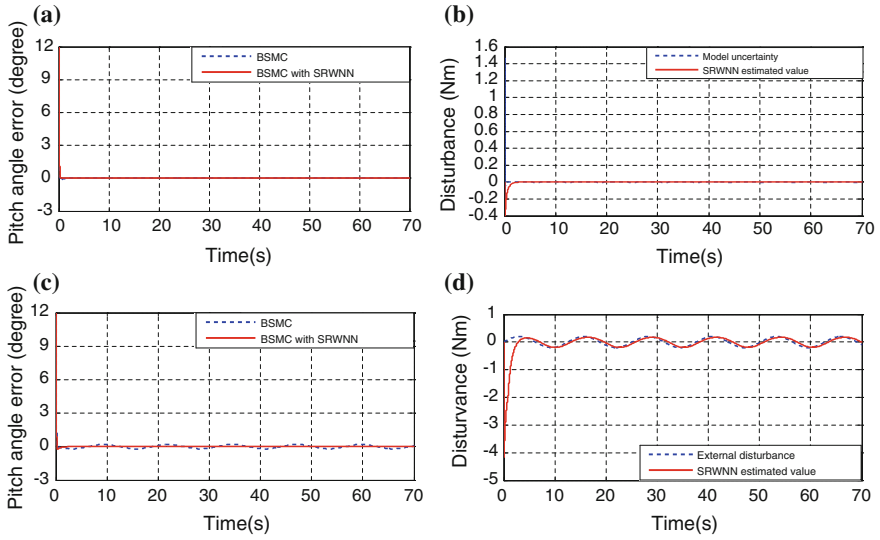
Fig. 8.5 The pitch control comparison result under uncertainties. **a** Pitch angle error under model uncertainties. **b** SRWNN result under model uncertainties. **c** Pitch angle error under external disturbance. **d** SRWNN result under external disturbance
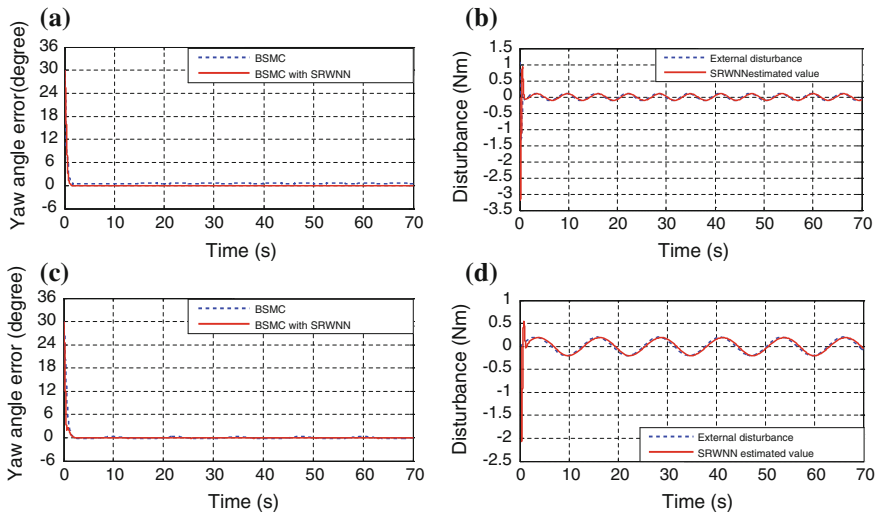
Fig. 8.6 The yaw control comparison result under uncertainties. **a** Yaw angle error under model uncertainties. **b** SRWNN result under model uncertainties. **c** Yaw angle error under external disturbance. **d** SRWNN result under external disturbance

disturbances. Furthermore, the satisfied uncertainties estimation performance with SRWNN observer is clearly corroborated.

Hence, simulation results highlight the claim that BSMC with SRWNN method can offer better attitude control performance and stronger robustness than BSMC method in the presence of model uncertainties and external disturbances. It is evident that the proposed method is better suited in dealing with the robust control problem of the eight-rotor with uncertainties.

8.5 Conclusion

In this paper, the robust attitude control strategy is presented for a coaxial eight-rotor UAV involving the model uncertainties and external disturbances. The eight-rotor that has higher drive capacity and stronger robustness than quad-rotor is modeled. Then, a robust BSMC with SRWNN method is proposed as the attitude controller of the eight-rotor with uncertainties. The combinative method of back-stepping control and sliding mode control has the improved robustness and simplified design procedure. The SRWNN observer can effectively estimate the lumped uncertainties, whose weights can be trained online by adaptive laws derived from Lyapunov stability theory. Then, the uniformly ultimate stability of the eight-rotor system is guaranteed. Finally, simulation results demonstrate the BSMC with SRWNN method adopted in the eight-rotor has great control performance and strong robustness under model uncertainty and time-varying external disturbance.

References

1. Nagaty A, Saeedi S, Thibault C et al (2013) Control and navigation framework for quadrotor helicopters. J Intell Robot Syst 70(1–4):1–12
2. Mohammadi M, Shahri AM (2013) Adaptive nonlinear stabilization control for a quadrotor UAV: theory, simulation and experimentation. J Intell Robot Syst 72(1):105–122
3. Besnard L, Shtessel YB, Landrum B (2012) Quadrotor vehicle control via sliding mode controller driven by sliding mode disturbance observer. J Franklin Inst 349(2):658–684
4. Liu H, Bai YQ, Lu G et al (2013) Robust attitude control of uncertain quadrotors. IET Control Theory A 7(11):1583–15895
5. Lin FJ, Shen PH, Hsu SP (2002) Adaptive backstepping sliding mode control for linear induction motor drive. IEE Proc Electr Power Appl 149(3):184–194
6. Ku CC, Lee KY (1995) Diagonal recurrent neural networks for dynamic systems control. IEEE Trans Neural Netw 6(1):144–156
7. Zhang QH, Benveniste A (1992) Wavelet networks. IEEE Trans Neural Netw 3(6):889–898

8. Yoo SJ, Park JB, Choi YH (2006) Adaptive dynamic surface control of flexible-joint robots using self-recurrent wavelet neural network. IEEE Trans Syst Man Syst 36(6):1342–1355
9. Zuo Z (2010) Trajectory tracking control design with command-filtered compensation for a quadrotor. IET Control Theory Appl 4(11):2343–2355
10. Oussar Y, Rivals I, Personnaz G (1998) Training wavelet networks for nonlinear dynamic input-output modelling. Neurocomputing 20(1–3):173–188
11. Slotine JJE, Li WP (1991) Applied nonlinear control. Prentice-Hall, Englewood Cliffs

Chapter 9
Hardware-in-the-Loop Simulations for Connected Vehicle

Yulin Ma, Youchun Xu and Jianshi Li

Abstract Connected vehicle is a typical application that is demonstrated in intelligent transport systems. Hardware-in-the-loop simulations put discrete events, finite states transition, and continuous vehicle dynamics modeling together to conveniently and effectively achieve the integration and test of connected vehicle system. The emphasis and difficulty of the connected vehicle system are discussed, including loosely coupled distributed architecture, information sharing, and conflict resolution mechanism among vehicles, roadsides and information center, and collaborative control scheme driven by discrete event flow, and results of cooperative driving for connected vehicle via HILS are also given.

Keywords Connected vehicle · Hardware-in-the-loop simulations · Loosely coupled distributed architecture · Hybrid automata · Collaborative control

9.1 Introduction

Nowadays, the insertion of Intelligent Transportation Systems (ITS) in the society is a fact, due to a big number of projects, demonstrations, and researches that have been carried out around the world. Connected vehicle (CV) is a typical application that is demonstrated by using the technology of Internet of Things (IoT) in the ITS. Connected vehicle systems (CVs) need to function properly in a vast amount of different traffic scenarios and road conditions [1]. Therefore, the design and validation of such systems are challenging, and requires a test environment that encompasses the different aspects of traffic at various scales.

Hardware-in-the-loop simulation (HILS) is one of the high-tech approaches that combines theory, numerical simulation, software, digital communications, data acquisition, instrumentation and control to give a mechatronic system. It is

Y. Ma (✉) · Y. Xu · J. Li
Department of Military Vehicle, Military Transportation University, Tianjin, China
e-mail: mayulin1983@163.com
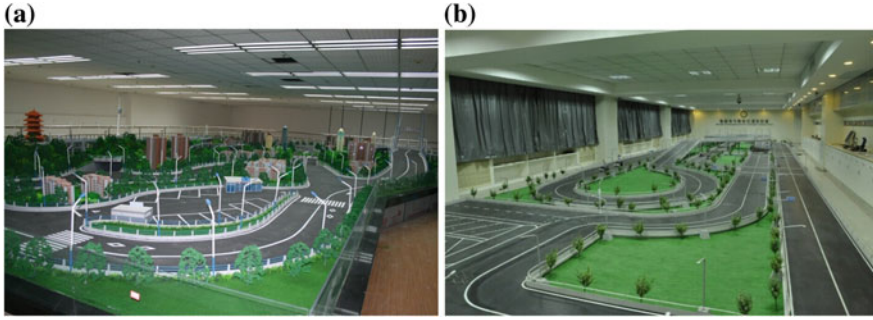
Fig. 9.1 The HILS in Wuhan University of Technology and Military Transportation University. **a** WUTS, **b** MTUS

generally known that the HILS systems are closed-loop systems consisting of many math models, physical hardware components, and subsystems connected through extensive electrical interface by means of CarMaker, dSPACE, CAN buses, MATLAB/SIMULINK, and VehSim-RT®. For example, [2–5] had used HILS to gain good effect in the research of intelligent vehicle. In China, the flexible, versatile HILS are WUTS developed by Wuhan University of Technology [6] and MTUS by Military Transportation University [7]. Both of them are typical of mechatronic, scale testbed consist of scale vehicles running on the simulated road, as shown in Fig. 9.1.

Motivated by the powerful function and wide purpose of HILS, this paper is going to develop a HIL-based connected vehicle system by means of AMTS. First, key points and difficult points in the integration and test of CVs are described. After a brief introduction to AMTS, different states are given corresponding to the candidate maneuvers of CV, and a hybrid automata is developed to perform transitions between these states. Once a desired state is activated, the specific maneuver is executed by a combined longitudinal and lateral controller design. In the AMTS, various cooperative scenarios are considered and the corresponding performance of the controller is shown in the end.

9.2 Emphasis and Difficulty

Essentially, CVs mainly reflect the hybrid logic of the whole ITS in the following three aspects. First, the physical structure of CVs is composed of onboard vehicle subsystem, roadside subsystem, and service center. Second, the information structure includes sensors networks, inter-vehicle communication networks, road-to-vehicle communication networks, and wide area networks. Last but not least, the system operation includes the responses to both discrete transient event and continuous vehicle dynamics. These three aspects are interrelated and interact on each other, collectively determining the cooperative driving for CVs. Therefore, in

order to realize the effectiveness of CVs, the loosely coupled distributed system architecture, information sharing and conflict resolution mechanism, and collaborative control scheme driven by discrete event flow should be explored in depth.

9.2.1 Loosely Coupled Distributed System Architecture

According to the hybrid logic of CVs, a distributed system architecture that includes onboard vehicles, roadsides, and service center should be developed to instruct the cooperative behavior of CV, and a decentralized variable structure should be also developed to instruct the autonomous behavior of the individual vehicle. Meanwhile, the loosely coupled design of information structure should be used to develop the knowledge service models of CVs. On the one hand, this hierarchy from onboard vehicles, through roadsides, then to service center, can weaken the dependence of different onboard control units on information interaction between themselves. On the other hand, this updating from the raw data, through information processing, then to the required knowledge, can form necessary knowledge service flow of CVs. Therefore, according to the configuration of "soft bus plus components", the dynamic and static data classification and fusion, multichannel communication protocol, and network management at foreground and background need be designed, and the knowledge service models should be verified by using message queues and topic-based method [8]. Through the integration of physical and information structure, the simplicity, flexibility, and robustness of CVs will be improved.

9.2.2 Information Sharing and Conflict Resolution Mechanism

The cooperative driving for CVs is actually the process of information sharing and competition among vehicles, roadsides, and service center. So, the analysis of this process should be divided into two parts. One is transitions between different states corresponding to the candidate maneuvers of CV, the other is conflict resolution in the process of information interaction. Usually, the hybrid automata of CVs are developed by using finite state machine and Petri net to analyze the cooperative behaviors [9]. In terms of states transitions, according to different types of information, an event-driven system is developed by using different event types, such as direct event, broadcasting event, binding event, and so on. Once the states transitions are well performed, the appropriate state can be activated. A hybrid control strategy for CVs includes the cooperative maneuvers of the leader, the controlled vehicle, and the following vehicles. In terms of conflict resolution, timed automata and fuzzy inference are used to analyze the conflict type of events in the information distribution mechanism, such as different types of events can trigger the

execution of other parallel states within one specific state. In addition, a hierarchical structure is used for the consistency of conflict detection, and a utility function developed by implicit events and time logic events is used to eliminate the conflict. Thus, the accuracy of the information distribution could be improved. Meanwhile, the hybrid automata for CVs are verified by the simulation tool of Stateflow and SimEvents.

9.2.3 Collaborative Control Scheme Driven by Discrete Event Flow

A collaborative control scheme driven by discrete event flow should be designed according to the transitions and activations of the corresponding states. In the conventional hybrid control method, a simple and direct commands or logic conditions are used for both transitions and activations. For example, the default cruising speed for connected vehicles is 30 km/s, or the spacing error for connected vehicles is maintained within 1 m, or the vehicle should merge into the front platoon of vehicles by accelerating maneuver. However, according to the knowledge service models and the conflict resolution mechanism of CVs, the optimal driving states for CV covering arbitrary lane, road sector, intersection, even the whole traffic should be obtained. For example, the maximum length of CV is 10 cars within the road sector, or the 30 % of the total cars in this road sector will enter into other sectors at the next road junction. Therefore, the performance criteria that determine the max-flow of CV should be developed by using optimal control and adaptive control methods. In this way, not only can a steady target be tracked quickly, such as cruising speed at 30 m/s, or spacing error within 1 m, but also can a smooth states transition be done from original state to the activated state, such as the following maneuver is switched to the lane-changing maneuver, last but not least, according to the process of knowledge service, when the length of a platoon of several vehicles is close to "the maximum length within the road sector", it can be realized that the 30 % of the total cars in this road sector will enter into other sectors at the next road junction. Meanwhile, a Lyapunov method is used to analyze the influence that communication delay, parameters uncertainty, and disturbance have on the driving stability for CV. On the other hand, the Poincaré maps are used to analyze the stabilizability of CVs under states transitions.

9.3 Case Study

The HILS has often been developed as a scale version of vehicles and roadway. Take an example of AMTS, it is a one-twelfth scale version whose area is 200 m^2 and accommodates up to 100 scale vehicles running on the roadway. The AMTS includes three parts: scale roadway, scale vehicles, and monitor console. The scale

roadway has different kinds of road infrastructures, such as highway, bridges, ramps, U-turns, and intersections. The scale vehicles are equipped with micro PC, power supply module, actuation module that drives the steering and driving motors, wireless network interface controllers that communicates among vehicles, roadside, and monitor console, and indispensable onboard sensors, including digital camera as image recognition of the road surface, RFID reader as vehicle positioning, and ultrasonic, optical encoder, and accelerator as vehicle motion acquisition. The monitor console is actually a server-based some software interfaces, which manages vehicles and roadway databases, coordinate the whole mechatronic systems, online adjusts controller, and intervenes HILS in real time. According to the emphasis and difficulty of CVs, a distributed structure and a hybrid control strategy are illustrated in Figs. 9.2 and 9.3, respectively.

According to a three-degree-of-freedom vehicle model given by [6], the vehicle model is developed by using MATALB/SIMULINK, as shown in Fig. 9.4, which includes longitudinal motion, lateral motion, and yaw motion. The vehicle parameters are listed in Table 9.1.

In terms of cooperative maneuvers for CV, such as cruising, following, merging, splitting, lane changing, and overtaking, each state corresponds to the candidate maneuver, and a hybrid automata can be developed to achieve transitions between
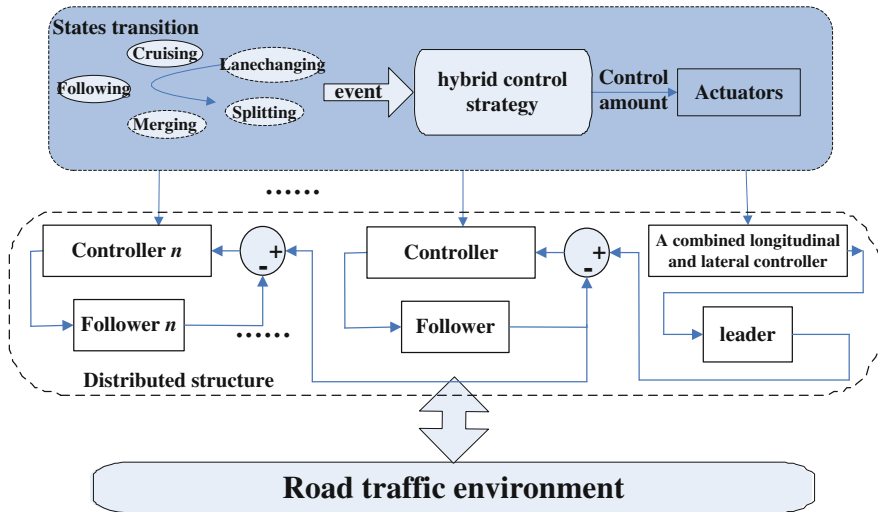
Fig. 9.2 The distributed structure of CVs
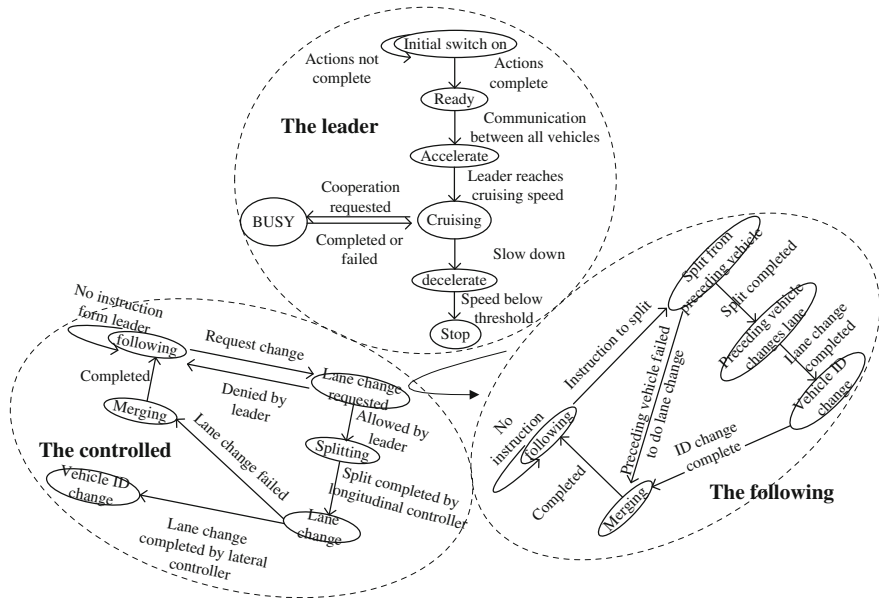
Fig. 9.3 A hybrid control strategy for CVs
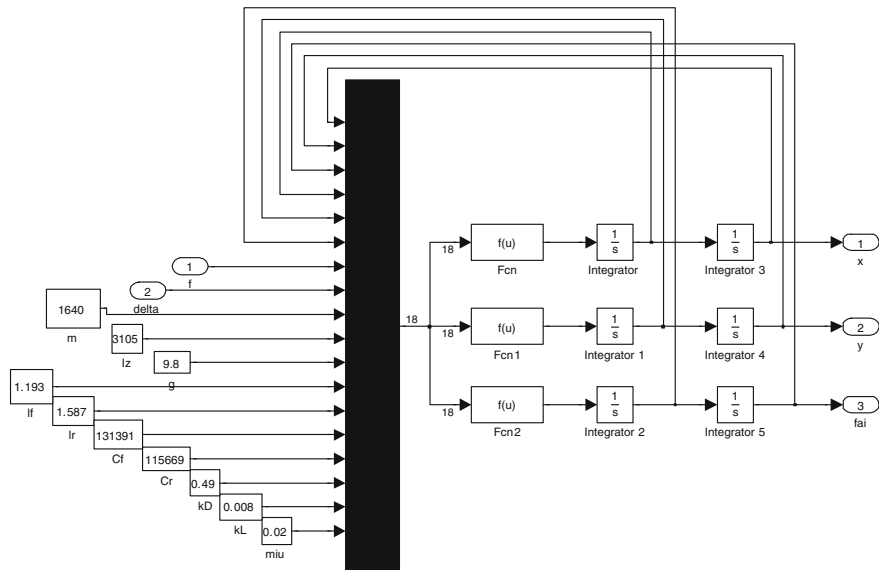
Fig. 9.4 The vehicle model

Table 9.1 The vehicle parameters

Parameters	Description	Parameters	Description
m/kg	Total mass	k_L/Ns^2 m^{-2}	Aerodynamic lift parameter
I_z/kg m^2	Yaw inertial	g/m s^{-2}	Gravity acceleration
l_f/m	Distance from front axle to center of gravity	g/m s^{-2}	Gravity acceleration
l_r/m	Distance from rear axle to center of gravity	f/N	Traction force
C_f/N rad^{-1}	Front cornering stiffness	delta/rad	Steering wheel angle,
C_r/N rad^{-1}	Rear cornering stiffness	x/m	Longitudinal position
μ	Rolling friction coefficient	y/m	Lateral position
k_D/Ns^2 m^{-2}	Aerodynamic drag parameter	fai/rad	Yaw angle

these states, and it is implemented by using Stateflow module in MATALB/SIM-ULINK or other unified modeling languages. So, as long as the monitor console sends the command according to the knowledge service flow and the conflict resolution mechanism of CVs, the onboard control unit can perform states transitions to achieve optimal collaborative control with each other in CVs. The hybrid automata developed by Stateflow is shown in Fig. 9.5, and it includes cruising, following, and lane-changing three fundament states. The conditions of states transitions are composed of the lane position, the length of CV, the desired speed, and spacing of CV.
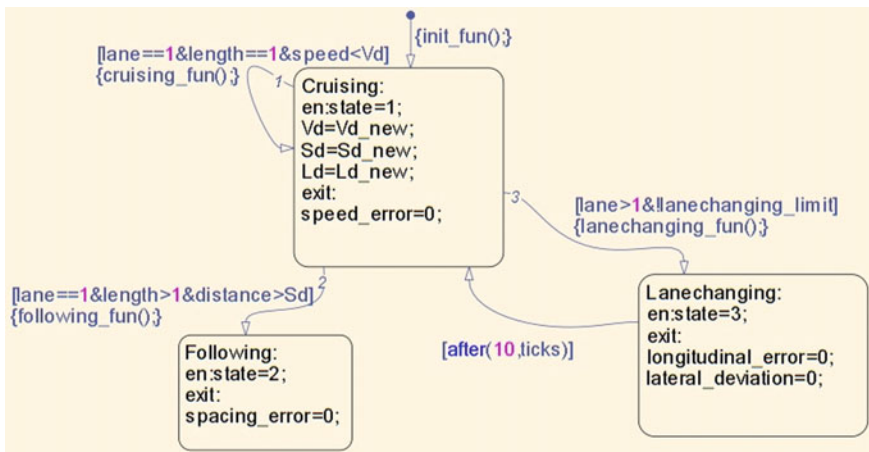
Fig. 9.5 The hybrid automata development

Once a desired state is activated, the specific maneuver can be executed by a combined longitudinal and lateral controller designed by some control methods like PID, SMC, MPC, and LQR. Here, taking SMC as example, after a sliding surface that employs both longitudinal error and lateral error is defined, the combined longitudinal and lateral controller for the corresponding vehicle can be designed by Terminal Sliding Mode Control method [7]. The simulations of following and lane-changing maneuvers are given. In the following maneuver simulation for a five-vehicle platoon, the leading vehicle is assumed to accelerate from 0 to 30 m/s at 2 m/s^2. After the vehicle reaches 30 m/s, it begins to decelerate to 10 m/s at -2 m/s^2. The desired spacing is 12 m. The simulation results are shown in Fig. 9.6. While in the lane-changing maneuver simulation, according to a trapezoidal-based lateral acceleration method, the lane-changing trajectory is first planned and then the lateral motion is tracked. The simulation results are as shown in Fig. 9.7, and the red line denotes the actual vehicle motion, while the blue line denotes the desired vehicle motion.
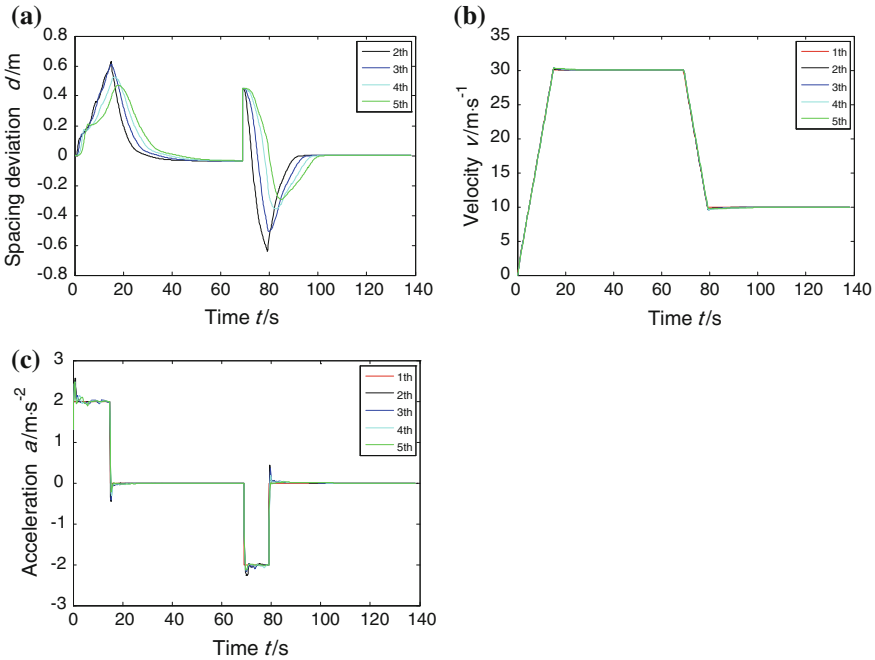
Fig. 9.6 Five-vehicle platoon following maneuver simulation. **a** Spacing error profiles, **b** velocity profiles, **c** acceleration profiles
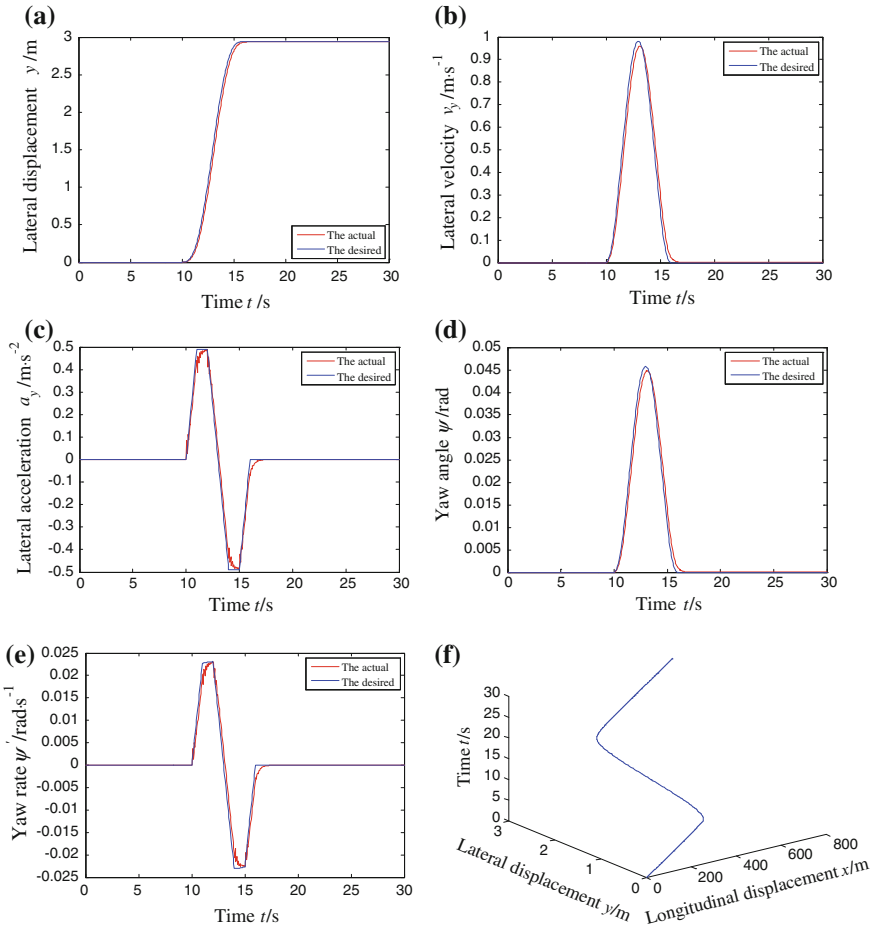
Fig. 9.7 Lane-changing maneuver simulation. **a** Lateral displacement profiles, **b** lateral velocity profiles, **c** lateral acceleration profiles, **d** yaw angle profiles, **e** yaw rate profiles, **f** 3D profiles

9.4 Conclusions

The HILS is inexpensive, easily reconfigurable, and safe enough to attempt cooperative maneuvers for CV. A HIL-based connected vehicle system is developed including scale roadway, scale vehicles, and monitor console. The distributed structure and hybrid control strategy for CVs are given. Because of each state corresponding to the candidate maneuver, after states transition and activation, the specific maneuver is executed by a combined longitudinal and lateral controller. Besides, we demonstrate HILS use in connected vehicle, such as following and lane-changing cases. It will be a priority to design the knowledge service models, event-flow models, and performance criteria that determine the maximum vehicle flow in the next work.

References

1. Tideman M, van Noort M (2013) A simulation tool suite for developing connected vehicle systems. In: Proceedings of IEEE intelligent vehicles symposium, Gold Coast, Australia, pp 713–718, 23–26 June 2013
2. Gietelink O, Ploeg J, De Schutter B et al (2006) Development of advanced driver assistance systems with vehicle hardware-in-the-loop simulations. Veh Syst Dyn 44(7):569–590
3. Deng WW, Lee YH, Zhao A (2008) Hardware-in-the-loop simulation for autonomous driving. In: Proceedings of the 34th annual conference of IEEE industrial electronics, Orlando, USA, pp 1742–1747, 10–13 Nov 2008
4. Vanholme B, Gruyer D, Glaser S et al (2010) Fast prototyping of a highly autonomous cooperative driving system for public roads. In: Proceedings of IEEE intelligent vehicles symposium, San Diego, USA, pp 135–142, 21–24 June 2010
5. Swanson KS, Brown AA, Brennan SN et al (2013) Extending driving simulator capabilities toward hardware-in-the-loop testbeds and remote vehicle interfaces. In: Proceedings of IEEE intelligent vehicles symposium, Gold Coast, Australia, pp 122–127, 23–26 June 2013
6. Ma YL, Wu Q, Yan XP et al (2013) The hardware-in-the-loop simulator: a mechatronic testbed for cooperative vehicles maneuvers. Int J ITS Res 11(1):11–22
7. Ma YL, Xu YC, Wu Q et al (2014) Hybrid control for cooperative vehicle-platoon via the hardware-in-the-loop simulator. In: Proceedings of 16th international IEEE annual conference on intelligent transportation systems, The Hague, The Netherland, pp 2373–2378, 6–9 Oct 2014
8. Li LX, Jin Z, Li G (2011) Modeling and verifying services of internet of things based on timed automata. Chin J Comput 34(8):1365–1377 (in Chinese)
9. Hou LS, Jin Z, Wu BD (2006) Requirement driven web service modeling and verifying. Sci China Ser-E Inf Sci 36:1189–1219 (in Chinese)

Chapter 10
Research on Mobile Robot Task Planning and Execution System in Intelligent Environments

Fang Fang

Abstract According to the application requirements for mobile robot, the robot task planning and control mechanism in distributed intelligent environment is studied. The general task planning and execution system architecture are studied and established in the dynamic intelligent environment. According to the needs of autonomous systems, extended hierarchical task nets planning modeling for robot's autonomous task accomplishment are studied. Efficient optimal introductory task resolver algorithm based on task nets and methods of converting task dispatching scheme to robot's action sets are proposed. Related experiments are also conducted in order to verify the feasibility and effectiveness of the system.

Keywords Mobile robot · Task planning · Execution system · Intelligent environment

10.1 Introduction

In the future, mobile robots will become human convenient and friendly assistants. First of all, they need to be able to adapt to coexist with people harmoniously in highly dynamic application environment [1, 2]. Here task planning plays a key role according to the known environment model, task requirements, and the application of interactive functions and information. At the same time, in order to effectively reduce the cost of robots and improve the robot's ability to perform a task, intelligent environment or intelligent space [3–5] which is widespread and with relatively low cost combined with a robot has become an inevitable trend.

Robot planning study is rooted in the fact that all kinds of robots are in a noisy environment model, all sensory information is uncertain to some extent, so the robots

F. Fang (✉)
Key Laboratory of Measurement and Control of CSE, School of Automation,
Southeast University, Nanjing 210096, Jiangsu, People's Republic of China
e-mail: ffang@seu.edu.cn

need to integrate perception and execution to plan directly. Hoffman and Breazeal [6] pointed that the interaction and teamwork of robots and humans can be greatly improved if the former can anticipate the forthcoming actions of the latter. The robots should acquire knowledge about people's current and predicted future activities and use such knowledge to plan their actions accordingly. An intelligent environment can monitor the service object and people in its space through its complex joint perception and execution ability. In man–machine joint task planning system human aware task planner (HATP) proposed by Montreuil [7], and Galindo's human–machine collaborative planning method proposed by [8], the robot does not consider the human's behavior habits, and only provides robot planner with the prediction of the behavior of the human. Mausam Weld's [9] CoMDPs (concurrent markov processes) method is entirely the extension of markov decision processes (MDPs), and puts forward how to calculate a series of planning behavior which can be executed safely and have a certain duration at the same time. However, this method is only fit for a single robot agent and random actions execution time greatly increases the computational burden; so it is not suitable for robot online task planning problem. For the above application, this paper researches on robot task planning with people present making full use of intelligent service components and optimizes the service function through the robot online task planning and execution.

10.2 Decisional System Framework

According to the distribution and characteristics of autonomy of the component-based robot system as well as the dynamic characteristics of the observation environment, we classify the whole system into three different levels according to the intelligent level of the component. The robot is the most intelligent component in the system which can monitor all other intelligent components in the system and make plans as a whole. Followed by this are the other intelligent components in the system which can improve performance and resolve conflicts through mutual coordination. The humans encountered by the robot are represented by entities called "InterAction Agents" (IAAs). IAAs solve human conflicts/blocking and unfriendliness through interaction and negotiation with robot. This paper establishes a robot-centered distributed system with high reliability which introduces the advantages of centralized structure on the basis of fully distributed structure, and studies the robot−human aware dynamic task planning and control mechanism.

The system control architecture shown in Fig. 10.1 is devised for robot decision making and action in a human aware environment. The whole system consists of a decisional layer and functional layer. The decisional layer is composed of three components: The task planner (HATP), task agenda, and the supervision and execution module (SVE). HATP is the decisional kernel concerning timing constraints, physical security constraints, human aware constraints, action efficiency constraints, etc. SVE constitutes the decision kernel, which is based on an incremental context-based task refinement in a human context. The supervision and
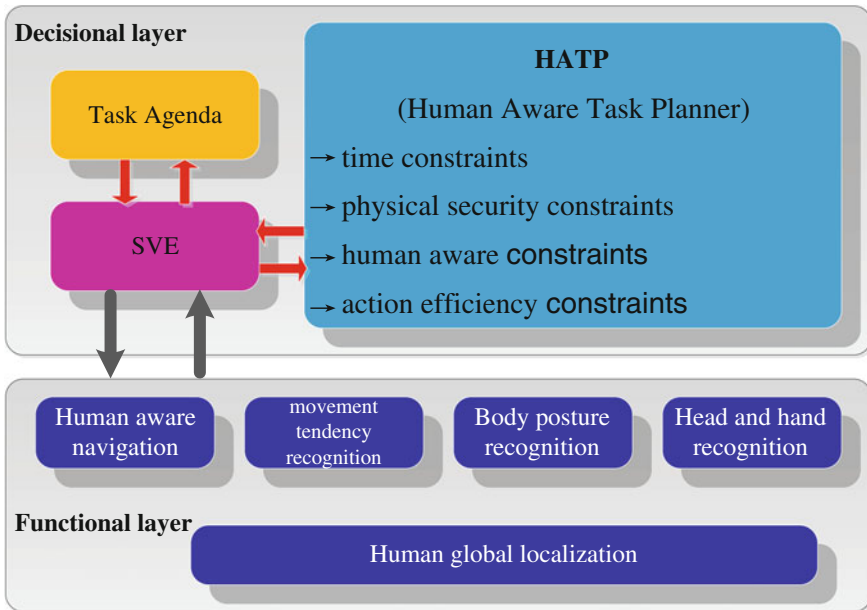
Fig. 10.1 Planning and decision-making model structure of the robot system

execution module takes into account not only the task achievement, but also communication and monitoring needed to support interactive task achievement in a flexible way. The functional layer consists of human aware navigation module, human global localization module, movement tendency recognition module, body posture recognition module, etc.

10.3 Mission Planning Methods

Hierarchical task network planning methods (HTN) are introduced and expanded. Probabilistic model is used to represent its application framework. Then robot hierarchical task network planner A*-HTN, which is based on A* algorithm, is proposed. On this basis, information reasoning combined with robot probabilistic model is done to accomplish the planning system concerning external information. At the same time, online probability learning method is proposed; so that robot can replan or repair the task when task fails. The structure using extended hierarchical task network planning methods is shown in Fig. 10.2.

Robot autonomous planning model mainly contains related planning language model, optional action sets, and constraints related to operation action, planning time constraints (PTC), action duration constraints (ADC), efficiency constraints (EC), physical security constraints (PSC), and interaction constraints (IC). Except
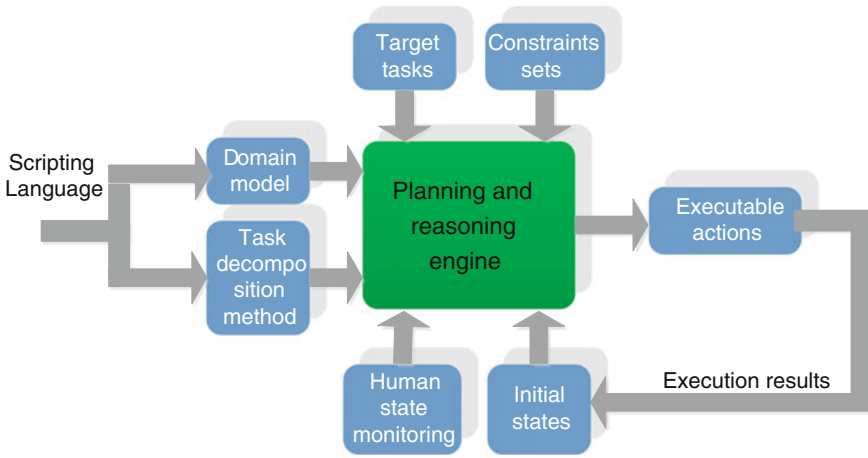
Fig. 10.2 Robot autonomous planning system framework

planning model, task decomposition method library which is used in the solving process of A*-HTN planning method is different from the general planning system. It is used to descript the definition of complex task and its decomposition method. When solving domain model and decomposition method library, it is treated as a knowledge library of inference engine. Planning requests contain the robot system's initial state collection, target task collection (not the target state collection), and constraints collection. Both of them and intermediate data produced by planning system form the database of inference engine. Under the support of the knowledge library and database, inference engine uses the TNBFSS method based on A* algorithm to accomplish iterative search which finally gets an executable action plan. After the action plan is executed, the target status is used as the new initial state in the inference engine by the new planning process. At the same time, when robot fails to perform tasks, implementation monitoring module will contrast the feedback action plan with the anticipation to confirm whether to enter the circulatory system of replan or planning patch. When dynamic information is missing, robot can complete the task more efficiently in this way. What is more, it can make the system more efficient and the robot more autonomous.

In order to achieve the human aware task plan and execution, the comity and many other social habits are quantified and integrated in consideration space for mission planning according to the events schedule agenda of service object. In this consideration space, task planner uses the given task as the constraints to calculate the optimal behavior. We have realized the human aware behavior goal of the robot which both guarantees the security of human and robot and adapts the psychological feelings. Now, considering n individual's status $H_k^1, \ldots, H_k^n$ and global pose of the robot r_k, we use the rule functions fcriterion to calculate the cost of robot, as shown in formula (10.1):

$$\text{Cost} = f_{\text{criteria}}(\text{robot, people, environment}) = f_{\text{criteria}}(r_k, H_k^1, \ldots H_k^n, M) \quad (10.1)$$

Five social habits or psychology principles are considered in fcriterion, including not infringing on others' personal space, minimum area of human–robot interaction, maintaining visibility to others, and complying with the travel side.

HTN algorithm could decompose to get a minimum number of behavior actions. But optimal planning is not only related to the number of actions, but also to behavior action itself. Each motion has different utility value according to its type and execution results, and some motions may execute to fail. Actually, the largest success probability of any action is less than one; so the traditional HTN algorithm which adapts the static environment is not suitable. Uncertainties must be regarded. A*-HTN planner can meet this requirement. The utility value of each type operation a is defined as $u(a, r)$, if a executes successfully then $r = 1$, if not then $r = 0$. The planner gets the action collection b which has the maximum expected utility ($E[u(b)]$), $b = (a_1, a_2, \ldots a_k) = a_i^k$

$$u(b, r) = \prod_{i=1}^{k} u(a_i, r_i) \quad (10.2)$$

$$E[u(b)] = \sum_{r \in \{0,1\}} p(r|b) u(b, r) = \sum_{r} p(r|b) \prod_{i=1}^{k} u(a_i, r_i) \quad (10.3)$$

When execution fails, $u(a, 0) = 0$, then formula (10.3) becomes

$$E[u(b)] = p(r = 1 \Big| b) \prod_{i=1}^{k} u(a_i, r_i = 1) = \underbrace{\prod_{i=1}^{k} p(r_i = 1 | r_1^{i-1} = 1, b)}_{\theta(a_i; b)} \prod_{i=1}^{k} u(a_i, r_i = 1)$$

$$(10.4)$$

10.4 System Experiment and Verification

We use the example of sending and receiving things to verify the feasibility and effectiveness of the system. Staff A will send a thing to staff B. He first calls the robot name. Voice sensor in the room catches his voice and sends to the robot. Robot sends the audio information to voice recognition server to recognize it, thus judging that someone is calling him and where the staff A is. Then the robot moves to the office room to search where the staff A is. There are many staffs in this room; staff A uses uniform color markers (its function is similar to the color marks on the robot) to show his location to the global camera. He puts the thing on the tray of robot and tells the robot to deliver it to staff B. The target name captured and recognized is told to
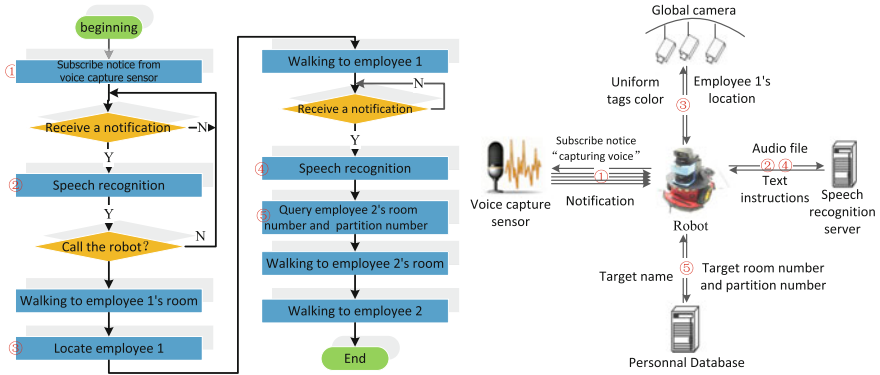
Fig. 10.3 Task flows for delivery in office

the robot in the same way. The robot finds the name of staff B in the staff library and finds his office room number. A global map is downloaded from the environment model library. The robot plans a way to the room of staff B, then sets it out. On its way, the robot uses the global camera to locate and track itself. When it arrives at the room of staff B, the robot downloads the local map of this room from the environment model library. And it plans a way to go behind staff B. The implementation method used is as shown in Fig. 10.3.

This scene test was realized. The feasibility and effectivity of the system are validated by establishing the mission process, analyzing and matching the subtasks, and planning the task by itself.

10.5 Conclusion

The basic framework of robot task planning and execution system in distributed intelligent environment is presented in this paper. The common mission planning and control system architecture and logical hierarchy is also put forward and established. An efficient optimal introductory task resolver algorithm based on task nets and methods of converting task dispatching scheme to robot's action sets is proposed. The task planning, distribution, and implementation are completed through constant interaction between robots, intelligent components, and people. Through a series of human–machine harmony rules, task assignment has certain adaptability to the service people. The architecture effectively solves the bottleneck problem of the large amount of calculation in planning process through dispersing machine intelligence into the intelligent components.

References

1. Karola P, Sebastian W, Christian SJ et al (2011) Attitude of German museum visitors towards an interactive art guide robot. In: Proceedings of the 6th ACM/IEEE international conference on human-robot interaction, Lausanne, Switzerland, pp 227–228
2. Taha T, Miro JV, Dissanayake G (2011) A POMDP framework for modelling human interaction with assistive robots. In: IEEE international conference on robots and automation, Shanghai, China, pp 544–549
3. Luo RC, Zhan JW, Cheng WH et al (2009) Network-based multimodal human-robot interactions in ubiquitous computing environment. In: IEEE international conference on robotics and biomimetics (ROBIO), Bangkok, Thailand, pp 131–136
4. Jin X (2010) Development and applications of smart space service components for mobile robot enhancement. School of Automation, Southeast University, Nanjing (in Chinese)
5. Qian K, Ma X, Dai X, Jin X (2011) Semantic service composition mechanism for component-based robotic system. In: Proceeding of 37th annual conference of IEEE Industrial Electronics Society, Melbourne, Australia, pp 3192–3197
6. Hoffman G, Breazeal C (2007) Cost-based anticipatory action selection for human-robot fluency. IEEE Trans Robot 23(5):592–661
7. Montreuil V, Clodict A, Ransan M et al (2007) Planning human centered robot activities. In: IEEE international conference on systems, man and cybernetics, Montreal, Cook Islands, pp 2476–2481
8. Galindo C, Fernandez-Madrigal J-A, Gonzalez J (2008) Multihierarchical interactive task planning: application to mobile robotics. IEEE Trans Syst Man Cybern Part B-Cybern 38 (3):785–798
9. Mausam Weld DS (2008) Planning with durative actions in stochastic domains. J Artif Intell Res 31:33–82

Chapter 11
Terrain Data Real-Time Analysis Based on Point Cloud for Mars Rover

Haoruo Zhang, Yuanjie Tan and Qixin Cao

Abstract With the development of space exploration, more and more aerospace researchers pay attention to Mars and Mars rover that has a capability of autonomous navigation will gradually become the focus of the study. Above all, we need to realize a real-time modeling and analysis of unknown environment, providing necessary real-time information for Mars rover motion planning, and ultimately achieving autonomous navigation. First, the research content is briefly introduced. Then, visual sensor on Mars rover is used to acquire 3D point cloud area in real-time environment and 3D grid map is created to reduce the complexity of 3D map for real-time analysis. Third, relying on the established 3D grid map, terrain and environmental information are analyzed and identified and necessary information for Mars rover motion planning is provided.

Keywords Vision sensor · 3D point cloud · 3D grid map · Obstacle crossing possibility · Obstacle feature

11.1 Introduction

The research is to achieve modeling and terrain data real-time analysis of environment based on point cloud for the Mars rover. The target is to establish stereo vision sensor system on Mars rover, and to achieve 3D point cloud creating, modeling, and real-time environmental analysis. According to the particular rover model, stereo vision sensor is established and is connected to the rover on-board computer, writing the program using an open source PCL library based on Microsoft Visual C++. Then Mars rover motion planning is combined with Webots robot simulation environment, finally running the program on the Mars rover.

H. Zhang (✉) · Y. Tan · Q. Cao
Institute of Robotics, Shanghai Jiao Tong University, No. 800 Dongchuan Road,
Minhang, Shanghai, China
e-mail: haoruozhang@foxmail.com
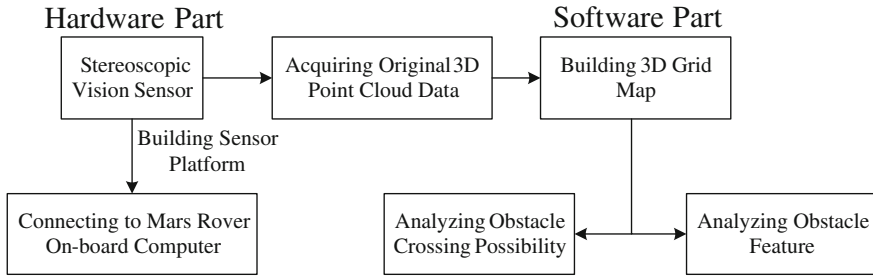
Fig. 11.1 Modeling and terrain data analysis system of environment for Mars rover

And the research is to study the methods to solve the problem about terrain point cloud data analysis for Mars rover. And finding the method to reduce the complexity of the 3D point cloud map, and also creating 3D grid map which have sufficient amount of information in a short time [1]. Due to the complex environment on Mars, studying about how to get further information on the environment analysis is to identify the area which can be passed through or not, the area part of the characteristic data is calculated by obstacle features analysis, and the data is provided to motion planning for Mars rover [2].

The main framework for modeling and terrain data analysis system is as follows (Fig. 11.1).

11.2 Original 3D Point Cloud Data Acquisition and Processing

The research is to study the methods to solve the problem about terrain point cloud data analysis for Mars rover, and we can utilize the stereo vision sensor to acquire original 3D point cloud data, for example, Bumblebee2 [3]. The research mostly focuses on the 3D point cloud processing, and uses Kinect sensor as stereo vision sensor temporarily. And the sensor platform is built on the Mars rover which is six-wheeled rocker type mobile robot. And the stereo vision sensor platform can adjust the vision angle in a certain range.

11.2.1 Original 3D Point Cloud Data Acquisition

First, stereo vision sensor is used to get depth image and color image of the current environment in general. And the original 3D point cloud map can be built by depth image and color image [4]. The research also proposes a method to build the
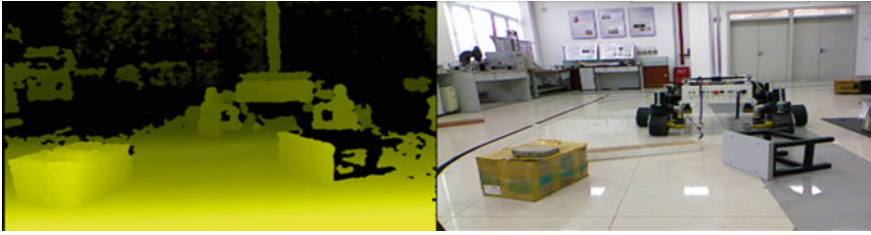
Fig. 11.2 Original environment data acquisition

original 3D point cloud map. The research uses stereo vision sensor to acquire depth image and color image of original environment, as follows (Fig. 11.2).

Left side of the image is the depth image and right side is the color image. The research builds the 3D point cloud by integrating depth image and color image, as follows.

In general stereo vision sensor coordinate system, Z-axis is the normal axis of the lens, the depth value of each pixel in the depth image represents the Z value of the actual coordinate space; X, Y is the index position of the depth image of each pixel (X is column, Y as row), so X, Y coordinate space needs to be converted to the actual X, Y value.

First, the field view of stereo vision sensor is acquired, including horizontal and vertical viewing angles.

Second, the proportion of unit conversion is calculated (Fig. 11.3).

Angle α is horizontal viewing angle and angle β is vertical viewing angle.

$$\text{Real World } X \text{ to } Z = 2\tan(\alpha/2), \quad \text{Real World } Y \text{ to } Z = 2\tan(\beta/2) \qquad (11.1)$$

Third, the actual environment of X, Y values is calculated. And nXRes is the pixel value in the depth image in the width direction, nYRes is the pixel value in the height direction (Fig. 11.4 and Table 11.1).

Fig. 11.3 Proportion of unit conversion
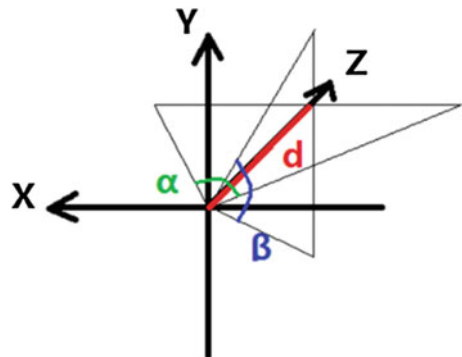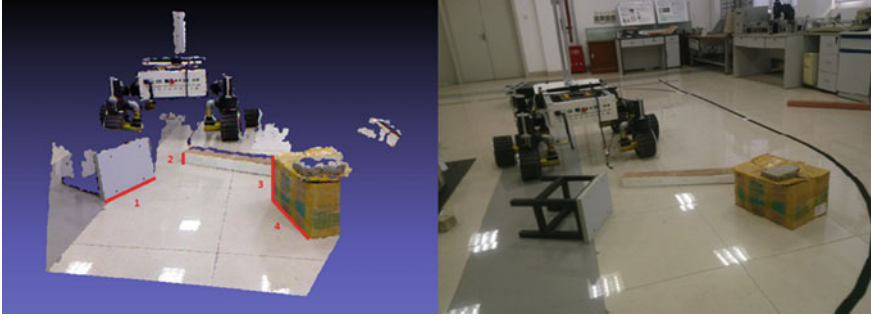
Fig. 11.4 Comparison between actual environment and 3D point cloud

Feature	Actual value (m)	3D value (m)	Errors (%)
1	0.3530	0.35182	0.33433
2	0.0600	0.05927	1.21667
3	0.2260	0.22435	0.73009
4	0.3820	0.38104	0.25131

Table 11.1 Errors between actual value and 3D point cloud value

$$\text{Normalized } X = X/nX\text{Res} - 0.5, \quad \text{Normalized } Y = 0.5 - Y/nY\text{Res} \quad (11.2)$$

$$X = \text{Normalized } X \times Z \times \text{Real World } X \text{ to } Z \quad (11.3)$$

$$Y = \text{Normalized } Y \times Z \times \text{Real World } X \text{ to } Z \quad (11.4)$$

11.2.2 Building 3D Grid Map

Mars rover motion planning needs large amounts of real-time environment data [5]. Therefore, it is necessary to build a 3D grid map; in this way, it can reduce the complexity of creating maps, and reduce running time of the algorithm (Fig. 11.5).

PCL open source library filter module has filter function that can remove unwanted points in the 3D point cloud data with different filters [6]. And the research uses filter module class ApproximateVoxelGrid to simplify 3D point cloud map. Class ApproximateVoxelGrid can generate 3D grid map with the input of original 3D point cloud map, and the research takes advantage of all the center of the grid to approximate point sets that are contained in the grid.

This research chooses 3D grid size of 0.05 m. The data points are reduced from 163,209 to 2440 points, and the size of point cloud file reduces from 7078 to 82 KB, ensuring the environmental characteristics of the information simplify data.
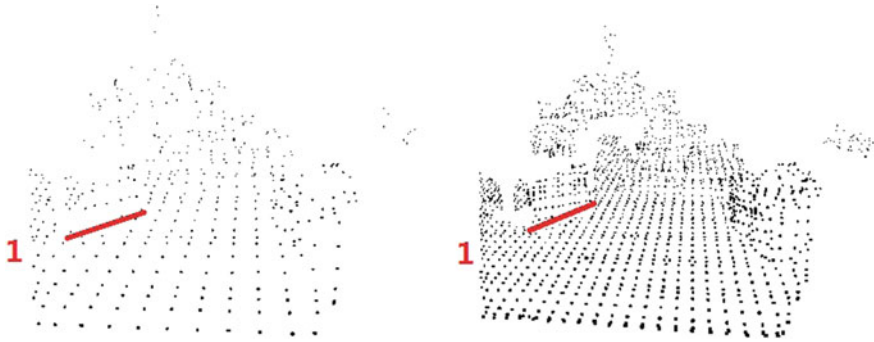
Fig. 11.5 3D grid map (size 0.1 m *left*, size 0.05 m *right*)

11.3 Terrain Data Analysis of Single-Frame 3D Grid Map

As for terrain data analysis, the coordinate system of 3D grid map needs to be changed [7]. The current coordinate values obtained from 3D grid map, based on stereo vision sensor coordinate system, must be transformed into a coordinate system of Mars rover.

11.3.1 Analyzing Obstacle Crossing Possibility

The research also gained some motion data of Mars rover about obstacle crossing from physical experiments; for example, the rover's wheels cannot pass through slope of about 30° or more and the height of the obstacle radius rover wheels (11 cm) above. So the research needs to search all data points on the 3D grid map to detect whether the obstacle, whose slope angle is more than 30°, exists or not. So, we need to search all the data points of the 3D grid map and find out the point sets (two points) that meat some requirements. First, the difference between X values of the two points is less than 0.1 m, while the difference between Y values of the two points is greater than 0.05 m. In this way, the two points in the point set are closest with each other in the 3D grid map (grid size 0.05 m), and they have different Y values.

Then, calculating the slope between two points in all point sets. If the point set whose slope angle is more than 30°, the algorithm will judge whether the point set is located on the area that the wheels of Mars rover will pass through or not. And X value of the area is more than 0.2 m or less than −0.2 m.

And if X value of points is less than 0.2 m and more than −0.2 m, the algorithm will judge whether Z value of these points is less than the bottom height of Mars rover or not; for example, if Z value is more than 0.32 m, the area could not be passed through. In addition, if the point set whose slope angle is more than 30°

Fig. 11.6 Flow diagram of obstacle crossing possibility analysis
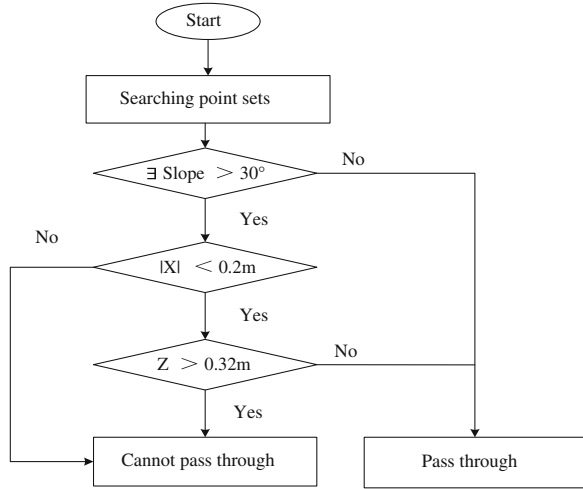
which is located in the area whose *X* value is less than 0.2 m and more than −0.2 m, then the current terrain cannot be passed through (Fig. 11.6).

11.3.2 Analyzing Obstacle Feature

After analyzing obstacle crossing possibility, if the current 3D grid map can be passed through, it is necessary to analyze the obstacle feature. In this way, Mars rover could take a different strategy under different conditions of obstacle feature.

In the algorithm, the input is a pointer of point cloud, and the output is a variable named "workcase." During the experiment, the main analysis is about some relatively simple obstacle feature. If the value of "workcase" is 1, it indicates that the ground is flat; 2 indicates uphill straightly; 3 indicates uphill straightly on left side; 4 indicates uphill diagonally on left side; 5 indicates uphill straightly on right side; 6 indicates uphill diagonally on right side; 7 indicates uphill diagonally; 8 indicates downhill straightly; and 9 or 10 indicates downhill on one side (left and right).

First, the algorithm will judge whether the area is "workcase" 1 or not by average and variance of *Z* value. Then the algorithm selects four arrays of data points whose *X* value are −0.45, −0.25, 0.25, and 0.45 m, respectively. And the *Y* value of data points in every array is sorted by size. In addition, the algorithm will search the points whose *Z* value is more than 0.05 m in every array and assign the least *Y* value to variable distance. Second, the algorithm will judge whether the difference between distances (*X* value −0.45 and 0.45 m) is less than 0.1 m or not. And the difference can be signed by Diff (−0.45 to 0.45). The other terrain data analysis is as follows (Fig. 11.7).
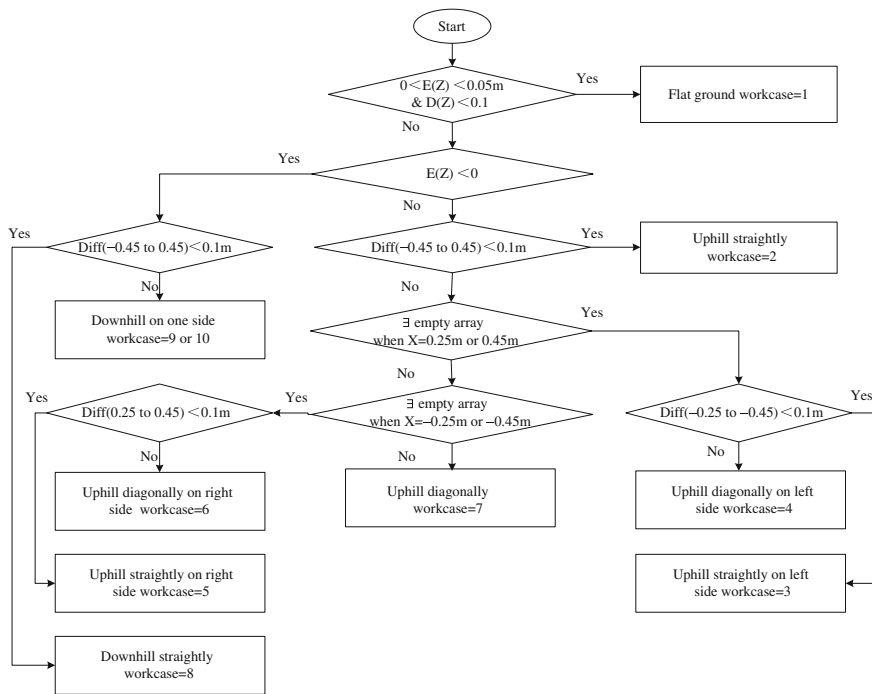
Fig. 11.7 Flow diagram of obstacle feature analysis

11.3.3 Experiments Under Webots Robot Simulation Environment

See Fig. 11.8 and Table 11.2.

Table 11.2 Errors between actual value and analysis value in experiments

Obstacle feature	Actual value		Analysis value	Errors (%)
2	Distance	0.6750 m	0.6763 m	0.1926
	Gradient	20.0°	20.0021°	0.0105
3	Distance	0.4740 m	0.4750 m	0.2110
	Gradient	20.0°	20.0014°	0.0070
4	Alpha	−26.0°	−26.6887°	2.6488
8	Distance	1.2950 m	1.3007 m	0.4402
	Gradient	−11.5°	−11.4787°	0.1852
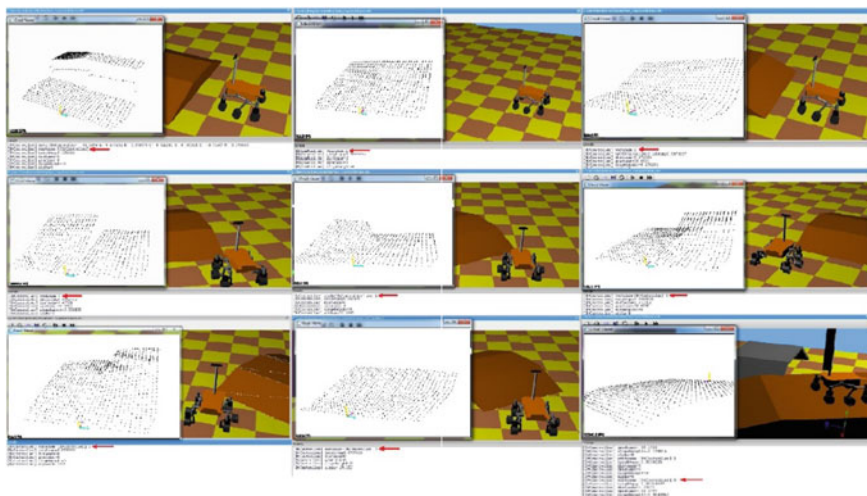
Fig. 11.8 Algorithm experiments under Webots robot simulation environment

11.4 Conclusion

Considering the size of Mars rover, errors between actual value and analysis value are within the acceptable range. According to Fig. 11.8, the algorithm can realize obstacle feature recognition and get result in a short time about 0.5 s. In conclusion, simulation experiments verify the accuracy and real time of the algorithm.

References

1. Andreasson H, Treptow A, Duckett T (2005) Localization for mobile robots using panoramic vision, local features and particle filter. In: Proceedings of the 2005 IEEE international conference on robotics and automation (ICRA 2005), pp 3348–3353
2. Bajracharya M, Maimone MW, Helmick D (2008) Autonomy for mars rovers: Past, present, and future. Computer 41(12):44–50
3. Kim IH, Kim DE, Cha YS et al (2007) An embodiment of stereo vision system for mobile robot for real-time measuring distance and object tracking. In: International conference on control, automation and systems, ICCAS'07. IEEE, pp 1029–1033
4. Matthies L, Kelly A, Litwin T et al (1996) Obstacle detection for unmanned ground vehicles: a progress report. Springer, London
5. Manduchi R, Castano A, Talukder A et al (2005) Obstacle detection and terrain classification for autonomous off-road navigation. Auton Robots 18(1):81–102

6. Nguyen DV, Kuhnert L, Schlemper J et al (2010) Terrain classification based on structure for autonomous navigation in complex environments. In: 2010 third international conference on communications and electronics (ICCE), IEEE, pp 163–168
7. Su L, Luo C, Zhu F (2006) Obtaining obstacle information by an omnidirectional stereo vision system. In: 2006 IEEE international conference on information acquisition, IEEE, pp 48–52

Chapter 12
Motion Planning Algorithm Based on Environmental Information for Mars Rover

Yuanjie Tan, Haoruo Zhang and Qixin Cao

Abstract In this paper, we propose a motion planning algorithm for Mars Rover to realize the smooth and steady action when crossing obstacles and ultimately achieve the purpose of autonomous movement. The research described in this paper includes the following aspects. First, finish kinematics modeling and analyze some basic movement patterns when the rover is doing planar motion and get the results of the inverse kinematics. Then validate the result in the virtual simulation environment. Second, conduct the kinematics analysis for the Mars rover when it crosses some specific obstacles such as climbing a slope. Third, get the optimized strategy of motion planning and determine the overall plan scheme when crossing obstacles.

Keywords Kinematics modeling · Inverse kinematics equations · Crossing obstacles · Motion planning strategies

12.1 Introduction

In the past, the motion planning of the traditional robot mainly concentrated on path planning. This way actually regards the robot as a whole to study how it can effectively avoid obstacles in the environment. But on Mars, due to extremely complex pavements and environment, the Mars rover cannot be regarded as a black box. The structure of the robot, the over-obstacle capacity, and many other aspects should be taken into account. The most important thing for the Mars rover is how to overcome the obstacles efficiently and ensure its safety, autonomy, and high efficiency of its movement at the same time [1].

Y. Tan (✉) · H. Zhang · Q. Cao
Institute of Robotics, Shanghai Jiao Tong University, No. 800 Dongchuan Road, Minhang, Shanghai, China
e-mail: ilovedotayouxi@163.com

The research mainly studies how the Mars Rover analyzes the environment information after obtaining the real-time environmental picture and decides how to control the motion of the 10° of freedom based on the information [2] (Fig. 12.1).

12.2 Planning Algorithm of Planar Motion for Mars Rover

The simplest situation is that the Mars rover moves on a plane without any obstacles. It has various kinds of basic movement patterns, namely: straight forward, backward, stop; spin around; rotation of large radius.

On the plane, any movement can be seen as a superposition of these three basic movement patterns. Viewing from the center of mass of the Mars rover, the movement can be equivalent to two speeds: linear velocity V and angular velocity ω. Therefore, it is necessary to know the relationship between the rover's overall linear velocity V, the rotation angular velocity ω, and its six wheel's speed. According to the structural characteristics of the rover, an inverse kinematics equations of motion on the plane is established [3].

The six wheels are denoted as No. 0–5 in the anticlockwise direction, θ refers to the angle between the line connected by front wheels and the rover's centroid and the horizontal direction. $\beta[i]$ means the pose angle of the No. i wheel (Fig. 12.2).

Fig. 12.2 The kinematics analysis of planar motion
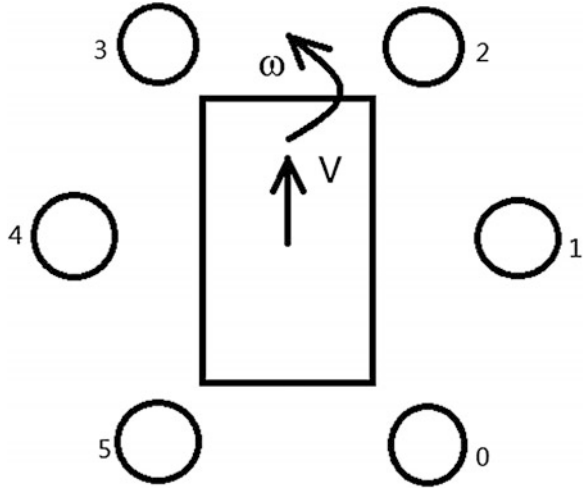
$$\beta[0] = a\tan((\omega * L * \sin(\theta))/(V - \omega * L * \cos(\theta))) \qquad (12.1)$$

$$\beta[2] = -a\tan((\omega * L * \sin(\theta))/(V - \omega * L * \cos(\theta))) \qquad (12.2)$$

$$\beta[3] = -a\tan((\omega * L * \sin(\theta))/(V + \omega * L * \cos(\theta))) \qquad (12.3)$$

$$\beta[5] = a\tan((\omega * L * \sin(\theta))/(V + \omega * L * \cos(\theta))) \qquad (12.4)$$

$$V[0] = -(V - \omega * L * \cos(\theta))/\cos(\beta[0]) \qquad (12.5)$$

$$V[1] = -(V - \omega * L) \qquad (12.6)$$

$$V[2] = -(V - \omega * L * \cos(\theta))/\cos(\beta[2]) \qquad (12.7)$$

$$V[3] = (V + \omega * L * \cos(\theta))/\cos(\beta[3]) \qquad (12.8)$$

$$V[4] = (V + \omega * L) \qquad (12.9)$$

$$V[5] = (V + \omega * L * \cos(\theta))/\cos\beta([5]) \qquad (12.10)$$

12.3   Planning Algorithm of Crossing Over Obstacles and Simulation Verification

Three factors needs to be considered when the Mars rover goes through obstacles in a real-time environment: security, stability, economy. The rover can efficiently go through obstacles if its motion planning method meets these three conditions.

Security is to determine the strongest ability of going through obstacles and this can provide a theoretical basis for the rover's traversability. Stability is that the rover can keep its direction of motion unchanged after going through obstacles. That means it can self-correct its direction when it deviates from its original direction. Economy means that most of the current planning methods set the same motion parameters for each wheel, this planning method will result in the parasitic power loss. The reason is the incoordination between different drive units which may result in wheel's slip. So kinematic analysis need be done when the rover goes through obstacles. By this way, a more efficient pattern for crossing obstacles can be achieved [4].

12.3.1 Motion Planning of Uphill

The whole idea for the motion plan of climbing is to keep the motor's rotation speed of the wheels which are on the ground constant, then the speed of the wheel which is on the slope changes in real time. According to the geometric relationship, the relationship between the speed of the wheels on the slope and the speed of the wheels on the ground can be solved in the ideal situation. Controlling the speed of the uphill wheels based on this solution will reduce the possibility of the occurrence that other wheels slip so that the power consumption of the motor achieves a minimum value.

This method first analyzes one situation of uphill: Only the front wheel climbs on the slope while the middle and the back wheel move on the ground. It sets the original moments which means $t = 0$ corresponds to the moment that the front wheel begins to climb on the slope (Fig. 12.3).

In the analysis, the overall forward speed of the rover is denoted as V, the speed of the uphill wheel u, the slope angle θ (Fig. 12.4).

Fig. 12.3 Mars rover in Webots simulation environment
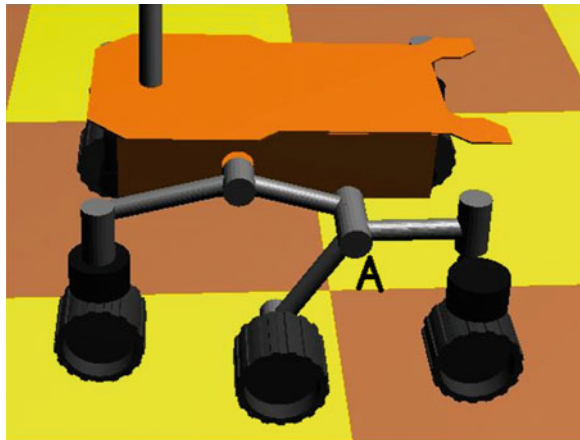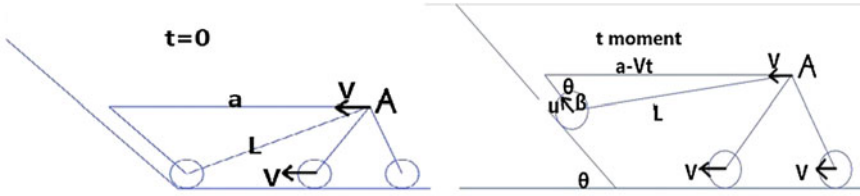
Fig. 12.4 The kinematic analysis of the uphill of the Mars rover

By the triangle law of cosines:

$$\frac{L}{\sin \theta} = \frac{a - Vt}{\sin \beta} \tag{12.11}$$

By the rule that the speed along the direction of the rod should be the same:

$$V \cos(180 - \theta - \beta) = u \cos(180 - \beta) \tag{12.12}$$

$$L = 0.68 \tag{12.13}$$

$$a = 0.62 + \frac{0.28}{\tan \theta} \tag{12.14}$$

$$u = \frac{\cos(\theta + \beta)}{\cos \beta} V = \frac{\cos(\theta + \mathrm{pi} - a \sin(\frac{a - Vt}{L} \sin \theta))}{\cos(\mathrm{pi} - a \sin(\frac{a - Vt}{L} \sin \theta))} V \tag{12.15}$$

If the climbing wheel is denoted as No. 1, the other wheels are denoted as 2–6, the motion planning equation is:

$$V_1 = \frac{\cos(\theta + \mathrm{pi} - a \sin(\frac{a - Vt}{L} \sin \theta))}{\cos(\mathrm{pi} - a \sin(\frac{a - Vt}{L} \sin \theta))} V \tag{12.16}$$

$$V_2 = V_3 = V_4 = V_5 = V_6 = V \tag{12.17}$$

Note that the speed of the climbing wheel changes with time while the other wheels' speed is consistent with the overall rover forward speed. The rover uses DC servo motor which can achieve real-time change in velocity.

According to the results of the above plan, the speed curve of the front wheel when climbing 30° and 20° slope is as follows (Fig. 12.5).

The unit of time is taken as 64 ms because the cycle that the Webots program updates all of the values is 64 ms.
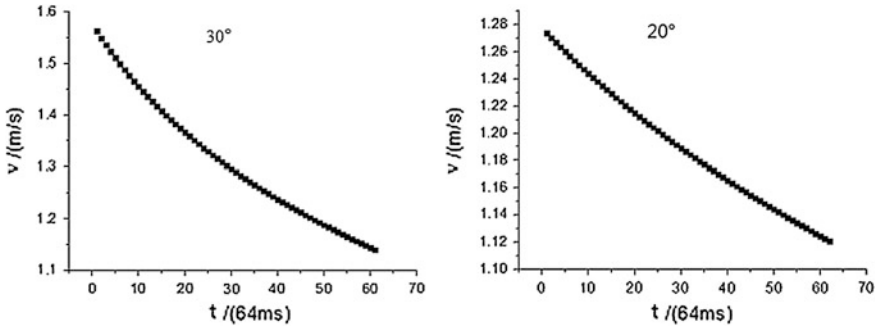
Fig. 12.5 The speed *curve* of the front wheel when climbing 30° and 20° slope

12.3.2 *Webots Simulation Verification*

In Webots, this method makes the simulation of the above planning strategy. Since the slip of the wheel may happen in real environments, it will be difficult to see the difference between different strategies. In Webots simulation, this method sets the coefficient of friction between the wheels and the ground or the slope to a very big value to ensure the wheels' pure rolling. In this situation, the results of simulation will be more obvious.

When the rover climbs with its six wheels at the same speed, it can be seen that the middle wheel hangs in the air. This phenomenon is not difficult to understand. Since the front wheel is uphill, the rear wheel moves forward on the ground, if these two wheels keep the same speed, then the body will inevitably be compressed resulting in the middle wheel idle off the ground. At the same time, the rear wheel on the ground bears much larger load. Besides, the motor is damaged due to the unreasonable velocity distribution (Fig. 12.6).

When the process of climbing is controlled by the results calculated above, that means the speed of the climbing wheels change in real-time, the middle wheel is
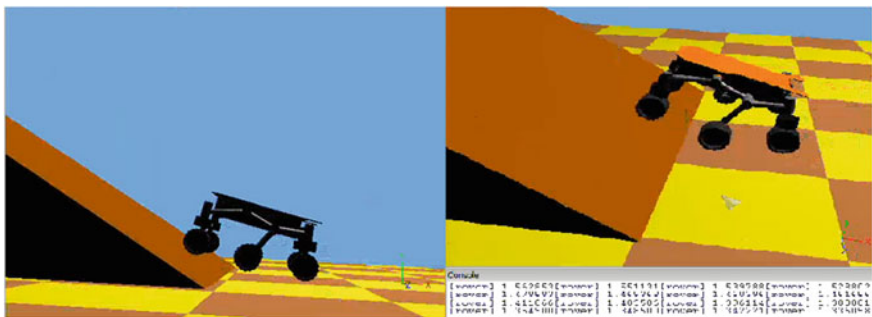
Fig. 12.6 The simulation of the process of uphill using two different planning strategies

always close to the ground and the entire body can smoothly climb on the slope. The data shown in the console area in the bottom of the right figure is the real-time speed of the uphill wheel. This planning strategy which confirms to the kinematic and geometry relationship can achieve the optimization of energy and protection of the motor, so that the rover can theoretically cross obstacles efficiently.

The other kinds of climbing such as downhill are analyzed and verified using the similar approaches, the process of derivation is omitted here.

12.4 Overall Planning Algorithm for Crossing Over Obstacles

To combine the motion planning algorithm with the vision algorithm, the planning strategy need be changed according to the real-time working conditions of the rover [5].

The visual part of the algorithm analyzes nine kinds of simple working conditions of the rover including uphill, climbing across the vertical ladder or simply not able to pass the obstacle. The motion planning part will take the corresponding planning strategy to control the motion of the rover based on the working condition it gets from the vision part [6].

For example, when the working condition is determined to be No 7 which corresponds to straight uphill of the rover, the visual algorithm will return some parameters to the motion planning algorithm such as the distance from the rover to the slope, the slope angle, and the height of the slope.

The following figure is a world model established in Webots virtual simulation environment to verify the effectiveness of the motion control strategy (Fig. 12.7).

This method actually combines all kinds of obstacles to make a target database. Based on this idea, the overall planning algorithm can be summarized as follows.

First, Kinect vision sensor mounted on the rover gets an image of real-time environmental information, the image mosaic algorithm can obtain a 4×4 matrix after coping with this image, and then get the rover's pose information. At the same

Fig. 12.7 World model established in Webots virtual simulation environment
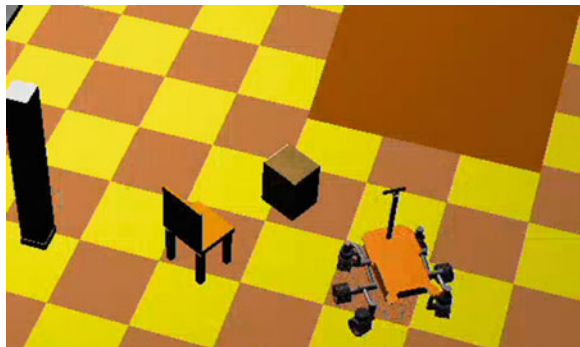
time, the vision algorithm recognizes the obstacle and compares it with the standard obstacle in the target database established previously. Then some of the characteristic parameters can be obtained and the current working condition of the rover is determined [7].

If the obstacle is beyond the rover's crossing ability, a fuzzy path planning need be done, the main task is to bypass the obstacle and the specific method is to plan the path of the rover. However, this is not the focus of this method. If the obstacle is within the rover's crossing ability, the motion planning involving 10° of freedom need be done to achieve the efficiency of going through obstacles. According to the type of the obstacles and characteristic parameters, strategy for going through obstacles can be determined. This method focuses on the rotation velocity and poses planning of each wheel based on the strategy discussed previously.

12.5 Conclusion

In this paper, we propose a motion planning algorithm for Mars Rover and validate its effectiveness in the virtual simulation environment. We achieve the purpose of autonomous movement by determining the overall plan scheme when crossing obstacles.

References

1. Hayati S, Volpe R, Balaram J et al (1997) The Rocky 7 Rover: a Mars science craft prototype. In: 1997 IEEE international conference on robotics and atuomation, pp 2458–2464
2. Volpe R, Balaram J, Ohm T et al (1997) Rocky 7: a next generation Mars rover prototype. Adv Robot 11(4):341–358
3. Muir PF, Neumann CP (1987) Kinematic modeling of wheeled mobile robots. Int J Robot Syst 4(2):282–340
4. Matijevic J (1997) Sojourner: The Mars pathfinder micro-rover flight experiment. Space Technol 17(3):143–149
5. Mishkin AH, Morrison JC, Nguyen TT et al (1998) Experiences with operations and autonomy of the Mars pathfinder microrover. IEEE Aerosp Conf Proc 1998:337–351
6. Cheng Y, Maimone MW, Matthies L (2005) Visual odometry on the Mars exploration rovers. In: 2005 international conference on systems, man and cybernetics, pp 903–910
7. Bunschoten R (2003) Mapping and localization from a panoramic vision sensor. Universiteit van Amsterdam [Host], p 128

Chapter 13
Error Correction of Support Vector Regression Model for Copper-Matte Converting Process

Jun Chen, Xiaoqi Peng and Xiuming Tang

Abstract To improve the performance of copper-matte Peirce-Smith Converting (PSC), the influence of local process data to ε-support vector regression (SVR) model for converting process is studied. This paper proposes an Error Correction method for ε-Support Vector Regression (EC_SVR), in which the influence of local support vector to prediction results is considered. Two EC_SVR models for slag weight and blowing time of S1 period (that is, the first slag producing period of PSC) are developed by the real production data. Simulation results show that EC_SVR model can significantly improve prediction accuracy and generalization of the converting decision variable in S1 period.

Keywords Support vector regression · Error correction · Copper-matte converting · Prediction accuracy · Generalization

13.1 Introduction

Converting is the second half of the smelting/converting sequence by which most of the world's Cu–Fe-sulfide concentrates are made into metallic copper. It is most often carried out in the cylindrical Peircee-Smith converter [1]. PSC is a 'batch' process. Converting takes place in two stages: (a) the slag-forming stage when

J. Chen · X. Peng (✉)
School of Information Science and Engineering, Central South University,
No. 932 LuShan Road, Changsha, China
e-mail: pengxq126@126.com

J. Chen
e-mail: 97chenjun@gmail.com

J. Chen · X. Tang
Institute of Information and Electrical Engineering, Hunan University of Science
and Technology, Taoyuan Road, Xiangtan, China
e-mail: tangxm2873@sina.com

Fe and S are oxidized to FeO, Fe_3O_4 and SO_2, silica flux is added to form a liquid slag with FeO and Fe_3O_4. (b) The copper-making stage when the sulfur in Cu_2S is oxidized to SO_2. Copper is not appreciably oxidized until it is almost devoid of S. The objective of optimization decision model for PSC is to obtain higher output with more superior quality of crude molten copper and lower energy consumption.

In the last two decades, researchers started to make use of the large amounts of data measured and stored in the PSC process to build optimization decision model. Hu et al. [2] developed an Artificial Neural Network (ANN) prediction model to the range of converting endpoint. Song et al. [3] proposed to extract some laws from lots of production data using the data mining technology, to forecast slag weight of PSC, Song et al. [4] developed two optimal decision making models, respectively, for flux amount and blowing time of S1 period based on combined ANN. Yao et al. [5] developed a model to predict the composition of the slag using partial least squares and ANN methods jointly.

Data-driven model is probably closer to real converting process than mechanism models in theory, meanwhile, the mainly used data-driven method is ANN, in which the optimal number of hidden nodes is problem dependent and unknown in advance. Support vector machine, a set of classification and regression techniques, has played an important role in model building over the past decades. It is grounded in the framework of statistical learning theory and the principles of structural risk minimization [6]. But SVR model is usually built with global data distribution, not considering the local changes of converting process and its consequence to model. Consequently, research on EC-SVR model for copper-matte converting process is important and attractive.

Inspired by the research works mentioned above and the reasons that would cause errors to the forecast model, EC_SVR model are proposed. We use the local data of copper-matte converting process to correct SVR model, two EC_SVR model for slag weight and blowing time of S1 period are developed.

13.2 Support Vector Regression

Suppose we have a training data set $T = \{(x_1, y_1), \ldots, (x_l, y_l)\} \in (X \times Y)$ generated from an unknown probability distribution function $P(x, y)$, where X denotes the space of the input patterns $x_i (i = 1, \ldots, l)$ (e.g. $X = R^n$), for instance, control variable and state variable of matte converting. $y_i \in Y = R$ is a target output, l is the number of sample. In ε-insensitive support vector regression (ε-SVR) [7], our goal is to find an optimization decision function $f(x) = (\mathbf{w} \bullet x) + b$ in a function set $\mathbb{F}$, where the vector $\mathbf{w} \in R^n$ and bias $b \in R$. Based on the structural risk minimization principle, the upper bound of expected risk should be minimized. Here $c(x, y, f) = |y - f(x)|_\varepsilon = \max\{0, |y - f(x)| - \varepsilon\}$ is a ε-insensitive loss function, which has fixed width and symmetrical structure, ε is a pre-selected positive number.

It is a common method to handle nonlinear regression problems by mapping input samples x_i to a high-dimension linear feature space with a nonlinear mapping $\phi(x)$. The linear SVR model is formulated to predict output in the high-dimension feature space.

Nonlinear ε-SVR primal optimization problem can be represented as:

$$\min_{\mathbf{w}\in\mathbf{R}^n,\xi,\xi^*\in\mathbf{R}^l,b\in\mathbf{R}} \frac{1}{2}||\mathbf{w}||^2 + \frac{C}{l}\sum_{i=1}^{l}\left(\xi_i + \xi_i^*\right)$$

$$\text{s.t.}\quad ((\mathbf{w}\bullet\phi(x_i)) + b) - y_i \leq \varepsilon + \xi_i, i = 1,2,\ldots,l$$
$$y_i - ((\mathbf{w}\bullet\phi(x_i)) + b) \leq \varepsilon + \xi_i^*, i = 1,2,\ldots,l$$
$$\xi_i, \xi_i^* \geq 0, i = 1,2,\ldots,l \quad (13.1)$$

The penalty parameter $C > 0$ determines the trade-off between fault sample and model complexity by controlling the punishment degree of error classification sample. ξ and ξ^* are slack variables used to enhance prediction accuracy. The Lagrange function from the primal optimization problem is expressed as

$$L\left(\mathbf{w}, b, \xi^{(*)}\right) = \frac{1}{2}||\mathbf{w}||^2 + \frac{C}{l}\sum_{i=1}^{l}\left(\xi_i + \xi_i^*\right) - \sum_{i=1}^{l}\left(\eta_i\xi_i + \eta_i^*\xi_i^*\right)$$

$$- \sum_{i=1}^{l}\alpha_i(\varepsilon + \xi_i + y_i - (\mathbf{w}\bullet\phi(x_i)) - b)$$

$$- \sum_{i=1}^{l}\alpha_i^*\left(\varepsilon + \xi_i^* - y_i + (\mathbf{w}\bullet\phi(x_i)) + b\right) \quad (13.2)$$

where, $\alpha_i, \alpha_i^*, \eta_i, \eta_i^*$ are nonnegative Lagrange multipliers. The primal constrained optimization problem (13.1) can be solved under the Karush-Kuhn-Tucker (KKT) conditions, the dual optimization problem can be obtained as

$$\min_{\boldsymbol{\alpha},\boldsymbol{\alpha}^*\in\mathbf{R}^l} \frac{1}{2}\sum_{i,j=1}^{l}\left(\alpha_i^* - \alpha_i\right)\left(\alpha_j^* - \alpha_j\right)K\left(x_i, x_j\right) + \varepsilon\sum_{i=1}^{l}\left(\alpha_i^* + \alpha_i\right) - \sum_{i=1}^{l}y_i\left(\alpha_i^* - \alpha_i\right)$$

$$\text{s.t.}\sum_{i=1}^{l}\left(\alpha_i - \alpha_i^*\right) = 0, 0 \leq \alpha_i^*, \alpha_i \leq \frac{C}{l}, i = 1,2,\ldots,l \quad (13.3)$$

In which kernel function $K(x_i, x_j) = \langle\phi(x_i), \phi(x_j)\rangle$ is based on the Mercer's theorem. The solution of the dual problem yields the nonlinear regression function $f(x)$, and b is a constant term

$$f(x) = \sum_{i=1}^{l} \left(\alpha_i^* - \alpha_i \right) K(x_i, x) + b \qquad (13.4)$$

$$b = y_j - \sum_{i=1}^{l} \left(\alpha_i^* - \alpha_i \right) K\left(x_i, x_j \right) + \varepsilon \qquad (13.5)$$

where training points x_i whose $\alpha_i, \alpha_i^* \neq 0$, are referred as support vectors.

13.2.1 Boundary Characteristic Analysis of ε-SVR

ε-insensitive loss tube(ε-tube) of ε-SVR in linear space and high-dimension feature space are shown in Figs. 13.1 and 13.2, respectively.

If the input and output of the training samples (x_i, y_i) lie inside the ε-tube, then $\xi_i^* = \xi_i = 0$. In conjunction with the constraints of Eq. (13.1), we have

$$\varepsilon + \xi_i + y_i - (\mathbf{w} \bullet \phi(x_i)) - b > 0 \qquad (13.6)$$

Fig. 13.1 ε-tube linear space feature of single variable
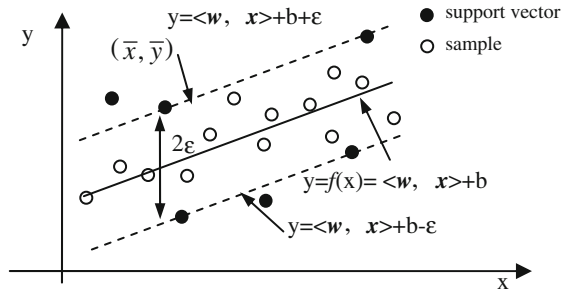
Fig. 13.2 ε-tube space feature in high-dimension feature space
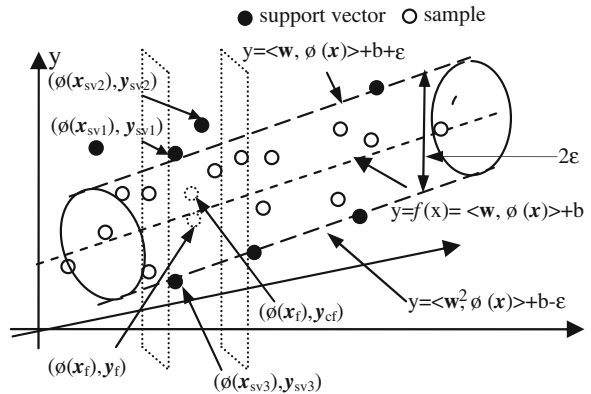
$$\varepsilon + \xi_i^* - y_i + (\mathbf{w} \bullet \phi(x_i)) + b > 0 \tag{13.7}$$

Combining KKT conditions and Eq. (13.2) allows us to conclude that

$$\alpha_i(\varepsilon + \xi_i + y_i - (\mathbf{w} \bullet \phi(x_i)) - b) = 0 \tag{13.8}$$

$$\alpha_i^*\left(\varepsilon + \xi_i^* - y_i + (\mathbf{w} \bullet \phi(x_i)) + b\right) = 0 \tag{13.9}$$

$$\left(\frac{C}{l} - \alpha_i\right)\xi = 0 \tag{13.10}$$

$$\left(\frac{C}{l} - \alpha_i^*\right)\xi^* = 0 \tag{13.11}$$

Combining Eqs. (13.6)–(13.9), we have $\alpha_i^* = \alpha_i = 0$, i.e., the training samples lie inside the ε-tube, which makes no contribution to decision function of regression Eq. (13.4).

If the training samples (x_i, y_i) lie on ε-tube boundary, from Figs. 13.1 and 13.2, we can observe $\xi_i^* = \xi_i = 0$, when $((\mathbf{w} \bullet \phi(x_i)) + b) - y_i = \varepsilon + \xi_i^*$, then $\varepsilon + \xi_i^* + y_i - (\mathbf{w} \bullet \phi(x_i)) - b = 2\varepsilon$. Combining Eqs. (13.8)–(13.10), we have $\alpha_i^* = 0$, $\alpha_i \in (0, \frac{C}{l})$. Similarly, when $\alpha_i = 0$, we have $\alpha_i^* \in (0, \frac{C}{l})$.

If the training samples (x_i, y_i) lie outside the ε-tube, we can observe $\xi_i^* \neq 0$. Combining Eqs. (13.8) and (13.11), we have $\alpha_i^* = \frac{C}{l}$, $\alpha_i = 0$. Similarly, when $\xi_i \neq 0$, we have $\alpha_i = \frac{C}{l}$, $\alpha_i^* = 0$.

This allows us to draw several useful conclusions.

(1) if the training samples (x_i, y_i) lie inside the ε-tube, then $\alpha_i^* = \alpha_i = 0$.
(2) if the training samples (x_i, y_i) lie on ε-tube boundary or lie outside the ε-tube, then both α_i, α_i^* cannot be 0.

As a result of analysis, the training error of ε-SVR is mainly produced by the training sample that lies outside ε-tube boundary. ε-tube of single variable linear ε-SVR in linear space is shown in Fig. 13.1. It depicts the error situation graphically. When the training samples (x_i, y_i) lie inside the ε-tube, these samples do not produce error; while the training samples $(\bar{x}, \bar{y})$ lie outside the ε-tube, error will be produced, which equals $\varepsilon - |\bar{y} - f(\bar{x})|$. It is clear that the local data of predicted sample should be taken into account and a smooth and close ε-tube should be constructed to fit the contour of data distribution, and then we can get the ε-SVR model with small prediction error and good generalization performance.

13.3 Error Correction of Support Vector Regression Model

ε-tube of the traditional ε-insensitive support vector regression have fixed width and symmetrical structure, shown in Fig. 13.2. For the input vector x_f, the regression predicted output y_f can be computed by decision function of regression Eq. (13.4). According to local regression fitting characteristics of the statistical models [8], a good expected regression vector $(\phi(x_f), y_{cf})$ should move with ε-tube constraints toward support vectors $(\phi(x_{sv1}), y_{sv1})$, $(\phi(x_{sv2}), y_{sv2})$, which lies in the local area between hyperplane δ and hyperplane γ, i.e., a good regression vector $(\phi(x_f), y_{cf})$ should be decided by global support vectors and local support vectors in the area of $(\phi(x_f), y_f)$.

From the analysis of Sect. 13.2.1, we found that the support vectors lying outside the ε-tube is the main source of the ε-SVR training error. It will influence the expected output of decision function of regression Eq. (13.4). The farther the distance of the support vector lies outside ε-tube to expected regression vector $(\phi(x_f), y_{cf})$, the less it contributes to decision function of regression, and vice versa. Define the paradigm of one vector in the feature space as $\|(\phi(x), y)\| = \sqrt{(\phi(x), y) \bullet (\phi(x), y)}$, then Euclidean distance of support vector to the regression predict vector $(\phi(x_f), y_f)$ is expressed as:

$$d_2((\phi(x_{sv}), y_{sv}), (\phi(x_f), y_f)) = \sqrt{\|\phi(x_{sv}) - \phi(x_f)\|^2 + (y_{sv} - y_f)^2} \qquad (13.12)$$

where, $(\phi(x_{sv}), y_{sv})$ is the support vector in high-dimension feature space, $(\phi(x_f), y_f)$ is the regression predict vector.

The centre of hypersphere is $(\phi(x_f), y_f)$, which contains k-nearest support vector $(\phi(x_{sv_i}), y_{sv_i}), i = 1, 2, \ldots, k$ around the vector $(\phi(x_f), y_f)$ in high-dimension feature space.

The relationship of space vectors in feature space is shown in Fig. 13.3, where those k-nearest support vectors $(\phi(x_{sv_i}), y_{sv_i}), i = 1, 2, \ldots, k$ create a local support vector set $\Omega = \big\{(\phi(x_f), y_f), (\phi(x_{sv_i}), y_{sv_i}), i = 1, \ldots, k\big\}$.

Fig. 13.3 The effect of local support vector in high-dimension feature space
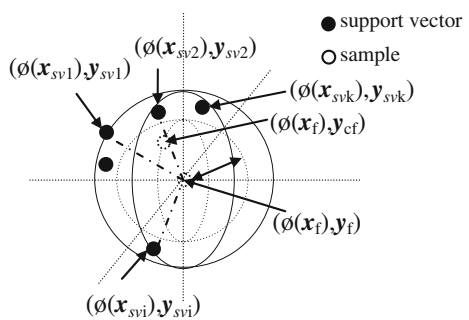
An expected regression vector $(\phi(x_f), y_{cf})$ should lie inside the hypersphere, whose center is $(\phi(x_f), y_f)$ and radius is ε, at the same time, a reasonable criterion for choosing an expected regression vector $(\phi(x_f), y_{cf})$ to minimize the sum of Euclidean distance of $(\phi(x_f), y_{cf})$ to $(\phi(x_f), y_f)$ and local support vector $(\phi(x_{sv_i}), y_{sv_i})$ is proposed.

The objective function is

$$\min_{y_{cf} \in \mathbf{R}} \sqrt{\sum_i^k \left\| \phi(x_f) - \phi(x_{sv_i}) \right\|^2 + (y_{cf} - y_{sv_i})^2}$$

$$\text{s.t} \ -\varepsilon \leq y_{cf} - y_{sv_i} \leq \varepsilon, i = 1, \ldots, k \tag{13.13}$$

The solution of constrained optimization problems Eq. (13.13) is the error corrected predict y_{cf}.

The Euclidean distance $\left\| \phi(x_f) - \phi(x_i) \right\|^2$ can be solved by kernel function $K(x_i, x_j) = \langle \phi(x_i), \phi(x_j) \rangle$ as follows.

$$\left\| \phi(x_f) - \phi(x_i) \right\|^2 = \langle \phi(x_f), \phi(x_f) \rangle + \langle \phi(x_i), \phi(x_i) \rangle - 2\langle \phi(x_f), \phi(x_i) \rangle$$
$$= K(x_f, x_f) + K(x_i, x_i) - 2K(x_f, x_i) \tag{13.14}$$

13.3.1 The Procedure of EC_SVR Model

The details of the error correction of SVR model are shown as follows:

Step 1. Given the training data set T, the parameter ε of ε-SVR is selected by experience, train the ε-SVR model with the parameter of kernel and the regularization coefficient C optimized by tenfold cross-validation.

Step 2. Solve the optimization problem (13.3) by using the training dataset T, compute the ε-SVR decision function of regression (13.4).

Step 3. Get all support vector, create a global support vector set Ω_{sv}

Step 4. Giving the input vector x_f, compute the regression predict y_f by decision function of regression (13.4), then create an implicit regression vector $(\phi(x_f), y_{cf})$ in high-dimension feature space.

Step 5. Find the k-nearest support vector $(\phi(x_{sv_i}), y_{sv_i}), i = 1, 2, \ldots, k$ of implicit regression vector $(\phi(x_f), y_f)$ in the global support vector set Ω_{sv}, create a local support vector set Ω, the Euclidean distance of the nearest support vector to $(\phi(x_f), y_f)$ should be less than or equal to 2ε, otherwise, decrease the k value, i.e., decrease the local support vector number for error correction.

Step 6. Solve the constrained optimization problems (13.13), obtain the error corrected regression predict y_{cf}.

13.4 EC_SVR Model for Copper-Matte Converting Process

There are 318 instances data in the converting lifetime of 2# PSC in a copper smelter. Each instance data contains two slag-forming as stage S1 and S2, two copper making stage as B1 and B2, which has 42 attributes. The attributes in slag forming periods of S1 and S2 are as follows: copper matte content, flux content, slag, blast volume, converting time, oxygen content, copper matte grade, copper in slag, SiO_2 in slag, copper in copper matte, cold material (bed material, indium beryllium, black copper, dust, and cladding), and refining slag. The attributes in periods of B1 and B2 are as follows: blast volume, converting time, oxygen, blister copper, copper in slag, SiO_2 in slag, cold material of B (waste copper, residue, impurities, scrap copper, cladding, dust, bed material, indium beryllium, etc.), and refining slag. The attributes of instance are selected and merged based on the process mechanism of copper matte converting and analysis purpose. Then the samples of 2# furnace in a copper smelter with missing data are eliminated, and good data are used to form an optimal original sample set, which includes attributes as copper matte content, flux content, cold material with plenty abundant copper, cold material with less copper, copper matte grade, converting time, blast volume, oxygen content, slag, Cu in slag.

The value of the data was normalized between 0 and 1. The (Gaussian) radial basis function (RBF) kernel is a popular kernel function used in support vector regression. It is defined as

$$k(x_i, x_j) = \exp(-\|x_i - x_j\|^2/(2\delta^2)) \tag{13.15}$$

Experiments are conducted using the LIBSVM [9] to solve the SVR model, in order to typically evaluate the different performance of regression model.

Root mean square errors (RMSE) are applied as performance indices to evaluate the efficacy of the SVR model fitting, it is defined as

$$\text{RMSE} = \sqrt{\frac{1}{n}\sum_{i=1}^{n}(y_{ti} - y_{pi})^2} \tag{13.16}$$

The Squared Correlation Coefficient (SCC) is chosen as a measure of the model generalization performance [10], it is defined as

$$\text{SCC} = \frac{(n\sum_{i=1}^{N}y_{ti}y_{pi} - \sum_{i=1}^{n}y_{ti}\sum_{i=1}^{n}y_{pi})}{\sum_{i=1}^{n}(y_{ti} - \bar{y}_t)^2\sum_{i=1}^{n}(y_{pi} - \bar{y}_p)^2} \tag{13.17}$$

where y_{ti} represents the target value (observation value) of the ith sample; y_{pi} is the prediction value of the ith sample; $\bar{y}_t$ and $\bar{y}_p$ denote the mean value of y_t and y_p, respectively.

13.4.1 EC_SVR Model for Slag Weight and Blowing Time

Slag weight in slag forming periods is an important variable for copper matte converting, and its accurate prediction value can help operators remove slag and cast slag correctly, which will improve blister copper quality and decrease copper content in slag. Meanwhile, the blast system influences furnace life, productivity, melts temperature and throughput a lot. Increasing blasting intensity and oxygen ratio will shorten converting time, but higher melt temperature will accelerate the consumption of refractory lining. Blast time control is the last operation of slag forming periods S1, deficiency of blast time or too much will both lead to more copper lose in slag [1]. Therefore, developing the prediction model of Slag Weight and blast time are important to enhance the copper matte economic indictor.

During one furnace life, the working conditions (e.g., lining corrosion, Slagging on tuyere) of PSC will change according to converting numbers. The accurate prediction of slag output and blowing time for one specific period S1 have stronger correlation with neighboring converting process, which shows apparent local properties and provide practical basis for SVR model error correction.

Copper-Matte Converting Process is carried out in the cylindrical PSC. Output of slag is closely related to matte grade, copper content, flux content, cold material content, blast velocity, oxygen ratio of air, blast time, etc. The optimal decision problem of blast time is related to matte grade, copper content, flux content, cold material content, blast velocity, oxygen ratio of air, etc. So we choose 8 variables of S1 period including copper matte content, flux content, low copper cold material content, high copper cold material content, matte grade, blowing rate, and oxygen content to build slag output forecasting model. Similarly, 7 variables are chosen to build blowing time forecasting model, including all mentioned above except blowing rate. 218 sets data selected from 318 at random are used as training data sets, the rest 100 sets are used as testing data set to assess the regression model of slag output and blowing time.

To make a comparison, between the ε-SVR and EC_SVR, we derive RMSE as fitting degree index, SCC as model generalization ability index. The results are shown in Table 13.1.

As shown in Table 13.1, the performance indicators of EC_SVR can significantly improve performance of Copper-Matte Converting Process, decrease the RMSE from 40.35 to 15.91 % and from 36.08 to 12.72 %, increase the SCC from 29.19 to 33.70 % and from 43.01 to 45.52 %, in predicting slag weight and blowing time of S1 period, respectively.

Table 13.1 Performance compared between EC_SVR and ε-SVR

	RMSE		Performance comparison	SCC		Performance comparison
	ε-SVR	EC_SVR	RMSE the rate of change (%)	ε-SVR	EC_SVR	SCC the rate of change (%)
Slag weight	0.4035	0.1591	↓60.57	0.2919	0.3370	↑15.45
Blowing time	0.3608	0.1272	↓64.74	0.4301	0.4552	↑5.835

13.5 Conclusion

An error correction method is proposed, which is proved to be effective in the SVR model. Two EC-SVR models of slag weight and blowing time in S1 period of a smelter in China are developed, they are proved to be able to improve the performance indicators significantly, which can also be applied to the optimization decision making problems of other complex industrial process.

References

1. King MJ, Sole KC, Davenport WG (2011) Extractive metallurgy of copper, 5th edn. Elsevier, Oxford
2. Hu Z, Mei C, Peng X (2002) Intelligent decision and endpoint prediction system for PS furnace matte converting process. Nonferrous Metals-Beijing 54(1):40–42
3. Song Y, Peng X, Tang Y, Tang L, Wang W (2007) Forecast slag weight of copper matte converting in ps converter based on data mining. Control Instrum Chem Ind 34(2):17–19
4. Song Y, Peng X, Dong W, Hu Z (2011) Data driven optimal decision making modelling for copper-matte converting process. J Comput Inf Syst 7(3):754–761
5. Yao JF, Mei C, Peng XQ, Zhou AL, Wu DH (2002) Intelligent decision support system of operation-optimization in copper smelting converter. J Central South Univ Technol 9 (2):138–141 (in Chinese)
6. Vapnik V (2000) The nature of statistical learning theory. Springer, New York
7. Smola AJ, Schölkopf B (2004) A tutorial on support vector regression. Stat Comput 14 (3):199–222
8. Amberg M, Lüthi M, Vetter T (2010) Local regression based statistical model fitting. Pattern Recognition. Springer, Berlin, pp 452–461

9. Chang CC, Lin CJ (2011) LIBSVM: a library for support vector machines. In: ACM transactions on intelligent systems and technology (TIST) 2(3):27
10. Ni YQ, Hua XG, Fan KQ, Ko JM (2005) Correlating modal properties with temperature using long-term monitoring data and support vector machine technique. Eng Struct 27 (12):1762–1773

Chapter 14
Modeling Based on the Extreme Learning Machine for Raw Cement Mill Grinding Process

Xiaofeng Lin and Jinbo Liang

Abstract Vertical grinding mill is the main grinding equipment for the new-type dry cement raw meal production, raw material grinding process in cement industries accounts for approximately 50–60 % of the total energy consumption. The dynamic characteristics of the variables in the raw material vertical mill grinding process are strongly coupled, nonlinear, and large time lag. The process of parameter adjustment requires too much human intervention, it is difficult to establish a precise mathematical model. To address these problems, we use extreme learning machine network, establish production quotas predictive model of cement raw material vertical mill grinding process, combined with the cement raw material vertical mill grinding process data obtained from a cement plant, the model is trained and tested. Experimental results show that the proposed modeling method is effective to achieve the online estimation of the key indicator parameters for the vertical mill grinding process, lying foundation for parameters optimization online of the vertical mill grinding production process, and providing reference value for the energy consumption reducing.

Keywords Vertical mill · Extreme learning machine · Raw meal fineness · Grinding pressure difference · Data pre-processing

14.1 Introduction

Vertical cement mill (vertical mill) is a machine that plays an important role in the raw meal production process of the new-type dry cement, and it is a set breakage, drying, grinding, transport in one [1]. Raw material grinding process is a vital and energy consumption link in the cement production. According to statistics,

X. Lin · J. Liang (✉)
School of Electrical Engineering, Guangxi University, No. 100 DaXue Road, Nanning, China
e-mail: ljinbony@126.com

raw material grinding process account for approximately 50–60 % of the total production cost [2].

Consequently, reducing the energy consumption in the raw material grinding process, improving the stability of the manufacture process and quality of the products, adjusting the technological index timely and objectively is needed urgently, so as to upgrade the production efficiency and optimize the production process.

Due to the cement-grinding process production has the characteristics of strong coupling, multivariables, and nonlinearity, it is difficult to build a precise math model for it. The key parameter is unable to detect online, and the setting of the parameters is mainly depend on the workers' experience, which makes it a subjective and hysteretic process.

With the development of the intelligent control and the control demand of some complicated systems, soft measurement technology rise sharply, it involved in many fields, such as petrochemical and environmental protection. Though the forward neural networks have many advantages, which make it widely used in the soft measurement and modeling, it has drawbacks of falling into local minima and slow learning rate [3].

Extreme learning machine (ELM) is a learning method for single-layer forward neural networks (SLFNS) proposed by Huang et al. [4]. It avoids the problems in the gradient descent learning method likes suffering from local minima, long training time, and so on. It ensures whether the network has good generalization performance, and the learning time is improved significantly as well.

To address the problems in cement-grinding process production, the ELM is applied to model the process of raw cement vertical mill grinding, and the measured data obtained from a cement plant is used to train and test the model. The results show that the method proposed is effective.

14.2 The Process of Raw Cement Vertical Mill Grinding

The grinding process of raw cement vertical mill consists of grinding and powder selecting [5]. First stage: The mixture material is sent to the feed throat by the feeding belt machine, entering the grinding machine from the feeding pipe, and falling to the center of the millstones. Then, under the thrust between the material and the force of centrifugal, the mixture material moves to the grinding layer. Second stage: After grinded, the mixture material keep moving to the edge of the millstone until it comes across the heat gas which come from the wind ring. The large partial of powder falls to the bottom of the machine. Then, the outer-circulation makes it back to the grinding machine. Conversely, the fine powder is taken up by high-speed stream. The unqualified fine powder will drop-down the millstones and continue to grinding after the powder selected by the separator. And the qualified fine powder is wind discharged by vertical mill grinding machine. After cyclone separator measures the selected powder and when the requirements of fine
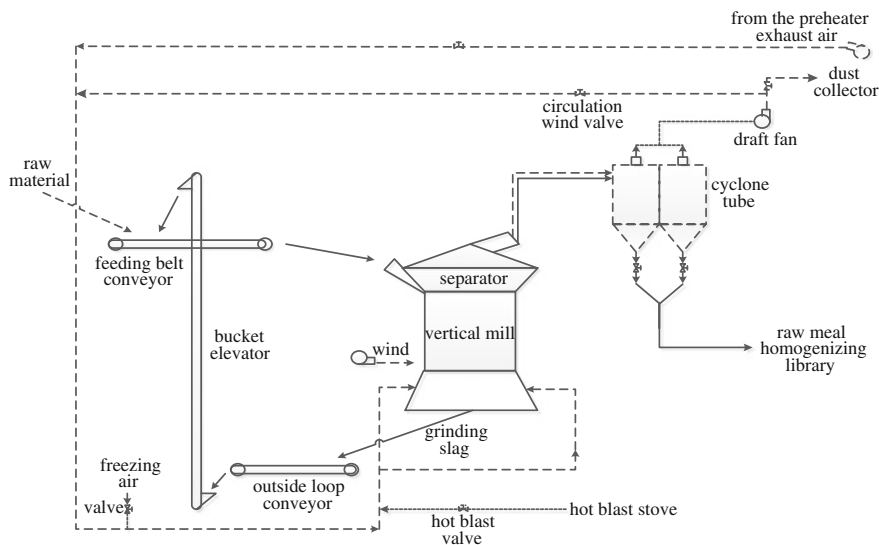
Fig. 14.1 Raw material vertical roller mill grinding circuit

powder is met, it is collected by the dust collector for the finished product of raw
material. The process is shown in Fig. 14.1.

In the production process of raw material grinding, A timely adjustment control
on changes of material and equipment operating parameters is an essential part of
the system to ensure operation stable. The main factors affecting the stability of the
system [6]:

(1) Feeding quantity. A stable volume of feed mill is prerequisite for differential
pressure within the grinding. When volume of feed is insufficient, material
layer on the disk becomes unstable; while amount of wind is certain, then
pressure differential will be reduced. When feeding excessive, "plow material"
phenomenon will appear on the disk, not only easily leads to "full grind," but
will also make pressure differential rise within the grinding.

(2) Feeding air temperature. The high temperature make the material loose, the
material is thin layered, feedback increased, and thus the pressure inside the
mill increased; On the contrary, the material moisture will be larger, grinding
and separator efficiency will be reduced, and it will reduce the pressure inside
the mill, so output is affected.

(3) Grinding pressure. Too small grinding pressure is not sufficiently for finely
grounding the material which results in an increase amount of slag spit and
higher grinding efficiency, as well as power consumption increases, which is
easy to cause vibration.

(4) Separator speed. The speed of the separator directly affects the raw material
fineness index. Either separator speed is too large or too small, it will directly
affect the quality of the final collection of the raw material grinding particles.

(5) Circulating air valve opening. Size of the wind also directly affects the raw material fineness index. Adjusting the amount of wind mill is generally circulating the air through the control valve opening to achieve.

From the above, we can see that the two most important quality evaluations are the mill pressure and raw material fineness in the entire vertical mill grinding process. The size of the raw materials fineness directly affects the calcinations of the subsequent cement. Factors that affect the two key indicators, pressure inside the mill and raw material fineness, are feeding quantity, temperature into the mill, grinding pressure, separator speed, and circulating air valve opening. Therefore, it is regarded as a control variable.

14.3 Modeling of Production Index for Vertical Mill Raw Material Grinding Process

14.3.1 Extreme Learning Machine

The network topology of the ELM is shown in Fig. 14.2.

As named in Huang et al. $a_i, b_i, i = 1, \ldots, L$. is called the hidden layer input parameters of the neural network; The ith column of a_i, b_i are the ith hidden node output with respect to inputs parameters. $\beta_1, \ldots, \beta_i, \ldots, \beta_L$ is called the hidden layer output matrix. $x_j (j \in 1, \ldots, n)$ is the number of input neurons. L denotes the number of hidden layer neurons. $o_j (j \in 1, \ldots, n)$ denotes the number of output neurons.

The core learning method of the ELM, we can summarize as three-step learning model as following:

Given a training set $\{(x_i, t_i)\}_{i=1}^{N} \subset R^n \times R^n$, hidden node output function $g(\bullet)$, and the number of hidden nodes L. we can do

First: Assign randomly hidden node parameters $a_i, b_i, i = 1, \ldots, L$.

Second: Calculate the hidden layer output matrix $H = g(a, b, x)$

Fig. 14.2 The architecture of extreme learning machine network

n input nodes L hidden nodes   output node
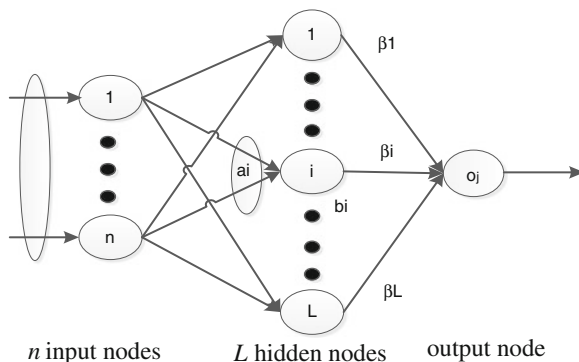
Finally: Calculate the output weight (β): $\beta = H^{-1} \bullet T$ where $T = \{t_j\}_{i=1}^{N}$, H^{-1} is the Moore-Penrose generalized inverse of hidden layer output matrix of the neural network.

Consider a supervised learning problem. For example, we have the training sample set with N groups of samples $\{X, Y\} = \{x_i, y_i\}_{i=1}^{N}$, where $x_i \in R^{n_i}$, $y_i \in R^{n_o}$ is a regression tasks, where n_i and n_0 are the dimensions of input and output data, respectively [7].

An obvious characteristics of extreme learning machines is that the parameters of the hidden mapping functions can be randomly set, according to any continuous probability distribution on $(-1, 1)$. The only free parameters that need to be optimized are the output weights between the hidden neurons and the output nodes. By doing so, training extreme learning machines is equivalent to solving a regularized least squares problem.

In the first, assume that the numbers of hidden layers neurons is n_h. We denote by $h(x_i) \in R^{1 \times n_h}$ the output vector of the hidden layer with respect to the x_i, $\beta \in R^{n_h \times n_o}$ is the output weights that connect the hidden layer with the output layer. Then, the outputs of the network are given by

$$f(x_i) = h(x_i) \bullet \beta, i = 1, \ldots, N. \tag{14.1}$$

In the second, minimizing the sum of the squared losses of the prediction errors, calculate the output weights.

$$\min_{\beta^{n_h \times n_o}} \frac{1}{2} \|\beta\|^2 + \frac{C}{2} \sum_{i=1}^{N} \|e_i\|^2 \tag{14.2}$$
$$\text{st}: h(x_i) \bullet \beta = y_i^T - e_i^T, \quad i = 1, \ldots, N.$$

In the formulation of (14.2), the first item in the objective function is a regularization item which controls the complexity of the model, $e_i \in R^{n_o}$ is the error vector with respect to the ith training pattern, and C is a penalty coefficient on the errors of training process.

To eliminate the constraint conditions of objective function, obtain the following equivalent unconstrained optimization problem.

$$\min_{\beta \in R^{n_h \times n_o}} L_{\text{ELM}} = \frac{1}{2} \|\beta\|^2 + \frac{C}{2} \sum_{i=1}^{N} \|Y - H \bullet \beta\|^2. \tag{14.3}$$

where $H = [h(x_1)^T, \ldots, h(x_N)^T]^T \in R^{N \times n_h}$.

The above problem is widely known as regularized least squares. Set the gradient of ELM with respect to β to 0. We can get the formulation

$$\nabla L_{\text{ELM}} = \beta + CH^T(Y - H \bullet \beta) = 0. \tag{14.4}$$

If the number of rows of H are more than the number of columns, and H is of full column rank, which is usually the case where the number of training patterns are greater than the number of the hidden neurons, then

$$\beta^* = \left(H^T H + \frac{I_{n_h}}{C}\right)^{-1} H^T Y. \tag{14.5}$$

where I_{n_h} is an identity matrix of dimension n_h.

On the contrary, If H have more columns than rows, and is of full row rank. HH^T is invertible matrix. In this case, β may have the number of solutions without end. So we confine β to be a linear combination of the rows of $H : \beta = H^T \alpha$. ($\alpha \in R^{N \times n_o}$). Multiplying both side of formulation (14.4) by $(HH^T)^{-1} H$. We have

$$\alpha + C(Y - HH^T \alpha) = 0, \tag{14.6}$$

$$\beta^* = H^T \alpha^* = H^T \left(HH^T + \frac{I_N}{C}\right)^{-1} Y. \tag{14.7}$$

where I_N is a dimension of N identity matrix.

Accordingly, compared to the hidden neurons, in the case where training patterns are plentiful, we use the formulation (14.5) to calculate the output weights, otherwise we use the formulation (14.7).

14.3.2 Data Pre-processing

According to the data form which the actual grinding process of a cement plant of 5000 t/d production line is gathered. Those records data include online and offline testing data. The original data collected from the cement plant cannot be used directly. It must be preprocessed.

First, subjective error must be eliminated using the way of limiting amplitude to eliminate the data which is over the amplitude according to the variable scope of operation in the process of production. And the average value is greater than three times the standard deviation the data; Second, For the random error, the data were smoothed by using seven point linear smoothing method. Algorithm is as follows:

(1) For the N-dimensional vector $x = (x_1, x_2, \ldots, x_n)^T$, Standardization of original data is as follows:

$$x_{ij}^* = \frac{x_{ij} - \overline{x_i}}{\sqrt{S_{ij}^*}}, \overline{x}_i = \frac{1}{n}\sum_{i=1}^{n} x_{ij}, S_{ij}^* = \frac{1}{n-1}\sum_{i=1}^{n}(x_{ij} - \overline{x_i})^2 \tag{14.8}$$

(2) Calculated correlation matrix R

$$R = \frac{1}{n-1}X^{*T}X^* \tag{14.9}$$

where X^* is a standardized data matrix, X^{*T} is the transpose.
(3) Calculating a correlation matrix (R) of the eigenvalues (λ_i) and the corresponding eigenvectors orthogonal unit. Variance contribution rate is the main ingredient.

$$g_i = \lambda_i \Big/ \sum_{i=1}^{m} \lambda_i \times 100\,\% \tag{14.10}$$

Accumulated variance contribution rates are as follows:

$$\sum_{i=1}^{p} g_i = \sum_{i=1}^{p} \lambda_{i_i} \Big/ \sum_{i=1}^{m} \lambda_i \times 100\,\% \tag{14.11}$$

After data processing, The part of the data shown in Table 14.1.

14.3.3 Simulation Results and Analysis

Through the above analysis, online index which includes the feed quantity(t/h), separator speed (rpm), circulating air valve opening (%), feeding air temperature (°C), and grinding pressure difference (kpa), offline data is raw meal fineness

Table 14.1 Part of the data of raw material production process of cement plant

Circulating air valve opening (%)	Separator speed (rpm)	Feeding air temperature (°C)	Feeding quantity (t/h)	Raw meal fineness (%)	Grinding pressure difference (kPa)
40	39.3	156	435	22.63	6045
40	39.3	154	435	22.08	5920
40	39.3	160	435	24.06	5836
45	39.5	163	435	21.99	5943
45	39.5	154	440	21.34	5862
45	39.5	152	440	20.65	5772
45	39.5	156	440	21.39	5861
40	39.5	158	440	21.76	5731
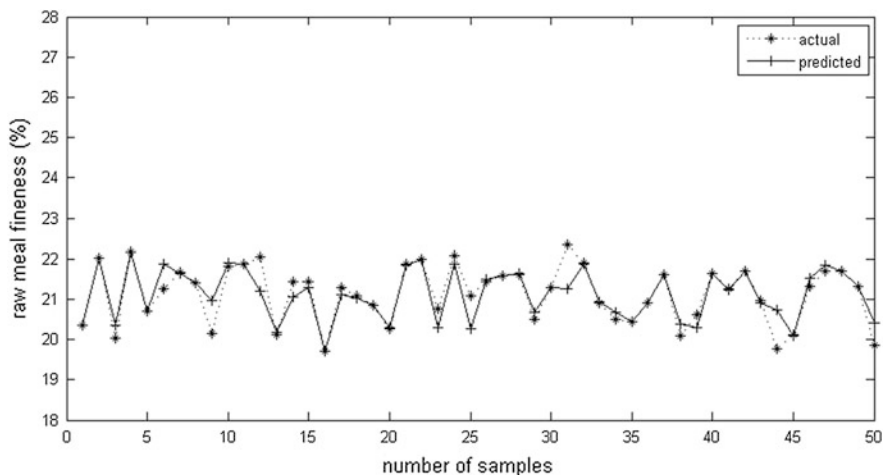
Fig. 14.3 Generalization curve of raw meal fineness of ELM prediction model

index (%). The two indexes of mill pressure difference and raw meal fineness as the output parameters of index prediction model in the process of roller mill grinding; feeding quantity, the temperature of the ground wind, the rotating speed of separator, and the valve opening cycle wind are the input variables.

We take 450 groups of valid data which are divided into training data set and test data set according to the ratio of 8:1; 400 groups of data are the training data, 50 groups of data are test data. Each group of data contains six data, the former four data are used as the network inputs, they represent the physical meaning as follows: The valve opening cycle wind, the rotating speed of separator, the temperature of the ground wind, and grinding feed rate; the last two data are used as the network inputs, they represent the physical meaning namely: Raw meal fineness and the differential pressure within the vertical grinding machine.

Modeling based on ELM for raw cement mill grinding process. After initialization, the network's relevant parameters are as follows: The hidden layer parameters are 50, after training and prediction of ELM network model in a loop. The raw meal grinding fineness and the pressure differential fitting diagrams are as following (Figs. 14.3 and 14.4).

The same data and network structure were used to establish the BP network model. The related parameters of the network are as follows: The hidden layer nodes is 50, the input neurons is 4, the output neurons is 2, the network learning rate is 0.01, the error precision is 0.05, and the largest number of training is 2000 times. The performance comparison of the two kinds of model is shown in Table 14.2.

Through the Table 14.2, we can see that ELM has the index of faster speed and smaller error compared with the BP model. ELM can reflect the mapping relationship among the key process indicators in the process of raw cement vertical mill grinding.
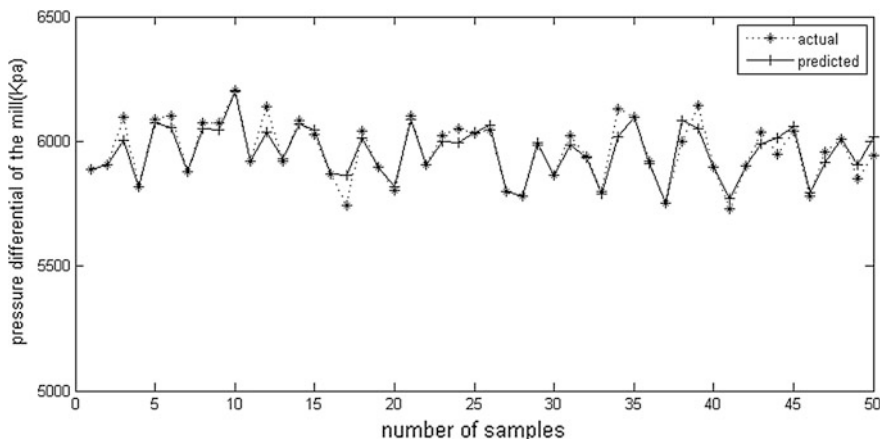
Fig. 14.4 Generalization curve of pressure differential of the mill of ELM prediction model

Table 14.2 The performance comparison of ELM and BP model

Items	ELM	BP
RMSE of raw meal fineness	0.0093	0.0148
RMSE of grinding pressure	1.9728	2.7322
The maximum relative error of raw meal fineness	7.21 %	9.95 %
The maximum relative error of grinding pressure	3.48 %	7.31 %
Training time	0.33 s	50.00 s
Number of iterations	10	234

14.4 Conclusion

The raw material grinding in the cement mill for production of cement is one of the most energy-demanding processes in cement industry. In cement plants, 50–60 % of the total energy consumption is due to grinding of raw materials. The process of parameter adjustment requires too much of human intervention. Online measurement of quality parameters of cement fineness is crucial for the proper quality maintenance. And it will optimize the energy consumption for the mill. In this paper, extreme learning machine learning methods establishment of a raw material vertical mill grinding index prediction model for online measurement quality parameter is used. By using the data of online and offline variables from vertical mill grinding cement raw material production process, tests of records in a cement plant for the ELM model training and testing are obtained. Experimental results show that the method is effective. It can reflect the mapping between the key process indicators of cement raw material vertical mill grinding production process. It is observed that the model based on the extreme learning machine holds good promise to be implemented online for real-time estimation of cement fitness and

grinding pressure which will certainly help the plant operators in maintaining proper cement quality and in reducing energy losses has a certain reference value.

References

1. Xiao ZM, Li JL (2006) Cement technology. Chemical Industry Press, Beijing (in Chinese)
2. Liu ZJ (2005) The new dry cement technology. China Building Materials Industry Press, Beijing (in Chinese)
3. Ajaya KP, Hare KM (2013) A hybrid soft sensing approach of a cement mill using principal component analysis and artificial neural networks. In: IEEE international advance computing conference (IACC), pp 713–718
4. Huang GB, Zhu QY, Siew CK (2006) Extreme learning machine: theory and applications. J Neuron-Comput 70:489–501
5. Chen SL, Zhao CF (2006) Crushing and grinding of cement production technology and equipment. Chemical Industry Press, Beijing (in Chinese)
6. Zhou ZL, Zhou JY (2009) Cement grinding process and equipment. Chemical Industry Press, Beijing (in Chinese)
7. Huang G, Jatinder ND, Song SJ (2014) Semi-supervised and unsupervised extreme learning machines. IEEE Trans Cybern 44(12):2405–2417

Chapter 15
The Analysis of Lunar Environment Suitability

Haiyuan Yue, Yang Jia, Zhiying Wang, Fan Yang and Xilun Ding

Abstract According to the lunar surface DEM (digital elevation model) data, combined with the various constraints of rover, such as the terrain, illumination, obstacles, mobile performance, the areas which can work on were analyzed and were expressed as different suitability. The terrain suitability, temperature suitability, illumination suitability, energy suitability, and communications suitability of the lunar surface are introduced at first. Then a comprehensive suitability evaluation was analyzed by applying the fuzzy logic method. The lunar surface environment was analyzed more comprehensively. Suitability will provide the basis for lunar teleoperation.

Keywords Lunar · Environment · Suitability · Terrain · Temperature · Illumination · Energy · Communication

15.1 Introduction

Due to the complexity of the lunar surface environment, the safety and reliability of rover in the lunar surface are significant. Teleoperation center in the earth needs to analyze and assess the environment around the rover rapidly, according to both rover features and the environment around the rover. We can obtain the surrounding workable environment, supplying support for the teleoperation task decision, according to the suitability of the lunar surface environment analysis.

H. Yue (✉) · F. Yang · X. Ding
Beihang University, Beijing, China
e-mail: haiyuan_yue@me.buaa.edu.cn

Y. Jia
China Academy of Space Technology, Beijing, China

Z. Wang
Harbin Institute of Technology Shenzhen Institute, Beijing, China

Environmental analysis mainly focused on the analysis of the terrain at present [1]. Researchers design the path planning algorithm through the information of the terrain. Some researchers analyze the traversability of terrain taking account of the four indicators of the terrain like placing safety, traversing safety, stepped safety, and roughness analysis, the same used in the path planning [2]. A popular model is the digital elevation model (DEM) [3]. DEMs are grid maps storing the overall terrain height of a certain metrical patch (e.g., 1 m × 1 m). By considering height differences between neighboring cells, traversability scores can be computed [3, 4].

Most of researchers consider only the terrain suitability during the environmental suitability analysis. Otherwise, the lunar surface and other planetary environments are complex. Not only the terrain, but also the characteristics of the planetary environment, like the illumination, temperature, energy, and communications of the lunar surface integrated are all required [5, 6]. In this paper, based on the digital elevation model of the moon, five aspects of the terrain, illumination, temperature, energy and communication suitability analysis are made, comprehensive environmental analysis model are got which can obtain a more accurate work area.

15.2 Analysis of Suitability

Suitability is raised to characterize the suitable work area of the lunar surface. In order to reduce the workload of the follow-up analysis, first, image from satellite with high resolution is analyzed. The environment suitability is estimated crudely. Then online collected image, whose resolution is lower, is estimated. According to the size of the robot and obstacle clearance capacity, DEM data are analyzed, setting a threshold to exclude large elevation values n a block of topographic maps, from all directions through the obstacles. Concavo convex obstacles are considered together. For example, a deep crater is considered as a high obstacle, the robot cannot traverse. Suitability values can be expressed as nonthrough, and marked by corresponding colors.

This paper studies the suitability based on the special nature of the planet environment. After the obstacle coarse filter, DEM data will be analyzed in five aspects, which are terrain suitability, illumination suitability, temperature suitability, energy suitability, and communication suitability. Also a comprehensive suitability evaluation will be analyzed.

To analyze the suitability of the environment, the DEM data are partitioned into several grids. The method of grid size setting is as follows. First the map is divided into several squares in the size of circumscribed square of the rover body in a horizontal plane projection, and then subdivided into 3 × 3 small grid. The dividing method can get the accurate analysis of the state before and after the rover movement. The division of the grid is shown in Fig. 15.1. In the grid of the size of the rover body, the rover body can pivot turn, oriented in any direction without having to get out the grid. In this paper, the analysis of the suitability can be

Fig. 15.1 Division of the grid
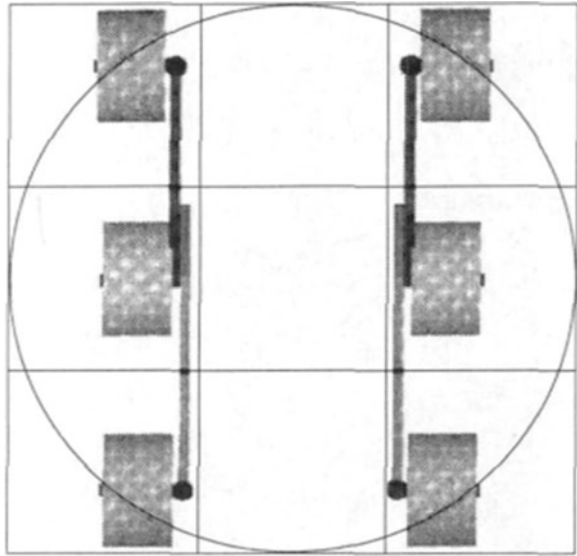
analyzed in eight directions, moving in different directions as shown in Fig. 15.2, respectively. The following section is analyzed on the basis of division in such grid.

15.2.1 The Terrain Suitability

The terrain suitability refers the description of the traversability of the terrain and the mobile performance of the rover.

Terrain suitability analysis not only concerned about the terrain data, but also the performance of the rover about the climbing obstacle capability. The static, climbing, obstacle, and roughness are all considered to analyze terrain suitability [2].

Static suitability is the suitability of the rover stationary placing.

Fig. 15.2 Map division and the direction of moving
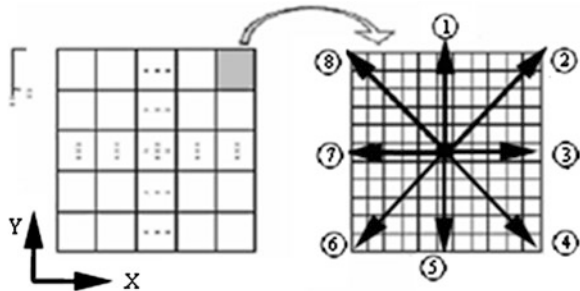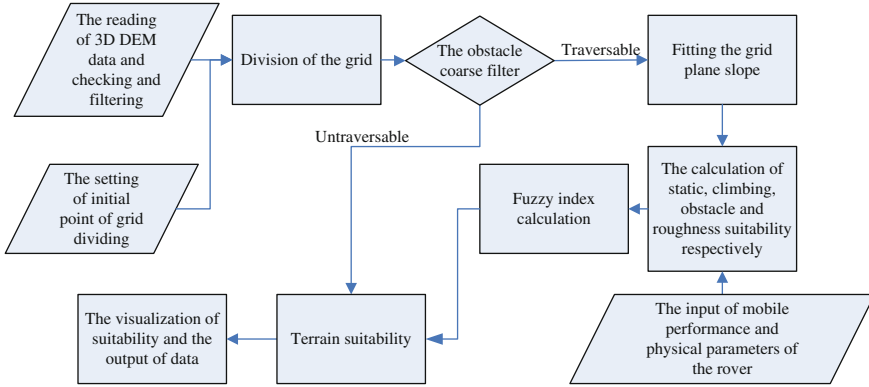
Fig. 15.3 The flowchart of terrain suitability

Climbing suitability is the suitability of the rover moving. Slope is an important factor affecting the safety of the rover, that represent the climbing ability of the rover.

Obstacle suitability is the safety of the rover stepping over the obstacle. This is a rover characterization of the obstacle capability.

Roughness suitability is the roughness of the terrain, when rover walk in a rough terrain, the roughness becomes an important factor (Fig. 15.3).

15.2.2 The Illumination Suitability

Illumination suitability describes the analysis of the terrain illumination shadows and the conditions for the camera imaging. The normal work of the rover like the cameras is influenced by the illumination. The illumination needs be considered to acquire a more accurate workable area.

First, the direction of incidence of the sun can be determined by ephemeris. Combined the position and orientation of the rover, with the position and attitude of the camera, front lighting or back lighting of the camera can be determined. The camera facing the sun is considered as backlight. If the camera is at backlight, then the illumination suitability is marked as not suitable. If the grid is a shaded area, it also is marked as not suitable. Assuming that the camera will receive the reflected light intensity I, the camera photosensitive threshold is $(I_{\min}, I_{\max})$, then the illumination suitability is calculated as follows:

$$\tau = \frac{I - I_{\min}}{I_{\max} - I_{\min}} \tag{15.1}$$
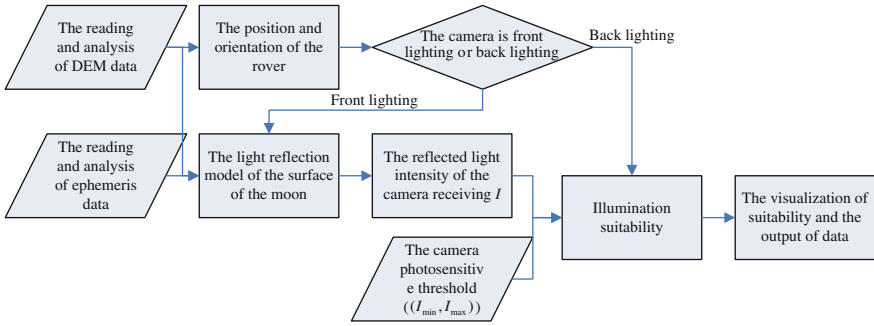
Fig. 15.4 The flowchart of illumination suitability

where τ is the illumination suitability. If $I \geq I_{max}$ or $I < I_{min}$, the illumination suitability of the area is unsuitable. Whatever the value of τ bigger than 1 or smaller than zero, the illumination suitability of the area is unsuitable. The values from 0 to 1 represent different illumination.

The calculation flowchart of Illumination suitability is shown in Fig. 15.4.

15.2.3 The Temperature Suitability

The temperature suitability describes the survival and adaptability of the rover in the lunar surface concerning the temperature condition of lunar surface.

The calculations of the temperature suitability need to determine the shadow area of the terrain. The shaded area can be considered as unsuitable and labeled unfit. The rest area is calculated based on the temperature indicator. First, temperature T in the latitude and longitude coordinates (l, b) is calculated. Then assume that the highest temperature which the rover can bear is T_{max}, the lowest temperature is T_{min}, and the regulating temperature which can be obtained according to the power balancing thermal is ΔT. The temperature suitability is calculated as follows:

$$H = \left| \frac{T - \Delta T}{T\max} \right| \tag{15.2}$$

where H represents the high temperature factor. When $H \leq 1$, the rover can work; when $H > 1$, the rover can't work.

$$L = \left| \frac{T\min}{T + \Delta T} \right| \tag{15.3}$$

where L represents the low temperature factor. When $L \leq 1$, the rover can work; when $L > 1$, the rover can't work.
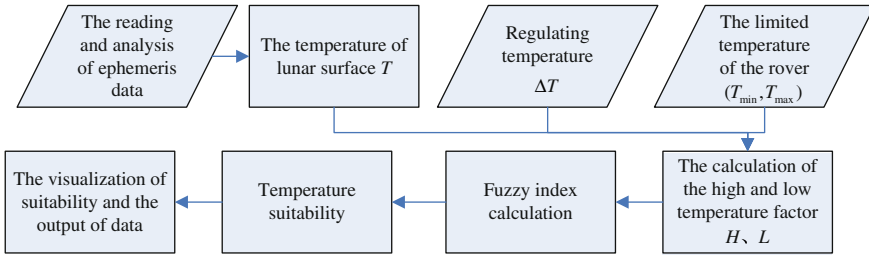
Fig. 15.5 The flowchart of temperature suitability

Choose the larger one from the H and L as the final temperature suitability value. When its value is greater than 1 that does not work and less than or equal to 1 can work. The suitability becomes bad from small to large.

The calculation flowchart of temperature suitability is shown in Fig. 15.5. The environment temperature in the lunar has a great impact on the rover's normal work. The temperature suitability can be got by analyzing the current temperature, combined with the rover's thermal system, to ensure the normal operation of the device.

15.2.4 The Energy Suitability

The energy suitability describes the analysis of the solar wing energy output capacity, combined the terrain around the rover, under the conditions of maintaining the current state of the rover's solar wing. Assuming that the original energy of the battery at the time is P_0, the maximum capacity is P_{max}, p_g is the output energy of the solar wing, P_i is the power demand. Then the energy suitability is expressed as

$$\tau = \frac{P_g + P_o - P_i}{P_{max}} \tag{15.4}$$

where τ is the continuous value between 0 and 1.

The calculation flowchart of energy suitability is shown in Fig. 15.6. In order to ensure that the energy requirements can be satisfactory, the analysis of the energy suitability is needed. We can determine whether this field can satisfy the energy demand of rover, based on the analysis of the energy suitability.
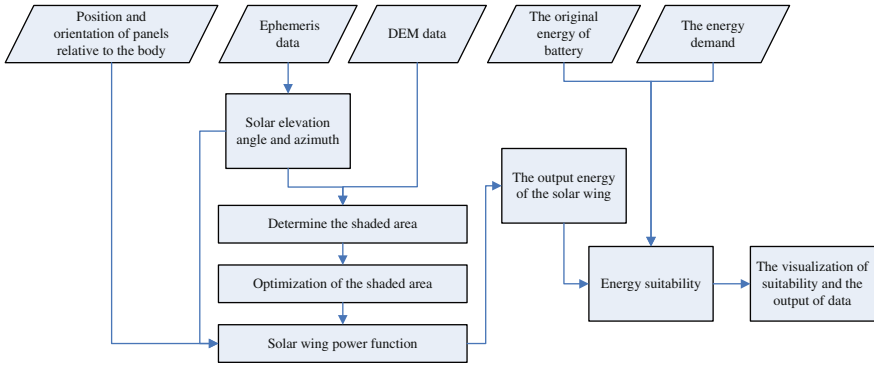
Fig. 15.6 The flowchart of energy suitability

15.2.5 The Communication Suitability of Communication

The communication suitability describes the analysis of the communication condition of the omni directional and directional antenna, combined the surrounding terrain of the rover and ephemeris, under the conditions of maintaining the current state of the rover

Calculated by the ephemeris, when the elevation angle is less than 0 or completely obscured, the communication suitability is labeled as unsuitable. Then the communication suitability is expressed as

$$Q = 1 - \frac{\alpha - \alpha_{shadow}}{\alpha} \tag{15.5}$$

where Q is the communication suitability, α is the communication angle, α_{shadow} is the obscured angle. When Q is less than 0, the field is not suitable. When the value of Q is between 0 and 1, it indicates different suitability.

The calculation flowchart of communication suitability is shown in Fig. 15.7. The analysis of communication is in order to analyze the influence of environment on the rover's communication.

15.2.6 The Comprehensive Suitability

Comprehensive suitability considers the above five factors, analyzing the environment in different modes of operation comprehensively.

Comprehensive suitability is based on five aspects like terrain, illumination, temperature, energy, and communication suitability which combines the demand for specific tasks or work mode by several fuzzy analysis algorithm to obtain the
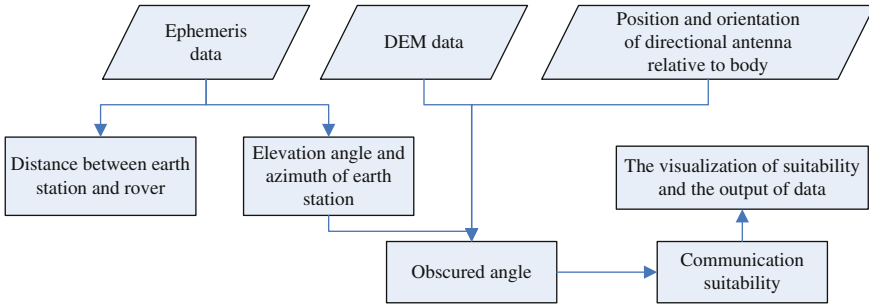
Fig. 15.7 The flowchart of communication suitability

best comprehensive suitability, which can be the comprehensive evaluation criteria for the suitability of the rover.

The fuzzy logic method is introduced as follows.

Assume that $f_{\text{fuzzy}}(X, Y)$ is the function of the fuzzy analysis algorithm considering the X and Y at the same time. The basic idea of the fuzzy analysis algorithm is:

First, fuzzy subset of two input and single output system is set up. Two inputs like A and B can be divided into several set, like $A = \{A_1, A_2, A_3\}$; $B = \{B_1, B_2, B_3\}$, output $C = \{C_1, C_2, C_3, C_4, C_5\}$.

Then the fuzzy rules are established, as shown in the following Table 15.1.

Where if input is A_1 and B_1, then output is C_1 and so on. Using fuzzy analysis method repeatedly based on above algorithm, the comprehensive suitability can be got.

The comprehensive suitability function is expressed as

$$F = f_{\text{fuzzy}}(f_{\text{fuzzy}}(f_{\text{fuzzy}}(f_1(X_1), f_2(X_2)), f_{\text{fuzzy}}(f_3(X_3), f_4(X_4))), f_5(X_5)) \qquad (15.6)$$

where $f_i(X_i)$ represents the function of the different suitability; X_i represents the various parameters which influence the suitability

According to the requirements of different tasks, the weight coefficient of each input in the comprehensive analysis can be changed to obtain the desired value of suitability.

Table 15.1 Fuzzy rules

A	B_1	B_2	B_3
B			
A_1	C_1	C_2	C_3
A_2	C_2	C_4	C_3
A_3	C_3	C_3	C_5

15.3 The Result

This paper takes the 1024 × 1024 DEM data of img format as the testing object. It assumes that the terrain data grid already divided according to the actual needs. Figure 15.8 is the original terrain data. The areas of the dark color are lower. The figure includes four different depths of the craters, and three long ditches. The elevation value of the rest is close.

Set the basic parameters as follows: Patroller wheel radius of 0.3 m, maximum inclination of angle of 15°, the wheel width of 0.2 m, the solar elevation angle of 30°, windsurfing x angle and y angles are 30° base station elevation angle of 30°, and the base station azimuth angle of 120°. Analysis assumes that the direction of the front of the patrol is due north to the fixed.

Only after terrain Suitability graphics, as shown in Fig. 15.9.

Under the same conditions, considering the terrain, light, temperature, energy, communication, comprehensive suitability results shown in Fig. 15.10.

In the above example, white represents inappropriate area, black represents the appropriate area; and it can also be seen that more available working area is considered only in the terrain suitability, a combination of other factors, i.e., consider the consolidated suitability, the available working area can be significantly less, this is in line with the truth.

Fig. 15.8 Original testing figure
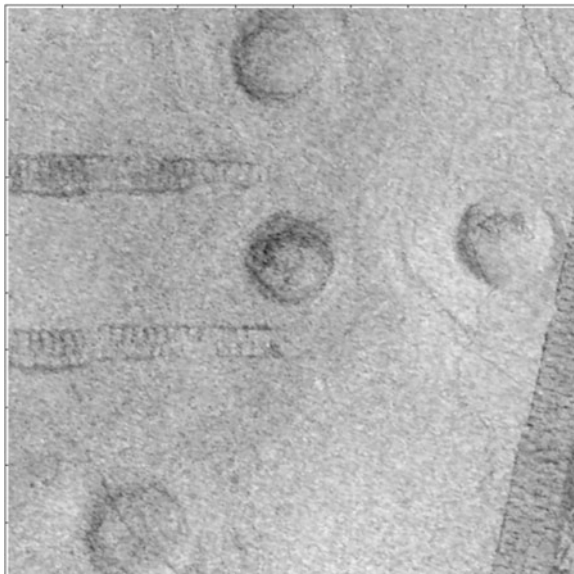
Fig. 15.9 The result of terrain suitability
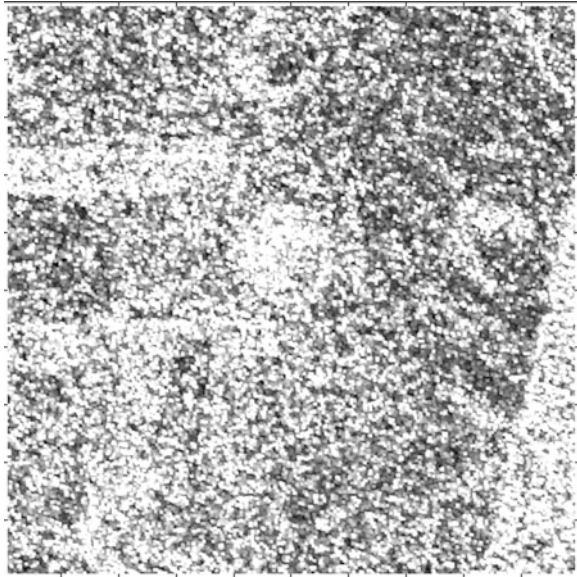
Fig. 15.10 The result of comprehensive suitability
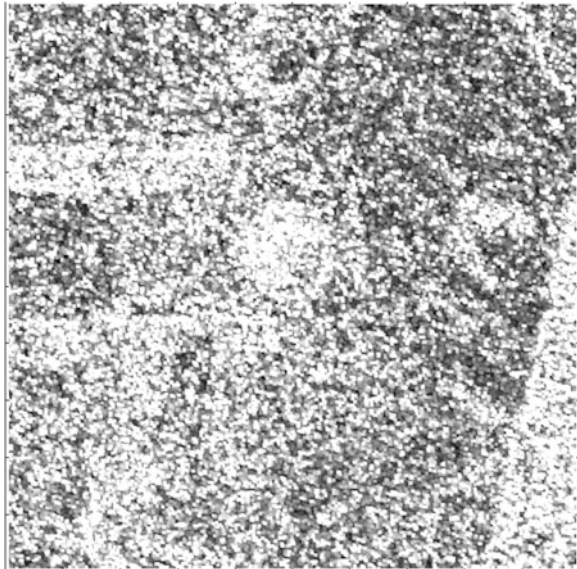
15.4 Conclusions

This paper, combines the special environment of the lunar surface, considering the five indicators of the terrain, lighting, temperature, energy, communications, and the use of fuzzy logic algorithm; proposes a comprehensive suitability evaluation

method of lunar rover lunar surface; analyzes the suitable of the environment of the lunar surface and making it a more comprehensive environmental analysis of the lunar rover around. The results show that, to analyze the suitability of the lunar rover in the lunar surface only from one side is not comprehensive, such as from terrain suitability. To make the lunar rover working successful on the lunar surface, the comprehensive suitability evaluation is necessary. The article only gives the suitability of the environment. The next step plans to do the path planning analysis which is based on the given suitability analysis. According different planning combine different task suitability analysis to plan path, in order to get a more reasonable path.

References

1. Laubach SL, Burdick J, Matthies L (1998) An autonomous path planner implemented on the Roeky7 prototype microrover. In: The 1998 IEEE international conference on robotics and automation, Belgium
2. Liu J, Chen J (2009) Traversability based path algorithm for lunar rovers. Chinese Space Technol (in Chinese)
3. Braun T, Bitsch H (2008) Visual terrain traversability estimation using a combined slope/elevation model. In: KI '08 Proceedings of the 31st annual German conference on advances in artificial intelligence
4. Shirkhodale A, Amrani R (2005) Soft computing for visual terrain perception and traversability assessment by planetary robotic systems. Syst Man Cybern
5. Jin G-G, Lee H-S (2010) Fuzzy-based speed estimation for navigation of unmanned robots. Int J Control Autom Syst 8(2)
6. Shirkhodaie A, Amrani R, Chawla N, Vicks T (2004) Traversable terrain modeling and performance measurement of mobile robots. In: Performance metrics for intelligent systems workshop, NIST, 24–26 Aug 2004

Chapter 16
Genetic Algorithm for Solving the Inverse Kinematics Problem for General 6R Robots

Zhen Sui, Li Jiang, Yan-Tao Tian and Wei Jiang

Abstract The problem of inverse kinematics for general 6R robots was provided for calculation process, and also exist many inverse kinematics and geometric structure which did not meet the PIEPER criterion. In order to solve these problems, an inverse kinematics algorithm with high accuracy based on multiple population genetic algorithm (MPGA) was proposed. Multiple population was performed to accelerate the convergence rate and avoid the defect of the least part point. For illustrating the performance of the MPGA, the simulation results attained from MPGA are compared with those obtained from well-known single-population genetic algorithm (SGA). Experiments on Panasonic TA1400 robot verified that the algorithm could calculate all globally optimal solutions of general geometric structure and the pose error also can have up to two digits after the decimal point. So this algorithm can be used to guarantee higher control accuracy.

Keywords Robots · Inverse kinematics · Genetic algorithm · Globally optimal solutions

16.1 Introduction

Now, robot was widely used in welding, spray paint, trajectory tracking control, and so on. For multipoint stretch forming for the curved surface of sheet metal, the vector of joint variables at the desired goal position of the robotic manipulator is unknown; so teaching method cannot used to solve that. In order to solve this problem, inverse kinematics of the robot must be worked out. Qiu et al. [1] researched multipoint stretch forming for the curved surface of sheet metal, through

---

Z. Sui (✉) · L. Jiang · Y.-T. Tian · W. Jiang
College of Communication Engineering, Jilin University,
No 5988 RenMin Road, NanGuan, Changchun City, China
e-mail: suizhen@jlu.edu.cn

certain geometry constraints to get the special solution. But this solution showed when curvature radius is larger, the space line error also get larger. In terms of the 6 DOF robot, Cheng et al. [2] thrown an inverse kinematics algorithm based on the analyses of characteristics of symbolic preprocessing and matrix decomposition. However, when the structure of the robot does not have a closed-form solution, this approach does not work at all. Liu et al. [3] on the basis of inverse kinematics analysis of robot, using secondary coding method of SGA to solve the inverse kinematics solution, but the convergence speed and convergence precision of the algorithm cannot be ensured when the degree of freedom mechanical arm is increased. Literature [4–6] through a variety of improved genetic algorithm to is calculate the inverse kinematics solution. However, the speed and convergence precision of the proposed algorithm were not significantly improved. MPGA divides all populations into several populations, then through artificial selection and immigration operation [7] to form a new population by selecting the best individuals from each category. So the convergence speed of genetic algorithms [8] and inversion precision were significantly improved using this mechanism. Finally, after taking 6 DOF robot TA1400 as an example, the general mechanical structure robot inverse kinematics was solved by using the proposed novel inverse kinematics subproblem solution, and realized intelligent robot trajectory planning.

16.2 Inverse Kinematics Problem

Figure 16.1 is the kinematic diagram of Panasonic TA1400 robot when revolute joint is zero. Kinematic model of robot is built according to the special mechanical structures.

$^{i-1}_{i}T$ is a transformation matrices [9] which is resulted from the coordinate system $i-1$ and coordinate system i. The homogeneous transformation matrix for a single joint is expressed as:

Fig. 16.1 Kinematic diagram of Panasonic TA1400 robot
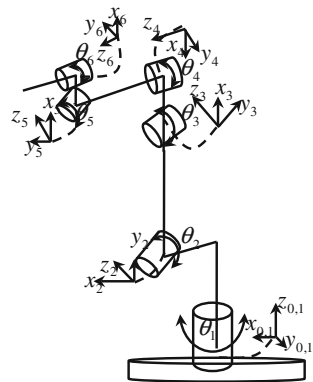
$$
{}^{i-1}_{i}T = \begin{bmatrix} c\theta_i & -s\theta_i & 0 & a_{i-1} \\ s\theta_i c\alpha_{i-1} & c\theta_i c\alpha_{i-1} & -s\alpha_{i-1} & -s\alpha_{i-1}d_i \\ s\theta_i s\alpha_{i-1} & c\theta_i s\alpha_{i-1} & c\alpha_{i-1} & c\alpha_{i-1}d_i \\ 0 & 0 & 0 & 1 \end{bmatrix} \tag{16.1}
$$

where $c\theta_i = \cos(\theta_i)$, $s\theta_i = \sin(\theta)_i$, θ_i is the angle between x_{i-1} and x_i axes measured about z_i axis, α_i is the angle between z_i and z_{i+1} axes measured about x_i axis, a_i is the distance from z_i to z_{i+1} axes measured along x_i axis and d_i is the distance from x_{i-1} to x_i axes measured along z_i axis. Using DH parameters, $T_0, T_1, T_2, T_3, T_4, T_5$ can be obtained.

The forward kinematics of the end-effector with respect to the base frame is obtained by multiplying all of the ${}^{i-1}_{i}T, i = 0, 1\ldots6$ matrices.

$$
{}^{0}_{6}T = \prod_{i=1}^{6} {}^{i-1}_{i}T = \begin{bmatrix} r_{11} & r_{12} & r_{13} & p_x \\ r_{21} & r_{22} & r_{23} & p_y \\ r_{31} & r_{32} & r_{33} & p_z \\ 0 & 0 & 0 & 1 \end{bmatrix} \tag{16.2}
$$

where γ_{ij} represent the rotational elements of transformation matrix (i and $j = 1, 2$ and 3) and p_x, p_y, p_z are the elements of position vector. In analytical solution technique, it should be started by equating the known transformation (Eq. 16.2) with the product of below link transformations.

$$
F(\theta_1, \theta_2, \theta_3, \theta_4, \theta_5, \theta_6) = {}^{0}_{6}T \tag{16.3}
$$

For a 6 joint variables robot, the forward kinematics equation can be used to compute the Cartesian coordinates of the robot when the joint angles are known. However, the joint angles must be computed for any given real-world Cartesian coordinate system in an industrial application. In Eq. (16.4), the inverse kinematics is shown as the function

$$
F_{\text{inverse kinematics}} = {}^{0}_{6}T = F(\theta_1, \theta_2, \theta_3, \theta_4, \theta_5, \theta_6) \tag{16.4}
$$

For robot working in an obstacle free environment, the performance criterion for multiplicity resolution can be taken as the minimization of the total joint displacement.

$$
\Delta\theta = \|\{\theta\} - \{\theta_{\text{cur}}\}\| \tag{16.5}
$$

where $\|\bullet\|$ denotes the Euclidean distance, $\{\theta_{\text{cur}}\} = \{\theta_{1,\text{cur}}\theta_{2,\text{cur}} \cdots \theta_{6,\text{cur}}\}^T$ represents the vector of joint variables at the current configuration of the robotic manipulator and $\{\theta\} = \{\theta_1\theta_2 \cdots \theta_6\}^T$ represents the unknown vector of joint variables at the desired goal position of the robotic manipulator.

In order to achieve a desired position $\{^oP_{w,\text{des}}\}$ of the robot, Eq. (16.4) can be used to form a constraint vector equation of the form

$$\{^oP_w\} - \{^oP_{w,\text{des}}\} = \{0\} \tag{16.6}$$

When current position $\{^oP_w\}$ and target position is equal, then inverse kinematics is worked out.

The limits on the joint variable values can be expressed as

$$\theta_k^l \leq \theta_k \leq \theta_k^u, k = 1, 2, \ldots m \tag{16.7}$$

where θ_k^l and θ_k^u represent the lower and upper limits of the joint variables

The inverse kinematics problem solution involves the solution of the nonlinear transcendental vector equation given in Eq. (16.6) subject to the constraints given in Eq. (16.7). This problem can be stated as the optimization problem

$$\text{Min} \quad \left\| \{^oP_w\} - \{^oP_{w,\text{des}}\} \right\| \tag{16.8}$$

Subject to $\theta_k^l \leq \theta_k \leq \theta_k^u, k = 1, 2, \ldots m$

The objective function of the optimization problem stated in Eq. (16.8) is multimodal in nature and has zero value at the optimal points.

The multiplicity resolution involves the solution of the following problem

Min $\quad \Delta\theta$

Subject to

$$\{^oP_w\} - \{^oP_{w,\text{des}}\} = \{0\} \tag{16.9}$$

$\theta_k^l \leq \theta_k \leq \theta_k^u, k = 1, 2, \ldots m$

The solution of the optimization problem given by Eq. (16.9) involves the comparison of the total joint displacement $\Delta\theta$ values at the multiple solutions of the multimodal problem given in Eq. (16.8).

16.3 Evolutionary Approach

The MPGA with immigration operation and artificial selection was proposed to solve complex high-dimensional optimization problems. The population evolution is implemented by the operators of agents such as competition and cooperation with the dynamic neighboring environment and self-learning operator with their own knowledge. This mechanism improves the global convergence ability and efficiently prevents the algorithm from the local optimization and early matures. Figure 16.2 shows the process of multiple population genetic algorithm.
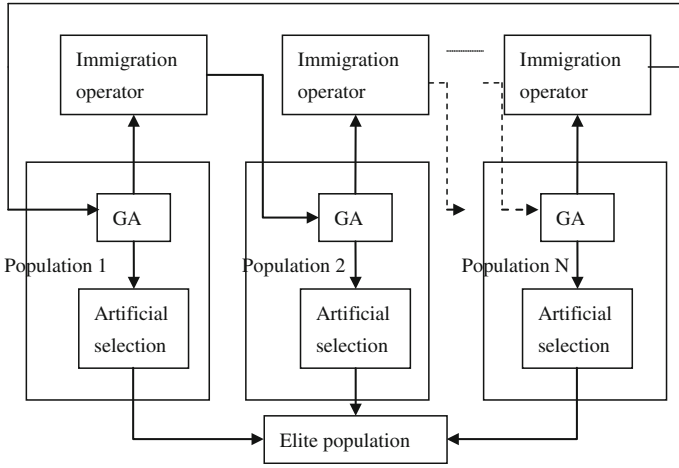
Fig. 16.2 Multiple population genetic algorithm

Specific steps:

Step 1. Initialization parameters

Individual species N, population numbers M, Crossover probability P_c, Mutation probability P_m. Maximum Permissible position Error E-position, Maximum Permissible orientation Error E-gesture.

where P_c is determined by Eq. (16.10), P_m is determined by Eq. (16.11).

$$P_c = 0.7 + (0.9 - 0.7) \times \text{rand}(MP, 1) \qquad (16.10)$$

$$P_m = 0.001 + (0.05 - 0.001) \times \text{rand}(MP, 1) \qquad (16.11)$$

where MP denotes population numbers, $\text{rand}(MP, 1)$ returns an MP-by-1 matrix containing pseudorandom values drawn from the standard uniform distribution on the open interval (0, 1).

Different crossover and mutation parameters are introduced in different population evolution which improves the total performance of genetic algorithm greatly.

Step 2. Immigration operation

Immigration operation is used to find out the best and worst individuals of the current population, and then substitute the best individual for the worst individual in the population. By using this mechanism, it will help to accelerate the convergence speed of the algorithm.

Step 3. Genetic Algorithm
Step 4. Artificial selection

Artificial selection operation is used to record the best individual and the code of the best individual in each population, and then find out the optimal individual in all of the population. The optimal individual in all of the population is the optimum selection finally.

Step 5. Evolution over, output optimization solution

Based on the optimal individual which was operated by artificial selection, using forward kinematics algorithm, calculate the end location-posture of the robot.
If the position is less than E-position and gesture is less than E-gesture
Get an inverse kinematics solution of the optimal results.
Else
Go to Step 2.

16.4 Simulation Experiments

The effectiveness and performance of the presented algorithms are verified by the experiment (two-link robot and TA1400 robot) and comparative analysis.

16.4.1 Two-Link Robot

Simulation experiments were performed on a two-link robot shown in Fig. 16.3. The inverse kinematics problem for the two-link robot can be stated as

$$\min \left(\begin{array}{c} (a_1 c_1 c_2 - a_1 s_1 s_2 + a_2 c_1)^2 - x^2 \\ + (a_1 s_1 c_2 + a_1 c_1 s_2 + a_2 s_1)^2 - y^2 \end{array} \right), a_1 = 40, a_2 = 30 \qquad (16.12)$$

Fig. 16.3 Two-link robot
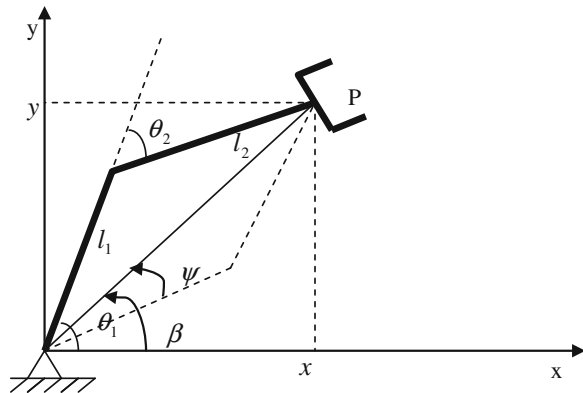
Table 16.1   Results of simulation experiments performed on two-link robot

No	Position (X,Y)	Results using SGA			Results using MPGA		
		θ_1(rad)	θ_2(rad)	Position error	θ_1(rad)	θ_2(rad)	Position error
1	(20, 45)	2.0933	−1.602	0.0011	2.0999	−1.602	1.6136e-8
		0.2129	1.5973	6.5551e-4	0.2052	1.602	5.3839e-8
2	(−30, 35)	−2.977	−1.7237	1.0540e-4	−2.9742	−1.7277	3.6630e-9
		1.2533	1.7226	1.7091e-4	1.2499	1.7277	1.7964e-8

where $c_i = \cos(\theta_i)$, $s_i = \sin(\theta_i)$ X, Y denote the numerical values of the Cartesian coordinates at the desired position of the robot.

The following control parameters were used for the SGA: Population size = 40, Crossover probability = 0.7, and Mutation probability = 0.3. The control parameters were used for the MPGA is the same for SGA, but mutation probability is determined by Eq. (16.11), crossover probability is determined by Eq. (16.10).

Table 16.1 shows the values of the joint variables obtained using the SGA and MPGA and geometric solution. The minimum positioning errors of the two-link robot for the values of the joint variables obtained using these strategies are also given in the table. Table 16.1 shows that the minimum positioning errors obtained using MPGA are less compared to the minimum positioning errors obtained using SGA. Figure 16.4 shows the variation of the minimum positioning error for the inverse kinematics problem using the two GA strategies for simulation experiments
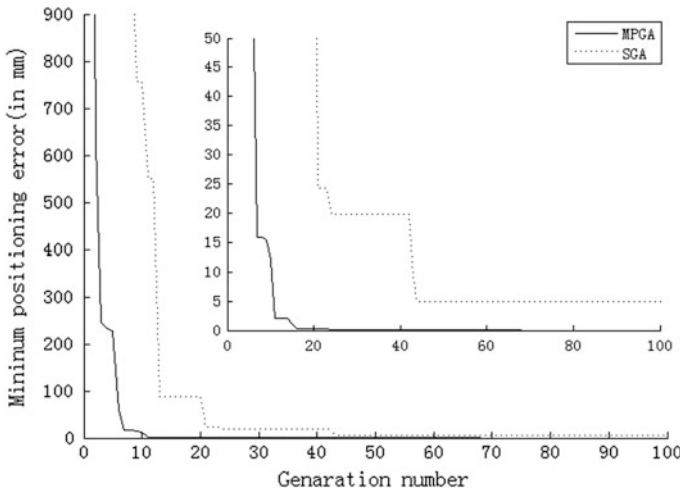
Fig. 16.4   Variation of minimum positioning error with generations for simulation experiment no. 1 of two-link robot using SGA and MPGA separately

no. 1. Figure 16.4 shows that the generation number and minimum positioning errors obtained using MPGA are less compared to the generation number and minimum positioning errors obtained using SGA.

16.4.2 TA1400 6R Robot

The inverse kinematics problem for the TA1400 robot can be stated as:

$$
\min \left\| \left\{ \begin{array}{cccc} r_{11} & r_{12} & r_{13} & p_x \\ r_{21} & r_{22} & r_{23} & p_y \\ r_{31} & r_{32} & r_{33} & p_z \\ 0 & 0 & 0 & 1 \end{array} \right\} - \left\{ \begin{array}{cccc} \hat{r}_{11} & \hat{r}_{12} & \hat{r}_{13} & \hat{p}_x \\ \hat{r}_{21} & \hat{r}_{22} & \hat{r}_{23} & \hat{p}_y \\ \hat{r}_{31} & \hat{r}_{32} & \hat{r}_{33} & \hat{p}_z \\ 0 & 0 & 0 & 1 \end{array} \right\} \right\| \tag{16.13}
$$

where $\hat{\gamma}_{ij}$ represent the rotational elements of the desired vector transformation matrix (i and j = 1, 2, and 3) and $\hat{p}_x$, $\hat{p}_y$, $\hat{p}_z$ are the elements of the desired position vector.

In order to solve nonlinear and transcendental equation inverse kinematical, we use the MPGA strategy. If robot terminal execution position posture can be stated as: $T_{\text{end}} = \begin{bmatrix} T_1 & T_2 & T_3 & T_4 \end{bmatrix}^T$

Where T_1 = [0.2500 −0.0580 0.9665 500]; T_2 = [0.4330 0.8995 −0.0580 200]; T_3 = [−0.8660 0.4330 0.2500 600]; T_4 = [0 0 0 1]. Table 16.2 shows that the minimum positioning errors obtained using MPGA is less than two digits after the decimal point while gesture error is lesser. The results in Table 16.2 show that MPGA have high-precision and stability.

When the degree of freedom is from 2 to 6, what can be observed from Fig. 16.5 is that MPGA can work well, while SGA cannot convergence to global optimal. The simulation experiment of TA1400 verifies the superiority of the MPGA to the traditional SGA.

Figure 16.6 (I) establishs TA1400 robot model in Robotics Toolbox of MAT-LAB. So when plugging vector of joint variables at the desired goal position of the robotic manipulator of Table 16.2 into TA1400 robot model in Robotics Toolbox of MATLAB, Fig. 16.6 is got.

Where A-H represent the positions of the robotic manipulator are resulted in vector of joint variables in Table 16.2.

Figure 16.7 is the experiment of TA1400 robot. Computational results are presented to demonstrate the effectiveness of the algorithm.

Figure 16.7a: Sketch maps of TA1400 robot. Figure 16.7b: Robot is working. Figure 16.7c: Trajectory.

Table 16.2 Results of simulation experiments performed on TA1400 robot

No	θ_1	θ_2	θ_3	θ_4	θ_5	θ_6	Position error	Gesture error
1	−2.5594	−2.1347	−0.8202	2.4501	1.1751	−2.5528	0.0016	−1.6981e-4
2	−2.5863	1.645	−2.7265	0.7481	0.9381	−0.2075	0.0010	−2.8240e-4
3	−2.4962	1.8064	−2.7834	−2.3348	−1.0801	2.9431	0.0015	−2.3192e-4
4	−2.524	−2.2788	−0.8129	−0.6731	−1.2722	0.4927	0.0012	−2.6917e-4
5	0.6138	1.9732	−1.3722	0.6570	−1.3423	−3.0457	0.0012	−2.0097e-4
6	0.5714	−1.2114	−2.1766	−0.6860	1.1096	−2.5179	6.6952e-4	−2.3425e-4
7	0.5766	2.2624	−1.3601	−2.4328	1.1084	−0.0906	5.7352e-4	−2.0762e-4
8	0.61239	−0.8466	−2.2299	2.4895	−1.3801	0.4200	3.6146e-4	−2.9013e-4
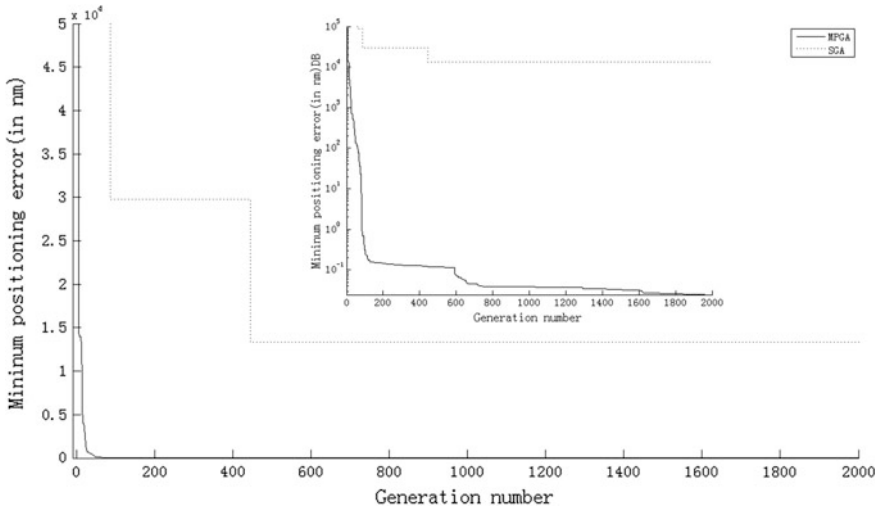
Fig. 16.5 Variation of minimum positioning error with generations for simulation experiment of TA1400 robot using SGA and MPGA
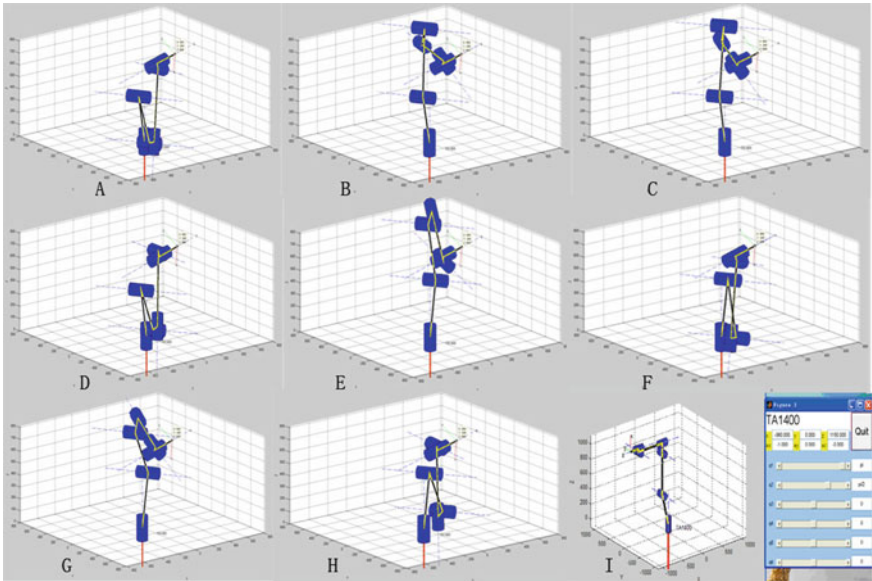
Fig. 16.6 Result in Robotics Toolbox of MATLAB of TA1400 robot at T_{end}
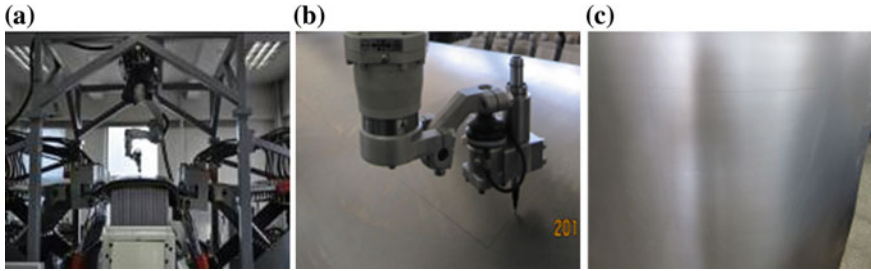
Fig. 16.7 Actual experiment

16.5 Conclusion

Compared with the SGA, MPGA makes the global solution more efficient and accelerate the convergence speed. Besides, MPGA improves its genetic choose operation by introducing the immigration operator and artificial selection.

MPGA solves inverse kinematics of 6R robots by optimizing objective function which was decided by present position vector and desired position vector. While referring to algebraic methods, when the last three consecutive axes of 6 DOF robot does not intersect at a point or the robot does not meet PIEPER criterion which is caused by mechanical parameters error, algebraic methods can not solve these problems.

References

1. Qiu N, Sui Z, Mingzhe L et al (2013) Algorithm of 6-DOF robot trajectory planning applied to special marking. J Jilin Univ (Eng Technol Ed) 5(48):1307–1313 (in Chinese)
2. Cheng YL, Zhu SQ, Liu SG et al (2008) Inverse kinematics of 6R robots based on the orthogonal character of rotation sub-matrix. Robot 30(2):160–164 (in Chinese)
3. Liu Y-C, Huang Y-M, Wang X-Y et al (1998) Genetic algorithm for solving the inverse kinematics problem of Robot. Robot 20(6):421–426 (in Chinese)
4. Kalra P, Mahapatra PB, Aggarwal DK (2006) An evolutionary approach for solving the multimodal inverse kinematics problem of industrial robots. Mech Mach Theory 41:1213–1229
5. Dong Y, Yang T, Li W (2012) Algorithm based on analytical method and genetic algorithm for inverse kinematics of redundant manipulator. Comput Simul 3:239–243
6. Lin M, Wang G, Lin Y (2012) Robot inverse kinematics based on improved genetic algorithm. J Jiangsu Univ Sci Technol (Nat Sci Ed) 26(4):370–375 (in Chinese)
7. Shi F, Wang H, Hu F et al (2011) 30 case analysis of MATLAB intelligent algorithm. Beihang University Press, Beijing (in Chinese)
8. Lei Y-J et al (2006) Genetic algorithm toolbox and its application of MATLAB. Xidian university press, Xian (in Chinese)
9. Craig JJ (2006) Introduction to robotics: mechanics and control [M] 3rd ed. China Machine Press, Beijing (in Chinese)

Chapter 17
Fixed Time Synchronization of Complex Dynamical Networks

Yingjiang Zhou and Changyin Sun

Abstract This paper studies the protocol of fixed time synchronization of multiagent systems. First, under appropriate criterion, classical continuous fixed time synchronization protocol is proposed for the multiagent systems. Then, in order to reduce the conservative of the convergence time, a more accurate estimate is provided. Finally, simulation example is performed to illustrate the effectiveness of the theoretical results.

Keywords Synchronization · Multiagent systems · Pinning control · Fixed time

17.1 Introduction

The synchronization theory of multiagent systems has received much attention in recent years and many interesting results have discussed from different angles. This is partly due to its wide applications in many areas, such as cooperative control of unmanned Air Vehicles, cooperative control of multi-interceptor system for near-space hypersonic vehicles, robotic teams, electrical power grids, sensor networks, and interpersonal relationship network.

Up to now, most of the existing works on synchronization problems are asymptotic synchronization results. In [1], for the fixed and switching topology networks, classical consensus protocols have been introduced, and the algebraic connectivity has defined to determine the convergence rate. The locally and globally adaptive synchronization of an uncertain complex dynamical network has been investigated [2]. For the multiagents system with time-varying delays, a general

Y. Zhou · C. Sun (✉)
School of Automation, Southeast University, Nanjing 210096, China
e-mail: cysun@seu.edu.cn

Y. Zhou
School of Automation, Nanjing University of Posts and Telecommunications,
Nanjing 210023, China

criterion was given in [3], where the network sizes can be extended to be much larger compared to those very small ones studied in [4, 5]. Recently, a new kind of synchronization protocol has studied for the inherent delayed nonlinear dynamics and intermittent communications [6].

The convergence rate of the asymptotic results is at best exponential with infinite settling time. In the practical systems, finite time synchronization results are much better. And there are many research results about finite time synchronization. Several kinds of finite time synchronization protocols have been investigated in [7–9] by using the finite time theorem [10]. The finite time distributed consensus problem for multiagent systems was studied by using a binary consensus protocol and the pinning control scheme [11]. The key point in finite time result is that the power exponent is less than one. The convergence time of the above finite time results depends on the initial conditions of the agents. But in some practical applications, it is required to achieve synchronization in a prescribed time.

The main objective of this paper is to design protocols that achieve fixed time synchronization, that is to say the convergence settling time is regardless of the initial states. The definition of fixed time was proposed in [12], where the criterion for fixed time attractive was also given. Fixed time algorithms can be also found in [13–15]. In [14], a fixed time control protocol for a specific formation control problem was designed. In [15], a fixed time average-consensus protocol for a weighted undirected network was designed.

The contributions of this paper are summarized as follows. Based on classical nonlinear complex dynamic networks, fixed time synchronization problem has been discussed. Specifically, under appropriate criterion, the complex dynamic networks were proved to achieve fixed time synchronization. The fixed time synchronization method can effectively avoid the convergence time depending on the initial state. These results have important practical implications for network synchronization of practical engineering applications.

The rest of this paper is organized as follows. In Sect. 17.2, some preliminaries and problem statement are briefly outlined. The fixed time synchronization criterion for complex networks is given in Sect. 17.3. In Sect. 17.4, simulation example is given to verify the proposed results. Finally, conclusions are included in Sect. 17.5.

17.2 Preliminaries and Problem Statement

In this section, first, some basic algebraic graph concepts will be presented. Then, the problem statement is introduced. Last, some lemmas are given.

The graph in this paper is undirected and do not contain self-edges. For the algebraic graph $G = \{V, E, A\}$, $V = \{v_i, i = 1, \ldots, n\}$ means a set of nodes, $E \subseteq V \times V$ means a set of edges, and $A = [a_{ij}] \in R^{n \times n}$ means a weighted adjacency matrix. An edge E_{ij} in graph G is denoted by the ordered pair means that agent j can access the state information of agent i. If there is a connection between agent j and i,

i.e., $(v_i, v_j) \in E$, then $a_{ij} = a_{ji} > 0$; otherwise, $a_{ij} = a_{ji} = 0$ ($i \neq j$, $i, j = 1, \ldots, n$). Furthermore, we assume that $a_{ii} = 0$ for all $i \in \{1, \ldots, n\}$. The Laplacian matrix of graph G is $L = [l_{ij}] \in R^{n \times n}$, where $l_{ii} = \sum_{j=1}^{n} a_{ij}$ and $l_{ij} = -a_{ij}$, $i \neq j$. A path in the graph G represents a way to get from an origin node v_i to a destination node v_j by traversing edges in the graph. An undirected network G is connected if there is a path between any pair of distinct nodes.

Suppose that $\text{sig}(x)^\alpha = \text{sign}(x)|x|^\alpha$.

There are n agents. Each agent dynamics is given as follows:

$$\dot{x}_i = f(x_i, t) + u_i, \tag{17.1}$$

where u_i is a protocol of both system dynamics and information transmission among the n agents. Now, consider the following classical fixed time protocol:

$$u_i = c_1 \text{sig}\left(\sum_{j=1}^{n} a_{ij}(x_j - x_i)\right)^{\alpha_1} + c_2 \text{sig}\left(\sum_{j=1}^{n} a_{ij}(x_j - x_i)\right)^{\alpha_2} + c_3 \sum_{j=1}^{n} a_{ij}(x_j - x_i) \tag{17.2}$$

where c_k, $k = 1, 2, 3$, are the coupling strength, $\alpha_1 \in (0, 1)$, $\alpha_2 > 1$.

For the multiagent system (17.1), the disturbance $f(x_i, t)$ should satisfy the following condition.

Assumption 17.1 There exists constants k_i such that

$$(x_i - y)^T (f(x_i, t) - f(y, t)) \leq (x_i - y)^T k_i (x_i - y) \tag{17.3}$$

Note that Assumption (17.3) is very mild.

The objective of control in this paper is to find appropriate controller (17.2) such that the solutions of the controlled network (17.1) fixed time synchronize.

Definition 17.1 The multiagent systems (17.1) is said to reach fixed time synchronization, if for any initial condition, there exists a fixed settling time T_0, which is not connect with initial condition, such that $\lim\limits_{t \to T_0}(x_i(t) - s(t)) = 0$, for $i = 1, 2, \ldots, n$.

When the controlled complex network (17.2) achieves synchronization, the coupling terms and control inputs will automatically vanish. This indicates that any solution $x_i(t)$ of any single node is also a solution of the synchronized coupled network.

Last, some lemmas which will be used in the following sections are introduced.

Lemma 17.1 [1] For a connected undirected graph G, the Laplacian matrix L of G has the following properties. $x^T L x = \frac{1}{2} \sum_{i=1}^{n} \sum_{j=1}^{n} a_{ij}(x_i - x_j)^2$, for any $x \in \mathbb{R}^n$, which implies that L is positive semi-definite. 0 is a simple eigenvalue of L and $\mathbf{1}$ is

the associated eigenvector. Assume that the eigenvalues of L are denoted by 0, $\lambda_2, \ldots, \lambda_n$ satisfying $0 \leq \lambda_2 \leq \ldots \leq \lambda_n$. Then the second smallest eigenvalue $\lambda_2 > 0$. Furthermore, if $\mathbf{1}^T x = 0$, then $x^T L x \geq \lambda_2 x^T x$.

Lemma 17.2 [12] If there exists a continuous radially unbounded function V : $\mathbb{R}^n \to \mathbb{R}_+ \cup \{0\}$ such that

(1) $V(x) = 0 \Leftrightarrow x = 0$;
(2) for some $\alpha, \beta, p, q, k > 0$, $pk < 1$, and $qk > 1$, any solution $x(t)$ satisfied the inequality $D^* V(x(t)) \leq -\left(\alpha V^p(x(t)) + \beta V^q(x(t))\right)^k$,

then, the origin is globally fixed time stable and the following estimate holds:

$$T(x_0) \leq \frac{1}{\alpha^k(1 - pk)} + \frac{1}{\beta^k(qk - 1)}, \ \forall x_0 \in \mathbb{R}^n.$$

Lemma 17.2 presents quite a conservative settling time estimate. A more accurate estimate is provided in the next lemma. Consider the case where the constants p and q are of the form $p = 1 - \frac{1}{2\gamma}$ and $q = 1 + \frac{1}{2\gamma}$, $\gamma > 1$.

Lemma 17.3 [12] If there exists a continuous radially unbounded function V : $\mathbb{R}^n \to \mathbb{R}_+ \cup \{0\}$ such that

(1) $V(x) = 0 \Leftrightarrow x = 0$;
(2) for some $\alpha, \beta > 0$, $p = 1 - \frac{1}{2\gamma}$, $q = 1 + \frac{1}{2\gamma}$, and $\gamma > 1$, any solution $x(t)$ satisfied the inequality $D^* V(x(t)) \leq -\alpha V^p(x(t)) - \beta V^q(x(t))$,

then, the origin is globally fixed time stable and the following estimate of the settling time function holds:

$$T(x_0) \leq T_{\max} := \frac{\pi \gamma}{\sqrt{\alpha \beta}}, \ \forall x_0 \in \mathbb{R}^n.$$

17.3 Fixed Time Synchronization Criterion for Complex Networks

In this section, for the undirected network, the global fixed time synchronization of complex dynamical networks is established with protocol (17.2).

Theorem 17.1 Suppose that Assumption (17.3) holds. The controlled undirected networks (17.1) and (17.2) are globally fixed time synchronizations if the following condition is satisfied:

$$k_i < c_3 \lambda_2, \tag{17.4}$$

and the fixed settling time T satisfies that $T \le T(x_0) \le \dfrac{1}{2^{\frac{\alpha_1-1}{2}}\lambda_2^{\frac{1+\alpha_1}{2}}c_1(1-\alpha_1)}$
$+ \dfrac{1}{n^{\frac{1-\alpha_2}{2}}2^{\frac{\alpha_2-1}{2}}\lambda_2^{\frac{1+\alpha_2}{2}}c_2(\alpha_2-1)}.$
where λ_2, is the second smallest eigenvalue of matrix L.

Proof Consider the following positive Lyapunov functional candidate:

$$V(t) = \frac{1}{2}x^T L x = \frac{1}{4}\sum_{i=1}^{n}\sum_{j=1}^{n}a_{ij}(x_i - x_j)^2 \qquad (17.5)$$

Set $q_i = \sum_{j=1}^{n}a_{ij}(x_i - x_j)$, then protocol (17.2) can be transformed to the following form

$$u_i = -c_1\mathrm{sig}q_i^{\alpha_1} - c_2\mathrm{sig}q_i^{\alpha_2} - c_3 q_i.$$

Taking the derivative of $V(t)$ yields,

$$\dot{V}(t) = x^T L\dot{x} = \sum_{i=1}^{n}\sum_{j=1}^{n}a_{ij}(x_i - x_j)\dot{x}_i = \sum_{i=1}^{n}q_i\dot{x}_i$$

$$= \sum_{i=1}^{n}\sum_{j=1}^{n}a_{ij}(x_i - x_j)(f_i + u_i)$$

$$= \frac{1}{2}\sum_{i=1}^{n}\sum_{j=1}^{n}a_{ij}(x_i - x_j)(f_i - f_j) - c_3\sum_{i=1}^{n}q_i^2 - c_1\sum_{i=1}^{n}(q_i^2)^{\frac{1+\alpha_1}{2}} - c_2\sum_{i=1}^{n}(q_i^2)^{\frac{1+\alpha_2}{2}}$$

$$\le \frac{1}{2}k_i\sum_{i=1}^{n}\sum_{j=1}^{n}a_{ij}(x_i - x_j)^2 - c_3\sum_{i=1}^{n}q_i^2 - c_1(\sum_{i=1}^{n}q_i^2)^{\frac{1+\alpha_1}{2}} - c_2 n^{\frac{1-\alpha_2}{2}}(\sum_{i=1}^{n}q_i^2)^{\frac{1+\alpha_2}{2}}$$

Since $Lx = [q_1, \ldots, q_n]^T$, we have $\sum_{i=1}^{n}q_i^2 = (Lx)^T Lx = x^T L^2 x$. Let $L^{\frac{1}{2}}\mathbf{1} = s = [s_1, \ldots, s_n]^T$. Then, $s^T s = (L^{\frac{1}{2}}\mathbf{1})^T L^{\frac{1}{2}}\mathbf{1} = \mathbf{1}L\mathbf{1} = 0$, which means $s = \mathbf{0}$. Then, $\mathbf{1}^T L^{\frac{1}{2}}x = s^T x = 0$. So, we can get,

$$\sum_{i=1}^{n}q_i^2 = (L^{\frac{1}{2}}x)^T L(L^{\frac{1}{2}}x) \ge \lambda_2 x^T Lx = 2\lambda_2 V.$$

And we can get,

$$\dot{V}(t) \le 2k_i V - 2c_3\lambda_2 V - c_1(2\lambda_2 V)^{\frac{1+\alpha_1}{2}} - c_2 n^{\frac{1-\alpha_2}{2}}(2\lambda_2 V)^{\frac{1+\alpha_2}{2}}$$

$$= 2(k_i - c_3\lambda_2)V - c_1(2\lambda_2)^{\frac{1+\alpha_1}{2}}V^{\frac{1+\alpha_1}{2}} - c_2 n^{\frac{1-\alpha_2}{2}}(2\lambda_2)^{\frac{1+\alpha_2}{2}}V^{\frac{1+\alpha_2}{2}}$$

Now, we can get the conclusion.

If $k_i < c_3\lambda_2$, $\dot{V}(t) < -c_1(2\lambda_2)^{\frac{1+\alpha_1}{2}}V^{\frac{1+\alpha_1}{2}} - c_2 n^{\frac{1-\alpha_2}{2}}(2\lambda_2)^{\frac{1+\alpha_2}{2}}V^{\frac{1+\alpha_2}{2}}$. By Lemma 17.2, we obtain the fixed time result. And the convergence time satisfied

$$T \leq T(x_0) \leq \frac{1}{2^{\frac{\alpha_1-1}{2}}\lambda_2^{\frac{1+\alpha_1}{2}}c_1(1-\alpha_1)} + \frac{1}{n^{\frac{1-\alpha_2}{2}}2^{\frac{\alpha_2-1}{2}}\lambda_2^{\frac{1+\alpha_2}{2}}c_2(\alpha_2-1)}.$$

In order to get a more accurate estimate of convergence time, the following Corollary is provided by using Lemma 17.3.

Corollary 17.1 Suppose that Assumption (17.3) holds. The parameters α_1 and α_2 in the protocol (2) are selected as $\alpha_1 = 1 - \frac{1}{\gamma}$ and $\alpha_2 = 1 + \frac{1}{\gamma}$, $\gamma > 1$, then, with the same conditions as Theorem 17.1, the settling time can be estimated as follows:

$$T(x_0) \leq T_{\max} := \frac{\pi\gamma}{2\lambda_2\sqrt{c_1 c_2}n^{\frac{1-\alpha_2}{4}}}. \tag{17.6}$$

Remark 17.1 In fact, there are many kinds of fixed time strategies, here just consider one typical form, see Eq. (17.2). Through simple extend or exchange, many other fixed time control strategies can be derived.

17.4 Simulation Example

In this section, simulation example is listed to illustrate the effectiveness of the method proposed in this paper.

Consider the undirected multiagent systems with the topology shown in Fig. 17.1.

By using classical protocol (17.2), fixed time synchronization problem has been showed. The disturbance f_i is chose as $f_i = 2\sin x_i$. Choose the following initial conditions: $x(0) = [5 \quad -3 \quad 6 \quad -4 \quad 1]^T$. The control gains are selected as $c_1 = c_2 = c_3 = 5$, $\alpha_1 = 0.5$, and $\alpha_2 = 10$.

Fig. 17.1 The topology of the multiagent systems
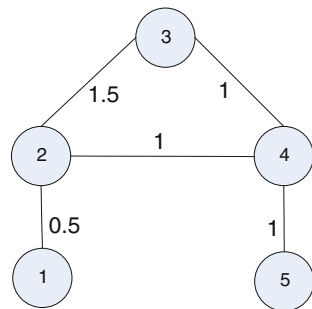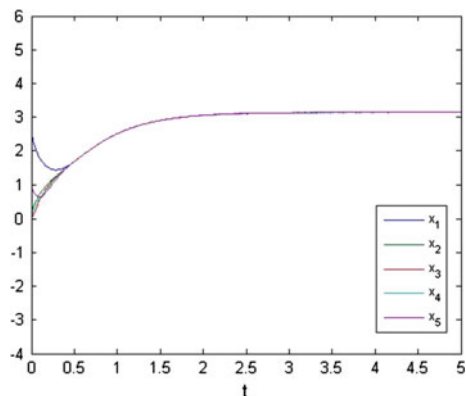
   From the analysis in Sect. 1.3, if we choose protocol (17.2), all the states will
achieve fixed time synchronization as seen in Fig. 17.2. And the convergence time
T satisfies $T \leq T(x_0) \leq 62.9$ s. From Fig. 17.2, we know all states will converge to
the same when $t \geq 1$ s.

17.5 Conclusion

From the practical applications point, the fixed time results are much better than the
asymptotic and simple finite time results. In this paper, the protocol of fixed time
synchronization of multiagent systems has been considered. Under some appro-
priate criteria, classical continuous fixed time synchronization protocol is proposed
for the multiagent systems.

References

1. Olfati-Saber R, Murray R (2004) Consensus problems in networks of agents with switching
   topology and time-delays. IEEE Trans Autom Control 49(9):1520–1533
2. Zhou J, Lu J, Lü J (2006) Adaptive synchronization of an uncertain complex dynamical
   network. IEEE Trans Autom Control 51(4):652–656
3. Yu W, Cao J, Lü J (2008) Global synchronization of linearly hybrid coupled networks with
   time-varying delay. SIAM J Appl Dyn Syst 7(1):108–133
4. Cao J, Li P, Wang W (2006) Global synchronization in arrays of delayed neural networks with
   constant and delayed coupling. Phys Lett 353(4):318–325

5. Wang W, Cao J (2006) Synchronization in an array of linearly coupled networks with time-varying delay. Phys A 366:197–211
6. Wen G, Duan Z, Yu W, Chen G (2013) Consensus of second-order multi-agent systems with delayed nonlinear dynamics and intermittent communications. Int J Control 86(2):322–331
7. Wang L, Xiao F (2010) Finite-time consensus problems for networks of dynamic agents. IEEE Trans Autom Control 55(4):950–955
8. Xiao F, Wang L, Chen J, Gao Y (2009) Finite-time formation control for multi-agent systems. Automatica 45(11):2605–2611
9. Li S, Du H, Lin X (2011) Finite-time consensus algorithm for multi-agent systems with double-integrator dynamics. Automatica 47(8):1706–1712
10. Bhat S, Bernstein D (2000) Finite-time stability of continuous autonomous systems. SIAM J Control Optim 38(3):751–766
11. Chen G, Lewis F, Xie L (2011) Finite-time distributed consensus via binary control protocols. Automatica 47(9):1962–1968
12. Polyakov A (2012) Nonlinear feedback design for fixed-time stabilization of linear control systems. IEEE Trans Autom Control 57(8):2106–2110
13. Levant A (2013) On fixed and finite time stability in sliding mode control. In: Proceedings of 52nd IEEE conference on decision and control. Florence, Italy, IEEE, pp 4260–4265
14. Parsegv S, Polyakov A, Shcherbakov P (2013) Nonlinear fixed-time control protocol for uniform allocation of agents on a segment. In: Proceedings of 51nd IEEE conference on decision and control. Maui, USA, IEEE, pp 7732–7737
15. Parsegv S, Polyakov A, Shcherbakov P (2013) On fixed and finite time stability in sliding mode control. In: Proceedings of 4th IFAC workshop on distributed estimation and control in networked systems. Koblenz, Germany, pp 110–115

Chapter 18
Review and Research Issues on Underactuated Finger Mechanism

Licheng Wu, Yanxuan Kong and Xiali Li

Abstract The current typical prototypes, design methods, and analysis theory on underactuated finger mechanism are reviewed. Primary existing problems are also pointed out according to some analyses. Finally, several important directions in future research are proposed.

18.1 Introduction

Researchers have investigated different types of robotic hands for achieving grasp and handling of objects. Several successful designs for humanoid and non-humanoid hands have been developed in the past, like those that are used, for example, in the Stanford/JPL Hand [1], DLR Hand [2], BUAA Hand [3], Colobi Hand [4], Barrett Hand [5, 6], TUAT/Karlsruhe Hand [7], Turin Hand [8], TBM Hand [9], MA-I Hand [10], SARAH Hand [11, 12], MIT Hand [13] and the RCH-1 Hand [14]. Most of the available multi-fingered prototypes have a high number of degrees of freedom, a complex actuation, and a high cost. Most of those hands are still used for enhanced applications, laboratory tests, or research projects. However, even in the market, hands are available for industrial and non-industrial applications, for example, the Barrett Hand [6], SARAH Hand [12], ROBOSOFT Hand [15].

Many robotic hands focus on simulating the overall appearance and action of a biologic hand, while neglecting other equally important features such as size, weight, and real-time control. Conventional robotic hand, such as in [16], are relatively complex, large, heavy, and difficult to be installed in a robot arm with the

L. Wu (✉) · Y. Kong · X. Li
Minzu University of China, Beijing 100081, China
e-mail: wulicheng@tsinghua.edu.cn

size like a human. The complexity of conventional robotic hand is also very expensive and difficult to manufacture and maintain. However, although the robotic hand has many normal DOFs, the driver and control system need to be big and be difficult to control. In some sense, a robotic hand with more DOFs is more dexterous. And the number of the DOFs directly determines the ability of a hand to bend around an object and adapt to its shape.

An important point on designing a robotic hand is how to decrease the volume, weight, and power cost. Therefore, designing a robotic hand with fewer drivers becomes an interesting direction. However, it becomes a challenge that how to design a robotic hand with feature of compact, low cost and easy operation but still keep the number of DOFs to support the ability of grasp adaptively different object. A hot researched way is to utilize fingers with underactuated driving mechanisms.

18.2 Typical Underactuated Finger Mechanism

Currently, there are two main types of underactuated finger mechanisms, namely tendon-actuated mechanisms and linkage-based mechanisms as outlined in [17]. Typical tendon-actuated mechanisms can be easily built with compact architectures as shown in Fig. 18.1a. However, tendon-actuated mechanisms can only exert small grasping forces. The other disadvantage of tendon systems is that they are strongly affected by friction and elasticity [18]. Some patents are issued on development of robotic hand with tendons mechanisms in [19, 20]. A tendons mechanism for an underactuated prosthetic hand is reported in [21, 22]. An optimal design problem is discussed as related to the diameter and location of the pulleys in [23]. A two degree of freedom/one-actuator finger is presented with isotropic force characteristics in [24]. Here, force-isotropic means that the intensity of the forces exerted at the center of each phalanx, and on the grasped object, are identical. A design of an UFM in TBM hand is presented in [25]. Some preliminary results on a cosmetic prosthetic hand with tendon driven underactuated mechanism and compliant joints are also presented in [26].

For applications where large grasping forces are requested, linkage-based mechanisms are more convenient. A US patent [27] and its improved version [28] were published in 1998 and 2003. As shown in Fig. 18.1b, this kind of linkage UFM is successfully designed through mimicking the transmission structure of tendon driven underactuated mechanism. The prototype built with this kind of linkage finger mechanism is shown in Fig. 18.1c. As shown in Fig. 18.1c, the mechanism proposed in [27, 28] can hardly be built in a compact design, especially when the mechanism is demanded to be embedded within the finger body with a human size during the whole motion of grasp operation. The thumb of TH-1 hand of Tsinghua University has a prismatic passive joint that is driven by a spring [29]. An improved version for TH-2 hand as shown in Fig. 18.1d is reported in [30]. A vital problem of this thumb mechanism of TH-1 and 2 hand is that the prismatic passive joint (a rack) is fixed at the height direction of the finger. The rack can have
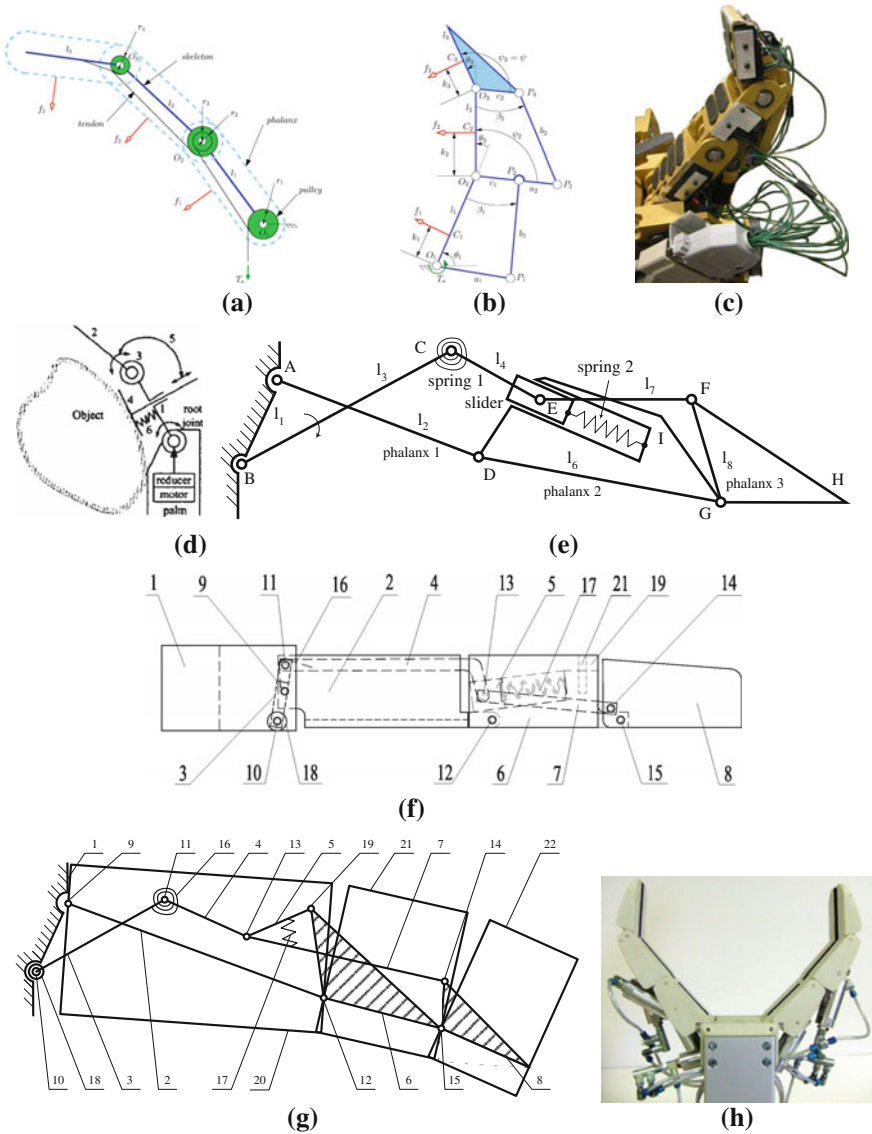
Fig. 18.1 Several typical underactuated finger mechanisms: **a** a tendon-actuated UFM, **b** a kind of Linkage UFM with the same transmission structure of tendon-actuated UFM, **c** a prototype built with linkage UFM as shown in (**b**), **d** UFM of thumb of TH-2 hand, **e** 8 links UFM, **f** a design of 8 link UFM, **g** pneumatic robotic fingers, **h** Linkage UFM with all revolute joints

very short stroke. For realizing effective turning action of the next phalanx, the prismatic passive joint, namely the rack need to be built with very huge transmission ratio. This means that a finger with this kind of mechanism can only put very small grasping force, even smaller than tendon driven mechanisms can do.

Therefore, this kind of mechanism cannot be utilized for finger with more than three phalanxes. Then, Licheng Wu et al. proposed a kind of 8-link underactuated finger mechanism in [31] as shown in Fig. 18.1e. This kind of 8-link mechanism has the feature of compact structure and capability of big grasping power. A design scheme of this 8-link mechanism limited the size as human finger is shown in Fig. 18.1f. A shortage of this mechanism is containing a prismatic joint with tiny size to make against of facture and maintaining. Recently, an enhanced version of this kind of 8-link UFM with all revolute joints was announced as a patent [32], as shown in Fig. 18.1g. Obviously, this design with all revolute joints should overcome the former version's shortage of containing a tiny prismatic joint, as announced by its inventors Licheng Wu and Xiali Li. Besides, a pneumatically driven underactuated hand is reported in [33] as shown in Fig. 18.1h. Through automatically distributing of gas, the hand can adaptively grasp object with different size and shape. However, pneumatic driven system not only has big volume and mass, but also is not easy to control.

18.3 Research on Design and Analysis of UFM

In the design and analysis of UFM, Zollo et al. propose a bionic approach to the design of an anthropomorphic artificial hand able to mimic the natural motion of the human fingers [34]. In [35], an architecture of two-DOF underactuated fingers is proposed and a simulation tool is designed to analyze their behaviors. Luo et al. [36] analyzed the features of three-finger grasping. Wu et al. [37, 38] finished the kinematical modeling and static analysis of proposed linkage UFM, discussed the intrinsic mechanism and deduction of equivalent mechanism preliminarily, and simulation analysis was conducted with Matlab; then the mechanical design and dynamics simulation of adaptively grasping objects with different shape and sizes were accomplished. Cai et al. [39] researched the control issues of five-finger underactuated hand based on electrical signals. [40] proposed an optimized method for designing humanoid robot finger size with the goal of optimizing weight sum of bionic fingers' natural motion, fulfilled dimensions design by searching optimization, nevertheless, the applicability and effect remains to be improved. With regard to a type of three-joint UFM, Khakpour and Birglen [41] proposed an algorithm for grasping process simulation which is based on statics and kinematics. With regard to tendon actuation and artificial tendon actuation of UFM, Balasubramanian and Dollar [42, 43] discussed the problems of working space and grasping ability. As a whole, the present design of linkage underactuated mechanism is implemented by intuition, bionics or the testing, and adjustment based on computer simulation result, the related design theory is still scarce [44].

In UFM, each phalanx's grasping force of an object cannot regulate independently, as the drive is less than the DOFs. In addition, since the UFM itself contains elastic component, when the contact force of phalanxes is larger, the fingers are likely to show rollback phenomenon [44], resulting in grasping instability and even

shooting out of the object. All these factors definitively impact on the grasping performance of underactuated fingers. But there is few research on the mechanical property and grasping stability of linkage underactuated mechanism for the present. In previous research, the grasping stability of objects in different conditions including different configuration and grasping force distribution were discussed; nevertheless, for underactuated fingers which contain elastic components, an overall stability analysis should include the stability of finger mechanism itself. Only objects and finger mechanism that both remain stable can establish stable grasping. The instability of mechanism itself resulted in rollback phenomenon, and it should be researched by analyzing the stability of UFM itself. Birglen and Gosselin discussed the relation between driving force and grasping force in [44], but the jacobian matrix derivation method they used applied to this mechanism type only, which cannot be used in other type of underactuated mechanism. Gosselin et al. [45] proposed an idea of analyzing the stability of two-finger underactuated hand, they also proposed a method of keeping grasping configuration stable when increasing driving force. However, the stability problem is not discussed in their research, and in their conclusion exists great limitations since the spring force is totally ignored in the relevant research. In other words, the grasping stability of UFM, especially the comprehensive analysis method, which contains stability analysis of UFM itself, remains to be studied.

In conclusion, the analysis and design theory of UFM at present is inadequate and still needs further study.

18.4 Research Prospect

The current research in the design and analysis of UFM is inadequate, which should be studied further. On the other hand, there are some limitations in all of the existing UFM, therefore it is necessary to study new UFM. In this paper, some future research points and relevant technical methods are proposed as follows.

1. To research the equivalent of UFM and the design method based on equivalent mechanism (as defined in [31, 32]). To research and analyze the UFM which is equivalent to an intrinsic mechanism of simple single DOF system under the action of spring element at different grasping stages. To research and deduce different methods of equivalent mechanism at different grasping stages. To research the design method of dimension based on equivalent mechanism.

   On the one hand, when the passive joints linked by elastic elements are free from external force and ignoring the inertia force, there will be no joint movement, which is equivalent to a kind of fix joint. On the other hand, when a phalanx grasping object, its movement is often constrained, then some related joints of finger mechanism will be constrained [31]. Then analyze the condition of spring force and phalanx movement under constraint in different grasping states (for example, freedom of all phalanxes, single phalanx grasp, certain

phalanxes grasp, all phalanx grasp) by exporting some related fixedly attached joints from equivalent mechanism. Establish an integrated table of grasping states and equivalent mechanism. The finger dimensions are given with maximizing reachable workspace as principal design index, and factors such as the degree of finger mimics a human finger and transmission efficiency are considered. According to the order from the phalanx nearest to palm to farthest phalanx, the single DOF equivalent mechanism of each phalanx is designed when the phalanx moves without constraint until all the dimension design of UFM are finished.

2. To research the grasping force analysis methods of UFM and the design method of elastic element parameters. Generally, the initial state of present UFM is simply set fingers as fully straightened, and the elastic force of elastic element in the initial state is zero. However, the observation of human and other creatures reveals that biological fingers are not fully straightened in normal state but between the state of fully straightened and the state of rolled to the limit. Therefore, when the fingers straighten fully, the elastic element in fingers has certain pre-tightening force. Although you must overcome the pre-tightening force first to open fingers while grasping large objects, but then the pre-tightening force of the elastic element can assist grasping. The effect of pre-tightening force on fingers' mechanical property, especially its relationship with grasping stability, is a problem worthy of studying.

   Therefore in the future, the derivation method of Jacobian matrix among grasping force and driving force and elastic force should be studied. Define and study the grasping stability of finger mechanism. Research the relationship between grasping configuration and grasping stability, as well as the relationship among elastic element parameters, pre-tightening force, and grasping stability. Then the design methods of elastic element parameters of UFM and pre-tightening force will be proposed.

   The Jacobian matrix among grasping force and driving force and elastic force can be deduced based on its physical significance by using the technique that drives only one separate joint with unit force at each time. Analyze the mechanical stability of the UFM itself to deduce the relationship between grasping configuration and grasping stability, and then deduce the stable grasping subspace of the reachable workspace. Plug spring coefficient and initial stroke into the jacobian matrix to deduce the explicit relation with the grasping force, and then deduce the relationship between pre-tightening force and grasping stability. According to the above relations, the design goal of spring coefficient and pre-tightening force is to optimize adjustable amplitude of grasping force under typical full contact grasping configuration.

3. The movement mechanism analysis of the hand grasping and the variable topology mechanisms synthesis of UFM. Build a more accurate movement model of human fingers through the analysis of human fingers' anatomical structures and the observations of actual movement situation. Discover the underactuated motion law of the finger grasping on the basis of the human

fingers' behavior structure characteristics and the adaptive motion mechanism of grasping and the variable topology analysis of different driving ways switches. To do this, human fingers' movement identification is studied. Establish the recognition system of accurate grasp and dynamic grasping movements. The means of merging the movement topology of UFM and control feasibility is taken into account to reproduce the switch between the movement mechanism of hand grasping and different driving ways. To achieve joint movement as more as possible with less drivers so that the flexibility and manipulability can be improved without increasing fingers' volume and weight.

4. The analysis of the nonholonomic kinematics and mechanics of UFM. The analysis objects include the kinematics and mechanics of single finger UFM as well as kinematics, statics, dynamics of the entire UFM. To study the input–output relations and corresponding forward-inverse algorithm of the kinematics and dynamics with higher pairs point contact surfaces, which provides the basis of control policy. Underactuated system has the second-order nonholonomic properties, this makes modeling and control more difficult on the one hand, on the other hand this provides a broader scope to optimize the design of finger grasping.

Aiming at the innovation theory and method of dynamic modeling and parameter identification, which are built on accurate grasping and dynamic grasping of objects with different physical properties, mechanical modular design, and optimization problems of position-force hybrid control are studied, the redundant and fault-tolerant problems of finger mechanism in a complex environment are studied as well. The research also includes basic theoretical approaches and key techniques of target identification and autonomous location, system self-reconfiguration, and reliable guaranteed cost control in fault conditions, etc.

5. To develop a new underactuated finger principle prototype and implement related scientific experiments. Rotational joints are used to substitute translational joints existing in 8 links UFM (as shown in Fig. 18.1f), then develop a new type of full rotation articulated UFM. This development could reduce the manufacturing cost and increase maintainability on the basis of inheriting the advantages of the original mechanism. The research process should pay attention to digital simulation and experiment of system kinematics, dynamics, motion planning, and control problems. Then use semi-physical simulation of Hardware-in-the-loop system to improve the credibility of key problems' simulation. The hardware solution can be employing control system composed of embedded ARM MPU and DSP device, taking advantage of ARM chips' system management and control performance and fast processing speed of DSP. Meanwhile, implanting embedded operating system ARM-Linux in ARM and using powerful networking functionality of Linux system could make the fingers' control system access Ethernet at any time, that is, Plug and Play, which make the remote monitoring and control of fingers more convenient. Then any single finger's status information could be uploaded in package to main control computer and pc through WLAN in order to run more complex control algorithm.

18.5 Conclusions

In this paper, the present typical UFMs are discussed, the analysis and the design theory are reviewed, then some shortcomings and problems that need to be further investigated are pointed out, and on this basis the next focus of UFM is predicated, and the research methods are proposed primarily.

References

1. Mason MT, Salisbury JK (1985) Robots hands and the mechanics of manipulation. MIT Press, Cambridge
2. Butterfass J, Grebenstein M, Liu H, Hirzinger G (2001) DLR-hand II: next generation of a dexterous robot hand. In: IEEE international conference on robotics and automation, Seoul, pp 109–114
3. Zhang Y, Han Z, Zhan H, Shang X, Wang T, Guo W (2001) Design and control of the BUAA four-fingered hand. In: IEEE transaction on robotics and automation, pp 2517–2522
4. Gosselin CM, Mountambault S, Gosselin CJ (1993) Manus colobi: preliminary results on the design of a mechanical hand for industrial applications. In: 19th ASME design automation conference, vol 65, issue 1, pp 585–592
5. Townsend WT (2000) The barrett hand grasper—programmable flexible parts handling and assembly. Ind Robot Int J 27:181–188
6. Barrett Hand. http://www.barretttechnology.com
7. Fukaya N, Toyama S, Asfour T, Dillmann R (2000) Design of the TUAT/Karlsruhe humanoid hand. In: IEEE/RSJ international conference on intelligent robots and systems, Takamatsu, pp 1754–1759
8. Raparelli T, Mattiazzo G, Mauro S, Velardocchia M (2000) Design and development of a pneumatic anthropomorphic hand. J Robot Syst 17(1):1–15
9. Dechev N, Cleghorn WL, Nauman S (1999) Multiple finger, passive adaptive grasp prosthetic hand. Mech Mach Theory 36:1157–1173
10. Suares R, Grosch P (2004) Dexterous robotic hand MA-I software and hardware architecture. Intelligent Manipulation and Grasping, Genova, pp 91–96
11. Martin E, Desbiens AL, Laliberté T, Gosselin C (2004) SARAH hand used for space operation on STVF robot. Intelligent Manipulation and Grasping, Genova, pp 279–284
12. SARAH Hand. http://www.robot.gmc.ulaval.ca/recherche/theme04_a.html
13. Edsinger-Gonzales A (2004) Design of a compliant and force sensing hand for a humanoid robot. Intelligent Manipulation and Grasping, Genova, pp 291–295
14. Roccella S, Carrozza MC, Cappiello G, Dario P, Cabibihan JJ, Zecca M, Hiwa H, Itoh K, Matsumoto M, Takanishi A (2004) Design, fabrication and preliminary results of a novel anthropomorphic hand for humanoid robotics: RCH-1. In: IEEE/RSJ international conference on intelligent robots and systems, Sendai, pp 266–271
15. ROBOSOFT Hand. http://www.robosoft.fr/SHEET/05Grippers/1002ROBOSOFT3FINGER/3Finger.html
16. Qian X, Zhang Q (1996) The driver method and application of a driver mechanism of phalanx joint. China patent no. 1136988A

17. Ceccarelli M, Tavolieri C, Lu Z (2006) Design considerations for underactuated grasp with a one D.O.F. anthropomorphic finger mechanism. In: Proceedings of 2006 IEEE/RSJ international conference on intelligent robots and systems (IROS 2006), Beijing, China, pp 1611–1616, 9–15 Oct 2006

18. Ceccarelli M (2004) Fundamentals of mechanics of robotic manipulation. Kluwer/Springer, Dordrecht

19. Mullen JF (1972) US patent 3694021, 26 Sept 1972

20. Crisman JD, Kanojia C, Zeid I (1996) US patent 5570920, 5 Nov 1996

21. Massa B, Roccella S, Carrozza MC, Dario P (2002) Design and development of an underactuated prosthetic hand. In: Proceedings of the 2002 IEEE international conference on robotics and automation, Washington, DC, pp 3374–3379

22. Carrozza MC, Suppo C, Sebastiani F, Massa B, Vecchi F, Lazzarini R, Cutkosky MR, Dario P (2004) The SPRING hand: development of a self-adaptive prosthesis for restoring natural grasping. Auton Robot 16:125–141

23. Cabas R, Cabas LM, Balaguer C (2006) Optimized design of the underactuated robotic hand. In: Proceedings of the 2006 IEEE international conference on robotics and automation (ICRA 2006), Orlando, pp 982–987

24. Krut S (2005) A force-isotropic underactuated finger. In: Proceedings of the 2005 IEEE international conference on robotics and automation (ICRA 2005), Barcelona, pp 2314–2319

25. Dechev N, Cleghorn WL, Naumann S (2001) Multiple finger, passive adaptive grasp prosthetic hand. Mech Mach Theory 36:1157–1173

26. Carrozza MC, Cappiello G, Stellin G, Zaccone F, Vecchi F, Micera S, Dario P (2005) A cosmetic prosthetic hand with tendon driven under-actuated mechanism and compliant joints: ongoing research and preliminary results. In: Proceedings of the 2005 IEEE international conference on robotics and automation (ICRA 2005), Barcelona, pp 2661–2666

27. Gosselin C, Laliberte T (1998) US patent 5762390, 9 June 1998

28. Laliberte T, Gosselin C (2003) Actuation system for highly underactuated gripping mechanism. US patent 6505870, 14 Jan 2003

29. Zhang W, Chen Q, Sun Z (2003) Under-actuated humanoid robot hand with changeable grasping force. J Tsinghua Univ (Sci Tech) 43(8):1143–1147

30. Zhang W, Chen Q, Sun Z, Zhao D (2004) Passive adaptive grasp multi-fingered humanoid robot hand with high under-actuated function. In: Proceedings of the 2004 IEEE international conference on robotics and automation, New Orleans, LA, pp 2216–2221

31. Wu L, Carbone G, Ceccarelli M (2009) Design an underactuated mechanism for a 1 active DOF finger operation. Mech Mach Theory 44(2):336–348

32. Wu L, Li X (2013) A kind of linkage underactuated finger mechanism with all revolute joints. Chinese patent CN 103358315 A, 23 Oct 2013

33. Bégoc V, Krut S, Dombre E, Durand C, Pierrot F (2007) Mechanical design of a new pneumatically driven underactuated hand. In: 2007 IEEE international conference on robotics and automation, Roma, Italy, pp 927–933, 10–14 April 2007

34. Zollo L, Roccella S, Guglielmelli E, Carrozza MC, Dario P (2007) Biomechatronic design and control of an anthropomorphic artificial hand for prosthetic and robotic applications. IEEE/ASME Trans Mechatron 12(4):418–429

35. Laliberte T, Gosselin CM (1998) Simulation and design of underactuated mechanical hands. Mech Mach Theory 33:39–57

36. Luo M, Mei T, Wang X, Yu Y (2004) Grasp characteristics of an underactuated robot hand. In: Proceedings of the 2004 IEEE international conference on robotics and automation, New Orleans, LA, pp 2236–2241

37. Wu L, Carbone G, Ceccarelli M (2009) Designing an underactuated mechanism for a 1 active DOF finger operation. Mech Mach Theory 44(2):336–348

38. Wu L, Ceccarelli M (2009) A numerical simulation for design and operation of an underactuated finger mechanism for larm hand. Mech Des Struct and Mach 37(1):86–112

39. Zhao J, Jiang L, Shi S, Cai H, Liu H, Hirzinger G (2006) A five-fingered underactuated prosthetic hand system. In: Proceedings of the 2006 IEEE international conference on mechatronics and automation, Luoyang, pp 1453–1458, 25–28 June 2006

40. Nava Rodriguez NE, Carbone G, Ceccarelli M (2006) Optimal design of driving mechanism in a 1-DOF anthropomorphic finger. Mech Mach Theory 41:897–911

41. Khakpour H, Birglen L (2013) Numerical analysis of the grasp configuration of a planar 3-DOF linkage-driven underactuated finger. J Comput Nonlinear Dyn 8. doi: 10.1115/1.4007359

42. Balasubramanian R, Dollar AM (2011) Performance of serial underactuated mechanisms: number of degrees of freedom and actuators. In: 2011 IEEE/RSJ international conference on intelligent robots and systems, San Francisco, CA, USA, pp 1823–1829, 25–30 Sept 2011

43. Balasubramanian R, Dollar AM (2011) A comparison of workspace and force capabilities between classes of underactuated mechanisms. In: 2011 IEEE international conference on robotics and automation, Shanghai, China, pp 3489–3496, 9–13 May 2011

44. Birglen L, Gosselin CM (2004) Kinetostatic analysis of underactuated fingers. IEEE Trans Robot Autom 20(2):211–221

45. Birglen L, Gosselin CM (2006) Grasp-state plane analysis of two-phalanx underactuated fingers. Mech Mach Theory 41:807–822

Chapter 19
Quasi-equivalent Coupling Motion Model of Two-Wheeled Differentially Driven Mobile Robot

Niu Wang, Zhihu Ruan, Bingxin Ran and Rongzheng Fang

Abstract Due to the presence of nonholonomic constraints of two-wheeled differentially driven mobile robot (TWDDMR), and the left and right wheel motors are affected by constraint reaction generating resistance moment, the TWDDMR has a strong dynamics coupling problem. By introducing the dynamic coupling into dynamic structure of double closed-loop drive system (DLDCM), the dynamic mechanism model of drive system with coupling is obtained. Then, the quasi-equivalent modeling (QEM) approach is used to simplify the mechanism model so as to get the quasi-equivalent dynamic model as well as corresponding state-space equations. And the quasi-equivalent state-space motion model is obtained through integration of the kinematic model into quasi-equivalent dynamic model. Then, by using speed response data of the actual system and combining with genetic algorithm to accurately identify the model parameters. Finally, through experiments results of the TWDDMR motion model and the second-order model, respectively, comparing with the actual system which demonstrates the effectiveness of the proposing method and model.

Keywords TWDDMR · Dynamics coupling · Quasi-equivalent modeling · Model identification · Genetic algorithms

19.1 Introduction

Two-wheeled differentially driven mobile robot (TWDDM) is a common wheeled mobile robot, generally uses two double loop direct current motors (DLDCM, Double Loop Direct Current Motor) as the drive of system. The application of TWDDM is wide, its motion systems with nonholonomic constraints and strong

N. Wang (✉) · Z. Ruan · B. Ran · R. Fang
College of Automation, Chongqing University, Room 2009, The Main Classroom Building,
Area A, No.174, Shazheng Street, Shapingba District, Chongqing, China
e-mail: wangniuwn123@163.com

nonlinearity. Including load changes, dynamics strongly coupling and other factors have a greater impact on motion of TWDDM. For motion model of TWDDM, according to the voltage balance equation and torque balance equation of DCM, [1, 2] obtain DLDCM Second-order decoupled model (SDM, second-order decoupled model), but SDM has ignored the presence of nonlinear in dynamical systems of TWDDM, and compared to the actual system it has large differences in the process of accelerating dynamic response [3]. In order to get closer to the actual model of DLDCM, [4] studies the saturation nonlinear of DLDCM, and obtains nonlinear model of DLDCM, so that results of model response are close to test results of actual platform, but the model is very complex and difficult to apply to the actual system. In [5] is proposed a robust adaptive control method of dynamic model with parameter uncertainties and external disturbances. Dong and Kuhnert [6] propose model parameters and nonparametric uncertain tracking control method of TWDDM. But they are mainly aimed at the controller design on the basis of model parameters uncertainty, but the controller structure is complex and difficult to apply to the actual system. In order to obtain a DLDCM model which is more simplified and easy to actual application, [7, 8] make DLDCM simplifying saturated nonlinear state-space model by using QEM. And the state-space model is more close to the real system under the condition for load constant of TWDDM, once load of TWDDM changes, the model cannot reflect the true wheel speed response process of TWDDM. In [9] is derived the nonlinear differential between input torque and speed of TWDDM. And it gets system state equation of TWDDM, but it does not research TWDDM drive system dynamics, and only on the simulation platform without comparing the data of simulation platform to actual platform, so it cannot ensure that research can move to the physical platform. In [10] is obtained the soccer robot's motor model parameters under different load conditions by using curve fitting method, to a certain extent, it can alternate the variable load drive system model of TWDDM, but it has a large amount of experiment work, and curve fitting has a big error. So it is difficult to apply to other robotic platform. In [11] the formation control problem of multiple nonholonomic mobile robots is aimed at, including actuator and formation dynamics, and designs a new control strategy that combination of kinematic and driver enter voltage controller by back stepping, but the dynamic model does not reflect the coupling relationship between the two motor systems. The motion model of TWDDM basing on quasi-equivalent model of DLDCM with variable load is obtained in [12] , but TWDDM as a whole, contains two pairs of closed-loop drive system. TWDDM with the nonholonomic constraint, so two motors have strong coupling on the underlying dynamic character [9]. But such quasi-equivalent model of DLDCM with variable load only applies to a single motor and does not reflect the coupling relationship between the two-way motor systems.

This paper is based on quasi-equivalent model of DLDCM with variable load, combining Lagrange dynamics equation of TWDDM to obtain the dynamics model of drive system for TWDDM with coupling relationship. Using QEM method to simplify the above dynamics coupled model, we can obtain quasi-equivalent dynamics coupling model of TWDDM, and combining with kinematic model of

TWDDM, we can obtain quasi-equivalent coupling motion model of TWDDM. Then by using speed response data of the actual system and combining with genetic algorithm to accurately identify the model parameters. Finally, experiments results of motion model of TWDDMR demonstrate effectiveness of the proposing method and model comparing with the actual system.

19.2 Quasi-Equivalent Coupling Motion Model

19.2.1 Kinematics Model of TWDDM

The geometric structure diagram of TWDDM is as shown in Fig. 19.1.

Velocity matrix of TWDDM relative to the world coordinate system is $\dot{V}_c = \begin{bmatrix} \dot{x}_c & \dot{y}_c & \dot{\theta} \end{bmatrix}^T$, and angular velocity of the left and right driving wheels is $v = \begin{bmatrix} \dot{\hat{\varphi}}_l & \dot{\hat{\varphi}}_r \end{bmatrix}^T$, velocity of TWDDM in the body coordinate system is $V_R = \begin{bmatrix} R_{\dot{x}_c} & R_{\dot{y}_c} & \dot{\theta} \end{bmatrix}^T$. The length of the two driving wheel axis is l, and radius of each driving wheel is r. Assume that movement of TWDDM meets the condition of pure rolling and no slip, and kinematics equation of TWDDM is easy to get by rigid body mechanics.

Equation (19.1) multiplies by the rotation matrix that can be transformed to speed of TWDDM of the world coordinate system.

The generalized pose of TWDDM is $q = [x_c, y_c, \theta, \hat{\varphi}_l, \hat{\varphi}_r]^T$, and then Eqs. (19.2) and (19.3) can be rewritten as follows.

$$V_R = \begin{bmatrix} R_{\dot{x}_c} \\ R_{\dot{y}_c} \\ \dot{\theta} \end{bmatrix} = \frac{r}{l} \begin{bmatrix} \frac{l}{2} & \frac{l}{2} \\ 0 & 0 \\ -1 & 1 \end{bmatrix} \begin{bmatrix} \dot{\hat{\varphi}}_l \\ \dot{\hat{\varphi}}_r \end{bmatrix} \tag{19.1}$$

Fig. 19.1 Geometry structure diagram of TWDDM
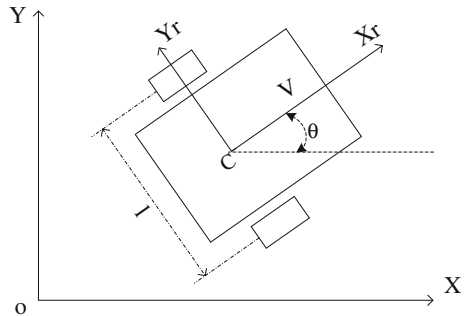
$$\begin{bmatrix} \dot{x}_c \\ \dot{y}_c \\ \dot{\theta} \end{bmatrix} = \begin{bmatrix} \cos\theta & -\sin\theta & 0 \\ \sin\theta & \cos\theta & 0 \\ 0 & 0 & 1 \end{bmatrix} V_R = \begin{bmatrix} \frac{r\cos\theta}{2} & \frac{r\cos\theta}{2} \\ \frac{r\sin\theta}{2} & \frac{r\sin\theta}{2} \\ -1 & 1 \end{bmatrix} \begin{bmatrix} \dot{\hat{\phi}}_l \\ \dot{\hat{\phi}}_r \end{bmatrix} \tag{19.2}$$

$$\dot{q} = S(q)v \tag{19.3}$$

where:

$$S(q) = \begin{bmatrix} \frac{r\cos\theta}{2} & \frac{r\sin\theta}{2} & -\frac{r}{l} & 1 & 0 \\ \frac{r\cos\theta}{2} & \frac{r\sin\theta}{2} & \frac{r}{l} & 1 & 0 \end{bmatrix}^T \tag{19.4}$$

$$A(q)\dot{q} = 0 \tag{19.5}$$

$$A(q) = \begin{bmatrix} \sin\theta & -\cos\theta & 0 & 0 & 0 \\ -\cos\theta & -\sin\theta & \frac{l}{2} & r & 0 \\ -\cos\theta & -\sin\theta & \frac{l}{2} & 0 & r \end{bmatrix} \tag{19.6}$$

The generalized velocity is verified to satisfy the nonholonomic constraint equations by Eq. (19.5).

19.2.2 Dynamics Coupling Model of TWDDM

In Fig. 19.1, the overall mass of TWDDM is m, including mass of two wheels and mass of two drive motors and mass of TWDDM platform. The z-axis is perpendicular to the body coordinate system $X_r C Y_r$, and moment of inertia of TWDDM is J_z around the z-axis, and the moment of inertia of the motor shafts of left and right wheels are, respectively, J_l and J_r, then moment of inertia of the output shaft are, respectively, $\hat{J}_l$ and $\hat{J}_r$. Torque of the left and right wheels of the motor shaft are, respectively, T_l and T_r, and then conversion to the output shaft are, respectively, $\hat{T}_l$ and $\hat{T}_r$. The angular displacement of the motor shaft for left and right wheels are, respectively, $\hat{\phi}_l$ and $\hat{\phi}_r$, and then conversion to the output shaft are, respectively, $\hat{\phi}_l$ and $\hat{\phi}_r$. TWDDM is also subject to binding during the movement, left and right wheels subjecting to binding of X direction are, respectively, $\hat{F}_{xl}$ and $\hat{F}_{xr}$. The sum of Y direction under the constraints reaction is $\hat{F}_y$. To make force analysis of TWDDM, respectively, in the x direction, y direction, z direction, and the axial of the two driving wheels. Through torque balance equations, we can get the following Eq. (19.7).

$$
\begin{cases}
m\ddot{x}_c - (\hat{F}_{xl} + \hat{F}_{xr})\cos\theta + \hat{F}_y\sin\theta = 0 \\
m\ddot{x}_c - (\hat{F}_{xl} + \hat{F}_{xr})\sin\theta - \hat{F}_y\cos\theta = 0 \\
J_z\ddot{\theta} + \frac{l}{2}(\hat{F}_{xr} - \hat{F}_{xl}) = 0 \\
\hat{J}_l\ddot{\varphi}_l + \hat{F}_{xl}r = \hat{T}_l \\
\hat{J}_r\ddot{\varphi}_r + \hat{F}_{xr}r = \hat{T}_r
\end{cases}
\tag{19.7}
$$

$$
M\ddot{q} = E\tau - A^T(q)\lambda
\tag{19.8}
$$

$$
\begin{cases}
M = \mathrm{diag}\{\, m \quad m \quad J_z \quad \hat{J}_l \quad \hat{J}_r \,\} \\
E = \begin{bmatrix} 0 & 0 & 0 & 1 & 0 \\ 0 & 0 & 0 & 0 & 1 \end{bmatrix}^T \\
\lambda = \begin{bmatrix} \hat{F}_y & \hat{F}_{xl} & \hat{F}_{xr} \end{bmatrix}^T \\
\tau = \begin{bmatrix} \hat{T}_l & \hat{T}_r \end{bmatrix}^T
\end{cases}
\tag{19.9}
$$

The above equation can be written as the Lagrange standard equations form (19.8) and (19.9).

By using Eqs. (19.4) and (19.6), (19.10) can be obtained.

Both ends of the Lagrange Eq. (19.8) multiply by $S^T(q)$ at the same time, and which substitutes into Eq. (19.10). Then Lagrangian can be eliminated to Eq. (19.11).

To take derivatives of at both ends of the Eq. (19.3), and which substitutes into Eq. (19.11), then the kinetic equation of TWDDM can be got as follows Eq. (19.12).

$$
A(q)S(q) = 0
\tag{19.10}
$$

$$
\tau = S^T(q)M\ddot{q}
\tag{19.11}
$$

$$
\dot{v} = -\left(S^T(q)MS(q)\right)^{-1}S^T(q)M\dot{S}(q)v + \left(S^T(q)MS(q)\right)^{-1}\tau
\tag{19.12}
$$

Through simplifying the above equation, the nonlinear differential equations between each wheel speed and drive torque of TWDDM can be obtained as follows Eq. (19.13).

Because the actual has the motor speed reducer, and the reduction ratio is i, the parameter of the output shaft can be switched to the motor shaft of the drive motor, and by using Eq. (19.13) we can obtain Eq. (19.14).

In practice, people often use the wheel speed (n) instead of the wheel angular velocity ($\dot{\varphi}$), therefore left and right wheels speed are, respectively, n_l and n_r, and $\dot{\varphi} = \frac{2\pi n}{60}$, then Eq. (19.14) can be obtained as follows.

where:

$$\begin{cases} \ddot{\hat{\phi}}_l = {}^l\hat{\lambda}_l\hat{T}_l + {}^r\hat{\lambda}_l\hat{T}_r \\ \ddot{\hat{\phi}}_r = {}^l\hat{\lambda}_r\hat{T}_l + {}^r\hat{\lambda}_r\hat{T}_r \end{cases} \tag{19.13}$$

$$\begin{cases} \ddot{\phi}_l = {}^l\lambda_l T_l + {}^r\lambda_l T_r \\ \ddot{\phi}_r = {}^l\lambda_r T_l + {}^r\lambda_r T_r \end{cases} \tag{19.14}$$

$$\begin{cases} \dot{n}_l = {}^l\lambda_l T_l + {}^r\lambda_l T_r \\ \dot{n}_r = {}^l\lambda_r T_l + {}^r\lambda_r T_r \end{cases} \tag{19.15}$$

$$\begin{cases} {}^l\lambda_l = 30 \cdot i^{2l}\hat{\lambda}_l/\pi \\ {}^r\lambda_l = 30 \cdot i^{2r}\hat{\lambda}_l/\pi \\ {}^l\lambda_r = 30 \cdot i^{2l}\hat{\lambda}_r/\pi \\ {}^r\lambda_r = 30 \cdot i^{2r}\hat{\lambda}_r/\pi \end{cases} \tag{19.16}$$

For the actual TWDDM, each wheel commonly is using DLDCM. DLDCM has better dynamic performance relative to the single loop control system, which mainly is reflected in the fast starting speed. Figure 19.2 is a single DLDCM dynamic block diagram.

By using Eqs. (19.15) with (19.17) we can get Eq. (19.18) as follows.

$$\begin{cases} \tau_l = L_l/R_l & \tau_r = L_r/R_r \\ T_{el} = C_{ml}I_l & T_{er} = C_{mr}I_r \\ E_l = C_{el}n_l & E_r = C_{er}n_r \\ U_l - E_l = R_l(I_l + \tau_l\dot{I}_l) & U_r - E_r = R_r(I_r + \tau_r\dot{I}_r) \\ T_l = T_{el} - T_{Ll} & T_r = T_{er} - T_{Lr} \\ T_{Ll} = (1 - \eta_l)T_{el} & T_{Lr} = (1 - \eta_r)T_{er} \end{cases} \tag{19.17}$$
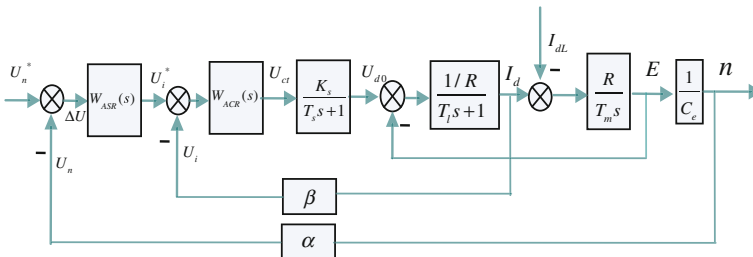
Fig. 19.2 Dynamic structure of DLDCM

$$\begin{cases} \dot{I}_l(t) = -\frac{I_l(t)}{\tau_l} - \frac{E_l(t)}{L_l} + \frac{U_l(t)}{L_l} \\ \dot{E}_l(t) = {}^l\lambda_l C_{el} C_{ml} \eta_l I_l + {}^r\lambda_l C_{el} C_{mr} \eta_r I_r \\ \dot{I}_r(t) = -\frac{I_r(t)}{\tau_r} - \frac{E_r(t)}{L_r} + \frac{U_r(t)}{L_r} \\ \dot{E}_l(t) = {}^l\lambda_r C_{er} C_{ml} \eta_l I_l + {}^r\lambda_r C_{er} C_{mr} \eta_r I_r \end{cases} \tag{19.18}$$

19.2.3 Quasi-equivalent Dynamic Coupling Model

By using methods of the characteristic analysis and QEM to simplify DLDCM model into a state-space model, Fig. 19.3 shows the dynamic coupling model of drive system for TWDDM after QEM simplification.

The state variables of the system are defined as x_1, x_2, x_3, x_4. Left and right wheels of TWDDM are all normal rotation direction, which is turning as an example.

(1)   The system state equation:
   S_1 State—Left and right wheel motors are working in an unsaturated zone:

$$\begin{bmatrix} \dot{x}_1 \\ \dot{x}_2 \\ \dot{x}_3 \\ \dot{x}_4 \end{bmatrix} = \begin{bmatrix} 0 & -\alpha_l T_{l2}/J_L & 0 & 0 \\ T_{l1} & -K_l\alpha_l T_{l2}/J_L & K_{lr}T_{r1} & -K_{lr}K_r\alpha_r T_{r2}/J_R \\ 0 & 0 & 0 & -\alpha_r T_{r2}/J_R \\ K_{rl}T_{l1} & -K_{rl}K_l\alpha_l T_{l2}/J_L & T_{r1} & -K_r\alpha_r T_{r2}/J_R \end{bmatrix} \begin{bmatrix} x_1 \\ x_2 \\ x_3 \\ x_4 \end{bmatrix}$$
$$+ \begin{bmatrix} 1 & 0 \\ K_l & K_{lr}K_r \\ 0 & 1 \\ K_{rl}K_l & K_r \end{bmatrix} \begin{bmatrix} U_l \\ U_r \end{bmatrix}$$

$$\tag{19.19}$$
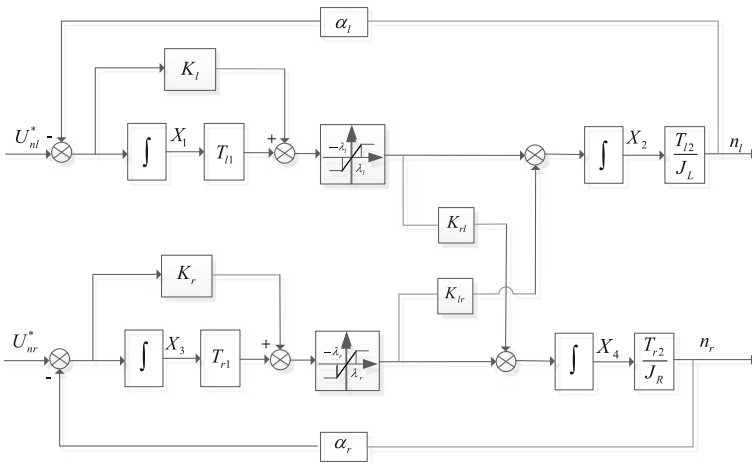
Fig. 19.3 Quasi-equivalent model of TWDDM

S_2 State—Left wheel motor is working in saturated zone; Right wheel motor is working in the unsaturated zone as in Eq. (19.20).

S_3 State—Right wheel motor is working in saturated zone; Left wheel motor is working in the unsaturated zone as in Eq. (19.21).

$$\begin{cases} x_1 = \frac{(\lambda_l - K_l U_l + \alpha_l K_l T_{l2} x_2 / J_L)}{T_{l1}} \\ \dot{x}_2 = \lambda_l + K_{lr}(T_{r1} x_3 - \frac{K_r \alpha_r x_4 T_{r2}}{J_R} + K_r U_r) \\ \dot{x}_3 = U_r - \frac{\alpha_r x_4 T_{r2}}{J_R} \\ \dot{x}_4 = K_{rl} \lambda_l + T_{r1} x_3 - \frac{K_r \alpha_r x_4 T_{r2}}{J_R} + K_r U_r \end{cases} \tag{19.20}$$

$$\begin{cases} \dot{x}_1 = U_l - \frac{\alpha_l T_{l2} x_2}{J_L} \\ \dot{x}_2 = K_{lr} \lambda_r + T_{l1} x_1 - \frac{K_l \alpha_l T_{l2} x_2}{J_L} + K_l U_l \\ x_3 = \frac{(\lambda_r - K_r U_r + \alpha_r K_r T_{r2} x_4 / J_R)}{T_{r1}} \\ \dot{x}_4 = \lambda_r + K_{rl}\left(T_{l1} x_1 - \frac{K_l \alpha_l T_{l2} x_2}{J_L} + K_l U_l\right) \end{cases} \tag{19.21}$$

S_4 State—Left and right wheel motors are working in the saturated zone as in Eq. (19.22).

(2) The system output equation as in Eq. (19.23).

$$\begin{cases} x_1 = (\lambda_l - K_l U_l + \alpha_l K_l T_{l2} x_2 / J_L)/T_{l1} \\ \dot{x}_2 = \lambda_l + K_{lr} \lambda_r \\ x_3 = (\lambda_r - K_r U_r + \alpha_r K_r T_{r2} x_4 / J_R)/T_{r1} \\ \dot{x}_4 = \lambda_r + K_{rl} \lambda_l \end{cases} \tag{19.22}$$

$$y = \begin{bmatrix} n_l \\ n_r \end{bmatrix} = \begin{bmatrix} 0 & T_{l2}/J_L & 0 & 0 \\ 0 & 0 & 0 & T_{r2}/J_R \end{bmatrix} \begin{bmatrix} x_1 \\ x_2 \\ x_3 \\ x_4 \end{bmatrix} \tag{19.23}$$

And the discriminant formulas for each state:

$$S = \begin{cases} S_1 & \left(K_l U_l - \frac{K_l \alpha_l T_{l2} x_2}{J_L} + T_{l1} x_1 < \lambda_l\right) \cap \left(K_r U_r - \frac{K_r \alpha_r T_{r2} x_4}{J_R} + T_{r1} x_3 < \lambda_r\right) \\ S_2 & \left(K_l U_l - \frac{K_l \alpha_l T_{l2} x_2}{J_L} + T_{l1} x_1 > \lambda_l\right) \cap \left(K_r U_r - \frac{K_r \alpha_r T_{r2} x_4}{J_R} + T_{r1} x_3 < \lambda_r\right) \\ S_3 & \left(K_l U_l - \frac{K_l \alpha_l T_{l2} x_2}{J_L} + T_{l1} x_1 < \lambda_l\right) \cap \left(K_r U_r - \frac{K_r \alpha_r T_{r2} x_4}{J_R} + T_{r1} x_3 > \lambda_r\right) \\ S_4 & \left(K_l U_l - \frac{K_l \alpha_l T_{l2} x_2}{J_L} + T_{l1} x_1 > \lambda_l\right) \cap \left(K_r U_r - \frac{K_r \alpha_r T_{r2} x_4}{J_R} + T_{r1} x_3 > \lambda_r\right) \end{cases} \tag{19.24}$$

Above all the state-space expressions constitute a complete dynamic coupling model of TWDDM. Among them, X1, X2 are, respectively, given speed of driving
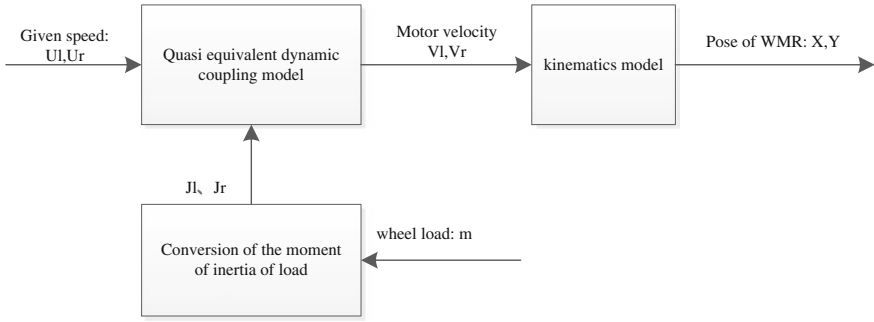
Fig. 19.4 Structure of quasi-equivalent motion model of TWDDM

motor for left and right wheels. Y is the system output speed matrix. $T_{l1}, T_{l2}, K_l, \alpha_l, \lambda_l, K_{lr}, T_{r1}, T_{r2}, K_r, \alpha_r, \lambda_r, K_{rl}$ are parameters of system model, and they are also the inherent parameters of the system, and they are constant too.

19.2.4 Quasi-equivalent Coupling Motion Model of TWDDM

In fact, $^l\lambda_l$ and $^r\lambda_l$ are related to the amount of rotation inertia and revolver. The coupling coefficient is inherent to the TWDDM parameter, and it is approximated as a determined amount.

In fact, $^l\lambda_l$ and $^r\lambda_l$ are all certain amount associating with moment of inertia of the left wheel. The coupling coefficient is the intrinsic parameters of TWDDM, and it is approximately determining a certain amount. Changes of TWDDM load is mainly reflected in the changes of $^l\lambda_l$. When TWDDM load changes, average overall mass of TWDDM will be assigned to the two wheels, so that the moment of inertia of each drive wheel system is changed. Similarly, parameters ($^r\lambda_r$ and $^l\lambda_r$) of the right wheel model have the same properties, and $^l\lambda_l = 30i^2/\pi J_L, {}^r\lambda_r = 30i^2/\pi J_R$. Therefore, J_L and J_R are equivalent moment of inertia for load of TWDDM converting to driving system in Fig. 19.4. Therefore, the quasi-equivalent coupling motion model of TWDDM is established in this paper, which not only can reflect change of load of TWDDM, but also reflects the dynamics coupling relation of drive system.

19.3 Accurate Identification of Model Parameters

For model parameters, this paper uses genetic algorithm tuning [13, 14]. Genetic algorithm is a kind of optimization search algorithm which has wide applicability.

According to the principle of genetic algorithm introduced above, setting evaluation function is an important step for parameter identification. This article selects the average error between speed response of motor model and the actual motor speed value as a fitness function under the condition of step input:

$$f(z) = \frac{\sum_{i=1}^{m} |n_{lc}(i) - n_{ls}(i)|}{m} + \frac{\sum_{i=1}^{m} |n_{rc}(i) - n_{rs}(i)|}{m} \qquad (19.25)$$

In the Eq. (19.25), $n_{lc}(i)$ and $n_{ls}(i)$ are, respectively, speed of actual platform and model for left wheel at the ith sampling time. Similarly, $n_{lc}(i)$ and $n_{ls}(i)$ are, respectively, speed of actual platform and model for left wheel at the ith sampling time. M is the number of sampling. Therefore, problems of model parameter optimization by using the improved genetic algorithm, which can be summed up in realization of the objective function $Minf(z)$ $(L < Z < U)$. Among them, L and U are the feasible solution space of the model parameters (Z).

19.4 Experiments

19.4.1 Experimental Design and Evaluation Index

Quantitative comparison of the curve by using following the evaluation index:

The average error is as in Eq. (19.26).

The m is the total number of sampling, and the difference between the actual data values of the system for sampling point i and calculated values of model is written as follows in Eq. (19.27).

$y_c(i)$ and $y_s(i)$, respectively, are speed value for the actual system and model, respectively, in the sampling time i. The maximum error is as in Eq. (19.28).

$$EX = \frac{\sum_{i=1}^{m} |e(i)|}{m} \qquad (19.26)$$

$$e(i) = y_c(i) - y_s(i) \qquad (19.27)$$

$$M_D = \max(|e(1)|, |e(2)|, \ldots, |e(m)|) \qquad (19.28)$$

19.4.2 Experimental Data Analysis

19.4.2.1 Model Parameter Identification

Table 19.1 shows that using improved genetic algorithm to identify the quasi-equivalent coupling motion model parameters of TWDDM.

Table 19.1 Parameter identification of quasi-equivalent coupling motion model for TWDDM

T_{l1}	T_{l2}	K_l	α_l	λ_l	K_{lr}
38.410	0.188	1.633	0.991	261.431	0.046
T_{r1}	T_{r2}	K_r	α_r	λ_r	K_{rl}
98.105	0.175	2.838	0.999	282.242	0.042
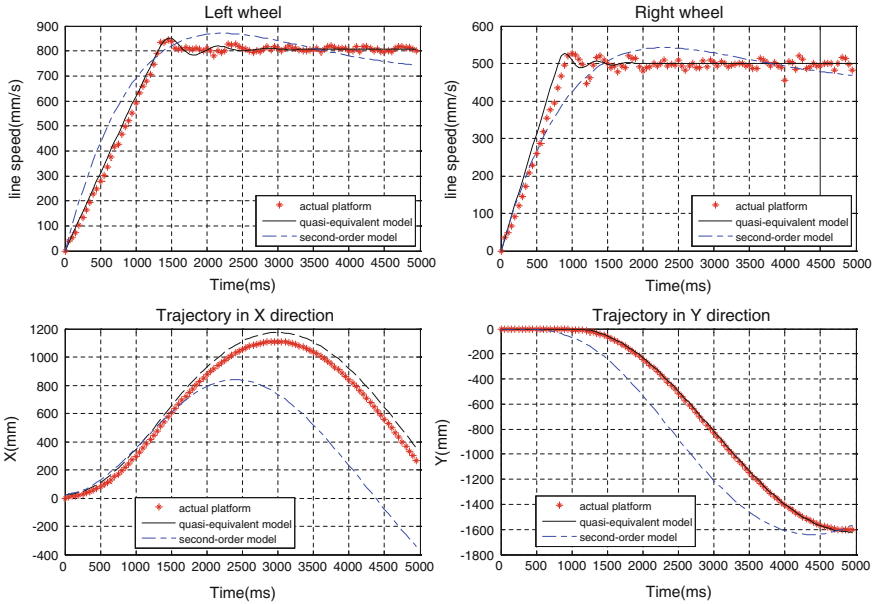
Fig. 19.5 Responses of models and physical system for (800, 500) mm/s under 4.5 kg

19.4.2.2 Model Validation

Two experiments are designed for quasi-equivalent coupling motion model of the TWDDM and the second-order decoupled model of existing, respectively, comparing with the response of the actual output. There are two comparative experiments for different wheel speeds and different loads, and specific response curve is shown in Figs. 19.5 and 19.6.

From the above evaluation indexes of Tables 19.2 and 19.3, the above two experiments indicate that the proposing quasi-equivalent coupling motion model of TWDDM is closer to the actual system than the second-order decoupled model in the wheel speed and the trajectory.
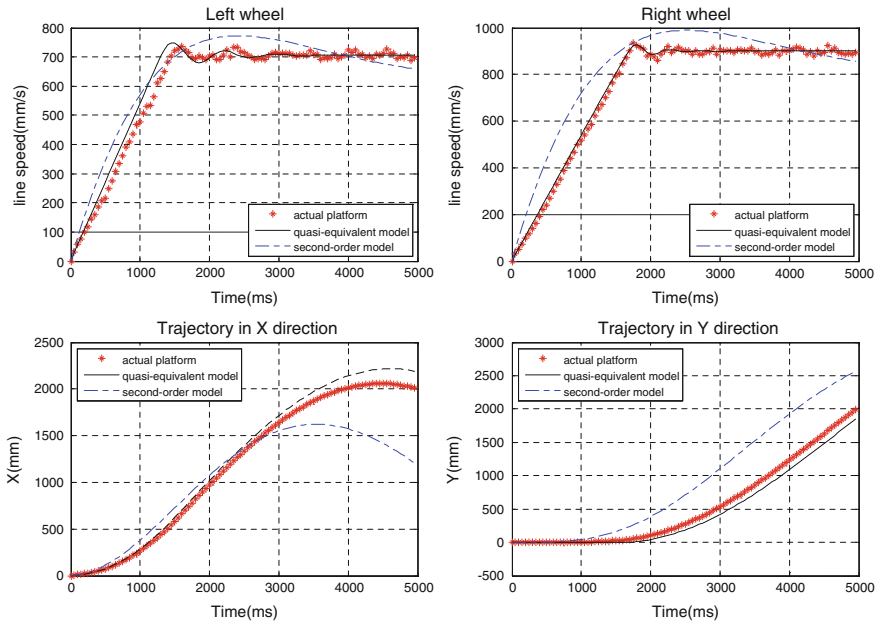
Fig. 19.6 Responses of models and physical system for (700, 900) mm/s under 9 kg

Table 19.2 Error evaluation of (800,500) mm/s under 4.5 kg

	Index/mm	Left wheel	Right wheel	Trajectory
TWDDM motion model	EX	14.06	15.26	40.80
	MD	41.80	70.40	74.30
Second-order model	EX	56.10	28.43	460.00
	MD	164.40	109.50	860.00

Table 19.3 Error evaluation of (700,900) mm/s under 9 kg

	Index/mm	Left wheel	Right wheel	Trajectory
TWDDM motion model	EX	19.90	11.59	140.00
	MD	86.90	32.20	319.00
Second-order model	EX	48.70	82.10	550.00
	MD	126.70	211.70	1360.00

19.5 Conclusions

This paper is based on quasi-equivalent model of DLDCM with variable load, combining Lagrange dynamics equation of TWDDM to obtain the dynamics model of drive system for TWDDM with coupling relationship. Using QEM method to simplify the above dynamics coupled model, we can obtain quasi-equivalent dynamics coupling model of TWDDM, and combining with kinematic model of TWDDM, we can obtain quasi-equivalent coupling motion model of TWDDM. Then by using speed response data of the actual system and combining with genetic algorithm to accurately identify the model parameters. Finally, experiments results of motion model of TWDDMR demonstrate effectiveness of the proposing method and model comparing with the actual system.

References

1. Ruxun Z, Zhang Z, Qi Y (2006) Direct identification of DC electromotor model parameter. Comput Simul 23(6):113–115 (in Chinese)
2. Jiang L, Yang J, Yang Z, Zhang Z (2008) Design proposal for robot servo system based on MatlabRTW. J S China Univ Technol (Nat Sci Ed) 36(9):136–139 (in Chinese)
3. Lyshevski SE (1999) Nonlinear control of mechatronic systems with permanent-magnet DC motors. Mechatronics 9:539–552 (in Chinese)
4. Pakorn S, Hiroaki S, Masatoshi H et al (2006) The effects of controller saturation on dynamic characteristics of commercial positioning systems and their countermeasures. In: 2006 SICE-ICASE international joint conference, Busan, South Korea, pp 880–883
5. Kim MS, Shin JH, Hong SG, Lee JJ (2003) Designing a robust adaptive dynamic controller for nonholonomic mobile robots under modeling uncertainties and disturbances. Mechatronics 13 (5):507–519
6. Dong W, Kuhnert KD (2005) Robust adaptive control of nonholonomic mobile robot with parameter and nonparameter uncertainties. IEEE Trans Rob 21(2):261–266
7. Wang N, LI Z, Li Y, Pan Y (2008) Motion system simulation of two wheeled robot with DC motor drive system. J Syst Simul, 20(17):4633–4646 (in Chinese)
8. Li Y, Wang Niu Z (2008) Modeling and identification of double loop DC motor(DLM) control system. Control Theory Appl 25(6):1077–1080 (in Chinese)
9. Chen X, Li C, Li G, Luo Y (2008) Dynamic model based motor control for wheeled mobile robots. Robot 30(4):326–332 (in Chinese)
10. Wu Y, Li Z, Wang N (2009) Modeling of double loop DC motor control system under variable load. J SE Univ (Nat Sci Ed) 39(S1):172–176 (in Chinese)
11. Li Y, Zhu L, Sun M (2014) Formation self-adaptation control problem of mobile robot including actuator dynamics. Comput Eng Appl 50(1):235–240 (in Chinese)
12. Ruan Z, Wang N, Ran B (2014) Motion model of two-wheel differential drive mobile robot under variable load. In: The 6th international conference on mechanical and electronics engineering, Beijing, China (in Chinese)

13. Li Z, Zhang H, Gu J et al (2008) Dynamic parameters identification of three-link acrobat on horizontal bar. Control Theory Appl 25(2):242–246, 252 (in Chinese)
14. Jiangong GU (2006) The application of GAs in human-simulated intelligent control. Chongqing University, Chongqing (in Chinese)

Chapter 20
Humanware Model in Novel Decision System

**Xianjun Zhu, Jie Yang, Yin Sheng, Zhipeng Wang
and Xianzhong Zhou**

Abstract How to integrate human (expert) into the procedure of decision-making is an important issue for the next generation of decision support systems (DSS). Based on the concepts related to humanware (Hw) in our research, including Hw, Hw technology, HW service, and Hw and knowledge, the framework of novel decision systems (NDS) is presented. Then this paper proposes the structure of Hw model (HwM), which describes the key component and implement steps in detail. HwM can convert human (expert) into one component, so as to facilitated Hw to participate in the procedure of decision-making. Finally, a case study demonstrates that Hw can be engaged in the procedure of decision-making.

Keyword DSS · Human–computer interaction (HCI) · NDS · HwM

20.1 Introduction

In the 1970s, G. Anthony Gorry presented first the concept of DSS [1]. Based on this concept, a large number of qualitative and quantitative models are proposed to solve a series of representative decision support problems [2–5]. However, more and more decision tasks (problems) are too complicated to be described by a quantitative or qualitative model, e.g., qualitative, fuzzy, and uncertainty tasks (problems) [6–9]. Researchers began to seek a new way to blend human into the procedure of decision-making.

At the beginning of this century, the progress of Internet technology promotes the development of HCI technology [10], especially the fourth generation of HCI. DSS research also enters into a new stage. For example, case-based decision aids as a methodology for building systems in which people and machines work together to

X. Zhu · J. Yang · Y. Sheng · Z. Wang · X. Zhou (✉)
Department of Control and System Engineering, School of Management and Engineering,
Nanjing University, 22 Hankou Road, Nanjing 210093, Jiangsu, China
e-mail: zhouxz@nju.edu.cn

solve problems [11]. A large number of scholars are engaged in researching DSS that is based on network environment. Their studies are also based on the traditional DSS in essence, which only has two kinds of research patterns. One pattern is that human has priority, and computer is just an auxiliary tool, such as expert system. The other is that computer has priority, human is a watcher and participate in a small amount of work, such as people in the loop. In both patterns, humans always act as the external factor of DSS.

We try to build a new model, which can blend human (expert) in the procedure of decision-making, and also seek to design architecture to convert human (expert) into Hw, and that can be retrieved and invoked in the procedure of decision-making.

20.2 Concepts Related to Humanware

20.2.1 Humanware

Definition 20.1 Humanware (Hw). Hw is a carrier of human (expert) and interface, as well as the relationship of two elements. Hw is an important component of the NDS.

Human (expert) of Hw has the following characteristics:

- it is a normal person, which is a personalized description statistically and has bounded rational and personalized;
- it is a carrier of natural intelligence, which can provide knowledge, experience, and wisdom during the procedure of decision-making;
- it is a decision-maker, which can provide all kinds of support such as information, function, algorithm, etc.

Interface of Hw has dual functions, i.e., expression and presentation. The expression can help Hw to get data and information about the decision tasks (problems). The presentation can help Hw to show their abilities and the role they can bear.

20.2.2 Humanware Service

Definition 20.2 Humanware Service (HwS). In the NDS, HwS is a kind of special service provided by Hw, which is the service-oriented and modularization.

HwS can solve the semi-(un-)structured problems that cannot be solved by DSS, such as analysis, judge, advice, etc. It can assume the specific role in the procedure

of decision-making, and collaborate with others. Everyone can register and become an HwS in NDS.

HwS in the library is defined as a 7-tuple: <ID, Name, Category, Function, Input, Output, QoS>, where: ID is an identification which indicates that each service has an ID that is different from any other service; Name is defined to the service, and is nonuniqueness in the library; Category is the token of the classification of services, i.e., 0 is Software Service, 1 is Soft-HwS, 2 is Hard-HwS; Function is the ability description of HwS; Input and Output are the request and response parameters between HwS and system; QoS (Quality of Service) is the assessment to the HwS by the system and users.

20.2.3 Humanware and Knowledge

In the procedure of decision-making, Hw can provide various types of support, such as knowledge, experience, wisdom, etc. Knowledge is the most important factor. Figure 20.1 shows the relationship of knowledge and HwS.

Knowledge has two parts, i.e., tacit knowledge and explicit knowledge. Tacit knowledge is that cannot be expressed but can be used by human in the procedure of making, such as judgment of the situation. Others are explicit knowledge. A part of explicit knowledge can be encoded, including available software, computing, and symbolic inference, and so forth. The other part of explicit knowledge cannot be encoded, but human can understand, such as the content evaluation of pictures.

According to the classification of knowledge mentioned above, the vast majority of knowledge exists in Hw. HwS is a formal representation of Hw, so HwS has knowledge.

Fig. 20.1 Hw service and knowledge

Humanware and Knowledge

Not Code Knowledge **Explicit**

Tacit Knowledge **Tacit**

Code Knowledge **Explicit**
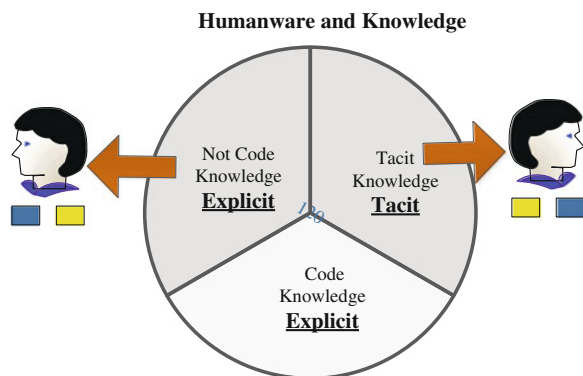
20.3 The Novel Decision System

According to the theory of system science, the function of the system behavior is decided by the composition of system elements and their relationships (structure). The traditional DSS has two elements, i.e., hardware and software. Based on the traditional DSS, NDS has a new element, i.e., Hw. So the status of NDS likes a troika.

NDS has three core elements, i.e., hardware, software, and Hw, and they have same status and role. During the procedure of making decision, Hw can provide its unique intelligence (individual knowledge, experience and wisdom). At the same time, Hw can closely collaborate with hardware and software under the network environment. For example, three kinds of wares can be unified: registration, management, and invocation, so as to achieve the decision tasks (problems).

Figure 20.2 is the NDS model, the relationship of each factor show as follows:

- Decision tasks (problems) is the core of the NDS, they are dispatched to three kinds of ware. Then three kinds of ware will send decision result to the NDS. NDS receive feedback information and change the state of decision node;
- Hardware is a kind of exist in physical form and combination together. According the function of information processing, hardware can be divided into several types, such as information storage, information media, information gathering, and information transmission, etc.;
- Software is based on the software knowledge, and as the form of code runs on all kinds of services. Software has several types, i.e., basic software, middleware, application software, and embedded software, etc.;

Fig. 20.2 Hw and knowledge

The novel decision system model
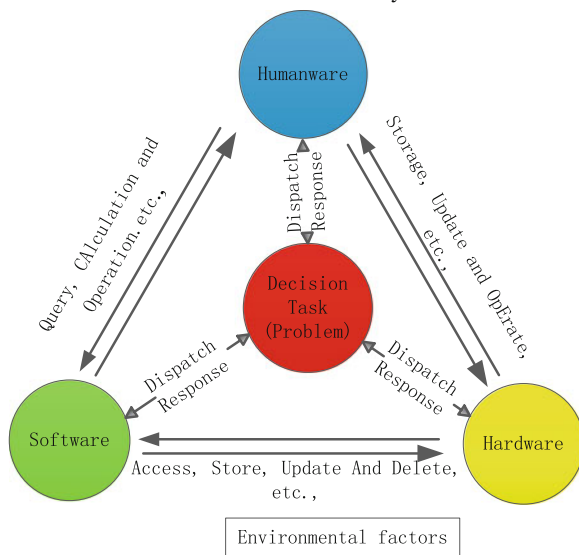
- Hw is based on conversion of natural human, who having a unique wisdom. It can collaborate with hardware and software under the network environment. It can be unified management, scheduling, enabling;
- Environmental factor is an indispensable part outside of the NDS, for example the network bandwidth of coastal area is obviously higher than of inland.

20.4 Humanware Model

In the NDS, HwM is an abstract object of Hw, which takes part in the procedure of decision-making. It has six components, these are Request Reception/Gather Device and Data Flow, Information Gate/Enhance, Multimodal Convert Protocols, Adaptive Push, Multi-channel expression and presentation device, and Hw, as shown in Fig. 20.3.

20.4.1 Overview of Hw Model

The main components of HwM are shown as follows:

- *Request Reception/Gather Device and Data Flow*: Request Reception between Hw and NDS takes in charge of receiving request and returning response of decision tasks (problems). First, in the procedure of decision-making, this component helps HwS obtaining other data and information from various
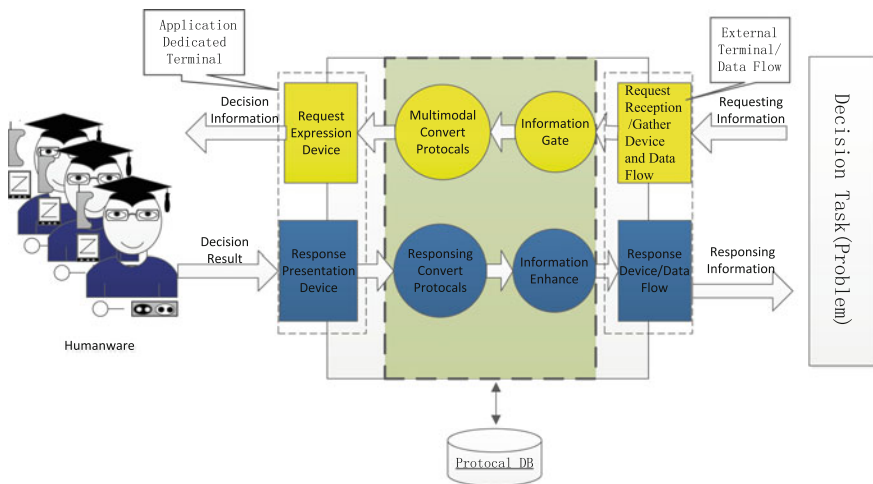
Fig. 20.3 Hw model

sources. Second, the state of decision node can be changed according by the content of response;

- *Information Gate/Enhance*: The data and information coming from the external device are very complicated. So the gate is responsible for choosing information for Hw, and form an unified reference information. The enhanced device is responsible for adding information filtered out by the gate device on the decision result, these information may be useful for the subsequent processing;
- *Multimodal Convert Protocols*: There are many formats of data and information filtered by the gate device, such as pictures, statistical data, video, audio, etc. They are fused to form a unified information format, i.e., statistics, speech, etc. Different formats of information can convert freely and smoothly according by the multimodal covert protocols;
- *Adaptive Push*: It is based on many technologies, e.g., data mining technology, natural language processing technology. Through digging Hw personal qualities, such as command art, preferences, etc. it can achieve ultimately that the appropriate information format is sent to the appropriate Hw;
- *Multi-channel expression and presentation device*: With the developing of eye tracking, speech recognition, gesture recognition technology (contact and non-contact), sensory feedback, and other HCI technologic, Hw can interact with several devices at the same time. Interaction with multiple channels can be used in the procedure, such as feeling channels, touch channels, etc. A lot of inter-action technologies improve the accuracy and efficient greatly, such as the precise interaction, three peacekeeping operator directly, and the procedure of biphasic interaction, etc.

20.4.2 Implement Procedure

Hw participating in the procedure of decision-making has the following steps:

Step 1: decision tasks (problems) are assigned to Hw. Hw can get the request of tasks, and Hw also can get other data and information through the other sources and channels;

Step 2: the information gate filtrate the data and information that is obtained from the step 1, then get the related data and information for the current decision tasks (problems);

Step 3: all kind of data and information are merged together and form a unified format, i.e., statistical information, voice information, touchscreen information, eye tracker information, etc.;

Step 4: under the network environment, Hw face different kinds of HCI device during the procedure of decision-making. Therefore, reference infor-mation should be shown on the appropriate devices autonomous;

Step 5: Hw integrate all kinds of information and make decisions. If the reference information is not enough, the process should return to the step 2;

Step 6: the decision result is accurate, and sent back to the NDS. Therefore, the presentation device is used to accept decision result;

Step 7: according the convert protocol, the decision result is converted into the unified format that be accepted by NDS.

Step 8: the information filtering out in the step 2 is attached to the decision result that may be useful for the other process;

Step 9: The response content is sent back to the NDS, the node state of decision-making process is modified;

Step 10: End.
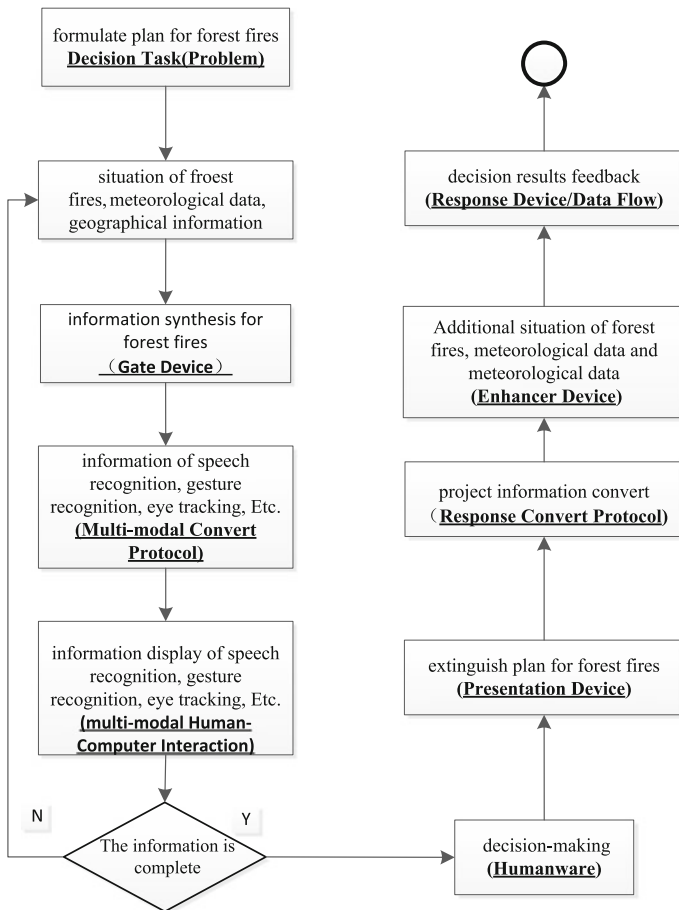
Fig. 20.4 Formulation procedure of extinguish plan for forest fires

20.5 An Illustrative Example

In this chapter, we give a formulation procedure plan for extinguishing forest fires, so as to demonstrate the Hw Model how to be engaged in the procedure of decision-making. The process is shown in Fig. 20.4.

The information of forest fires includes: (1) site information comes from the frontline firefighters; (2) detection information collects from all kinds of monitoring device; (3) surveillance information gathered by unmanned device; (4) the information of equipment, materials; (5) weather information including recent, present, and future.

Fusion information can be shown on an intuitive display of the video or audio message, which is suitable for video or audio information broadcast and display equipment.

The plan must be very clear and can been formed feedback information, which will be sent to the procedure of decision-making.

20.6 Conclusion

This paper proposes a new decision model called NDS model, which blend Hw into the procedure of decision-making first. Then, we design the Hw model, and expound the implement procedure of Hw model invoking in the procedure of decision-making in detail. Finally, an example is given to illustrate that Hw model is feasible and effective.

The protocol research is the next topic, including the protocol of request/response exchange, the protocol of information covert, and the protocol of adaptive push, etc.

References

1. Gorry A, Scott Morton MS (1971) A framework for information systems. Sloan Manage Rev 13(1):56–79
2. Jarke M, Radermacher FJ (1998) The AI potential of model management and its central role in decision support. Decis Support Syst 4(4):387–404
3. Fraser MM, Hipel KW (1989) An architecture for integrating expert systems. Decis Support Syst 5(3):263–276
4. Turban E (1996) Implementing decision support systems: a survey. In: IEEE conference, man and cybernetics, IEEE Press, Beijing, pp 2540–2545
5. Carlsson C, Turban E (2002) Decision support systems: directions for the next decade. Decis Support Syst 33(2):163–176

6. Bringsjord S (1998) Computationalism is dead; now what? J Exp Theor Artif Intell 10(4): 393–402
7. Ribeiro RA, Powell PL, Baldwin JF (1995) Uncertainty in decision-making: an abductive perspective. Decis Support Syst 13(2):183–193
8. Fetzer JH (1998) People are not computers: though processes are not computational procedures. J Exp Theor Artif Intell 10(4):371–391
9. Hamscher W, Kiang MY, Lang R (1995) Qualitative reasoning in business, finance and economics: introduction. Decis Support Syst 13(2):183–193
10. Zhu ZX (1994) Human ergonomics. Zhejiang Education Press, Hangzhou, pp 17–24 (in Chinese)
11. Kolodneer JL (1991) Improving human decision making through case-based decision aiding. AI magazine 12(2):52–68

Chapter 21
Control System Design of Self-balanced Bicycles by Control Moment Gyroscope

Jiarui He and Mingguo Zhao

Abstract The unmanned bicycle, as a type of unmanned vehicles, has become a research hotspot recently, and one of the most challenging problems for its realization is the method to keep the bicycle balanced. In this paper, we analyze the dynamic model of self-balanced bicycles using a Control Moment Gyroscope (CMG). The gyroscopic theory shows that by making the spinning flywheel precess, the CMG module generates a moment to resist the gravitational moment and keep the bicycle balanced. According to the gyroscopic theory, we design the mechanical structure and control system of the CMG device and use state feedback control to configure the poles in order to keep the system stable. We obtain the possible feedback coefficient according to the behavior of our system by MATLAB simulations and then adjust the feedback coefficient to get a more stable and robust system through physical experiments. The results of our physical experiments show that the feedback control method can been used to keep the bicycle balanced.

Keywords Balanced · Control system design · Control moment gyroscope · State feedback

21.1 Introduction

Many institutions and enterprises are researching unmanned vehicles and have achieved some significant progress in recent years, unmanned bicycle as a widely used vehicle is a research hotspot. Compared to automobiles, bicycles have more flexibilities due to the small size and more difficulties due to the two-wheeled structure. Bicycles can go through small alleys and other narrow spaces, while

J. He (✉) · M. Zhao
Robot Control Laboratory, Tsinghua Univerisity, Beijing 100084, China
e-mail: hjr13@mails.tsinghua.edu.cn

M. Zhao
e-mail: mgzhao@mail.tsinghua.edu.cn

automobiles cannot. Bicycles will fall down when the forward velocity is very low, while automobiles do not have this problem. Therefore, the first step to design unmanned bicycles is to make the bicycle self-balanced.

The methods to achieve a self-balanced bicycle are mainly classified into four types. The first type is using a control moment gyroscope (CMG); Beznos et al. use gyroscopic stabilization to balance a bicycle in 1998 [1], and Harun Yetkin introduces a sliding mode controller (SMC) to control a CMG in 2014 [2]. The CMG method can provide a large torque, but energy consumption of CMG is very high because the flywheel is spinning all the time. The second type is mass balancing; Getz and Marsden balance the bicycle by swinging a massive ball in 1995 [3], and Masaki Yamakita and Atsuo Utano use a massive balancer to control the bicycle for trajectory tracking in 2005 [4]. The mechanical structure of mass balancing is simple, but the torque this method could provide is small. The third type is steering control; J. Fajans et al. introduce the theory of steering control in the American Journal of Physics in 1999 [5], and Tanaka and Murakami use steering control to achieve the balance of a bicycle in 2004 [6]. The energy consumption of steering control is low, but it cannot balance the bicycle at low forward velocity. The forth type is using a reaction wheel; Murata Manufacturing utilizes a reaction wheel to balance the bicycle and produces the well-known self-balancing robot bicycle called Murata Boy in 2005 [7]. The response time of the reaction wheel is short, and the output torque is limited, so it is suitable for the balance of a small bicycle.

In this paper, the bicycle is massive and its center of mass is high, so we choose CMG method to generate a large torque to balance the bicycle. We design the mechanical structure of self-balanced bicycle based on an electric bicycle as showed in Fig. 21.1, the CMG module is installed in the backseat of bicycle. The detail of CMG module is showed as Fig. 21.2. According to CMG theory, the flywheel is spinning fast and we make the gimbal and flywheel precess with an angular rate; the gimbal will generate a moment to resist the gravitational moment, we can control this moment to keep the bicycle balanced.

Fig. 21.1 Self-balanced bicycle

Fig. 21.2 CMG device
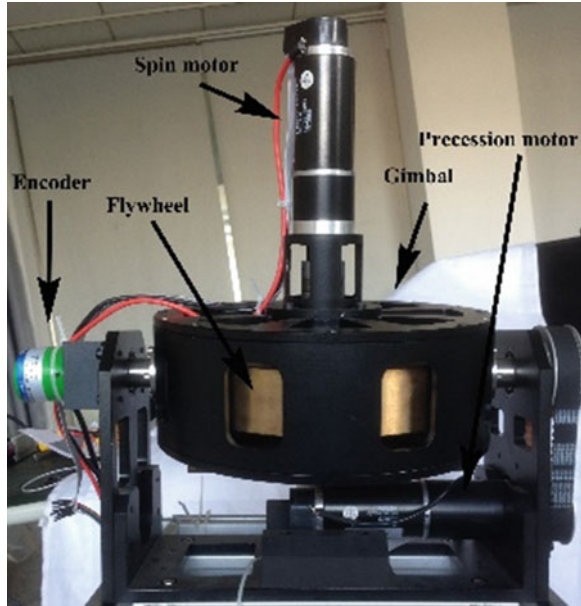
The outline of the paper is as follows. In Sect. 21.2, the reference coordinate system is introduced, the dynamic equations are derived. Section 21.3 shows the results of simulations and physical experiments. Section 21.4 presents the conclusion and thoughts about future work.

21.2 Dynamic Model of CMG-Controlled Bicycle

As Fig. 21.3 shows, O_h is a fixed point on the ground, O_g is the geometric center of the gimbal and flywheel. We define three local coordinate systems: horizon coordinate system $O_h - x^h y^h z^h$, bike coordinate system $O_g - x^b y^b z^b$, gimbal coordinate system $O_g - x^g y^g z^g$.

The relative motion of bicycle is consisted of three parts: The body rotates around x^h-axis with lean angle α and lean angular rate $\dot{\alpha}$; the gimbal and flywheel rotate around y^b-axis with precession angle β and precession angular rate $\dot{\beta}$; the flywheel rotates around Z^g-axis with spin angular rate $\dot{\gamma}$.

In order to prevent confusion, we define the part of bicycle excluding the gimbal and flywheel as body. The dynamic model can be divided into two parts: The movement of body, the movement of gimbal and flywheel.
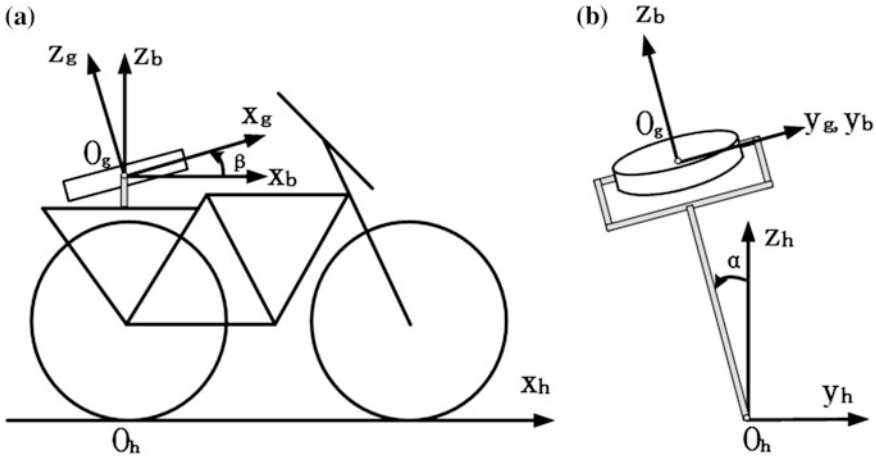
Fig. 21.3 Coordinate systems **a** Side view **b** Front View

21.2.1 The Movement of Body

Ignore the factor of friction, this part has two inputs which have effects on the movement of body. One input is the gravity, another input is the moment τ_b imposed by gimbal in the x^b-axis direction. m_b is the mass of the body, l_b is the height of the body's COG in relation to the ground.

Define generalized coordinates as follows:

$$X_b = \begin{bmatrix} -l_b\sin\alpha \\ l_b\cos\alpha \\ \alpha \end{bmatrix}, \quad F_b = \begin{bmatrix} 0 \\ -m_b g \\ -\tau^b \end{bmatrix}, \quad M_b = \text{diag}(m_b, m_b, I_x^b) \tag{21.1}$$

21.2.2 The Movement of Gimbal and Flywheel

The movement of gimbal and flywheel can be divided into two parts. The first part is that gimbal and flywheel roll around x^h-axis, caused by the torque generated by the gravity. We define that: m_{gf} is the mass of the gimbal and flywheel, l_{gf} is the height of the gimbal and flywheel's COG in relation to the ground. Define generalized coordinates as follows:

$$X_{cmg} = \begin{bmatrix} -l_{gf}\sin\alpha \\ l_{gf}\cos\alpha \end{bmatrix}, \quad F_{cmg} = \begin{bmatrix} 0 \\ -m_{gf} g \end{bmatrix}, \quad M_{cmg} = \text{diag}(m_{gf}, m_{gf}) \tag{21.2}$$

The other part is gimbal and flywheel's rolling around y^b-axis and flywheel's rolling around Z^g-axis. The precession motor provides a moment τ_{pre} to drive the

Fig. 21.4 The relation
between τ_{rea} and τ_b
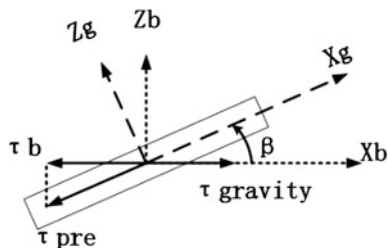
gimbal and flywheel to precess, the spin motor provides a moment τ_{spin} to drive the
flywheel to spin. Besides, the body give a reaction moment τ_{rea} to the gimbal.

The relation between τ_{rea} and τ_b is showed as Fig. 21.4, τ_b is the component of
τ_{rea} in x^g-axis direction, $\tau_{\text{rea}} = \tau_b/\cos\beta$.

We set $O_g - x^g y^g z^g$ as the global coordinate system, so the resultant moment is
$\tau = [\tau_b/\cos\beta, \tau_{\text{pre}}, \tau_{\text{spin}}]^T$.

The angular rate of the body ω_b, the angular rate of the gimbal ω_g, the angular
rate of the flywheel ω_f, the angular momentum of gimbal, and flywheel H are
showed as follows:

$$\omega_b = R_y^{-1}(\beta) \times R_x^{-1}(\alpha) \times [\dot\alpha, 0, 0]^T = [\dot\alpha\cos\beta, 0, \dot\alpha\sin\beta]^T$$

$$\omega_g = \left[\dot\alpha\cos\beta, \dot\beta, \dot\alpha\sin\beta\right]^T, \omega_f = \left[\dot\alpha\cos\beta, \dot\beta, \dot\alpha\sin\beta + \dot\gamma\right]^T$$

$$H = H_p + H_s = I_g\omega_g + I_f\omega_f$$

where

$$R_x(\alpha) = \begin{bmatrix} 1 & 0 & 0 \\ 0 & \cos\alpha & \sin\alpha \\ 0 & -\sin\alpha & \cos\alpha \end{bmatrix}, R_y(\beta) = \begin{bmatrix} \cos\beta & 0 & -\sin\beta \\ 0 & 1 & 0 \\ \sin\beta & 0 & \cos\beta \end{bmatrix}$$

$$I_g = \text{diag}\left(I_x^g, I_y^g, I_z^g\right), I_f = \text{diag}\left(I_x^f, I_y^f, I_z^f\right)$$

The differential of H is $H_d = I_g\dot\omega_g + I_f\dot\omega_f + \omega_g \times H_f$. Where $\omega_g \times H_f$ is the
moment generated by the precession of gimbal and flywheel.

21.2.3 The Movement of Whole Bicycle

According to Sects. 2.1 and 2.2, we define generalized coordinates as follows:

$$q = [\alpha, \beta, \gamma]^T, X = [X_b, X_{\text{cmg}}, \alpha, \beta, \gamma]^T$$

$$\text{Left} = [M_b \ddot{X}_b; M_{\text{cmg}} \ddot{X}_{\text{cmg}}; H_d], \text{Right} = [F_b; F_{\text{cmg}}; \tau]$$

Define $= \frac{\partial X}{\partial q}$, and use $J^T \cdot \text{Left} = J^T \cdot \text{Right}$, we can obtain dynamic equation of bicycle:

$$
\begin{bmatrix}
\ddot{\alpha}\left[m_{gf}\left(l_{gf}\right)^2 + m_b(l_b)^2 + I_x^b + I_x^f\cos\beta + I_x^g\cos\beta\right] + I_z^f\dot{\beta}\dot{\gamma} + (I_x^f - I_z^f)\dot{\beta}\dot{\alpha}\sin\beta \\
\ddot{\beta}\left(I_y^f + I_y^g\right) - I_x^f\dot{\alpha}^2\cos\beta\sin\beta - I_z^f\dot{\alpha}\cos\beta(\dot{\gamma} - \dot{\alpha}\sin\beta) \\
\ddot{\gamma}I_z^f - \ddot{\alpha}(I_z^f + I_z^g)\sin\beta
\end{bmatrix}
$$
$$
= \begin{bmatrix}
m_{gf}gl_{gf}\sin\alpha + m_bgl_b\sin\alpha \\
\tau_{pre} \\
\tau_{spin}
\end{bmatrix}
\tag{21.3}
$$

By controlling the spin motor, we can keep $\dot{\gamma}$ to be a constant, $\ddot{\gamma} = 0$ is founded. Linearization of the movement equation around the equilibrium position $(\alpha = \dot{\alpha} = \beta = \dot{\beta} = 0)$ yields:

$$
\begin{cases}
I_x\ddot{\alpha} + H_z\dot{\beta} = H_z\alpha \\
I_y\ddot{\beta} - H_z\dot{\alpha} = \tau_{pre} \\
I_x\ddot{\gamma}I_z^f = \tau_{spin}
\end{cases}
$$

where, $I_x = I_x^b + I_x^f + I_x^g + m_{gf}l_{gf}^2 + m_bl_b^2$, $H_z = I_z^f\dot{\gamma}$, $M_x = m_{gf}\, gl_{gf} + m_bgl_b$, $I_y = I_y^f + I_y^g$, $I_z = I_z^f$.

Due to $\ddot{\gamma} = 0$, we can ignore $\ddot{\gamma}I_z^f = \tau_{spin}$. Letting $x = [\alpha, \dot{\alpha}, \beta, \dot{\beta}]^T$, $\tau_{pre} = K_i i$, K_i, is torque constant of motor. The state equation of system is given as:

$$
\begin{bmatrix}
\dot{\alpha} \\
\ddot{\alpha} \\
\dot{\beta} \\
\ddot{\beta}
\end{bmatrix}
=
\begin{bmatrix}
0 & 1 & 0 & 0 \\
\frac{M_x}{I_x} & 0 & 0 & -\frac{H_z}{I_x} \\
0 & 0 & 0 & 1 \\
0 & \frac{H_z}{I_y} & 0 & 0
\end{bmatrix}
\begin{bmatrix}
\alpha \\
\dot{\alpha} \\
\beta \\
\dot{\beta}
\end{bmatrix}
+
\begin{bmatrix}
0 \\
0 \\
0 \\
\frac{K_i}{I_y}
\end{bmatrix}
i = Ax + Bu
$$
$$
y = \begin{bmatrix}
1 & 0 & 0 & 0 \\
0 & 0 & 1 & 0
\end{bmatrix}
\begin{bmatrix}
\alpha \\
\dot{\alpha} \\
\beta \\
\dot{\beta}
\end{bmatrix}
= Cx
\tag{21.4}
$$

The rank of controllability matrix is 4, the system is fully controlled. As we all know, the typical indicators of systemic stability is the place of systemic poles.

We can find that two poles of the system are zero, the system is unstable. However, we can use state feedback to configure the poles to keep the system stable:

$$u = i = -kx \tag{21.5}$$

21.3 Simulation and Experiment

To prevent the damage to the instruments, we test the CMG module on an experimental device built by aluminum profiles instead of test on bicycle directly, as is showed in Fig. 21.5. We install an absolute encoder on the ground to test α and $\dot{\alpha}$. The controller is NI-CompactRio-9024, and the reconfigurable embedded chassis is NI-CompactRio-9114.

Define the height of the whole device CoM as l_{dev}, the parameters of experimental device is as Table 21.1.

Substituting the above parameters, the state equation is obtained

$$\dot{x} = \begin{bmatrix} 0 & 1 & 0 & 0 \\ 12.81 & 0 & 0 & -0.55 \\ 0 & 0 & 0 & 1 \\ 0 & 93.98 & 0 & 0 \end{bmatrix} x + \begin{bmatrix} 0 \\ 0 \\ 0 \\ 0.77 \end{bmatrix} u$$

$$y = \begin{bmatrix} 1 & 0 & 0 & 0 \\ 0 & 0 & 1 & 0 \end{bmatrix} x \tag{21.6}$$

Fig. 21.5 Experimental device

Table 21.1 Parameter values

Parameter	Value	Unit
$[m_f, m_g, m_b]$	[10.513, 6.357, 9.77]	kg
l_{dev}	0.66	m
$[I_x^f, I_y^f, I_z^f]$	[297.98, 297.98, 559.46]	kg × cm^2
I_y^g	782.83	kg × cm^2
I_x	134539.8	kg × cm^2
K_i	0.0603	Nm/A
$\dot{\gamma}$	22.0	r/s

To verify the effect of feedback, we use MATLAB to simulate the behavior of the system. To simplify the complexity of system, we introduce the concept of dominant poles, the dominant poles are located in the specified trapezoidal region and the other poles are located far away from the dominant poles.

The number and place of dominant poles is estimated by simulation and tested by experiment. When we set the poles at [−50, −1.5, −1.5 + i, −1.5−i], the feedback coefficient k is [−2588.7, −506.2, −24.7, 70.7], the states change as Fig. 21.6.

According to the result of simulation, the states approach to the steady state after a few seconds as expected.
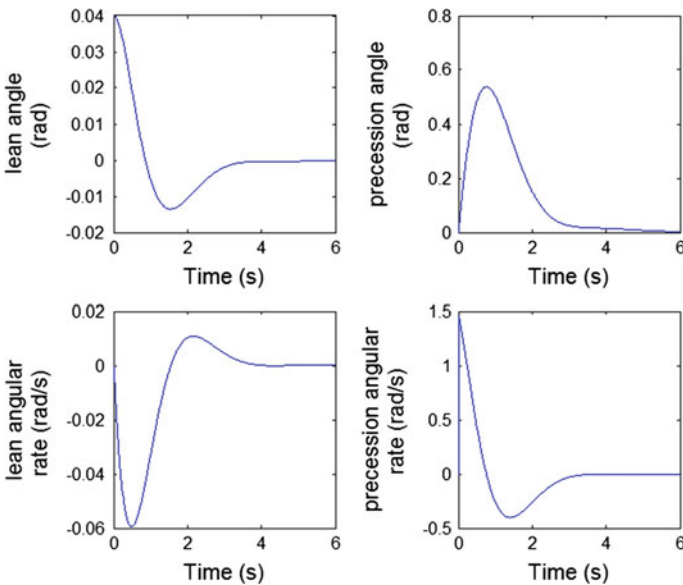
Fig. 21.6 Simulation result
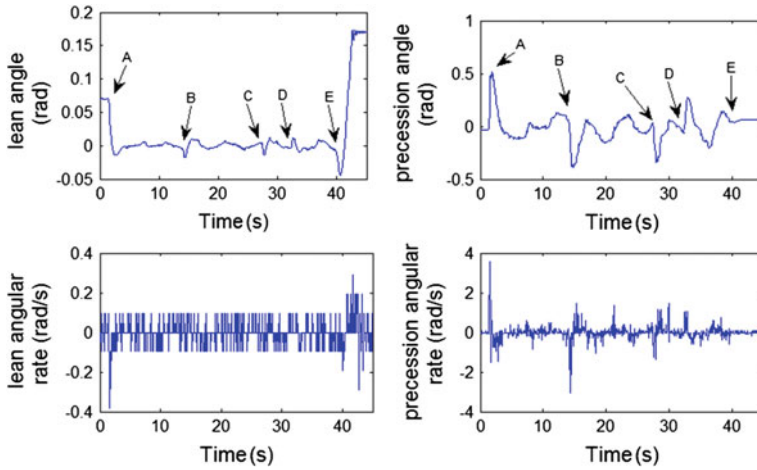
Fig. 21.7 Experiment result

In the experiments, we set the poles the same as simulation parameters, the feedback coefficient k is $[-2588.7, -506.2, -24.7, 70.7]$. A data collected from the experiment on the CMG device is as Fig. 21.7. The precession motor begin to work at point A, lean angle of point A is 0.0675 rad. After about 3.3 s, the system is running around the steady state. At the points B, C, and D we impose an instant impact on the body, the system deviates from the original state and returns to the steady state. At point E, the precession motor stops working, the device falls down quickly. The result of the experiment shows that feedback control method can been used to keep the bicycle balanced.

21.4 Conclusion and Future Work

To solve the problem that bicycles fall down at low forward velocity, we design state feedback control system to keep the bicycle balanced with a CMG. The results of simulation and physical experiments show that state feedback control can keep the bicycle self-balanced stably and can resist certain instant disturbance.

The first step to make the bicycle balanced is completed by state feedback control. However, the CMG method has some disadvantages; the energy consumption is very high. In addition, since the CMG device imposes a vertical torque $\tau_{rea}\sin\beta$ to the bicycle as shown in Fig. 21.4, the front wheel of the bicycle may leave the ground and the bicycle may even fall backwards. In the future, we will combine steering control with the CMG method to reduce energy consumption and utilize double gyroscopes to eliminate the effect of the vertical torque.

References

1. Beznos AV et al (1998) Control of autonomous motion of two-wheel bicycle with gyroscopic stabilisation. Robot Autom 3:2670–2675
2. Yetkin H et al (2014) Gyroscopic stabilization of an unmanned bicycle. In: American control conference, pp 4549–4554
3. Getz NH, Marsden JE (1995) Control for an autonomous bicycle. Robot Autom 2:1397–1402
4. Yamakita M, Utano A (2005) Automatic control of bicycles with a balancer. In: Advanced intelligent mechatronics, pp 1245–1250
5. Fajans J (2000) Steering in bicycles and motorcycles. Am J Phys 68(7):654–659
6. Tanaka Y, Murakami T (2004) Self sustaining bicycle robot with steering controller. In: Proceedings of 2004 IEEE advanced motion, control confrence 193–197
7. The Murata Boy Website (2005). http://www.murataboy.com/en-global

Chapter 22
Laser-Based Obstacle Avoidance and Road Quality Detection for Autonomous Bicycles

Sotirios Stasinopoulos and Mingguo Zhao

Abstract This paper presents a novel design and implementation approach for a laser range sensor (LRS)-based obstacle avoidance and road quality detection system specifically created to be used onboard an autonomous bicycle. The system uses the measurements from a single LSR to detect dynamic obstacles inside the bicycle's environment and avoid the ones whose paths intersect with its own. The LSR's mechanical base and rotating mechanism were specially designed to fit the lightweight structure of the bicycle and a specific rotation pattern on the bicycle's sagittal plane was created to maximize sensing efficiency. The RANSAC Line Detection algorithm is applied to detect the ground line, assess the road surface quality, and avoid bumps or holes on the bicycle path. Our experimental results show promising bicycle behavior and reliable obstacle avoidance at different speeds.

Keywords Laser range sensor (LRS) · Obstacle avoidance · Road surface quality · RANSAC · Autonomous bicycle

22.1 Introduction and Related Research

In the past decade, numerous research efforts focused on autonomous vehicles and their transition from the field of academic research to real-life applications. In order to be truly autonomous, a vehicle must be aware of its surroundings, perceive the objects within it, and avoid any obstacles that may cross its path, while maintaining

S. Stasinopoulos (✉) · M. Zhao
Robot Control Laboratory, Department of Automation,
Tsinghua University, Beijing, China
e-mail: stasinopouloss10@mails.tsinghua.edu.cn

M. Zhao
e-mail: mgzhao@mail.tsinghua.edu.cn

its original course. Following the advances in sensor technologies, modern autonomous vehicles combine a variety of sensory systems in order to "see" the world. While the greatest part of scientific attention has been devoted toward realizing the fully autonomous car, many benefits would come from research the automation of other types of vehicles as well.

This paper is part of a series of papers that focus on the autonomous bicycle, its control, obstacle detection and avoidance, and path planning systems. Here, we specifically describe the obstacle detection and avoidance part, along with a feature for detecting the road quality. The novelty of our system resides in the adaptation of the traditional laser-based obstacle detection and avoidance system to the special characteristics of an autonomous bicycle, which differentiate its requirements in environment perception from cars and other vehicles. Bicycles' long, narrow, and lightweight structure prevents the integration of numerous and over-complicated sensor systems. Due to their shape and size, their ability to change direction relatively easily, and their rather low cruising speeds, bicycles should be able to coexist on the road with other vehicles in close proximity and to continue on their path if obstacles do not pose an immediate threat to their course. In addition, given their natural instability, balance is of great importance to bicycles, making the detection of road surface abnormalities crucial to a smooth cruise. Our system through careful design and processing makes full use of a single Laser Range Sensor (LRS) to adjust to the autonomous bicycle's specifications.

The theoretical basis of autonomous vehicles and obstacle avoidance has been firmly set over the past decades. Mainly following principles of automatic control as explained thoroughly by Dorf [1], recent publications have introduced perception and navigation systems mainly for autonomous cars. One of the first efforts pertaining to an autonomous bicycle was made by Getz and Marsden [2], where the stabilization and control methodologies of such two-wheeled vehicles were examined. Other teams [3–5], studied autonomous bicycles as well, but mainly from the control aspect, without adequate research focusing on the perception and navigation problems that are introduced by the special characteristics of bicycles.

In our paper, we make use of the advances in sensor systems and especially in LRSs. In addition, we utilize the "RANdom SAmple Consensus" (RANSAC), an iterative method that is used to estimate parameters of a mathematical model from a set of data containing outliers. The algorithm published [6] has been used in various vehicle applications including wall and road lane detection and tracking [7]. We use RANSAC to extract the road surface model in front of our vehicle and detect possible road abnormalities.

Our paper is organized as follows: the Design and Theoretical Model for our obstacle avoidance and road surface quality detection are analyzed in Sects. 22.2 and 22.3. Our experimental setup is described in Sect. 22.4, while Sect. 22.5 presents our experimental procedure results. Conclusions and discussion for future work are provided in Sect. 22.6.

22.2 Design

Contrary to various autonomous vehicle designs that integrate a number of environment monitoring sensor systems and later combine their measurements through different sensor fusion models, we decided our design to maintain a minimalistic character and include only one outdoor LRS of wide Field of View (FoV)-270° for a number of reasons. At first, based on our bicycle's long-narrow shape, low height, and lightweight design, the integration of various sensors onboard would be practically impossible without disrupting the advantages of these characteristics. Second, our aim is a solution that could possibly result in a future product; therefore, we had to restrict the overall cost and not include additional sensors or more LRS sensors, confining the design to only the essential single LRS. Finally, since our requirements include high detection speed of random moving obstacles on the bicycle's path, we chose the implementation of a fast minimalistic algorithm without any need for time-consuming sensor fusion. Of course, using only one sensor has its disadvantages as well, in case the sensor fails to detect some obstacles, but given the accuracy of modern LRS sensors, that failure could only have too short of a duration to affect our system.

The exact mounting position of our LRS and its motion pattern was carefully selected in order to cover the largest FoV possible. The sensor, its rotating frame, and corresponding motor are mounted in the front part of the bicycle in the place of the headlight, as shown in Fig. 22.1 (left), in order to monitor the frontal and lateral FoV, while remaining aligned with the bicycle's main body orientation, without hindering steering in any way. Instead of choosing a complex rotation pattern, we make our sensor rotate vertically while scanning horizontally, covering thus various levels in front of the bicycle, while always maintaining a view of the sides of the bicycle. A more complex rotation mechanism is virtually inapplicable in the confined space onboard the bicycle and could interfere with its balance and steering. The rotation of our LRS satisfies these limitations, but is not constant during the bicycle's movement. In order to ensure the vehicle's ability to cruise in close proximity with other moving vehicles and correct its course only when collision is eminent, obstacle detection is only performed on a desired horizontal level each time, as will be explained in the following section.
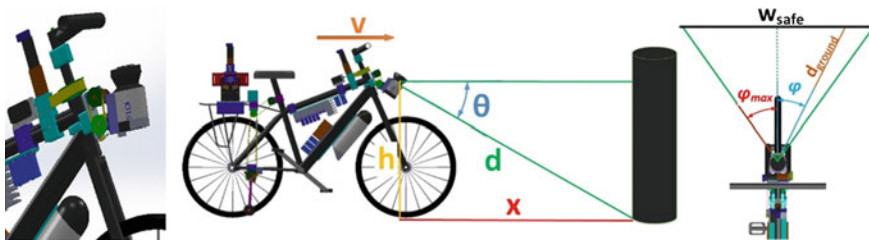
Fig. 22.1 The design of the LRS rotation system (*left*), the obstacle detection model (*middle*) and the bicycle's safe passage and ground distance at each LRS scan measurement (*right*)

22.3 Theoretical Model

Given our one-level LRS, our obstacle detection takes place at one horizontal plane at each instant, while this plane due to our vertical rotation mechanism has the ability to rotate and intersect with the ground plane at a desired distance from the sensor and subsequently the vehicle. This intersection is our Obstacle Detection Horizon (ODH) which we calculate each time based on our bicycle's speed. Based on bicycles' sensitivity to obstacles on the ground even of small height, such as bumps and sidewalks, and to road abnormalities, such as small holes or train tracks, we have to always be in a position to detect potentially dangerous to our bicycle's smooth cruise spots within our path and avoid them, while staying on our intended course. However, since our goal is an autonomous bicycle that can move within cluttered environments and only avoid objects that pose an immediate threat, we set our ODH close to our vehicle, until the point where given our speed we can safely and timely perform the orientation change maneuvers and maintain stability.

Obstacle Detection Horizon Calculation In order to calculate the safe ODH for our vehicle, we need to take into account the total delay that is inserted into our system by its different parts, from the moment an obstacle is detected until the evasive change in direction is performed. Therefore, we must include the delay introduced by the LRS response time $t_{d,\text{LRS}}$, the delay from our computer processing $t_{d,\text{proc}}$, the delay from our bicycle control system $t_{d,\text{control}}$ and the delay inserted by the actual change of direction $t_{d,\text{change}}$. The total delay $t_{d,\text{total}}$ thus becomes $t_{d,\text{total}} = t_{d,\text{LRS}} + t_{d,\text{proc}} + t_{d,\text{control}} + t_{d,\text{change}}$. Of course, some of the above delays may overlap to a certain extent, but in this modeling we consider them sequential.

Our bicycle can travel a distance of $x_{d,\text{total}} = t_{d,\text{total}} * v$, where v is the speed of the bicycle, as can be seen in Fig. 22.1 (middle). In order to detect obstacles only when they intersect with our path's danger zone, while letting the other dynamic objects of our environment move freely without interfering with our planned course, we constantly adjust the angle with the level plane θ of the ODH to $x_{d,\text{total}}$. Given the height h of our LRS during its rotation is linearly approximated as

$$h = h_{\text{low}} + (h_{\text{level}} - h_{\text{low}}) \frac{\theta_{\text{low}} - \theta}{\theta_{\text{low}}} \qquad (22.1)$$

where h_{low} is the height of the LRS at the lowest allowed rotation position of our configuration, so that the LRS does not register information from the front wheel, θ_{low} is the angle at that lowest position and h_{level} is the height of the LRS when it is aligned with the level plane. Therefore, since $\tan \theta = h/x$, we have

$$\theta = \tan^{-1} \frac{h}{v * t_{d,\text{total}}} \qquad (22.2)$$

which represents the angle of rotation for the LRS with regard to the bicycle's speed and defines our ODH. As the speed v increases, the rotation angle θ decreases, making our ODH extend to even further objects in the distance, since the distance covered during an evasive maneuver becomes greater and more objects are within our path's danger zone.

Obstacle Detection and Avoidance Although we are able to monitor objects approaching the bicycle from the sides and adjust our course accordingly, at this point we only choose to avoid obstacles within our bicycle's safe passage. Given our bicycle's width is w_b, we define our safe passage's width along our path as double that width, i.e., $w_{safe} = 2w_b$. We choose this to ensure the safety of our bicycle, but also we try to keep that passage as narrow as possible so that our bicycle can cruise closely along other vehicles without recognizing them as obstacles.

Given the rotation angle θ and the LRS height h, the ground is at distance

$$d_{ground} = \frac{\frac{h}{\sin\theta}}{\cos\varphi} \pm d_{error} \qquad (22.3)$$

where d_{error} refers to the systematic measurement error introduced by the LRS, that needs to be taken into consideration in order to make our detection system more robust, and φ is the angle at which each LRS scan intersects with the ground in front of the bicycle within our safe passage's width as can be seen in Fig. 22.1 (right). The range of the angle φ is $[-\varphi_{safe}, \varphi_{safe}]$, where φ_{safe} sets the limits of our safe passage and is calculated as

$$\varphi_{safe} = \tan^{-1}\frac{(w_{safe}/2) * \sin\theta}{h} \qquad (22.4)$$

Each time an object is detected at a distance $d < d_{ground}$, we have to examine whether its width w_{obs} is at least equal to a minimum width $w_{obs,threshold}$. Given our LRS's scanning accuracy and its angular range, we calculate over each scan at a specific vertical rotation θ, the number of points $n_{obs,threshold}$ in the LRS's range that correspond to $w_{obs,threshold}$, approximating at each instant our detection horizon by the distance of the ground from the LRS in the bicycle's sagittal plane $d_{gnd,sag} = h/\sin\theta$. If the number of consecutive points of a detected object is greater than $n_{obs,threshold}$, the object is considered an actual obstacle and we store the angular position of the point in the middle of its width.

After and obstacle is verified to lie within our path, we perform evasive maneuvers, steering the bicycle away from the obstacle, in the opposite direction from where it was detected. This action is performed repeatedly with angular step $\alpha_{change,step}$ to ensure a smooth shift in the bicycle's direction, until the obstacle is no longer within our path. In the presence of more than one obstacle, the closest one is considered as a more eminent collision danger, so it is avoided first. If an obstacle remains within collision course, the bicycle reduces its speed and attempts a change of direction of greater angular value. After a total angular direction change of

$\alpha_{change,total}$ and the avoidance of the obstacle, we begin to adjust its course again with angular step $\alpha_{change,step}$ to the opposite direction, until the entire angular direction change is reversed and we resume our original course.

Road Surface Quality Detection using RANSAC The input to the RANSAC algorithm is a set of observed data values, a parameterized model which can explain or be fitted to the observations, and some confidence parameters. RANSAC achieves its goal by iteratively selecting a random subset of the original data. These data are hypothetical inliers and this hypothesis is then tested as follows:

1. A model is fitted to the hypothetical inliers.
2. All other data are tested against the model and hypothetical inliers are selected.
3. The model is good if sufficiently many points have been classified as inliers.
4. The model is re-estimated from all hypothetical inliers.
5. The model is evaluated by estimating the error of the inliers relative to it.

This procedure is repeated a fixed number of times until the refined model has an error lower than the last saved model.

In our attempt, we use the laser scan measurements from the LRS, convert them to a point cloud, and provide them as input to the RANSAC algorithm. Given the low dimensionality of our data, the algorithm estimates the model that corresponds to the road surface after a few iterations. After the calculation of the inlier measurement points, we study the remaining outliers to locate road abnormalities, such holes, ditches, or train tracks that could disrupt our bicycle's rather fragile stability. In a similar manner to the detection of obstacles, we compare groups of sequential outliers against a minimum road abnormality width $w_{abn,threshold}$ to determine whether there are spots on the road that need to be avoided. We note here that $w_{abn,threshold}$ must be set according to our bicycle's wheel width, in order to avoid having our wheels trapped in relatively narrow tracks or ditches.

22.4 Experimental Setup

Our experimental setup includes the implemented autonomous bicycle according to our design, as seen in Fig. 22.2. Our system comprises an Intel NUC for the onboard processing of the LRS scan measurements over ROS and a Compact RIO controller for coordinating the motors of the bicycle, after receiving the control signal over serial port from the NUC. Using a SICK LMS-111 outdoor sensor of 270° FoV, we scan multiple horizontal levels with our vertical rotation mechanism. For our implementation, we have an approximate total reaction delay time of $t_{d,total} = 1$ s, design parameters $h_{level} = 0.92$ m, $h_{low} = 0.84$ m, $\theta_{low} = 46.4°$, and a bicycle width of $w_b = 0.8$ m, making our safe passage width $w_{safe} = 1.6$ m. Our LRS's systematic error is $d_{error} = 2$ %, while the chosen threshold for obstacle width is $w_{obs,threshold} = 0.1$ m, for road abnormalities is $w_{abn,threshold} = 0.05$ m and the angular correction step is $\alpha_{change,step} = 3°$.

Fig. 22.2 The implemented autonomous bicycle (*left*) and the LRS rotation mechanism (*right*)

Given this configuration, we test our system in both indoor and outdoor surroundings. For the indoor test, we select a building corridor and test if the vehicle will detect the obstacles on its path, while ignoring the surrounding walls and obstacles that do not interfere with its safe passage. For the outdoor test, we choose a road with bumps and ditches to prove the efficiency of both the obstacle detection and the road surface quality techniques. In both tests, the vehicle moves with a speed of $v \approx 10$ km/h, making the angle with the level plane $\theta \approx 17.9°$ and subsequently setting our ODH in the bicycle's sagittal plane at $d_{\mathrm{gnd,sag}} = 2.89 \pm 2\%$ m.

22.5 Experimental Results

In both indoor and outdoor experiments Fig. 22.3, our system can reliably detect obstacles within our path that may cause collision and differentiate them from other obstacles outside our safe passage within the environments of high clutter.
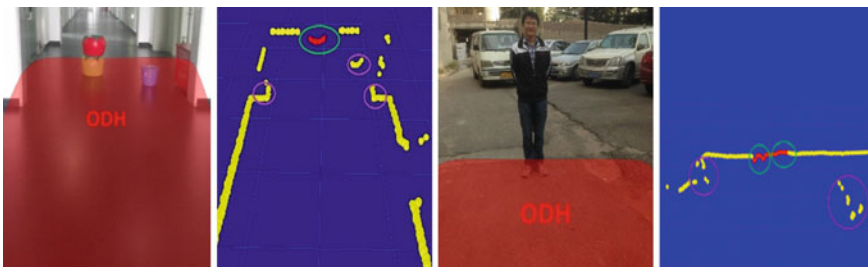
Fig. 22.3 Experimental results of the indoor (*left*) and the outdoor (*right*) experiment. The detected obstacles and road abnormalities within our path are marked with *red*, compared to the other *yellow* points of the scan, and are circled with *green*, while obstacles outside our passage, thus not detected, are circled with *purple*

Moreover, with the application of the RANSAC algorithm, the road surface on our ODH is correctly modeled and the abnormalities are more easily detected, as can be seen in our outdoor results, where the road ditch is detected and marked with red.

22.6 Conclusions and Discussion

In this paper, we introduced a novel design and implementation approach for a LRS-based obstacle avoidance and road quality detection system specifically created to be used onboard an autonomous bicycle. Through studying the specifications and needs of autonomous bicycles, we took full advantage of a single LRS's measurements and developed a system that permits our bicycle to perceive its surroundings, while maintaining a smooth and balanced cruise and co-existing with other dynamic obstacles if they do not pose immediate threat to its safe passage. Our experimental results support the efficiency of our system and the advantageous characteristics of our autonomous bicycle design.

Despite our promising results, there is room for a number of further developments for our system. Future work includes evolving our path planning methodology in order to include field techniques for the obstacles and the final goal, like in [8, 9], but we will need to formulate a real-time solution adjusted to our specialized obstacle and road tracking method. In addition, more systematic modeling of obstacles could be examined, probably adopting the recently proposed avoidance system by Cherubini and Chaumette [10]. More advanced road abnormalities modeling with RANSAC could also be achieved if ideas for separate abnormality modeling could be integrated [11]. Finally, more field tests with the autonomous bicycle in unknown terrains will be needed to verify the proper behavior of our system.

References

1. Dorf RC (1995) Modern control systems. Addison-Wesley Longman Publishing Co., Inc, Boston
2. Getz NH, Marsden JE (1995) Control for an autonomous bicycle. In: Proceedings of the 1995 IEEE international conference on robotics and automation, pp 1397–1402
3. Keo L, Masaki Y (2008) Trajectory control for an autonomous bicycle with balancer. In: IEEE/ASME international conference on advanced intelligent mechatronics, pp 676–681
4. Sharma HD, Umashankar N (2006) A robotic model (ROBI) of autonomous bicycle system. In: IEEE international conference on computational intelligence for modelling, control and automation, pp 107–107
5. Yavin Y (1999) Stabilization and control of the motion of an autonomous bicycle using a rotor for tilting moment. Comput Methods Appl Mech Eng 178:233–243
6. Fischler MA, Bolles RC (1981) Random sample consensus: a paradigm for model fitting with applications to image analysis and automated cartography. Commun ACM 24:381–395

7. Borkar A, Hayes M, Smith MT (2009) Robust lane detection and tracking with ransac and Kalman filter. In: ICIP, pp 3261–3264
8. Borenstein J, Koren Y (1989) Real-time obstacle avoidance for fast mobile robots. IEEE Trans Syst Man Cybern 19:1179–1187
9. Khatib O (1986) Real-time obstacle avoidance for manipulators and mobile robots. Int J Rob Res 5:90–98
10. Cherubini A, Chaumette F (2013) Visual navigation of a mobile robot with laser-based collision avoidance. Int J Rob Res 32:189–205
11. Schnabel R, Wahl R, Klein R (2007) Efficient RANSAC for point‑cloud shape detection. Computer graphics forum, 2007. Wiley Online Library, pp 214–226

Chapter 23
System Identification Research for Tank Stabilized Sight System Based on GA

Bin Han, Tianqing Chang and Kuifeng Su

Abstract Building model for Tank Sight Stabilized System by traditional mechanism method is difficult because of its complex internal structure. A method which combines classical step response method and the genetic algorithm to identify a certain type Tank Sight Stabilized System is proposed. It obtains the step response curve of Sight Stabilizing platform in certain conditions based on DSP system and Cubic spline method. It determines the order of the model based on priori knowledge and identifies the parameter of the model using GA. Finally,the effectiveness of the method is checked by using step response property label error evaluating method. The result shows that the method can be identified precisely with the identification model of Tank Sight Stabilized System.

Keywords Tank sight stabilized system · System identification modeling · Genetic algorithms · Cubic spline

23.1 Introduction

Tank stabilized sighting system uses the characteristics of fixed axis of inertial devices to isolate the interference of the vehicle, so it can guarantee the steadiness of sight in inertial space and its performance affects the performance of Tank Weapon System. The system model is the basic information of design of control system and the accuracy of this model has a direct impact on the performance of the control system. The method of system modeling can be divided into two categories according to the nature currently: mechanism modeling and system identification modeling. In addition, the development and application of intelligent algorithms is very fast in recent years, GA has been widely used on system identification modeling [1].

B. Han (✉) · T. Chang · K. Su
Graduate Student, No. 21, Dujiakan Street, Fengtai District, Beijing 100072, People's Republic of China
e-mail: han-b08@163.com

Research on stabilized sight system started late in our country; the research on system identification of tank stabilized sight system always stays on the mechanism modeling and simulation. As tank stabilized sight system has a complex internal structure, there are a few modeling methods that can be used for the experiment, so far domestic. A lot of research on the stabilized sight platform used mechanism modeling method, and these studies do not make any verification of the application of the method [2–6]. Taking into account the actual situation that the motor only reverses within a limited angle when tank stabilized sight system works, it chooses the method that combines classical step response method and the genetic algorithm to identify a certain type Tank Sight Stabilized System.

23.2 Acquisition of the Object Step Response Curve

To obtain an accurate model of the control object, get the object step response curve first using the control system and experimental platform, as seen in Fig. 23.1.

To ensure stable operation of the tank stabilized sight system, the experimental data is obtained in the case of current loop closed. In order to improve the accuracy of the data sampled in the system, take 0.2 ms as the data sampling period considering the control system operation speed. Take the square wave whose amplitude is 0.5 and period is 60 ms as input signal instead of step wave. Use DSP system to sample input and output data. In order to achieve the effect of filtering, it samples data at eight points simultaneously and takes the average of the data as output data.

Figure 23.2 shows the input data and output data. Horizontal dashed line the step input signal sampling curve, starts from zero. The points stands for output data sampling points. The solid polyline stands for output data which is a restored step response curve. There is little noise in the output signal because of filtering as seen
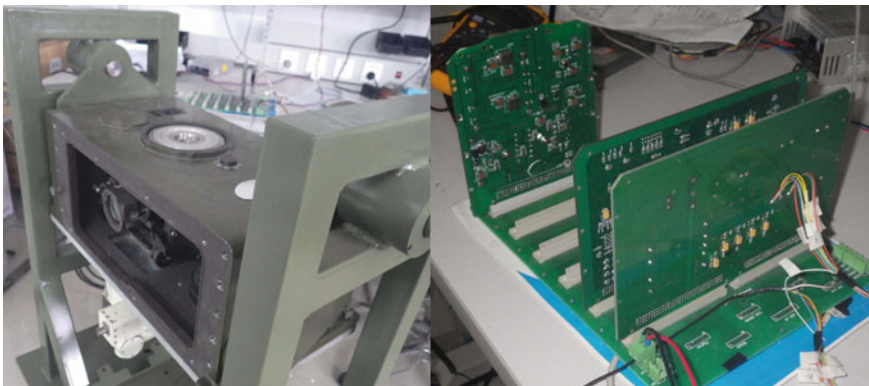
Fig. 23.1 The control system and experimental platform
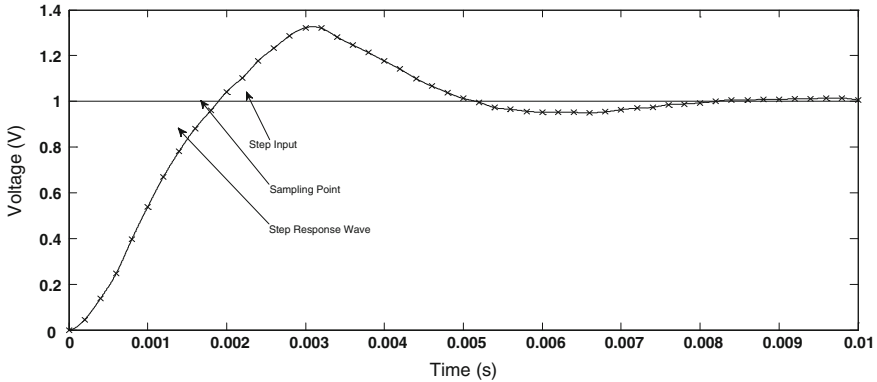
Fig. 23.2 Input data and output data

in the figure; however, the effect of the reduction step response curve is relatively poor. The output data needs to do further interpolation processing in order to get step wave which can reflect the performance of the control system completely.

Currently, interpolation method commonly used is linear, lagrange, HEMIT, Newton, Piecewise etc. It takes cubic as interpolation method to make the curve continuous and the derivative continuous according to the actual needs [7]. It uses the spline function to achieve cubic spline interpolation and select 5000 interpolation points at equal intervals in the range. The interpolation image is intercepted as seen in Fig. 23.3. As seen that cubic spline interpolation has a significant effect on the curve smoothing. It improves the accuracy of the calculation of overshoot, adjustment time, and rising time.
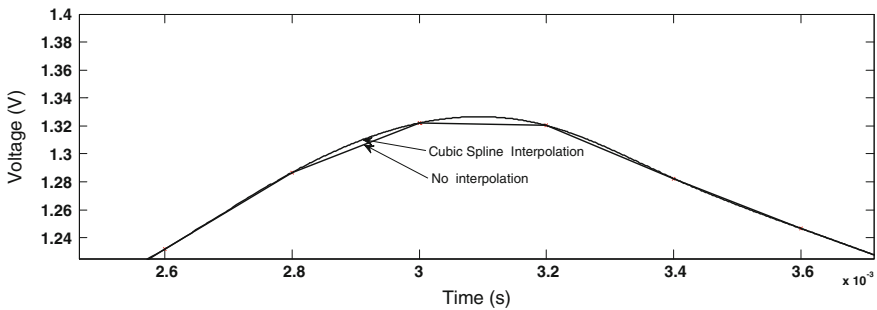
Fig. 23.3 Effect contrast of cubic spline interpolation processing
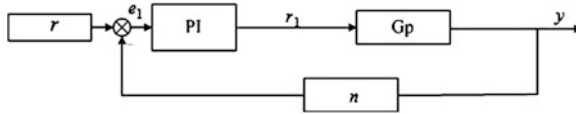
Fig. 23.4 The structure of the experimental control system

23.3 Determination of the Model Order to Be Identified

The experimental system is current closed loop during data sampling and the model to be identified is the motor model actually, so take the current loop into consideration separately and ignore the rest in the experiment. The structure of the experimental control system is shown in Fig. 23.4. The feedback factor of current loop is n and $n = 1$ during the experiment. The controller of current loop is PI controller and $k_p = 1.5$, $k_i = 0.04$ in the experiment. In order to measure motor model transfer function, take the current loop as a whole to do system identification and then calculate the motor model transfer function.

The control model of DC torque motor input voltage and armature input current is first order. The current closed-loop model transfer function becomes second-order when considering PI controller parameters and unit negative feedback. Determine the current closed-loop model transfer function is second-order without delays according to the shape of step response curve [8]. As shown:

$$G(s) = \frac{1}{a_w^2 s^2 + 2\xi a_w s + 1} \tag{23.1}$$

Therefore, the parameter need to be identified are a_w and ξ. The max input voltage is 10 V, the applied voltage in the experiment is 1 V, and the homologous steady voltage is 1 V. It uses the acquisition voltage value to calculate the identification directly in order to guide the controller designing and calculating more easily.

23.4 Identification of the Model Parameters

After the order of the model to be identified is determined, the model parameters can be acquired according to the input and output data based on a certain identification algorithm. The paper uses genetic algorithms for parameter identification. As a global optimization Swarm Optimization, GA has the advantage of parallel operations and global optimization and it has made great progress terms of theoretical research and engineering applications. The algorithm running takes a long time because of its iterative calculation. The paper uses variable place and probability mutation operator to make the convergence speed faster. In order to get better identification results, it designs the fitness function specially. The crossover in the paper is a uniform crossover.

23.4.1 The Design of GA

To improve the running speed and effect of GA, it designs the GA. Take two parameters coupled binary coded as individual sample. The select operator of GA saves the best individual and the mutation operator is random mutation operator. The mutation probability and mutation place ranges adaptively as the evolution algebra ranges [9]. As shown:

$$\begin{cases} p_m = 0.1 - (0.1 - 0.001)\frac{t}{T} \\ n = N - t \end{cases} \tag{23.2}$$

Set M as the size of the population, $X_i(i = 1,2,…M)$ as individual, designs the fitness function specially, takes overshoot, adjustment time, and rising time weighted as fitness function. The algorithm steps are as follows:

Step 1: Set algebraic calculations as $t = 0$, use random number generate the initial population P_o;

Step 2: Extract chromosomal, restore parameter values, calculated the each individual's fitness and sort it;

Step 3: Judge whether the algebra reach the maximum evolution, algorithm terminates if yes, turn step 4 if no, turn step 2;

Step 4: Produce some chromosomes according to select options with probability P_v;

Step 5: Produce some chromosomes according to crossover operation with probability P_c;

Step 6: Produce some chromosomes according to mutation operation with probability P_m;

Step 7: $t + 1 \rightarrow t$, turn step 2.

23.4.2 Designing of Fitness Function

The traditional genetic function uses the squared error of sample points during system identification. The effects of identification are really poor after the algorithms runs enough iterations, as seen in Fig. 23.5. The reason is that the error of non-critical points affected the error of key points. The fitness function needs to be designed if better effect of identification wanted.

Enhance the role of adjustment of the key points, ignore the error of second point, design fitness function. Use step response performance indicators: overshoot error e_{MP}, rising time error e_{TR}, peak time error e_{TP}, adjustment time error e_{TS} weighted as fitness function of the ith iteration. As shown:
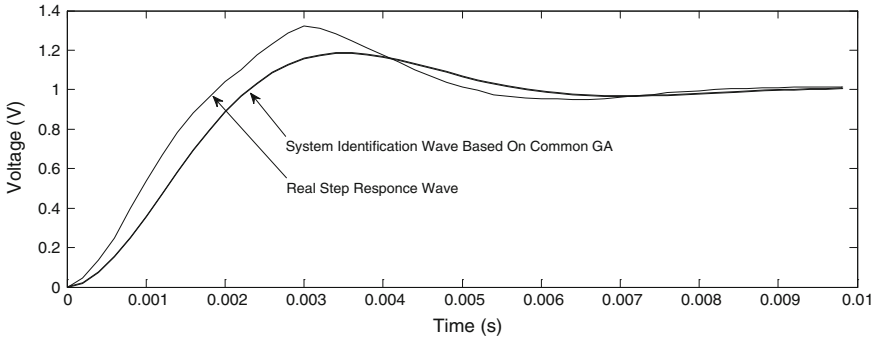
Fig. 23.5 Traditional fitness function identification results

$$f_i(x) = a_{i1}e_{MP}(x) + a_{i2}e_{TR}(x) + a_{i3}e_{TP}(x) + a_{i4}e_{TS}(x) \qquad (23.3)$$

The fitness function coefficients a_{ij} decided by experience and adaptive method. The formula is as shown:

$$\begin{cases} a_{i1} = 0.25 + 0.2\frac{e_{mp}(i-1)}{e_{mp}(i-1)+e_{tr}(i-1)+e_{tp}(i-1)+e_{ts}(i-1)} \\ a_{i2} = 0.15 + 0.2\frac{e_{tr}(i-1)}{e_{mp}(i-1)+e_{tr}(i-1)+e_{tp}(i-1)+e_{ts}(i-1)} \\ a_{i3} = 0.18 + 0.2\frac{e_{tp}(i-1)}{e_{mp}(i-1)+e_{tr}(i-1)+e_{tp}(i-1)+e_{ts}(i-1)} \\ a_{i4} = 0.22 + 0.2\frac{e_{ts}(i-1)}{e_{mp}(i-1)+e_{tr}(i-1)+e_{tp}(i-1)+e_{ts}(i-1)} \end{cases} \qquad (23.4)$$

$e_{mp}(i-1)$, $e_{tr}(i-1)$, $e_{tp}(i-1)$, $e_{ts}(i-1)$ in the formula is the best individual's overshoot error e_{MP}, rising time error e_{TR}, peak time error e_{TP}, adjustment time error e_{TS} of the ith iteration. Taking the same iterations and the number of initial population, the result of the experiment as shown in Fig. 23.6. It can be derived from the analysis that the improved fitness function plays an important role in accelerating convergence and enhancing system identification effect.
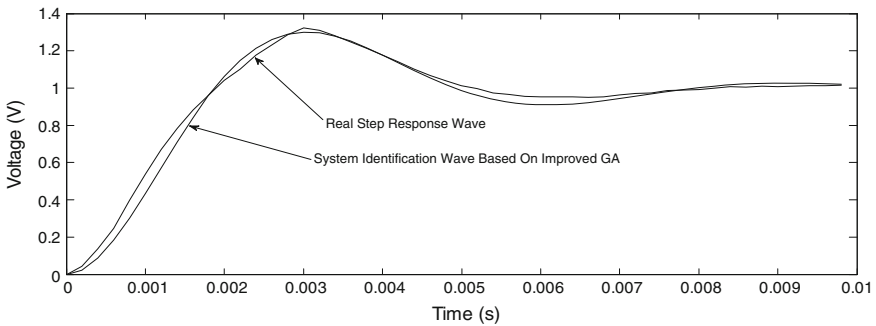
Fig. 23.6 Improved fitness function identification results

Table 23.1 Quantitative analysis of the identification effect

Performance indicators	Real output	Identification output	Percentage error (%)
Rising time e_{tr} (ms)	1.877	1.898	1.12
Adjustment time e_{ts} (ms)	6.598	7.109	7.74
Peak time e_{tp} (ms)	3.005	3.008	0.1
Overshoot e_{mp} (V)	0.322	0.302	6.2

23.4.3 Simulation and Experiment

Write improved genetic algorithm in MATLAB [10], take overshoot error e_{MP}, rising time error e_{TR}, peak time error e_{TP}, adjustment time error e_{TS} weighted as fitness function, population is set to 100, binary coding, the length of chromosome is 40 and parameter 20. The result of parameter identification is $a_w = 0.000903$, $\xi = 0.359$ after iterating 100 times. The model transfer function system identified is shown:

$$G(s) = \frac{1}{8.154e - 7s^2 + 6.484e - 4s + 1} \tag{23.5}$$

23.5 System Identification Evaluation

Measurement noise and the error in the approach can make error in system identification. The effect of the system identification needs quantitative evaluation and verification. As a common means of evaluating the quality of the control performance of control system, it uses the error of step response performance indicators between the actual system curve and identification model curve. The experiment majorly compares the error of overshoot and rising time and adjustment time between identification simulation curve and actual system curve to evaluate the effect of system identification.

Use step response performance indicators to analyze the effect of the identification quantitatively, as seen in Table 23.1. It can be inferred that the model identified is effective.

23.6 Conclusion

The paper proposes a method which combines classical step response method and the genetic algorithm to identify a certain type Tank Sight Stabilized System. Design the experiment of sampling input and output data, get step response curve of controlled object through cubic spline Interpolation, determine the structure and

order of the model to be identified, and get the controlled object model by parameter identification based on improved Genetic Algorithms. Finally, use step response performance indicators error method to analyze the effect of the identification quantitatively. The result shows that the model identified is effective.

References

1. Li Y, Zhang K (2003) Xitong Bianshi Lilun Ji Yingyong. National defence industry press, Beijing
2. Xie J (2013) Design of line-of-sight control system for armored vehicle. Academy of Armored Force Engineering
3. Liu Q, Hu H, Liu J, Er L (2003) Research on the parameter identification of friction model for servo systems based on genetic algorithms. Syst Eng Electron 25(1):77–80
4. Zhang D (2006) Research on digital control of upper reflector aim-stabilization system. Tianjin University
5. Zhang J Research on active disturbance rejection control of digital aim-stabilization system. Tianjin University
6. Dou L, Zong Q, Liu W (2009) Progress of the research on identification for control oriented. Syst Eng Electron 31(1):158–164
7. Liu S, Tang F (2007) Study on system identification method based on genetic algorithms. Syst Eng Theor Pract 3:134–139
8. Yang J (2010) The parameter identification of servo system. Xian University of Electronic Science
9. Xie M, Zhao W, Lu D, Wang B (2012) Research on mathematical model identification of steering gear based on genetic algorithms. Comput Measur Control 2:428–430
10. Ni B, Xiao D (2006) System identification and simulation toolbox under MATLAB environment. J Syst Simul 18(6):1493–1496

Chapter 24
Controller Design of Flexible Double-Inverted Pendulum with Uncertainties Based on T-S Fuzzy Inference System

Jimin Yu, Liangsheng Nan and Linyan Huang

Abstract Mathematical modeling of the flexible double-inverted pendulum with uncertain friction coefficient is presented by Lagrange function in this paper. Based on Takagi-Sugeno fuzzy inference and parallel distributed compensation (PDC) theory, the controller design approach is proposed. Based on the concept of effective maximum overlap-rules group, the stability condition of T-S fuzzy system for flexible double-inverted pendulum is relaxed to finding a local public positive definite matrix. As a result, stability conservativeness of T-S fuzzy system is decreased. According to the new relaxed stability condition, linear matrix inequalities are designed for solving the feedback gain of each subsystem, and the controller based on parallel distributed compensation is given. Simulation results show that the designed controller can effectively control the uncertain flexible double-inverted pendulum.

Keyword Flexible double-inverted pendulum • Adaptive fuzzy control • T-S fuzzy systems

24.1 Introduction

Inverted pendulum system is a nonlinear, multivariable, strong coupling, and unstable experimental device. The controls to inverted pendulum have two aspects: Stability control and swing-up control, which are often used to verify various control algorithms such as the classical control theory [1, 2], the modern control theory [3], and a variety of intelligent control methods [4–6].

Flexible double-inverted pendulum system is more complex and more difficult to control. Currently, as an important branch of modern control theory, linear optimal

J. Yu · L. Nan (✉) · L. Huang
College of Automation, Chongqing University of Posts and Telecommunications, No. 2, Chongwen Road, Nan'an District, Chongqing, China
e-mail: nlsheng@163.com

control theory has achieved fruitful results in the stability control of inverted pendulum. Reference [7] presented fuzzy control of double-inverted pendulum based on information fusion, which simplifies the design process of fuzzy controller. Recently, the stability of nonlinear uncertain system-based T-S fuzzy model is becoming a hot topic [8–11].

In addition, current researches focus mainly on the regular inverted pendulum. Little attention has been paid to the flexible-inverted pendulum. In this paper, free oscillation link is introduced into the linear inverted pendulum, free spring system. Based on T-S fuzzy inference mechanism, the controller design approach to the nonlinear flexible double-inverted pendulum with uncertainties is investigated.

24.2 The Mathematical Model of Linear Flexible Double-Inverted Pendulum System

When ignoring the air resistance, linear flexible double-inverted pendulum system can be seen as a combination of the spring, homogeneous pendulum, and car. The structure is shown in Fig. 24.1.

This paper uses the Lagrange equations of analytical mechanics to derive mathematical model of flexible-inverted pendulum system. Therefore, the Lagrange equation of inverted pendulum system that suffers conservative force and dissipative force at the same time should be expressed as follows:

$$\frac{\mathrm{d}}{\mathrm{d}t}\left(\frac{\partial T}{\partial \dot{q}_i}\right) - \frac{\partial T}{\partial q_i} + \frac{\partial V}{\partial q_i} + \frac{\partial D}{\partial \dot{q}_i} = F_{q_i} \tag{24.1}$$

In Eq. (24.1), q_i are the generalized coordinates, F_{q_i} are the generalized forces of effecting on the system. T, V, and D are the system's kinetic energy, potential energy, and dissipated energy, respectively. And,

Fig. 24.1 The structure of flexible double-inverted pendulum
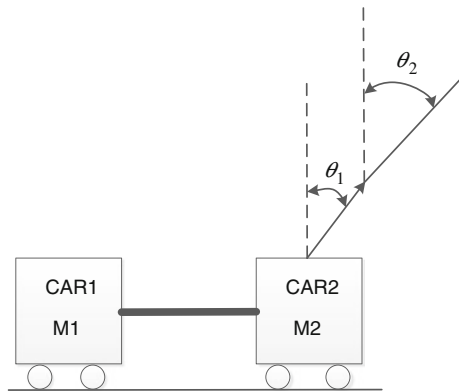
$$V = \sum_{i=0}^{n} V_i, \ T = \sum_{i=0}^{n} T_i \quad \text{and} \quad D = \sum_{i=0}^{n} D_i$$

where n is the number of pendulums, T_i is the kinetic energy of cars and pendulums, V_i is the potential energy of cars and pendulums, D_i is the dissipated energy of cars and pendulums.

In this system the kinetic energy, potential energy and dissipated energy are as follows:

$$
\begin{aligned}
T &= \frac{1}{2}M_1\dot{x}_1^2 + \frac{1}{2}M_2\dot{x}_2^2 + \frac{1}{2}J_1\dot{\theta}^2 + \frac{1}{2}m_1\left[\left(\dot{x}_2 + l_1\dot{\theta}_1\cos\theta_1\right)^2 + \left(l_1\dot{\theta}_1\sin\theta_1\right)^2\right]J_1\dot{\theta}_1^2 \\
&\quad + \frac{1}{2}J_2\dot{\theta}_2^2 + \frac{1}{2}m_2\left[\left(\dot{x}_2 + L\dot{\theta}_1\cos\theta_1 + l_2\dot{\theta}_2\cos\theta_2\right)^2 + \left(L\dot{\theta}_1\sin\theta_1 + l_2\dot{\theta}_2\sin\theta_2\right)^2\right] \\
&= \frac{1}{2}M_1\dot{x}_1^2 + \frac{1}{2}(M_2 + m_1 + m_2)\dot{x}_1^2 + \frac{1}{2}\left(J_1 + m_1l_1^2 + m_2L^2\right)\dot{\theta}_1^2 + \frac{1}{2}\left(J_2 + m_2l_2^2\right)\dot{\theta}_2^2 \\
&\quad - m_2Ll_2\dot{\theta}_2\cos(\theta_2 - \theta_1)\dot{\theta}_1 + (m_1l_1 + m_2L)\dot{\theta}_1\dot{x}_2\cos\theta_1 + M_2l_2\dot{\theta}_2\dot{x}_2\cos\theta_2 \\
V &= V_0 + V_K + V_1 + V_2 = m_1gl_1\cos\theta_1 + m_2g(L\cos\theta_1 + l_2\cos\theta_2) \\
D &= D_0 + D_1 + D_2 + D_3 = \frac{1}{2}c_1\dot{x}_1^2 + \frac{1}{2}c_2\dot{x}_2^2 + \frac{1}{2}f_1\dot{\theta}^2 + \frac{1}{2}f_2\left(\dot{\theta}_2 - \dot{\theta}_1\right)^2
\end{aligned}
$$

Taking T, V, and D into the Eq. (24.1), we can get the kinematic model of flexible-inverted pendulum

$$
\begin{cases}
M_1\ddot{x}_1 + c_1\dot{x}_1 = u + k(x_2 - x_1) \\
(M_2 + m_1 + m_2)\ddot{x}_2 + (m_1l_1 + m_2L)\cos\theta_1\ddot{\theta}_1 + m_2l_2\cos\theta_2\ddot{\theta} \\
\quad + F_0\dot{x} - (m_1l_1 + m_2L)\sin\theta_1\dot{\theta}_1 - M_2l_2\sin\theta_2\dot{\theta}_2^2 = -k(x_2 - x_1) \\
(m_1l_1 + m_2L)\cos\theta_1\ddot{x}_2 + \left(J_1 + m_1l_1^2 + m_2L^2\right)\ddot{\theta}_1 + m_2Ll_2\cos(\theta_2 - \theta_1)\ddot{\theta}_2 \\
\quad + (f_1 + f_2)\dot{\theta}_1 + \left[-m_2Ll_2\sin(\theta_2 - \theta_1)\dot{\theta}_2 - F_2\right]\dot{\theta}_2 = (m_1l_1 + m_2L)g\sin\theta_1 \\
m_2l_2\cos\theta_2\ddot{x}_2 + m_2Ll_2\cos(\theta_2 - \theta_1)\ddot{\theta}_1 + \left(J_2 + m_2l_2^2\right)\ddot{\theta}_2 \\
\quad + \left[m_2Ll_2\sin(\theta_2 - \theta_1)\dot{\theta}_1 - f_2\right]\dot{\theta}_1 + f_2\dot{\theta}_2 = m_2gl_2\sin\theta_2
\end{cases}
\tag{24.2}
$$

Then, the state-space model of flexible double-inverted pendulum is given as follows:

$$
\begin{cases}
\dot{X} = A(t)C + B(t)u \\
Y = C(t)X
\end{cases}
\tag{24.3}
$$

In addition, $X = [x_1, x_2, \theta_1, \theta_2, \dot{x}_1, \dot{x}_2, \dot{\theta}_1, \dot{\theta}_2]^T$, $A(t) = \begin{bmatrix} \text{zeros}(4) & \text{diag}([1, 1, 1, 1]) \\ A21 & A22 \end{bmatrix}$,

$A21 = \text{inv}(M) \times N^*$, $A22 = -\text{inv}(M) \times F$, $B(t) = [B1; B2]$, $B1 = \text{zeros}(4, 1)$, $B2 = \text{inv}(M^*) \times [1 \quad 0 \quad 0 \quad 0]^T$, $C(t) = [\text{diag}([1, 1, 1, 1]) \quad \text{zeros}(4)]$

$$M(\theta_1, \theta_2) = \begin{bmatrix} M_1 & 0 & 0 & 0 \\ 0 & M_2 + m_1 + m_2 & (m_1l_1 + m_2L_1)\cos\theta_1 & m_2l_2\cos\theta_2 \\ 0 & (m_1l_1 + m_2L_1)\cos\theta_1 & J_1 + m_1l_1^2 + m_2L_1^2 & m_2L_1l_2\cos(\theta_2 - \theta_1) \\ 0 & m_2l_2\cos\theta_2 & m_2L_1l_2\cos(\theta_2 - \theta_1) & J_2 + m_2l_2^2 \end{bmatrix}$$

$$F\left(\theta_1, \theta_2, \dot{\theta}_1, \dot{\theta}_2\right) = \begin{bmatrix} c_1 & 0 & 0 & 0 \\ 0 & c_2 & -(m_1l_1 + m_2L_1)\sin\theta_1\dot{\theta}_1 & -m_2l_2\sin\theta_2\dot{\theta}_2 \\ 0 & 0 & f_1 + f_2 & -m_2L_1l_2\sin(\theta_2 - \theta_1)\dot{\theta}_2 - f_2 \\ 0 & 0 & m_2L_1l_2\sin(\theta_2 - \theta_1)\dot{\theta}_1 - f_2 & f_2 \end{bmatrix}$$

$$N^* = \begin{bmatrix} -K & K & 0 & 0 \\ K & -K & 0 & 0 \\ 0 & 0 & (m_1l_1 + m_2L)g & 0 \\ 0 & 0 & 0 & m_2gl_2 \end{bmatrix}.$$

24.3 Controller Design of Uncertain System Based on T-S Fuzzy Inference System

24.3.1 T-S Fuzzy Inference System Controller Design

T-S continuous nonlinear uncertain fuzzy systems are expressed as follows:

Plant Rule i: If v_1 is F_1^i and v_2 is about F_2^i and … v_p is F_p^i, Then

$$\begin{cases} \dot{x}(t) = (A_i + \Delta A_i(t))x(t) + (B_i + \Delta B_i(t))u(t) \\ y(t) = C_i x(t) \end{cases} \tag{24.4}$$

where v_j is the premise variable, F_j^i is the membership function of rule i, $x(t)$ represents state variables, $u(t)$ represents control inputs, $A_i = R^{n \times n}$, $B_i = R^{n \times m}$. $\Delta A_i, \Delta B_i$ are time-varying matrixes with appropriate dimension and represent parameter uncertainties section of fuzzy model.

Assume 24.1 Uncertainty matrixes ΔA_i and ΔB_i are norm bounded and can be deconstructed as follows:

$$[\Delta A_i, \Delta B_i] = D_i F_i(t)[E_{1i}, E_{2i}] \tag{24.5}$$

where D_i, E_{1i} and E_{2i} are known real constant matrices with certain dimension. $F_i(t)$ is lebesgue-measurable unknown matrix function, which satisfied $F_i(t)^T F_i(t) \leq I$.

According to the defuzzification of fuzzy system, the total outputs of fuzzy model with uncertainties described by (24.4) are as follows:

$$\dot{x}(t) = \sum_{i=1}^{r} h_i(x(t))((A_i + \Delta A_i(t))x(t) + (B_i + \Delta B_i(t))u(t)) \qquad (24.6)$$

where h_i is the membership function under rule i, $h_i = \prod_{k=1}^{r} F_k^i(x_k(t))$ and $\sum_{i=1}^{r} h_i(x(t)) = 1$.

PDC controller is natural and simple for T-S fuzzy system. For each local linear subsystem under a fuzzy rule, there is a state feedback controller as follows:

Control rule If v_1 is F_1^i and v_2 is about F_2^i and … v_p is F_p^i, Then

$$u(t) = K_i x(t) \qquad (24.7)$$

According to the fuzzy rules of (24.7), the PDC controller of continuous non-linear system (24.6) is

$$u(t) = \sum_{i=1}^{r} h_i K_i x(t) \qquad (24.8)$$

Taking (24.8) into (24.6) and according to the assume 24.1, we can get

$$
\begin{aligned}
\dot{x}(t) =& \sum_{i=1}^{r} \sum_{k=1}^{r} h_i(x(t)) h_k(x(t))((A_i + \Delta A_i(t))x(t) + (B_i + \Delta B_i(t))u(t)) \\
=& \sum_{i=1}^{r} h_i^2(x(t))(A_i + B_i K_i + D_i F_i(E_{1i} + E_{2i} K_i))x(t) + D_k F_k(E_{1k} + E_{2k} K_i)x(t) \\
&+ 2 \sum_{i<k}^{r} h_i(x(t)) h_k(x(t)) \frac{1}{2}(A_i + B_i K_k + A_k + B_k K_i + D_i F_i(E_{1i} + E_{2i} K_k))
\end{aligned}
$$
$$(24.9)$$

24.3.2 The Stable Condition of Continuous Nonlinear System

Definition 24.1 If there is a set, which has minimum–maximum overlapping rules group and contains all the fuzzy rules of the system, then the set is named as effective maximum overlapping group set (EMORGs), and the maximum overlapping rules groups are named effective maximum overlapping group (EMORG).

Lemma 24.1 *For given constant matrices D, E and symmetric constant matrix S, if there exit some positive constants $\varepsilon > 0$ satisfying*

$$S + \begin{bmatrix} \varepsilon^{-1} E^T & \varepsilon D \end{bmatrix} \begin{bmatrix} R & 0 \\ 0 & I \end{bmatrix} \begin{bmatrix} \varepsilon^{-1} E \\ \varepsilon D \end{bmatrix} < 0$$

Then, the following inequality holds

$$S + DFE + E^{\mathrm{T}} F^{\mathrm{T}} D^{\mathrm{T}} < 0$$

where $F^{\mathrm{T}} F \leq 0$.

Theorem 24.1 *For fuzzy system* (24.9) *with standard fuzzy partition (SFP) inputs, if there exit matrices K_i, scalars $\varepsilon_{ik}(i, k = 1, 2, \ldots, r)$ and local shared positive definite symmetric matrix P_l in each EMORG satisfying inequalities* (24.10) *and* (24.11), *then* (24.9) *is asymptotically stable in large-scale at equilibrium point.*

$$\Phi_{ii} + \varepsilon_{ii}^{-1}(E_{1i} + E_{2i}K_i)^T(E_{1i} + E_{2i}K_i) + \varepsilon_{ii}P_lD_i(P_lD_i)^T \leq 0 \qquad (24.10)$$

where $i \in \{$the sequence numbers of rules included in $G_l\}$;

$$\begin{aligned} &\Phi_{ii} + \varepsilon_{ik}^{-1}(E_{1i} + E_{2i}K_k)^T(E_{1i} + E_{2i}K_k) + \varepsilon_{ik}^{-1}(E_{1k} + E_{2k}K_i)^T(E_{1k} + E_{2k}K_i) \\ &\quad + \varepsilon_{ik}P_lD_i(P_lD_i)^T + \varepsilon_{ik}P_lD_k(P_lD_k)^T \leq 0 \end{aligned} \qquad (24.11)$$

where $i, k \in \{$the sequence numbers of rules included in $G_l\}$, $i < k$, and Φ_{ii}, Φ_{ik} are as follows:

$$\begin{aligned} \Phi_{ii} &= A_i^{\mathrm{T}} P_l + P_l A_i + K_i^{\mathrm{T}} B_i^{\mathrm{T}} P_l + P_l B_i K_i \\ \Phi_{ik} &= A_i^{\mathrm{T}} P_l + P_l A_i + A_k^{\mathrm{T}} P_l + P_l A_k + K_k^{\mathrm{T}} B_i^{\mathrm{T}} P_l + P_l B_i K_k + K_i^{\mathrm{T}} B_k^{\mathrm{T}} P_l + P_l B_k K_i \end{aligned}$$

G_l represents the lth EMORG, and $l = 1, 2, \ldots, s$,
  where

$$s = \begin{cases} \prod\limits_{j=1}^{n} \left(\frac{q_j + 1}{2} \right), & q_j \in \text{Odd Set}; \\ \prod\limits_{j=1}^{n} \left(\frac{q_j}{2} \right), & q_j \in \text{Even Set}; \\ \prod\limits_{q_{j'} \in \text{odd}} \left(\frac{q_{j'}}{2} \right) \prod\limits_{q_{j''} \in \text{even}} \left(\frac{q_{j''} + 1}{2} \right), & j', j'' \in \{1, 2, \ldots, n\}, q_j \text{ are others} \end{cases} \qquad (24.12)$$

q_j represents the number of fuzzy partition of the jth input.

Considering a non-singular matrix $F(x) \in R^{n \times n}$ as follows:

$$F(x) = \begin{bmatrix} F_{11}(x) & F_{12}(x) \\ F_{21}(x) & F_{22}(x) \end{bmatrix}$$

where $F_{11}(x)$ is $r \times r$.

   According to Lemma 24.1 and Theorem 24.1, we can get a new stability condition as follows:

Theorem 24.2 *For fuzzy system* (24.9) *with standard fuzzy partition (SFP) inputs, if there exit matrices* K_i, *scalars* $\varepsilon_{ik}(i, k = 1, 2, \ldots, r)$ *and local shared positive definite symmetric matrix* P_l *in each EMORG satisfying inequalities* (24.13) *and* (24.14), *then* (24.9) *is asymptotically stable in large-scale at equilibrium point*:

$$
\begin{bmatrix}
\Psi_{ii} & * & * \\
E_{1i}Q + M_{1i} & -\varepsilon_{ii}I & * \\
D_i^T & 0 & -\varepsilon_{ii}^{-1}I
\end{bmatrix} < 0
\tag{24.13}
$$

where $i, k \in \{$the sequence numbers of rules included in $G_l\}$

$$
\begin{bmatrix}
\Psi_{ik} & * & * & * & * \\
E_{1i}Q + E_{2i}M_{lk} & -\varepsilon_{ik}I & * & * & * \\
E_{1i}Q + E_{2i}M_{li} & 0 & -\varepsilon_{ik}I & * & * \\
D_i^T & 0 & 0 & -\varepsilon_{ik}^{-1}I & * \\
D_k^T & 0 & 0 & 0 & -\varepsilon_{ik}^{-1}I
\end{bmatrix} < 0
\tag{24.14}
$$

where $i, k \in \{$the sequence numbers of rules included in $G_l\}$, $i < k$, *and* Ψ_{ii}, Ψ_{ik} *are as follows*:

$$
\Psi_{ii} = QA_i^T + A_iQ + M_{li}^T B_i^T + B_i M_{li},
$$
$$
\Psi_{ik} = QA_i^T + A_iQ + QA_k^T + A_kQ + M_{lk}^T B_i^T + B_i M_{lk} + M_{li}^T B_k^T
$$
$$
\quad\quad + B_k M_{li} + K_k^T B_i^T P_l + P_l B_i K_k + K_i^T B_k^T P_l + P_l B_k K_i
$$

where $Q = P_l^{-1}$, $M_{li} = K_i P_l^{-1}$, * *represents elements in symmetrical position*, G_l *represents the lth EMORG*, $l = 1, 2, \ldots, q, q = \prod_{j=1}^{n} (m_j - 1)$, m_j *represents the jth input's fuzzy partitions*.

Note 1 for theory 2, the number of LMIs to ensure the fuzzy system's stability is $[2^{n-1}(2^n + 1)] \prod_{j=1}^{n} (m_j - 1)$.

24.4 T-S fuzzy Modeling and Controller Design of Flexible Double-Inverted Pendulum

Let the domain of input variables θ_1 and θ_2 be $\left[-\frac{\pi}{2}, -\frac{\pi}{2}\right]$, $\dot{\theta}_1$ and $\dot{\theta}_2$ be $[-10, 10]$. There are three membership functions of θ_1 and θ_2. There are two membership functions of $\dot{\theta}_1$, $\dot{\theta}_2$. According to the nonlinear model of flexible double-inverted pendulum, we take θ_1, θ_2, $\dot{\theta}_1$ and $\dot{\theta}_2$ as premise variables. Let e denote θ_1, θ_2, $\dot{\theta}_1$ and $\dot{\theta}_2$. When $e \to 0$, $\sin e \to m$, $\cos e \to 1$;

When $e \to \pm^{\pi}/_2$, $\sin e \to \pm 1 \to {^2}/_{\pi}e$, $\cos e \to 0 \to \cos(88°)$;

According to Theory 2, we can get the feedback gains of each local linear subsystem.

In this paper we have

$$-5\,\mathrm{N\,m/s} \le \Delta c_1 = \Delta c_2 \le 5\,\mathrm{N\,m/s}, \quad -0.002\,\mathrm{N\,m/s} \le \Delta f_1 \le 0.002\,\mathrm{N\,m/s}$$
$$-0.001\,\mathrm{N\,m/s} \le \Delta f_2 = 0.001\,\mathrm{N\,m/s}$$

$$D_i = D = \begin{bmatrix} \text{zeros}(4) & \text{zeros}(4) \\ \text{zeros}(4) & \Psi \end{bmatrix}, \quad \Psi = \begin{bmatrix} -3.3333 & 0 & 0 & 0 \\ 0 & -3.2125 & 0.0048 & -0.0018 \\ 0 & 7.5245 & -0.1320 & 0.0728 \\ 0 & -1.5748 & 0.2771 & -0.1908 \end{bmatrix}, \quad E_{1i} = I, \quad E_{2i} = 0,$$

$$F_i = \begin{bmatrix} \text{zeros}(4) & \text{zeros}(4) \\ \text{zeros}(4) & \Theta \end{bmatrix} \quad \Theta = \sin(t)I \quad i = 1, 2, \ldots, 33.$$

According to (24.12), we get four EMORG of uncertain nonlinear flexible double-inverted pendulum system.

Furthermore, according to Theory 2, we can get the feedback gains of each linear subsystem by LMI as follows:

$K_1 = 10^3 \times [\, 1.3481 \quad -1.2035 \quad -4.0002 \quad 4.6702 \quad 0.0435 \quad -0.2794 \quad -0.1287 \quad 0.5839 \,]$

$K_2 = [\, 569.1627 \quad -424.5944 \quad 627.6283 \quad -403.7172 \quad 23.4184 \quad -61.4765 \quad -63.5059 \quad -98.6033 \,]$

$K_3 = 10^3 \times [\, 1.1653 \quad -1.0207 \quad 1.5061 \quad -1.5536 \quad 0.0393 \quad -0.1711 \quad -0.1916 \quad -0.3153 \,]$

$K_4 = [\, 568.4451 \quad -423.8768 \quad 627.4234 \quad 415.1406 \quad 23.3960 \quad -61.2878 \quad -63.3525 \quad 101.3644 \,]$

$K_5 = 10^3 \times [\, 1.1496 \quad -1.0050 \quad 1.4832 \quad 1.5616 \quad 0.0390 \quad -0.1680 \quad -0.1877 \quad 0.3175 \,]$

$K_6 = [\, 568.4451 \quad -423.8768 \quad 627.4234 \quad 415.1406 \quad 23.3960 \quad -61.2878 \quad -63.3525 \quad 101.3644 \,]$

$K_7 = 10^3 \times [\, 1.1496 \quad -1.0050 \quad 1.4832 \quad 1.5616 \quad 0.0390 \quad -0.1680 \quad -0.1877 \quad 0.3175 \,]$

$K_8 = [\, 569.1627 \quad -424.5944 \quad 627.6283 \quad -403.7172 \quad 23.4184 \quad -61.4765 \quad -63.5059 \quad -98.6033 \,]$

$K_9 = 10^3 \times [\, 1.1653 \quad -1.0207 \quad 1.5061 \quad -1.5536 \quad 0.0393 \quad -0.1711 \quad -0.1916 \quad -0.3153 \,]$

$K_{10} = 10^3 \times [\, 0.6010 \quad -0.4564 \quad -1.5858 \quad 0.6679 \quad 0.0244 \quad -0.0672 \quad -0.4869 \quad -0.0495 \,]$

$K_{11} = 10^3 \times [\, 1.1557 \quad -1.0112 \quad 5.8189 \quad 1.5292 \quad 0.0391 \quad -0.1670 \quad 1.4318 \quad -0.1349 \,]$

$K_{12} = 10^3 \times [\, 0.6005 \quad -0.4560 \quad 1.6320 \quad 0.6681 \quad 0.0244 \quad -0.0671 \quad 0.5009 \quad -0.0495 \,]$

$K_{13} = 10^3 \times [\, 1.1706 \quad -1.0260 \quad -5.7855 \quad 1.5523 \quad 0.0395 \quad -0.1699 \quad -1.4198 \quad -0.1375 \,]$

$K_{14} = 10^3 \times [\, 0.6005 \quad -0.4560 \quad 1.6320 \quad 0.6681 \quad 0.0244 \quad -0.0671 \quad 0.5009 \quad -0.0495 \,]$

$K_{15} = 10^3 \times [\, 1.1706 \quad -1.0260 \quad -5.7855 \quad 1.5523 \quad 0.0395 \quad -0.1699 \quad -1.4198 \quad -0.1375 \,]$

$K_{16} = 10^3 \times [\, 0.6010 \quad -0.4564 \quad -1.5858 \quad 0.6679 \quad 0.0244 \quad -0.0672 \quad -0.4869 \quad -0.0495 \,]$

$K_{17} = 10^4 \times [\, 0.0847 \quad -0.0803 \quad -6.2638 \quad 7.2026 \quad 0.0031 \quad -0.0218 \quad -0.2709 \quad 1.1123 \,]$

$K_{18} = 10^4 \times [\, 0.0994 \quad -0.0850 \quad -7.4938 \quad 9.6149 \quad 0.0035 \quad -0.0144 \quad -0.146 \quad 11.5250 \,]$

$K_{19} = 10^4 \times [\, 0.0995 \quad -0.0851 \quad -7.4739 \quad 9.5905 \quad 0.0035 \quad -0.0144 \quad -0.1482 \quad 1.5210 \,]$

$K_{20} = 10^4 \times [\, 0.0996 \quad -0.0851 \quad -7.4771 \quad 9.5939 \quad 0.0035 \quad -0.0144 \quad -0.1482 \quad 1.5222 \,]$

$K_{21} = 10^4 \times [\, 0.0853 \quad -0.0807 \quad -6.2890 \quad 7.2535 \quad 0.0032 \quad -0.0217 \quad -0.2705 \quad 1.1203 \,]$

$K_{22} = 10^4 \times [\, 0.0854 \quad -0.0808 \quad -6.2919 \quad 7.2565 \quad 0.0032 \quad -0.0218 \quad -0.2706 \quad 1.1213 \,]$

$K_{23} = 10^4 \times [\, 0.0852 \quad -0.0807 \quad -6.3073 \quad 7.2745 \quad 0.0032 \quad -0.0217 \quad -0.2689 \quad 1.1243 \,]$

$$K_{24} = 10^4 \times [\,0.0852 \quad -0.0806 \quad -6.3044 \quad 7.2716 \quad 0.0032 \quad -0.0217 \quad -0.2689 \quad 1.1233\,]$$
$$K_{25} = 10^4 \times [\,0.0879 \quad -0.0834 \quad 4.1732 \quad -3.2196 \quad 0.0032 \quad -0.0225 \quad 1.5745 \quad -0.8154\,]$$
$$K_{26} = 10^4 \times [\,0.0876 \quad -0.0831 \quad 4.1817 \quad -3.2251 \quad 0.0032 \quad -0.0224 \quad 1.5774 \quad -0.8162\,]$$
$$K_{27} = 10^4 \times [\,0.0881 \quad -0.0835 \quad 4.1638 \quad -3.2128 \quad 0.0032 \quad -0.0226 \quad 1.5686 \quad -0.8129\,]$$
$$K_{28} = 10^4 \times [\,0.0884 \quad -0.0839 \quad 4.1552 \quad -3.2073 \quad 0.0032 \quad -0.0227 \quad 1.5657 \quad -0.8120\,]$$
$$K_{29} = 10^4 \times [\,0.0881 \quad -0.0835 \quad 4.1638 \quad -3.2128 \quad 0.0032 \quad -0.0226 \quad 1.5686 \quad -0.8129\,]$$
$$K_{30} = 10^4 \times [\,0.0884 \quad -0.0839 \quad 4.1552 \quad -3.2073 \quad 0.0032 \quad -0.0227 \quad 1.5657 \quad -0.8120\,]$$
$$K_{31} = 10^4 \times [\,0.0879 \quad -0.0834 \quad 4.1732 \quad -3.2196 \quad 0.0032 \quad -0.0225 \quad 1.5745 \quad -0.8154\,]$$
$$K_{32} = 10^4 \times [\,0.0876 \quad -0.0831 \quad 4.1817 \quad -3.2251 \quad 0.0032 \quad -0.0224 \quad 1.5774 \quad -0.8162\,]$$
$$K_{33} = 10^4 \times [\,0.0873 \quad -0.0835 \quad 4.1629 \quad -3.1198 \quad 0.0032 \quad -0.0229 \quad 1.5738 \quad -0.8056\,]$$

$$
P_1 = 1.0e - 002 \times
\begin{bmatrix}
0.0553 & -0.0359 & -0.2761 & 0.0162 & 0.0010 & 0.0197 & -0.4387 & 0.0003 \\
-0.0359 & 0.0350 & 0.0235 & 0.0021 & -0.0008 & 0.0064 & 0.3615 & -0.0056 \\
-0.2761 & 0.0235 & 3.8412 & -0.3240 & -0.0037 & -0.3557 & 1.1414 & 0.0763 \\
0.0162 & 0.0021 & -0.3240 & 0.2429 & 0.0006 & 0.0271 & -0.0320 & -0.0554 \\
0.0010 & -0.0008 & -0.0037 & 0.0006 & 0.0010 & 0.0000 & 0.0046 & -0.0001 \\
0.0197 & 0.0064 & -0.3557 & 0.0271 & 0.0000 & 0.0396 & -0.0287 & -0.0108 \\
-0.4387 & 0.3615 & 1.1414 & -0.0320 & 0.0046 & -0.0287 & 4.2285 & -0.0320 \\
0.0003 & -0.0056 & 0.0763 & -0.0554 & -0.0001 & -0.0108 & -0.0320 & 0.2037
\end{bmatrix}
$$

$$
P_2 = 1.0e - 003 \times
\begin{bmatrix}
0.0709 & 0.0313 & -0.0610 & 0.0586 & 0.0271 & 0.1844 & -0.1417 & -0.0766 \\
-0.0663 & 0.9497 & -0.4743 & 0.5335 & 0.2527 & 1.5635 & -0.8512 & -0.8609 \\
0.0032 & -0.5429 & 0.3602 & -0.3501 & -0.1582 & -1.0274 & 0.5842 & 0.5639 \\
-0.0065 & 0.5825 & -0.3370 & 0.4709 & 0.1814 & 0.9999 & -0.5520 & -0.4993 \\
-0.0018 & 0.2813 & -0.1570 & 0.1854 & 0.0963 & 0.4828 & -0.2904 & -0.2715 \\
0.0006 & 1.7516 & -1.0228 & 1.0300 & 0.4837 & 3.5377 & -1.6518 & -1.5655 \\
-0.0379 & -0.9278 & 0.5651 & -0.5431 & -0.2812 & -1.6016 & 1.4044 & 1.2911 \\
0.0235 & -0.9543 & 0.5505 & -0.5193 & -0.2703 & -1.5374 & 1.2976 & 1.3329
\end{bmatrix}
$$

$$
P_3 = 1.0e - 003 \times
\begin{bmatrix}
0.9044 & -0.7266 & -0.3481 & -0.0032 & 0.0071 & 0.2764 & 0.3645 & 0.6367 \\
-0.7266 & 0.6323 & 0.2015 & 0.0762 & 0.0111 & -0.1094 & -0.6029 & -0.5555 \\
-0.3481 & 0.2015 & 0.5045 & -0.2254 & -0.0404 & -0.2878 & 0.6838 & -0.1737 \\
-0.0032 & 0.0762 & -0.2254 & 0.2071 & 0.0334 & 0.1621 & -0.7069 & -0.0710 \\
0.0071 & 0.0111 & -0.0404 & 0.0334 & 0.0072 & 0.0401 & -0.1437 & -0.0099 \\
0.2764 & -0.1094 & -0.2878 & 0.1621 & 0.0401 & 0.3494 & -0.5821 & 0.0918 \\
0.3645 & -0.6029 & 0.6838 & -0.7069 & -0.1437 & -0.5821 & 3.2724 & 0.5220 \\
0.6367 & -0.5555 & -0.1737 & -0.0710 & -0.0099 & 0.0918 & 0.5220 & 0.5377
\end{bmatrix}
$$

$$
P_4 = 1.0e - 002 \times
\begin{bmatrix}
4.9730 & -5.3609 & 0.1990 & -0.2799 & -0.0729 & -2.0270 & 1.0952 & -0.0695 \\
-5.3609 & 5.7864 & -0.2323 & 0.3039 & 0.0801 & 2.2018 & -1.2000 & 0.0763 \\
0.1990 & -0.2323 & 0.0851 & -0.0152 & -0.0061 & -0.1219 & 0.0843 & -0.0075 \\
-0.2799 & 0.3039 & -0.0152 & 0.0231 & 0.0050 & 0.1187 & -0.0793 & 0.0041 \\
-0.0729 & 0.0801 & -0.0061 & 0.0050 & 0.0015 & 0.0331 & -0.0232 & 0.0013 \\
-2.0270 & 2.2018 & -0.1219 & 0.1187 & 0.0331 & 0.8645 & -0.4884 & 0.0314 \\
1.0952 & -1.2000 & 0.0843 & -0.0793 & -0.0232 & -0.4884 & 0.3758 & -0.0211 \\
-0.0695 & 0.0763 & -0.0075 & 0.0041 & 0.0013 & 0.0314 & -0.0211 & 0.0062
\end{bmatrix}
$$
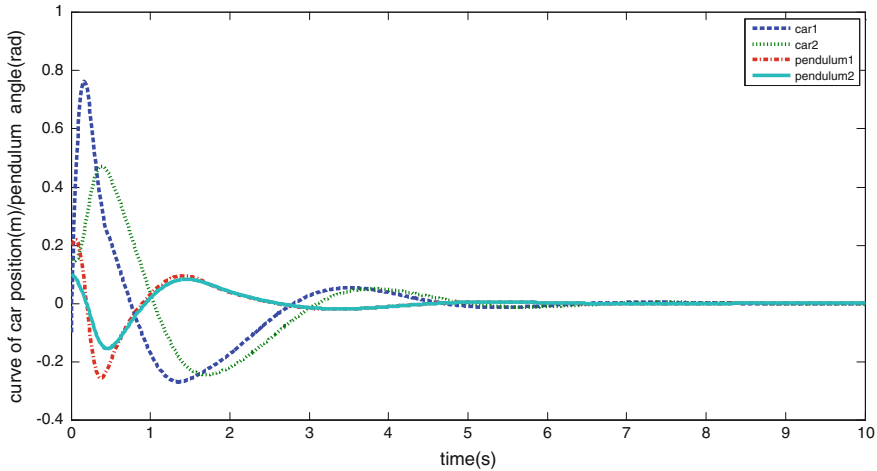
Fig. 24.2 Simulation results

24.5 Simulation

Triangular membership function is selected from the membership functions of the toolbox in MATLAB,and the functions are Trimf.

$$
\begin{cases}
F_1^1 = \mathrm{trim}f\left(\theta_1, \left[-\frac{\pi}{2}, 0, \frac{\pi}{2}\right]\right) & \theta_1 \to 0 \\
F_1^2 = \mathrm{trim}f\left(\theta_1, \left[-\frac{\pi}{2}, -\frac{\pi}{2}, 0\right]\right) & \theta_1 \to -\frac{\pi}{2} \\
F_1^3 = \mathrm{trim}f\left(\theta_1, \left[0, 0, \frac{\pi}{2}\right]\right) & \theta_1 \to \frac{\pi}{2}
\end{cases}
\qquad
\begin{cases}
F_2^1 = \mathrm{trim}f\left(\theta_2, \left[-\frac{\pi}{2}, 0, \frac{\pi}{2}\right]\right) & \theta_2 \to 0 \\
F_2^2 = \mathrm{trim}f\left(\theta_2, \left[-\frac{\pi}{2}, -\frac{\pi}{2}, 0\right]\right) & \theta_2 \to -\frac{\pi}{2} \\
F_2^3 = \mathrm{trim}f\left(\theta_2, \left[0, 0, \frac{\pi}{2}\right]\right) & \theta_2 \to \frac{\pi}{2}
\end{cases}
$$

$$
\begin{cases}
F_3^1 = \mathrm{trim}f\left(\dot{\theta}_1, [-10, -10, 10]\right) & \dot{\theta}_1 \to -10 \\
F_3^2 = \mathrm{trim}f\left(\dot{\theta}_1, [-10, 10, 10]\right) & \dot{\theta}_1 \to 10
\end{cases}
\qquad
\begin{cases}
F_4^1 = \mathrm{trim}f\left(\dot{\theta}_2, [-10, -10, 10]\right) & \dot{\theta}_2 \to -10 \\
F_4^2 = \mathrm{trim}f\left(\dot{\theta}_2, [-10, 10, 10]\right) & \dot{\theta}_2 \to 10
\end{cases}
$$

Taking K_i and F_k^i into the Eq. (24.7), we can get the controller. Initial-state variables are [−0.1 0.2 0.2 0.1 0 0 0 0]. The Simulation curve of flexible double-inverted pendulum base on T-S fuzzy controller is shown as in Fig. 24.2. According to the simulation results, we can get that the T-S fuzzy controller keeps the system stable in the balance point at 5th second.

24.6 Conclusion

As there exits many uncertainties and external disturbances in the actual control process, it is difficult to establish the accurate mathematical model of flexible double-inverted pendulum system. In this paper, T-S fuzzy method is used to model

the flexible double-inverted pendulum system with uncertain parameters, which will approach to the actual control system with the greatest approximation. In addition, on the basis of the improved sufficient conditions for the stability of T-S fuzzy systems, the fuzzy controller is designed. The proposed method can decrease the conservation of the original T-S fuzzy system stability by reducing the number of linear matrix inequalities.

References

1. Hadjili ML, Kara K (2011) Modelling and control using Takagi-Sugeno fuzzy models. In: IEEE Saudi international, pp 1–6
2. Wang JJ (2011) Simulation studies of inverted pendulum based on PID controllers. Simul Model Pract Theory 19(1):440–449
3. Yan X, Jiang H (2005) Control method study on a single inverted pendulum in simulation environment. Measur Contr Technol 24(7):37–39
4. Chen N, Zhang Z, Liu F et al (2010) Adaptive fuzzy control for balancing double inverted pendulums. In: International conference on IEEE, pp 543–548
5. Žilić T, Pavković D, Zorc D (2009) Modeling and control of a pneumatically actuated inverted pendulum. ISA Trans 48(3):327–335
6. Tatikonda RC, Battula VP, Kumar V (2010) Control of inverted pendulum using adaptive neuro fuzzy inference structure (ANFIS). In Circuits and Systems (ISCAS) on, IEEE, pp 1348–1351
7. Fan Y, Sang Y, Liu B (2011) A fuzzy control method based on information integration for double inverted pendulum. In: Second international conference on, IEEE, pp 24–27
8. Yao J, Chai Y (2007) Swing-up control of double inverted pendulum based on adaptive neuro-fuzzy inference system. In: Fourth international conference on, IEEE, vol 4, pp 195–198
9. Gong CZ, Wang AH (2005) Stability analysis of fuzzy control for a class of complex uncertain nonlinear systems. Guangzhou, China
10. Fang CH, Liu YS, Kau SW et al (2006) A new LMI-based approach to relaxed quadratic stabilization of TS fuzzy control systems. IEEE Trans Fuzzy Syst 14(3):386–397
11. Wang X, Wang S, Wang K, Hong W (2012) Adaptive fuzzy robust control of a class of nonlinear systems via small gain theorem . In: 10th IEEE international conference, pp 559–564

Chapter 25
Research on the EEG Recognition for Brain–Computer Interface of Speech Based on DIVA Model

Shaobai Zhang and You Zeng

Abstract Direction Into Velocities of Articulators (DIVA) model can be more accurately described as a mathematical model, it shows the role of the human brain involved in speech production and speech understanding by the region, it can simulate the pronunciation process and play a key role in speech BCI design. In order to realize the speech BCI system, we used wavelet packet decomposition and support vector machine (SVM) in EEG signal processing during the speech in this study according to the forecast of DIVA model and the conclusions of DIVA-related researches. Result shows that the eigenvector extracted by the method worked out fine in the classification of EEG signal, it provided a new way to design a speech-related BCI system. In addition, the conclusions of this study also proved the forecast of brain activation during the speech of DIVA model.

Keywords Brain–computer interface · EEG · DIVA model · Wavelet packet decomposition · SVM

25.1 Introduction

In recent years, a growing number of researchers and scholars are dedicated to the research and development of brain–computer interface technology, which can serve as a bridge between human brain and computer and communicate human thinking to computer [1, 2]. It is a brand new form of human–machine interaction. A complete

S. Zhang (✉) · Y. Zeng
Computer Department, Nanjing University of Posts and Telecommunications,
Nanjing 210046, Jiangsu, China
e-mail: adzsb@163.com

Y. Zeng
e-mail: zzengyyou@163.com

brain–computer interface system consists of EEG acquisition module, feature extraction module, feature classification module, and facility directive module, among which the extraction of EEG features and feature classification are the hardcore of the entire system.

This paper proposes a feature extraction and classification method specific to speech EEG signals, and aims at the implementation of speech brain–computer interface which is a relatively complex brain–computer interface. Designing a speech brain–computer interface system [3] meeting the application requirements entails full knowledge of the related functions of the brain regions dealing with speech production and comprehension. Huge efforts by many recent researchers in researching and exploring the mechanism of speech production and calculation model acquisition have been paid off with fruitful results, among which the Directions Into Velocities of Articulators [4] (DIVA) model put forward by Professor Frank H. Guenther of the speech lab of Boston University has been widely applied in researches of speech production and acquisition [5]. Prof. Guenther's DIVA model gives an accurate elucidation toward the kinematics data of human vocal organs and the working mechanism of related brain regions, on which basis Prof. Guenther therewith designed a neural analytic system [6]-based apparatus (speech brain–computer interface system), with which what a user wants to express can be delivered in voice by the voice synthesis system, while all that is needed for the user is to think about it. And through the combination with brain–computer interface technology, the user can have direct control over voice output at a response speed much higher than that of the typing system used by the renowned scientist Mr. Hawking. This neural analytic system is composed of two parts: brain–computer interface (BCI) and the voice synthesis system DIVA. Here in BCI, the EEG is acquired through a wireless neural electrode which is permanently implanted into the cerebral cortex of the patient, while the detected EEG used to drive the continuous "movements" of the voice synthesizer which provides the patient with real-time voice output.

Presently, to design a Chinese neural analytic system [7] that can "read" Chinese speakers' thinking process, domestic researchers must focus on two key aspects: first, finding out the differences of cerebral processing mechanisms in pronouncing English and Chinese; second, finding out an EEG classification method suitable for Chinese pronunciation. In this study, we conducted experiments with the pronunciation of both Chinese Pinyin and English letters, and keep records of the experimental subjects' EEG in the pronunciation of both languages, and then following the relevant definitions in the DIVA model, we processed the EEG data through wavelet packet decomposition (WPD) and extracted the eigenvectors, which is then imported into SVM for classification and recognition. As the experiment result turned out, the classification method adopted in this research has high recognition precision and is proved to be an EEG classification and recognition method suitable for Chinese pronunciation, which provides a new idea for the design of Chinese neural analytic system, and meanwhile the examination of the

classification results also confirmed the DIVA model as well as domestic researchers' relevant speculations about the cerebral activations in speech production [8].

25.2 Introduction of DIVA Model

As shown in Fig. 25.1, DIVA model is composed by a feedforward control subsystem, a feedback control subsystem, and a Maeda simulation articulatory model [9]. In the training stage, the model produces a time series that describes the variation of articulatory velocity and position changes of articulators according to some rule with the training speech as an input.

One of the important features of the development of DIVA model is the one-to-one correspondence between model modules and relevant regions in the cerebral cortex. In the new DIVA model established in 2011 [10], Dr. Frank H. Guenther described the relation of DIVA components and the regions of brain in the Montreal Neurological Institute (MNI) framework. The premotor, motion, audition, and somatosensory regions in the pallium and epencephalia has been accurately defined in the new model. In this experiment, we used these definitions of DIVA model, and the result of our experiment also proved some forecast of DIVA. Thus, DIVA model becomes a basic framework that can be used to explain experimental data from all sources and provide consistent descriptions to speech neural processes.
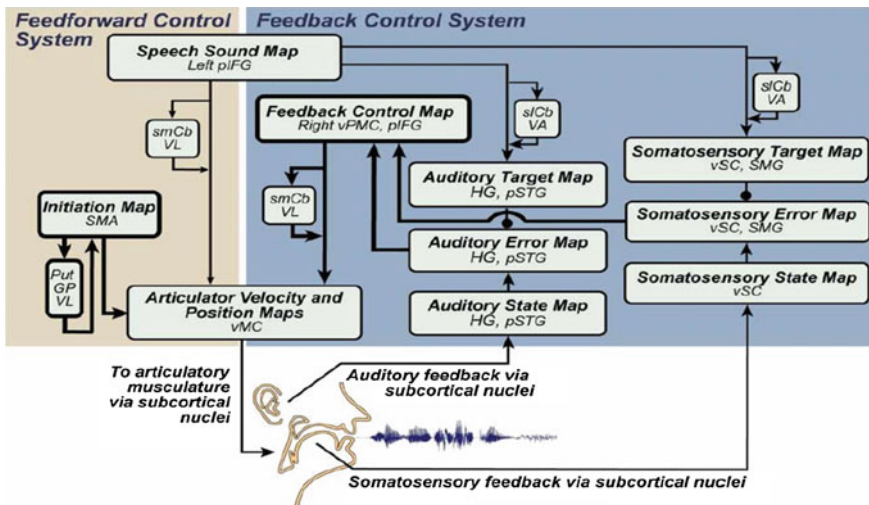
Fig. 25.1 A schematic diagram of DIVA model

25.3 Methods

25.3.1 Participants and Procedures

The experimental subject is a native Chinese speaking male with good health, who has certain experience with EEG acquisition experiments. This experiment adopts brain wave scanner and EEG headset with 128 electrodes to record the EEG signals, with the impedance of each electrode being under 5000 Ωm and the signal sample frequency being 500 Hz. The subject remained in clear consciousness throughout the EEG acquisition, and completed 80 times of pronunciation task of the Chinese pinyin J and the English letter J respectively, with the duration of each pronunciation being 600 ms and the pronunciation started 100 ms each time after the initiation of each pronunciation task. This experiment was completed within one day.

25.3.2 Pretreatment of the Experimental Data

Since EEG signals above 30 Hz are valueless, we adopted a 0.3–30 Hz bandpass filter in the EEG signal acquisition process. And considering that the EOG and kinesis of the subject have substantial impact on the signal generation, we eliminated the electrooculogram and mechanomyography impacts from the acquired EEG signals through visual inspection before further analyzing the EEG signals.

25.3.3 Selection of Channel

According to the predictions in DIVA model and relevant conclusions of researches about phonological processing brain mechanisms, the cerebral region controlling the movement of vocal organs is located in the precentral gyrus, therefore we adopted the EEG signals acquired (Fig. 25.2) in the encephalic region as speculated in the DIVA model when extracting and classifying the features of EEG signals of Chinese speakers.

25.3.4 Processing Tools for the Experimental Data

25.3.4.1 EEGLAB

This research adopts the EEGLAB toolkit in the environment of MATLAB R2010b to read the EEG signals acquired in the experiment. EEGLAB toolkit is a processing tool specific to EEG data process, whose build-in pop loadset function

Fig. 25.2 The electrode position of the EEG headset adopted in the experiment
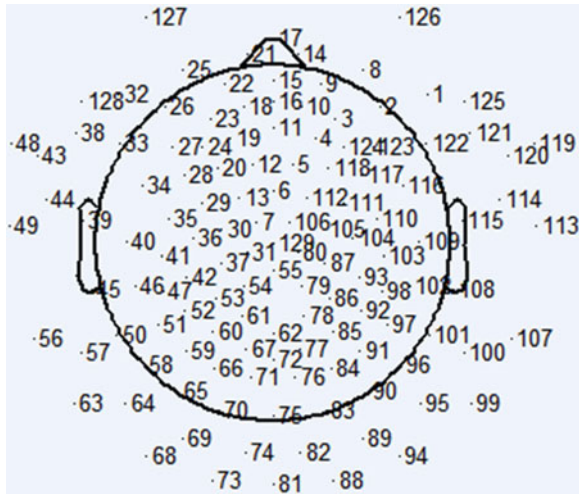
Fig. 25.3 EEG waveform of the subject pronouncing the English letter "J"
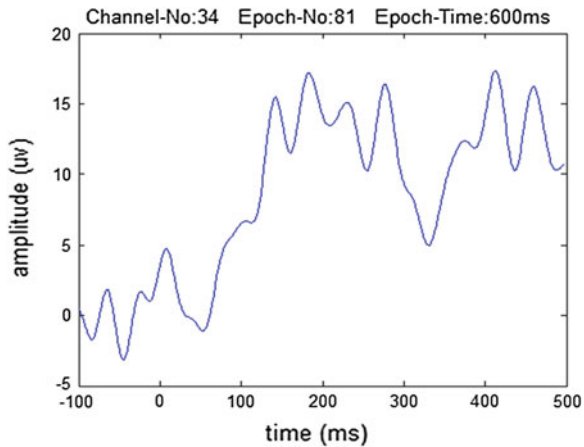
(Figs. 25.3 and 25.4 shows the waveform of EEG signals read through the pop loadset function) also offers us great convenience in the feature extraction suing WPD and the classification using SVM.

25.3.4.2 LibSVM Toolkit

LibSVM toolkit is a simple, easy-to-use, efficient, and effective SVM model recognition and regress software package developed by Taiwan University Associate Professor Lin Zhiren et al. This software engages in relatively less parameter adjustment with SVM and provides a great number of default parameters that could

Fig. 25.4 EEG waveform of
the subject pronouncing the
Chinese pinyin "J"
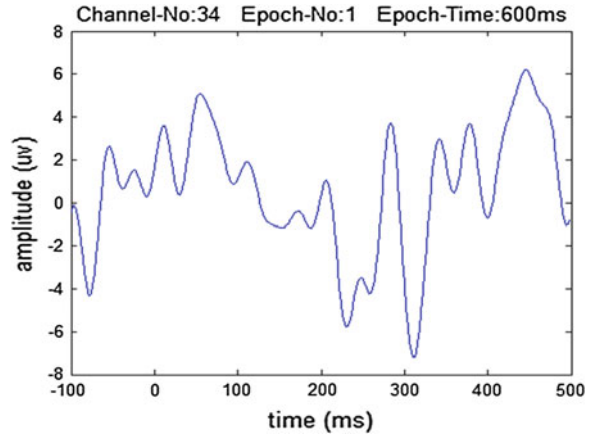
be used to solve many problems; it also provides the function of cross validation. In
this research, we adopt LibSVM toolkit to classify the features of EEG signals.

25.4 The Feature Extraction of EEG Signals

25.4.1 Wavelet Packet Decomposition and Its Characteristics

25.4.1.1 The Characteristics of Wavelet Packet Decomposition

WPD is an extension of wavelet decomposition, that is, it further decomposes the
high frequency detail signals left over by wavelet transform (WT) so as to enhance
the frequency resolution. As is shown in Figs. 25.5 and 25.6, because the two
exporting frequency bands reduce by half through orthogonal decomposition, the
sampling frequency can be reduced by half without any loss of information.

Fig. 25.5 Wavelet
decomposition of signals
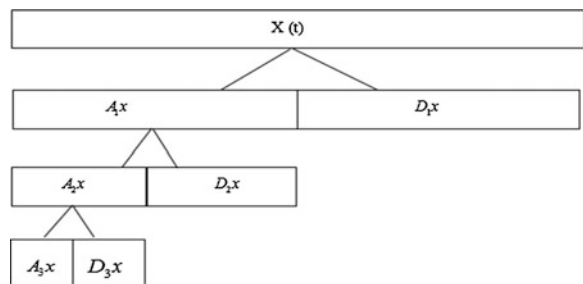
Fig. 25.6 Wavelet packet
decomposition of signals
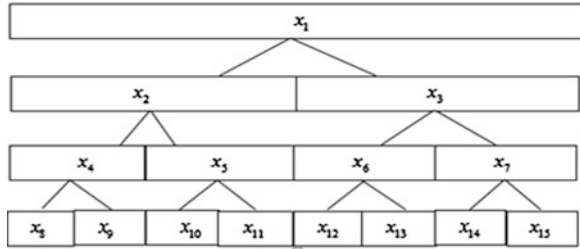
For any wavelet series shown in 25.1:

$$D_j x(t) = \sum_n d_n^j \varphi(2^j t - n) = \sum_n d_n^j w_1(2^j t - n) \tag{25.1}$$

Can be decomposed into the orthogonal sum of wavelet packet component:

$$D_{j,k,m} x(t) = \sum_n d_n^{j,k,m} w_{2^k+m}(2^{j-k} t - n) \quad m = 0, 1, \ldots, 2^{k-1} \tag{25.2}$$

Here into $D_{j,0,0} x(t) = D_j x(t)$. For signal $X(t)$, if $j = 0$, then $k = 0$ and $m = 0$, standing for the original signal $X(t)$ itself at the frequency resolution level j, written down as $X1$. If decomposed for 1 time, namely $k = 1$, $m = 0$, 1, then the result at the first level of wavelet decomposition is decomposed signals $X2$ and $X3$. If decomposed for 2 times, namely $k = 2$, $m = 0$, 1, 2, 3, then the results of the second level of wavelet decomposition are the decomposed signals $X2$, $X3$ and $X6$, $X7$, and the like.

25.4.1.2 Wavelet-Decomposed Signal Energy

As a result of adopting WPD, all decomposition frequency bands are mutually independent, and there is neither redundant information nor missed information, and the energy remains in consistent conservation.

$$E(n) = \sum_{k=1}^{N} |g_n(k)|^2 \quad n = 0, 1, 2, \ldots, 2^m - 1 \tag{25.3}$$

Here, n stands for the serial number of frequency bands.

25.4.1.3 The Advantages of Processing EEG Signals with Wavelet Packet Decomposition

EEG signals are nonstable and nonleaner random signals, while WPD provides just the right way of analyzing nonstable random signals at frequency domain and time

domain simultaneously. WPD can realize orthogonal decomposition for signals within full spectrum band, thus achieving better localization of frequency domains; it can also self-adaptively choose the corresponding frequency bands in accordance with the signal features and matches the signal features with signal frequency spectrums, thus advancing the time-frequency resolution. These advantages endow it high suitability for processing EEG signals.

25.4.2 Feature Extraction of Experimental Data

Under sober and relaxed conditions, that is, when there is no input of sensory irritation, human's motor cortex can record a type of electric signals within the range of 9–13 Hz, which is often referred to as rhythm. When the test subject is executing certain movement task (even it is merely imaginary without and actual body movement), the rhythm will undergo substantial changes, either strengthened or weakened. In BCI system, this change of rhythm can be used to recognize different imaginary body movement.

Since the key consideration here is the signals within the range of 9–13 Hz, this paper adopts Db2 wavelet function to deliver a six-layer WPD of the EEG signals acquired in the experiment and orthogonally decomposed them into 32 independent frequency bands: 0–7.8125, 7.8125–15.6250 Hz, and the like. The sinusoidal signals within the range of 9–13 Hz are put under the second frequency band. We use the decomposition coefficient and energy value at the layer as the eigenvectors and import these eigenvectors into the SVM model for classification training and recognition.

25.5 Classification and Prediction of Eigenvectors

25.5.1 Support Vector Machine (SVM) Model

SVM is a type of machine learning method based on statistical learning theories, and developed rapidly ever since was put forward for the first time by Boser, Guyon, Vapnik et al. in COLT-92. Up to now it has been successfully applied in many intelligent information acquisition and processing areas. The basic idea of SVM model is to map the input vectors to a high-dimensional eigenspace through preset nonlinear mapping (kernel function).

$$(x_i, y_i), \quad i = 1, 2, \ldots, n \tag{25.4}$$

Here x_i stands for the eigenvector; n stands for the sample size; y_i stands for the category mark number. SVM will find out an optimal classification hyperplane and import error penalty to deliver balanced optimization within this sample space, so that it can separate the two types of data points correctly to the utmost and keep

these two types of data point as far as possible from the classification hyperplane. Here SVM solves the problem, constructs classification hyperplane, and obtains the decision function through constructing a constrained optimization problem, specifically through constructing a quadratic programing with leaner inequality constraint conditions (constrained quadratic programing).

25.5.2 Classification of Experimental Data

The experimental data is split into English letter group and Chinese pinyin group, with each group including the EEG signals of 80 times of pronunciation. We import the eigenvectors obtained in the WPD of the first 40 EEG signals in each group into SVM, and take the first 20 eigenvectors of each group as training sample, and the other 20 ones as test sample. Both training set and test set are normalized into the interval [0, 1]. The entire sample space is divided into two categories: the EEG signals from the pronunciations of the English letter J falling into category 0, while that from the pronunciation of the Chinese Pinyin J falling into category 1, thus the classification of the signals from the subject's pronunciation of both the English letter and the Chinese pinyin is completed.

25.6 Experimental Results and Analysis

25.6.1 Experimental Results

As shown in Figs. 25.7 and 25.8 are the classification results of EEG signals obtained in the pronunciation of the two types of pronunciation tasks through SVM model; Fig. 25.7 is the classification results of the EEG signals obtained through

Fig. 25.7 Classification results of the EEG signals obtained through channel no. 46
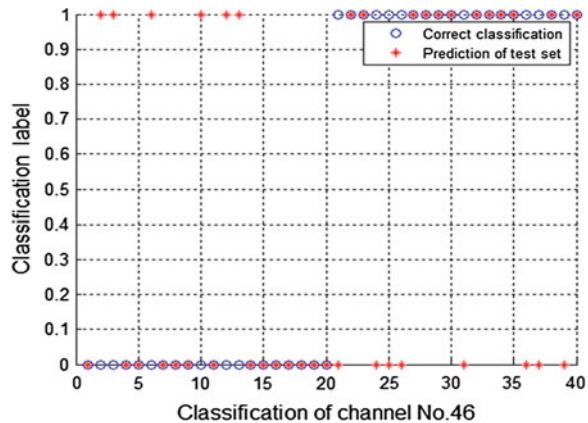
Fig. 25.8 Classification results of the EEG signals obtained through channel no. 35
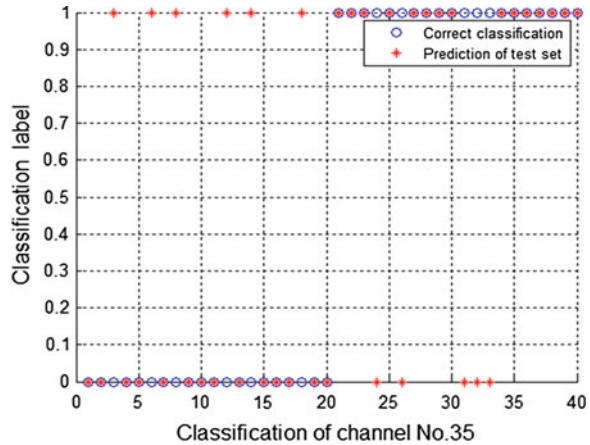
electrode No. 46, while Fig. 25.8 is the classification result of the EEG signals obtained through electrode No. 35.

As we can see from the classification result diagrams, in the classification of the EEG signals through Channel 46 the rate of SVM's recognition of the EEG signal feature test sample obtained from the subject's pronunciation of the English letter J reaches as high as 70 %, which is apparently higher than that of the Chinese pinyin J (55 %), while in the classification through Channel 35 the rate of SVM's recognition of the EEG signal feature test set sample obtained from the subject's pronunciation of the Chinese pinyin J reaches as high as 75 %, which is apparently higher than that of the English letter J (55 %). What is different from both situations with the above-mentioned two channels, where there are considerably huge differences in the classification accuracy, is that in the classification through Channel 42 SVM's average recognition rates of the EEG signal feature test set samples obtained from the two types of pronunciation tasks both reach above 65 % (Fig. 25.9).

Furthermore, in the classification and recognition of the EEG signals through the channels mentioned above, SVM classifier's recognition rate of the training set samples reaches above 75 %.

25.6.2 Results

From the experimental results as interpreted in Sect. 25.6.1 it is obvious that the data collected through channel 35 has high EEG signal recognition performance, while the experiment with channel 46 turns out to be the opposite, which we think is caused by the difference in brain processing mechanisms and the different activated brain regions in pronouncing Chinese pinyin and English letters. DIVA model holds that the passageways in gyrus frontalis inferior and veutro brain areas are activated in the process of pronouncing English letters, while domestic

Fig. 25.9 Classification results of the EEG signals obtained through channel (electrode) no. 42
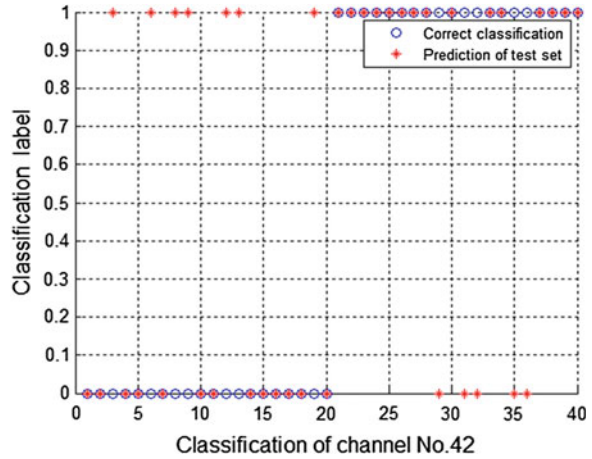
researchers find that the activated regions in pronouncing Chinese speeches include the left bottom of parietal lobe and the left precentral gyrus, and etc. The results of this experiment are roughly in line with that of previous research conclusions and confirm the DIVA model's prediction about the cerebral regions to be activated in the process of pronunciation as well as the research conclusions of existing domestic literature concerning the regions to be activated in the pronunciation of Chinese.

In addition, since channel 42 lies between channel 35 and channel 46, the EEG data acquired through channel 42 can provide significant reference for the pronunciation process of both languages; therefore, if we adopt the EEG signal features obtained through 42 in the design of brain–computer interface system for the pronunciation of both English letters and Chinese pinyin, we will surely be paid off with a brain–computer interface with higher performance.

25.7 Discussion

This paper uses WPD and SVM model to classify the EEG signal features in pronunciation of both English letters and Chinese pinyin. The accuracy of signal recognition is high enough for the classification of the EEG signals in pronunciation tasks, which provides with the implementation of Chinese speech brain–computer interface system with an effective EEG signal classification method. And besides the classification and recognition of EEG signals, this paper has also verified DIVA model's predictions concerning the cerebral activation during pronunciation tasks, and the differences in classification accuracy for the EEG signals acquired in different electrode positions also conform with the conclusions of the FMRI experiments by previous researchers [11].

References

1. Guenther FH, Brumberg JS, Nieto-Castanon A et al (2008) A brain-computer interface for real-time speech synthesis by a locked-in individual implanted with a neurotrophic electrode. In: Neuroscience meeting planner 2008
2. Sellers EW, Krusienski DJ, McFarland DJ et al (2006) A P300 event-related potential brain–computer interface (BCI): the effects of matrix size and inter stimulus interval on performance. Biol Psychol 73(3):242–252
3. Brumberg JS, Nieto-Castanon A, Kennedy PR et al (2010) Brain–computer interfaces for speech communication. Speech Commun 52(4):367–379
4. Guenther FH (1994) A neural network model of speech acquisition and motor equivalent speech production. Biol Cybern 72(1):43–53
5. Branski RC, Peck KK (2008) Neuroimaging in communication sciences and disorders. Ear Hear 29(6):971
6. Guenther FH, Brumberg JS, Wright EJ et al (2009) A wireless brain-machine interface for real-time speech synthesis. PLoS ONE 4(12):e8218
7. Shaobai Z, Han Y, Li J, Cheng X (2012) Research on improved mean shift algorithm base on local distribution in EEG signal classification. J Artif Intell Res 3(3):117–122
8. Lei X, Yang P, Yao D (2009) An empirical Bayesian framework for brain–computer interfaces. IEEE Trans Neural Syst Rehabil Eng 17(6):521–529
9. Guenther FH, Ghosh SS, Tourville JA (2006) Neural modeling and imaging of the cortical interactions underlying syllable production. Brain Lang 96(3):280–301
10. Guenther FH, Vladusich T (2012) A neural theory of speech acquisition and production. J Neurolinguistics 25(5):408–422
11. Golfinopoulos E, Tourville JA, Bohland JW et al (2011) fMRI investigation of unexpected somatosensory feedback perturbation during speech. Neuroimage 55(3):1324–1338

Chapter 26
Research on the Mechanism of Intelligent Transportation Systems on Improving Road Safety

Wenfeng Liu and Bin Li

Abstract Road safety has been a serious global problem. This paper first summarizes the impact of "human factor" on the road traffic crashes; secondly, it analyzes the importance of the "human factor" in the road traffic system through constructing a conventional road traffic system model; thirdly, through in-depth analysis of driver's information processing and "driving ability" and its limitations, it clarifies the importance of the "driving ability" on road safety; finally, according to the technical characteristics of ITS, it proposes a new road traffic system model under the effects of ITS, and then comparing with the conventional model, it makes clear that the ITS technologies will improve and protect the "driving ability", and thus effectively enhance road safety. This study will have active significance on the following in-depth studies on the potential benefits and advantages of ITS technologies on road safety in the future.

Keywords Intelligent transport technologies · ITS · Road safety · Driving ability · Mechanism · Traffic crash prevention · Accident warning

26.1 Introduction

There are around 1.2 million deaths each year, and between 20 and 50 million injuries, on the world's roads. To put these deaths into context, the numbers are similar to deaths from tuberculosis, and more than the number of deaths from malaria. Overall, road traffic deaths rank tenth as a leading cause for death. For people aged between 5 and 44, road traffic crashes are among the top three causes of death. Not only is this problem bad, it is getting worse. WHO estimates that by 2030, if nothing is done, road traffic deaths will rank fifth as a leading cause of

W. Liu (✉) · B. Li
Associate research fellow, Research Institute of Highway, MOT, No. 8,
Xitucheng Road, Haidian District, Beijing, China
e-mail: wenfeng@itsc.com.cn

death, rather than the current tenth place. In addition to the large social and human costs resulting from these deaths, there is a substantial economic cost. WHO estimated the annual global cost to be USD 518 billion, between 1 and 3 % of the gross national product. This is in excess of the total amount of development assistance provided to low- and middle-income countries [1].

Road traffic crashes statistics show that the human factor is the main cause for road traffic crashes, 80–90 % of the crashes are concerned with the driver. According to Japanese police reports, "delays in recognition" and "errors in operation and judgment" account for about 75 % of all traffic accidents in Japan, in which, "delays in recognition" account for 47 %, "errors in judgment" account for 16 %, and "errors in operation" account for 12 %. In all collision accidents, 41 % is due to the delay in recognition of the obstructions, 39 % is due to the errors in operation, 13 % is due to the errors of judgment, and 7 % is due to the defect of the ability [2].

Based on these statistical data, we find that the human factor, especially the limitations of drivers on the driving risk recognition, judgment, and decision-making have great impacts on road safety.

26.2 Mechanism of the Driver's Perception and Decision-Making During Driving

26.2.1 Conventional Road Traffic System Model

In a typical road traffic system, people, vehicles, roads, and the environment are the four main integral parts, which are always changing and interactive when the driver is driving the vehicle.

When the driver is driving the vehicle, the road is the entity object on which the vehicle is attached, and the factors of the road, such as road alignment, traffic signal signs, traffic control measures, are the constraints to the vehicle's movement. The environmental factors along the route, such as traffic flow status, weather conditions and light conditions, are the constraints to the vehicle's movement, and any vehicle's movements will have an impact on the environment in turn. The driver is the core of the whole system, who is the information processor and the decision maker in the system. They manipulate vehicle movements to complete the driving task by constantly collecting and processing information from the road, vehicle and environment, and then make judgments and decisions in accordance with their perception of the situations they face, based on their attitudes, knowledge, and experience.

A typical road traffic system and its inner relationship could be described by the model shown Fig. 26.1.
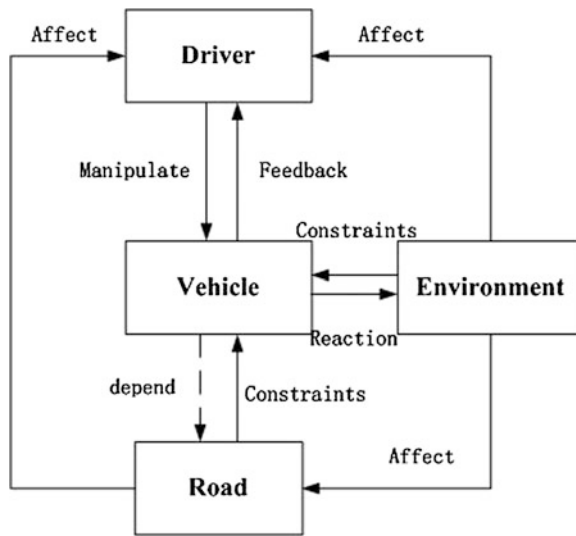
Fig. 26.1 Conventional road traffic system model

26.2.2 The Information Processing of the Driver in Driving

During driving, the driver will first try to accept all kinds of information, such as road signs and markings, traffic signals, vehicles, pedestrians, bicycles, weather and light conditions, from the external environment and inner vehicle environment through their senses (mainly by eyes or ears), then transmit all the information to the brain. Through a series of reactions, the brain will have a comprehensive understanding of the things, which is the perception. On the basis of perception, the brain forms the "depth perception", including visual distance, estimated speed, and time. Finally, the brain will send the instruction, which is based on the judgments from the depth perception, to the hands and feet to control or operate the vehicle. Overall, the process of the driver in driving the vehicle is a continuous iterative process of the perception, judgment, and decision-making, which could be abstracted as the "Perception—Judgment decisions—Operation" simplified model (Fig. 26.2).
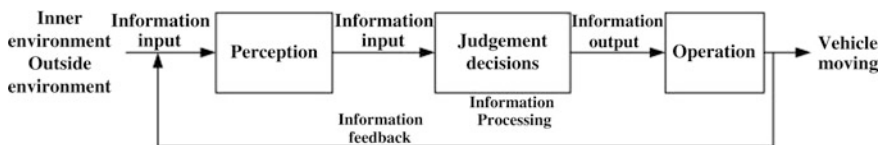
Fig. 26.2 The simplified information processing model of the driver in driving

26.3 The Limitations of Driver's Driving Ability

26.3.1 The Definition of Driving Ability

The driver's capacities of perception, attention, responsiveness, and operation during the driving process are collectively called the driving ability here. Driving ability is highly correlated with road safety. If the driver makes an error in any task of the information collection, processing, judgment, and decision-making, it is likely to cause traffic crashes. However, the driver's driving ability has limitations.

26.3.2 The Limitations of Driving Ability

In Table 26.1 can be found that people's own abilities of perception, attention, responsiveness, and dynamic judgment have limitations, which will bring difficulties and uncertainty to a driver for completion of a driving task safely and successfully; the changes in external factors, such as velocity, weather conditions, light intensity, will produce a significant reduction effect on these driver's abilities, especially in the state of high-speed movement, the driver's abilities on moving sight, field of vision, dynamic judgment, reaction time, speed and distance judgment, and attention allocation will be limited, which will have great effects on the driving safety; in addition, the driver will be stimulated and impacted by continuous multi-source information from inner- or external of the vehicle during driving, but due to the limitations on the capability of awareness and information processing, it is hard to make real-time and comprehensive feature extraction from multi-source information, and unable to accurately identify and forecast the traffic situation. The limitations of the driving ability are the main reason for "human factor" which could to be the most important factor causing traffic crashes.

26.4 The Affect of ITS on the Driving Ability

Intelligent Transportation Systems (ITS) refers to information and communication technology (applied to transport infrastructure and vehicles) that improve transport outcomes such as transport safety, transport productivity, travel reliability, informed travel choices, social equity, environmental performance, and network operation resilience [3].

When ITS technologies are added to the traditional road transport system, the conventional road traffic system model would be changed (shown as Fig. 26.3). In the new model, ITS technologies could establish close, active, and stable mutual information transmission and processing contact between the driver and the road traffic environment, so that it could provide the driver with timely, accurate,

Table 26.1 Limitations and impact factors of driving ability

Aspect	Sub-item	Impact factors	Correlation	Description or examples
Perception	Sight	Velocity	Negative correlation	The driver could see the traffic sign outside 240 m which is in front of the vehicle when the speed is in 60 km/h, while he can only see the traffic sign outside 160 m in 80 km/h
		Light intensity and contrast	Positive correlation	It is pruned to make traffic crash at night or twilight
	Vision	Velocity	Negative correlation	The driver could see the object outside 24 m which is on both side of the vehicle when the speed is in 64 km/h, while he can only see the object outside 33 m in 90 km/h
	Illusion	Special terrain and road alignment	–	In the concave road section, it is easy to judge the downhill as on a flat road, and also easy to judge that the degree of an upward slope is more great than it actually being
Attention	Distribution of attention	Complexity of the environment	Negative correlation	The driver could pay attention to 4–6 targets at the same time
Responsiveness	Reaction time	Velocity complexity of the environment	Positive correlation	It usually takes 2.5 s when the driver determines the safe stopping distance
Dynamic judgment	–	Velocity	Negative correlation	It usually takes 2 s when the driver tries to observe the environment from the rearview mirror and make judgment and actions

effective, continuous warning information support to compensate for his physical and mental limitations and the reduced driving ability due to adverse weather conditions, slippery road surface, at nights and so on, could ensure the driver to find and identify the potential risks on the route timely and effective, have sufficient time to make the correct decision and operation, then the traffic crashes could be reduced significantly which are caused by the driver's perception delay, errors of judgment and operational, and thus the level of road safety could be effectively enhanced.

From the perspective of driving risk information, ITS technologies could provide the driver with an early warning information system from roadside and inner-vehicles. In this case, the tasks of perception of the road traffic environment will be
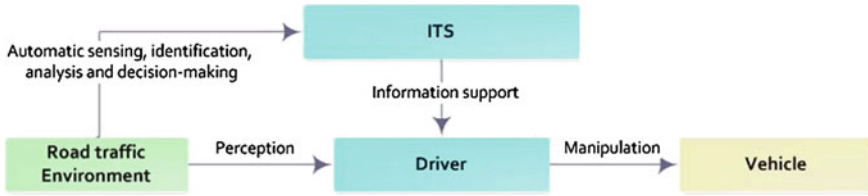
Fig. 26.3 New road traffic system model under the effects of ITS
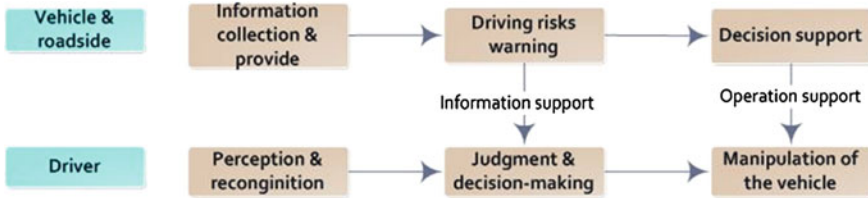
Fig. 26.4 The logical structure of the active warning information by ITS technologies to the driver

completed by the driver and ITS together, especially the task of real time perception of traffic environmental and part of the decision-making and control tasks. So the driver's work will be replaced to some extent by the ITS equipments on the road-side or inner-vehicle, the limit or lack of driver's driving ability will be made up, especially under unfavorable conditions such as adverse weather conditions, wet or slippy road surface, and at nights, etc., so that it will be ensured to complete the driving task safely. The logical structure of the active warning information by ITS technologies to the driver is shown in Fig. 26.4.

ITS technologies can build up a new road traffic environment, in which the functionality of existing road infrastructure is expanded and extended, the driver's driving ability is improved, especially, the driver's perception, judgment, and decision-making ability is effectively improved when they are facing all kinds of risks in the road traffic environment.

26.5 Conclusion

In the past few decades, the EU, US, Japan, and other highly motorized countries or regions significantly improved their road safety conditions by taking an integrated approach to "conventional" road safety measures, such as improving transport infrastructure, road user education, and law enforcement. Despite these efforts the number of road accidents and the number of road victims are still unacceptably high. Furthermore, the contributions from many of these "conventional" safety measures are reaching their limits, and further improvements in safety by these measures are becoming more and more difficult to achieve at a reasonable cost.

Currently, the EU [4–6], U.S. [7], Japan [8] and other major developed countries or regions have been increasingly concerned about the possibility and method of applying ITS technologies to improve road safety, and have set the road safety goals as the main task of each ITS development phase in their ITS development strategy. In the future, more and more attention will be focused on the research and practice of the application of ITS to improve road safety in developing countries.

This paper first summarizes the impact of "human factor" on road traffic crashes; secondly, it analyzes the importance of the "human factor" in the road traffic system through constructing a conventional road traffic system model; thirdly, through in-depth analysis of driver's information processing and "driving ability" and its limitations, it clarifies the importance of the "driving ability" on road safety; finally, according to the technical characteristics of ITS, it proposes a new road traffic system model under the effects of ITS, and then by comparing with the conventional model, it makes clear that the ITS technologies will improve and protect the "driving ability", and thus will effectively enhance road safety. This study will have active significance on the following in-depth studies on the potential benefits and advantages of ITS technologies on road safety in the future.

References

1. World Health Organization (2009) Global status report on road safety, Switzerland
2. Cabinet Office 2008 (2008)—White paper on traffic safety in Japan, Government of Japan
3. GB/T 20839-2007 (2007) Intelligent transport systems—general terminology (in Chinese)
4. COM (2003) 311 (2003) European road safety action programme, halving the number of road accident victims in the European Union by 2010: a shared responsibility
5. DIRECTIVE 2010/40/EU (2010) Directive 2010/40/EU of the European parliament and of the council of 7 July 2010 on the framework for the deployment of intelligent transport systems in the field of road transport and for interfaces with other modes of transport
6. REGULATION (EC) No 661/2009 (2009) The European parliament and of the council of 13 July 2009 concerning type-approval requirements for the general safety of motor vehicles, their trailers and systems, components and separate technical units intended there for
7. Department of Transportation (2009) ITS strategic research plan, 2010–2014, Washington
8. Highway Industry Development Organization (2011) ITS Handbook 2011 pp 9–15

Chapter 27
Study on Auto Decision-Making and Its Simulation Control for Vessel Collision Avoidance

Lina Li, Guoquan Chen and Guoding Li

Abstract A general Personifying Intelligent Decision-making for Vessel Collision Avoidance (short for PIDVCA) algorithm for simulating the ordinary practice and fine seamanship of the navigator emphatically discussed after two typical examples under the multi-ship encountering situation for marine radar simulation training are explained, and its core PIDVCA mathematical model are derived, the typical simulation examples based on the ship intelligent handling control simulation (shot for SIHCS) platform are analyzed and the predicted result is acquired.

Keywords Multi-ship encountering situation · PIDVCA mathematical model · PIDVCA algorithm · Ordinary practice of navigator · Simulation example

27.1 Introduction

For the fact that more than 90 % of collisions are caused by human factors [1], it is necessary to develop the vessel intelligent collision avoidance navigator (short for VICAN) [2] with the function of intelligent decision-making for vessel collision avoidance. To simulate for experienced seamen abiding to the International Regulations for Preventing Collisions at Sea (short for COLREGS below) and the ordinary practice of them in taking action to avoid ship collision is meaningful. To solve this problem, first, a PIDVCA method and its evaluation criteria have to be constructed to ensure the rationality and effectiveness of the anti-collision decision-making scheme. Second, various kinds of PIDVCA mathematical models have to be established as a basis for the quantitative analysis of PIDVCA method. In addition, to complete the simulation of the fine seamanship and logic thinking of experienced seamen, we also need to design a series of PIDVCA algorithms to

L. Li (✉) · G. Chen · G. Li
Institute of Navigation of Jimei University, No. 1 JiaGeng Road, Jimei District, Xiamei, China
e-mail: lln668@163.com

realize the organic integration between qualitative and quantitative analysis. In 20-year' theoretical research, the theory of PIDVCA has been formed [3–8].

In this paper, the general PIDVCA algorithm for simulating the ordinary practice and fine seamanship of excellent seamen under the multi-ship encountering situation emphatically is discussed, and the core PIDVCA mathematical model is derived from geometric analysis and the PIDVCA algorithm is verified by analysis of some simulation examples.

27.2 Enlightenment Received from the Training Example of Marine Radar Simulator

27.2.1 Description of Two Typical Examples

The decision making for collision avoidance under the multi-ship meeting situation (simply called for multi-ship anti-collision) is hard for navigators. Therefore, the multi-ship anti-collision training is the main content in the marine radar simulator. The training practice is usually set to poor visibility in the open sea and the minimum DCPA is set to 2 nm according to the COLREGS. The geometry analysis of the two typical multi-vessel meeting situation instance used in radar simulator is shown in Fig. 27.1a, b, here the Co represent the course of own ship (short for OS). They are used to checkout whether the trainees hold the suitable opportune to take action and recovery original course and the altering course (short for AC) of own ship (short for OS). The target ships (short for TS) 1, 2, and 3 are shown in the radar display screen currently and C1, C2, and C3 are the corresponding position points, respectively. The TS1 and TS2 with OS exist potential collision risk, while the TS3 has none risk with OS. If the OS is taken the collision avoidance scheme by turning
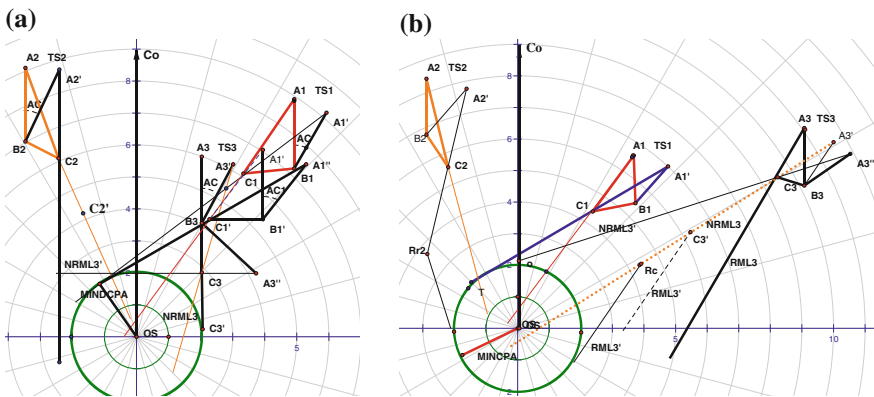
Fig. 27.1 Geometric analysis for the multi-vessel anti-collision instances

course to starboard at once which will result in that the TS3 would pass from OS within the minDCPA. Whether the collision risk would really exist between OS and TS3 after OS being taken action? If so, how the trainer plans the new anti-collision scheme based on the TS3?

27.2.2 What Action Being Taken?

For the students in the school, most of whom selected the most dangerous TS1 and take anti-collision action by the COLREGS of two vessel meeting situation and the AC of OS was determined by the ARPA's trialling function of Radar. As shown in the Fig. 27.1a, b, when the heading of OS is altered AC to starboard at B3A3′ though both of the TS1 and TS2 can be avoided at the same time, the NRML3 (relative motion line) of the TS3 would intrude into the minDCPA circle which is a potential danger to OS. So the AC of OS is increased to B3A3″ until the NRML3′ (new relative motion line) of TS3 passed out of the minDCPA circle. These kinds of the anti-collision schemes can be surely safe but not be the most reasonable and economical.

However, for the same problem to the experienced captain, on the opportunity of steer rudder (short for Tsr) under the AC of OS, whether or not in potential collision risk for the TS, they made different judgment and action from the students in school. They turned OS's heading starboard AC1 when the TS3 passed from own ship's abeam, as shown in the Fig. 27.1a, and turned AC starboard to B1A′ immediately but not AC1 to B3A″ in the Fig. 27.1b, according to the relative speed and position of the TS3 with their intuition and experience.

27.3 PIDVCA Mathematical Models

One of the key techniques is the establishment of PIDVCA mathematical models that the "personification" intelligence for machine is realized. PIDVCA mathematical models are used for quantizing some important notion that is involved in COLREGS and proposed by PIDVCA theory and the dynamic anti-collision information for obtaining real time. They are Included various anti-collision parameters (such as the TS movement factor, collision parameter and PIDVCA scheme) computing model based on analytic geometry, judgment value estimating model, the TS encountering character model, the TS encountering attribute model, and the dynamic optimizing object function. They are present by mathematical equation [5].

C_0 and V_0 in Fig. 27.2 are represented the ship's course and speed, V_t and V_r are stand for the speed and relative movement speed of TS; RML and NRML represent, respectively, the relative movement line before and after the course of OS is altered,
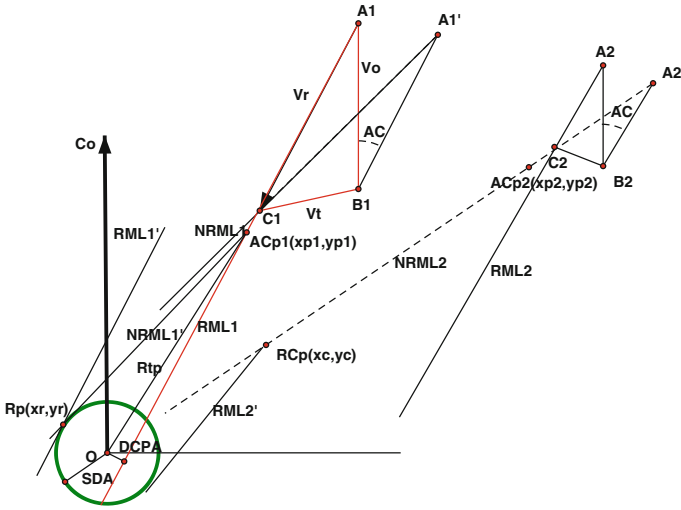
Fig. 27.2 Geometric sketch for OS being altered AC and its restoring confine point

NRML′ is the parallel lines for NRML. SDA is stand for Safe Distance of Approach, and also the threshold for the potential risk of collision judgment.

27.3.1 Quantizing Model of PIDVCA Scheme

PIDVCA scheme includes the opportunity of initial steering rudder (stand for Tisr), amplitude of altering course (stand for AC) and predicted restore point (stand for Rp) or opportunity (stand for Tr) of collision avoidance.

Tisr is calculated by the same method as the last opportunity of steering rudder (Tln) [4].

If the Tisr has been missed, AC computing model is derived from the speed vector triangle $A1' B1 C1$ as shown in Fig. 27.2:

$$AC = Crn[n] - a\sin\left(\frac{Vt[n] \times \sin(Crn[n] - Ct[n] + C_0)}{V_0}\right) \times 180/\pi - 180 \quad (27.1)$$

Tr is the predicted time of dangerous TS1 sailing from $ACp1(xp1, yp1)$ to $Rp(x_r, y_r)$, the predicted restoring point $Rp(x_r, y_r)$ is the crossover point of NRML1′ and RML1′ as shown Fig. 27.2. Obviously the computing model of Tr is as following:

$$RML1' : y[n] = x[n]\cot Cr[n] + {SDA[n]}\big/{\sin Cr[n]} \quad (27.2)$$

$$\text{NRML1}' : y[n] = x[n] \cot \text{Crn}[n] + \frac{\text{SDA}[n]}{\sin \text{Crn}[n]} \tag{27.3}$$

Solving the crossover point above RML1 and NRML1′, then Rp(x_r, y_r) is:

$$
\begin{aligned}
x_r &= \left(\frac{\text{SDA}[n]}{\sin(\text{Crn}[n])} - \frac{\text{SDA}[n]}{\sin(\text{Cr}[n])} \right) \div \left(\frac{1}{\tan(\text{Cr}[n])} - \frac{1}{\tan(\text{Crn}[n])} \right) \\
y_r &= \frac{x_r}{\tan(\text{Cr}[n])} + \frac{\text{SDA}[n]}{\sin(\text{Cr}[n])}
\end{aligned}
\tag{27.4}
$$

In formula (27.4), Cr and Crn are not included with the 0, 90°, 180° and 270°. Then, the computing model of Tr is:

$$\text{Tr}[n] = \frac{\sqrt{(\text{Xp}[n] - x_r)^2 + (textYp[n] - y_r)^2} \times 60}{\text{Vrn}[n]} \tag{27.5}$$

Here, n is the number of the most dangerous TS.

27.3.2 PIDVCA Scheme's Verifying Models Under Multi-vessel Encountering Situation

The verifying models of PIDVCA scheme are composed the computing models of predicting TS's parameters and restoring confine time (short for Tc) for new dangerous TS. As shown in Fig. 27.2, Tc is the sailing time that new dangerous TS2 from ACp2 ($xp2$, $yp2$) (altering course point) to RCp (x_c, y_c) (restoring confine point), and its computing model method is the same as the Tr. Firstly solving the crossover point of RML2′ and NRML2, and RCp (x_c, y_c) as following:

$$
\begin{aligned}
x_c &= \left(\frac{\text{CPAn}[i]}{\sin(\text{Crn}[i])} + \frac{\text{SDA}[i]}{\sin(\text{Cr}[i])} \right) \div \left(\frac{1}{\tan(\text{Cr}[i])} - \frac{1}{\tan(\text{Crn}[i])} \right) \\
y_c &= \frac{x_c}{\tan(\text{Crn}[i])} + \frac{\text{CPAn}[i]}{\sin(\text{Crn}[i])}
\end{aligned}
\tag{27.6}
$$

Then, the Tc is computed following:

$$\text{Tc}[i] = \frac{\sqrt{(\text{Xp}[i] - x_c)^2 + (\text{Yp}[i] - y_c)^2} \times 60}{\text{Vrn}[i]} \tag{27.7}$$

In formula (27.6), Cr and Crn are not included with the 0, 90°, 180°and 270°.

27.4 PIDVCA Algorithms

27.4.1 Composition of PIDVCA Algorithms

The PIDVCA algorithm is used to realize the combination of the qualitative analysis based on "COLREGS" and quantitative calculation processing of the ordinary practice and fine seamanship of seamen, in order to obtain real-time dynamic collision avoidance knowledge. In addition, it is described by flowcharts, decision trees, decision tables or mathematical equations. The algorithm is divided into two part, they are initial PIDVCA scheme generation algorithm and PIDVCA scheme verification and optimization algorithm.

The initial PIDVCA generation algorithm is constituted by TS parameter solving algorithm, TS rendezvous character identification algorithm, TS potential risk analysis algorithm, dynamic risk evaluation algorithm (for multi-vessel), the encountering attribute recognition algorithm of potentially dangerous TS and the anti-collision attribute recognition algorithm for OS with the TS, the analysis and classification algorithm for potentially dangerous TS encountering situation and PIDVCA scheme generating algorithm.

The PIDVCA verification and optimization algorithm is consisted of forecasting TS potential risk analysis algorithm, generic algorithm for simulating the ordinary practice of experienced seamen, space searching optimization algorithm, time space searching optimization algorithm, coordination anti-collision optimization algorithm, dynamic optimization of local PIDVCA scheme algorithm, PIDVCA scheme generation algorithm and decision-making algorithm in immediately dangerous situation.

27.4.2 Generic Algorithm for Simulating the Ordinary Practice of Navigator

Based on the anti-collision methods of the experienced captain and the chief mate taken in the two typical examples, the flowchart of PIDVCA generic algorithm for simulating the ordinary practice and fine seamanship of navigator is designed as shown in the virtual box of Fig. 27.3. The Trr, Tcc and L-PAE in Fig. 27.3 are separately stand for the value of max{Tr[i]}, min{Tc[i]} and level of predicted anti-collision effect.

27.5 Simulation Control Test

In order to ensure PIDVCA schemes to be reasonable, effective, and optimized, this method is embedded in the PIDVCA theoretical models [4], the intelligent code in the process knowledge as the carrier is compiled into an executable PIDVCA program files, guiding the PIDVCA formation.
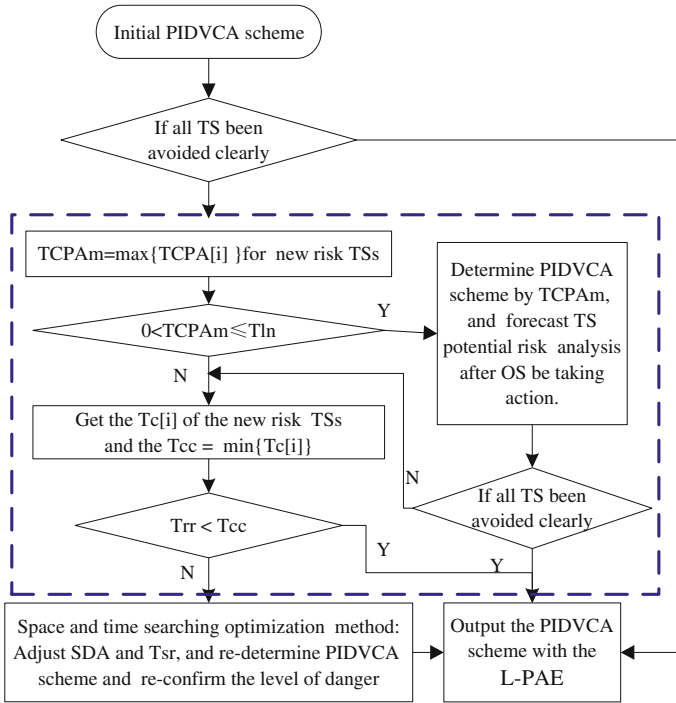
Fig. 27.3 PIDVCA generic algorithm flowchart for simulating the ordinary practice and fine seamanship of experienced seamen

27.5.1 SIHC Simulation Platform

To validate the algorithm of PIDVCA, we developed a simulation platform with the name of "the ship intelligent handling control (SIHCS) platform", which is based on the ship maneuver simulating model and electronic chart display and information system (ECDIS). The SIHCS platform is constructed by making good use of the existing technology of ship handling simulator. It is composed of one console computer and five OS servers and one TS server. The OS in the platform see each other through ECDIS. The console, OS, and TS servers are high-performance PC and linked by local network. The SIHCS possesses all functions of ship handling simulator. The software of OS server also has an interface for users. We integrate the PIDVCA algorithm together with the Self tuning fuzzy PID autopilot algorithm into the SIHCS platform in the form of dynamic link library. Thus, the SIHCS platform is used to carry out simulating test on the process monitor for vessel automatic collision avoidance.
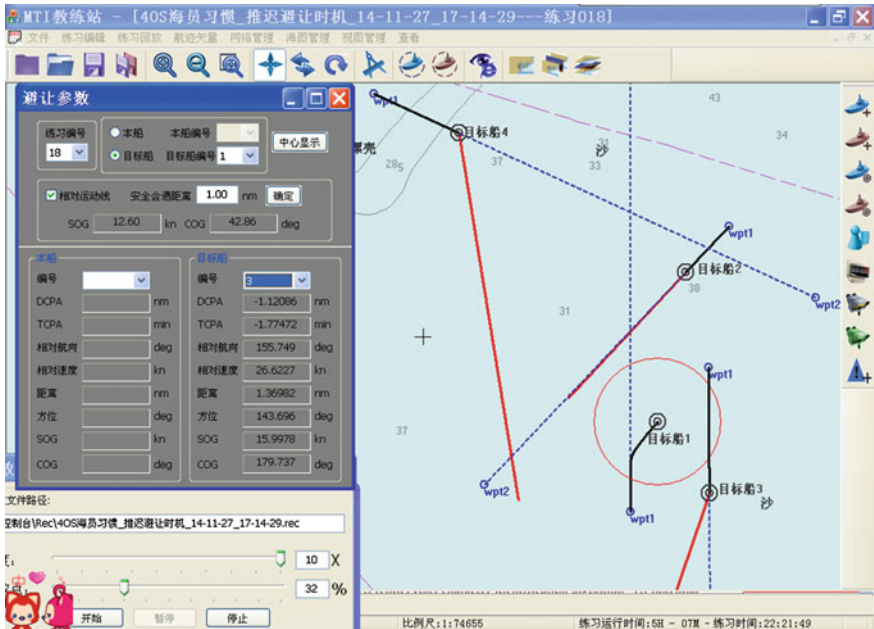
Fig. 27.4 Replay chart of the automatic anti-collision process for simulating first example

27.5.2 PIDVCA Scheme and Its Simulation Control

The simulation playback figure of the examples, which is realized the automatic generation of PIDVCA scheme and the automatic anti-collision monitoring process in the SIHC Simulation platform are shown as Figs. 27.4 and 27.5. The TS1 is loaded PIDCVA algorithm and defined as OS, but the target ships TS2, TS3, and TS4, are not loaded the algorithm. Two examples are similar to the marine simulator's ones discussed above. TS2 is the most dangerous to OS, but TS3 is safe.

By calling TS parameter solving algorithm, TS rendezvous character identification algorithm, TS potential risk analysis algorithm, the encountering attribute algorithm, and the anti-collision attribute recognition algorithm, dynamic risk evaluation algorithm, the analysis and classification of dangerous target encountering situation algorithm in turn, as well as related PIDVCA mathematical model, PIDVCA scheme of OS for first and second example are, respectively, with Tisr: 3.24 min, AC: 42°, Trr: 12.3 min and Tisr: 0, AC: 46°, Trr: 8.6 min, the related information for the TS2, TS3, and TS4 relative to OS in initial meeting situation is, respectively, shown in the Tables 27.1 and 27.2, except for DCPAn (DCPA between TS and OS after OS being altered AC). The results of simulation are
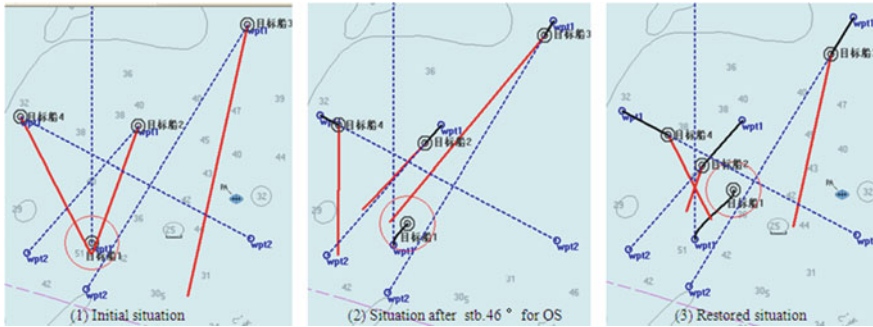
Fig. 27.5 Replay chart of the automatic anti-collision process for simulating second example

Table 27.1 Anti-collision information for OS relative to TS2, TS3, and TS4 for Fig. 27.4

	Ct (Deg.)	Vt (kn)	Cr (Deg.)	Vr (kn)	TCPA (min)	DCPA (nm)	SDA (nm)	DCPAn (nm)
TS2	223.6	8.0	196.7	19.2	14.7	−0.2	1.23	1.29
TS3	180.0	16.0	180.0	28.5	4.7	−1.23	1.59	−1.21
TS4	114.6	12.0	148.2	20.7	25.3	0.01	1.09	2.38

Table 27.2 Anti-collision information for OS relative to TS2, TS3, and TS4 for Fig. 27.5

	Ct (Deg.)	Vt (kn)	Cr (Deg.)	Vr (kn)	TCPA (min)	DCPA (nm)	SDA (nm)	DCPAn (nm)
TS2	223.3	14.0	200.1	27.0	10.11	−0.05	1.50	1.54
TS3	212.1	10.0	192.5	24.1	22.6	–3.91	1.33	0.61
TS4	116.9	12.0	152.1	23.0	13.8	0.22	1.09	2.4

presented that PIDVCA algorithms have a good simulation for the opportunity of steering rudder and restore course taken by experienced captain, also have a good judge for multi-ship meeting collision avoidance risk. In Fig. 27.5, by calling (27.6) and (27.7) to calculate the Tc of TS3, the result of Tc is 12.5 min, apparently, the Trr (8.6 min) is less than Tcc. That means the potential collision danger between OS and TS3 is disappeared naturally after OS be restored course. So the initial PID-VCA scheme (Tisr: 0, AC: 46°, Trr: 8.6 min) is effective. According to the results of calculation, the DCPA between OS and TS2 is −2.38 nm after restoring the original course of OS. Apparently, there is no collision risk between OS and TS3 actually (Table 27.3).

Table 27.3 L-PAE: level of predicted anti-collision

L-PAE	Connotation
Safety class: 0	Only changed the course by OS (Own ship) according to COLREGS or ordinary practice, satisfy with DCPA ≥SDA
Secondary safety class: 1 Close quarter situation	Only changed the course by OS according to COLREGS or ordinary practice, just satisfy with SDAmin < DCPA < SDA
Safety class: 2 (only for multi-vessels)	Only changed its original anti-collision course direction by OS, according to ordinary practice in multi-vessels, satisfy with DCPA ≥SDA
Secondary safety class: 3 Close quarter situation (only for multi-vessels)	Only changed its original anti-collision course direction by OS, according to ordinary practice in multi-vessels just satisfy with SDAmin < DCPA < SDA
Urgent class: 4 Immediate danger situation	Only changed the course by OS can't be avoided collision with DCPA < SDAmin

27.6 Conclusions

Enlightenment from two marine radar simulator training practices that reflect the ordinary practice of navigator and the fine seamanship is obtained, the PIDVCA generic algorithm that the machine to simulate and implement the anti-collision decision-making method of the experienced captains is sketched, emphatically discussed and verified by two simulation control examples. The simulating experiments for typical multi-vessel collision avoidance are shown that the PIDVCA algorithm is the rationality and validity, and the objective of research has been achieved. And a lot of simulating experiments have been done to prove the integrity of PIDVCA mathematical model in recent research. However, the PIDVCA algorithm on multi-vessel encountering is very complicated, it should be further optimized and make more simulating experiments to improve its practicality.

References

1. Liu H (2008) Reflect on collisions and their causes 4:8–10 (in Chinese)
2. Li L, Yang S, Suo Y (2008) Vessel intelligent collision avoidance navigator (VICAN). Chinese patent, No. 200720007317 (in Chinese)
3. Li L, Yang S, Suo Y, Chen G, Wang J (2008) Automation method for personifying intelligent decision-making for vessel collision avoidance. In: Proceedings of IEEE ICAL 2008 conference, vol 09, pp 876–1881
4. Li L,Yang S, Xiong Z et al (2009) Study on the theoretical framework of personifying intelligent decision-making for vessel collision avoidance. Navig China 6:30–34 (in Chinese)
5. Li Lina, Chen G, Shao Z, Xiong Z, Yang S, Sun H (2011) The construction of the PIDVCA system and its appraisal standard. J Dalian Marit Univ Sci Technol 37(4):1–7 (in Chinese)

6. Li L, Chen G, Yang S, Wei Z (2010) Mechanism for constructing the dynamic collision avoidance knowledge-base by machine learning. In: The proceeding of international conference on manufacturing automation, pp 279–285
7. Chen G, Yin Y, Li L, Yang S, Suo Y (2010) Mechanism and simulation of personifying intelligent decision- making for vessel collision avoidance. In: The proceedings of 2010 international conference on computer application and system modeling, ICCASM 2010, pp V4681–V4686
8. Chen G, Yin Y, Li L, Yang S, Suo Y (2012) The PIDVCA method in the application of intelligent navigation simulator. In: The proceedings of 17th international navigation simulator lecturers conference

Chapter 28
Dynamic Partitioning Methods for Control Sub-area Based on Fuzzy Clustering Analysis

Zhengwu Wang, Kangkang Tan and Ping Zhang

Abstract Area coordination control is an important measure to ease urban traffic. Sub-area partitioning is a basis of area coordination control and the partitioning accuracy affects the global control efficiency. Traditional sub-area partitioning is based on qualitative principles related to period, flow, distance, and so on, without establishing a system of sub-area partitioning indexes and without considering quantitative partitioning methods and so the sub-area partitioning is subjective and optional. In this paper, a system of sub-area partitioning indexes is established considering indexes such as distance, period, continuity of traffic flow and dispersion. The sub-area is divided by two stages: one is to preliminarily select intersection of sub-area excluding those of big period difference and long distance; the other is to describe intersections' traffic state and physical relationship and to cluster intersections based on fuzzy clustering analysis. Compared to traditional partitioning method of sub-area, the method presented in the paper can bring less system delay that proves the method is effective.

Keywords Traffic engineering · Control sub-area · Dynamic partitioning · Means clustering analysis

28.1 Introduction

The control sub-area [1] is a secondary control area, according to traffic characteristic of different areas, divided from a control range of a road network with a large area. Each sub-area has different control strategies and control plans. These independent secondary areas are sub-areas. The sub-area partitioning may enable traffic control to extend from points to area and so the traffic flow may be organized and optimized in a greater scope to elevate working efficiency of each intersection.

Z. Wang (✉) · K. Tan
Changsha University of Science and Technology, Changsha, Hunan Province, China

P. Zhang
Hunan Province, Zhuzhou, China

Many researches have been done by scholars on partitioning of control sub-area. The partitioning methods may fall in two categories: static partitioning method and dynamic partitioning method. A static partitioning method is to divide sub-areas according to signal periods, intervals of intersections and traffic flow, etc. The partitioned sub-area is fixed within a control period. A dynamic method is on the basis of the static partitioning method considering real changes of traffic flow. It makes the sub-area partitioning may be in response to changes of traffic flow and sub-area boundaries can be determined in real time.

Many scholars have studied the dynamic partitioning methods of sub-areas. Yagoda et al. [2] divided sub-areas in accordance with relational indexes of adjacent intersections, for which a relational model is established with distance, period, and traffic flow as parameters. Li [3] presented a dynamic distributive concept of urban network and embedded it in the sub-area partitioning for dynamic traffic assignment. Jianzhang [4] added indexes of road network topology to the sub-area partitioning algorithm. Shang Deshen [5], introduced traffic network reliability to evaluate and screen preliminarily selected sub-areas until the sub-areas are finally determined. Li [6], proposed a fuzzy dynamic partitioning method of traffic control sub-areas based on fuzzy inference. Wong [7] built a partitioning process of dynamic sub-areas in line with TRANSYT in view of a nonlinear relation between signal periods and regional delay. Yagoda [8] studied the index system, threshold values, and algorithms of dynamic sub-areas.

So far the following methods are used for dynamic sub-area partitioning: an index system and partitioning principles are established and then the sub-areas are divided according to real-time information based on partitioning principles. These partitioning methods are mainly qualitative and the partitioning basis is the physical characteristic of road network, rarely considering the characteristic of traffic flow. Therefore, in this paper both the physical characteristics and traffic characteristics of road network are considered and an index system of sub-area partitioning is built. To make the sub-area partitioning quantitative, a sub-area partitioning method based on Fuzzy C-Means (FCM) is established in the paper in making the sub-area partitioning more operable.

28.2 Partitioning of Control Sub-areas Based on Fuzzy Clustering

28.2.1 Selection of Partitioning Indexes of Control Sub-areas

Partitioning indexes of sub-area mainly include the following:

(1) Distance

All intersections are adjacent within a control sub-area and the distance should be in a certain range. If the distance extends the range, traffic flow that leaves from the upstream intersections may disperse gradually as the running distance increases

and it will be in a random situation when reaching downstream intersections, which affects the coordination control. Generally, the range of coordination control of intersections L is less than 600 m.

(2) Period

The signal period comprehensively reflects the characteristics of traffic flow characteristics. Close signal periods may, to certain extent, indicate similar traffic flow characteristics of adjacent intersections. Therefore the signal period is an important index of sub-area partitioning. Generally speaking, within the same sub-area, periods of different intersections should be in the range of (0.75C, 1.5C) where C is the intermediate period.

(3) Continuity of traffic flow

Intersections based on period and distance principles may not be similar on their traffic flow characteristics. Therefore, it is insufficient to divide sub-areas only considering the period index, but the indexes should be determined additionally in two respects—continuity and dispersion of traffic flow. Continuity mainly consists of two indexes: saturation of intersection and spreading range of congestion space of road sections.

(4) Dispersion of traffic flow

If vehicles arrive uniformly within the whole period, same number of stopping cars and same delays will be generated within the red light time, regardless of the locations of the red light time occurs. Conversely, pulsed vehicle flow may increase efficiency of coordination control. Hence the dispersion of vehicle flow should be taken into account in partitioning sub-areas.

28.2.2 Process of Dynamic Partitioning of Control Sub-areas

The process of dynamic partitioning of control sub-areas determined in the paper is as shown in Fig. 28.1. Sub-areas are divided by two stages: as for first stage, intersections with large distances and periods not in an appropriate range are excluded from the sub-area; after partitioning of second stage, more similar intersections are clustered in the same sub-area.

28.2.3 Computation of Partitioning Indexes of Sub-areas

Control sub-area partitioning of second stage is performed based on clustering analysis. Relevant indexes are first calculated for each intersection and intersections are clustered in line with fuzzy clustering analysis. The indexes adopted include those related to distance, period, traffic flow dispersion, and continuity.
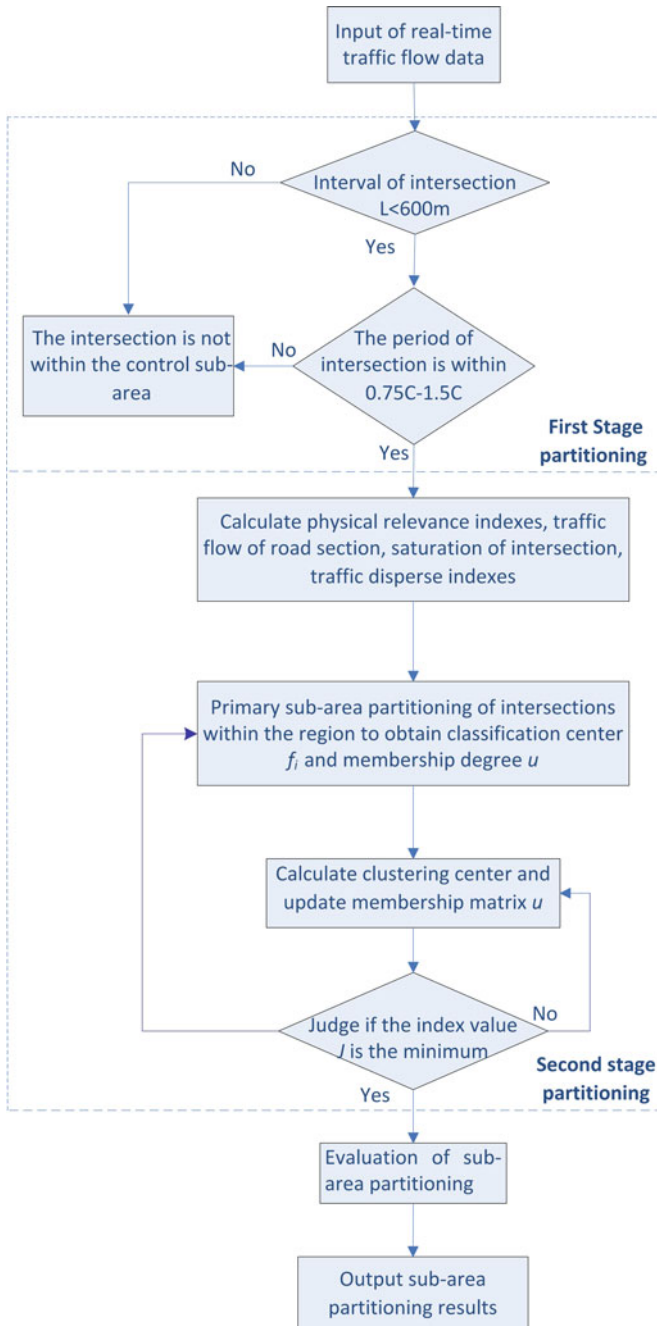
Fig. 28.1 Process of control sub-area partitioning

Computation models are mainly as follows:

(1) Physical correlation characteristics of intersection

Physical correlation characteristics indicate the correlation between links and nodes, commonly by notation of adjacency matrixes or weight matrixes. Assume p is the number of nodes, L_{ij} is the distance between intersection i and j, w_{ij} is the link weight of intersection i and j; and the weight matrix W is expressed as below:

$$W = \left(W_{ij}\right)_{p \times p} \tag{28.1}$$

where $W_{ij} = \begin{cases} L_{ij} & \text{if existing link between intersection } i \text{ and } j \\ 0 & \text{else} \end{cases}$

(2) Saturation of intersection

The saturation y_i of intersection i is calculated according to Eq. (28.2).

$$y_i(t) = \sum_{j-1}^{k} \frac{q_{ij}(t)}{N_{ij}(t)} \tag{28.2}$$

where $q_{ij}(t)$, and $N_{ij}(t)$, respectively, represent the flow rate, capacity of entrance j of intersection i in t time period, and k is the number of entrances of intersection k.

(3) Spreading range of congestion space in single road section

It mainly reflects gathering and dissipation of queuing vehicles and may be represented with the queuing length of vehicles in the road section. See the computation model as below [9]:

$$L_a(t) = \begin{cases} L_a(t-1) + A_a(t) - D_a(t) & \text{if } L_a(t-1) + A_a(t) > D_a(t) \\ 0 & \text{else} \end{cases} \tag{28.3}$$

where $L_a(t), A_a(t), D_a(t)$ are, respectively, the queuing length, accumulated arrivals, and leaving vehicles of section a in t time period, and the difference is the number of vehicles left behind the stop line.

(4) Traffic dispersion

Traffic dispersion is a significant index describing traffic situation. A pulse index $PF_i(t)$ of traffic flow is selected in this paper to measure the traffic disperse.

$$PF_i(t) = \frac{Q_{i,30\%}(t) + Q_{i,70\%}(t)}{2 \times AQ_i(t)} \tag{28.4}$$

where $Q_{i,30\%}(t), Q_{i,70\%}$, respectively, represent 30 % and 70 % of maximum arrivals of intersection i within the signal period of time period t. $AQ_i(t)$ represents the arriving vehicles of intersection i within the signal period of time period t.

28.2.4 Fuzzy Clustering of Intersection

In the second stage, the clustering scheme of intersection is determined according to physical indexes and traffic situation. The range of control sub-area is determined based on Fuzzy C-Means because it has the following characteristics: (1) fuzzy clustering analysis is a process to divide elements into classes based on their similarity to satisfy the partitioning requirement of control sub-areas. (2) many kinds of factors can be taken into consideration and it is free from restriction of classes and number of parameters; (3) compared to correlation method, FCM algorithm optimizes the whole system instead of only comparison between two objectives.

FCM algorithm is first proposed by Dunn and developed by Bezdek [10]. Classes are divided in sub-area partitioning of fuzzy clustering analysis based on the similarity of $X = (X_1, X_2, \ldots, X_p)_{p \times m}$. Assume m indexes in x_k of intersection X_k is $x_k = (x_{1k}, x_{2k}, \ldots, x_{mk})$ and $k = 1, 2, \ldots p$. g classes are contained in the intersection set and the center of classes is $f = (f_1, f_2, \ldots, f_g)$. The index of center of classes may be represented by $f_i = (f_{1i}, f_{2i}, \ldots, f_{mi})$ where $i = 1, 2, \ldots, g$ and then the steps of sub-area partitioning of fuzzy clustering analysis can be described as follows:

Step 1: Calculating indexes.
Step 2: Initializing partitioning: preliminarily divide all intersections into g sub-areas and let the indexes of key intersections be the initial clustering center f_i^0. Determine each intersection's weight of the sub-area, i.e., initial membership matrix u, $u = (u_{ik})_{g \times p}, u_{ik} \in [0, 1]$, and $\sum_{i-1}^{g} u_{ik} = 1$.
Step 3: Iteration: Continually update and optimize the clustering center and membership matrix to obtain the best scheme.
         Step 3.1: Update membership degree according to the following rules.

$$\text{If } \| x_k - f_i^l \| > 0, \quad \text{then} \quad u_{ik}^{l+1} = \frac{1}{\sum_{j=1}^{g} \left(\frac{\|x_k - f_i^l\|}{\|x_k - f_j^l\|} \right)^{\frac{2}{\alpha - 1}}} \qquad (28.5)$$

$$\text{If } \| x_k - f_i^l \| = 0, \quad \text{then} \quad u_{ik}^{l+1} = 1$$

where u_{ik} represents the weight of intersection k being a member of the control sub-area; $\alpha \geq 1$ (2.0 taken in this paper); l is number of iteration steps.
         Step 3.2: Update clustering center: calculate the clustering center according to the Eq. (28.6).

$$f_i^l = \frac{\sum_{k=1}^{p} \left(u_{ik}^l \right)^{\alpha} x_k}{\sum_{k=1}^{p} \left(u_{ik}^l \right)^{\alpha}} \qquad (28.6)$$

Step 4: Judge convergence: if the membership matrix u^l satisfies requirement of convergence, stop circulating.

Step 5: Divide sub-areas: after the above four steps, two series, the clustering center and membership degree, can be obtained, $U = \left(u^1, u^2, \ldots, u^l\right)$ and $F = \left(f^1, f^2, \ldots, f^l\right)$. The minimum (u^*, f^*) of index value $J(u, f)$ is obtained from these two series and the index value $J(u, f)$ is defined as below:

$$J(u,f) = \sum_{k=1}^{m} \sum_{i=1}^{g} (u_{ik})^{\alpha} \| x_k - f_i \|^2 \tag{28.7}$$

According to (u^*, f^*), control sub-area partitioning can be obtained. $J(u,f)$ is the weighted sum of square of distances from sample x_k to each clustering center f_i with the weight being $(u_{ik})^{\alpha}$ where u_{ik} is the membership degree of the intersection X_k as a member of class i. Square error clustering criteria is actually used for $J(u,f)$. Therefore, the best fuzzy partition should be the stable point of minimum variance of $J(u,f)$ and the stable point is the corresponding point of $\min\{J(u,f)\}$.

Step 6: delay analysis.

28.3 Example Analysis

An application research is done based on the network as shown in Fig. 28.2 where Numbers are intervals of intersections. The network includes two perpendicular trunk roads KH and AC and 7 branch roads. Tables 28.1 and 28.2 are traffic data of road network in time period of t_1 and t_2.

Fig. 28.2 Road network
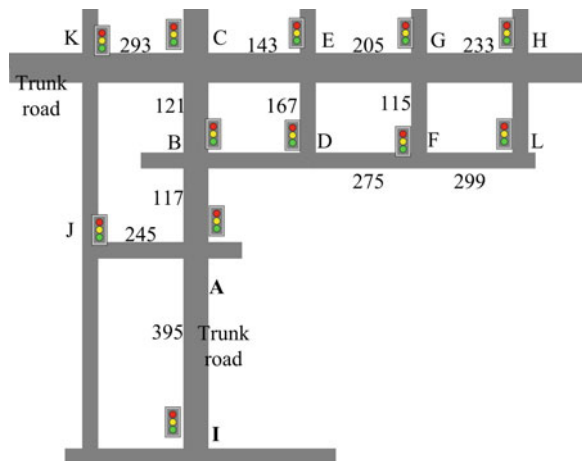
Table 28.1 Traffic data in time period t_1 of regional road network

Intersection	Period C (s)	Green light time (s)	Traffic flow of green time (pcu/h)	Arriving rate (pcu/h)	Leaving rate (pcu/h)	Number of vehicles in a period (pcu)
A	120	66	730	793	747	25
B	94	52	684	733	700	18
C	132	70	966	1056	977	36
D	90	50	422	471	432	11
E	98	56	837	897	850	24
F	84	40	345	379	367	9
G	95	50	776	813	790	21
H	68	40	709	763	724	14
I	88	48	669	699	680	17
J	66	38	552	580	561	10
K	63	36	523	559	538	10

Table 28.2 Traffic data in time period t_1 of regional road network

Intersection	Period C (s)	Green light time (s)	Traffic flow of green time (pcu/h)	Arriving rate (pcu/h)	Leaving rate (pcu/h)	Number of vehicles in a period (pcu)
A	114	71	718	713	677	28
B	101	49	644	773	670	13
C	142	73	908	1356	897	35
D	79	49	382	401	453	18
E	84	57	767	808	861	25
F	79	40	385	317	372	9
G	106	57	737	837	700	25
H	61	34	714	768	727	16
I	95	43	637	649	661	15
J	71	41	507	556	571	12
K	58	40	492	534	598	7

Sub-areas are partitioned by two methods. One is based on FCM, the other is the traditional qualitative method based on period, distance, and traffic flow. The results are obtained shown by Table 28.3.

Signal coordination control is realized in the same sub-area with same signal period and phase difference to obtain the delay of each intersection. The total delay of vehicles based on FCM algorithm is 1855.69 s while it is 2721.7 s based on the traditional method. So the method based on FCM algorithm is effective.

Table 28.3 Results of control sub-area partitioning

No. of sub-area	Qualitative analysis	Clustering analysis	
	Intersections	Intersections	
		t_1	t_2
1	K, J	K, C	K, C, E
2	C, E, G	E, G, H, F	G, H
3		B, J, A	J, A
4	D, F		D, F
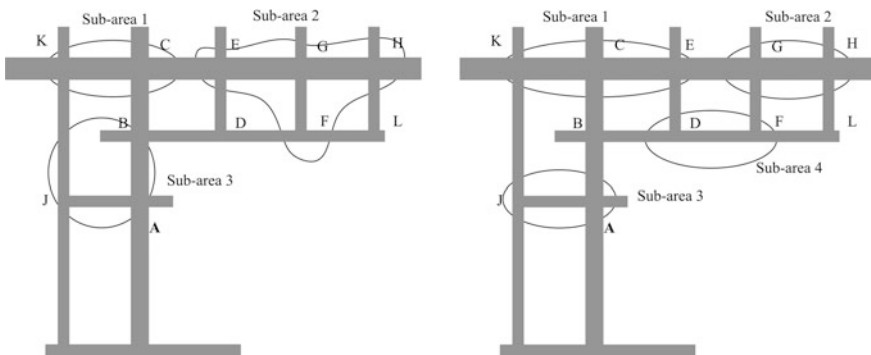
Fig. 28.3 Sub-areas in time period t_1 and t_2

28.4 Conclusions

Sub-area partitioning is the foundation of regional traffic control. The sub-area partitioning method based on Fuzzy C-Means is proposed in the paper. The experiment results show this method is effective (Fig. 28.3).

References

1. Mo H, Peng G, Yun M (2002) Automatic partitioning of traffic control sub-areas under guidance. J Traffic Transp Eng 2(2): 67–72 (in Chinese)
2. Yagoda N et al (1973) Subdivision of signal systems into control areas. Traffic Eng 43(12):42–45
3. Li R, Gong X (2006) Traffic network time-space division of dynamic traffic assignment. J Grad Sch Chin Acad Sci 4(23):520–525 (in Chinese)
4. Zhangjian Z, Wei H (2008) Design and implementation of traffic zone division oriented to coordinated traffic signal control. China Acad J Electron Publ House 211–215 (in Chinese)

5. Shang D, Shi J (2007) The transportation controlled area dynamic division research. Road Traffic Saf 7(1):27–29 (in Chinese)
6. Li R, Huapu L (2008) research on traffic signal control sub-area fuzzy automatic division method. J Wuhan Univ Technol 32(3):381–384 (in Chinese)
7. Wong SC (2002) Group-based optimization of a time-dependent TRANSYT traffic model for area traffic control. Trans Res Part B Methodol 36(4):291–312
8. Yagoda C (1985) How to decide the interconnection of isolated traffic signals. In: Proceedings of the 17th conference on winter simulation, 1985, pp 445–453
9. Liu J (2007) The research on the diffusion of recurrent congestion on urban road and forecasting method. Master Dissertation of Jilin University, 2007, vol 9 (in Chinese)
10. Bezdek JC (1981) Pattern recognition with fuzzy objective function algorithms. Plenum Press, New York

Chapter 29
Research on Water Quality Monitoring Section Optimization Based on Multi-agent Model

Sen Peng, Xiaofeng Lian, Xiaoyi Wang and Jiping Xu

Abstract In order to conduct reasonable and effective water quality (WQ) section monitoring of lakes, water reservoirs, and rivers this paper presents a multiagent model to optimize the WQ monitoring sections. First, the paper establishes a normalized matrix based on the original WQ monitoring data and from the data extracted principal/nonprincipal components as effective WQ features. Then, multi-WQ-agents model is built including comprehensive evaluation scores (CES) of principal/nonprincipal components in each WQ-agent and interaction rules of WQ-agents on the basis of the multiagent theory, in which the adjacent WQ-agents can be merged or split according to the similarity of CES. Therefore, the research realizes merge in the coarse segmentation of all WQ-agents, called as $Agent^{\#}$. On the condition that the number of $Agent^{\#}$s is smaller than the predefined threshold, the $Agent^{\#}$s would be spilt further in the fine segmentation, called as $Agent*s$. Finally, the central points of $Agent*$ are selected as the measuring samples of WQ monitoring sections. The result shows that multiagent model can improve the monitoring quality, cut cost, and provides a creative measure of WQ monitoring section optimization.

Keywords Water quality monitoring · Section optimization · Multi-WQ-Agent model · Coarse/fine segmentation

29.1 Introduction

Water is essential for living creatures which is necessary for living and production [1]. WQ monitoring is of great significance in prevention and control of pollution in water bodies [2]. It is a complicated system engineering to assess variations of water quality [3] by monitoring and measuring water pollutant type, concentration,

S. Peng · X. Lian (✉) · X. Wang · J. Xu
School of Computer and Information Engineering, Beijing Technology and Business University, Beijing 10048, China
e-mail: lianxf@th.btbu.edu.cn

and trends. The choice of WQ monitoring sections is generally considered of monitoring purpose and section type. Traditional lake monitoring sections were distributed in average size, and the center of each grid is taken as the measuring point. It is simple, but the traditional monitoring sections always have the same or similar results to the adjacent waste monitoring resources. Therefore, optimization is necessary. The purpose of section optimization is getting the best overall function with minimum cost and maximum efficiency [4, 5]. This method is based on multiagent can reduce the redundant construction and reflect the overall water conditions objectively.

This paper proposes multi-WQ-agents optimization model based on the interaction of the WQ-agents simulating the process of WQ monitoring section optimization. Intelligent WQ-agents can perceive the environment through sensors, act on the environment through effectors, and communicate with other agents. Agent model simulation can better grasp the relationship and interactive collaboration among agents [6]. In this paper, the method according to multiagent constructs a multi-WQ-agent model with two elements calculated by PCA, then determines similar degree of adjacent WQ-agents through collaboration and communication, and finally realizes the optimization of WQ monitoring sections by WQ-agents' merger and split in coarse and fine segmentation separately.

29.2 WQ-Agent Model Based on PCA

PCA is a statistical analysis method mapping to low-dimensional space from high-dimensional data, and the integrated indicators of principal components are independent. PCA can not only simplify the evaluation system, but also reduce the overlapping and redundancy of information. This analysis has certain superiority in comparability, quantitative, and qualitative analysis of integration degree, and the selection of index weight. PCA is used to analyze various factors and the CES of the principal/nonprimary components is taken as element of multi-WQ-agent simulation model.

29.2.1 The Basic Principle of PCA

Let $x_1, x_2, \ldots, x_n$ are initial variables. Some principal variables $z_1, z_2, \ldots, z_p (p < n)$ can be selected by the PCA method, in which the ith component is expressed as $z_i = l_{i1}x_1 + l_{i2}x_2 + \cdots + l_{in}x_n$, and l is the weight of initial variables. z_i and $z_j (i \neq j, i, j \in [1, m])$ are independent, where z_1 is the component with largest variance of all the linear combinations with respect to $x_1, x_2, \ldots, x_n$; z_2 is the component with largest variance of all the linear combinations with respect to $x_1, x_2, \ldots, x_n$ irrelevant with z_1; similarly, z_p is the component with largest variance of all the linear combinations with respect to $x_1, x_2, \ldots, x_n$ irrelevant with $z_1, z_2, \ldots, z_{p-1}$ [7].

The overall procedure of PCA calculation is described as follows [8]:

1. Construct the original variable matrix **X**.

$$\mathbf{X} = \begin{bmatrix} x_{11} & x_{12} & \cdots & x_{1n} \\ x_{21} & x_{22} & \cdots & x_{2n} \\ \vdots & \vdots & \vdots & \vdots \\ x_{m1} & x_{m2} & \cdots & x_{mn} \end{bmatrix} \tag{29.1}$$

2. To eliminate the impact of the original data's dimension and order of magnitude, use the Z-score transformation to standardize matrix **X**:

$$x'_{ij} = \frac{x_{ij} - \bar{x}_j}{S_j} \tag{29.2}$$

where

x_{ij} an element of matrix **X**

$\bar{x}_j = \frac{1}{m}\sum_{i=1}^{m} x_{ij}$ mean of all the elements

$S_j = \sqrt{\frac{1}{m-1}\sum_{i=1}^{m} (x_{ij} - \bar{x}_j)^2}$ variance of all the elements

3. Calculate correlation matrix R of the normalized data, then calculate matrix R's eigen value $\lambda_i (i = 1, 2, \ldots, n)$ and corresponding eigenvectors $l_i = (l_{i1}, l_{i2}, \ldots, l_{in})$, Where λ_i is variance of component z_i.

4. Calculate the contribution rate $e_i = \lambda_i / \sum_{i=1}^{n} \lambda_i$, and determine the number of principal components according to the cumulative variance contribution rate $\alpha = \sum_{i=1}^{p} e_i$ ($\alpha \geq 85$ %, normally), where p is the number of principal component.

5. Determine the expression of principal component $z_i (i = 1, \ldots, p)$.

6. Determine the comprehensive CES of principal/nonprincipal components

$$\begin{cases} Z = \sum_{k=1}^{p} e_k z_k \\ \bar{Z} = \sum_{k=p+1}^{n} e_k z_k \end{cases} \tag{29.3}$$

$$\begin{cases} e_k = \frac{\lambda_k}{\lambda_1 + \lambda_2 + \cdots + \lambda_p}, & \text{if} \quad k \leq p \\ e_k = \frac{\lambda_k}{\lambda_{p+1} + \lambda_{p+2} + \cdots + \lambda_n}, & \text{otherwise} \quad k > p \end{cases} \tag{29.4}$$

If $k \leq p$, e_k indicates weight of principal component, i.e. variance contribution rate of principal component; Otherwise, it indicates weight of nonprincipal component weight.
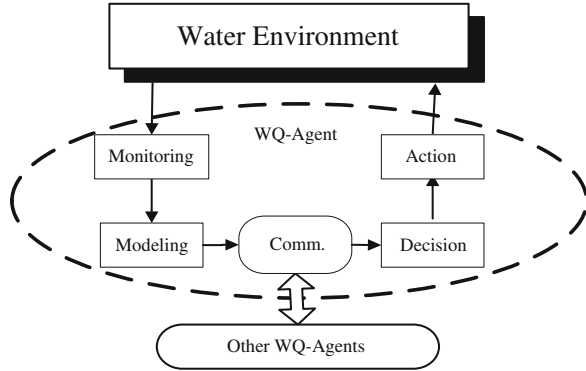
29.2.2 WQ-Agent Model

In general, the basic structure of the agent can be classified into three types: Deliberative agent, reactive agent, and hybrid agent [9, 10]. A WQ-agent presented in this paper, as a hybrid agent, is able to make decision and response intelligently based on the water environment. Figure 29.1 shows the model of the WQ-agent.

WQ-agent can perceive WQ parameters measured by special sensors, act on the environment through deflectors, and communicate with other WQ-agents. Moreover, each WQ-agent with its own knowledge, objectives, and competencies can calculate the CES of principal and nonprincipal component by PCA method mentioned above as two elements of WQ-agent model, i.e., Z and $\overline{Z}$. WQ-agent simulation system constructed in this paper is a system composed of multiple WQ-agents which can interact with each other.

29.3 Multi-WQ-Agent Partition Criteria and Optimization

29.3.1 Multi-WQ-Agents Model

WQ-agent Simulation System (ASS) is defined as a quadruple [11, 12]:

$$\text{ASS} = \left\langle \text{Agents, } EP, R_p, R_c \right\rangle \tag{29.5}$$

where

- Agents = {Agent1, Agent2, ..., Agent$N$}, means a set of WQ-agent for water monitoring section, in which the number of agents is N.
- EP = {pH, EC, TD, DO, AN...}, means WQ monitoring parameters, including *PH*, electrical conductivity, turbidity degree, dissolved oxygen, ammonia nitrogen, etc.
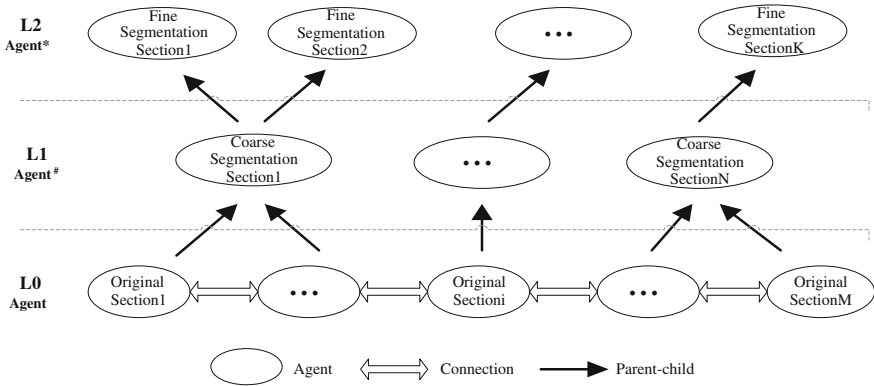
Fig. 29.2 Multi-WQ-agent organizational structure

- $R_c = \{\langle \text{Agent}i, \text{Agent}j \rangle | \text{Agent}i \in \text{Agents} \land \text{Agent}j \in \text{Agents} \land S(\text{Agent}i, \text{Agent}j)$ $i, j \in N\}$, is a connection relationship set, in which $S(x, y)$ is true if there has a connection relationship between x and y, otherwise, false.
- $R_p = \{\langle \text{Agent}i, \text{Agent}j \rangle | \text{Agent}i \in \text{Agents} \land \text{Agent}j \in \text{Agents} \land P(\text{Agent}i, \text{Agent}j)$ $i, j \in N\}$, is a parent-child relationship set, in which $P(x, y)$ is true if there has a parent-child relationship between x and y, otherwise, false.

As shown in Fig. 29.2, basic structure of multi-WQ-agent model is a three-layer hierarchical structure consisting of original agent, coarse segmentation agent, and fine segmentation agent, record as *Agent*, *Agent#*, and *Agent**, respectively, in which $N < K < M$. There are two elements in an original agent, i.e., Z and $\bar{Z}$; connection means *Agents* belong to the relationship set R_c in $L0$; parent−child means the agents belong to the set R_p exist the subordinate relationship.

29.3.2 Layer L0–L1: Coarse Segmentation Model

Layer $L0$–$L1$ is the primary phase for the section optimization. In $L0$, Z is taken as the evaluation parameter. If there is high similarity between two adjacent agents, they would be merged together. Thereby, according to the coarse segmentation method, *Agent#* (the number is N) can be obtained from all of *Agents* (the number is M) as follows:

$L0$: Set an array $\mathbf{Z} = [Z_1, Z_2, \ldots, Z_i, \ldots, Z_M]$, in which each element is the CES of principle component of each *Agent*. In addition, the evaluation threshold for similarity is set as ε.

```
Initialize coarse segmentation sections' number N = 1
for i=1 to M
 initialize a=0;
 for j=i to M
 if |z_i − z_j| ≤ ε  & <Agenti and Agentj are adjacent> then
S(Agenti,Agentj) =1 ;
        else  S(Agenti,Agentj) =0  and set a=1;
 end for j
 Agenti ∈ Agent#N
if a=1 then N=N+1;
 end for i
```

Finally, we can get the number of $Agent^{\#}$ in $L1$.

29.3.3 Layer L1–L2: Fine Segmentation Model

After the procedure of coarse segmentation, if the number of $Agent^{\#}$ N is less than the predefined number, the fine segmentation should be implemented in the process of layer $L1$ to $L2$. Now, $\bar{Z}$ is taken as the evaluation parameter from $Agent$ in $L0$, the detail as follows:

$L1$: Set an array $\bar{\mathbf{Z}} = [\bar{Z}_1, \bar{Z}_2, \ldots, \bar{Z}_i, \ldots, \bar{Z}_M]$, in which each element is the CES of nonprinciple component of each $Agent$. In addition, the evaluation threshold for similarity is set as ξ.

```
Initialize fine segmentation sections' number K = 1
for i=1 to M
 initialize b=0;
 for j=i to M
 if |Z_i − Z_j| > ξ then  S(Agenti,Agentj) =0 ;
 if S(Agenti,Agentj) =0 then b=1;
 end for j
 Agenti ∈ Agent*K
if b=1 then K=K+1;
 end for i
```

Thus we can get the number K of $Agent^{*}$ in $L2$, which satisfies the constraint of the predefined threshold. Next, by calculating the arithmetic mean, the location of each monitoring section can be determined, that is, the final optimized WQ monitoring section is the center of each monitoring region.

29.4 Experimental Results and Analysis

As an example, Beihai Lake in Beijing is chosen to illustrate the procedure of monitoring section optimization. First, according to the size, we divide the Beihai Lake into nine grids averagely, and the center of each grid is set as the sample point of monitoring section; nine water quality parameters including PH, electrical conductivity, turbidity degree, dissolved oxygen, ammonia nitrogen, transparency, total nitrogen, total phosphorus, and chlorophyll are collected separately by water surveillance ship. Then, using SPSS software, the principal/nonprincipal components can be calculated from the above WQ parameters which are analyzed by PCA method. The variance contribution rate of principal/nonprincipal components can be obtained in Table 29.1.

As shown in Table 29.1, comprehensive variance contribution rate of the first four principal components reaches 87.16 %, means that 87.16 % information of original variables is offered and the rest is offered by the nonprincipal components. The weight of WQ parameters in each component is shown in Table 29.2, through which the value of components z can be calculated.

Therefore, CES can be calculated by Eq. 29.6, and the results are shown in Table 29.3.

$$\begin{cases} Z = e_1 z_1 + e_2 z_2 + e_3 z_3 + e_4 z_4 \\ \bar{Z} = e_5 z_5 + e_6 z_6 + e_7 z_7 + e_8 z_8 \end{cases} \qquad (29.6)$$

According to the value Z in coarse segmentation, Beihai Lake is divided into four $Agent^{\#}s$ from nine $Agents$. For the predefined threshold five is larger than four, then it is divided into five $Agent*s$ according to the value $\bar{Z}$ in fine segmentation following.

Table 29.1 PCA analysis of the total variance of WQ parameters

Component index	Initial eigenvalues			Extraction loaded sum of squares		
	Total	Variance percentage	Cumulative	Total	Percentage of variance	Cumulative
1	2.716	30.174	30.174	2.716	30.174	30.174
2	2.373	26.371	56.545	2.373	26.371	56.545
3	1.826	20.293	76.838	1.826	20.293	76.838
4	0.929	10.324	87.162	0.929	10.324	87.162
5	0.582	6.465	93.626	0.582	6.465	93.626
6	0.469	5.212	98.838	0.469	5.212	98.838
7	0.070	0.777	99.616	0.070	0.777	99.616
8	0.035	0.384	100.000	0.035	0.384	100.000
9	6.073E-17	6.748E-16	100.000			

Table 29.2 Principal component matrix

WQ Para	Components							
	1	2	3	4	5	6	7	8
pH	−0.634	0.365	0.627	−0.050	−0.175	−0.152	0.013	0.122
EC	−0.098	0.826	−0.059	−0.160	0.363	−0.376	0.060	−0.054
TD	0.528	0.002	0.680	−0.359	0.260	0.236	−0.080	−0.014
DO	−0.467	0.680	0.356	0.022	−0.373	0.206	−0.001	−0.106
AN	0.782	0.285	−0.301	0.308	−0.305	−0.165	−0.051	0.000
Tra	−0.494	0.280	−0.722	−0.137	0.092	0.352	0.068	0.034
Chl	−0.361	−0.661	0.404	0.488	0.132	−0.017	0.109	−0.047
TP	0.900	0.259	0.234	−0.058	−0.098	0.126	0.194	0.028
TN	0.112	0.657	0.107	0.645	0.290	0.197	−0.055	0.037

Table 29.3 WQ-agent elements

Agent no.	1	2	3	4	5	6	7	8	9
Z	−1.58	−0.82	−0.64	−0.03	0.15	0.12	0.36	1.36	1.08
$\bar{Z}$	0.05	0.14	−0.05	−0.21	0.13	0.69	−0.38	0.24	−0.64

As seen from Fig. 29.3, multi-WQ-agents optimization refers to the merge and spilt process of WQ monitoring sections. The monitoring sections of Beihai Lake are optimized to five WQ sections from nine through coarse segmentation and fine segmentation, in which the final layout of monitoring section is the geometric center.
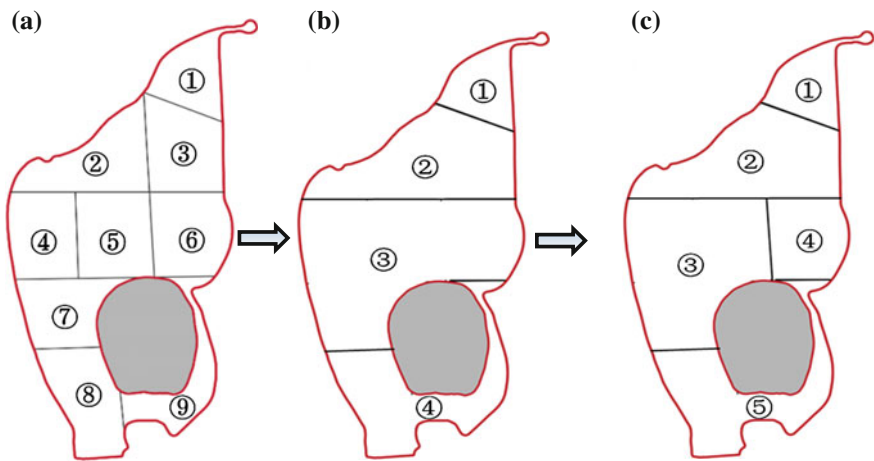
Fig. 29.3 Multi-WQ-agents optimization process of Beihai lake. **a** Original sections, **b** coarse segmentation sections, **c** fine segmentation sections

29.5 Conclusion

This paper proposes a WQ monitoring section optimization method based on multiagent model. Taking CES of principal/nonprincipal components as two elements, multi-WQ-agents set up a communication with each other, and the optimized *Agents** are obtained through coarse/fine segmentation according to the similarity of adjacent agents. The method with layered instruction can reflect overall WQ conditions effectively, and optimize WQ monitoring sections visually.

References

1. Dong S, Liu Z, Wang X, Zhao X (2012) Intelligent agent modeling and simulating of algal bloom formation mechanism. J Jiangnan University (Nat Sci Ed) 11(4):412–417 (in Chinese)
2. Park SY, Choi JH, Wang S et al (2006) Design of a water quality monitoring network in a large river system using the genetic algorithm. Ecol Model 199(3):289–297
3. Ouyang Y (2005) Evaluation of river water quality monitoring stations by principal component analysis. Water Res 39(12):2621–2635
4. Wenqiang W, Chen Q, Li J, Chen G (2010) Optimization of river water quality monitoring sections. Acta Sci Circumstantiae 30(8):1537–1542 (in Chinese)
5. Fei M, Li J (2006) Research on river water quality monitoring sections optimization settings— taking an example of South Canal. J Environ Sci Manag (8):171–172 (in Chinese)
6. Liao S, Hongwei L, Chen J, Dai J (2006) Research on conceptual framework for Agent-based modeling and simulation. J Syst Simul 18(2):616–620 (in Chinese)
7. Fang H, Sun S, Zhu Y, Xiao Z, Shi F (2009) Principal component analysis apply in water quality assessment. Environ Sci Manag 34(12):152–154 (in Chinese)
8. Wang M, Liang C (2010) Study on water quality assessment based on principle component analysis. J Water Resour Water Eng 21(6):140–142 (in Chinese)
9. Meng Z (2003) The design and implement of agent modeling in complex system distributed simulation platform D National University of Defense Technology. (in Chinese)
10. Jing P (2010) Study on multi-Agent simulation and optimization of multi-water resources integrated allocation and control in Tianjin D Tianjin University (in Chinese)
11. Ni J, Li J, Fan X (2007) A complex system simulation platform based on multi-agent. J Comput Simul 24(12):283–286 (in Chinese)
12. Niu W (2007) The study on modeling and simulation for water resources multi-agent system based on system evolution algorithm D Hehai University (in Chinese)

Chapter 30
Load Frequency Control of Two-Area Interconnected Power System Using Fuzzy Logic-Based PI Control Method

Aimin An, Yixin Chen, Haochen Zhang, Fuchao Liu and Jingjing Zheng

Abstract Load frequency control (LFC) plays an important role to maintain the system frequency and tie-line flow at their respective scheduled values during normal period in the power system. Generally, the conventional control strategies, such as PI and PID control algorithms are applied for LFC in practical power systems. However, good control performance could not be guaranteed by using such traditional control strategies when external disturbances occur. In order to overcome the drawbacks, fuzzy logic-based proportional integral (FLPI) controller is proposed for an efficient LFC performance in this paper. Considering the reason that various disturbances and uncertainty consisting of load variation, modeling error, and structure change exist in power system, fuzzy logic modeling method is used for improving the robust performance. And a PI control strategy based on Ziegler-Nichols is used to eliminate or reduce the frequency deviation, tie-line deviation, and area control error. Finally, simulation results demonstrate that the proposed method can stabilize the two-area power system; the performance indices including settling time and overshoots of the tie-line power and frequency deviations can also be improved through the proposed method.

Keywords Load frequency control · Two-area interconnected power system · Fuzzy logic based proportional integral control · Tie-line power · Frequency deviations

A. An (✉) · Y. Chen · H. Zhang
School of Electrical and Information Engineering, Lanzhou University
of Technology, Lanzhou 730050, China
e-mail: anaiminll@163.com

F. Liu · J. Zheng
Institute of Electrical Power Science, Electrical Power Company
of Gansu Province of State Grid, Lanzhou 730050, Gansu, China

30.1 Introduction

Large-scale power systems are normally composed of several control areas, the various areas are interconnected through tie lines. The tie lines are utilized for energy transmission or exchange between areas and provide interarea support in case of abnormal conditions [1]. Area load changes will lead to imbalance between power generation and power demand, and as a result it will deviate from its nominal value. These mismatches must be corrected via supplementary control strategies [2]. Automatic generation control (AGC) is a very important measures in power system operation and control to ensure the performance and sufficient and reliable electric power supply with good quality. AGC is a feedback control system that adjusting the generator output power to remain defined frequency [3]. It is also known as LFC, which main objective is to minimize the deviations of frequency and tie-line power and to reduce their steady-state errors to zero and whenever there is a change in load demands [4].

For a multiarea power system, the frequency deviations and tie-line power are weighted together by a linear combination to a single variable called as the area control error (ACE) [5]. In order to eliminate or reduce such changes in the operating conditions and system parameters, a number of controllers are employed for getting better dynamic performance. The most commonly used is conventional proportional integral (PI) controllers [6]. However, they are slightly simple for implementation and their performances are very satisfactory, the tuning process is complicated and usually requires explicit parameter values. The transient response of the system will have overshoots and undershoots, when the complexity in the system increase due to disturbance existence. In order to improve the performance of the system, some intelligent control strategies are proposed. The fuzzy control rule is used to modeling the dynamics of power system considering various disturbances. Fuzzy logic is imposed and it must cope up with the dynamics of the power system. A PI controller based on intelligent system would be suitable for controlling the system. Many researchers have used fuzzy logic controllers for load frequency control of power system with and without nonlinearities [7–9], and, the results are observed that the transient response is oscillatory and time to reach the steady state is more.

Considering the reason that various disturbances and uncertainties consisting of load variation, modeling error and structure change exist in power system; fuzzy logic modeling method is used for improving the robust performance. And, a PI control strategy based on Ziegler-Nichols is used to eliminate or reduce the frequency deviation, tie-line deviation, and area control error. In this paper, a FLPI control strategy is proposed to improve the dynamic performance of power system under a sudden load changes. In the study, for simplicity purpose, the effects of generation rate constraint (GRC) and governor dead band have not been accounted for. The performance of the LFC is compared with conventional PI controller when one-step load disturbance is given in either areas of the system.

   The paper is organized as follows. The Introduction is given in Sect. 30.1, and
the dynamic model of the two-area interconnected power system is presented in
Sect. 30.2. A PI controller based on Ziegler-Nichols method is presented in
Sect. 30.3. The fuzzy logic-based PI controller is proposed, and its membership
function and control rules is designed in Sect. 30.4. In Sect. 30.5, the simulation is
implemented to verify the performance of the proposed controller that applied to a
real two-area power system, and a comparison is made with the classical PID.
Finally, the conclusion is offered in Sect. 30.7.

30.2 Two-Area Interconnected Power System

LFC is used to regulate the power flow between different areas while holding the
frequency constant. In the power system, the system frequency will rise when the
load decreases; similarly, the frequency may drop if the load increases. Generally,
for power system operation, it is desirable to maintain the frequency as the constant,
ideal case is that the frequency deviation $\Delta\omega$ is zero. The power flow through
different tie lines must be scheduled according to power demand. A conceptual
diagram of the interconnected areas is shown in Fig. 30.1.

30.2.1 Dynamic of Difference Component

In this work, two-area thermal−thermal power system will be analyzed. Each area
feeds its user pool and tie-line allows the electrical power to flow between areas
[10]. It is assumed that each area has only one equivalent generator and is equipped
with governor-turbine system. Generally, a power system with a reheated turbine
consists of four parts, governor, reheater, turbine, and generator. Their respective
dynamics are formulated as transfer function as follows: Transfer function of
governor dynamics is $\frac{1}{T_g s+1}$, Transfer function of reheater dynamics is $\frac{K_r T_r s+1}{T_r s+1}$,
Transfer function of turbine dynamics is $\frac{1}{T_t s+1}$, Transfer function of generator
dynamics is $\frac{K_p}{T_p s+1}$.
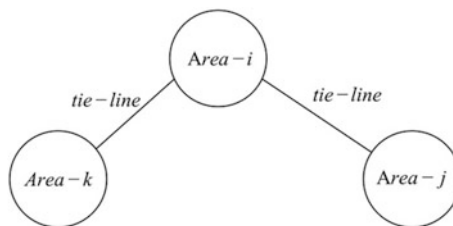
Fig. 30.1 Interconnected areas in a power system

30.2.2 Frequency Deviation, Tie-Line Power Deviation and Area Control Error

The overall generator-load dynamic relationship between the incremental mismatch power $(\Delta P_{\text{mech}} - \Delta P_L)$ and frequency deviation $\Delta\omega$ can be expressed as

$$\Delta\omega = \frac{K_p}{T_p s + 1}(\Delta P_{\text{mech}} - \Delta P_L) \tag{30.1}$$

The total tie-line power between area-1 and area-2 can be calculated as

$$\Delta P_{\text{tie}12} = \frac{2\pi T_{12}}{s}(\Delta\omega_1 - \Delta\omega_2) \tag{30.2}$$

Area control error indicates the power mismatch between the area load and generation. The ACE for control area-1 and area-2 can be expressed as a summation of frequency multiplied by a bias factor β_i and tie-line power.

$$\text{ACE}_i = \Delta P_{\text{tie}12} + \beta\Delta\omega_i \tag{30.3}$$

Based on analysis above, the model for a two-area power system can be expressed as shown in Fig. 30.2.

30.2.3 State Space Model of Two-Area Interconnected Power System

The overall system can be modeled as a multivariable system in the following form

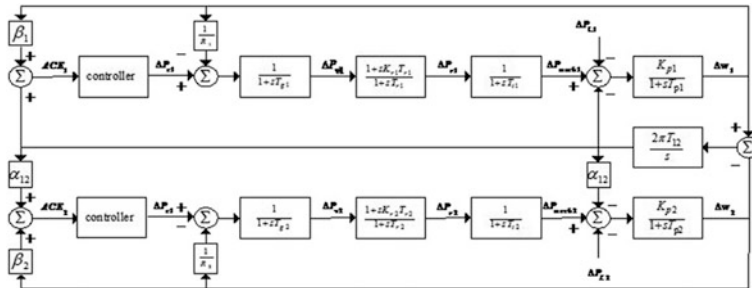$$\dot{X} = Ax + Bu + Rd \tag{30.4}$$

Fig. 30.2 Schematic diagram of two-area power system

$$y = Cx \tag{30.5}$$

where A is the system matrix, B, R, and C is the input, disturbance distribution, and output matrices. x, u, d are state, control signal, and disturbance vectors, respectively.

$$x = [\Delta\omega_1, \Delta P_{v1}, \Delta P_{r1}, \Delta P_{mech1}, \Delta\omega_2, \Delta P_{v2}, \Delta P_{r3}, \Delta P_{mech2}, \Delta P_{tie12,}]^T \tag{30.6}$$

$$u = [u_1, u_2]^T, \, d = [P_{L1}, P_{L2}]^T \tag{30.7}$$

The system output is given as

$$y = [\Delta\omega_1, \Delta\omega_2, \Delta P_{tie12}, ACE_1, ACE_2]^T \tag{30.8}$$

30.3 Conventional PI Controller Based on Ziegler-Nichols

As an efficient loop feedback mechanism widely used in industrial engineering, PI control algorithm is also used in the power systems. The control algorithm design involves two separate parameters, namely, proportional gain K_p and integral time parameter T_i. The proportional action determines the reaction based on the current error, the integral action determines the reaction based on the sum of recent errors, and the weighted sum of these two actions is used to adjust the process via the final control element. If the input error $e(t)$ and output $u(t)$ are given, the relationship between $e(t)$ and $u(t)$ is

$$u(t) = K_p[e(t) + \frac{1}{T_i} \int e(t)dt] \tag{30.9}$$

The transfer function of a PI controller has the following form

$$G_c(s) = K_p + \frac{K_i}{s} \tag{30.10}$$

In this work PI algorithm is used as controller, and the parameters K_p and T_i are tuned using the Ziegler-Nichols method. The Ziegler-Nichols tuning method is a heuristic method of tuning a PID controller, and the Ziegler-Nichols tuning rule is meant to give PID loops best disturbance rejection [11]. The calculation of the parameter K_p and T_i in the PI controller consists of following four procedures:

step 1. Reduce the integrator gains to 0;
step 2. Increase K_c from 0 to some critical value $K_p = K_c$ at which sustained oscillations occur;
step 3. Note the value K_c and the corresponding period of sustained oscillation, T_c;

Table 30.1 The Ziegler-
Nichols rules

Controllers	K_p	T_i
P	$0.5K_c$	
PI	$0.4K_c$	$0.8T_c$

step 4. Calculate the controller parameter values according to Table 30.1, and use
these parameter values in the controller.

## 30.4 Fuzzy Logic-Based Proportional Integral Controller

In the real world, power system contains many different kinds of uncertainties due
to unpredictable load variations, system modeling errors, and change of the power
system structure. Hence, a controller with strong robust performance is needed, and
the fuzzy control strategy is suitable for controlling this process. However, the
process manipulated fuzzy control has the steady-state error; so, it is necessary to
use the integral elements to eliminate the steady-state error, and the PI control
strategy is considered naturally.

The concept of fuzzy logic was developed by Zadeh in [1], it is a thinking
process or problem-solving control methodology incorporated in control system
engineering to control systems when some inputs are either imprecise or the
mathematical models do not exist at all. A fuzzy logic controller consist of four
section namely fuzzifier, rule base, inference engine, and defuzzifier [12]. The
proposed FLPI controller is shown in Fig. 30.2. The controller has two input
signals, namely, ACE and AĊE, and the output signal of the fuzzy logic controller
is the input signal of the conventional PI controller. Finally, the output signal from
the conventional PI controller called the control signal is used for controlling the
LFC in the interconnected power system. The calculation of the control action in
the FLPI controller consists of following four steps Fig. 30.3:

step 1. Calculate ACE and AĊE;
step 2. Convert the ACE and AĊE into fuzzy variables, linguistic variables such
as NB, NS, ZO, PS, PB;
step 3. Evaluate the decision rules shown in rules given below using the com-
positional rule of inference;
step 4. Calculate the deterministic input required to regulate the process.

The number of linguistic terms used for each linguistic variable determines the
quality of control which can be achieved using fuzzy logic controller. Generally, as
the number of linguistic terms increases, the quality of control improves but this
improvement comes at a cost of increased complexity on account of computational
time and memory requirements due to increased number of rules. Therefore, a
compromise between the quality of control and complexity involved is needed to

Fig. 30.3 Structure of FLPI controller
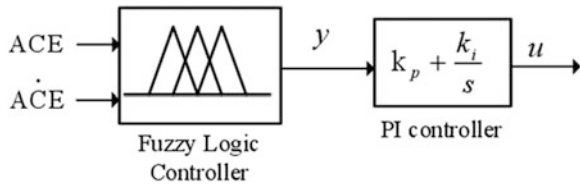
Fig. 30.4 Triangular membership functions
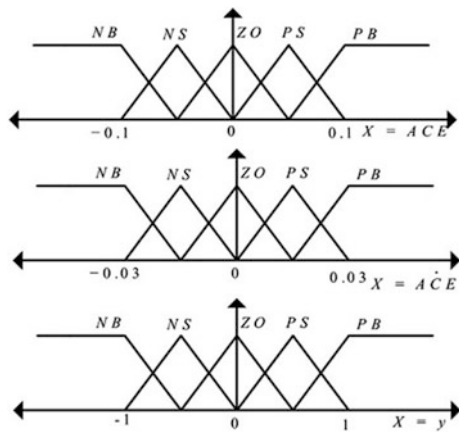
choose the number of linguistic terms, each one of which is represented by a membership function, for each linguistic variable. In this study, five linguistic terms have been chosen for each of the three linguistic variables. The membership functions of FLPI controller are presented in Fig. 30.4.

Fuzzy rules are conditional statement that specifies the relationship among fuzzy variables. These rules help us to describe the control action in quantitative terms and have been obtained by examining the output response to corresponding inputs to the fuzzy controller. The rules, as used in this study, for the FLPI are given in Table 30.2. If ACE is ZO and $\dot{ACE}$ is PS then output y is NS (Fig. 30.3).

Table 30.2 Fuzzy control rules

ACE $\dot{ACE}$	NB	NS	ZO	PS	PB
NB	PB	PB	PB	PS	ZO
NS	PB	PB	PS	ZO	ZO
ZO	PS	PS	ZO	NS	NS
PS	ZO	ZO	NS	NB	NB
PB	ZO	NS	NB	NB	NB

Table 30.3 Parameters for interconnected power system

Symbol	Quantity	Value
T_{gi}	Speed governor time constant	0.08
R_i	Governor speed regulation parameter	2.4
T_{pi}	Power system time constant	20
T_{ti}	Turbine time constant	0.3
K_{ri}	Steam turbine reheat constant	0.33
β_i	Frequency bias constant	0.5
T_{12}	Synchronizing coefficient	0.707
K_{pi}	Power system gain	120
T_{ri}	Steam turbine reheat time constant	10

30.5 Simulation and Discussion

Simulations were performed using the conventional PI and FLPI controllers applied to a two-area interconnected power system as shown in Fig. 30.2 by applying 0.01 p.u MW step load disturbance to both areas. Most of the two-area interconnected power system parameters are provided in the Table 30.3 and some parameters have modified [9, 13]. Two-performance criteria such as overshoots and settling time were considered in the simulation for the system dynamic parameter, frequency deviation in both the areas and tie-line power deviation.

By varying the load 0.01 in two-area with PI controller and FLPI controller, the steady-state error is minimized to zero. From Figs. 30.5, 30.6, 30.7, 30.8, and 30.9, it is found that conventional PI controller does not provide good control performance and it takes more settling time to settle down the steady-state error, due to the fixed value of PI controller. But FLPI controller provides better control performance than PI controller, the settling time and overshoot are reduced considerably.

Fig. 30.5 The frequency deviation of the area-1
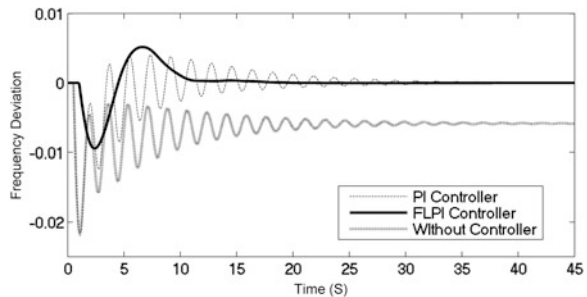
Fig. 30.6 The frequency deviation of the area-2
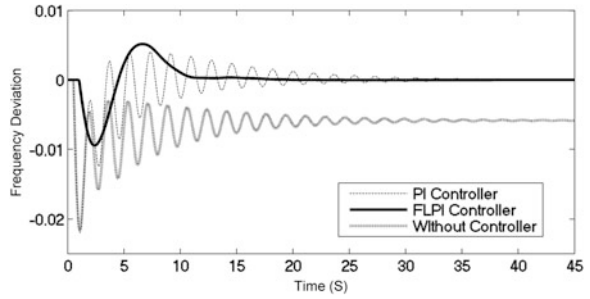
Fig. 30.7 Tie-line power deviation in two-area
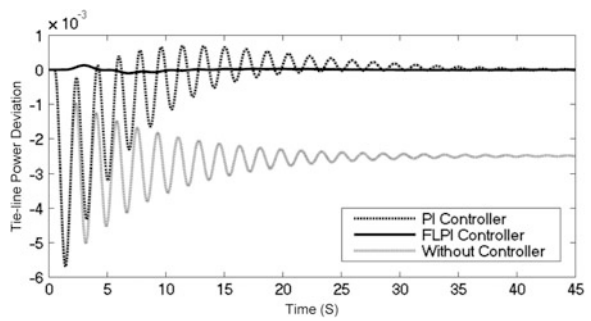
Fig. 30.8 Area control error in area-1
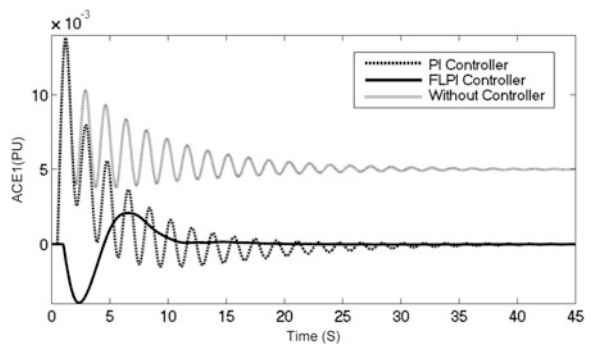
Fig. 30.9 Area control error
in area-2
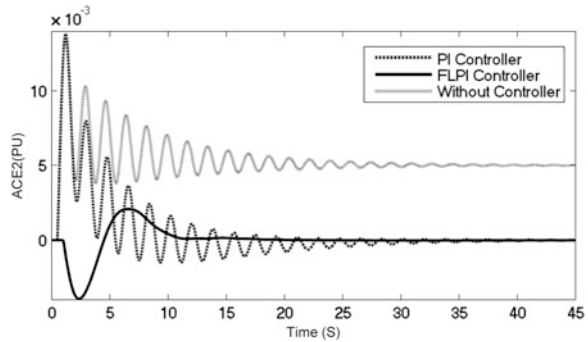
30.6 Conclusion

In this paper, a FLPI controller is proposed for LFC of a two-area interconnected power system. The system is disturbed by giving one-step load perturbation in area-1 and area-2, the dynamic parameters such as frequency deviations and tie-line power deviation are taken to verify the controller performance, which is also justified through ACE. The simulation results demonstrate that the proposed FLPI controller performs significantly better than conventional PI controller in the areas of settling time and overshoot. Therefore, the performance of FLPI controller better than PI controller.

References

1. Grigsby L (2012) Power system stability and control, vol 5. CRC press, Boca Raton
2. Gonen T (2013) Modern power system analysis. CRC Press, Boca Raton
3. Bengiamin N, Chan W (1978) Multilevel load-frequency control of interconnected power systems. Proc Inst Electr Eng 125(6):521–526
4. Wood A, Wollenberg B (2012) Power generation, operation, and control. Wiley, New York
5. Sahu R, Panda S, Yegireddy N (2014) A novel hybrid DEPS optimized fuzzy PI/PID controller for load frequency control of multi-area interconnected power systems. J Process Control 24(10):1596–1608
6. Kumari R, Avtar M (2011) Automatic generation control of multi area power system using PID controller. Int J Eng Trends Technol (IJETT) 4(5):1976–1980
7. Ellithy K, Metwally K (2012) Design of decentralized fuzzy logic load frequency controller. Int J Intell Syst Appl (IJISA) 4(2):66–75
8. Rajarathna S (2012) Performance analysis of LFC of two area system using PI and fuzzy logic controller. Int J Adv Res Sci Eng 1(2):42–44

9. Ramanand K, Sankeswari P (2013) Load frequency control using fuzzy logic controller of two area thermal-thermal power system. Int J Emerg Technol Adv Eng 3(9):655–659
10. Saadat H (2002) Power systems analysis. McGraw-Hill, New York
11. Valério D, Costa J (2006) Tuning of fractional PID controllers with Ziegler–Nichols-type rules. Sig Process 86(10):2771–2784
12. Ross T (2013) Fuzzy logic with engineering applications, vol 686. Wiley, New York
13. Çam E, Kocaarslan İ (2005) A fuzzy gain scheduling PI controller application for an interconnected electrical power system. Electr Power Syst Res 73(3):267–274
14. Klir G, Yuan B (1995) Fuzzy sets and fuzzy logic, vol 4. Prentice Hal, New Jersey

Chapter 31
Research on the Comprehensive Analysis and Early Warning Expressway Weather Information System

Wenfeng Liu, Xun Li and Li Zhang

Abstract This paper reviewed the development of the road weather information system in the developed countries and summarized the problems of its applications on expressway in China; second, proposed a new approach to achieve the dedicated weather information services on expressway through the in-depth data fusion of the macro-meteorological observation and forecasting data from meteorological sector and the road weather information system (RWIS) observation data and video surveillance data from the devices along the expressway; third, described the architecture, functions, process, and interface of the comprehensive analysis and early warning expressway weather information system; and finally, introduced the demonstration case and its results of the system's application on the Jing-jin-tang expressway.

Keywords Road weather information system · RWIS · Expressway · Adverse weather · Road safety · Traveler information services · Early warning

31.1 Introduce

Expressway is the core of the national highway network, by the end of 2012; the mileage of expressway in China had reached 96,200 km [1], and the national expressway network in China had basically been formed. Today and in the future, the national expressway network is playing a more and more important role in supporting the economic development and people travel safely and conveniently.

It is a main feature of the expressway that its severity of traffic crashes, including the injury and death rate, is much higher than the ordinary highway. Especially under the adverse weather conditions, it will lead to the dangerous road conditions

W. Liu (✉) · X. Li · L. Zhang
Research Institute of Highway, MOT, No. 8, Xitucheng Road, Haidian District,
Beijing, China
e-mail: wenfeng@itsc.com.cn

such as low visibility, road area of ice (water, snow) and slip, etc., on some highway sections, which contains a variety of diving risks and even maybe lead to serious accident. Statistics data shows that: On contrast with 2011, the number of deaths had a growth due to the adverse weather conditions, and the number of deaths caused by traffic accidents under the inclement weather conditions including rain, snow, and fog had a 13.3 % growth in nationwide in 2012. The casualty rate of traffic crash on expressway under fog condition is highest, which had reached 2.67 person/crash; followed by under-snow condition, the casualty rate reached 2.3 person/crash; the casualty rate in rainy season was 2.18 person/crash; and finally, the casualty rate in cloudy and sunny days is lowest, which was closed to 2 person/ crash. While the casualty rate of traffic crash on expressway in case of road surface with water had reached 2.38 person/crash, which was much higher than it under other road conditions [2].

The high sensitivity of traffic on expressway to weather conditions has great influence and constraints on the pursuit of the "high-speed, efficient, safe, and comfortable" modern highway transport system. Under the global warming environment, the frequency of weather disasters is increasing, and its intensity is enhancing; it has become the maximum nonhuman factor threatening the safety of expressway, which were weather disasters (fog, rain, icy pavement, etc.) and the geological disasters (mudslides, landslides, etc.) caused by them. It could be foreseeable that the impact of adverse weather conditions on expressway's operation will be more prominent, with the continued growth of expressway mileage, vehicle fleet, and adverse weather conditions.

31.2 Development Status and Main Problems

Road weather information system (RWIS) is a combination of technologies that collects, transmits, models, and disseminates weather and road condition information [3]. The application of the RWIS will reduce the negative effects of adverse weather conditions on mobility and safety. The RWIS will help the road authorities and normal traveler to face the adverse weather conditions on the roads and make decisions.

Currently, more and more countries pay attention to the research and application of the RWIS, such as the United States [3, 4], Finland [5, 6], Sweden [7, 8], etc. A series of national or regional RWIS has been built and applied. The RWIS has been widely used in road traffic information services, road traffic control and management, road maintenance, and other areas. Several countries have launched or are being undertaken to form the standards or guides of RWIS to prompt the application of the RWIS, which include: RWIS data elements, RWIS Siting, communication, and calibration, and the RWIS information promulgating, etc.

From the 1990s, twentieth century, the RWIS stations were applied in China, which were used in the Jing-Jin-Tang expressway between Beijing and Tianjin [9]. With the rapid development of highways (especially the expressways) in China, the highway operation and management departments pay more and more attention to

road safety, the demand of the travelers on the weather information services along the highway is being increasing.

But the conventional meteorological observation and forecast methods were mainly for planar large-scale objects, while the expressway was showing zonal distribution characteristics, and the demand of the meteorological information service along the expressway was dotted need. The relationship among the RWIS information and the public travel, road traffic management, and road maintenance is not strong; because the RWIS stations along the highway or expressway could not provide directly the suggestion or decision of travel, traffic management, or road maintenance in the adverse weather conditions to the traveler or the authorities, which need the support of lots of comprehensive data processing technologies and disposal strategy. And also, it is lack of a useful, simple, and intuitive information system to help the local expressway or highway authorities or companies to carry out the real-time expressway weather information collecting, transmitting, processing, and promulgating. So that, the ability of the expressway operation and management sector or meteorological sector to monitor, forecast, early warning, dispose, and service on the adverse traffic weather conditions was still unable to meet the expressway's traveler's needs.

31.3 Research on the Monitoring Data Fusion and Early Warning Method of the Expressway Meteorological States

31.3.1 Research on the Data Fusion of the Meteorological and Expressway Management Sector

The RWIS stations along the expressway, which was constructed and operated by the expressway management sector, could directly monitor a single point or small area's traffic meteorological environmental data with high accuracy; but the RWIS station is expensive and difficult to maintain, so it was hard to layout with high density in the large scale. However, the monitoring and maintenance teams of the expressway management sector had accumulated many years' data about the road surface states in different weather conditions along the expressway.

The meteorological monitoring and forecasting works of the meteorological sectors were mainly focus on a region, while their study on impact of the different weather conditions on expressway's surface states in was limited. However, the meteorological sectors had developed many new macro-meteorological observations technologies, including: Satellite clouds observation, radar observation, etc., which had formed a meteorological observation grid network with high-spatial and temporal resolution. Meanwhile, the meteorological sectors had accumulated many years of regional meteorological historical data, and had unique forecasting and early warning capabilities about the adverse weather conditions.
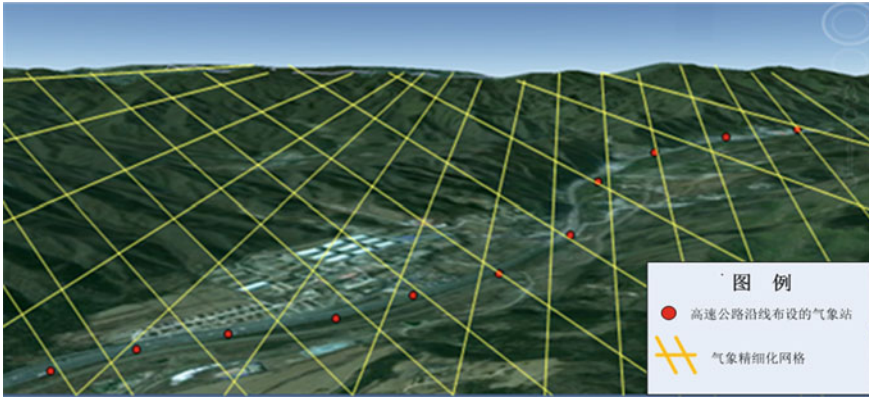
Fig. 31.1 Schematic of the in-depth road weather information data fusion method on considering of the ribbon characteristic of expressway

Therefore, the paper proposed that the meteorological information service on expressway could not only rely on the RWIS stations along the expressway, but should be laid on the data of the RWIS stations along the expressway as a benchmark, and highly integrated the macroeconomic meteorological observation and forecasting data by the meteorological sectors, then through the data assimilation and inversion to get the road weather conditions in real-time or in next few hours.

The schematic of the in-depth data fusion method was shown as Fig. 31.1.

In Fig. 31.1, the yellow grid lines were shown the meteorological observation grid with 1 km resolution that the meteorological sector could offer, and the red points were the RWIS stations along the expressway supported by the expressway management. It could effectively improve the density and accuracy of the monitoring data of the expressway's meteorological states through the data assimilation and inversion techniques on the meteorological weather observation grid. While it could effectively ensure the accuracy of the meteorological sector's observed data on the specific points by the data of the RWIS stations along the expressway, the data of the RWIS stations could be an effective and valuable reference and benchmark for the meteorological sector forecasting the expressway surface's state under different weather conditions.

31.3.2 Research on the Warning Strategies of Expressway Under the Adverse Weather Conditions

Through the comparative analysis of historical traffic accidents data and the corresponding meteorological data, this paper made clear the main type of adverse weather conditions which had great impact on the road safety of the Jing-jin-tang expressway; then calculated the theory speed limit value under different weather conditions,

Table 31.1 The warning strategies of expressway under the adverse weather conditions (first grade, blue)

Grade	Condition	Weather conditions	Warning strategies
First grade blue	Condition 1	200 m < visibility ≤ 500 m	Fog, speed limit ≤80 km, the vehicle spacing ≥150 m
	Condition 2	One hour rainfall intensity 10.0–14.9 mm/h, or one minute rainfall intensity 0.8–1.2 mm/min, and 200 m < visibility ≤ 500 m	Rain, poor vision, speed limit ≤60 km, the vehicle spacing ≥100 m
	Condition 3	(10 min) Average wind 5–6 grade (8.0–13.8 m/s), or (10 min maximum) gust 7 (13.9–17.1 m/s)	Wind, speed limit ≤80 km, the vehicle spacing ≥150 m (dangerous goods freight vehicle is prohibited through the traffic control expressway section)
	Condition 4	Snow or sleet, (12 h rainfall 0.1–0.9 mm or 24 h rainfall 0.1–2.4 mm)	Snow, speed limit ≤60 km, the vehicle spacing ≥100 m
	Condition 5	Snow thickness <1.0 cm	Covered by snow, speed limit ≤80 km, the vehicle spacing ≥150 m
	Condition 6	Dust, 200 m < visibility ≤ 500 m	Dust, poor vision, speed limit ≤80 km, the vehicle spacing ≥150 m

including sunny, rain, snow, and road surface state (dry, wet, water, ice), and tested the speed limit value by the average driver's reaction time and braking distance under different speeds; Finally, verified reasonable speed value under different weather conditions through the analysis of the driver's psychological changes under adverse weather conditions by questionnaire, and also collected the driver's suggestions on the service content and manner of the RWIS on expressway network.

On the basis above, the paper adopted a hierarchical manner to divide the adverse weather conditions into four grades: Blue, yellow, orange, and red, on considering of the experience of expressway traffic management and control measures; then to propose a set of safely driving behavior recommendations and control measures corresponding to different grades, finally, formed the early warning strategies. The early warning strategies under the first grade (grade blue) on expressway had been shown as Table 31.1.

31.4 Development of the System

31.4.1 System Functions

The system changed the service concept and tradition of the meteorological information in the field of transportation, used the conventional meteorological data, including temperature, humidity, wind, pressure, precipitation, and others, to

get the practical information, including the visibility, road surface temperatures, icy pavement, road surface conditions, highway speed limits, and others, which had met the needs of the drivers and the expressway management sectors.

The main technical functions of the system include

- using B/S architecture, relying on the Internet for data transmission.
- being able to access multiple sources dynamic road weather monitoring data.
- being able to transfer meteorological grading rules and freedom to customize the driving behavior according the proposed rules.
- being able to use a variety of query and statistical functions, and multiangle comparison and statistical analysis on the historical RWIS observation data.
- being able to publish meteorological monitoring data and the driving behavior recommendation on the target expressway sections through automatic or manual mode.
- being able to communicate with the traffic flow management and control system and the travel information service system.

31.4.2 System Architecture

The system architecture of the comprehensive analysis and early warning expressway weather information system is shown as Fig. 31.2.

The development of the "Expressway icy & visibility forecast module" in the Fig. 31.2 was relying on the existed weather forecast and warning system in the meteorological sector. The module had concerned on the expressway's linear
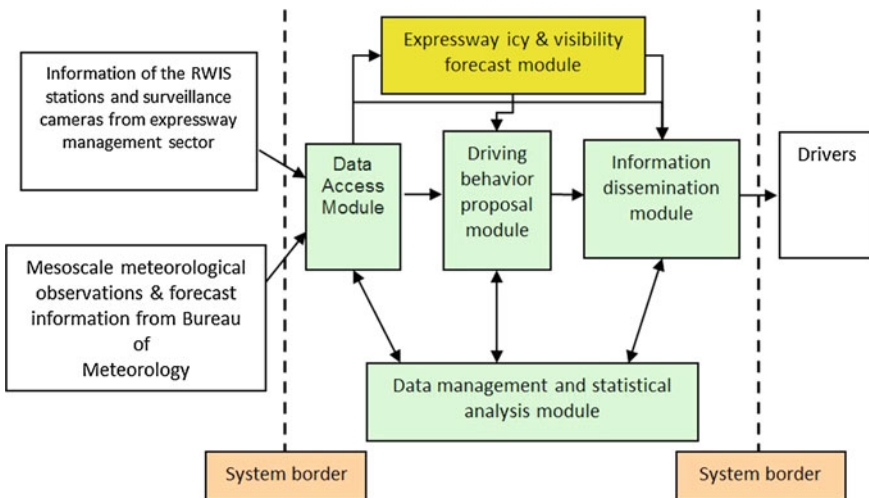
Fig. 31.2 The system architecture of the comprehensive analysis and early warning expressway weather information system

features, utilized the integrated meteorological observation data by the system, targeted on the two key objectives: Visibility and road surface icing, which had great impact on the travel safety on the expressway, and used kinetic and statistical methods to achieve the relative forecast functions, then the forecasts and warnings results would be fed back to the system.

31.4.3 System Process

The system process of the comprehensive analysis and early warning expressway weather information system is shown as Fig. 31.3.
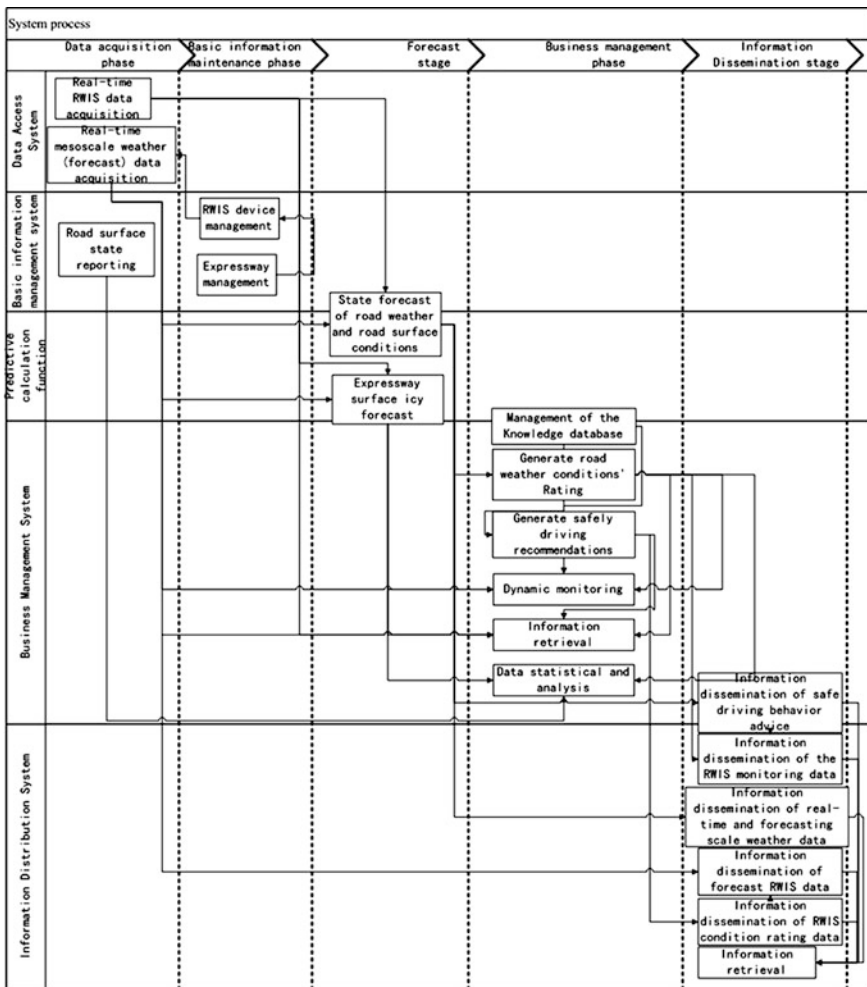
Fig. 31.3 The system process of the comprehensive analysis and early warning expressway weather information system

Fig. 31.4 The interface of the comprehensive analysis and early warning expressway weather information system

31.4.4 Human–Machine Interface of the System

A typical interface of the comprehensive analysis and early warning expressway weather information system is shown as Fig. 31.4. In addition to the meteorological monitoring and forecast data along the expressway and the surrounding area, the system also effectively integrated the data of the video surveillance equipment along the expressway (usually 1 point/2 km), which was constructed and operated by the expressway management sector. The video surveillance equipment's information was a very helpful means for the traffic management team to intuitive feel and understand the road meteorology state, while it could help them to make a qualitative confirmation and judgment on the early warning weather information more quickly and intuitive.

31.5 Demonstration Application

The Jing-jin-tang Expressway is a intercity rapid aisle between Beijing and Tianjin, which are the two municipalities in China, its total length is 142.69 km. In October 2011, the comprehensive analysis and early warning expressway weather information system had complete its deployment in the monitoring and management center of the Jing-jin-tang Expressway, then began its demonstration application (see Fig. 31.5).

Fig. 31.5 Demonstration application of the comprehensive analysis and early warning expressway weather information system

In the demonstration application, the system had integrates the data of seven road weather monitoring stations and multichannel video surveillance cameras from the expressway operation and management sector, as well as the data of three road weather monitoring stations, ten precipitation monitoring network nodes (BJ-RUC) and the forecasting outputs about the wind speed, visibility, road surface temperature, road surface conditions, and snow depth on road surface from the Beijing meteorological sector. The system could provide driving behavior's recommendations under adverse weather conditions for the drivers, who wanted to chose the Jing-jin-tang expressway as their route; could conduct the statistics and comparative analysis of the historical road weather data of the expressway, could achieve the real-time monitoring on the visibility and road conditions and the forecasting and early warning in the next 3 h, the accuracy rate of the early warning had been over 90 %.

After the application of the system, the capacity and efficiency of the monitoring, forecasting, early warning, disposal, and service under the adverse weather conditions along the expressway had been effectively improved. the number of highway closed caused by the rain, snow, and fog had been reduced 50 %, the traffic crashes rate of 1 hundred million vehicle kilometers under the adverse weather conditions had been reduced 30 %, and the black point or section of road safety had been significantly reduced. It should be noted here that these effects were the jointly outputs of the system and other traffic management measures and technologies, such as active traffic flow guidance technology, traffic broadcast system along the expressway, etc.

31.6 Conclusion

The comprehensive analysis and early warning expressway weather information system has focused on the driver's demands on the travel safety information services under adverse weather conditions, and combined with the characteristics and

their respective advantages of the transportation and meteorological sectors, it could effectively improve the expressway's safety and reliability under adverse weather conditions.

References

1. http://www.moc.gov.cn/ (in Chinese)
2. The traffic management bureau of the ministry of public security of the people's republic of china. Traffic accident statistics annual report of the People's Republic of China 2011–2012, 2012–2013 (in Chinese)
3. http://www.fhwa.dot.gov/weather/best_practices/CaseStudiesFINALv2-RPT.pdf
4. http://www.fhwa.dot.gov/weather/publications/RWIS_brochure.pdf
5. http://www.vaisala.com/en/Pages/default.aspx
6. Toivonen K, Kantonen J (2001) Road weather information system in finland. Transp Res Rec 1741:21–25
7. http://www.trafikverket.se/en/startpage/
8. Axelson L (2000) Development and use of the Swedish road weather information system. http://www.rwis.net/pdf/rwis.pdf
9. Li C (2009) The demands of the RWIS on highway. In: Presentation on the conference (Nanjing, China, 2009-12-22) (in Chinese)

Chapter 32
Fluctuation Analysis of Runoff Time Series Under Coarse-Graining Network Modeling Method

Qiang Tang, Jie Liu and HongLing Liu

Abstract Based on coarse-graining complex networks modeling method, the fluctuation characteristic of the daily runoff series of the Yangtze River in China and the Ocumlgee River in America are investigated in this paper, respectively. First, the related runoff time series were transformed into discrete symbolic sequences by coarse-graining preprocessing method, and then, related complex networks were created. Dynamic statistical features and topology parameters of the two fluctuation networks, such as clustering coefficient (CC), characteristic path length (CPL), and betweenness centrality example, from 2-June to 19-June in (BC) of nodes, are calculated and compared with each other. It can be found that, the clustering coefficients of both networks are much larger than random networks with the same scale, and both characteristic path lengths are as small as random networks with the same scale. It indicated that the short-range correlation exists in different fluctuation patterns of the discrete symbolic sequences obtained by the coarse-graining method. Furthermore, it can be found that, the betweenness centrality of different node is obvious different from each other in both networks, which means that some fluctuation patterns have important significance and can be seen as a conversion precursor between the various fluctuation patterns. Also, the community analysis are also carried out and closer connections are revealed for further prediction research. These results indicates potential value for research on short-term prediction of runoff process.

Keywords Runoff time series · Fluctuation · Complex networks · Coarse graining · Clustering coefficient · Characteristic path length · Betweenness centrality · Community analysis

Q. Tang · J. Liu (✉) · H. Liu
College of Mathematics and Computer Science, Wuhan Textile University,
Wuhan 430200, China
e-mail: liujie@wtu.edu.cn

Q. Tang · J. Liu · H. Liu
Research Center of Nonlinear Science, Wuhan Textile University,
Wuhan 430200, China

32.1 Introduction

Since the discovery of small-world behavior [1] and the scale-free property [2], complex networks have attracted continuous attention [3–8]. Recently, some methods of time series analysis by constructing a complex network have been introduced and the study of time series, based on the complex networks, has recently received a lot of attention. Yang et al. constructed a weighted network from stock price time series and extracted its maximal spanning tree and understand the structure variation of stock market by analyzing the average path length, the influence of the center node, and the p-value for every maximal spanning tree [9]. Hu et al. built several spatial economic networks through the threshold method and the Minimal Spanning Tree method based on annual GDP of nine economic sectors from 1995–2010 in 31 Chinese provinces and autonomous regions and investigated the statistical properties of these networks [10].

In the field of hydrology, characterizing complicated dynamics of runoff time series is a fundamental problem of continuing interest. Chen and Rao investigated nonlinearity in monthly hydrologic time series with the Hinich test [11]. Their results indicate that all of the stationary segments of standardized monthly temperature and precipitation series are found to be either Gaussian or linear. Some of the standardized monthly streamflow and Palmer's drought severity index are found to be nonlinear. Wen Wang et al. investigated the streamflow data with four characteristic time scales (i.e., 1 year, 1 month, 1/3 month, and 1 day) of four rivers in order to study the character and type of nonlinearity that were present in the streamflow dynamics. It is found that there are stronger and more complicated nonlinear mechanisms acting at small timescales than at larger timescales [12].

In this work, we investigated the daily runoff series of two typical rivers, including the Ocmulgee River in the United States and the Yangtze River in China, from the view of complex networks by using coarse-graining process. Then some dynamic statistical features and topology parameters of three fluctuation networks corresponding to various daily runoff series, such as degree distribution, clustering coefficient, mean path length, betweenness centrality, and inverse participation ratio, are discussed.

32.2 The Coarse-Graining Process of Daily Runoff Series

A time series, e.g., daily runoff series, can be coarse-grained into limited and more understandable symbolism sequence in which each symbol represents an entire pattern of series fluctuations. Let $x(t)$ be the runoff at time t. The fluctuation of runoff $k(t)$ can be defined by

$$k(t) = \frac{x(t + \Delta t) - x(t)}{\Delta t}$$

where Δt is a time interval. Then we calculate all the moving slope of different fluctuation (1). According to the partition methods mentioned in Ref. [13], four feature symbols are defined as follows: $r(0 < k(t) < 1)$, $R(k(t) \geq 1)$, $d(-1 < k(t) < 0)$, and $D(k(t) \leq -1)$. Here, R is violent-up meta pattern; r is common-up meta pattern; d is common-down meta pattern; D is violent-down meta pattern. Therefore, a runoff series is transformed into a symbolic sequence, i.e.,

$$S = (S_1 S_2 S_3 \ldots), \ S_i \in (R, r, d, D)$$

For example, from 2-June to 19-June in 1943, the daily runoff series is: 3360, 2950, 2860, 2790, 2720, 2750, 2720, 2690, 2770, 2860, 2950, 3080, 4430, 5220, 5990, 6310, 6330, 6290, and 5790. Suppose $\Delta t = 1$ day, the corresponding symbolic sequence is: *D d d d r d d r r r r R R R R d r D*.

32.3 The Construction of Complex Networks Based on Coarse-Graining Method

For four feature symbols (R, r, d, D), we can get different string of symbol. We call a string made of n symbols an n-string which represents different patterns of runoff fluctuations. For example, if $n = 2$, there are 16 2-strings, i.e., ($RR, Rr, Rd, RD, rR, rr, rd, rD, dR, dr, dd, dD, DR, Dr, Dd, DD$). After the coarse-graining process, we can get a symbolic sequence which composed of different 2-strings. It is multivariate about interconnections and interactions between fluctuation patterns of runoff, the contents of interactions are message transmission of runoff; the format of interconnection is directed; the intensity level of involvement is different. Therefore a directed weigh networks, associated with the daily runoff series, could be constructed where a 2-string is a node. If the nodes i and j have multiple disjoint link paths, the magnitude w_{ij} of the number of multiple disjoint paths is assigned to the edge of nodes i and j as its weight. For example, if the network nodes are defined as 16 2-strings, the direct-link of symbolic sequence ($D d d d r d d r d d r d R R R d r D$) is

$$Dd \rightarrow dd \rightarrow rd \rightarrow dr \rightarrow dd \rightarrow rd \rightarrow RR \rightarrow Rd \rightarrow rD$$

Remark: According to the literatures of Lei , Feng G-L et al., [14]: for fluctuation Analysis of real timeseries, such as temperature time series, runoff time series, under coarse-graining modeling method, smaller time scale behaves much better than large scales. So 3-day fluctuation will be considered in the next section of this brief paper.

32.4 The Characteristics Analysis of Related Networks

The daily runoff series of two rivers are considered, i.e., the Yangtze River at Pingshan station in China and the Ocmulgee River at Macon in the United States from January 1, 1958 to December 31, 2007. Let $\Delta t = 1$ day, $n = 3$, then there are 64 fluctuation patterns, i.e., (*DDD*, *DDd*, *DDr*, *DDR*, *DdD*, *Ddd*, *Ddr*, *DdR*,…, *RRr*, *RRR*). First, two complex networks are constructed based on above-mentioned method from the above runoff series, respectively. Then, the clustering coefficient, mean path length, and betweenness centrality are calculated and compared as follows.

32.4.1 Clustering Coefficient and Characteristic Path Length

For the directed weigh networks, we can define the weighted clustering coefficient of a given node i as: [15]

$$C_i^w = \frac{1}{s_i(k_i - 1)} \sum_{j,k} \frac{w_{ij} + w_{ik}}{2} a_{ij} a_{jk} a_{ik}$$

where k_i is the degree number of node i, s_i is the node strength of node i, defined as

$$s_i = \sum_j w_{ij}$$

$\sum_{k > j} a_{ij} a_{jk} a_{ik}$ is the number of triangles including node i. The clustering coefficient C is then given by the average of C_i^w over all the nodes.

The characteristic path length of directed networks L is defined by Newman [16]:

$$L = \frac{1}{N(N - 1)} \sum_{i \neq j} d_{ij}$$

where N is the number of network nodes, d_{ij} is the distance between nodes i and j.

From Table 32.1 we can see that the clustering coefficients of networks are larger and mean path lengths are smaller, which indicates the short-range correlation exists in different fluctuation patterns and various fluctuation patterns have small size group variety. The mean path length represents the conversion time from a

Table 32.1 The clustering coefficients and characteristic path lengths of related networks

Networks	C	L
Ocumlgee	0.5128	1.6143
Yangtze	0.2176	1.6910

fluctuation pattern to another. So mean path lengths that are less than 2 indicate pattern conversion time is about 6 days, which has reference value for short-term prediction of runoff process.

32.4.2 Betweenness Centrality

The betweenness centrality (BC) is used to quantify the topological importance of a node in the network communications between each pair of nodes [14, 17, 18], i.e., BC at a certain node is interpreted as the net influence for a pattern of runoff fluctuation to affect or control other patterns in global network.

Let $c(i, j)$ be the number of the shortest pathways between a pair of nodes (i, j). Among them, the number of the shortest paths passing through a node k is denoted by $c_k(i, j)$ and then we have the fraction $g_k(i, j)$:

$$g_k(i,j) = c_k(i,j)/c(i,j)$$

Then the BC of the node k is defined as the accumulated amount of $g_k(i, j)$ over all pairs, i.e.,

$$g_k = \sum_{(i,j)} g_k(i,j) = \sum_{(i,j)} \frac{c_k(i,j)}{c(i,j)}$$

BC of every node among these networks are calculated and ranked in Tables 32.2 and 32.3. One can see that the BC sum of the nodes ranking in first 10 reaches up to 42 % (Ocumlgee river) and 34.5 % (Yangtze river) in total BC from Tables 32.2 and 32.3, respectively.

The betweenness centrality of different nodes (pattern) obviously behaves different from each other which means that some fluctuation patterns have important significance. It can be seen as a conversion precursor between the various fluctuation patterns for real runoff data analysis. It should be mentioned that, for Ocumlgee river, the betweenness centrality of three fluctuation patterns, *DDd*,

Table 32.2 The betweenness centrality of different nodes of the Ocumlgee River fluctuation networks
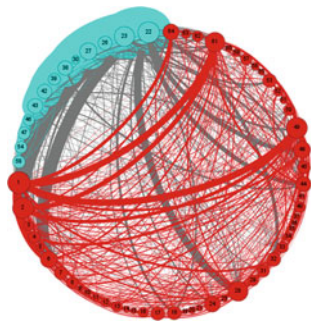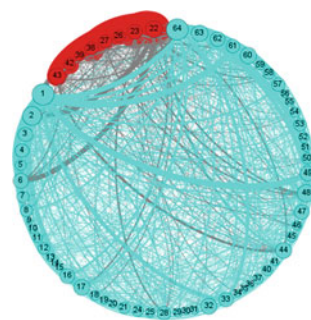
Node	DDd	RDD	RRR	dDd	Ddd	rRR	rRD	DDD
g_k (%)	7.1722	5.3583	5.2068	3.9204	3.8575	3.5080	3.3968	3.3891
Index	1	2	3	4	5	6	7	8
Node	RDR	dDD	ddR	DDR	drr	…	…	DrD
g_k (%)	3.1461	3.0411	2.8199	2.8165	2.8040	…	…	0
Index	9	10	11	12	13	…	…	64

Table 32.3 The betweenness centrality of different nodes of the Yangtze River fluctuation networks

Node	DrR	Ddd	dRr	rDD	DDR	rRr	rrR	RrR
gk (%)	4.3040	4.1586	4.1351	3.6258	3.3511	3.1881	3.1429	2.9407
Index	1	2	3	4	5	6	7	8
Node	DDr	dDD	Ddr	DdR	RRD	…	…	DRd
gk (%)	2.8445	2.8004	2.5520	2.4559	2.4088	…	…	0.0946
Index	9	10	11	12	13	…	…	64

RDD, and *RRR*, are greater than other, which indicate the importance of rapid increase pattern and rapid decrease pattern. For Yangtze river, the betweenness centrality of three fluctuation patterns, *DrR*, *Ddd*, and *dRr*, are greater than other, which indicate the importance of these three patterns.

Table 32.4 The community analysis of the Ocumlgee River and the Yangtze River fluctuation networks

Network type	Community analysis results (Color on line)
Ocumlgee River fluctuation networks: where the red nodes belong to the same community, in which the relationship between numbers and patterns are 22(*ddr*), 23(*ddR*), 26(*drr*), 27(*drR*), 30(*dRr*), 38(*rdd*), 39(*rdr*), 42(*rrd*), 43(*rrr*), 46(*rRd*), 47(*rRr*), 54(*Rdr*), 58(*Rrr*)	
Yangtze River fluctuation networks: where the red nodes belong to the same community, in which the relationship between numbers and patterns are 22(*ddr*), 23(*ddR*), 26(*drr*), 27(*drR*), 38(*rdd*), 39(*rdr*), 42(*rrd*), 43(*rrr*)	

32.4.3 Community Analysis

In this subsection, network community analysis technique [19] is used here to reveal some inherits of these two fluctuation networks. In Table 32.4, it can be found that, for the Ocumlgee River fluctuation network, the connections of red nodes '*ddr, ddR, drr, drR, dRr, rdd, rdr, rrd, rrr, rRd, rRr, Rdr, Rrr*' appears much closer than others, and the other green nodes are connected closer. For the Yangtze River fluctuation network, the connections of nodes '*ddr, ddR, drr, drR, rdd, rdr, rrd, rrr*' appears much closer than others, and the other green nodes are connected closer. These results certainly can be used in predicting possible fluctuation patterns for runoff time series in real life.

32.5 Conclusions

In summary, under a new viewpoint of complex networks, the topological features of two runoff complex networks constructed from the daily runoff series of two rivers by preprocessing coarse graining. To analyze the dynamics of the Runoff data, using homogenous partition of coarse graining process, the series of Chinese and American Runoff Time Series are transformed into symbolic sequences consisted of four characters (R, r, d, D). The vertices of the runoff fluctuation networks is symbol strings, and linked in the network's topology by time sequence. Our research shows that the clustering coefficients of both networks are large and mean path lengths are small. The number of characteristic path lengths indicate pattern conversion time is about 6 days. The betweenness centrality of different nodes behave obviously different, which means some nodes play crucial role in forming macroscopic patterns of runoff fluctuation and affecting other patterns. The community analysis are also carried out and closer connections are revealed for further prediction research. These results contribute to understanding the variation of runoff process and have reference value for short-term prediction of runoff process.

References

1. Watts DJ, Strogatz SH (1998) Collective dynamics of 'small-world' networks. Nature 393 (6684):440–442
2. Barabási AL, Albert R (1999) Emergence of scaling in random networks. Science 286 (5439):509–512
3. Albert R, Barabási AL (2002) Statistical mechanics of complex networks. Rev Mod Phys 74(1):47

4. Amaral LAN, Scala A, Barthelemy M, Stanley HE (2000) Classes of small-world networks. Proc Natl Acad Sci 97(21):11149–11152
5. Newman ME (2001) The structure of scientific collaboration networks. Proc Natl Acad Sci 98 (2):404–409
6. Faloutsos M, Faloutsos P, Faloutsos C (1999) ACM SIGCOMM'99. Comput Commun Rev 29(251):16
7. Guelzim N, Bottani S, Bourgine P, Képès F (2002) Topological and causal structure of the yeast transcriptional regulatory network. Nat Genet 31(1):60–63
8. Wang J, Yang H (2009) Complex network-based analysis of air temperature data in China. Mod Phys Lett B 23(14):1781–1789
9. Yang C, Shen Y, Xia B (2013) Evolution of Shanghai stock market based on maximal spanning trees. Mod Phys Lett B 27(03):1350022–19
10. Hu S, Yang H, Cai B, Yang C (2013) Research on spatial economic structure for different economic sectors from a perspective of a complex network. Phys A 392(17):3682–3697
11. Chen HL, Ramachandra Rao A (2003) Linearity analysis on stationary segments of hydrologic time series. J Hydrol 277(1):89–99
12. Wang W, Vrijling JK, Van Gelder PH, Ma J (2006) Testing for nonlinearity of streamflow processes at different timescales. J Hydrol 322(1):247–268
13. Li P, Wang BH (2007) Extracting hidden fluctuation patterns of Hang Seng stock index from network topologies. Phys A 378(2):519–526
14. Lei Z, Zhi-Qiang G, Rong Z et al (2008) An approach to research the topology of Chinese temperature sequence based on complex network. Acta Phys Sin 57(11):7380–7389 (in Chinese)
15. Chen Wei-Dong X, Hua GQ (2010) Dynamic analysis on the topological properties of the complex network of international oil prices. Acta Phys Sin 59(7):4514–4523 (in Chinese)
16. Newman ME (2001) Scientific collaboration networks. I. Network construction and fundamental results. Phys Rev E 64(1):016131
17. Barthelemy M (2004) Betweenness centrality in large complex networks. Eur Phys J B Condens Matter Complex Syst 38(2):163–168
18. Goh KI, Oh E, Kahng B, Kim D (2003) Betweenness centrality correlation in social networks. Phys Rev E 67(1):017101
19. Barrat A, Barthelemy M, Pastor-Satorras R, Vespignani A (2004) The architecture of complex weighted networks. Proc Natl Acad Sci USA 101(11):3747–3752

Chapter 33
Nonlinear Analysis of Typical Hydrological Time Series Under the Viewpoint of Visibility Graph Methods and Its Two Modification Versions

HongLing Liu, Qiang Tang and Jie Liu

Abstract Using visibility graph, horizontal visibility graph, and limited penetrable visibility graph methods, which are all proposed recently to change from time series to network graph, the hydrological time series of Umpqua river are analyzed under the view of complex network. After the establishment of related complex networks of this typical hydrological time series, basic network characteristics, such as degree distribution, average path length, clustering coefficient, graph density, and so on are calculated. Furthermore, community analysis of the three types of related complex networks are carried out. The similarities and differences of the three methods for network analysis are proposed. Finally, basic norms for modeling hydrological time series are proposed with comparison of the merits and drawbacks of the three methods. Results indicate that, for real hydrological time series, the related visibility and limited penetrable visibility networks behave obviously small-world property, while horizontal visibility network has not. Three networks have obviously the degree of distribution characteristics of scale-free networks. Overall, horizontal visibility graph showing scale-free feature most obviously (heavy-tailed is not obvious), visibility graph, and limited penetrable visibility graph networks have obvious bending head (heavy-tailed feature is more obvious). Based on the fitting results of three degree distribution curves, it can be seen that the coefficient absolute value of horizontal visibility network is the largest, which shows the sequence is of high sensitivity. In addition, according to the community analysis results, the limited penetrable visibility graph method is best for classifying withered water period, visibility graph method's ability is worse, horizontal visibility graph method's ability is worst, while through horizontal visibility graph, one can find the local minimum of hydrological time series easily, which is also consistent with the result of degree distribution.

J. Liu (✉)
College of Mathematics and Computer Science, Wuhan Textile University,
Wuhan 430200, China
e-mail: liujie@wtu.edu.cn

H. Liu · Q. Tang
Research Center of Nonlinear Science, Wuhan Textile University,
Wuhan 430200, China

33.1 Introduction

Most hydrological time series are nonlinear, due to their complexity. It is difficult to understand it through classical methods for uncovering its complete characteristics. The development of nonlinear science provides new ideas and methods for people to explore the hydrological time series. Complex network analysis is one of the most important nonlinear analysis methods proposed in recent years. Complex network can be used as an effective kind of abstract and description method for complex system. For any complex system with a number of units, it can always be abstracted into node (Units), and abstract edge (relationships between units). So, all measured systems can be considered as a complex network system [1]. Research on small world network model in complex networks is earlier and more. Small world networks include classical WS smallword network model, the NW smallword network model, Monasson smallword network model, and some other modified versions include the BW small word network model, etc. The complex network method provides a new perspective for the study of complex systems, it plays an important role in understanding the complex behavior of the real system, so it is widely applied to sociology, biology, physics, etc.

In the network construction methods in complex networks, visibility graph and horizontal visibility graph construction methods are easy to realize and the calculation efficiency, etc. Nowadays, these methods seem to be useful for analysis of financial time series and hydrological time series has a preliminary application, see [1–5] and reference therein. To solve the problems existing in these two kinds of methods (i.e., for differ same type of signals from each other, the adaptability of noise), in Ting-ting et al. [6] proposed the so-called limited penetrable visibility graph method, they used this method to extract statistical characteristic of complex network parameters from conductance fluctuating signals measured from oil-gas-water three-phase flow test. Their results show that, the characteristic parameter combination behaves in good recognition effect [6].

In this paper, by using the three kinds of commonly used network method, we establish complex network based on the daily runoff data of the America Oregon Umpqua river Elkton station. By computing network static statistics, the nonlinear properties were discussed. Also, similarities and differences between the three kinds of algorithms to describe the actual runoff series are discussed in detail. Finally, the advantages and disadvantages of the runoff sequence network construction methods are given.

33.2 Visibility Graph, Horizontal Visibility Graph, and Limited Penetrable Visibility Graph Network Models for Time Series

In 2008, Lacasa et al published the visibility graph method (VG) in [1]. In this paper, for a discrete time series, the data point is defined as a network node, data points satisfy the lines defining visibility criterion for the network edges, using the histogram bar represented as a time sequence of data points. If the histogram bar top is mutually visible, we consider these two points connective in the network [1]. In 2009, Luque et al proposed horizontal visibility graph (HVG), the definition of network nodes and edges of the horizontal visibility graph is the same as the Visibility Graph. If we can draw a horizontal line between the two points, and the line of sight is not through the histogram of the other, then we consider the two points are connective in the network [2]. Obviously, in the same time series, HVG is a subnetwork of VG [3]. Limited penetrable visibility graph (LPVG) is a newly proposed [6]. The basic idea can be described as follows. The definition of limited across the line of sight N, the visibility criterion based on VG method provisionsly, if two nodes are connective in the network, when and only when the times of the two histogram bars corresponding to node connection are truncated by another histogram is located in between is not bigger than N.

Assume that the time series for: $\{xi\}$, $(i = 1,…,N)$, the resulting complex network denoted as: $G = \langle V, E \rangle$, here $V = \{vi\}$ $(i = 1, …,N)$ is the set of nodes, $E = \{ei\}$, $(i = 1,…,N)$ is the connection matrix of the network. For ease of understanding, the three basic models are listed as follows (Table 33.1):

In this paper, therefore we select $N = 1$ in the next section since the noise level is very low according to real data. By selecting random sequence $X = [0.74, 0.39, 0.65, 0.17, 0.70, 0.03, 0.27, 0.04, 0.09, 0.82]$, three kinds of network construction methods based on network diagram of can be shown as in Fig. 33.1.

Table 33.1 Different visibility criterion of differences between three kinds of construction methods

Construction methods (Henceforth)	Visibility criterion
VG	If any of the $i < n < j$, both have $\frac{x_i - x_n}{i - n} > \frac{x_i - x_j}{i - j}$, then the i node and the j node is visual, otherwise invisible
HVG	If any of the $i < n < j$, both have $x_i, x_j > x_n$, then the i node and the j node is visual, otherwise invisible
LPVG	Define limited across the line of sight N, visibility criterion is based on VG method: If two nodes in the network are connective, when and only when the times of the two histogram bars corresponding to node connection are truncated by other histogram is located in between is not bigger than N
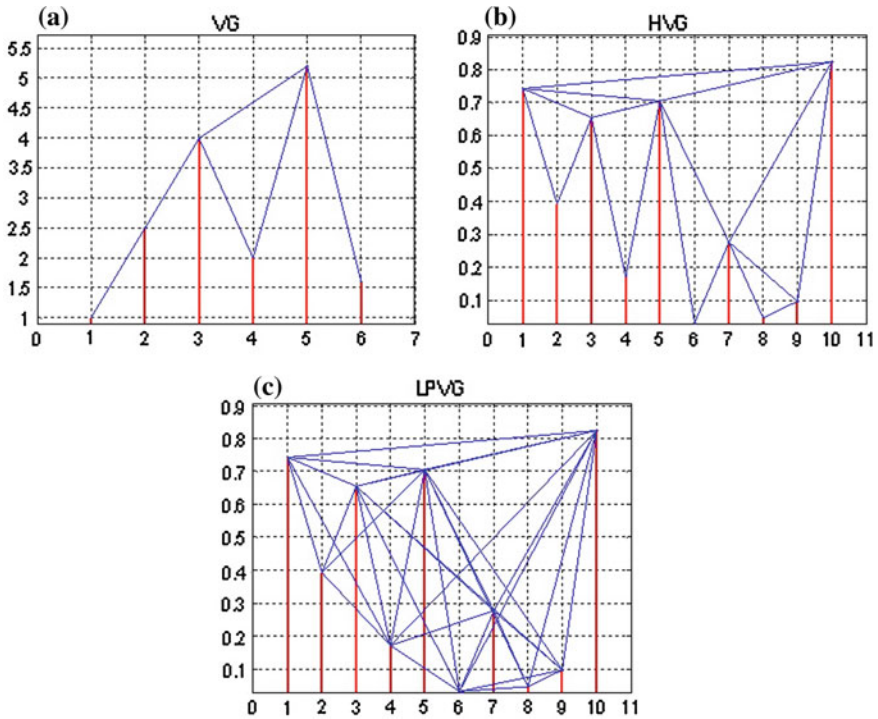
Fig. 33.1 Schematic diagram of three class network construction method based on the network. **a** *VG*, **b** *HVG*, **c** *LPVG*

33.3 Research and Analysis of Associated Digital Complex Network Characteristic of Daily Runoff Series

33.3.1 Analysis of Digital Characteristics of Associated Complex Network

This section will use three kinds of methods for establishing the corresponding associated complex network model and analysis for the America Oregon Umpqua river Elkton station which has 1347 daily runoff data from 2008.1.1 to 2011.9.8. Time series is listed as in Fig. 33.2.

Since most scholars believe that degree distribution parameters can be used to measure the frequency fluctuation pattern of sequence [5], in the next section, degree distribution of the associated networks generated by three methods are discussed first. The degree distribution analysis results can be seen in Fig. 33.3.

Generally speaking, horizontal visibility graph shows the most obvious scale-free feature, but the heavy tailed characteristics is not obvious. The head of VG and HVG degree distribution was bent, but the heavy tailed characteristics seems more
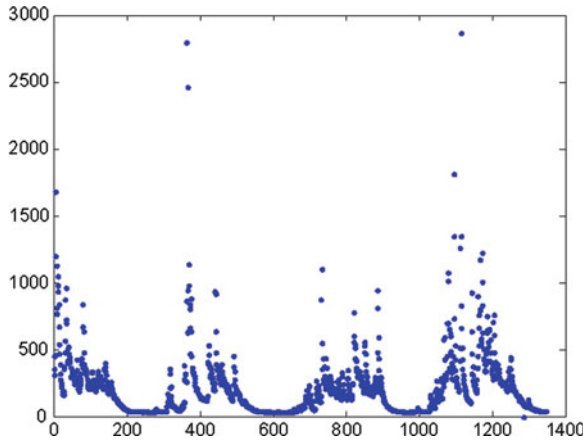
Fig. 33.2 The daily runoff data figure of Elkton station from 2008.1.1 to 2011.9.8
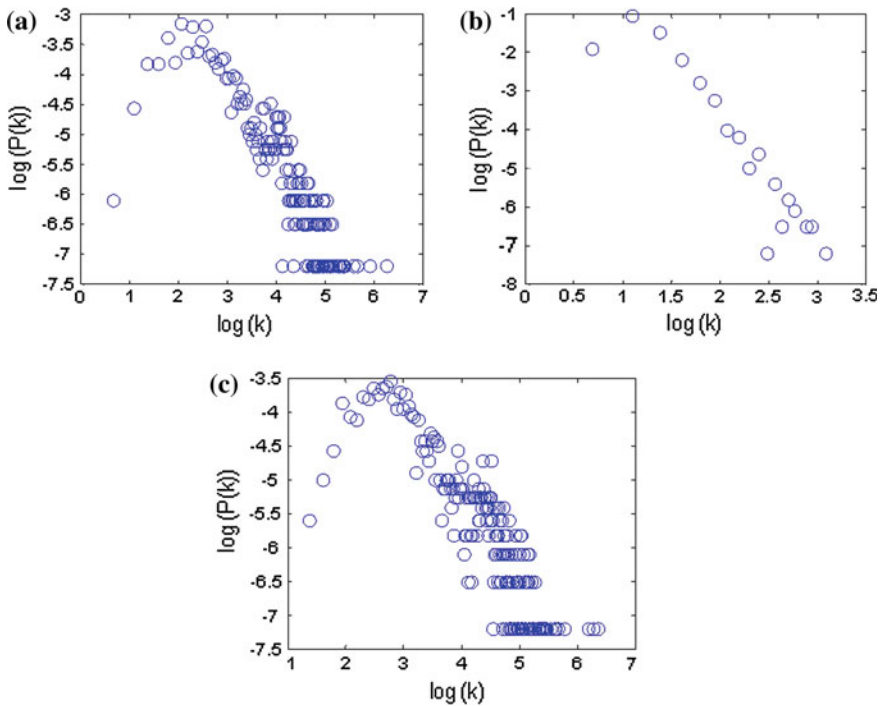
Fig. 33.3 The degree distribution for Umpqua river runoff series complex network using three different methods. **a** The degree distribution and fitting linear equation of VG $y = -1.2340x - 0.5454$; **b** The degree distribution and fitting linear equation of HVG $y = -3.4423x + 3.2043$; **c** The degree distribution and fitting linear equation of LPVG ($N = 1$) $y = -1.1653x - 0.6739$

Table 33.2 Comparative static network statistical characteristics to establish three kinds of networks

Characteristics	VG	HVG	LPVG
Network density	0.028	0.003	0.038
Network diameter	7.0	104.0	5.0
Average path length	2.897	20.850	2.703
Average clustering coefficient	0.755	0.493	0.788

obvious. From the results of three fitting curves, one can see that, with the HVG, the scaling coefficient absolute value approaches the maximum. HVG shows a higher sensitivity for description of the sequence sensitive. So, only for the time series with high fluctuations, HVG behaves better according to the results of this study.

This paper will also study the similarities and differences of other network static statistics associated with complex network model, numerical results for some typical characteristics of the calculation is shown in Table 33.2.

One can see from Table 33.2 that, for the corresponding associated networks, HVG is a kind of sparse network, its network density is small, which is close to the same scale stochastic network, and does not have the typical small world properties. That is to say, it is with larger diameter, and its average path is longer. VG and LPVG are typical small world networks, and its network density is large, with smaller diameter, and the average path is shorter. The related parameters-specific distribution map is shown in Fig. 33.3 in each sub-graph.

Finally, the basic evolution characteristics of associated network based on three kinds of methods in the evolution point are also investigated. Due to limited space, this paper only studies the evolution of the average path length of the related increasing networks. By setting 1992.7.9 runoff in Umpqua river runoff series as the starting point, we constructed the corresponding network models with three methods, then the average path lengths of the established networks are calculated as listed in Table 33.3.

The numerical results of Table 33.3 show that, according to the actual hydrological series, the network based on VG and LPVG have obvious smallworld characteristics, but the network obtained based on HVG does not have such smallworld character. In Fig. 33.4, the plot and the fitting curve of L value with the N regularity for this evolution time series is proposed. Table 33.4 gives the evaluation parameters for goodness of fitting.

Table 33.3 The average path length of the network model with different methods

$L(N)$ N	200	500	1000	3000	5000	7000
VG	2.26	3.139	3.059	3.736	3.808	4.074
HVG	10.42	22.229	15.238	22.453	19.800	21.475
LPVG ($N = 1$)	2.015	2.849	2.77	3.379	3.434	3.639
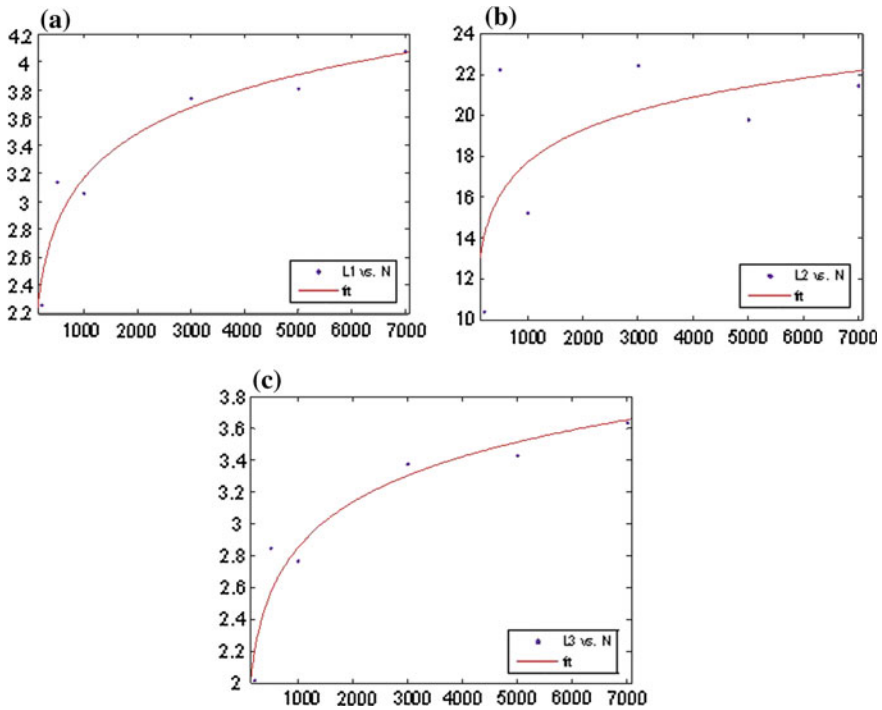
Fig. 33.4 The average path length and curve fitting of complex network using three different methods. **a** The average path length and curve fitting of VG($L1 = 0.460\ln(N) - 0.014$); **b** The average path length and curve fitting of HVG ($L2 = 2.301\ln(N) + 1.807$); **c** The average path length and curve fitting of LPVG ($N = 1$) ($L3 = 0.412\ln(N) + 0.003$)

Earlier studies have indicated that, if the average path length video network showed a logarithmic growth with the network scale, we can say it is fractal sequence [4, 5]. According to this standard, one can see that, the three kinds of networks have a similar role in finding fractal characteristics of time sequence. One can find Umpqua river runoff series has fractal characteristics, but VG and LPVG are more obvious. That is to say, from the analysis of the goodness of fit of data, VG and LPVG have better performance, HVG is not good. This also helps us in determining whether the daily runoff series have fractal properties VG and LPVG have a broad scope in future. Especially, in view of the strong anti-noise ability

Table 33.4 Characteristic index the fitting curves of L versus N under different methods

| Network methods	RSS	R-square	Adjusted R-square
VG	0.138	0.937	0.922
HVG	64.343	0.445	0.306
LPVG ($N = 1$)	0.129	0.928	0.910

LPVG, it is proposed that, for higher noise hydrological time historical data, one can use the LPVG method. The results of HVG is not better, it is suggested that this method should be avoided.

33.3.2 Communities Analysis of Complex Networks Based on Three Kinds of Methods

Community structure in the network refers to the vertices of the network that can be divided into groups, within the set of vertices connected is dense, comparison between groups of vertices connected sparse. In the study of the nature and function of the network, community structure has significant performance [7, 8], there are a lot of association classification algorithms, such as the famous community detection algorithms GN algorithm, NF algorithm et al. In addition, there are some special research methods of community structure module. In a word, study on community structure in the network is an important way to the network structure and function. Figure 33.5 shows the results of communities analysis of three kinds of network using software Gephi 0.8.2, statistical parameters are listed in Table 33.5.

From Table 33.5 one can find that, according to daily runoff series of Umpqua river, it is divided into 15 groups based on VG method, 30 groups based on HVG method, 11 groups based on LPVG ($N = 1$) method (Fig. 33.5). VG and LPVG show scale-free properties obviously, HVG shows an obvious class of stochastic
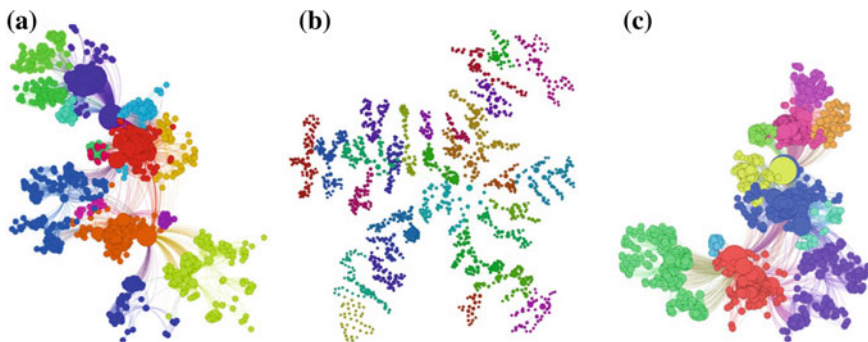
Fig. 33.5 Community chart of three types of networks (layout is Huyifan multilayer layout). **a** Community chart of VG. **b** Community chart of HVG. **c** Community chart of LPVG ($N = 1$)

Table 33.5 Comparative analysis of statistical characteristics of three types of network communities

Characteristics	VG	HVG	LPVG
Modularity	0.756	0.933	0.731
Modularity with resolution	0.756	0.933	0.731
Number of communities	15	30	11
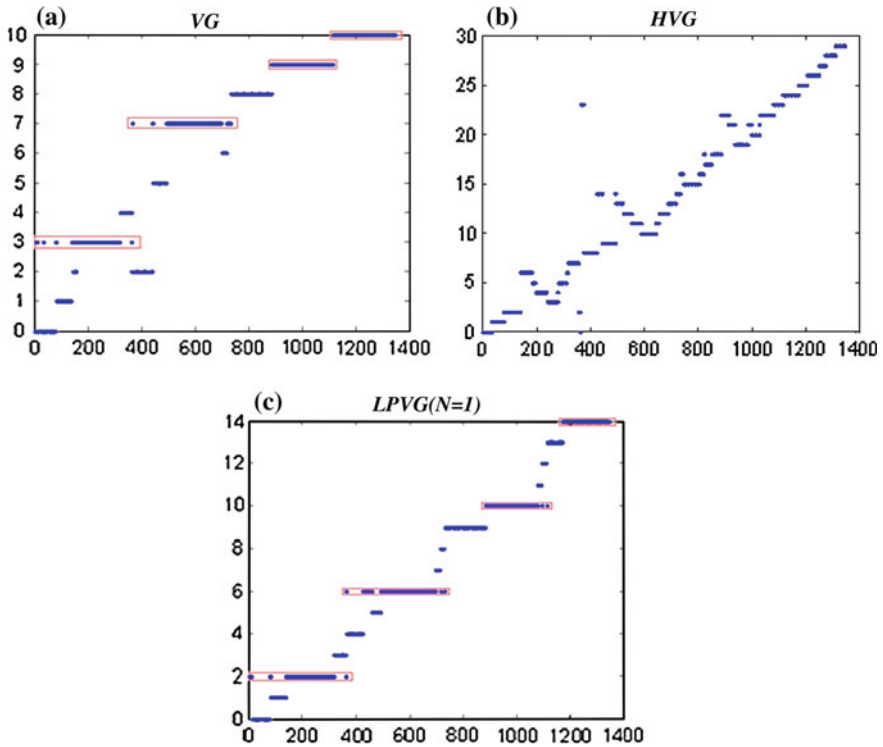
Fig. 33.6 Classification diagram of Community chart for three types of network (The *horizontal* axis is runoff $x(t_i)$ ($i = 1, 2, …, 1347$), The *vertical* axis is the moment the corresponding node runoff values belong to K_i ($i = 1, 2, …, k$) community.)

characteristics. Obviously, performance of VG and LPVG in this aspect is very close, but LPVG seems more obvious. This result and the earlier result on the distribution curve fitting goodness is completely consistent.

From Fig. 33.6, one can be seen clearly different node where the type of Association, now the sequence and the runoff time diagram (Fig. 33.1) for comparative study. From the community classification map of LPVG, one can find that daily runoff decreases gradually and tends to be stable from 1 to 100 nodes, so they are in the same class. From 100 to 200 nodes, the daily runoff reduces gradually from the stationary, so most of them are in the same class. From 200 to 300 nodes, day unchanged runoff, stay low, so most of them are in the same class. From 300 to 500 nodes, the daily runoff data are large at first and then become smaller, but in addition to individual mutation point, other data did not change much, so the classification categories are more, but most of them are in the same class, mutation into a category, from 500 to 800 nodes, except in the vicinity of the 750th node mutations. Other daily runoff data changed small, most of them are in the same class, mutation into a category. From 800 to 950 nodes, the daily runoff data

changed small, most of them are in the same class. From 950 to 1200 nodes, the daily runoff data gradually increase, most of them are in the same class. From 1200 to 1347 nodes, the daily runoff series gradually reduce, most of them are in the same class. The method of catastrophe does not reflect on about the 1200th node.

In the community classification of VG, some properties is the same as LPVG, one also see it is sensitive to mutation about the 1200th node.

In addition, by using rectangle marked the biggest club in Fig. 33.6a, c, it is easy to see that the communities analysis of LPVG has the strongest ability to distinguish between low flow period, VG can distinguish the two long dry season, but after the two segment length is close, it will be the dry season misjudgment, then HVG has distinguish ability in this respect, unable to distinguish between dry and wet season. But it is worth noting: in the classification diagram of HVG, one can see the three obvious breakpoints, they achieve local minima on about the 250th, 600th, 1000th node respectively, in the three nodes, the daily runoff precisely corresponding to a local minimum.

From the above analysis we can see, after constructing the associated networks of the runoff series based on VG and LPVG methods, through community analysis, by finding the biggest community, according to the association node number, it can be seen clearly that, the runoff in the basin of the dry season and the overall duration. after we construct the associated network runoff series based on HVG, by analyzing local minimum value in the community distribution curve, we can found local minima in corresponding runoff sequence. But whether can forecast this kind of analysis based on runoff? What is the internal mechanism of emergence of the phenomenon? These are still unknown for us all. These questions will be the future research topics to be studied.

33.4 Conclusion and Prospect

In this paper, in the perspective of complex network, based on the three methods of VG, HVG and LPVG which newly developed time series into a network graph analysis, we analyze the nonlinear properties and characterization on the daily runoff data of the America Oregon Umpqua river Elkton station. This paper first established complex associated network on the actual acquisition of runoff time series. Through calculation of basic network features, such as degree distribution, average path length, clustering coefficient, network density, we discuss the nonlinear nature. Numerical computation shows that, according to the actual hydrological series, the research results indicate that, according to the actual hydrological time series, visibility and limited penetrable visibility network have obvious small-world property, horizontal visibility do not have. In addition, the three networks have obviously the degree of distribution characteristics of scale-free networks. Overall, horizontal visibility graph showing scale-free feature is most obvious, heavy-tailed is not obvious; visibility graph and limited penetrable visibility graph have obvious bending head, heavy-tailed feature is more obvious. From the fitting

results of three degree distribution curve can be seen that: the coefficient absolute value of horizontal visibility network is the largest, this shows the sequence of high sensitivity. Also, according to the community analysis, we also find that, the limited penetrable visibility graph is good to classify withered water period, visibility graph's ability is bad, horizontal visibility graph's ability is worse. Through horizontal visibility graph, we can find the local minimum of hydrological time series, this is consistent to the result of degree distribution. Results of this paper also shows that, there are similar results in many aspects in VG and LPVG network establishing based on the real data, whether the analysis of static statistical character of network or community analysis can obtain similar results, but HVG networks' results with the difference between the two is relatively large, this can be very easy to see from our earlier analysis. The most obvious is the community classification, obviously, relatively large differences. Then whether the analysis results based on VG have potential significance needs further research. In this paper, we do not consider LPVG with larger N and other two kinds of networks of similarities and differences. In the near future, we will develop some comparative research in this area. In addition, we can analyze this kind of hydrological time series which contains a certain noise ratio and study the three kinds of networks for nonlinear analysis of anti-noise ability.

References

1. Lacasa L, Luque B, Ballesteros F, Luque J, Nuno JC (2008) From time series to complex networks: the visibility graph. Proc Natl Acad Sci 105(13):4972–4975
2. Nunez M, Lacasa L, Gomez JP, Luque B (2012) Visibility algorithms: a short review, New Frontiers in Graph Theory. intechweb.org. Edited by Yagang Zhang, Chapter 6:119–152
3. Zhao L, Tang Z, Wang J, Wang J, Yang H (2011) Time series analysis based upon complex network. J Univ Shanghai Sci Technol 33(1):47–66 (in Chinese)
4. Tang Q, Liu J (2009) Network analysis of Shanghai stock exchange composite index and Shenzhen stock exchange component index. In: Proceeding of WHICEB 2009, vol I, pp 883–887
5. Tang Q, Liu J, Liu HL (2010) Comparison of different daily streamflow series in US and China, under a viewpoint of complex networks. Mod Phys Lett B 24(14):1541–1547
6. Zhou T, Jin N, Gao Z, Luo Y (2012) Limited penetrable visibility graph for establishing complex network from time series. Acta Phys Sin 61(3):94–104 (in Chinese)
7. Brandes U (2001) A faster algorithm for betweenness centrality. J Math Soc 25(2):163–177
8. Vincent D, Blondel J-LG, Lambiotte R, Lefebvre E (2008) Fast unfolding of communities in large networks. J Stat Mech: Theory Exp 10:P1000

Chapter 34
Path Planning in Changing Environments Based on "Frame" Difference

Zhi Wang, Fang Xiao and Hong Liu

Abstract An effective path planner to solve difficult region problems in changing environments is proposed in this paper. When obstacles move at uncertain speeds, difficult regions change their characteristics accordingly. Identifying difficult regions is a thorny issue. A novel method using "Frame" Difference (FD) is presented in this paper, which is motivated by the idea of moving object detection. Changing regions are detected by FD and obstacle speed can be predicted qualitatively by counting the number of toggle points in those regions. Then, in order to adapt to different speeds, hybrid difference algorithm (HDA) which is a hybrid of adjacent frame difference or K-frame difference is proposed. HDA provides enough movement information of obstacles, and leads to safe path planning. Experiments conducted with a dual-manipulator system show that our method has lower replanning times and higher success rate than related planners, such as capacitor bridge builder and dynamic bridge builder.

Keywords Path planning · Changing environment · Frame difference · PRM

34.1 Introduction

During last two decades, with the development of sampling-based framework [1], a great progress of research in static environments has been obtained, especially rapidly-exploring randomized tree (RRT) [2] and probabilistic roadmap method

Z. Wang (✉)
University of Science and Technology, Beijing 100083, China
e-mail: zhiwang0503@163.com

F. Xiao
Shenzhen Graduate School of Peking University, Shenzhen 518055, China
e-mail: 1201213677@sz.pku.edu.cn

H. Liu
The Key Laboratory of Machine Perception, Peking University, Beijing 100087, China
e-mail: hongliu@pku.edu.cn

(PRM) [3]. In static environments, many variants of randomized algorithms are proposed for difficult region problems, like obstacle-based PRM [4], Bridge Test [5] and Gaussian Sampling Strategy [6]. However, in changing environments, due to the movement of obstacles in workspace (W-space), configurations occupied by obstacles (C-obstacle) will change accordingly. As a result, roadmap cannot accurately reflect the current state of the configuration space (C-space).

Dynamic Roadmap Method (DRM) [7], as a PRM derivative, computes mapping from W-space to C-space (W–C mapping) to solve problems in changing environments, instead of online collision detection. Dynamic bridge builder (DBB) [8] is a combination of DRM and bridge Test. Although DBB performs well on narrow passages identification, it cannot guarantee safety when obstacles are moving. Capacitor bridge builder (CBB) [2] has been proposed as a safe path planning method on the basis of DBB. However, CBB only identified "capacitor" bridges, it cannot cover all of difficult regions.

In this paper, "Frame" Difference (FD) [9] is used initially in path planning. In changing environments, continuous environments are discretized into static fragments. Each fragment is considered as a "frame," and we construct and update the roadmap in it. In preprocessing phase, points are sampled hierarchically. Then W–C mapping is computed with all points. In updating phase, though FD, changing regions are detected, and the number of toggle points is counted. In order to adapt to different speeds and provide enough movement information, hybrid difference algorithm (HDA) is proposed. After detecting changing regions, difficult regions are identified by bridge planner. Incremental points are activated around the safe endpoints of bridges. The overview of our method is illustrated in Fig. 34.1.

34.2 Safe Path Planning Based on "Frame" Difference

34.2.1 Hierarchy Sampling Strategy (HSS)

In changing environments with difficult regions, planning methods need to not only identify difficult regions accurately, but also increase sampling points in those regions rapidly. HSS reduces the size of W–C mapping by sampling useful points, in order to improve efficiency of path planning (Fig. 34.2).

34.2.2 Changing Regions Detection by "Frame" Difference

By comparing information with adjacent time fragments, changing regions can be detected and movement tendency can be predicted in the next-time fragment.
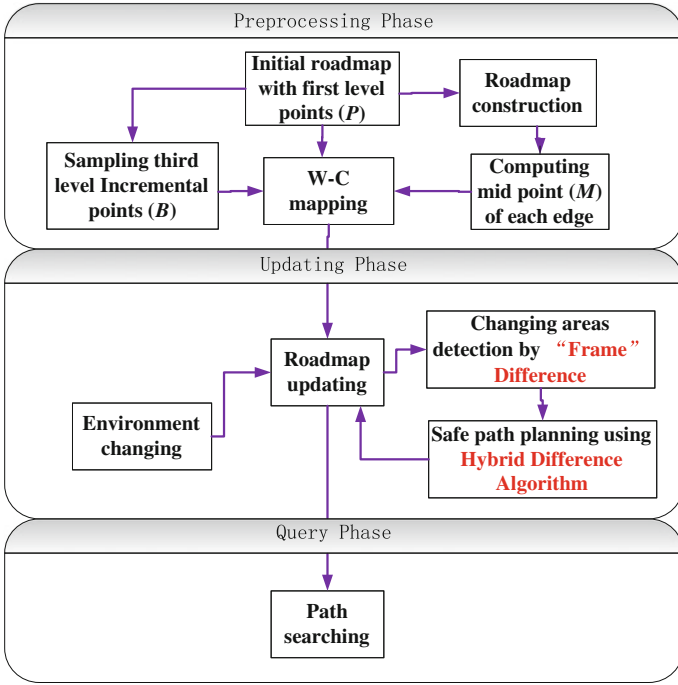
Fig. 34.1 Overview of our method

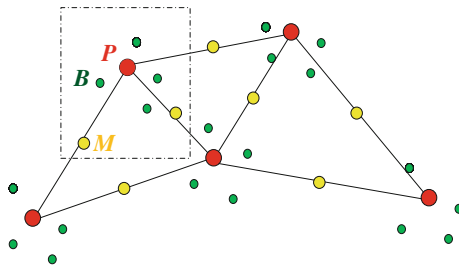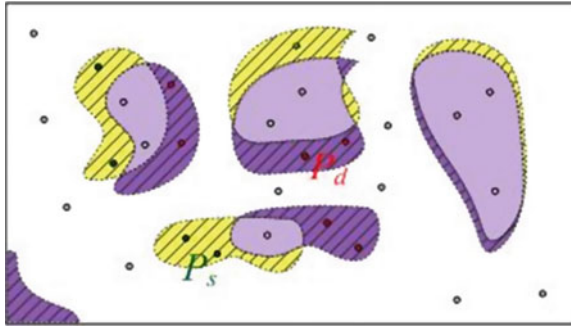**Fig. 34.2** Hierarchical sampling strategy. *Red*, *yellow*, *green* points are in first level (*P*), second level (*M*), and third level (*B*), respectively

Inspired by the moving object detection based on differenced frame process [9], continuous dynamic environments are discretized into static fragments. Each fragment is considered as a "frame," and we build and update the roadmap in it.

Fig. 34.3 Changing region detection. The regions in *purple* represent current C-obstacle and *yellow* represents their previous position. *Purple* with shadow presents the dangerous region and *yellow* with shadow presents the safe region. P_s is the set of safe points. P_d is the set of dangerous points

The simple way to detect changing regions may be to calculate the difference between previous frame and current frame, called Adjacent-FD. Changing regions are filled with shadow in Fig. 34.3.

$$D^t(p) = V^t(p) - V^{t-1}(p) \tag{34.1}$$

Here, for each $p \in P$, $D^t(p)$ represents the difference of validity of p between frame t and $t-1$. If $D^t(p) = 2$, it means that $V^t(q)$ toggles from -1 to 1. On the contrary, $D^t(p) = 2$ means $V^t(q)$ toggles from 1 to -1. After Adjacent-FD, the number of the toggle points is counted, denoted by N_t.

From another point of view, N_t indicates the motion amplitude of obstacles. If the number of toggle points N_t is larger than threshold T, it means movement speed is relatively fast. If N_t is smaller than T, it means slow and moderate.

34.2.3 Hybrid Difference Algorithm (HDA)

Adjacent-FD computed above is simple and easy to implement, but it cannot provide enough information for slower moving obstacles. Moving slowly means inadequate toggle points with a little information of movement tendency. For the purpose of making motion tendency to be obvious, K-FD is chosen as an improvement.

The new algorithm called K-FD uses current frame to minus previous K frames, respectively,

$$D_k^t(p) = V^t(p) - V^{t-k}(p) \quad (\text{for each } p \in P, k = 1, 2, \ldots, k) \tag{34.2}$$

$$D^t(p) = \bigcup_{k=1}^{K} D_k^t(p) \tag{34.3}$$

Here, $D_k^t(p)$ represents the difference of validity of p between frame t and $t-k$. $D^t(p)$ is the final difference we want. As long as the difference of adjacent K frames does exist, our method can detect it. If K is too small, motion regions are not that obvious. However, if K is too large, the detection will be too sensitive. Drawn from the experiments, K is set to be 3.

Algorithm 34.1: Hybrid Difference Algorithm

Input: $P = \{p_1 \cdots p_n\}$, Frame t, Frame t-1
Output: P_s , P_d
  1 **for** each point $p \in P$ **do**
  2   Compute Adjacent-FD:
          $D^t(p) = V^t(p) - V^{t-1}(p)$
  3   Compute the number of toggle points
          $N_t = \sum |D^t(p)| /2$
  4 **end for**
  5 **if** $N_t <$ threshold T **then**
      Obstacles move fast
      Compute K-FD:
  6   **for** $k \leqslant K$ **do**
  7        $D_k^t(p) = V^t(p) - V^{t-k}(p)$
  8        $D^t(p) += D_k^t(p)$
  9   **end for**
10 **else** $N_t \geqslant$ threshold T
11   Continue to use Adjacent-FD
12 **end if**
13 **if** $D^t(p) > 0$ **then**
14    $p \in P_s$
15 **else if** $D^t(p) < 0$ **then**
16    $p \in P_d$
17 **end if**

HDA is a hybrid of Adjacent-FD and K-FD. The purpose of using it is to guarantee the number of toggle points. When obstacles move slowly, HDA enables N_t to be enough to build bridges by choosing K-FD. When obstacles move fast, HDA choose Adjacent-FD as before. After HDA, we get $D^t(p)$, which is used to classify p. If $D^t(p)$ is positive, add p to P_s. If $D^t(p)$ is negative, add p to P_d. $D^t(p) = 0$ indicates no difference among K frames. Details are shown in Algorithm 34.1.

34.2.4 Bridge Builder and Boosting Strategy

A Dynamic Bridge Builder with HDA is used in this paper. As shown in Fig. 34.4, after classifying p, this kind of bridges will be flagged: One of the endpoints belongs to P_s, colored in green, the other endpoint belongs to P_d, colored in red, and the midpoint is in C-free, colored in yellow.

Fig. 34.4 Bridge builder and boost strategy. Bridges are built between P_s and P_d, and incremental points are activated around P_s
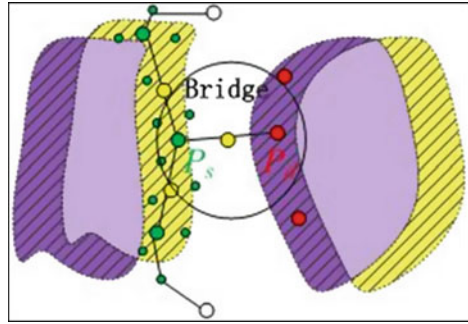
According to safe path planning, endpoints $p \in P_S$ are safer than other points, because they always behind obstacles. These points are chosen to be boost, which means incremental points around them will be activated, as shown in Fig. 34.4. Little green points are the third-level points around safe points. This boosting strategy makes more sampling points in safe regions, so that the path we searched will be relatively safe in a short time.

34.3 Experiment and Discussions

To evaluate the proposed method, simulated experiments are implemented in 3D scenario in hundreds of times. The proposed algorithm is mainly for the narrow passages in changing environments. Only when the narrow passages are included can reflect the superiority of it. In 3D W-space, there are two manipulators modeled by parameters of practical 6-DOF Kawasaki manipulators (FS03 N). The dual-manipulator system with 12-DOFs is planned to check the efficiency of algorithm in high-dimensional C-space. Here, we use Coldet2.1, which is popular and free, to conduct collision detection. All our experiments are performed on an ordinary personal computer with 3.00 GHz CPU and 2 GB memory. Experimental results are based on an average of 500 executions.

Generally, when a significant difficult region appears in W-space, C-space will be a corresponding difficult region. Hence, the experimental scenario (Fig. 34.5a) we set includes a number of difficult regions. It involves a rectangular board with a hole in the middle which is placed between two manipulators. The start configuration is randomized (Fig. 34.5b), and the goal configuration is a grasper docking motion through the hole which is difficult to complete (Fig. 34.5c). The rectangular board is always moving up and down at different speeds.

Table 34.1 shows the number of bridges built at different speed using our method. Because of the adaptability to speed, HDA can obtain enough toggle points
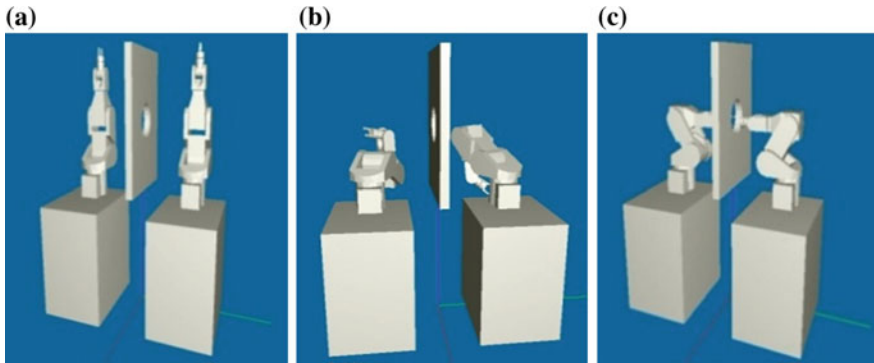
Fig. 34.5 a Simulation scenario. **b** A randomized start configuration. **c** A goal configuration

Table 34.1 Bridge builder results based on HDA

P	Speed	Num of bridges			Time (s)
		Max	Min	Ave	
1000	2	153	57	99	0.0037
	3	171	80	118	0.0038
	4	159	68	108	0.0037
2000	2	317	172	231	0.0046
	3	384	196	278	0.0048
	4	346	190	259	0.0048

in changing regions, although obstacles move slowly. As shown in Table 34.1, to different speed, the number of bridges which our method builds is almost the same.

As shown in Table 34.2, our method contributes to higher success planning rate (SPR) and lower average replanning times (ART) than other methods in the table. When obstacles move slowly, the number of toggle points in CBB is limited,

Table 34.2 Results of comparison experiment between HDA, CBB and DRM at different speeds

Method	Speed	SPR	ART	ST
Our method	2	94.13	14.91	9.05
	3	94.09	15.37	8.54
	4	94.10	15.39	8.36
CBB	2	91.98	28.33	16.01
	3	93.10	22.19	12.28
	4	94.03	16.83	9.39
DRM	2	90.47	48.72	48.11
	3	87.69	57.36	59.83
	4	81.70	70.04	71.29

leading to insufficient number of bridges. On the contrary, HDA can obtain suffi-
cient toggle points adaptively according to the speed. Although HDA need to
activate more incremental nodes, it gives rise to good performance in replanning, as
shown in the last two columns in Table 34.2. ART of our method is lower than
CBB and DRM. Meanwhile, ART of our method has no obvious change in different
speeds because of the adaptability. Moreover, compared with DRM, our bridge
builder using HDA costs less time with higher success rate.

34.4 Conclusions

Motivated by the idea of moving object detection based on differenced frame
process, our method uses "Frame" difference to detect difficult regions. A novel
hybrid difference algorithm (HDA) is presented in this paper, which is designed for
adapting uncertain speeds of obstacles in changing environments. Our method,
combined with bridge test, can identify the difficult regions fast and easily.
Experimental results in complex environment show that our method is superior to
previous methods in success planning rate (SPR), average peplanning times (ART)
and sum of time (ST). Generally speaking, HDA, as a method based on FD, is a
novel method to solve planning problems in real time.

References

1. Kavraki LE, Svestka P, Latombe JC, Overmars MH (1996) Probabilistic roadmaps for fast path planning in high-dimensional configuration spaces. IEEE Trans Robot Autom 12(4):566–580
2. Liu H, Zhang T (2012) A capacitor bridge builder based safe path planner for difficult regions identification in changing environments. In: IEEE/RSJ international conference on intelligent robots and systems, pp 3180–3186
3. Geraerts R, Overmars MH (2004) A comparative study of probabilistic roadmap planners. In: Algorithmic foundations of robotics V. Springer, Berlin, Heidelberg
4. Amato NM, Bayazit OB, Dale LK, Jones C, Vallejo D (1998) OBPRM: an obstacle-based PRM for 3D workspaces. In: Proceeding international workshop on algorithmic foundations of robotics, pp 155–168
5. Hsu D, Jiang T, Reif J, Sun Z (2003) The bridge test for sampling narrow passages with probabilistic roadmap planners. In: Proceedings IEEE international conference on robotics and automation, vol 3, pp 4420–4426
6. Boor V, Overmars MH, van der Stappen AF (1999) The Gaussian sampling strategy for probabilistic roadmap planners. In: Proceedings IEEE international conference on robotics and automation, vol 2, pp 1018–1023
7. Leven P, Hutchinson S (2002) A framework for real-time path planning in changing environments. Int J Robot Res 21(12):999–1030

8. Ding D, Liu H, Deng X, Zha H (2007) A dynamic bridge builder to identify difficult regions for path planning in changing environments. In: IEEE/RSJ international conference on intelligent robots and systems, pp 2925–2931
9. Zhan C, Duan X, Xu S, Song Z, Luo M (2007) An improved moving object detection algorithm based on frame difference and edge detection. In: Fourth international conference on image and graphics, pp 519–523

Chapter 35
Preliminary Design of a Flat-Staircase Intelligent Wheelchair

Zhengchao Zhou, Juanxiu Liu and Yifei Wu

Abstract The traditional manual wheelchairs and even electric wheelchairs do not have the function of climbing stairs, which limits freedom of the users. A flat-staircase intelligent wheelchair is presented in this article to improve the quality of the users' life, making them have more space and freedom. The article firstly introduces the mechanical structure of the intelligent wheelchair and elaborate the stair-climbing and flat-moving principle. Then according to the concept of modularization design, this article respectively puts forward the driving and controlling scheme of stair-climbing module and flat-moving module. Afterwards, the main controller hardware circuit based on TMS320F28335, operating lever hardware circuit and the driving hardware circuit of stair-climbing motor and flat-moving motor are given respectively. Next, the system software modules of the wheelchair is put forward and underlying driving program is written to realize motor control of brushless commutation and closed-loop speed control based on Partition PI algorithm. Then the joint debugging of the intelligent wheelchair is carried on and the test data figure is provided. Finally, the article summarizes the project and puts forward the prospects for future work.

Keywords Intelligent wheelchair · Climbing stairs · BLDC · DSP · IPM

35.1 Introduction

Population aging is becoming one of the major crises facing the world today. At present, China is the only country that the elderly population exceeded 200 million. At the same time, the number of lower limb disabilities increased year by year [1]. In order to facilitate the daily lives of the elderly and lower limb disabilities, various walking-aid devices emerged. Wheelchair becomes the most widely used walking-

Z. Zhou (✉) · J. Liu · Y. Wu
College of Automation, Nanjing University of Science and Technology,
Nanjing 20094, China
e-mail: gurvala@qq.com

aid device because of its smart, convenient, and simple operation. However, the traditional wheelchairs do not have the function of climbing stairs, which limits freedom of the users. A flat-staircase biservice intelligent wheelchair is presented in this article to improve the quality of the life of the elderly and the disabled.

Research and invention of flat-staircase biservice wheelchair has a history of hundreds of years. Over the last decade, foreign markets have launched a variety of commercial flat-staircase biservice intelligent wheelchairs. According to the different principle of stair-climbing, the flat-staircase intelligent wheelchairs are mainly divided into wheels-set type, crawler type, and walking type [2]. But most of these foreign wheelchairs have disadvantages of complex operation and high price that most Chinese consumers cannot afford them. Considering the market demand in China, it is significant to design a flat-staircase biservice intelligent wheelchair of simple operation and stable working, which Chinese consumers can afford. The flat-staircase biservice intelligent wheelchair presented in this article is semi-automatic, it belongs to wheels-set type wheelchair.

35.2 Mechanical Structure

The flat-staircase intelligent wheelchair adopts wheel-leg hybrid mode in structure, but there is no interference between the wheels and legs. Moving at grounds, the wheelchair is controlled by users independently. The intelligent wheelchair can be assisted by others to climb up and down the stairs. The intelligent wheelchair has a separate structure of wheels and legs that the stair-climbing module and the flat-moving module are designed independently [3]. The intelligent wheelchair consists of body, stair-climbing module, ground driving rear-wheels, solid guide-wheels, control driving device, operating lever, battery, and so on. Three-dimensional structure of the wheelchair is shown in Fig. 35.1.
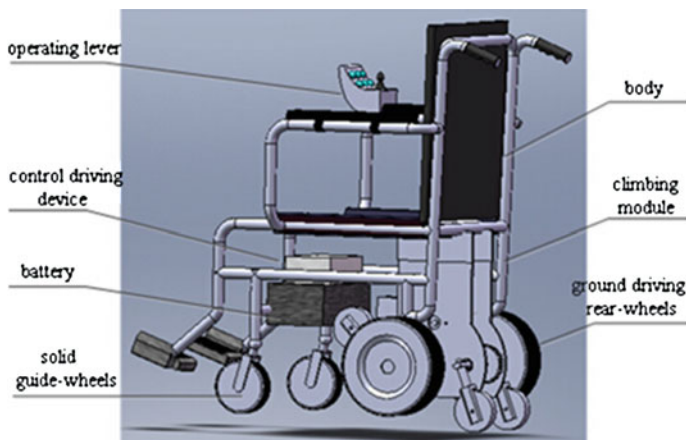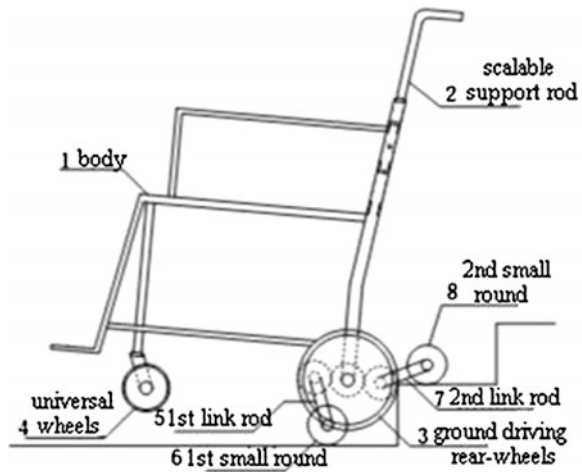

Fig. 35.1 Three-dimensional structure of the wheelchair

Fig. 35.2 Profile of the intelligent wheelchair

The intelligent wheelchair has four flat-wheels: two universal front-wheels, two driving rear-wheels. There are two brushless DC motors mounted in the rear-wheels hubs. When the wheelchair moves on the ground, two groups of climbing link rods and small rounds of the stair-climbing module adjust to the appropriate position which the ground do not contact with. The user makes the wheelchair move on the ground by the operating lever. The wheelchair moves straight forward and backward by the synchronous speed control of the rear-wheels and it makes a turn by the differential speed control of the rear-wheels. Profile of the intelligent wheelchair is shown in the Fig. 35.2.

The summary of stair-climbing module principle: when rear-wheels touch the edge of steps, the intelligent wheelchair begins the climbing mode. The helper behind tilts the wheelchair backwards an angle, then the climbing motor drives the transmission gear. 1st link rod and 2nd link rod revolve round clockwise their axes at a constant speed until the 1st small round first hit the ground. 1st small round plays a supporting role and applies pressure to the ground by the force of 1st link rod. The wheelchair is lifted gradually until 2nd small round touches the next step. At this time, 1st small round and 2nd small round touch the ground and the step respectively, both have the effect of supporting and applying force. The wheelchair is lifted again under the effect of both round until 1st link rod is perpendicular to the ground. After that, 1st small round begins to leave the ground, 2nd small round still touches the step and plays a role of supporting lift the wheelchair alone. Then the wheelchair is still lifted by 2nd small round and the helper. Finally, it climbs one step successfully. Repeating the above actions, the wheelchair climbs the stair in a way of semi-automatic [4].

35.3 Driving and Controlling Scheme

We put forward the driving and controlling scheme of the stair-climbing and flat-moving module. Motor is the core part of driving transmission to work and the basis of driving and controlling scheme. Brushless Direct Current Motor has the advantages of small volume, small internal friction, reliable operation, good speed performance. So we chose BLDCs as the stair-climbing motor and flat-moving (wheel hub) motor. The climbing movement and flat movement are driven by separate mode. The driving and controlling scheme of stair-climbing module is shown in Fig. 35.3.

The logic commutation, speed control, current control of the stair-climbing motor are completed by TMS320F28335. Speed feedback is realized by using eCAP module of TMS320F28335. Hall sensor is applied to the stair-climbing motor to measure current. Then we sample the output voltage by AD sampling module of TMS320F28335 and achieve closed-loop current control by software. Power amplifier of inverter bridge and current sampling are completed by Intelligent Power Module (IPM) circuit. IPM is an advanced power switch device which integrates the control, detection, protection circuit inside. The driving and controlling scheme of flat-moving module is shown in Fig. 35.4.

The speed measurement chip MC33039 can achieve the frequency doubling of hall signal. From the figure, the driving circuit that consists of MC33035 and MC33039 is mainly responsible for production of PWM, rotor decoding, logic commutation, closed-loop current control, and inverter driving. The main control circuit based on TMS320F28335 is mainly responsible for frequency sampling, speed calculation, and speed adjustment.
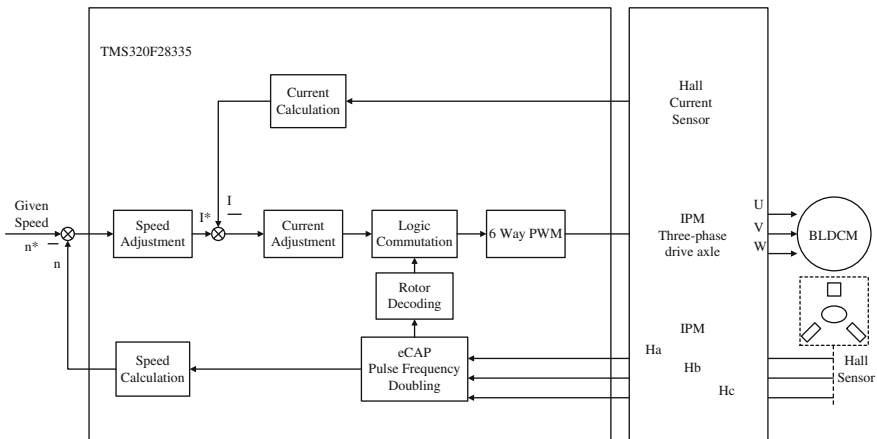
Fig. 35.3 Driving and controlling scheme of stair-climbing module
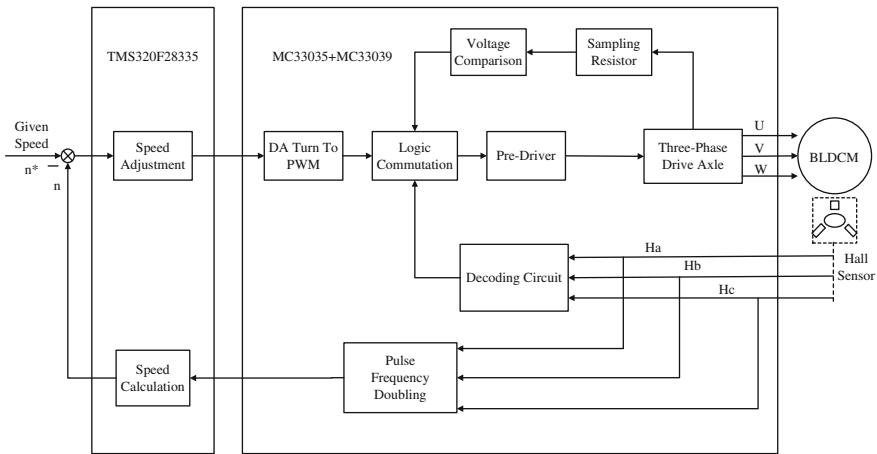
Fig. 35.4 Driving and controlling scheme of flat-moving module

35.4 Hardware Circuit

The structure diagram of the hardware circuit is shown in Fig. 35.5.

The control and driving system of this wheelchair first need to provide the users operating lever module, operating lever module will send operation intention and driving intention to the main control circuit through the communication circuit; The main control circuit and the driving circuit have to complete the speed and current closed-loop control not only of the wheel hub motors, but also of the stair-climbing motor.

The main control circuit is the core of the controlling and driving part of the intelligent wheelchair. Its main function is to receive the command signals from the operating lever circuit to achieve motor control algorithm. The main control circuit makes driving circuit drives the stair-climbing motor and flat-moving motors running.

Fig. 35.5 Structure diagram of the hardware circuit
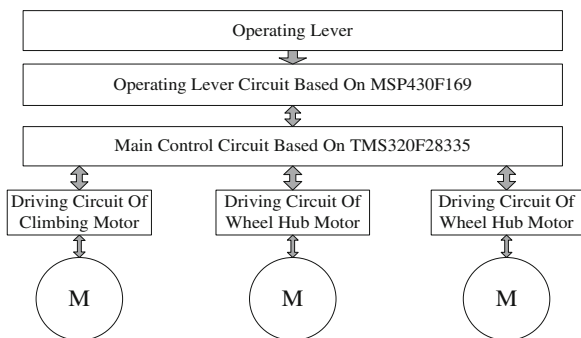
35.5 Software Design

The system software module is divided into two sections: a main controller TMS320F28335 and a operating lever controller MSP430F169. TMS320F28335 part has CAN communication module, speed control module, D/A driving module and initialization module, speed control module includes commutation module, speed detection module, control algorithm module, and pulse width modulation module; MSP430F169 part includes CAN communication module, key driving module, LCD driving module, A/D sampling module, and initialization module. The software module division is shown in Fig. 35.6.

Speed of the motor is adjusted by Partition PI control algorithm. The theory of Partitioned PI control algorithm is selecting the different values of PI parameter according to different feedback error. The feedback error is divided into large error area and small error area. At the large error area, increase the proportion value to make the system respond quickly; At the small feedback error area, increase the integration value to make the system work in steady state and ensure the system accuracy. Position type PI algorithm is shown as follows:

$$u(k) = K_p e(k) + u_I(k) = K_p e(k) + K_I e(k) + u_I(k-1) \qquad (35.1)$$

Each speed adjustment has updated the output value and integral value at the same time and limit the amplitude.
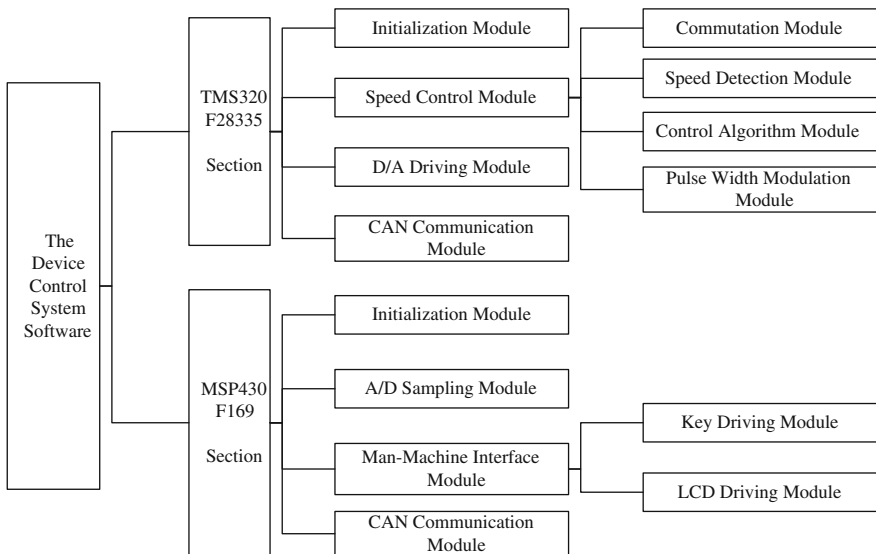
Fig. 35.6 The software module division

35.6 Joint Debugging

Experiment environment and platform of physical prototype is shown in Fig. 35.7.

The ground movement debugging: when the wheelchair moves straight, the given speed is 3 km/h, the rotational speed of wheel hub motors is 63 rpm. and the rotational speed of internal motor is 279 rpm, the control voltages of the left and right wheels are given 2.4 V and the directions are both forward. We get the speeds of left and right wheels by eCAP and the speed curves are shown in Fig. 35.8. When the wheelchair spot turn, the control voltages of the left and right wheels are given 2.4 V but the directions are opposite. The speed curves are shown in Fig. 35.9.

The climbing movement debugging: the wheelchair is not load-bearing and in human assisted, the speed and error curve of the first 10 s of climbing are shown in Figs. 35.10 and 35.11. Effects of backlash error by the transmission device, non-uniform friction, and external adjustment of helpers, speed fluctuates greatly.

Fig. 35.7 The experiment environment and platform

Fig. 35.8 Speed curves of straight move
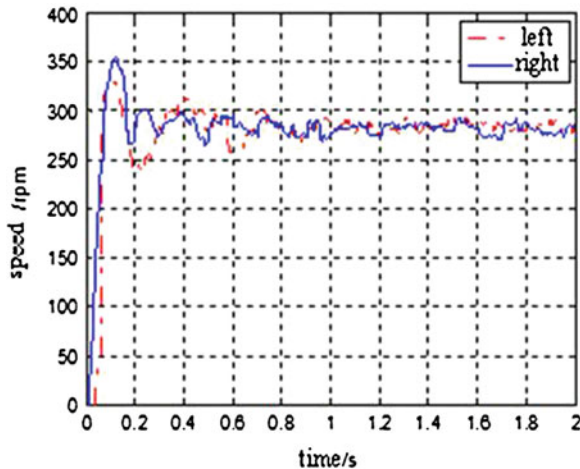
Fig. 35.9 Speed curves of spot turning

Fig. 35.10 Step response of 900 rpm

Fig. 35.11 Error curve of 900 rpm

35.7 Summary and Prospect

The debugging conditions and debugging results still lags far behind the actual climbing stairs, but debugging process verifies the feasibility of the transmission scheme of climbing module in principle and it also verifies the feasibility of control system. The above work can lay a good foundation to further improve the climbing module [5].

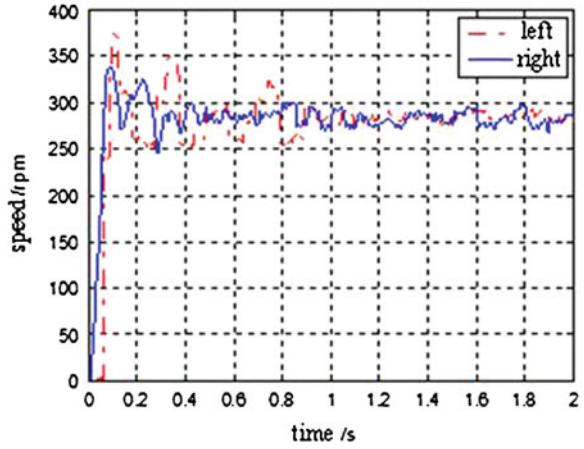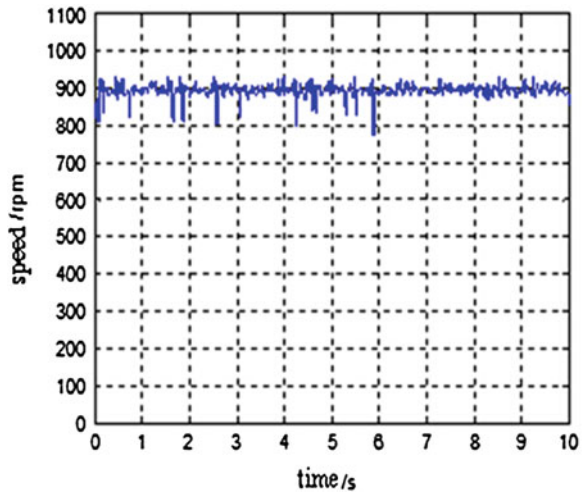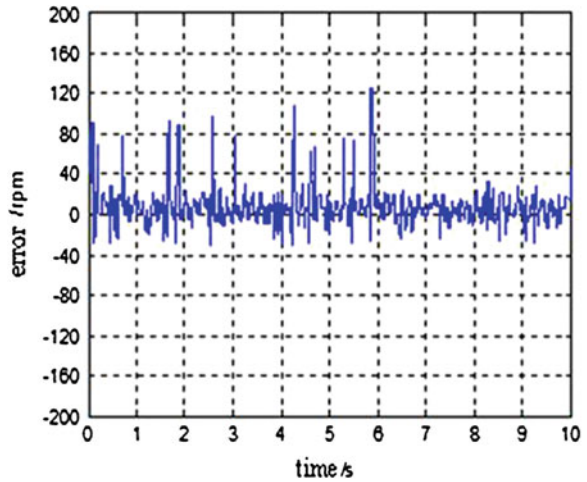Because design and development of wheelchair involves wide knowledge and design time is short, we need to make improvement and further research on the following aspects:

(1) By constraints of processing and assembly, it is difficult to conduct manned test for the wheelchair prototype. Later on we can make further improvement of materials, processing conditions and transmission size, and design test scheme.
(2) Install the touch, visual, infrared, attitude, and position sensors to prototype and research on information fusion, make it more user-friendly and intelligent [6].
(3) Conduct voltage and current safety monitoring of the battery, improve power supply scheme of the wheelchair and make it move off-line.

References

1. Chen CT, Pham HV (2012) On climbing winding stairs in an open mode for a new robotic wheelchair. Adv Robot 26(1–2):63–82
2. Arthanat S, Desmarais JM, Eikelberg P (2012) Consumer perspectives on the usability and value of the iBOT® wheelchair: findings from a case series. Disabil Rehabil: Assist Tech 7 (2):153–167
3. Tong Z (2014) The design of control system of flat-staircase biserve device based on aSPACE. Nanjing University of Science and Technology, Master's thesis, pp 9–10
4. Chen Q (2009) Flat-Staircase biserve walking-aid device. Chinese patent, 200910027397.2
5. Quaglia G, Franco W, Oderio R (2009) Wheelchair q, a mechanical concept for a stair climbing wheelchair. In: IEEE international conference on robotics and biomimetics (ROBIO), IEEE, pp 800–805
6. Morales R, Gonzalez A, Feliu V et al (2007) Environment adaptation of a new staircase-climbing wheelchair. Auton Robots 23(4):275–292

Chapter 36
A New Robot Manipulator Uncalibrated Visual Serving Control Method

Wang Niu, Liu Lang and Qiu Jing

Abstract This paper presents a new robot manipulator uncalibrated visual serving control method, which can conduct visual feedback control under the situation that the internal and external of camera parameters and the robot manipulator model are unknown, as well as without real-time computing the inverse of image Jacobian. First, the dual cameras biaxial parallel vision configuration is applied to detect the posture of the characteristics of robot manipulator end. Then, we select the specific feature points and lines in the image plane in order to represent the five degrees of freedom of the robot manipulator in cartesian space and design a PI controller. Finally, we realized the five degrees of freedom of the robot manipulator uncalibrated visual serving control in the actual physical platform, and the experiment results show that the effectiveness of the proposed control method under the dual cameras biaxial parallel vision configuration.

36.1 Introduction

Robot manipulator uncalibrated visual serving refers to its through constant iteration, real-time access and update the quantitative relationship between image space and working space, as well as it has no explicit calculate the internal and external parameters of the camera [1]. According to the number of camera in the uncalibrated visual serving system, it can be divided into monocular vision systems, binocular vision systems, and multipurpose vision system [2, 3]. The dual cameras vision configuration can get the three-dimensional information of the object without the object's geometry information. In the article [4], Wang et al. make robot

W. Niu (✉) · L. Lang · Q. Jing
College of Automation, Chongqing University, Chongqing 400030, China
e-mail: wangniuwn123@163.com

manipulator movement in the three-dimensional coordinate to decompose into the depth of focus movement Z-axis in one-dimensional and XY plane motion in two-dimensional by using stereomicroscopic vision system. Robot manipulator end is guided by the coarse and fine level of the depth visual in order to perform circular path tracking in the XY plane. In the paper [5], the automatically marking control systems with dual camera orthogonal vision configuration is successfully applied to gas bottles automatic marking by Chen. In the article [6], Harbin Institute of Technology using the orthogonal vision configuration developed the microscopic visual micro-manipulator control system that has been successfully used in optical fiber butt. But the dual cameras need to meet strictly orthogonal vision configuration so that it can achieve the corresponding functions in the article [4–6]. In reference [7] Liu et al. used the Kalman filtering estimation algorithm to estimate image Jacobian matrix and realized robot manipulator five degrees of freedom uncalibrated visual servo control under the eye-to-hand configuration of dual cameras. Paper [8] Assa et al. put forward the binocular camera sensor data fusion method, which two cameras use eye-in-hand and eye-to-hand configuration, to use ordered weighted average data fusion and extended Kalman filter algorithm to estimate pose and improve the accuracy of estimation and robustness. But the paper [7, 8] have to calculate the image Jacobian matrix or estimate the nonlinear mapping model so as to a large amount of calculation is needed. Paper [9] Chang, etc., calibrate the relationship between the camera and robot manipulator in advance, complete automated assembly cell phone cover by robot using the eye-in-hand binocular stereo vision system. Paper [10] Wang et al., designed a controller to realize grab the target task, which track the target by the camera eye-in-hand configuration and use the stereo vision to obtain the target depth information. But paper [9, 10] need to calibrate the camera parameters resulting in the complexity of uncalibrated visual serving is increased. In this paper, we proposed a new robot uncalibrated visual serving control method, which does not need the dual cameras strictly orthogonal and calculate the image Jacobian, as well as without estimating nonlinear models, and experiment realized robot manipulator five degrees of freedom uncalibrated visual serving by directly designing the vision controller in the image plane at last.

36.2 Vision Configuration and Camera Model

36.2.1 Vision Configuration

The dual camera eye-to-hand vision configuration and the depth information mutually compensate each other has been used in this paper. Ideally, two fixed cameras use orthogonal vision configuration that is shown in Fig. 36.1. The purpose of dual camera biaxial parallel vision configuration is not to reconstruct the position of the target in the world coordinate, but to make three-dimensional position

Fig. 36.1 Orthogonal vision configuration
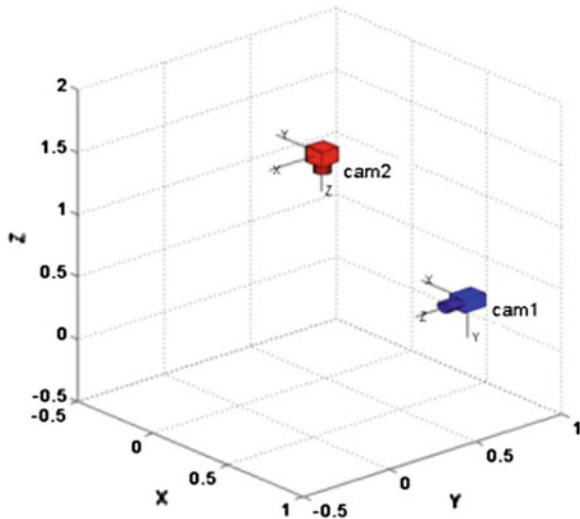
information into the two-dimensional position information of two planes and to avoid directly estimate the depth information of image features from the image plane. But the dual cameras orthogonal vision configuration has certain limitations in some engineering applications. Therefore, this paper proposes a dual camera biaxial parallel vision configuration method on the basis of dual cameras orthogonal vision configuration. The dual camera biaxial parallel vision configuration, as shown in Fig. 36.2, is that the X-axis of each dual camera coordinate are parallel with the world coordinate axis X, Y respectively, and the two camera rotation angle

Fig. 36.2 Biaxial parallel vision configuration
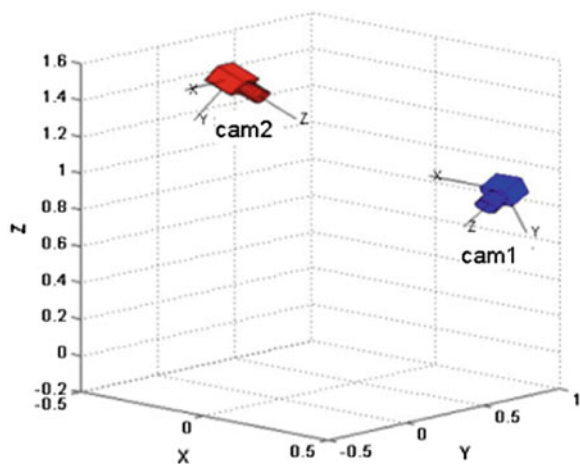
around the X-axis are ψ_1 and ψ_2. Compared to the dual cameras orthogonal vision configuration, the proposed method still able to achieve robot manipulator five degrees of freedom uncalibrated visual serving control with the camera rotate a certain angle around the X-axis. The camera1 clockwise rotate around the X-axis 30° and the camera2 counterclockwise rotate around the X-axis 60° based on dual camera using orthogonal vision configuration in the experiment.

36.2.2 Camera Model

The pinhole imaging model is commonly used to represent the camera model in machine vision, that is, the central perspective projection model [6, 11], and it is shown in Fig. 36.3. The coordinates of point P is (X, Y, Z) in the world coordinate and the coordinates of point P is (X_c, Y_c, Z_c) in the camera coordinate. The coordinates of the point P in the image coordinate is (x, y) and (u, v) is the pixel coordinates of the image plane, as well as (u_0, v_0) is the main center point of the pixel coordinates.

The camera coordinates (X_c, Y_c, Z_c) projected onto the two-dimensional image coordinate (x, y) is available according to the central perspective projection model.

$$x = f\frac{X_c}{Z_c}, \quad y = f\frac{Y_c}{Z_c} \tag{36.1}$$

The physical size of each pixel in the X-axis is dx and in the Y-axis is dy. Then we can change the physical coordinates (x, y) into the pixel coordinates (u, v) in the image coordinate

$$u = \frac{x}{\mathrm{d}x} + u_0, \ v = \frac{y}{\mathrm{d}y} + v_0 \tag{36.2}$$

Fig. 36.3 Central perspective model
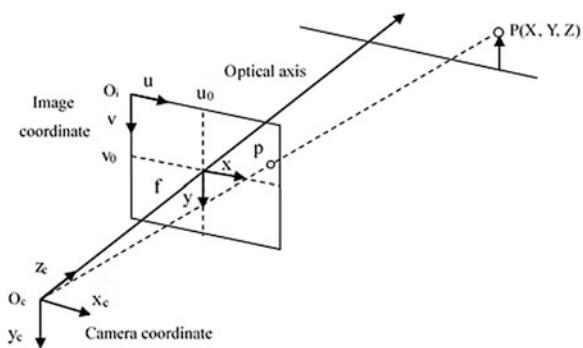
By formulas 36.1 and 36.2, we can get the transformation formula from the camera coordinates (X_c, Y_c, Z_c) to the image coordinates (u, v)

$$u = \alpha_x \frac{X_c}{Z_c} + u_0, \ v = \alpha_y \frac{Y_c}{Z_c} + v_0 \tag{36.3}$$

The posture of rigid body coordinate can represent by the fixed coordinate system or the Euler angles, and we choice the XYZ Euler angles rotation matrix to represent the posture of rigid body in this paper. The angle ψ, θ, ϕ are defined to stand for the rigid body rotate around the X-axis, Y-axis, Z-axis of the word coordinate respectively in Open Cv, and the expression of rotation matrix $\mathbf{R}_x, \mathbf{R}_y, \mathbf{R}_z$ are shown in Eq. 36.4 [12].

$$\mathbf{R}_x = \begin{bmatrix} 1 & 0 & 0 \\ 0 & \cos\psi & \sin\psi \\ 0 & -\sin\psi & \cos\psi \end{bmatrix}, \ \mathbf{R}_y = \begin{bmatrix} \cos\theta & 0 & -\sin\theta \\ 0 & 1 & 0 \\ \sin\theta & 0 & \cos\theta \end{bmatrix}, \ \mathbf{R}_z = \begin{bmatrix} \cos\phi & \sin\phi & 0 \\ -\sin\phi & \cos\phi & 0 \\ 0 & 0 & 1 \end{bmatrix} \tag{36.4}$$

According to the matrix expression of Open cv and rotation matrix and the dual camera biaxis parallel vision configuration in the Fig. 36.2, the homogeneous transformation matrix $\mathbf{R}_{cam1}$ and the translation vector $\mathbf{t}_{cam1}$ between the camera1 and the world coordinate can be expressed as formula 36.5.

$$\mathbf{R}_{cam1} = \mathbf{R}_x(-90° - \psi_1)\mathbf{R}_z(-180°) = \begin{bmatrix} -1 & 0 & 0 \\ 0 & \sin\psi_1 & -\cos\psi_1 \\ 0 & -\cos\psi_1 & -\sin\psi_1 \end{bmatrix}, \tag{36.5}$$

$$\mathbf{t}_{cam1} = \begin{bmatrix} 0.4 & 0.38 & 1.14 \end{bmatrix}$$

The homogeneous transformation matrix $\mathbf{R}_{cam2}$ and the translation vector $\mathbf{t}_{cam2}$ between the camera2 and the world coordinate can be expressed as formula 36.6.

$$\mathbf{R}_{cam2} = \mathbf{R}_x(-180° + \psi_2)\mathbf{R}_z(-90°) = \begin{bmatrix} 0 & -1 & 0 \\ -\cos\psi_2 & 0 & -\sin\psi_2 \\ \sin\psi_2 & 0 & -\cos\psi_2 \end{bmatrix}, \tag{36.6}$$

$$\mathbf{t}_{cam2} = \begin{bmatrix} 0.0 & 0.58 & 1.40 \end{bmatrix}$$

The transformation from the world coordinates (X_w, Y_w, Z_w) to the coordinates (X_c, Y_c, Z_c) of the camera coordinate is related to the position and attitude of the camera, which is determined by the internal and external parameters of camera. The external parameters of the camera can be expressed as a rotation matrix R_{cam} and translation vector t_{cam}. The transformation from the world coordinates (X_w, Y_w, Z_w) to the coordinate of the camera coordinate (X_c, Y_c, Z_c) represented by Eq. 36.7.

$$\begin{bmatrix} X_c \\ Y_c \\ Z_c \\ 1 \end{bmatrix} = \begin{bmatrix} \mathbf{R}_{cam} & \mathbf{t}_{cam} \\ 0 & 1 \end{bmatrix} \begin{bmatrix} X_w \\ Y_w \\ Z_w \\ 1 \end{bmatrix} \tag{36.7}$$

36.3 Image Feature Selection and Controller Design

36.3.1 Image Feature Selection

Image feature extraction and selection directly determine the controller design and the stability and robustness of the closed-loop control system. Commonly used image features such as points, lines, angles, area, images from, the optical flow field and Fourier descriptors, etc. Local image features, for instance, point and angle are relatively easy to extract and have a good environment adaptation ability and better robustness. Moreover, the number of image features should be greater than or equal to the degrees of freedom controlled by the robot manipulator in the uncalibrated visual serving process, while robot manipulator five degrees of freedom uncalibrated vision positioning need to select five image features at least. Therefore, the pixel coordinates of the characteristic points P_1 and the angle θ of P_1P_2 and U-axis in the Image plane of Cam1 and Cam2 are selected as Image features, so the image feature of this paper is $(U1_{p1}, V1_{p1}, U2_{p1}, V2_{p1}, \theta_1, \theta_2)$. In addition, the magenta and orange color block is the actual image features that we selected projected on the image plane in the actual system. The feature angle is the angle between the line connection magenta and orange color blocks and U-axis in the image plane and the feature point is the position of the orange color block in the image plane. The dual cameras projection model and the actual features on the image plane were shown in Figs. 36.4 and 36.5, respectively.

Fig. 36.4 The dual cameras projection model
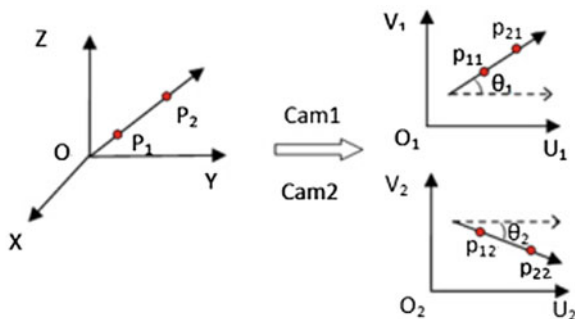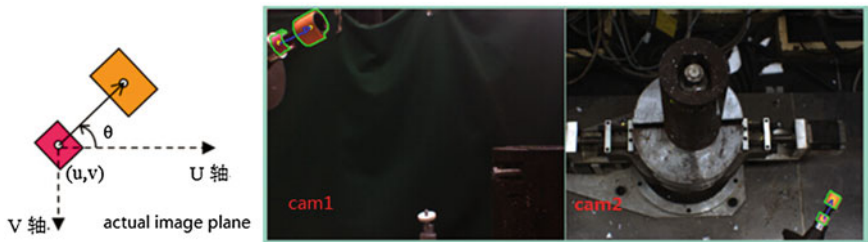
Fig. 36.5 The actual features on the image plane

36.3.2 Controller Design

Robot movement synthesized by the translational component along the X, Y, Z axis in the world coordinate. Thus, the controller design using off-line identification method to choose the key features to represent the robot manipulator movement, and the method is that manual control robot translate along the X_w, Y_w, Z_w axis and rotation around the Y_w, Z_w in the target neighborhood, then obtain the identification parameters from the collection of the sample data. According to the analysis of the sample data, we select characteristic quantity Δu_1 to reflect the movement of X_w axis, and characteristic quantity Δu_2 and Δv_1 to reflect the movement of Y_w and Z_w axes, respectively. Moreover, we chose θ_1 and θ_2 as a main feature quantity to represent the robot manipulator rotate around the Y_w and Z_w axes, respectively. Therefore, the controller based on image features can be described as

$$\begin{cases} \Delta X_w = a_1 \Delta u_1 \\ \Delta Y_w = a_2 \Delta u_2 \\ \Delta Z_w = a_3 \Delta v_1 \\ \Delta \mathrm{Rot} Y_w = a_4 \Delta \theta_1 \\ \Delta \mathrm{Rot} Z_w = a_5 \Delta \theta \end{cases} \tag{36.8}$$

In this paper, a proportional-integral controller is adopted by taking the robot needs to quickly eliminate static error converges to the desired attitude into account.

$$K_p E + K_i \int E \mathrm{d}_t - K_d \, \dot{q}(t) = \tau \tag{36.9}$$

where E is the error vector between the starting position and attitude and expectations pose, and $\dot{q}(t)$ is the Joint velocity vector. K_p is the proportional gain matrix and K_i is integral gain matrix. K_d is the Joint velocity feedback gain matrix.

36.4 Experiment

The image Jacobian matrix method and the proposed method conduct a comparison experiment in practical platform in order to reflect the superiority of the method proposed in this paper. The actual physical platform and software platform are shown in Fig. 36.6. The actual physical platform mainly composed by Denso robot VS6556, two industrial CCD cameras, image acquisition card, industrial PC, and terminal tools. Robot manipulator's maximum working range is 650–850 mm and the largest mass transportation is 6 kg with 6 degrees of freedom. The dual industrial cameras using high-speed industrial CCD camera of Micro-vision MV-VS078FC, which parameters contain the image resolution is 1024 × 768, with the focal length is 8 mm, and the physical dimensions of the horizontal and vertical pixels are 4.65 mm. The 1394 image acquisition card real-time capture the analog video signal that output from the high-speed industrial CCD. The PC is the model 610L of Advantech IPC.

The dual high-speed cameras using biaxial parallel vision configuration was used in this actual experimental platform. Denote the initial image feature vector in the image plane is (53.5, 112.9, 27.0, 870.5, 707.1, 60.0) and the initial pose of the robot manipulator end in the cartesian space is (275.6, −163.4, 453.7, −65.4, 42.4, 166.6). The desired image feature vector is (632.6, 536.8, −1.9, 520.9, 427.4, 95.7), and the desired pose of robot manipulator end in the cartesian space is (308.8, −260.3, 414.5, −94.1, 42.4, −178.5). After the experiment, the results show that the image feature vector is (632.1, 537.2, −1.7, 520.3, 427.6, 95.8) and the robot manipulator end's pose in cartesian space is (309.1, −260.4, 415.1, −94.8, 42.4, −179.1). In addition, the deviation vector is (−0.5, 0.4, 0.2, −0.6, 0.2, 0.1) compared with the desired image feature, as well as the deviation vector is (0.3, −0.1, 0.6, −0.7, 0.0, −0.6) compared with the expectations pose in cartesian space. According to the experimental data, we can know that the image plane point feature's and angle characteristic's deviation are less than a pixel or 1° and the cartesian spatial position's deviation is less than 1 mm, and attitude's deviation is
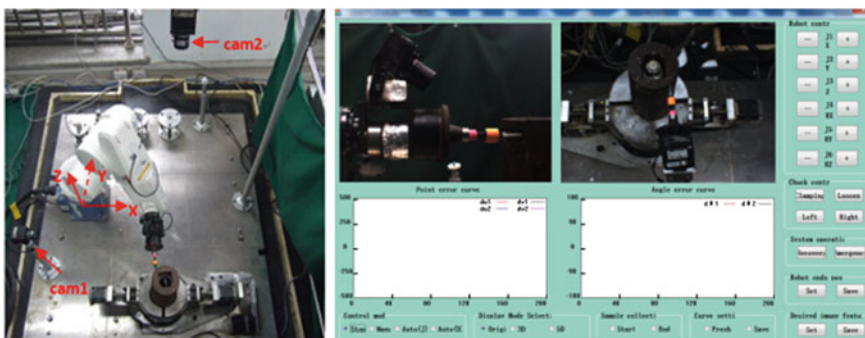
Fig. 36.6 The actual physical system and software platform

less than 1°. In this paper, the proposed dual camera biaxis parallel vision configuration, without having to calculate the image Jacobian matrix and the inverse of the image Jacobian matrix, which has not the situation of the image Jacobian matrix irreversible and avoid the amount of large calculation. Moreover, the deviation curve of feature point and angle characteristics in image 1 and 2 are shown in Figs. 36.7 and 36.8, respectively, and the position error curve and the attitude error curve in cartesian space are shown in Figs. 36.9 and 36.10. Finally, the point feature trajectory curve is smoothly in Cartesian space, which was shown in Fig. 36.11.

Fig. 36.7 Point deviation's curve in image 1 and 2
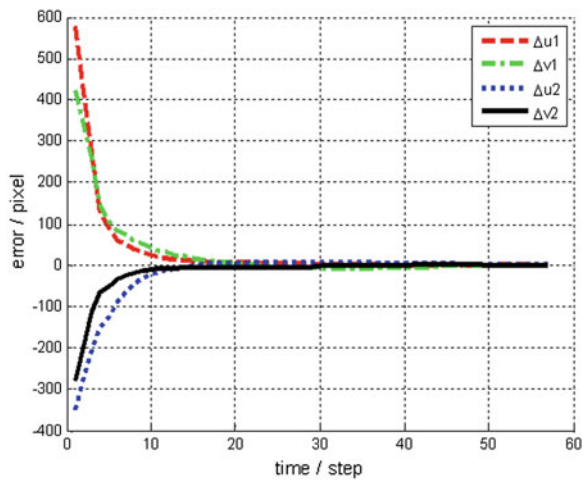
Fig. 36.8 Angle deviation's curve in image 1 and 2
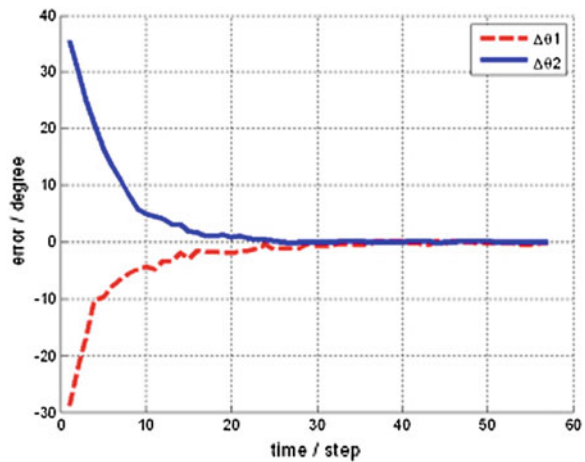
Fig. 36.9 Position error
curve in cartesian space
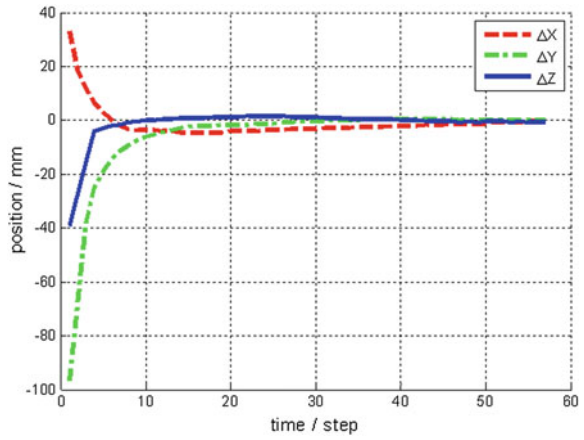
Fig. 36.10 Attitude error
curve in cartesian space
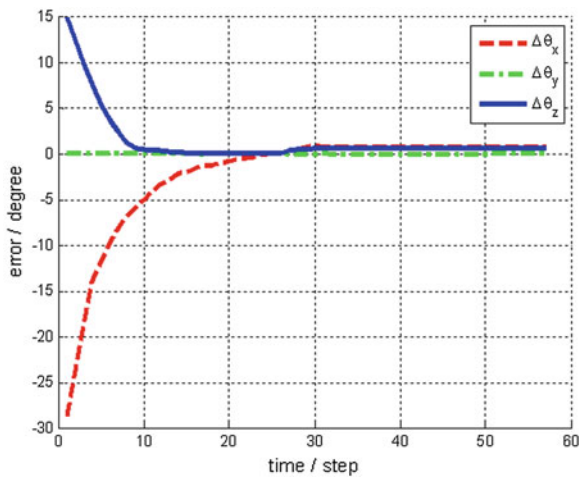
Fig. 36.11 Point trajectory
curve in cartesian space
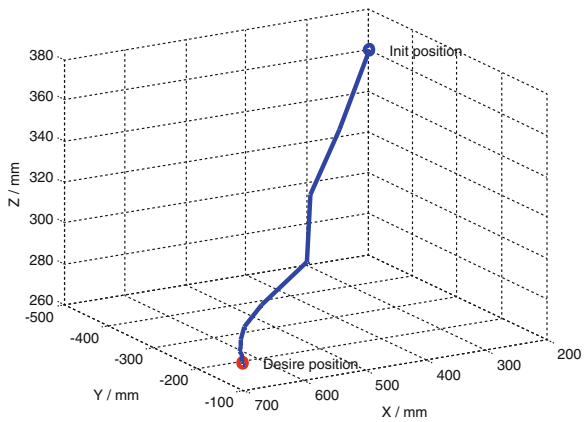
36.5 Conclusion

In this paper, we proposed an uncalibrated robot manipulator visual serving control method. First, the dual cameras biaxial parallel vision configuration was proposed and the point and angle image features in the camera image space were selected as image features. Then, we select the specific feature points and lines in the image plane in order to represent the robot manipulator's five degrees of freedom and designed a PI controller based on the proposed vision configuration. Finally, we verify the effectiveness and practicality of the proposed method in the robot manipulator five degrees of freedom uncalibrated vision control in the physical platform.

References

1. Han LW, Xu D, Tan M (2007) Approaching methods for camera characteristics in un-calibrated visual control system for robots. Cont Rol Decision 22(1):1–6 (in Chinese)
2. Chaumette F, Hutchinson S (2006) Visual servoing control part I: Basic approaches. IEEE Robot Autom Mag 13(4):82–90
3. Chaumette F, Hutchinson S (2007) Visual Servoing control part II: Advanced approaches. IEEE Robot Autom Mag 14(1):109–118
4. Wang M, Huang XH, Lv XD (2011) Un-calibrated vision servoing for micro-assembly robots based on image Jacobian model recognition. J Huazhong Univ Sci Tech (Natural Science Edition) 39(z2):60–63 (in Chinese)
5. Chen J, Jiang XM, Lu GD (2012) Development of automatic marking machine control system based on the orthogonal CCD feedback. Manuf Tech Mach Tool 2012(10):70–74 (in Chinese)
6. Xu D, Tan M, Li Y (2011) Vision measurement and control for robots. Defense Industry Press, Beijing, pp 228–230 (in Chinese)
7. Liu L, Wang N, Chuzhong Y, Wang D (2014) Kalman filter-based robot manipulator five degrees of freedom un-calibrated vision positioning. In: 2014 6th World Congress on international conference on mechanical and electronics engineering (ICMEE), IEEE, pp 914–919
8. Assa A, Janabi-Sharifi F (2010) A data fusion approach for multi-camera based visual servoing in. In: 2010 international symposium on optomechatronic technologies, ISOT 2010
9. Chang WC, Weng YH, Tsai YH et al (2011) Automatic robot assembly with eye-in-hand stereo vision. In: 2011 9th World Congress on intelligent control and automation (WCICA), IEEE, pp 914–919
10. Wang Y et al (2014) A modified image-based visual servoing controller with hybrid camera configuration for robust robotic grasping. Robotics Auton Syst. doi:10.1016/j.robot.2014.06.003
11. Liu YH, Wang H, Wang C, Lam K (2006) Un-calibrated visual servoinging of robots using a depth-independent interaction matrix. IEEE Tran Robotics 22(4):804–817
12. Corke P (2011) Robotics, vision and control: fundamental algorithms in MATLAB. Springer, Berlin. pp 223–333

Chapter 37
Methods Synthesis of Central Pattern Generator Inspired Biped Walking Control

Chengju Liu and Qijun Chen

Abstract Bio-inspired locomotion control method is one of the ways to promote the site application of biped robots. This paper synthesizes the main idea and structure of central pattern generator (CPG) inspired biped walking control methods into two kinds of common strategies: joint space control methods and workspace control methods. The key problems of these two approaches are deeply explored. Finally, the research direction of the CPG-inspired control method is discussed. The motivation of this paper is to synthesize the current mainly methods for biped robots to present a practical guide to researchers and engineers interested in the CPG-inspired control approaches.

Keywords Biped robot · Walking control · Central pattern generator (CPG) · Joint space control · Workspace control

37.1 Introduction

According to the research discoveries, CPGs are primarily responsible for generating coordinated, rhythmic movements of animals in real time, such as crawling, flying, swimming, hopping, walking, and running [1]. Based on the plausibility of CPG concept, it has attracted widespread interest in the field of robotics. It is hoped that achieve realistic control bionic robot-like rhythmic movement of animals, and the ability to adapt to the environment. Acting as a bio-inspired motion control mechanism, compared to the conventional control methods,

C. Liu (✉) · Q. Chen
School of Electronics and Information Engineering, Tongji University, Shanghai, China
e-mail: liuchengju@tongji.edu.cn

CPG has many features: (1) does not require accurate modeling of the control objective; (2) can produce rhythmic signals spontaneously; (3) has self-adaptability to the external uncertainty of the environment.

CPG-inspired control methods are first be used in the motion control bionic robot. Many CPG models are presented, including Huxley-Hodgkin model [2], Matsuoka model [3], etc. Inspired by lamprey's swimming CPG, Ijspeert's team has studied the motion of salamander and snake robots. In the joint space of a robot, one CPG unit was used to control one degree of freedom (DoF), and a distributed CPG network can generate complex coordinated multidimensional output signals to realize the swinging or serpentine locomotion [4]. Inagaki et al. [5] used Matsuoka-based CPG control network to control the three-dimensional movement of a snake-like robot. The successful exploration of CPG-based control projects in swimming and crawling robots set the foundation for the biological mechanism to control the motion of legged robots. Kimura's group has studied the locomotion control of quadruped robots based on neural oscillators [6]. Their studies mainly focus on using oscillators and reflexes to generate torque control signals or phase modulation signals in joint space to realize dynamic walking on irregular terrains.

So far there is no systematic motion system design method. Usually, for a specific application system, the control system is explored step by step: (1) Choose the CPG model; (2) The topology of the CPG network. The number of the oscillator units and the coupling topology of the network; (3) Parameters analyze of the network. Analyze the relationship of the parameters and the important qualities, such as frequency, amplitude, phase relations between the neurons, and the waveform of the oscillation signals; (4) How to use the output signals of the CPG network. What quantities of the oscillation signals are used as? For torque, position or phase et al.; (5) How to use the feedback information? Mainly solve the problem of how to add the feedback information to the network and the effect of the coupling term to the oscillation signals.

Recently, the biped robots have attracted more and more attentions. However, the redundant DoFs and moving center of mass (CoM) make it challenging to realize stable walking. During human walking, we just walk subconsciously. We do not need to consider the lift height and the moving span of the feet. We still can easily walk steadily, according to the biologists, which is thanks to the "nerve-muscle-skeletal" system for the regulation of movement. In view of this, in recent years, researchers have begun to model the CPGs biologically to investigate the biped rhythmic motion control. Taga's seminal contribution on neuromechanical simulations introduces CPGs to biped robot walking control [7, 8]. Nassour et al. [9] presented a CPG controller for the real-time balance of a simulated humanoid robot. The behavior of the robot emerges from dynamic interactions between the neural networks, the robot, and the simulated world. Or [10] have empirically explored the use of neural oscillators to realize biped stable locomotion control. Aoi and Tsuchiya [11] have proposed a locomotion control system for a biped robot to achieve robust walking using nonlinear oscillators. Oscillators are used to generate

the nominal trajectories of all the joints, and the nominal trajectories are modified using sensory feedback that depends on the posture and motion of the robot to achieve robust walking.

Summing up, there have two main difficulties exist for CPG-inspired biped locomotion controller design: (1) Many CPG units are required to control the multi-DoF for a biped robot, and thus, too many parameters need to be modulated in the CPG control network. To determine the relationship of the parameters and the oscillation signals is a between CPG unit rational connection topology structure and parameters, is a complex optimization problem; (2) That expected CPG-inspired control methods should have a certain self-adaption for the external environment changes and disturbances. However, the current reported results for the academic study of adaptive is still insufficient. Currently, most researches are mainly focused on a class of relatively simple movement patterns bionic robot control, such as snake-like robot. The problem for adaptive biped robot controller design has relatively few successful examples.

Compared with these existing reviews, this paper brings its own contribution by going more deeply into the technical aspects of how to use CPGs in biped walking control. In this paper, according to our research, we synthesize the current methods into two common methods of using CPGs in applications: joint space control method and workspace control method. We illustrate the basic idea, control structure as well as discuss several key issues during the application of the two control strategies. In the conclusion part, the research directions of the CPG-based control mechanism for robots.

37.2 Joint Space Control Methods

For the complex system of biped robots, the current CPG models do not have strong practicability. The current study mainly stays in the simulation stage or just rhythmic movement control for some joints of a biped robot. Currently, the mainly used methods are joint space control methods [7, 9, 10, 12–14]. In this method, one CPG unit is assigned to one DoF, and the distributed CPG network can generate complex coordinated multidimensional signals used as force or torque control to realize the coordinated motion. The architecture of this method is shown in Fig. 37.1, CPG network is the main part of control oscillation signals.

The rationality and effectiveness of the CPG network topology design affect the control result. Parameters optimization is very important for the entire control system, including offline parameters optimization and online optimization of the feedback loop.

Fig. 37.1 The architecture of joint space control method
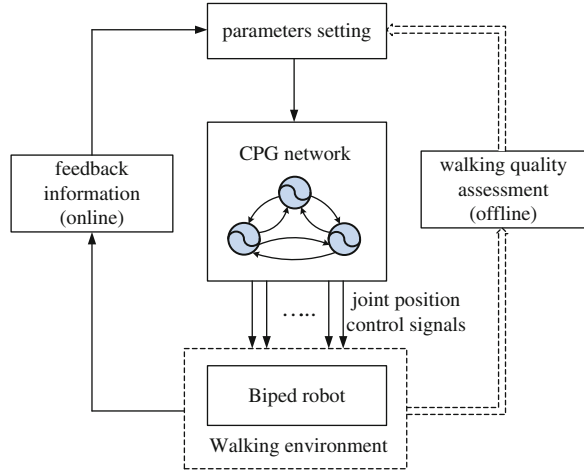
37.2.1 How to Use the CPG Units?

The general design method using one CPG unit is assigned to one DoF, and the distributed CPG network can generate complex coordinated multidimensional signals used as force or torque control to realize the coordinated motion.

The NAO robot is applied as an example to illustrate the basic idea and structure of the joint space control method. In this example, the DoFs related to locomotion on the two legs are only considered. Using one CPG unit to control one DoF will result in a complex distributed CPG network. To simplify the CPG network, a pitch-to-roll mapping link is employed. As Fig. 37.2 shows, the control signals of the DoFs in roll plane are mapped from the inhibited neural oscillators which controlled the DoFs in pitch plane. By optimizing the parameters of the network, all the neural oscillators become mutually entrained and oscillating in the same period. The final joint control signals can be obtained through amplitude transformation and result in a walking pattern for a biped robot.

37.2.2 How to Optimize the Parameters?

The parameters adjustment is a major difficulty for the joint space control method. In engineering applications, numerical analyze, computer simulation, and optimization methods are usually combined to explore the appropriate parameters. Finally, during the practical application, the obtained parameters are usually be carefully adjusted according to the actual control results. In particular, GA-based evolutionary techniques are frequently utilized to search and optimize the CPG network parameters to generate expected control signals [7, 15–17].
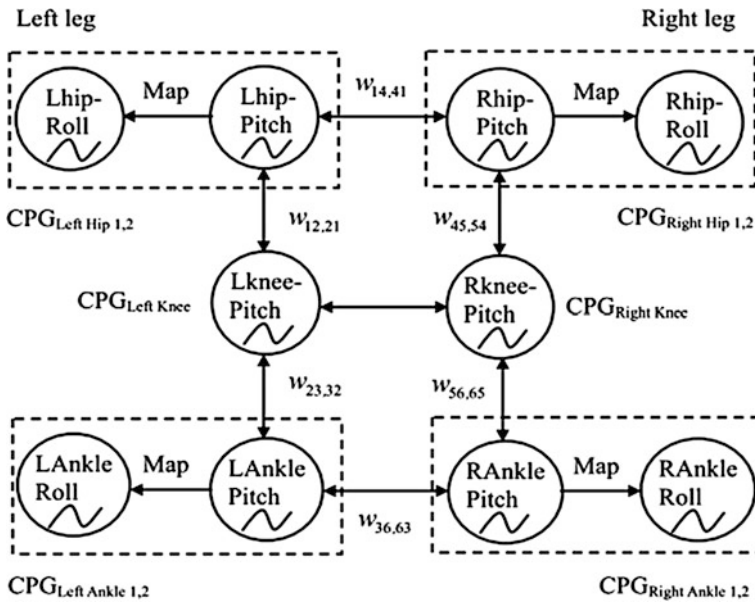
Fig. 37.2 The topology of CPG network

37.2.3 The Existing Key Problem

The state-of-art works of CPG-inspired methods are mostly using joint space control method. This method suits to the motion control of crawling robots such as snake-like robots. Its CPG network generates coordinated sine or quasi-sine joint control signals with appropriate phase relationships that realize various motion patterns. For legged robots, such as quadruped or humanoid robots, joint control signals are more complex than those the current CPG models can generate. With this CPG-joint control method, the stability of a walking robot can be realized by adjusting CPG parameters to generate appropriate coordinated joint control signals.

On the other hand, the mechanical configurations of the current robots, like NAO robot, are not designed exactly according to the legged animals. For example, on a robot, the joint is controlled by the motor, for a legged animal, the joint is controlled by muscles. So we cannot control a robot completely according to the biological mechanism.

Third, the effect of the feedback loop to the whole CPG network is very complex for this joint space control method. Several researchers have explored some approaches to solve the feedback design problem [8, 16, 18], however, the results of the roles of reflection are not obvious. So how to introduce a feedback signal to the joint space, and what form of the feedback information still need further research.

For biped robots, sometime, joint space control method cannot solve the environment adaptive control problem. How to generate specific control signals by CPG or how to combine the rhythmic signals with discrete signals will be a critical step, otherwise it will be difficult to achieve the flexibility in walking.

37.3 Workspace Control Methods

Another control approach is to assign the CPGs to some periodic variables to reflect the characteristics of walking gait [11, 19–22]. This method has several advantages. Assigning CPGs to the periodic variables during robot locomotion simplifies the connections between CPGs and feedback pathways from the environment. Walking pattern adjustment of robots is easier to realize than the CPG-joint space control method. This method can substantially reduce the number of CPGs and requires less tuning of the parameters. Aoi and Tsuchiya [11], Morimoto et al. [19] have explored the locomotion control methods in the task space of legged robots. In our previous work [21, 22], we proposed a novel workspace control method for biped adaptive locomotion. CPGs are used to generate toe trajectories online in workspace for a robot rather than to generate joint control signals in joint space. The block diagram of the proposed workspace control method is shown in Fig. 37.3. The control system architecture consists mainly of four parts: CPG network and the characteristics design module, perception feedback module, system parameters optimization module, the motion engine module.

The rhythm signals are generated using CPG module and using the rhythm signals, by design appropriate mapping function to generate periodic characteristics of biped robots. The environmental information is perceived using through sensors, and the information is sent to the rhythm generation module to modulate the periodic characteristics online to realize adaptability. The motion engine is used for mapping the adaptive characteristics to the joint space of the biped robot.
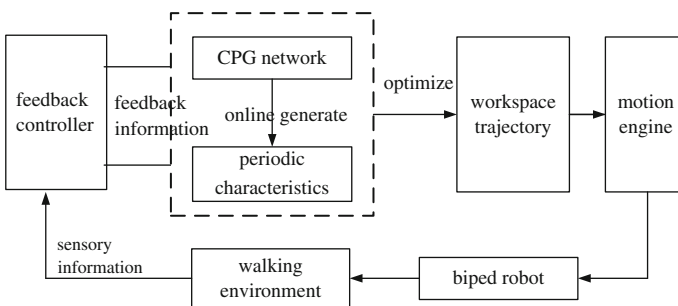
Fig. 37.3 The framework of the control system

37.3.1 How to Use CPG Units?

For a biped robot to walk on irregular terrains, the robot should have the capability to change the positions of the tips of its legs. At the same time, the adjustment of the position of its CoM is very important to improve walking stability. In order to improve the stability and adaptability, the modulation of swing foot trajectory and CoM trajectory should be combined. So in this example, the workspace trajectory generator is proposed based on four-coupled neural oscillators. A mapping function is designed to map periodical oscillation signals with specific phase relationships of the oscillator network to the swing foot trajectories. The CoM trajectories are also generated using CPG units. Thanks to the characteristics of CPGs, the output of the trajectory generators can be adjusted in real time.

37.3.2 How to Design the Feedback Loop?

Entraining of sensory feedback information is a key property of neural oscillators. In this example, biological reflexes are mimicked to make the neural oscillators autonomously adapt to different walking conditions without changing any of model parameters except the feedback term of CPG model. Figure 37.4 shows the basic framework of the sensory feedback paths designed in this example. The vestibulo-spinal reflex and ZMP-based feedback are used to modulate the generated trajectories in real time to improve the walking adaptability and stability. The feedback

Fig. 37.4 Overall architecture of sensory feedback paths
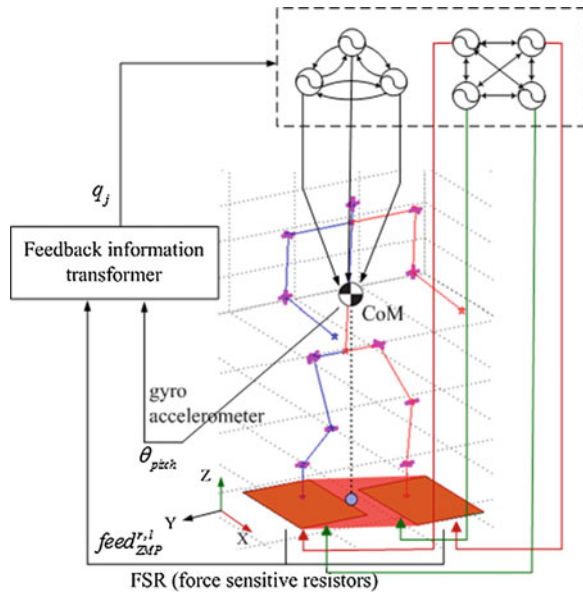
information transformer generates the feedback signals to the neural oscillators using sensory feedback information including the body attitude and ZMP distribution information from the robot.

37.3.3 How to Adjust the Parameters?

Staged parameter adjusting process can be used to derive the parameters. The first stage uses numerical simulation to analyze the effect of each parameter on the output signal. Then, an EA-based approach is applied to realize the walking pattern evolution for the whole system. The first stage aims to find the general relationships between parameters and output signals through computer numerical simulation. The connection weights are set as inhibitory connections in order to get the output signals with desired phase relationships. After the approximate range of the model parameters that can generate stable oscillation signals is obtained, EA-based evolution method is used to optimize the system parameters for the biped walking pattern.

37.4 Conclusion

In this paper, the application methods are synthesized as two common control strategies to introduce: joint space control methods and workspace control methods. Summarize and describe the main process during the engineering application, and pointed out the existing key problems. This paper is presented to provide a better understanding of how to use CPG concept to control biped locomotion. In this research field, the following key research questions maybe will become the research hot direction in the future: (1) How to design closed-loop CPGs which take sensory feedback into account? (2) Can CPGs be integrated with state-feedback driven control? (3) Are CPGs good choices for whole-body control and a larger class of motor behaviors apart from locomotion?

References

1. Delcomyn F (1980) Neural basis for rhythmic behaviour in animals. Science 210(4469): 492–498
2. Hodgkin AL, Huxley AF (1952) Currents carried by sodium and potassium ions through the membrane of the giant axon of loligo. J Physiol 116:449–472
3. Matsuoka K (1985) Sustained oscillations generated by mutually inhibiting neurons with adaptation. Biol Cybern 52:367–376
4. Ijspeert AJ, Crespi A, Ryczko D et al (2007) From swimming to walking with a salamander robot driven by a spinal cord model. Science 315:1416–1420

5. Inagaki S, Yuasa H, Suzuki T et al (2006) Wave CPG model for autonomous decentralized multi-legged robot: gait generation and walking speed control. Robot Auton Syst 54(2): 118–126

6. Kimura H, Fukuoka Y, Cohen AH (2007) Adaptive dynamic walking of a quadruped robot on natural ground based on biological concepts. Int J Robot Res 26(5):475–490

7. Taga G (1991) Self-organized control of bipedal locomotion by neural oscillators in unpredictable environment. Biol Cybern 65:147–159

8. Tan F, Fu CL, Chen K (2010) Biped blind walking on changing slope with reflex control system. In: Proceedings of IEEE inter conference on robotics and automation anchorage convention district, pp 1709–1714

9. Nassour J, Henaff P, Benouezdou F, Cheng G (2014) Multi-layered multi-pattern CPG for adaptive locomotion of humanoid robots. Biol Cybern. doi:10.1007/s00422-014-0592-8

10. Or J (2009) A hybrid CPG-ZMP controller for the real-time balance of a simulated flexible spine humanoid robot. IEEE Trans Syst Man Cybern -Part C: Appl Rev 39(5):547–561

11. Aoi S, Tsuchiya K (2005) Locomotion control of a biped robot using nonlinear oscillators. Auton Robot 19(3):219–232

12. Shan J, Cheng JS, Chen JP (2000) Design of central pattern generator for humanoid robot walking based on multi-objective GA. In Proceedings of IEEE international conference on intelligent robots and systems, pp 1930–1935

13. Dutra MS, de Pina Filho AC, Romano VF (2003) Modeling of a bipedal locomotor using coupled nonlinear oscillators of Van der Pol. Biol Cybern 88:286–292

14. Song KT, Hsieh H (2014) CPG-based control design for bipedal walking on unknown slope surfaces. In: Proceedings of IEEE international conference on robotics and automation, pp 5109–5114

15. Kim JJ, Lee JW, Lee JJ (2009) Central pattern generator parameter search for a biped walking robot using nonparametric estimation based particle swarm optimization. Int J Control Autom Syst 7(3):447–457

16. Park CS, Hong YD, Kim JH (2010) Full-body joint trajectory generation using an evolutionary central pattern generator for stable bipedal walking. In: Proceedings of IEEE/RSJ international conference on intelligent robots and systems, pp 160–165

17. Oliveira M, Matos V, Santos CP, Costa L (2013) Multi-objective parameter CPG optimization for gait generation of a biped robot. In Proceedings of IEEE international conference on robotics and automation, pp 3115–3120

18. Wolff K, Sandberg D, Wahde M (2008) Evolutionary optimization of a bipedal gait in a physical robot. In: World Congress on computational intelligence, pp 440–445

19. Morimoto J, Endo G, Nakanishi J et al (2008) A biologically inspired biped locomotion strategy for humanoid robots: modulation of sinusoidal patterns by a coupled oscillator model. IEEE Trans Rob 24(1):185–191

20. Ha I, Tamura Y, Asama H (2011) Gait pattern generation and stabilization for humanoid robot based on coupled oscillators. In: Proceedings of IEEE/RSJ international conference on intelligent robots and systems, pp 3207–3212

21. Liu CJ, Chen QJ, Wang DW (2011) CPG-inspired workspace trajectory generation and adaptive locomotion control for quadruped robots. IEEE Trans Syst Man Cybern-Part B 41 (3):867–880

22. Liu CJ, Wang DW, Chen QJ (2013) Central pattern generator inspired control for adaptive walking of biped robots. IEEE Trans Syst Man Cybern-Part A 43(5):1206–1215

Chapter 38
Improved EEG Analysis Models and Methods Using Blind Source Separation

Fasong Wang, Zhongyong Wang and Rui Li

Abstract Noninvasive assessing the physiological changes occurring inside the human brain is a challenging problem in biomedical engineering. These variations can be modeled as biomedical source signals that can be measured by several types of noninvasive brain imaging techniques such as electroencephalography (EEG). In this paper, after the perspective of linear blind source separation (BSS) model and characteristics of EEG are presented, the general and detailed definition of BSS model for EEG data analysis is given. Then based on the spatial structure and temporal or spectral information of the EEG signals, some state-of-the-art BSS techniques that can be used for analyzing EEG recordings are reviewed. A novel algorithm combining both high-order statistics and second-order statistics to achieve BSS for EEG is constructed. The paper concludes by discussing the influence of BSS for EEG research.

Keywords Blind source separation · Electroencephalogram · High-order statistics (HOS) · Second-order statistics (SOS) · Independent component analysis (ICA)

38.1 Introduction

In order to conclude that something is wrong or that the patients have a disease further processing is necessary. A common approach to the study of EEG is to describe patterns in space and time and link empirical findings with anatomical and physiological knowledge [1, 2]. Another approach that prevails in EEG signal analysis literature is BSS [3–5]. First being studied during the first half of the 1980s in the last century, BSS has enjoyed considerable interest worldwide only a decade later. BSS has a wide range of engineering applications today such as geophysical data processing, data mining, speech enhancement, image recognition, wireless

F. Wang (✉) · Z. Wang · R. Li
School of Information Engineering, Zhengzhou University, Zhengzhou 450001, China
e-mail: fasongwang@126.com

communications, and biological signal analysis [3, 4]. All these fruits come from the "blind" nature of the BSS problem formulation: no knowledge of mixing process or of source waveform is assumed. The BSS problem can be considered from different perspectives, based on various viewpoints, several hundred BSS algorithms have been proposed over the last 20 years with more added on every year. Generally, many methods are based on the cancelation of second-order statistics (SOS) and/or of high- order statistics (HOS). Their commonality characteristic is a certain degree of source spatial independence in the assumption, which is precisely modeled by the cancelation of those statistics. Both HOS and SOS have been employed with success in EEG. They are today established for denoising/ artifact rejection, improving brain computer interfaces and for increasing the SNR of single-trial time-locked responses [2].

38.2 BSS-Based EEG Analysis Model

Some phenomena strongly support the superposition principle of BSS [1, 2, 6], according to which the relation between neocortical dipolar fields and scalp potentials may be approximated by a system of linear equations. Then, let us denote the N EEG dipolar fields with fixed location and orientation in the analyzed time interval by the vector $\mathbf{s}(k) = (s_1(k), \ldots, s_N(k))^T$, and the observed scalp sensors measurement vector signals by $\mathbf{x}(k) = (x_1(k), \ldots, x_M(k))^T$. The mixing can be expressed as

$$\mathbf{x}(k) = \mathbf{H}\mathbf{s}(k) + \mathbf{v}(k), \tag{38.1}$$

where the matrix $\mathbf{H} = [h_{ij}] \in R^{M \times N}$ collects the mixing coefficients. However, some weak structural assumptions are often made: for example, it is typically assumed that the mixing matrix is square, that is, the number of source signals equals the number of observed signals ($M = N$), the mixing process $\mathbf{H}$ is defined by an even-determined (i.e., square) matrix and, provided that it is nonsingular, the underlying sources can be estimated by a linear transformation, which we will assume here as well. $\mathbf{v}(k) = (v_1(k), \ldots, v_N(k))^T$ is a vector of additive noise.

The task of BSS is to recover all the original signals from the observations $\mathbf{x}(k)$ simultaneously without the knowledge of $\mathbf{H}$ nor $\mathbf{s}(k)$. Let us consider a linear feed forward memoryless neural network which maps the observation $\mathbf{x}(k)$ to $\mathbf{y}(k)$ by the following linear transform:

$$\mathbf{y}(k) = \mathbf{W}\mathbf{x}(k) = \mathbf{W}\mathbf{H}\mathbf{s}(k) \tag{38.2}$$

where $\mathbf{W} = [w_{ij}] \in R^{N \times N}$ is a separating matrix, $\mathbf{y}(k) = (y_1(k), \ldots, y_N(k))^T$ is an estimate of the possibly scaled and permuted vector of $\mathbf{s}(k)$ and also the network output signals whose elements are statistically mutually independent, so that the

output signals $\mathbf{y}(k)$ are possibly scaled estimation of source signals $\mathbf{s}(k)$. As shown in [3–5], there are two indeterminacies in BSS: scaling ambiguity and permutation ambiguity. This implies that we can recover faithfully the source waveform out of a scale and permutation indeterminacy. The idea suits EEG well, since the waveform bears meaningful physiological and clinical information.

Using BSS model to analyze the EEG data, one should determine an objective function and an adequate optimization algorithm to run the computations required by the objective function. The statistical properties (e.g., consistency, asymptotic variance, robustness) of the BSS method depend on the choice of the objective or contrast function (a real function of a probability distribution), whereas the algorithmic properties (e.g., convergence speed, memory requirements, numerical stability) of the BSS method depend on the optimization algorithm.

38.3 SOS, HOS, and Hybrid Methods

38.3.1 SOS-Based Methods

EEG signals have a significant temporal (and spectral) structure. In this subsection we will describe the most popular BSS algorithms that use the temporal and spectral structure of the sources to perform the blind separation. The work using the SOS to achieve the BSS was initiated by Féty et al. [7]. Fety's method is based on the simultaneous diagonalization of the correlation matrices $\mathbf{R_x}(0)$ and $\mathbf{R_x}(1)$. Independently, Tong et al. [8] proposed a similar technique, namely the AMUSE (algorithm for multiple unknown signals extraction) technique, that achieves the BSS by the simultaneous diagonalization of two symmetric matrices $\mathbf{R_x}(0)$ and $(\mathbf{R_x}(\tau_k) + \mathbf{R_x^*}(\tau_k))/2$ with $\tau_k \neq 0$. This method has been extended in [9] where a generalized eigenvalue decomposition of a matrix pencil $(\mathbf{R_x}(\tau_1) + \mathbf{R_x}(\tau_2))$ is considered.

Later on, Belouchrani et al. [10] proposed the SOBI (second-order blind identification) algorithm that generalizes the previous methods to the case where more than two correlation matrices are used. In the SOBI algorithm, the separation is achieved in two steps; the first step is the whitening of the observed signal vector by linear transformation. The second step consists of applying a joint approximate diagonalization algorithm to a set of different time-lag correlation matrices of the whitened signal vector. A variant of SOBI has been presented that allowing direct signal separation from frequency domain data by exploiting the source correlation properties expressed in the time domain. This algorithm is referred to as f-SOBI, standing for "frequency domain SOBI" [11].

Numerous approaches have been proposed in recent years both for the formulation of the diagonalization criterion and for the algorithms considered for its minimization. One of the most popular and computationally appealing approach for

the joint diagonalization of a set of matrices $\mathbf{M}_1, \ldots \mathbf{M}_k$ is the unitary joint approximate diagonalization (JADE) [12], which minimizes the criterion

$$\sum_{k=1}^{K} \mathbf{off}(\mathbf{B}\mathbf{M}_k\mathbf{B}^*) \tag{38.3}$$

with respect to $\mathbf{B}$, subject to the unitary constraint $\mathbf{B}^*\mathbf{B} = \mathbf{I}$, where $\mathbf{off}(\mathbf{P}) = \sum_{i \neq j} |P_{ij}|^2$.

An iterative algorithm using relative gradient technique has been considered for the minimization of (38.3) without unitary constraint. An alternative approach for nonunitary approximate joint diagonalization has been proposed by Yeredor (the "AC-DC" algorithm [13]), which minimizes

$$\sum_{k=1}^{K} \left\| \mathbf{M}_k - \mathbf{A}^{\mathrm{T}}\mathbf{D}_k\mathbf{A}^* \right\|^2 \tag{38.4}$$

without constraining $\mathbf{A}$ to be unitary. In (38.4), $\mathbf{D}_k$ represent diagonal matrices.

A computationally efficient unconstrained minimization algorithm was proposed by Pham [14], whose target criterion is the Kullback—Leibler divergence between the $n \times n$ operand and the diagonal matrix with the same diagonal as the operand:

$$\sum_{k=1}^{K} \lambda_k [\log \det \mathrm{diag}(\mathbf{B}\mathbf{M}_k\mathbf{B}^*) - \log \det(\mathbf{B}\mathbf{M}_k\mathbf{B}^*)] \tag{38.5}$$

where $\lambda_k, k = 1, \ldots, K$ are positive scalar factors. This approach requires all the target matrices to be positive definite, which limits its applicability as a generic BSS tool. Another class BSS techniques based on SOS is the one using the maximum likelihood principle. This method uses the Gaussian asymptotic property of the discrete Fourier transform of the second-order stationary observations [3–5].

38.3.2 HOS-Based Methods

The HOS-based BSS methods are commonly called ICA. So we will discuss the ICA method in this subsection. ICA is usually performed by formulating a criterion of statistical dependence $\varphi(y)$, referred to as contrast function or contrast and minimizing it—sometimes referred to as minimum contrast estimation. The selection of specific contrast and numerical algorithm for its optimization gives rise to different ICA methods. Typically, decorrelation of the data using PCA is performed as a pre-processing stage. Some methods using orthogonal contrasts demand explicitly uncorrelated of the data. If the number of sources equals the number of mixtures, it is usually convenient to pose the problem as estimating the unmixing

matrix $\mathbf{W}$ and $\mathbf{W} = \arg\min_{\mathbf{W}} \varphi(\mathbf{Wx})$. If $M > N$, the first N principal components of x are used as the data.

Minimum contrast estimation is a general statistical estimation approach commonly used in ICA. Different multiunit contrast functions can be derived from different principles such as maximum likelihood (ML), information maximization (Informax), minimization mutual information (MMI). It can be shown that in many cases these contrasts are equivalent [3–5].

JADE can be described as follows: the matrix $\mathbf{W}$ diagonalizes $\mathbf{F}(\mathbf{M})$ for any matrix $\mathbf{M}$, that is, $\mathbf{WF}(\mathbf{M})\mathbf{W}^{\mathrm{T}}$ is diagonal. For ICA model, the matrix $\mathbf{F}(g)$ is of a linear combination of terms of the form $\mathbf{w}_i\mathbf{w}_i^{\mathrm{T}}$.

Thus, we can take a set of different matrices $\mathbf{M}_i$, $i = 1, \ldots, k$, and try to make the matrices $\mathbf{WF}(\mathbf{M}_i)\mathbf{W}^{\mathrm{T}}$ as diagonal as possible. In practice, the matrices $\mathbf{M}_i$ cannot be made exactly diagonal because the model does not hold exactly, and there are sampling errors too.

The diagonality of a matrix $\mathbf{Q} = \mathbf{WF}(\mathbf{M}_i)\mathbf{W}^{\mathrm{T}}$ can be measured, for example, as the sum of the squares of off-diagonal elements: $\sum_{k\neq l} q_{kl}^2$. Equivalently, because an orthogonal matrix $\mathbf{W}$ does not change the total sum of squares of a matrix, minimization of the sum of squares of off-diagonal elements is equivalent to the maximization of the sum of squares of diagonal elements. Thus, we could formulate the following measure:

$$ J(\mathbf{W}) = \sum_{i=1}^{k} \left\| \mathrm{diag}(\mathbf{WF}(\mathbf{M}_i)\mathbf{W}^T) \right\|^2 \tag{38.6} $$

where $\|\mathrm{diag}(g)\|^2$ means the sum of squares of the diagonal. Maximization of $J(g)$ is then one method of joint approximate diagonalization of the $\mathbf{F}(\mathbf{M}_i)$. Then the question is how do choose the matrices $\mathbf{M}_i$. A natural choice is to take the eigenmatrices of the cumulant tensor. Thus we have just n matrices that give all the relevant information on the cumulants, but they span the same subspace. This is the basic principle of the JADE algorithm.

Another benefit associated with this choice of $\mathbf{M}_i$ is that the joint diagonalization criterion is then a function of the distributions of $y = \mathbf{W}z$. In fact, after complicated manipulations, we can obtain $J(\mathbf{W}) = \sum_{ijkl \neq iikl} (\mathrm{cum}_{ijkl}^{(4)}(y_i, y_j, y_k, y_l))^2$. In other words, when $J(g)$ is minimized, the sum of the squared cross-cumulants of the y_i is also minimized. Thus, we can interpret the method as minimizing nonlinear correlations.

38.3.3 Proposed Algorithm via Both HOS and SOS

In many cases, ICA is applied on data sets that are not simply random vectors but multivariate time series, i.e., signals with time dependencies. However, ICA

completely ignores any time structure and uses only the marginal distributions of the estimated source signals. It was shown in the previous subsection, that under some restrictions, the time dependency information alone is sufficient to estimate the unknown source signals. Results obtained by these two different approaches to BSS are likely to improve if one exploits at the same time the spatial and the temporal information of the sources.

In real applications, the source signals maybe have asymmetric distribution, so the third-order statistics is very important, a hybrid BSS method for EEG source signals was derived in this subsection, the source signals are statistically independent in spatial and have various temporal structures. We can construct the novel cost function as:

$$J_1(\mathbf{W}) = \omega(2) \sum_{p=1}^{P} \sum_{i \neq j} (\mathrm{cum}_{ij}^{(2)}(\mathbf{y}))^2$$

$$+ \ \omega(3) \sum_{p=1}^{P} \sum_{ijk \neq ijj} (\mathrm{cum}_{ijk}^{(3)}(\mathbf{y}))^2 + \omega(4) \sum_{p=1}^{P} \sum_{ijkl \neq ijkk} (\mathrm{cum}_{ijkl}^{(4)}(\mathbf{y}))^2 \qquad (38.7)$$

where P represents the number of the time delays. $\omega(i)$, $i = 2, 3, 4$ are the weight of second-, third-, and fourth-order statistics and $\sum_{i=2}^{4} \omega(i) = 1$. $\mathrm{cum}_{ij}^{(2)}(\mathbf{y})$, $\mathrm{cum}_{ijk}^{(3)}(\mathbf{y})$ and $\mathrm{cum}_{ijkl}^{(4)}(\mathbf{y})$ are the second-, third-, and fourth-order cumulants of the source signals. Using JADE algorithm, we can optimize the above cost function and get the ideal result.

Based on the cost function (7), we can fully depend on the second-order time structure by setting $\omega(3)$ and $\omega(4)$ equal to zero and utilize the temporal structure of the source signals by $\sum_{p=1}^{P} \sum_{i \neq j} (\mathrm{cum}_{ij}^{(2)}(\mathbf{y}))^2$; If we set $\omega(2) = 0$, we can derive the high-order statistics $\sum_{p=1}^{P} \sum_{ijk \neq ijj} (\mathrm{cum}_{ijk}^{(3)}(\mathbf{y}))^2$ and $\sum_{p=1}^{P} \sum_{ijkl \neq ijkk} (\mathrm{cum}_{ijk}^{(4)}(\mathbf{y}))^2$ based ICA algorithm. If the source signals have spatial independent and temporal structure, we set different weights $\omega(i)$, $i = 2, 3, 4$, the proposed algorithm is derived.

38.4 Conclusion and Discussion

The problems of blind separation of source signals have received wide attention in various fields such as biomedical signal analysis and processing. Its use in EEG literature is currently growing very fast. Applications of BSS show special promise in the areas of noninvasive human brain imaging techniques to delineate the neural processes that underlie human cognition functions. When applied to EEG data BSS decomposes measured signals in a number of components. BSS implicitly estimates their orientation and explicitly estimates their waveform (out of a sign and energy arbitrariness) and mixing coefficients. Since checking the assumptions of the chosen BSS model and method is virtually impossible, the most credible arguments must

be founded upon neurophysiological knowledge, So, to extract the relevant information for diagnosis and therapy, expert knowledge in medicine and engineering is also required.

References

1. Mutihac R, Mutihac RC (2007) A comparative study of independent component analysis algorithms for electroencephalography. Romanian Reports Physic 59(3):827–853
2. Congedo M, Gouy-Pailler C, Jutten C (2008) On the blind source separation of human electroencephalogram by approximate joint diagonalization of second order statistics. Clin Neurophysiol 119:2677–2686
3. Cichocki A, Amari S (2002) Adaptive blind signal and image processing: learning algorithms and applications. Wiley, New York
4. Comon P, Jutten C (2010) Handbook of blind source separation independent component analysis and applications. Elsevier, Oxford
5. Wang FS, Li HW, Li R (2008) Unified nonparametric and parametric ICA algorithm for hybrid source signals and stability analysis. Int J Innov Comput Inform Cont 4(4):933–942
6. Nunez PL, Srinivasan R (2006) Electric field of the brain, 2nd edn. Oxford Univ Press, New York
7. Féty L, Uffelen J-P (1988) New methods for signal separation. Proceedings of the 14th conference on HF radio system and techniques, London, pp 226–230
8. Tong L, Liu RW, Soon VC, Huang Y-F (1991) Indeterminacy and identifiability of blind identification. IEEE Trans Circuits Syst 38(5):499–509
9. Choi S, Cichocki A, Belouchrani A (2002) Second order nonstationary source separation. J VLSI Sig Process 32(1–2):93–104
10. Belouchrani A, Abed-Meraim K, Cardoso J-F, Moulines E (1997) A blind source separation technique using second-order statistics. IEEE Trans Signal Process 45(2):434–444
11. Nuzillard D, Nuzillard J-M (2003) Second-order blind source separation in the Fourier space of data. Sig Process 83(3):627–631
12. Rutledge DN, Jouan-Rimbaud Bouveresse D (2013) Independent components analysis with the JADE algorithm. TrAC Trends Anal Chem 50:22–32
13. Yeredor A (2002) Non-orthogonal joint diagonalization in the least-squares sense with application in blind source separation. IEEE Trans Signal Process 50(7):1545–1553
14. Pham D-T (2001) Joint approximate diagonalization of positive definite matrices. SIAM J Matrix Anal Appl 22(4):1136–1152

Chapter 39
Stabilization in Networked Flexible Joint Manipulator Systems

Yi Liu, Jun Liu and Jin Zhou

Abstract This paper considers the stabilization issues in networked systems of single-link flexible joint manipulators. By using the multiinput multioutput (MIMO) feedback linearization techniques, we present a unified procedure for studying stabilization problems of the network consisting of N flexible joint manipulators. Some general criteria on both local and global stabilization for such network are proposed, and the corresponding control inputs at some specific controlled nodes can be explicitly presented. The procedure shows that the networked single-link flexible manipulator systems can always be stabilized using MIMO linearization strategies. Finally, numerical simulations are performed to demonstrate the feasibility and effectiveness of the proposed procedure.

Keywords Networked · Manipulator system · Stabilization · Linearization techniques

39.1 Introduction

Controllability of various complex networks has recently become a rather significant topic from various fields of science and engineering due to its potential applications involving computer systems, electric circuits, manufacturing processes, communication systems, aircraft, spacecraft, and robots [1]. In particular, stabilization of networked control systems, as one of the specific form of network controllability, has been an important issue in the design of nonlinear control

Y. Liu · J. Liu · J. Zhou (✉)
Shanghai Institute of Applied Mathematics and Mechanics, Shanghai 200072, China
e-mail: jzhou@shu.edu.c

J. Liu
Department of Mathematics, Jining University, Qufu 273155, Shandong Province, China

systems over the past decade. The objective of stabilization control design can be stated as follows: Given a physical system to be stabilization controlled and the specifications of its desired behavior, construct a feedback control law to make the closed-loop system display the equilibrium state. In general, the feedback linearization techniques are proposed as a fundamental framework for studying the stabilization problems in control design of nonlinear systems. In this direction, there are many important results focused on some typical nonlinear systems derived from some practical engineering problems. Among others, Sun et al. [2] addressed the problem of feedback stabilization of nonholonomic-chained systems within the framework of nonregular feedback linearization. Qian and Lin [3] studied the global stabilization problem of a class of planar system whose Jacobian linearization is neither controllable nor observable, and an output feedback-like control was proposed to solve such problem. Moreover, Souza and Maruyama [4] presented the input structure for a system of multiarticulated bodies, the corresponding stabilization strategy was given for such multibody systems.

On the other hand, flexible joint manipulator has become a typical and popular model for the control design of nonlinear mechanical systems in engineering applications. Therefore, there exists a well-developed theoretical frame of controllability for single flexible joint manipulator systems. For example, Meng et al. [5] proposed a novel scheme for researching posture stabilization in manipulator systems. Atesoglu and Ozgoren [6] presented the nonlinear modeling of a tripod type parallel manipulator, and a stabilization controller is designed for base disturbance attenuation. Ge and Chang [7] focused on the same issue in the controlling rigid flexible manipulators by using its inverse dynamics. However, considerably less attention has been dedicated to the various types of network dynamics, and even less to the stabilization problems of networked manipulator systems. Since network is regarded as a good tool to deal with a set of interactional systems, it is essential to investigate the stabilization issues of networked manipulator systems, indicating its good potential in engineering applications.

By inspired in part by the aforementioned works, we consider in this paper the stabilization problem in networked systems of single-link flexible joint manipulators. Based on the multi-input multi-output(MIMO) feedback linearization techniques, some general criteria on both local and global stabilization for the networks consisting of N flexible joint manipulators are derived analytically; and the corresponding control inputs at some specific controlled nodes can be explicitly presented through its analysis procedure. It is shown that the networked single-link flexible manipulator systems can always be stabilized by using MIMO linearization strategies. The structure of the paper is organized as follows. Section 39.2 contains the preliminaries; Sect. 39.3 is the main results. Application examples and its simulation results are presented in Sect. 39.4. The conclusion is finally given in Sect. 39.5.

39.2 Preliminaries

Consider the following state-space realization of a MIMO nonlinear system with n states, m inputs and m outputs, $m \leq n$ as

$$\dot{x} = F(x) + \sum_{p=1}^{m} G_p u_p$$

$$y_i = h_i(x), \ i = 1, 2, \ldots, m \tag{39.1}$$

where $u = [u_1, u_2, \ldots, u_m]^T$, $y = [y_1, y_2, \ldots, y_m]^T$, $x = [x_1, x_2, \ldots, x_n]^T$ are the inputs, outputs and states, respectively. $F(x)$ is a smooth vector field on R^n, $G_1, G_2, \ldots, G_m$ are smooth vector fields on R^m and $h(x)_1, h(x)_2, \ldots, h(x)_m$ are smooth scalar fields.

Definition 39.1 [8, 9] A nonlinear MIMO system of the form (39.1) is said to have a relative degree r_i with respect to an output y_i if the vector

$$L_G L_F^k h_i(x) \triangleq \left[L_{G_1} L_F^k h_i(x) \ldots L_{G_m} L_F^k h_i(x) \right] = 0, \quad k = 0, 1, \ldots, r_i - 2;$$
$$L_G L_F^k h_i(x) \triangleq \left[L_{G_1} L_F^k h_i(x) \ldots L_{G_m} L_F^k h_i(x) \right] \neq 0, \quad k = r_i - 1.$$

Specially, $r = \sum_{i=1}^{m} r_i$ is called the relative degree of system (39.1).

Definition 39.2 [10] If system (39.1) has a well-defined relative degree r_i for each output y_i then the decoupled matrix of the system is the following $m \times m$ matrix

$$\beta(x) = \begin{bmatrix} L_{G_1} L_F^{r_1-1} h_1(x) & \cdots & L_{G_m} L_F^{r_1-1} h_1(x) \\ \vdots & \ddots & \vdots \\ L_{G_1} L_F^{r_m-1} h_m(x) & \cdots & L_{G_m} L_F^{r_m-1} h_m(x) \end{bmatrix}. \tag{39.2}$$

If a system represented by (39.1) has well-defined relative degree r_i for all outputs y_i with $r = \sum_{i=1}^{m} r_i (r \leq n)$ and the matrix (39.2) has full row rank m, then we have

$$\xi^i = \begin{bmatrix} \xi_1^i \\ \xi_2^i \\ \vdots \\ \xi_{r_i}^i \end{bmatrix} = \begin{bmatrix} h_i(x) \\ L_F h_i(x) \\ \vdots \\ L_F^{r_i-1} h_i(x) \end{bmatrix}, \ i = 1, 2, \ldots, m,$$

$$\dot{\eta}_i = \Phi_{r+i}(\xi, \eta), \ i = 1, 2, \ldots, n - r$$

where $\Phi_{r+i}(\xi, \eta)$ are chosen such that the Jacobian matrix of $\xi_1^1, \ldots,$ $\xi_{r_1}^1, \ldots, \xi_1^m, \ldots, \xi_{r_1}^m, \eta_1, \ldots, \eta_{n-r}$ is nonsingular. This transforms system (39.1) to the normal form

$$
\begin{bmatrix} \dot{\xi}_1^i \\ \dot{\xi}_2^i \\ \vdots \\ \dot{\xi}_{r_i}^i \end{bmatrix} = \begin{bmatrix} L_F h_i(x) \\ \vdots \\ L_F^{r_i-1} h_i(x) \\ L_F^{r_i} h_i + \sum_{p=1}^m \beta_{ip}(\xi, \eta) u_p \end{bmatrix}, \quad i = 1, 2, \ldots, m. \tag{39.3}
$$

$$
\dot{\eta} = \Phi(\xi, \eta) \tag{39.4}
$$

Thus the control input can be written as

$$
\begin{bmatrix} u_1 \\ u_2 \\ \vdots \\ u_m \end{bmatrix} = \beta^{-1} \left[\begin{bmatrix} v_1 \\ v_2 \\ \vdots \\ v_m \end{bmatrix} - \begin{bmatrix} L_F^{r_1} h_1 \\ L_F^{r_2} h_2 \\ \vdots \\ L_F^{r_m} h_m \end{bmatrix} \right], \tag{39.5}
$$

which implies

$$
\left[y_1^{(r_1)}, \ldots, y_1^{(r_m)} \right]^T = [v_1, \ldots, v_m]^T. \tag{39.6}
$$

Therefore stabilization controller v_i in (39.6) can be designed to ensure stability of system (39.1).

Remark 39.1 Using MIMO linearization techniques, system (39.1) is divided into two parts: External part (39.3) and internal part (39.4) (called internal dynamics). Furthermore, for global stability of system (39.1), internal dynamics (39.4) should be stable while for local stability of the system, the zero dynamics ($\dot{\eta} = \Phi(0, \eta)$) should be stable.

39.3 Main Results

In this section, the networked nonlinear dynamical systems consisting of N single-link flexible joint manipulators are constructed. The aim of this section is to present a control scheme, with which the nonlinear networked systems of single-link flexible joint manipulators can be linearized and the input control can be found easily.

39.3.1 Problem Formulation

First, consider a single flexible joint manipulator system described in [11], its dynamic equation can be described as

$$I\ddot{q}_1 + MgL\sin q_1 + K(q_1 - q_2) = 0,$$
$$J\ddot{q}_2 - K(q_1 - q_2) = 0.$$
(39.7)

Here Coriolis force and frictions are ignored. In this system, q_1 and q_2 are the rotation angle of manipulator joint and engine, I and J are the rotational inertia of the manipulator and the engine, respectively, M is the mass of the manipulator, L is the length from the center of the manipulator to the end of the link, and K is joint stiffness.

Next, we consider the networked systems consisting of N nodes, which can be represented as follows:

$$\dot{x}_i(t) = f(x_i) + c \sum_{j=1}^{N} a_{ij} H x_j + \sum_{p=1}^{m} G_{ip} u_p, \quad (i = 1, 2, \ldots, N),$$
(39.8)

in which each node is a single flexible joint manipulator system, where $x_i = (q_{i1}, \dot{q}_{i1}, q_{i2}, \dot{q}_{i2})^T$, $f(x_i)$ is the node i's state-space realization of dynamic function (39.7), that is

$$f(x_i) = \begin{bmatrix} x_{i2} \\ -\frac{MgL}{I}\sin x_{i1} - \frac{K}{I}(x_{i1} - x_{i2}) \\ x_{i4} \\ \frac{K}{J}(x_{i1} - x_{i2}) \end{bmatrix},$$

H is the inner coupling matrix connecting different components of a state vector, c is the coupling strength and $G_{ip} \in R^4$ is the smooth vector field. a_{ij} is defined as follows: If there is a connection between i and $j(i \neq j)$, $a_{ij} = a_{ji} = 1$; otherwise, $a_{ij} = a_{ji} = 0$, $a_{ii} = -\sum_{j=1, j \neq i}^{N} a_{ij} = -k_i$, k_i is the degree of node i. Therefore, the networked system of flexible joint manipulators can be written as form (39.1), where $n = 4N$, $x = [x_1, x_2, \ldots, x_N]^T$, $F(x) = [F(x_1), F(x_2), \ldots, F(x_N)]^T$, $F(x_i) = f(x_i) + c \sum_{j=1}^{N} a_{ij} H x_j$, $G_p = [G_{1p}, \ldots, G_{Np}]^T (p = 1, 2, \ldots, m)$.

39.3.2 Stabilization Controller Design

As shown above, system (39.1) can be controlled by using Definition 39.1, with which the nonlinear networked systems can be transformed to a linear one if the nonlinear systems are MIMO linearizable. Furthermore, the scheme for stabilizing a

special kind of the nonlinear networked systems can be given according to the existing control theory.

Theorem 39.1 *Consider a networked flexible joint manipulator systems in the form of* (39.1). *Let* $i_1, i_2, \ldots, i_m$ *be the controlled nodes, and H, G satisfies that* $H_{ii} \neq 0, H_{ij} = 0(i \neq j), G_{i_k,i_k} = [0,0,0,1]^T, G_{ij} = 0(i,j \neq i_k, k = 1, \ldots, m)$. *Denote the state equations of uncontrolled nodes as subsystem* $\sum$, *then the following conditions hold:*

- *System* (39.1) *is of local stability, if* $\sum$ *is stable with* $x_{i_j} = 0(j = 1, \ldots, m)$;
- *System* (39.1) *is of global stability, if* $\sum$ *is stable with any* $x_{i_j}(j = 1, \ldots, m)$.

Specially, the input control of node i_k can be constructed as follows:

$$u_{i_k} = \frac{I}{K}\left(v_{i_k} - L_F^{r_{i_k}} x_{i_k,1}\right), \quad (k = 1, \ldots, m). \tag{39.9}$$

Proof Without loss of generality, we consider the case of $N = 3$, let node $i(i = 1, 2)$ be controlled nodes, and the corresponding outputs are given by $y_1 = x_{11}$, $y_2 = x_{41}$.

According the structure of G in Theorem 39.1, the relative degree r_i with respect to the output y_i can be calculated easily, that is, $r_i = 4(i = 1, 2)$, therefore $r = 8$. According to Definition 39.1, we have

$$\begin{bmatrix} \xi_1^i \\ \xi_2^i \\ \xi_3^i \\ \xi_4^i \end{bmatrix} = \begin{bmatrix} x_{i1} \\ x_{i2} + a_{i1}H_{11}x_{11} + a_{i2}H_{11}x_{21} + a_{i3}H_{11}x_{31} \\ \xi_3^i(x_{i1}, x_{i2}, x_{i3}, x_{11}, x_{12}, x_{21}, x_{22}, x_{31}, x_{32}) \\ \xi_4^i(x_{i1}, x_{i2}, x_{i3}, x_{i4}, x_{11}, x_{12}, x_{13}, x_{21}, x_{22}, x_{23}, x_{31}, x_{32}, x_{33}) \end{bmatrix}, \quad (i = 1, 2).$$

where

$$\xi_3^i(x_{i1}, x_{i2}, x_{i3}, x_{11}, x_{12}, x_{21}, x_{22}, x_{31}, x_{32}) = L_F \xi_2^i,$$
$$\xi_4^i(x_{i1}, x_{i2}, x_{i3}, x_{i4}, x_{11}, x_{12}, x_{13}, x_{21}, x_{22}, x_{23}, x_{31}, x_{32}, x_{33}) = L_F \xi_3^i.$$

$\eta_i(i = 1, 2, 3, 4)$ is chosen such that

$$\eta_i = x_{3i}. \tag{39.10}$$

To proof the theorem, there is need to know whether the Jacobian of $\xi_1^1, \ldots, \xi_4^1, \xi_1^2, \ldots, \xi_4^2, \eta_1, \ldots, \eta_4$ is nonsingular. Notice that if the Jacobian is nonsingular, then there exits new coordinate transformation which transforms the nonlinear system (39.1) to a linear one and according to (39.10), the internal dynamics are

the state equations of node 3 (subsystem $\sum$). Hence, the stability properties mentioned in this theorem can be determined by subsystem $\sum$ using Remark 39.1. Meanwhile, the input control (39.9) can be calculated by Definition 39.1.

Therefore, we consider the Jacobian matrix of $\xi_1^1, \ldots, \xi_4^1, \xi_1^2, \ldots, \xi_4^2, \eta_1, \ldots, \eta_4$ in the following

$$
\begin{bmatrix}
1 & 0 & 0 & 0 & 0 & 0 & 0 & 0 & 0 & 0 & 0 & 0 \\
a_{11}H_{11} & 1 & 0 & 0 & a_{12}H_{11} & 0 & 0 & 0 & a_{13}H_{11} & 0 & 0 & 0 \\
* & * & K/I & 0 & * & * & 0 & 0 & * & * & 0 & 0 \\
* & * & * & K/I & * & * & * & 0 & * & * & * & 0 \\
0 & 0 & 0 & 0 & 1 & 0 & 0 & 0 & 0 & 0 & 0 & 0 \\
a_{21}H_{11} & 0 & 0 & 0 & a_{22}H_{11} & 1 & 0 & 0 & a_{23}H_{11} & 0 & 0 & 0 \\
* & * & 0 & 0 & * & * & K/I & 0 & * & * & 0 & 0 \\
* & * & * & 0 & * & * & * & K/I & * & * & * & 0 \\
0 & 0 & 0 & 0 & 0 & 0 & 0 & 0 & 1 & 0 & 0 & 0 \\
0 & 0 & 0 & 0 & 0 & 0 & 0 & 0 & 0 & 1 & 0 & 0 \\
0 & 0 & 0 & 0 & 0 & 0 & 0 & 0 & 0 & 0 & 1 & 0 \\
0 & 0 & 0 & 0 & 0 & 0 & 0 & 0 & 0 & 0 & 0 & 1
\end{bmatrix}
$$

In this matrix, * is the elements containing a_{ij}, H_{ii}, M, g, L, I, J, K, and x. Obviously, the Jacobian is nonsingular. Hence, this completes the proof of Theorem 39.1. □

39.4 Examples and Simulations

This section will give an example to illustrate the proposed control analysis. For simplicity, we take four nodes case with star-shaped network in system (39.1) for example.

For system (39.1) with a star-shaped network, a_{ij} in (39.8) is presented as follows: $a_{11} = -3, a_{ii} = -1, a_{i1} = a_{1i} = 1(i = 2, 3, 4), a_{ij} = a_{ji} = 0(i < j)$. In addition, let $H_{ii} = 1, H_{ij} = 0(i \neq j)$, and G be the matrix which satisfy the conditions in Theorem 39.1 and the controlled nodes in this example is node 2.

Thus, to stabilize the manipulator joints of the networked system, the input is designed by Theorem 39.1 as follows:

$$
u_2 = \frac{I}{K}(v_2 - \alpha_2),
$$

where

$$
v_2 = -x_{21} - z_1 - 3z_2 - z_3;
$$

$$\alpha_2 = \frac{Kx_{14} + \frac{K(x_{21} - x_{23})}{J} - x_{24}}{I} - \frac{3K(x_{13} - x_{23} + x_{24})}{I} - 5(x_{11} - x_{31} + x_{32})$$

$$- \frac{3(gLM\sin x_{31} + I(-x_{12} + x_{32}) + K(x_{31} - x_{33}))}{I} - 5(x_{11} - x_{41} + x_{42})$$

$$- \frac{12(-gLM\sin x_{11} + K(-x_{11} + x_{13}) + I(-3x_{12} + x_{22} + x_{32} + x_{42}))}{I}$$

$$- \frac{3(gLM\sin x_{41} + I(-x_{12} + x_{42}) + K(x_{41} - x_{43}))}{I}$$

$$+ \frac{3K(-3x_{13} + x_{14} + x_{23} + x_{33} + x_{43})}{I}$$

$$+ \frac{(gLM\sin x_{21} + I(-x_{12} + x_{22}) + K(x_{21} - x_{23}))(-6I + K + gLM\cos x_{21})}{I^2}$$

$$- \frac{(3x_{11} - x_{12} - x_{21} - x_{31} - x_{41})(16I - 3K - gLM(2\cos x_{11} + \cos x_{21}))}{I}$$

$$+ \frac{1}{I}(x_{11} - x_{21} + x_{22})(-6I + 3K + gLM(3\cos x_{21} - (x_{11} - x_{21} + x_{22})(-\sin x_{21})));$$

$$z_1 = x_{11} - x_{21} + x_{22};$$

$$z_2 = -\frac{gLM\sin x_{21}}{I} - 4x_{11} + 2x_{12} + 2x_{21} - 2x_{22} - \frac{K(x_{21} - x_{23})}{I} + x_{31} + x_{41};$$

$$z_3 = \frac{1}{I}(K(-3x_{11} + 3x_{13} + 3x_{21} - x_{22} - 3x_{23} + x_{24})$$

$$+ I(16x_{11} - 12x_{12} - 6x_{21} + 6x_{22} - 5x_{31} + 3x_{32} - 5x_{41} + 3x_{42})$$

$$+ gLM(-2\sin x_{11} + 2\sin x_{21} - (x_{11} - x_{21} + x_{22})\cos x_{21}));$$

The systems' parameters are listed in Table 39.1.

The simulation results are shown in Fig. 39.1. In this figure, the results of the angular displacement curves of four nodes are plotted where node 2 is the controlled node. By use of the feedback linearization techniques, the manipulator's angular displacement of node 2 (Fig. 39.1b) can move to its equilibrium point quickly after a disturb, while the uncontrolled node 1,3,4 (Fig. 39.1a, c, d) can also be stable after a period of time, which indicates that the proposed stabilization controller design can achieve the desired effect.

Table 39.1 The system nominal parameters

Parameter	M	g	L	I	J	K	c
Value	1	9.8	1	10	1	1	1
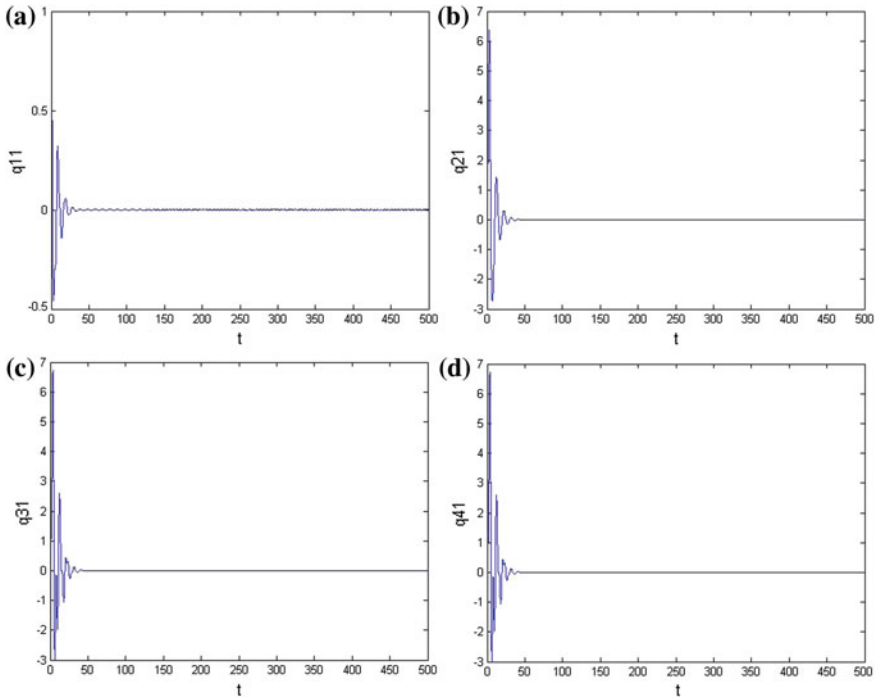
Fig. 39.1 The manipulator angular displacement curves of four nodes ((**a**), (**b**), (**c**) and (**d**) are the angular displacement curves of q_{11}, q_{21}, q_{31} and q_{41}, respectively.)

39.5 Conclusion

This paper considers the stabilization issues in networked systems of single-link flexible joint manipulators. By using the MIMO feedback linearization techniques, we present a unified procedure for studying stabilization problems of the network consisting of N flexible joint manipulators. Some general criteria on both local and global stabilization for such network are proposed, and the corresponding control inputs at some specific controlled nodes can be explicitly presented. The procedure shows that the networked single-link flexible manipulator systems can always be stabilized by using MIMO linearization strategies. Our future work includes the study of more general nonlinear dynamical models and network topologies.

References

1. Liu Y-Y, Slotine J-J, Barabasi A-L (2011) Controllability of complex networks. Nature 473 (7346):167–173. doi:10.1038/nature10011
2. Sun Z, Ge SS, Huo W, Lee TH (2000) Stabilization of nonholonomic chained systems via nonregular feedback linearization. In: Decision and control, IEEE, pp 1906–1911. doi:10.1109/CDC.2000.912141
3. Qian C, Lin W (2002) Output feedback stabilization of planar systems with uncontrollable/unobservable linearization. In: Decision and control, IEEE, pp 4324–4329. doi:10.1109/CDC.2002.1185051
4. de Souza EC, Maruyama N (2010) Feedback linearization for stabilization of a class of mobile, multibody systems. In: Decision and control, IEEE, pp 3590–3595. doi:10.1109/CDC.2010.5717336
5. Meng H, Cao L, Zhang Y, Gu J (2007) Posture stabilization of manipulator based on rotation platform. In: ICMA, IEEE, pp 88–93. doi:10.1109/ICMA.2007.4303521
6. Atesoglu O, Ozgoren MK (2008) The stabilization controller design for a tripod type parallel manipulator used for active suspension of a delicate device. In: CCA, IEEE, pp 1239–1246. doi:10.1109/CCA.2008.4629608
7. Ge XS, Chang J (2010) Tragectory tracking control of space rigid flexible manipulator. In: ICMTMA, IEEE, vol 782, pp 1047–1049. doi:10.1109/ICMTMA.2010.782
8. Kolavennu S, Palanki S, Cockburn JC (2001) Nonlinear control of nonsquare multivariable systems. Chem Eng Sci 56(6):2013–2110. doi:10.1016/S0009-2509(00)00470-X
9. Slotine J-JE, Li W (1991) Applied nonlinear control. Prentice Hall, Englewood Cliffs
10. Karimi HR, and Motlagh MRJ (2006) Robust feedback linearization control for a non linearizable MIMO nonlinear system in the presence of model uncertainties. In: IEEE, pp 965–970. doi:10.1109/SOLI.2006.328881
11. Marino R, Spang MW (1986) Nonlinear control techniques for flexible joint manipulators: a single case study. In: Robot, IEEE, pp 1030–1036. doi:10.1109/ROBOT.1986.1087613

Chapter 40
Design and Dynamic Analysis of an Underwater Manipulator

Wuxiang Zhang, Hongcheng Xu and Xilun Ding

Abstract Underwater Vehicle/Manipulator System (UVMS) is an important equipment for the exploitation of marine resources. The paper introduces a five-function manipulator, which is the main operating tool of UVMS and has four DOFs and a claw. All joints are driven by hydraulic cylinders for a better impermeability to seawater. A novel wrist mechanism utilizing groove cam is presented for achieving a rotation motion output. In addition, the dynamics of the manipulator interacting with the UVMS system is analyzed based on Kane's method. The effects from the fluid environment are also taken into consideration, which include added mass, drag force, and buoyancy. Finally, dynamic simulations of UVMS are performed to reveal the effect of the volume ratio between the manipulator and vehicle on the stability of UVMS and a critical ratio is found.

Keywords UVMS · Underwater manipulator · Wrist mechanism · Hydrodynamic forces · Volume ratio

40.1 Introduction

Underwater Vehicle/Manipulator System (UVMS) has been widely used in military and civil applications because of its capability of substituting human to perform underwater tasks in hazardous environment, such as underwater salvage, clearance,

W. Zhang (✉)
School of Mechanical Engineering and Automation, Beihang University,
100191 Beijing, China
e-mail: zhangwuxiang@buaa.edu.cn

H. Xu · X. Ding
State Key Laboratory of Robotics and System (HIT), 150006 Harbin, China
e-mail: xuhcheng@me.buaa.edu.cn

X. Ding
e-mail: xlding@buaa.edu.cn

and maintenance of underwater facilities. Underwater manipulator, as the main operating tool of UVMS, is subject to the limited payload capacity of the vehicle, corrosion, and permeation from seawater, as well as the high capability required in complex tasks, thus the optimal design of it is still in challenge.

Tremendous work on the design of underwater manipulator has been done by corporations and scholars. HLK-43000 [1] is a light-weight five-function manipulator and has been widely used in underwater tasks. Besides the grasping function, it has four DOFs: two on the shoulder, one on the elbow, and one on the wrist. Hydraulic actuators are used for driving. Electric cylinders are applied in ARM 5E [2] and the system can be controlled easily, but it may collapse if the seawater permeates. TITAN 4 [3] adopts another configuration: 1 DOF on the shoulder is shifted to the forearm, which increases the manipulator's dexterity. However, stability of UVMS would decrease since the mass center shifts away from the shoulder simultaneously, which aggrandizes the manipulator's influence on the vehicle. An et al. [4] designed a 3-DOF manipulator driven by electric motors whose axes are collinear with the axes of the correspondent joints.

Another problem encountered in the use of underwater manipulator is how to control it steadily. Unlike the manipulator on the ground, underwater manipulator suffers from the coupling interaction from the vehicle suspending in the water, that is, when the manipulator tries to reach the target, the vehicle will defect away from the original position and orientation, which will affect the operating accuracy of the manipulator in turn. Moreover, environment facts, such as the resistance and damping from the seawater, are non-negligible. To reduce the influences brought by the coupling interaction and the fluid environment for achieving accurate operation, the dynamic model of the UVMS system and the fluid environment is necessary to be developed. The dynamics of UVMS includes the multibody dynamics and hydrodynamics. For multibody dynamics, many methods can be chosen to establish the dynamic equations of the system, such as Newton-Euler, Lagrange method, Kane's method. Among these methods, Kane's method is characterized by the indifference of the internal forces and the lower computation cost [5]. Compared to multibody dynamics, hydrodynamics between the water and mechanical body is more complicated. Through analyzing the dynamics of Remote Operate Vehicle (ROV), Yuh et al. [6] identified 4 hydrodynamic forces which should be concerned: added mass, fluid acceleration, drag force, and buoyancy. Mcmillan et al. [7] further pointed out that the added mass can be represented by a 6×6 added inertia matrix. Fossen et al. [8] simplified the hydrodynamic model with two diagonal added inertia and damping matrices, considering the characteristic of the low velocity when UVMS was moving in the water. Levesque et al. [9] calculated the drag forces and momentums exerted on slender cylinder and square rods along the longitudinal axis. Zhang et al. [10] identified the hydrodynamic coefficients of a ROV via experiments.

In this paper, a five-function underwater manipulator with a novel wrist is introduced. Then, a dynamic model of the UVMS system is developed, and three hydrodynamic forces are discussed on the assumption that the flow velocity is

constant and there is no vortex. Simulations are performed to reveal the influence brought by the volume ratio between the manipulator and vehicle on the stability of the vehicle when the manipulator is moving.

40.2 Structure Design of the Underwater Manipulator

As stated previously, the manipulator has to cope with the contradiction between high capability and limited load of the vehicle, so cooperative design is necessary.

Balancing the mass and the capability, a five-function manipulator is designed in Fig. 40.1a. It contains four DOFs: shoulder rotating, upper arm lifting, elbow rotating, and wrist rotating. In addition, a claw is the end effector. The former three joints are used to ensure a reachability in 3-D space as well as the wrist rotating is designed for adjusting the orientation of the claw. The coordinate system of the manipulator is shown in Fig. 40.1b.

Instead of electric actuators which are sensitive to the permeation of seawater and hydraulic motors which need feedback control to maintain the position, hydraulic cylinders are chosen to drive all the joints and the claw for getting a high reliability of the entire system. The main parameters of the manipulator are shown in Table 40.1.

A novel wrist mechanism is designed in Fig. 40.2 for realizing the rotation motion output. Both cylinder-1 used for rotating the wrist and cylinder-2 for
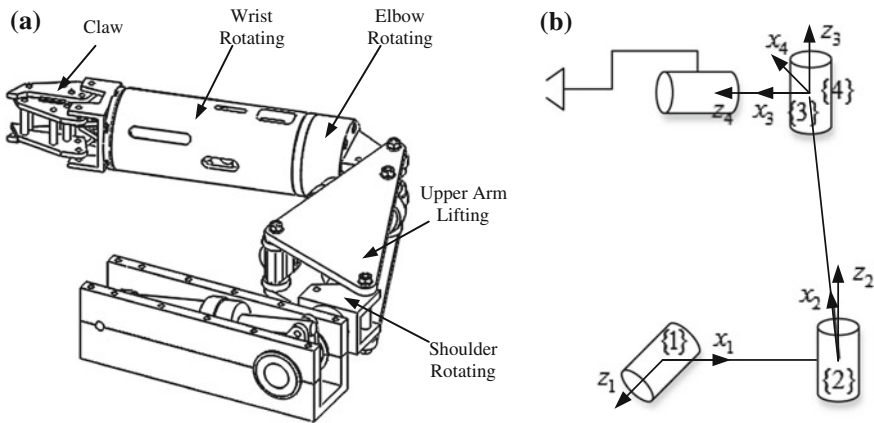
Fig. 40.1 The five-function underwater manipulator. **a** 3-D model, **b** coordinate system

Table 40.1 Main parameters of the manipulator

Length	Shoulder rotating	Upper arm lifting	Elbow rotating	Wrist rotating	Payload
650 mm	120°	90°	135°	180°	10 kg
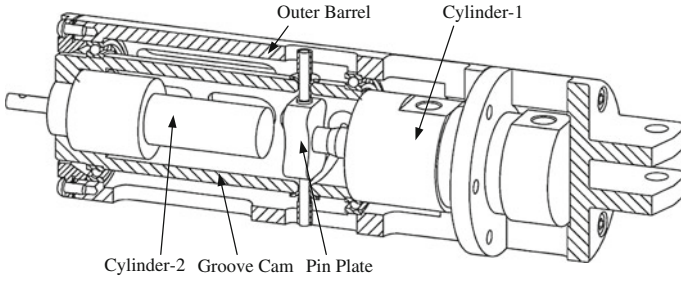
Fig. 40.2 Wrist mechanism

opening and closing the claw are embodied in the mechanism for reducing water resistance and interference. Groove cam rotates relative to the outer barrel, when the cylinder-1 drives the pins which pass through the helical groove on the groove cam to move along the axis of the outer barrel.

40.3 Dynamics of UVMS

UVMS is a nonlinear, strong-coupling, time-varying, and multibody system. The vehicle is suspending in the water when it works. Thus, when the manipulator tries to touch the target, the vehicle will defect away from the original position and orientation, which will affect the manipulator in turn. Moreover, ocean current and some other environment factors should be taken into consideration.

Figure 40.3 illustrates the coordinate system of a UVMS system equipped with the manipulator presented. {N} denotes the earth-fixed frame and {0} denotes the
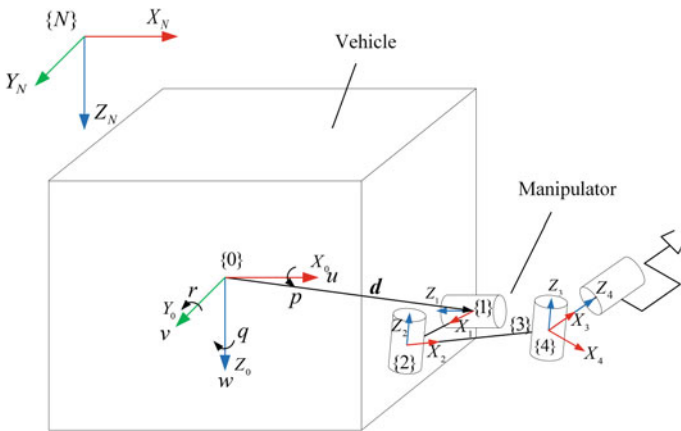
Fig. 40.3 The UVMS system

body-fixed frame located in the center of the vehicle. $\boldsymbol{d}$ is the position where the manipulator is planted. {1}, {2}, {3}, and {4} denote the body-fixed frames of each link on the manipulator, respectively.

The DOF of UVMS system is 10: six on the vehicle and four on the manipulator. Thus, 10 generalized speed are chosen here as

$$\dot{\boldsymbol{q}} = [u, v, w, p, q, r, \dot{\theta}_1, \dot{\theta}_2, \dot{\theta}_3, \dot{\theta}_4]^T \tag{40.1}$$

where $[u, v, w]^T$ and $[p, q, r]^T$ represent the linear and angular velocities of the vehicle expressed in body-fixed frame {0}. $\dot{\theta}_i (i = 1 \ldots 4)$ is the angular velocity of the i-th joint.

40.3.1 Hydrodynamics

The hydrodynamic model between the water and the body moving in it is complicated. It is necessary to simplify it for a practical application [11]. In the paper, three assumptions are made as a prerequisite: The flow velocity is constant, and there is no vortex; the velocity of UVMS is slow; the vehicle is equivalent to a cuboid and each link of the manipulator is equivalent to a cylinder. Therefore, three hydrodynamic forces including added mass, drag force, and buoyancy should be taken into consideration according to Reference [6].

40.3.1.1 Added Mass

When a body is accelerated through the seawater, the surrounding seawater will also be accelerated with the support from the body. Therefore, added mass force called added mass force whose direction is reverse is exerted on the body. It can be represented as a 6×6 matrix $\mathbf{I}_A$. The force $\boldsymbol{R}_A^*$ and momentum $\boldsymbol{T}_A^*$ applied on the body have the following form [5] as

$$\begin{bmatrix} \boldsymbol{R}_A^* \\ \boldsymbol{T}_A^* \end{bmatrix} = -\mathbf{I}_A \begin{bmatrix} \dot{\boldsymbol{v}}^{\text{rel}} \\ \dot{\boldsymbol{\omega}}^{\text{rel}} \end{bmatrix} - \begin{bmatrix} \tilde{\boldsymbol{\omega}}^{\text{rel}} & \mathbf{0} \\ \tilde{\boldsymbol{v}}^{\text{rel}} & \tilde{\boldsymbol{\omega}}^{\text{rel}} \end{bmatrix} \mathbf{I}_A \begin{bmatrix} \boldsymbol{v}^{\text{rel}} \\ \boldsymbol{\omega}^{\text{rel}} \end{bmatrix} \tag{40.2}$$

where $\boldsymbol{v}^{\text{rel}}$ and $\boldsymbol{\omega}^{\text{rel}}$ are the relative linear and angular velocities with respect to ocean current; $\tilde{\boldsymbol{v}}^{\text{rel}}$ and $\tilde{\boldsymbol{\omega}}^{\text{rel}}$ represent the operators $(\boldsymbol{v}^{\text{rel}} \times)$ and $(\boldsymbol{\omega}^{\text{rel}} \times)$, respectively.

40.3.1.2 Drag Force

Drag force is mainly caused by the impact of the ocean current. Theoretically, drag force should be derived by applying the potential theory and calculated via a surface

integral over the entire body. However, practically the drag force is calculated via an integral along the main axis based on strip theory according to the simplified formula [7, 9]

$$\mathrm{d}\boldsymbol{F}_D = \frac{1}{2}\rho C_D \|\boldsymbol{U}^\perp\| \boldsymbol{U}^\perp \cdot b \mathrm{d}x \tag{40.3}$$

where $\mathrm{d}\boldsymbol{F}_D$ represents the elementary drag force. ρ is the density of the fluid. C_D is the drag coefficient and $\boldsymbol{U}^\perp$ is the component of the flow velocity relative to the body whose direction is perpendicular to the axis. $b\mathrm{d}x$ represents the elementary area, in which b is the dimension in the plane normal to the axis and $\mathrm{d}x$ elementary length along the X-axis.

Since the shapes of the vehicle and links of the manipulator are different, we deal with them separately.

(a) Vehicle

When the vehicle pierces the water, there are at most 3 faces subject to the impact of the water. The distributions of the normal components of the relative flow velocities on the 3 pairs of opposite faces are symmetric. Therefore, without loss of generality, we can choose face Π_A, Π_B, and Π_C for analysis, as shown in Fig. 40.4. Instead of integrating over the whole face, we choose 2 symmetric axes of the face as the integrating direction.

The vehicle is sliced along the X_0-axis in Fig. 40.4a. The point P_1 on the symmetric axis is chosen as a reference point representing the whole strip. The relative velocity of the fluid $\boldsymbol{v}^r_{P_1}$ at P_1 is given as

$$\boldsymbol{v}^r_{P_1} = \boldsymbol{v}_{\mathrm{flow}} - (\boldsymbol{v}_0 + \boldsymbol{\omega}_0 \times \boldsymbol{r}_{P_1}) \tag{40.4}$$

where $\boldsymbol{v}_{\mathrm{flow}}$ is the velocity of the flow, relative to the earth; $\boldsymbol{r}_{P_1}$ is position vector of P_1, relative to the origin of frame $\{0\}$.
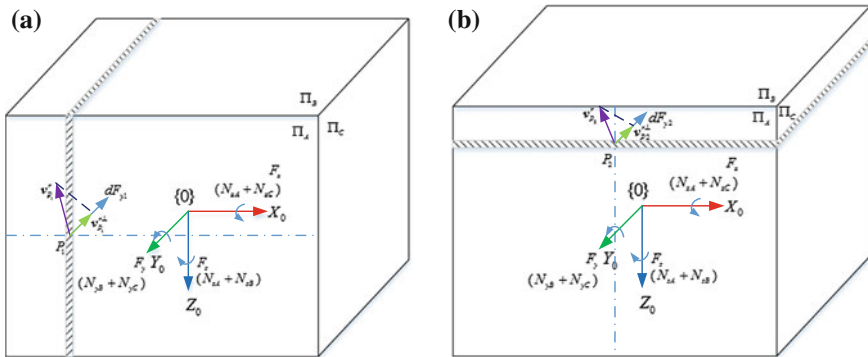

Fig. 40.4 Drag force exerted on the vehicle. **a** integral along X_0-axis over face Π_A; **b** integral along face Z_0-axis over face Π_A

The force tangent to the face is negligible in the paper. Based on Eq. (40.3), through integrating along the X_0-axis, we can obtain one of force $\boldsymbol{F}_y$ along Y_0-axis and a part of momentum N_z about Z_0-axis contributed by face Π_A as

$$\boldsymbol{F}_{y1} = \int\limits_{-l/2}^{l/2} \frac{1}{2_D} \left\| \boldsymbol{v}_{P_1}^{r\perp}(x) \right\| \boldsymbol{v}_{P_1}^{r\perp}(x) \cdot h\mathrm{d}x,$$

$$N_{zA} = \int\limits_{-l/2}^{l/2} \frac{1}{2} \rho C_D \left\| \boldsymbol{v}_{P_1}^{r\perp}(x) \right\| (\boldsymbol{v}_{P_1}^{r\perp}(x) \times \boldsymbol{r}_{P_1}) \cdot h\mathrm{d}x. \tag{40.5}$$

where l represents the length of the vehicle; $\boldsymbol{v}_{P_1}^{r\perp}(x)$ is the component of flow velocity normal to face Π_A; h is the height of the vehicle.

Similarly, the second one of force $\boldsymbol{F}_y$ and a part of momentum N_x about X_0-axis contributed by face Π_A can be calculated as

$$\boldsymbol{F}_{y2} = \int\limits_{-h/2}^{h/2} \frac{1}{2_D} \left\| \boldsymbol{v}_{P_2}^{r\perp}(x) \right\| \boldsymbol{v}_{P_2}^{r\perp}(x) \cdot l\mathrm{d}z,$$

$$N_{xA} = \int\limits_{-h/2}^{h/2} \frac{1}{2} \rho C_D \left\| \boldsymbol{v}_{P_2}^{r\perp}(x) \right\| (\boldsymbol{v}_{P_2}^{r\perp}(x) \times \boldsymbol{r}_{P_2}) \cdot l\mathrm{d}z \tag{40.6}$$

where $\boldsymbol{v}_{P_2}^{r\perp}(x)$ is the component of flow velocity at point P_2 normal to face Π_A; $\boldsymbol{r}_{P_2}$ is position vector of P_2, relative to the origin of frame $\{0\}$.

In the same way, we can obtain a series of forces and momentums: $\boldsymbol{F}_{x1}$, $\boldsymbol{F}_{x2}$; $\boldsymbol{F}_{z1}$, $\boldsymbol{F}_{z2}$; N_{yB}, N_{zB}; N_{xC}, N_{yC}. Thus, the resulting forces and momentums are given as

$$\begin{cases} \boldsymbol{F}_x = (\boldsymbol{F}_{x1} + \boldsymbol{F}_{x2})/2 \\ \boldsymbol{F}_y = (\boldsymbol{F}_{y1} + \boldsymbol{F}_{y2})/2, \\ \boldsymbol{F}_z = (\boldsymbol{F}_{z1} + \boldsymbol{F}_{z2})/2 \end{cases} \begin{cases} N_x = N_{xA} + N_{xC} \\ N_y = N_{yB} + N_{yC} \\ N_z = N_{zA} + N_{zB} \end{cases} \tag{40.7}$$

(b) Link of the Manipulator

The calculation of the drag force on each link of the manipulator is quite similar to that on the vehicle. The points on the longitudinal axis, i.e., X_i-axis, are chosen as the reference points and the component of relative flow velocity perpendicular to the X_i-axis is considered, as shown in Fig. 40.5. Link-3 and Link-4 are regarded as one link because of their coincidence at the origins. Hence, the drag force $\boldsymbol{F}_i$ and momentum N_i are described as
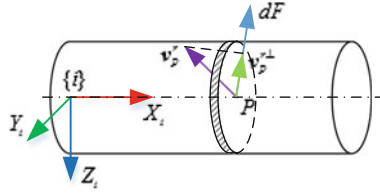
Fig. 40.5 Drag force on Link-i of the manipulator

$$F_i = \int_0^{l_i} \frac{1}{2}\rho C_D \|v_P^{r\perp}(x)\| v_P^{r\perp}(x) \cdot 2r_i \mathrm{d}x \quad (i = 1, 2, 3)$$

$$N_i = \int_0^{l_i} \frac{1}{2}\rho C_D \|v_P^{r\perp}(x)\| (v_P^{r\perp}(x) \times r_P) \cdot 2r_i \mathrm{d}x \quad (i = 1, 2, 3)$$

(40.8)

where l_i is length of the i-th link and $v_P^{r\perp}(x)$ is the component of flow velocity at a point P perpendicular to the longitudinal axis. r_P is the position vector of the point P relative to the origin of frame $\{i\}$. r_i is the radius of the cylinder.

40.3.1.3 Buoyancy and Gravity

Buoyancy and gravity are put together to deal with since their directions are collinear or parallel if the mass center and buoyancy center do not coincide. The resultant force R_{GBi} and momentum T_{GBi} of buoyancy and gravity are given as

$$\begin{bmatrix} R_{GBi} \\ T_{GBi} \end{bmatrix} = \begin{bmatrix} f_{Gi} + f_{Bi} \\ r_{Gi} \times f_{Gi} + r_{Bi} \times f_{Bi} \end{bmatrix}$$

(40.9)

where f_{Bi} and f_{Gi} are the buoyancy and gravity; r_{Bi} and r_{Gi} are the position vectors of buoyancy and mass centers.

40.3.2 Inertia and Control Forces

The generalized inertia force R_i^* and momentum T_i^* of each body can be given as

$$R_i^* = -m_i \cdot a_i, \quad T_i^* = -\mathbf{J}_i \cdot \alpha_i - \omega_i \times \mathbf{J}_i \cdot \omega_i$$

(40.10)

where m_i represents the mass; a_i and α_i represents the linear and angular accelerations; $\mathbf{J}_i$ represents the inertia matrix.

The vehicle is driven by the propellers planted in it, which can be equivalent to being applied by a resultant force $\boldsymbol{R}_{C0}$ and momentum $\boldsymbol{T}_{C0}$:

$$\boldsymbol{R}_{C0} = \begin{bmatrix} R_{Cx} & R_{Cy} & R_{Cz} \end{bmatrix}^T, \quad \boldsymbol{T}_{C0} = \begin{bmatrix} T_{Cx} & T_{Cy} & T_{Cz} \end{bmatrix}^T \tag{40.11}$$

There is also a control torque $\boldsymbol{T}_{Ci}$ on each joint:

$$\boldsymbol{T}_{Ci} = {}_{i}^{0}\mathbf{R} \cdot \begin{bmatrix} 0 & 0 & T_{Ci} \end{bmatrix}^T \tag{40.12}$$

where ${}_{i}^{0}\mathbf{R}$ is the transformation matrix from frame $\{0\}$ to frame $\{i\}$.

40.3.3 Dynamic Equations

From all the concerned forces calculated, the total generalized active force and inertia force [12] can be obtained as

$$\begin{aligned} F_r = &\sum_{i=0}^{4} \left[\frac{\partial \boldsymbol{\omega}_i}{\partial \dot{q}_r} \cdot (\boldsymbol{T}_{Di} + \boldsymbol{T}_{GBi}) + \frac{\partial \boldsymbol{v}_i}{\partial \dot{q}_r} \cdot (\boldsymbol{R}_{Di} + \boldsymbol{R}_{GBi}) \right] \\ &+ \left(\frac{\partial \boldsymbol{v}_0}{\partial \dot{q}_r} \cdot \boldsymbol{R}_{C0} + \frac{\partial \boldsymbol{\omega}_0}{\partial \dot{q}_r} \cdot \boldsymbol{T}_{C0} \right) + \sum_{i=1}^{4} \left(\frac{\partial \boldsymbol{\omega}_i}{\partial \dot{q}_r} - \frac{\partial \boldsymbol{\omega}_{i-1}}{\partial \dot{q}_r} \right) \cdot \boldsymbol{T}_{Ci} \quad (r = 1, \ldots, 10) \\ F_r^* = &\sum_{i=0}^{4} \left[\frac{\partial \boldsymbol{\omega}_i}{\partial \dot{q}_r} \cdot (\boldsymbol{R}_{Ai}^* + \boldsymbol{R}_i^*) + \frac{\partial \boldsymbol{v}_i}{\partial \dot{q}_r} \cdot (\boldsymbol{T}_{Ai}^* + \boldsymbol{T}_i^*) \right] \quad (r = 1, \ldots, 10) \end{aligned}$$

$$\tag{40.13}$$

According to Kane's method, the dynamic equation of the system is established as

$$F_r + F_r^* = 0 \quad (r = 1, \ldots, 10) \tag{40.14}$$

40.4 Simulation

Based on the dynamic equations derived previously, we perform simulations to test the stability of the vehicle at different volume ratio between the manipulator and the vehicle during the manipulator's working process. The parameters used for the simulations are shown in Table 40.2.

We use the dimensions of the vehicle in Table 40.2 as the normal dimensions and change the volume ratio by ±10 % and ±20 %. The system is static in still water initially, and the vehicle will defect when the manipulator is moving.

Table 40.2 Parameters for simulation

Vehicle		Manipulator		Environment	
Dimensions	700 mm × 500 mm × 500 mm	Link-1	Length: 50 mm	Gravity	9.8 m/s^2
			Radius: 40 mm		
			Mass: 0.16 kg		
Mass	70 kg	Link-2	Length: 50 mm	Density of seawater	1025 kg/m^3
			Radius: 40 mm		
			Mass: 0.16 kg		
		Link-3 and Link-4	Length: 50 mm		
			Radius: 40 mm		
			Mass: 0.16 kg		
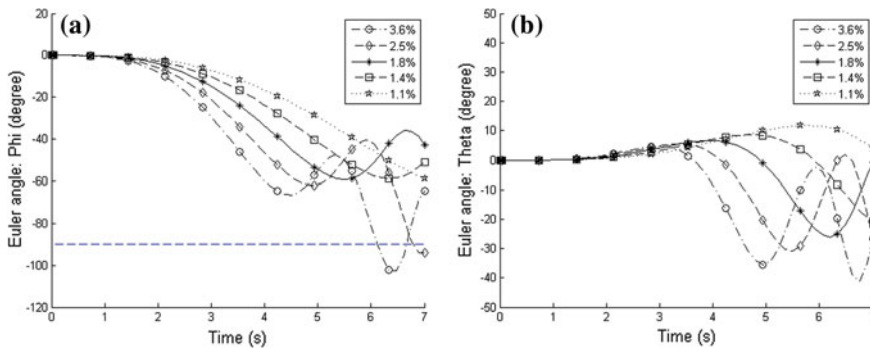
Fig. 40.6 Orientation deflection of the vehicle. **a** Euler angle: phi, **b** Euler angle: theta

The stability of the vehicle is evaluated by the Euler angle ϕ and θ. From the simulation results, as shown in Fig. 40.6, we can find that the lower the volume ratio between the manipulator and the vehicle is, the more stable the vehicle will be, and the vehicle will dip over 90° with a volume ratio bigger than 2.5 %.

40.5 Conclusion

In this paper, a five-function underwater manipulator is introduced for marine salvage, underwater clearance, and other underwater tasks. A novel wrist mechanism, which uses the less inner leakage cylinder as the actuator and the groove cam for transmission, is developed for a 180° rotation. The dynamic model of the entire UVMS composed of the manipulator and a ROV are analyzed including the effects from the fluid environment for providing basic information for its control system. Dynamic simulations are performed and the results show that with a lower volume ratio between the manipulator and the vehicle, the stability of the vehicle will be higher.

References

1. Hydro-Lek Remote Handling. Manipulator, http://www.hydro-lek.com/manipulators.php
2. ECA Robotics. Manipulator arms. http://www.eca-robotics.com/robotics-security-manipulator-arm.htm
3. Schilling Robotics. TITAN 4. http://www.fmctechnologies.com/en/SchillingRobotics.aspx
4. An J, Sun C et al (2009) Design and research on structure of underwater manipulator. Mech Eng Autom 91–92 (in Chinese)
5. Tarn T, Shoults G, Yang S (1996) A dynamic model of an underwater vehicle with a robotic manipulator using Kane's method. Underwater robots. Springer, New York, pp 195–209
6. Yuh J (1990) Modeling and control of underwater robotic vehicles. IEEE Trans Syst Man Cybern 20(6):1475–1483
7. McMillan S, Orin DE, McGhee RB (1995) Efficient dynamic simulation of an underwater vehicle with a robotic manipulator. IEEE Trans Syst Man Cybern 25(8):1194–1206
8. Fossen TI (1994). Guidance and control of ocean vehicles
9. Lévesque B, Richard MJ (1994) Dynamic analysis of a manipulator in a fluid environment. Int J Robot Res 13(3):221–231
10. Zhang Y, Xu G et al (2010) Measuration of the hydrodynamics coefficients of the microminiature open-shelf underwater vehicle. Ship Build China 51(1):63–72 (in Chinese)
11. Lamb H (1993) Hydrodynamics. Cambridge University Press, Cambridge
12. Kane TR, Levinson DA (1985) Dynamics, theory and applications. McGraw Hill, New York

Chapter 41
Human-Like Task Planning
for a Dual-Arm Robot Based
on Motion Primitives

Hongcheng Xu and Xilun Ding

Abstract Task planning has an important effect on the anthropomorphic characteristics of the motion of the humanoid robot. In this paper, human-like task planning for a dual-arm robot is discussed. A bottom-up task planning approach is proposed based on the motion primitives which imply the features of human motion, in order to obtain a human-like motion fundamentally. Unlike the traditional methods which decompose the task into a sequence of well-designed trajectories of the end-effector in task space, we ignore the trajectory planning temporarily, and assemble the motion primitives until the task is accomplished. Therefore, the human-like posture is guaranteed all the time, and there is no need to spend much time in solving the inverse kinematics of redundant manipulators and performing an optimization for a human-like posture. Two basic and specific tasks are analyzed based on the proposed approach. Finally, simulations are performed to verify the validation and feasibility, and the characteristics of the planned motion are discussed.

Keywords Task planning · Dual-arm robot · Motion primitive · Bottom-up approach

41.1 Introduction

As humanoid robots are gradually stepping into human society, the human-like motion of robots plays a significant role in enhancing the cooperation between the robots and humans, and accelerating the robot's pace of merging into the society.

H. Xu (✉) · X. Ding
School of Mechanical Engineering and Automation, Beihang University, Beijing, China
e-mail: xuhcheng@mail.buaa.edu.cn

X. Ding
e-mail: xlding@buaa.edu.cn

Different from the awkward and unpredictable motions planned using traditional methods which concentrate on predetermined performance indices, such as dexterity, joint limitation, obstacle avoidance, etc. [1, 2], recently humanoid robots are strongly expected to act in a human way so that they can be easily accepted when interacting with humans. Moreover, through transferring the human skills of dealing with tasks into the motion control of humanoid robots, humanoid robots can acquire the capability of generating new skills and flexibility of adapting to new environment.

Tremendous work on anthropomorphic motion planning of humanoid robots has been done. Zacharias et al. [3] employed Rapid Upper Limb Assessment (RULA) from ergonomics research to evaluate a human-like configuration. However, RULA is a discrete criterion; therefore it may obtain the same score within a range of the configurations and needs a secondary optimization. Park et al. [4] used Evolutionary Algorithm (EA)-based imitation learning, which collects the data captured from human motions and can generate a human-like motion. With this approach, massive experiments need to be conducted to collect enough data. Based on the opinion that motion primitives exist in the motion process of the human arm from neurophysiology [5], Ding and Fang [6] introduced the concepts of motion primitives and working plane to the motion planning of humanoid robots by combining different motion primitives and shifting between different working planes.

In task planning, it seems that most scholars intend to initially plan well-designed trajectories of the end-effector for task completion in task space and then perform motion planning based on the methods mentioned above to obtain a humanoid posture. Adorno et al. [7] did a lot of work on the dual position control trajectories of a dual-arm robot in task space. In [8], the iCub robot could draw a perfect circle in a 3-D space. However, performing trajectory planning firstly and then planning the motion is not essentially human-like, since human can neither draw an exactly straight line without a ruler nor a perfect circle without a compass. To make the robots complete the task really like human, Zöllner et al. [9] built a Programming by Demonstration (PbD) system to teach the robots how to achieve the work in a human-like way. But this method will take much time to train the robot and is difficult to be extended to different tasks. Our aim is to propose a bottom-up approach for human-like task planning based on our previous work on motion primitives, so that the robots move in a human-like way and are capable of adjusting to different tasks easily.

The rest of this paper is organized as follows. Section 41.2 introduces nine elementary motion primitives. Section 41.3 establishes a task planning framework based on motion primitives, and two basic and specific tasks are planned particularly based on the proposed method. In Sect. 41.4, simulations of accomplishing the basic tasks are performed, and the differences compared to traditional task planning method are discussed. Conclusions are drawn in Sect. 41.5.

41.2 Motion Primitives

According to the previous work by Fang and Ding [10], nine elementary motion primitives of the human arm have been defined, as shown in Table 41.1:

1. $\Delta - S_1$, Shoulder rotation about the axis S_Z of upper arm;
2. $\Delta - S_2$, Shoulder rotation about the axis S_X, which is perpendicular to the plane defined by the centers of the shoulder, elbow and wrist;
3. $\Delta - S_3$, Shoulder rotation about the axis S_Y, where $S_Y = S_Z \times S_X$;
4. $\Delta - S_4$, Shoulder rotation about the axis S_{SW} passing the centers of the shoulder and wrist;
5. $\Delta - E_1$, Elbow rotation about the axis E_Z of elbow;
6. $\Delta - W_1$, Wrist rotation about the axis W_Z along the fingers;
7. $\Delta - W_2$, Wrist rotation about the axis W_X, which is perpendicular to the palm;
8. $\Delta - W_3$, Wrist rotation out the axis W_Y, where $W_Y = W_Z \times W_X$;
9. $\Delta - W_4$, Wrist rotation about the axis W_{EW} passing the centers of the elbow and wrist.

The entire motion primitives repertoire can be spanned by applying a well-defined set of operations and transformations to these elementary primitives and by combining them according to well-defined syntactic rules [5]. Details on the rules of combining the motion primitives can be found in Ref. [11].

41.3 Task Planning

41.3.1 Framework of Task Planning

The framework of task planning is shown in Fig. 41.1. The main idea is to focus on the accomplishment of the task and try to simplify the motion of the manipulator by employing the features of the human arm motion which are implied in the motion primitives. Therefore, the trajectory of the end-effector is not strictly restricted initially. Motion primitive library contains the 9 elementary motion primitives as well as the others generated from them. Task planner connects the motion primitive library and the task, and is responsible to balance the efficiency of completing the specific task and the simplicity of the manipulator's motion and finally to determine how to select appropriate primitives to finish the task. After this, the trajectory of the end-effector has been determined and the task has been decomposed into a sequence of subtasks, each of which corresponds to a set of motion primitives. The motion primitive can be mapped into the joint space [6].

It should be noticed that ignoring the trajectory of end-effector temporarily does not lead to disorder and chaos. In fact, since the proposed approach is a bottom-up approach, i.e., from basic motion primitives up to a complex task, anthropomorphic

Table 41.1 Elementary motion primitives

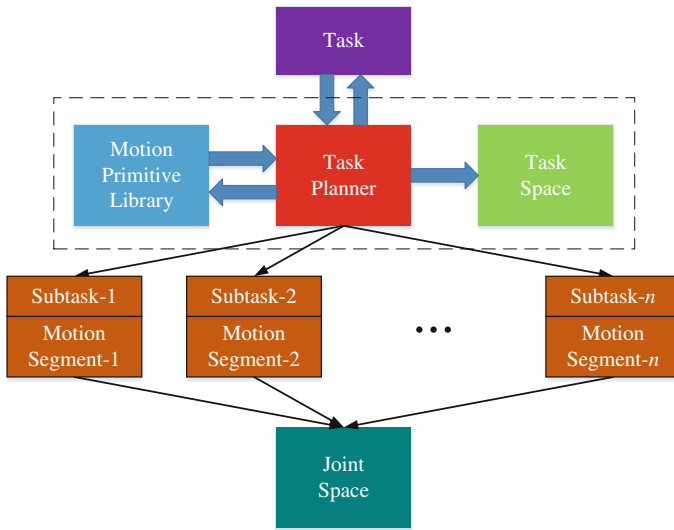| Shoulder		Elbow		Wrist	
Symbol	Chart	Symbol	Chart	Symbol	Chart
$\Delta - S_1$		$\Delta - E_1$		$\Delta - W_1$	
$\Delta - S_2$				$\Delta - W_2$	
$\Delta - S_3$				$\Delta - W_3$	
$\Delta - S_4$				$\Delta - W_4$	

Fig. 41.1 Framework of task planning

posture of the arm during the task execution is maintained all the time. Therefore, the trajectory of the arm end is much more natural.

41.3.2 Task Planning for Specific Tasks

Task planning for two basic and specific dual-arm tasks based on the proposed approach will be performed in this section: lifting a box and inserting a pen into the pen cap.

41.3.2.1 Lifting a Box

Considering the task of lifting a box with dual arms, there is no strict accuracy requirement for the position of the end point, that is, what is needed to be done is to lift the box and transfer it to an *appropriate* position near the body. The box may need to keep upright, which is required in common situations, e.g., when the box contains fluid. To simplify the motion and balance the payload on dual arms, the configurations of the dual arms are symmetrical and the box moves in the symmetrical plane of the body. The two palms will keep touching the box to prevent it from falling. Therefore, 3 goals need to be achieved: (1) Transfer the box to an *appropriate* position near the body; (2) Keep the palm touching the box; (3) Keep the box upright.
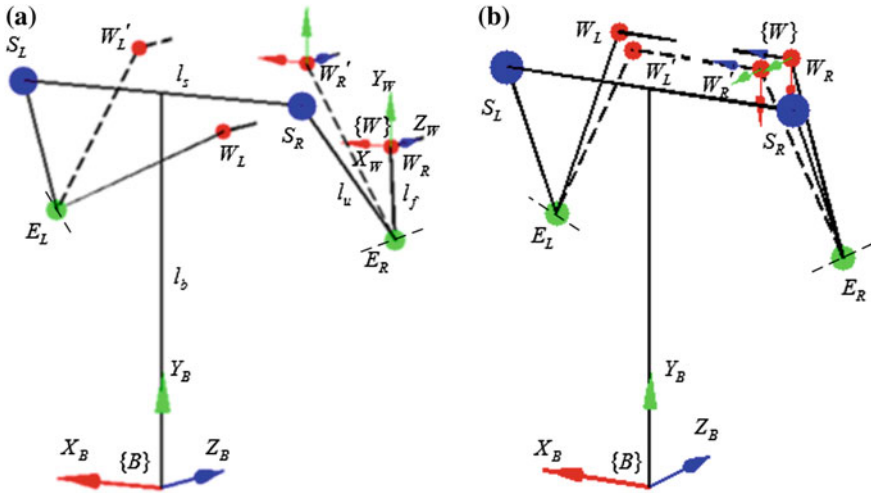
Fig. 41.2 Two specific tasks. **a** Lifting a box. **b** Inserting a pen into the pen cap

To achieve this task, motion primitives should be selected firstly. By analogy to the motions of humans when executing the task, if the initial configuration of the dual-arm robot is well posed, shoulder rotation $\Delta - S_1$ and elbow rotation $\Delta - E_1$ can be adequate for transferring, and wrist rotation $\Delta - W_1$, $\Delta - W_2$ and $\Delta - W_3$ need to be selected to satisfy the orientation requirements.

As shown in Fig. 41.2, an inertial reference frame $\{B\}$ is defined on the waist, and a body fixed frame $\{W\}$ on the wrist; l_b denotes the height of the body; l_s denotes the width of the shoulder; l_u and l_f denote the length of the upper arm and forearm, respectively; S_R, E_R and W_R represent the centers of the shoulder, elbow, and wrist on the right arm, respectively; while S_L, E_L and W_L correspond to the left arm. The initial orientation of $\{W\}$ is the same as $\{B\}$ and keeps the palm touching the box.

Because of the symmetry of dual arms, we only need to analyze one arm: the right arm is selected. The configuration of the body fixed frame $\{W\}$ in the global inertia frame $\{B\}$ is described as [12]:

$$\mathbf{g}_{BW} = e^{\hat{\xi}_1\theta_1} e^{\hat{\xi}_2\theta_2} e^{\hat{\xi}_3\theta_3} e^{\hat{\xi}_4\theta_4} e^{\hat{\xi}_5\theta_5} \mathbf{g}_{BW}(0) \qquad (41.1)$$

where $\mathbf{g}_{BW}(0) \in SE(3)$ is the initial configuration of $\{W\}$; $\theta_i \in R$ is the angle of the motion primitive $\Delta - S_1$, $\Delta - E_1$, $\Delta - W_1$, $\Delta - W_2$ or $\Delta - W_3$; $\hat{\xi}_i \in se(3)$ describes the screw of these motion primitives.

The spatial velocity of the wrist, which is measured at the origin of the global inertial frame $\{B\}$, is denoted by V_{BW}^B and can be calculated as

$$V_{BW}^B = \begin{bmatrix} v_{BW}^B \\ \omega_{BW}^B \end{bmatrix} = \mathbf{J}_{BW}^B(\boldsymbol{\theta})\dot{\boldsymbol{\theta}} \tag{41.2}$$

where v_{BW}^B and ω_{BW}^B are the linear velocity and angular velocity parts of the spatial velocity V_{BW}^B; $\mathbf{J}_{BW}^B(\boldsymbol{\theta}) = \begin{bmatrix} \boldsymbol{\xi}_1 & \boldsymbol{\xi}_2' & \boldsymbol{\xi}_3' & \boldsymbol{\xi}_4' & \boldsymbol{\xi}_5' \end{bmatrix}$, is the Jacobian matrix, and the ith column of $\mathbf{J}_{BW}^B(\boldsymbol{\theta})$ is given by

$$\boldsymbol{\xi}_i' = \mathrm{Ad}_{\exp(\hat{\xi}_1\theta_1)\cdots\exp(\hat{\xi}_{i-1}\theta_{i-1})}\boldsymbol{\xi}_i \tag{41.3}$$

The linear velocity of the point of wrist center can be calculated as:

$$\boldsymbol{v}_c = \begin{bmatrix} v_{cx} \\ v_{cy} \\ v_{cz} \end{bmatrix} = \omega_{BW}^B \times \boldsymbol{p}_c + v_{BW}^B \tag{41.4}$$

where v_{cx}, v_{cy} and v_{cz} are the coordinates of $\boldsymbol{v}_c$; $\boldsymbol{p}_c$ represents the position of wrist center, which is irrelevant to θ_3, θ_4 and θ_5, i.e., $\boldsymbol{p}_c = e^{\hat{\xi}_1\theta_1}e^{\hat{\xi}_2\theta_2}\boldsymbol{p}_{c0}$, where $\boldsymbol{p}_{c0}$ is the initial position of wrist center.

To achieve the 3 goals as mentioned above, the follow constraints should be satisfied:

$$\begin{cases} v_{cx} = 0, \\ \omega_{BW}^B = \mathbf{0} \end{cases} \tag{41.5}$$

Equation (41.5) supplies 4 equations and establishes the relationship among $\dot{\theta}_1$, $\dot{\theta}_2$, $\dot{\theta}_3$, $\dot{\theta}_4$ and $\dot{\theta}_5$. After the motion of the elbow is given, i.e., $\dot{\theta}_2$ is given, we can solve Eq. (41.5) and obtain the other joints' angular velocities.

41.3.2.2 Inserting a Pen into the Pen Cap

We perform an assembly task of inserting the pen into the pen cap in this subsection. Let the left arm hold the pen and the right arm hold the pen cap. Both the axes of the pen and pen cap are collinear with the axes W_Z along the left and right hand fingers. Symmetry of the body is still employed to simplify the motion. Dual arms move close to the symmetrical plane holding the pen and pen cap. The trajectories of the pen and pen cap do not need to be in a fixed plane, which can be seen frequently in traditional task planning. Therefore, 2 goals need to be achieved: (1) Move the pen or pen cap close to the symmetric plane; (2) Keep the axes of the pen and pen cap perpendicular to the symmetric plane. To achieve the goals as presented above, shoulder rotation $\Delta - S_1$ is selected for transferring and wrist rotation $\Delta - W_2$ and $\Delta - W_3$ for adjusting the orientation. Similar to the previous case, we can obtain the configuration of the body fixed frame:

$$\mathbf{g}_{BW} = e^{\hat{\xi}_1 \theta_1} e^{\hat{\xi}_2 \theta_2} e^{\hat{\xi}_3 \theta_3} \mathbf{g}_{BW}(0) \tag{41.6}$$

where θ_1, θ_2 and θ_3 are the angles of motion primitive $\Delta - S_1$, $\Delta - W_2$ and $\Delta - W_3$, respectively; and the spatial velocity:

$$\mathbf{V}_{BW}^B = \begin{bmatrix} \mathbf{v}_{BW}^B \\ \boldsymbol{\omega}_{BW}^B \end{bmatrix} = \mathbf{J}_{BW}^B(\boldsymbol{\theta})\dot{\boldsymbol{\theta}} \tag{41.7}$$

To achieve the goals, the following constraints should be satisfied:

$$\begin{cases} \omega_y = 0 \\ \omega_z = 0 \end{cases} \tag{41.8}$$

where ω_y and ω_y are the Y-axis and Z-axis components of the angular velocity $\boldsymbol{\omega}_{BW}^B$ of wrist center.

Equation (41.8) supplies 2 equations and establishes the relationship among $\dot{\theta}_1$, $\dot{\theta}_2$ and $\dot{\theta}_3$. After the motion of the shoulder rotation is given, i.e., $\dot{\theta}_2$ is given, we can solve the Eq. (41.8) and obtain the other joints' angular velocities.

41.4 Simulation and Discussion

Based on the task planning in the previous section, simulations are performed to verify the validation and feasibility. The parameters of the dual-arm robot are: $l_b = 500\,\text{mm}$, $l_s = 400\,\text{mm}$, $l_u = 250\,\text{mm}$, $l_f = 250\,\text{mm}$. The latest research results of neurophysiology showed that the motion velocity curve of the human arm can be characterized by a unimodal, bell-shaped tangential profile [5]. Here we use the consine function to fit the curve:

$$\omega(t) = \frac{\omega_{\max}}{2} \left(1 - \cos(\frac{2\pi}{t_{\text{total}}} \cdot t) \right) \tag{41.9}$$

where $\omega_{\max}$ is the maximum angular velocity; t_{total} is the total time spent in motion segment execution.

41.4.1 Lifting a Box

The initial rotation directions of the selected motion primitives on the right arm are: $\mathbf{S}_Z = \begin{bmatrix} -0.174 & -0.754 & 0.633 \end{bmatrix}^T$, $\mathbf{E}_Z = \begin{bmatrix} 0.453 & -0.814 & 0.316 \end{bmatrix}^T$, $\mathbf{W}_Z = \begin{bmatrix} 0 & 0 & 1 \end{bmatrix}^T$, $\mathbf{W}_X = \begin{bmatrix} 1 & 0 & 0 \end{bmatrix}^T$, and $\mathbf{W}_Y = \begin{bmatrix} 0 & 1 & 0 \end{bmatrix}^T$. Elbow rotation $\Delta - E_1$ moves according to the curve defined by Eq. (41.9), where $\omega_{\max} = 20°/s$ and
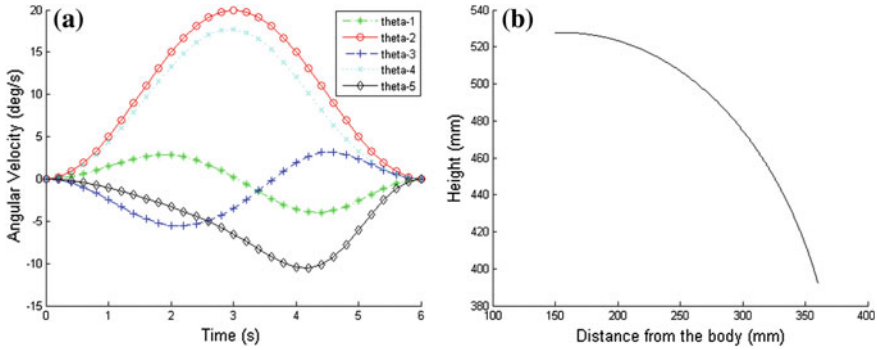
Fig. 41.3 Simulation results of lifting a box. **a** Motions of the motion primitives. **b** Trajectory of the end-effector in YZ plane

$t_{total} = 6$ s, other motions can be obtained through solving the Eq. (41.5), as shown in Fig. 41.3a. Choosing wrist center as the reference point, we can get the trajectory of the wrist, which is nearly an arc, as shown in Fig. 41.3b which only reflects the relationship between the Z-coordinate and X-coordinate, since Y-coordinate is constant.

Comparing the motions of the two motion primitives, shoulder rotation $\Delta - S_1$ and elbow rotation $\Delta - E_1$, which decide the position of the box, we can find that the angular velocity of elbow rotation $\Delta - E_1$ is much larger than that of shoulder rotation. Switching to the actual situation, the elbow is mainly responsible to the position, while the shoulder is adjusted slightly to keep the hand touching the box. The three motion primitives of the wrist seem to coordinate to adjust the orientation of the box, while wrist rotation $\Delta - W_2$ may be temporarily in charge in the interim of the motion, as shown in Fig. 41.3b.

41.4.2 Inserting a Pen into the Pen Cap

For the assembly task, the initial rotation directions are: $S_Z = \begin{bmatrix} 0 & -0.866 & 0.500 \end{bmatrix}^T$, $W_X = \begin{bmatrix} 0 & -1 & 0 \end{bmatrix}^T$, and $W_Y = \begin{bmatrix} 0 & 0 & -1 \end{bmatrix}^T$. Shoulder rotation $\Delta - S_1$ moves according to the curve defined by Eq. (41.9), where $\omega_{max} = 10°/s$ and $t_{total} = 3$ s, other motions can be obtained through solving the Eq. (41.8), as shown in Fig. 41.4a. The offsets in three axes can be seen in Fig. 41.4b. The offset in X-axis is 2 times bigger than that of wrist center with respect to its initial position, for both arms move close to each other and the diminution of the distance between the two wrists is required in the task.

Compared to the offsets in 3 axes, the offset in X-axis is obviously larger than that in another two axes. The offsets in Y-axis and Z-axis imply that the task is not executed in a fixed plane. Switching to the actual situation, these certain offsets can be endured if they do not lead to an uncomfortable posture.
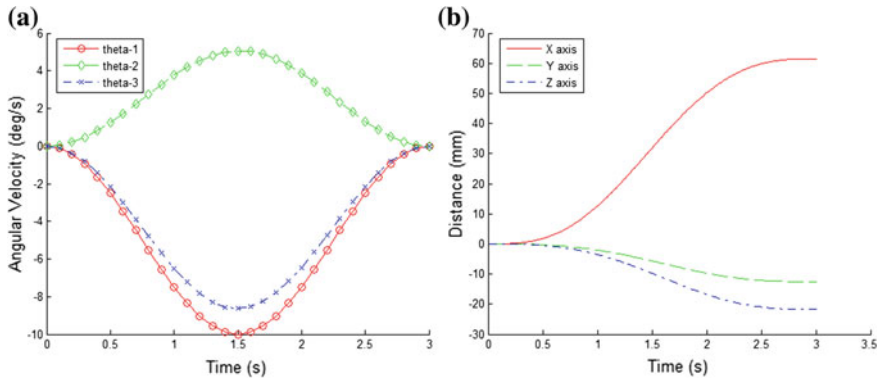
Fig. 41.4 Simulation results of inserting a pen into the pen cap. **a** Motions of the motion primitives. **b** Offset of the wrist in three axes

By analyzing how the task is executed and the simulation results, some characteristics of the proposed approach can be found, compared to the traditional methods:

1. Appropriate motion primitives are selected according to the necessary constraints extracted from the tasks, i.e., not all the DOFs of the arms are used and some of them may stay fixed. Therefore, the motion of the robot is simplified.
2. Discrepancies in the initial and final positions/orientations of the wrist may appear because of the release of the constraints. But they can be endured if not causing an uncomfortable posture. So the wrist is not strictly restricted and can float around the initial configuration in a reasonable volume.
3. Main motion primitive may exist during the task execution, which in real situation will alleviate the labor intensity of the brain. The main motion primitive controls the most concerned part of the task, while the others adjust according to the requirements of the tasks. This may indicate a direction to figure out the real-time control of the robot to deal with a complex task in a complicated environment.

41.5 Conclusion

This paper has proposed a bottom-up approach for human-like task planning. By assembling and combining the motion primitives which imply the features of human's motion, the robot is capable of moving human-likely throughout the task execution without time-consuming inverse kinematics problem. A task planner module is designed to enhance the relation between the task and the motion

primitives and enable the robot to be flexible to change and adjust by reselecting and recombining the motion primitives. Two basic and specific tasks are discussed and the simulation results have verified the validation and feasibility of the proposed approach.

References

1. Yoshikawa T (1985) Manipulability of robotic mechanisms. Int J Robot Res 4:3–9
2. Khatib O (1986) Real-time obstacle avoidance for manipulators and mobile robots. Int J Robot Res 5:90–98
3. Zacharias F, Schlette C, Schmidt F et al (2011) Making planned paths look more human-like in humanoid robot manipulation planning. In: IEEE international conference on robotics and automation (ICRA), pp 1192–1198
4. Park G-R, Kim K, Kim CH et al (2009) Human-like catching motion of humanoid using evolutionary algorithm(ea)-based imitation learning. In: IEEE international symposium on robot and human interactive communication, pp 809–815
5. Flash T, Hochner B (2005) Motor primitives in vertebrates and invertebrates. Curr Opin Neurobiol 15:660–666
6. Ding X, Fang C (2013) A novel method of motion planning for an anthropomorphic arm based on movement primitives. IEEE/ASME Trans Mechatron 18:624–636
7. Adorno BV, Fraisse P, Druon S (2010) Dual position control strategies using the cooperative dual task-space framework. In: IEEE/RSJ international conference on intelligent robots and systems (IROS), pp 3955–3960
8. Stollenga M, Pape L, Frank M et al (2013) Task-relevant roadmaps: a framework for humanoid motion planning. In: IEEE/RSJ international conference on intelligent robots and systems (IROS), pp 5772–5778
9. Zöllner R, Asfour T, Dillmann R (2004) Programming by demonstration: dual-arm manipulation tasks for humanoid robots. In: IEEE/RSJ international conference on intelligent robots and systems (IROS), pp 479–484
10. Fang C, Ding XL (2013) A set of basic movement primitives for anthropomorphic arms. In: IEEE international conference on mechatronics and automation (ICMA), pp 639–644
11. Fang C, Ding X (2013) A unified language for anthropomorphic arm motion. In: IEEE international conference on robotics and biomimetics (ROBIO), pp 522–529
12. Selig JM (2007) Geometric fundamentals of robotics. Springer, New York

Chapter 42
Design and Implementation of an Intelligent Cooking Robot Based on Internet of Things

Huailin Zhao, Xuyao Hao, Albert Wang and Chao Li

Abstract This paper designs a type of intelligent cooking robot, which can automatically complete cooking procedures such as heating, stir-frying, seasoning, and feeding and connect to the Internet via WiFi to achieve multiple functions like remote cooking, cooking instruction, and sharing of menu resource. The major part of the cooking robot consists of a small desk-type mechanism, which is managed by a microcontroller (MCU) to perform different cooking procedures. The robot is connected to the Internet via WiFi. By setting up a web server for the cooking menu management system, it parses cooking steps and methods into control commands and then sends these commands to the cooking robot. In this way, the cooking robot can be remotely operated by a computer or android phone. The experimental results show that the cooking robot can cook most Chinese cuisines and is easy to operate.

Keywords Cooking robot · Internet of things · WiFi · Mechanism · Circuit

42.1 Introduction

As smart home technology develops, the home robot has become increasingly popular. In particular, many technology research and development with respect to the home robot for cooking were carried out in China and other countries [1]. But most existing cooking robots can only carry out cooking in accordance with the fixed program, and they cannot cook through remote control. Besides they also cannot let users flexibly upload new cooking menu. As they lack good man–machine interface, in this paper, the cooking robot is connected with the web server

H. Zhao (✉) · X. Hao · C. Li
School of Electrical and Electronic Engineering, Shanghai Institute of Technology,
Shanghai 201418, China
e-mail: zhao_huailin@yahoo.com

H. Zhao · A. Wang
Department of Electrical Engineering, University of California, Riverside, CA 92521, USA

through the low-power WiFi technology based on the technology of the Internet of things. Users can realize the remote control to the cooking robot through the intelligent mobile phone. And the cooking robot can learn new cooking skill independently through the Internet.

Currently, the intelligent cooking device available in the market is mainly composed of two types: one type is the small cooking robot for ordinary consumers, such as the WiFi rice cooker mentioned in [1]. However, such robots are merely able to heat the food based on preset temperature curve and incapable of performing other functions like taking ingredients and stir-frying, so the intelligent automatic cooking is not achieved in the real sense; the other type is the large robot for production line, which is widely applied in fast food/food processing factories [2]. Despite its advantage in fully automatic cooking, the robot is relatively large, high-cost, and not portable, so it is difficult to use such robots as consumer products.

The proposed robot in this paper adopts a vertical cabinet. A special mechanism is used to simulate human hands and complete different actions like grabbing, throwing, and stir-frying. The eddy current heating method via electromagnetic induction is used for the temperature control of food. The robot is connected to the web server through WiFi signal to form an Internet of Things and achieve remote control. The features of the cooking robot include: 1. automatic remote cooking; 2. share online cooking menu; 3. cooking instruction and learning [3].

The overall implementation plan of the cooling robot is first introduced. The mechanic design of the robot and the connection to Internet via WiFi are then described. Finally, it is verified in actual tests that the proposed robot can perform the basic functions successfully, and some deficiencies in the design are also put forward.

42.2 System Description

The proposed robot is a type of intelligent WiFi cooking robot. The specific mechanism of the robot is managed by a microcontroller to simulate all necessary movements of human hands in cooking in a similar way that people control their actions with cerebellum. The robot is connected to the web server via WiFi signal for communication, and its operating condition is analyzed through a cooking menu database in the cloud server to give new action commands. In some sense, the robot is offered a "brain" to control itself. By simply clicking any menu to be cooked in the software in network terminals (mobile Apps) or computer terminals, users can send menu commands to the cloud server, which then controls each cooking procedure in accordance with the action commands in menu database.

As shown in Fig. 42.1, the overall system of the cooking robot consists of cooking robot, wireless router, cloud server, as well as the HCI terminal software of mobile phone and computer. The robot is able to perform cooking-related actions, such as taking ingredients, weighing, feeding, and stirring. It is connected to the user's personal wireless router via WiFi signal, while the wireless router serves as

Fig. 42.1 Block diagram of the cooking robot system
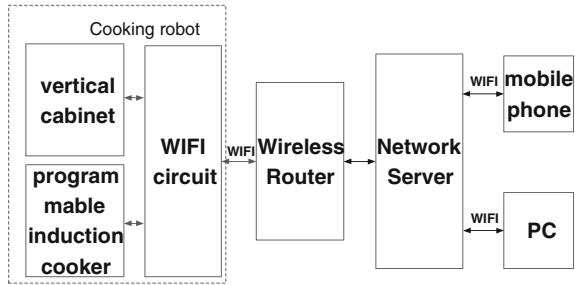
the signal transfer unit to set up the communication between the robot and the cloud server. The functions of the cloud server include: 1. receive the menu commands from the HCI terminal software of mobile phone and computer, decompose the menu commands into a group of motion-control commands based on the database of the menu management system, and send them to the cooking robot; 2. receive the commands from the robot's network communication feedback, access the cooking temperature and motion state of the robot, and forward them to the HCI terminal software of mobile phone and computer. The HCI software of mobile phone and computer communicates with the cloud server by means of WiFi or 3G signal to achieve remote control.

42.3 Mechanism of the Cooking Robot

As shown in Fig. 42.2, the mechanism of the cooking robot is mainly composed of three parts: 1. vertical cabinet; 2. stirrer; and 3. programmable induction cooker. The vertical cabinet is used to store food, grab the desired ingredients accurately through the internal mechanical drive, and feed them into the cookware (like pan) below. The stirrer is responsible for stirring the food during cooking and ensuring the food is heated evenly. The programmable induction cooker accesses the commands for temperature control from WiFi-based master control circuit board, and achieves the temperature control of food using the eddy current heating method via electromagnetic induction [4].

During automatic cooking, it is crucial to guarantee that robot can grab an accurate amount of ingredients for each food. This requires complicated design.

Figure 42.3 shows the 2D structure of the decomposed vertical cabinet. Inside the cabinet, there are grids for storage. The grids are placed separately around the rotary screw rod to facilitate the rotation and grabbing of the gripper [5]. A mechanism with two-degree-of-freedom motion is at the center of the cabinet. The gripper, driven by the rotation support, rotates around the screw rod. When it rotates to the grid in which the food should be took out, the rotation support stops rotating and the two-degree-of-freedom gripper moves the food to the weighing

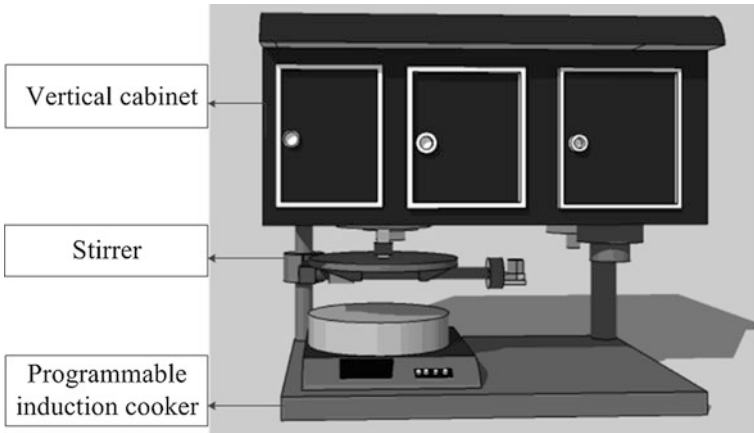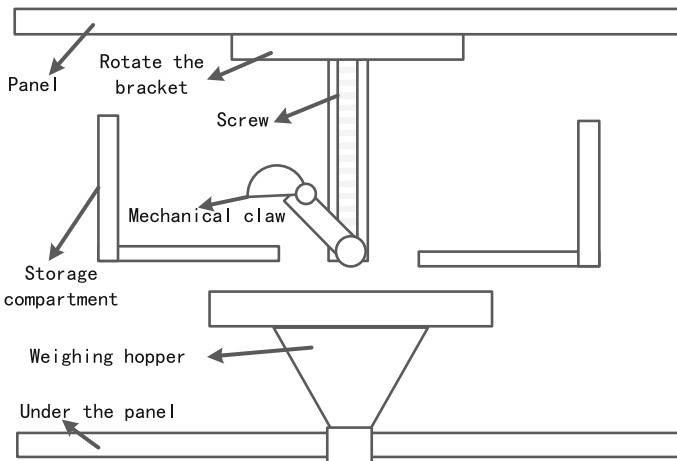**Fig. 42.2** Rending of the cooking robot

Fig. 42.3 2D structure of the decomposed vertical cabinet

hopper below, which can weigh the fallen food. In this way, a closed-loop control network for grabbing food is developed between the gripper and the weighing hopper to guarantee the robot can grab an accurate amount of food.

As stated above, one basic flow for automatic cooking is shown in Fig. 42.4.

Fig. 42.4 Flowchart of
automatic cooking
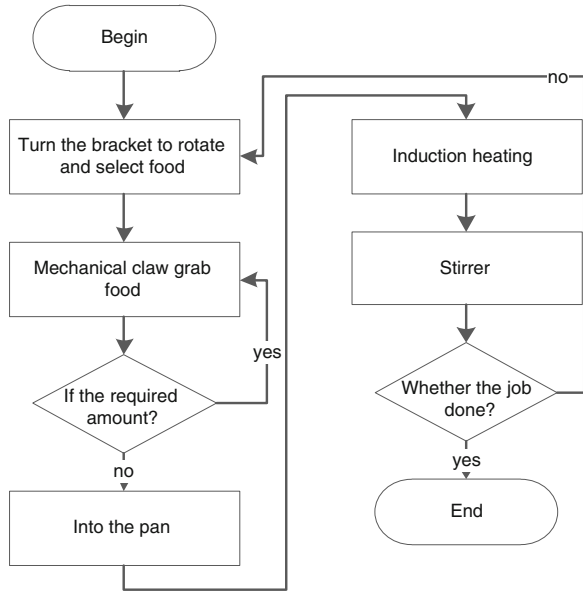
42.4 Hardware Circuit Design Method of the Cooking Robot

As shown in Fig. 42.5, the system's hardware circuit consists of three parts: 1. the programmable induction cooker which uses the ATmega64 microcontroller as master control unit and receives the temperature-control commands of WiFi-based master control via RS422 serial communication; 2. the WiFi-based master control circuit composed of STM32F407 and CC3000 Wireless network processor. In addition, STM32F407 is responsible for sampling in the robot's sensor system related to weighing, electric current and temperature, etc.; 3. the motor drive board which converts the PWM control signal of main control chip into the motor drive current so as to drive the motors of all mechanical joints in the system. Grating encoder is installed in each mechanical joint to form a PID closed-loop control network, so that the motion of mechanical joints can be controlled accurately [6].

As shown in Fig. 42.6, the WIFI CC3000 wireless network controller circuit control system. CC3000 is TI's latest launch of a low-power chip WIFI. It supports 802.11b/g integrated radio, modem and MAC, supports WLAN communication in the 2.4 GHz ISM band BSS station CCK and OFDM rates from 1 to 54 Mbps. CC3000 Smart Config™ WLAN provisioning tools allow customers to connect a headless device to a WLAN network using a smart phone, tablet, or PC. CC3000 work need a 32 k benchmark precision clock. In addition, due to the CC3000 operating voltage of 1.8, 3.3 V when using TTL level must be necessary to control the level of conversion.
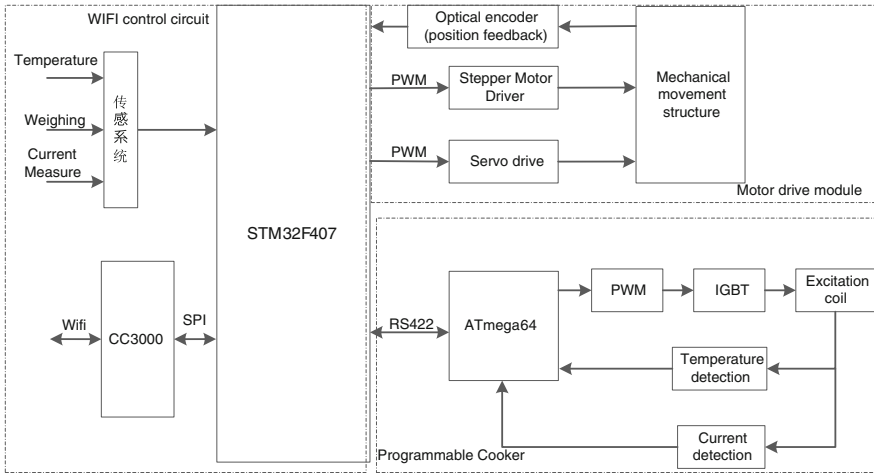
Fig. 42.5 Schematic diagram of the system's hardware circuit
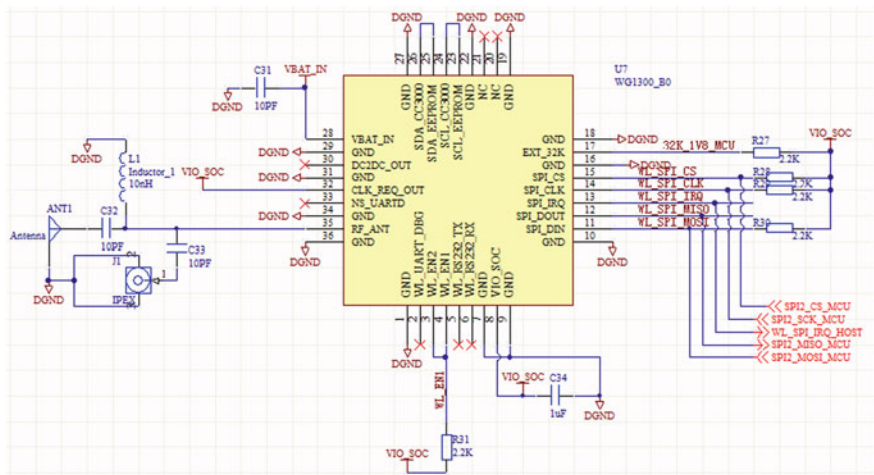
Fig. 42.6 WIFI control system diagram

42.5 Prototype and Test Results

Figure 42.7 shows the photo of the cooking robot. Because of the restrictions on the processing of mechanical parts, the cooking robot is actually assembled with the mechanism that uses the screw rod to drive the sliding of the gripper, instead of the above mechanism that applies the rotation of the vertical cabinet. However, their control effects and principles are basically the same.

Fig. 42.7 Photo of the cooking robot

Figure 42.8 shows the remote debugging software in the Windows system of the computer terminal. The debugging software is connected to the cloud server via WiFi signal and its remote control over the robot includes two types: manual control and automatic control. The robot can perform all control commands accurately, and complete automatic cooking in the mode of automatic control.

Every step of the cooking robot action is the one simulating the human hand, such as the temperature regulating, adding of the accessory food and the fully mixing. In the experiment, a high-level Chinese food cooker was invited to cook the by inviting a master of Chinese cuisine cooking red braised eggplant, and the cooking robot did the same dish. The comparison is shown in Table 42.1 [7].
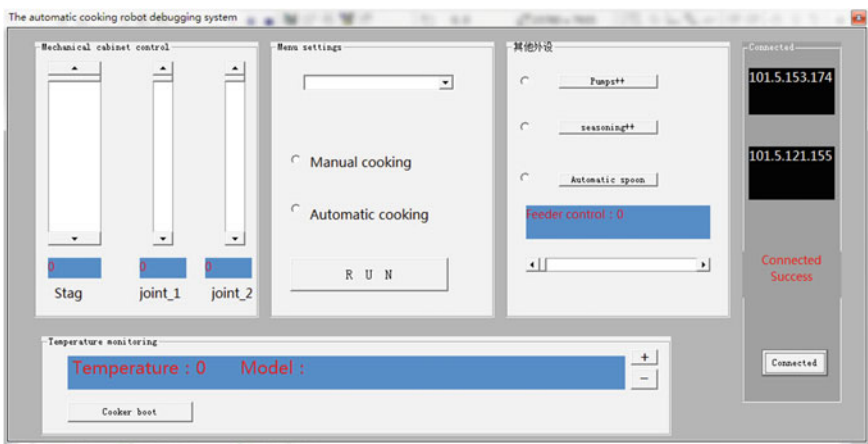

Fig. 42.8 Interface of computer terminal for remote control over host computer

Table 42.1 Cooking robot with the master chef cooking result contrast

Cooker	The robot (%)	The human cooker (%)
Colour and lustre	75	80
Taste	70	90
Simple sense	80	85
The aroma	74	74
Cooking time (Min)	21	29

42.6 Analysis of Experimental Results

The proposed cooking robot was awarded a prize in the Internet of Things Embedded Technology Contest held by STMicroelectronics in July, 2014, in which the manual and automatic cooking processes of Quick-Fried Shrimp Meat and Chinese Cabbage and Tofu Soup were demonstrated.

This paper introduces a type of automatic cooking robot based on Internet of Things, as well as its system composition, system function and basic features. The introduction focuses on the implementation principles of its mechanism and WiFi communication. With flexible and simple control methods, the robot can realizes the automatic cooking of Chinese food to some extent.

However, we also find some defects of the robot in actual use and test, including:

1. The ingredients are not kept in cold storage, so they will deteriorate if stored for a long term;
2. It is not easy to clean the oil stain and food chips after each automatic cooking.

The problems above will be improved in the future development.

References

1. Lee M, Xu K (2014) Cloud intelligent remote controllable integrated cooker. Products magazine. Hubei University College of Art and Design
2. Liu Y, Yan R, Liu X et al (2006) Applications crank block mechanism in the automatic cooking robot. Mech Eng 5:64–66
3. Zhu Y (2002) Household automatic cooking machine. Househ Appl Mag (3)20–21
4. Zhang S, Wu X (2013) Design and kinematics simulation for work movement mechanism of a novel cooking robot. Food Mech 7:92–94
5. Bao Z (2009) Feeding system design of automatic cooking robot. Mach Electron 04:59–63
6. SimpleLinkTM CC3000 Wi-Fi. TI instruments (2013)
7. Zhang J, Qi B, Zhou X, Liu X (2008) Analysis of the factor on influences the shredded meat mature degree for robot cooking. Food Sci Technol 7(34):110–114

Chapter 43
A Graph-Based Nonparametric Drivable Road Region Segmentation Approach for Driverless Car Based on LIDAR Data

Xiaolong Liu and Zhidong Deng

Abstract Road surface detection is one of the essential issues for autonomous driving. In this paper, we present a drivable road region detection approach using LIDAR data, where a nonparametric connected region representation is used to describe such a road region. First, an imaging of LIDAR data is conducted. Second, the gradient feature of road surface is extracted. Third, the flood fill algorithm is adopted to segment connected regions that express road surfaces. Using graph-based algorithm to deal with LIDAR data is a tentative way to segment drivable regions for driverless car. The experimental results show that the proposed approach is able to reliably detect drivable road regions under normal road conditions.

Keywords Drivable road region segmentation · Laser point clouds · Nonparametric · Driverless car

43.1 Introduction

To reliably detect drivable regions is essential to driverless car. Many researchers pay attention to such a hot spot topic in recent years, although it makes less significant advances. Among them, vision-based method is one of the most important branches in the field. Some methods use monocular camera to extract the road region by employing features with specific intensity, color, and texture as visual cues on the road surface [1–3]. Others use binocular or more cameras for road surface detection by utilizing 3D structural information [4–7]. Considering complexity of outdoor scenarios and lighting variation, however, traditional camera-based segmentation

X. Liu · Z. Deng (✉)
State Key Laboratory of Intelligent Technology and Systems,
Tsinghua National Laboratory for Information Science and Technology,
Department of Computer Science, Tsinghua University, Beijing 100084, China
e-mail: micheal@tsinghua.edu.cn

approaches are susceptible to environmental disturbances and cannot detect drivable road surface in a stable way.

The Light Detection and Ranging (LIDAR) can emit laser beam and receive its reflection. It can effectively avoid illumination disturbances in natural scenes. Such an active vision means has features like strong stability and abundant information, which is well suited to applications in outdoor environment.

The LIDAR data were used to detect road curb in 2007 [8]. In 2010, Shin et al. used a single LIDAR for outdoor patrol robots [9]. The LIDAR data is rather stable in the outdoor environment. But traditional road surface segmentation approaches often have assumption that road surfaces are planar. In [10], the RANSAC method was adopted to fit planar parameters. The grid cell method is also used in the expression of plane [11]. But there exist some restrictions for each of them. The road surface is not always available to planar fitting. Additionally, the grid cell method cannot deal with more complicated cases like hanging obstacles, i.e., the upper side of tunnel or the trees in natural scenes. In recent years, there are also many advances on real-time 3D laser imaging, automatic target recognition [12], and automatic pilot on driverless car [13].

Based on LIDAR data, this paper presents a drivable road region detection approach. It uses a nonparametric connected region representation to express such road regions. First, an imaging of LIDAR data is conducted. Second, a gradient feature of road surface is extracted. Third, the flood-filling algorithm is employed to make segmentation of connected regions that describe road surfaces. The use of graph-based algorithms for LIDAR data is a tentative way to drivable road region segmentation. The experimental results show that our approach can reliably detect drivable road regions under normal road conditions and be applicable to nonplanar surfaces and hanging obstacles.

43.2 A Nonparametric Drivable Region Segmentation Approach

Velodyne HDL-64E mounted on the roof provides a large amount of environmental information than previously available. The device has 5–15 Hz user-selectable frame rate and output rate of over 1.3 million laser points/s. After calibration, the LIDAR data are transformed to ones in Euclid coordinate frame. Figure 43.1 gives the illustration diagram of road model as laser scans are projected onto both horizontal road surface and shoulders.

The angle resolution of the LIDAR is 0.09°. Let us consider the LIDAR scan data ranging from left/right 45°. Assume x axis represents angle and y axis indicates laser scan data from 64 beams. The imaging of LIDAR data is shown in Fig. 43.2a.
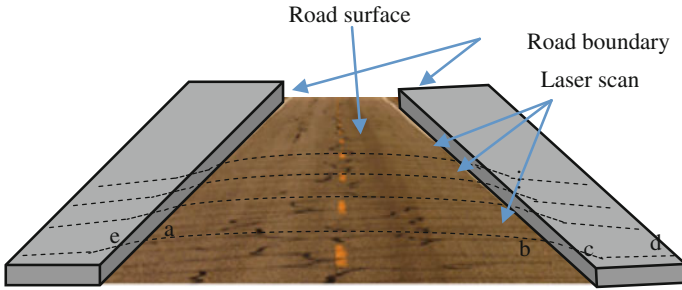
Fig. 43.1 The illustration diagram of road model
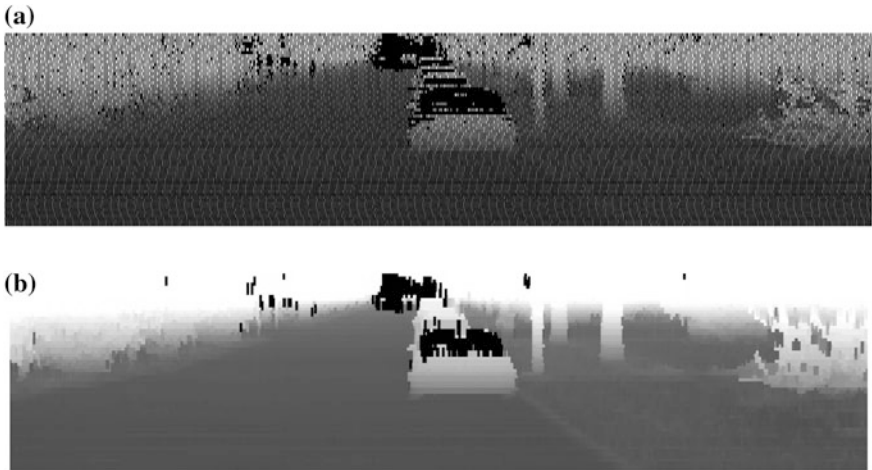
Fig. 43.2 The close operation for LIDAR imaging. **a** The imaging of LIDAR data. **b** The close operation

The image pixel value is converted by use of the formula below

$$G = ((x + 2.5) * 255)/(-1.5 + 2.5) \tag{43.1}$$

In the resulting expression, the LIDAR imaging is very similar to camera image. It is very clear to observe from such an imaging that there contain driving cars, trees, and road edges. In order to fill holes in the LIDAR imaging, the close operation is adopted, as shown in Fig. 43.2b. The close operation can be described as follows:

$$A^{\circ}B = (A \ominus B) \oplus \tag{43.2}$$

where the cell B is given by

1	1	1
1	1	1
1	1	1

Most of the holes are filled with the data nearby. Consequently, the road surface is connected together. The obstacles are isolated by the road and the other connected components.

The next step is to use the blur operation to remove the salient noise caused by the LIDAR itself and the surroundings. In this paper, we use the Gaussian kernel operator with a size of 3×5. It is a class of image-blurring filtering that uses Gaussian function, in order to calculate transformation for each pixel in image. The 2D Gaussian function is described below:
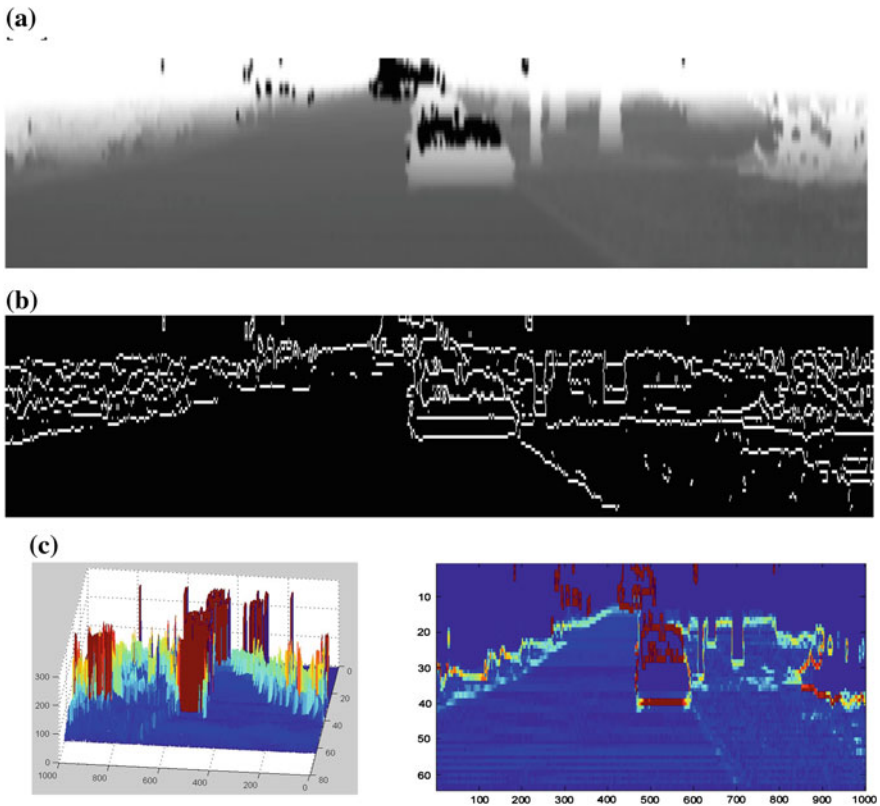
Fig. 43.3 The denoise and feature extraction process. **a** The Gaussian blur operation. **b** The Canny edge detection. **c** The 3D gradient histogram of the LIDAR data (*left*) and the height one, where *blue* indicates low and *red* high (*right*)

(a)

(b)

(c)
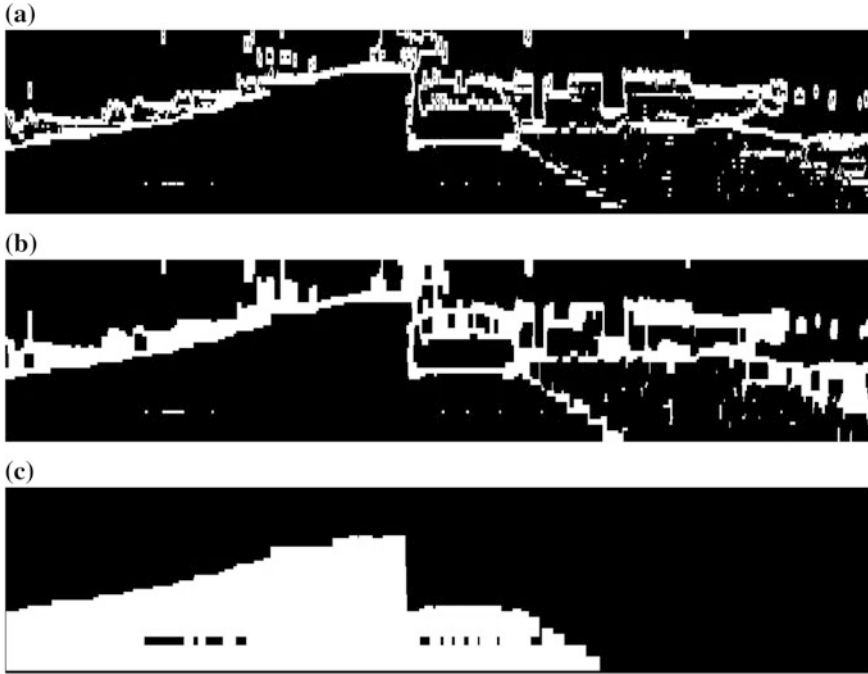
Fig. 43.4 The drivable region segmentation. **a** The binary image of the LIDAR data obtained using threshold of 40. **b** The close operation of the binary image. **c** The segmented road surface (marked in *white*)

$$G(x, y) = \frac{1}{2\pi\sigma^2} e^{-\frac{x^2+y^2}{2\sigma^2}} \tag{43.3}$$

where x is the distance from the origin in the horizontal axis, y the one from the origin in the vertical axis, and σ the standard deviation of Gaussian distribution [14].

The classical Canny edge detection algorithm is used to detect the road edge effectively. The road has mostly carved out by the pixels on the Canny edge. The Canny result compose the shape of the road. Next we conduct a gradient computation to extract road edges using the following formula:

$$G = \sqrt{\frac{d^2I}{dx^2} + \frac{d^2I}{dy^2}} \tag{43.4}$$

The gradient histogram acquired is shown in Fig. 43.3c. It is obvious that we can see the flatness of the road. If the road is not flat, the parametric expression should be a curved surface. Owing to the fact that the actual surface is unknown, it is very difficult to express it using a set of parameters. As a result, we present a nonparametric approach to represent road surfaces. It is based on the assumption that the region lying
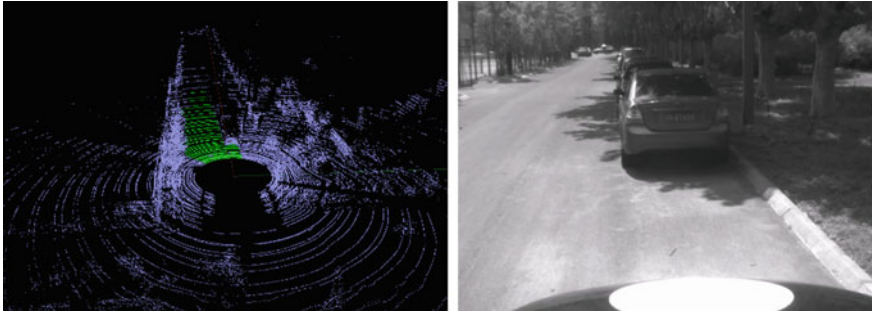
Fig. 43.5 The segmentation of drivable region marked in *green color* (*left*) and the corresponding camera image for the comparative reference (*right*)

in the front of driverless car is generally a drivable road surface. In fact, the vehicle is always running or parking on a road surface. This assumption makes sense. Consequently, this paper presents a drivable region detection approach based on the flood fill connection. First, the imaging of LIDAR data is converted into the binary image, as shown in Fig. 43.4a. But we can observe that there exist some holes or outliers in this image. Second, we exploited the close operator to remove part of them. In Fig. 43.4b, it is easy to see that the image quality is improved. Third, the flood fill algorithm is employed to carry out the connection of candidate drivable road regions shown in Fig. 43.4c, where we used the center of the image bottom as the seed point. Figure 43.5 shows the visualization of the above road segmentation.

Fig. 43.6 The satellite map for the roads near Tsinghua's gymnasium

43.3 Experimental Results

THU IV-2 driverless car developed by Tsinghua University is equipped with both Velodyne HDL-64E and digital cameras. The on-site test area, which is covered with a yellow rectangle, is the one near Tsinghua's gymnasium, as shown in Fig. 43.6. In this area, the road curb is not very clear. In addition, there is complicated traffic on the road, including cars, bikes, and pedestrians. Apparently, the proposed approach should be viewed to be effective and efficient, if such a road surface can be detected reliably.
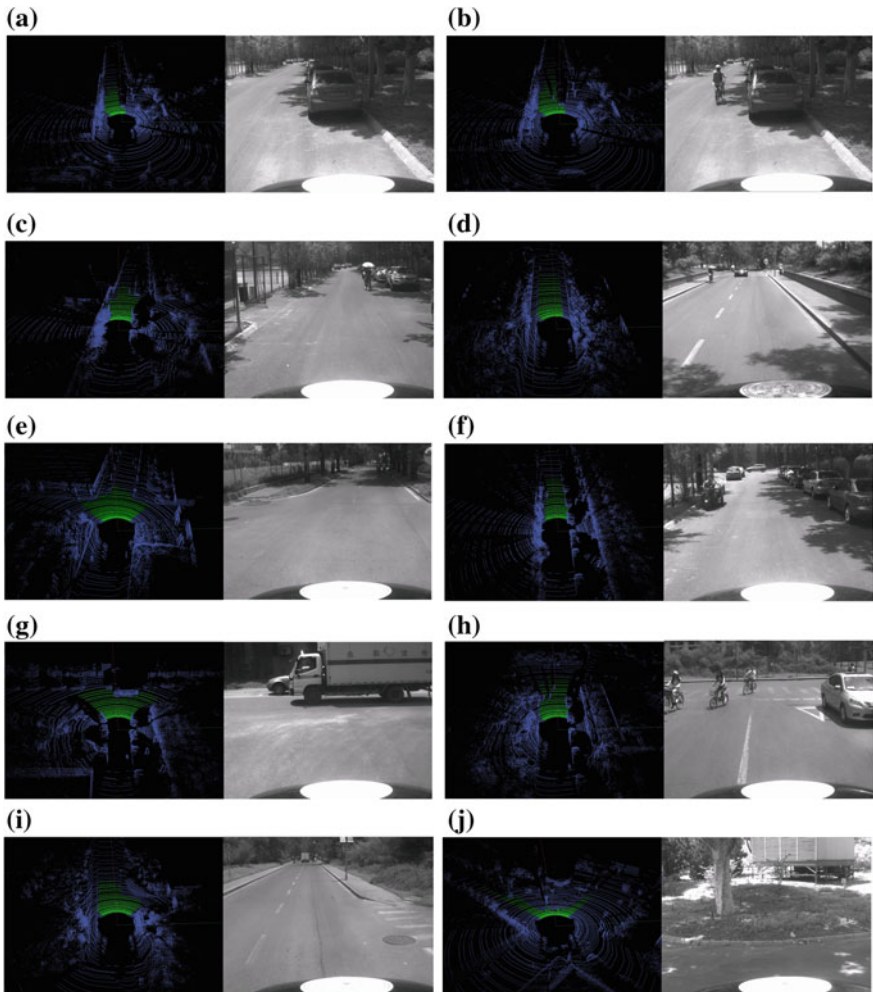

Fig. 43.7 The experimental results

The output rate of HDL is 10 Hz and the camera is 54 frame/s. Thus frame rate of both the HDL and the camera is not synchronous. But there is the nearest camera frame at each HDL data frame. The time interval of our digital camera is $1/54 = 0.0185$ s $= 18.5$ ms, which is quick enough when autonomously driving at 30 km/h. The drivable road region detection results under different scenarios are shown in Fig. 43.7.

From a collection of segmentation results in Fig. 43.7, bikes and vehicles located in the drivable road region can be identified very clearly, although the road curb is not very tall. The intersection can also be found. In Fig. 43.7, (a) shows the static obstacle of a car ahead and the low road curb near the grass can be detected. (b) gives one single bike detected. (c) demonstrates that the road curb is not continuous, but the connected region can also be achieved. (d) shows a long straight road. (e) precisely displays an intersection. (f) gives multiple static cars segmented out of the drivable region. (g) shows a moving car in the front of our driverless car. (h) illustrates a couple of segmented bikes. (i) demonstrates that our approach is able to connect the road regions together, just like that in (c), even if the road curb is not continuous. (j) shows the grass, together with the low road curb.

43.4 Conclusion

Based on LIDAR data, we present a graph-based drivable road region detection approach, where a nonparametric connected region representation is used to describe such road regions. First, an imaging of LIDAR data is done. Second, we extract gradient features of road surface. Third, the flood-filling algorithm is used to segment connected regions that express road surfaces. The experimental results demonstrate that our new approach can reliably detect drivable road regions under normal road conditions. Specifically, it is able to be applicable to nonplanar surfaces and hanging obstacles.

According to the actual experimental results, the segmented drivable road region is about 20 m far away in the front of the driverless car. Apparently, a new detection approach is required to segment the road surface in a longer distance. Additionally, the drivable region detection is not as stable as that used in obstacle detection. It cannot produce 100 % accuracy to extract road surface. In this case, the grid mapping information of road may be very important to significantly improve performance. For example, we could use it to provide ROIs to the drivable road region detection. This is potentially applied to unstructured roads. The detection of the drivable region in an unstructured road is worth being investigated in the future.

References

1. Bertozzi M, Broggi A, Fascioli A (2000) Vision-based intelligent vehicles: state of the art and perspectives. Robot Auton Syst 32:1–16
2. Sha Y, Zhang G, Yang Y (2007) A road detection algorithm by boosting using feature combination. In: Proceedings of the IEEE intelligent vehicles symposium, Istanbul, Turkey, pp 364–368
3. He Y, Wang H, Zhang B (2004) Color-based road detection in urban traffic scenes. IEEE Trans Intell Transp Syst 5(4):309–318
4. Guo C (2009) Drivable road region detection based on homography estimation with road appearance and driving state models. In: 4th International conference on autonomous robots and agents. ICARA 2009, 10–12 Feb 2009, pp 204–209
5. Lombardi P, Zanin M, Messelodi S (2005) Unified stereovision for ground, road, and obstacle detection. In: Proceedings of the IEEE intelligent vehicles symposium, Las Vegas, USA, pp 783–788
6. Hautiere N, Labayrade R, Perrolaz M et al (2006) Road scene analysis by stereovision: a robust and quasi-dense approach. In: Proceedings of the ninth international conference on control, automation, robotics and vision, Singapore, pp 1–6
7. Douillard B, Fox D, Ramos F et al (2008) Laser and vision based outdoor object mapping. In: Proceedings of robotics: science and systems (RSS)
8. Kim S-H, Roh C-W, Kang S-C et al (2007) Curb detection using laser range finder for reliable outdoor navigation. In: Proceedings of IEEE international conference on advanced robotics (ICAR'07) South Korea, pp 930–935
9. Shin Y, Jung C, Chung W (2010) Drivable road region detection using a single laser range finder for outdoor patrol robots. In: Intelligent vehicles symposium (IV), pp 877–882
10. Qian X, Ye C (2013) NCC-RANSAC: a fast plane extraction method for navigating a smart cane for the visually impaired. In: Automation science and engineering (CASE), pp 261–267
11. Armstrong E, Richmond R (2006) The application of inverse filters to 3D microscanning of LADAR imagery. In: Aerospace conference
12. Stone P, Beeson P, Mericli T et al (2007) DARPA urban challenge technical report. Austin robot technology, Technical report
13. Bohren J, Foote T, Keller J, Kushleyev A et al (2007) Little ben, the ben franklin racing team's entry in the 2007 DARPA urban challenge. J Field Robot 25:598–614
14. Linada G, George C (2001) Computer vision, 1st edn. Prentice Hall, New York

Chapter 44
Detection of Road Obstacles Using 3D Lidar Data via Road Plane Fitting

Xiong Chen and Zhidong Deng

Abstract Detection of road obstacles is essential for autonomous driving of intelligent vehicles on highways and urban roads. In this paper, we present a robust and accurate road obstacle detection method using 3D lidar data. First, we acquire a stable and accurate description of road curbs through double validations. Then, a RANSAC and least squares road plane fitting procedure is performed. Finally, obstacles including cars, trucks, pedestrians, and bikes are detected based on the road plane. Experimental results show good performances of the proposed method on various road situations.

Keywords Obstacle detection · Curb detection · Road fitting · Autonomous driving

44.1 Introduction

Robust detection of road obstacles is a major task in environment perception, which is crucial for intelligent vehicles to achieve safe autonomous driving. Road obstacles, including cars, trucks, pedestrians, and bikes arise constantly and unpredictably, which affects autonomous driving of intelligent vehicles to a significant extent. As intelligent vehicles are becoming more and more sophisticated, a sufficient understanding of surrounding environment will become increasingly important. However, this is not tractable due to mainly unpredictable strong noise brought by

X. Chen · Z. Deng (✉)
State Key Laboratory of Intelligent Technology and Systems, Tsinghua National Laboratory for Information Science and Technology, Department of Computer Science, Tsinghua University, Beijing 100084, China
e-mail: micheal@tsinghua.edu.c

both active sensors such as 3D lidars and passive sensors such as cameras usually equipped on intelligent vehicles. To handle this low signal-to-noise ratio data in real-time makes it even more difficult for autonomous driving of unmanned vehicles.

Obstacle detection has been studied for several decades. Immense amount of approaches utilized vision exclusively [1–3], whereas others focused on the use of 2D or 3D lidars [4–6], sometimes combined with vision [7]. Lidars are active sensors that are able to provide direct distance and intensity measurements of surrounding environment at high resolution without interference from weather, illumination, or shadow. The major difference between 2D lidars and 3D lidars is that each scanning of a 2D lidar is performed along a plane with a limited field of view (usually less than 180°), while a 3D lidar contains a large number of scanning planes with a broad field of view (even 360°), resulting in a cloud of 3D readings containing distance and intensity information within one single scanning period. This huge data makes a stable and accurate description of road curbs possible as a large amount of curb readings can be obtained in one scanning. As curbs define road boundaries, when appropriately modeled, they can be used to generate vehicle controlling parameters. Besides, once left and right curbs are successfully detected, lidar readings in between are mostly road and obstacles.

In this paper, we focus on the detection of urban road obstacles using Velodyne HDL-64E S2 3D lidar mounted on the top of our unmanned vehicle THIV-II (see in Fig. 44.1). We propose a method that robustly detects road obstacles in real-time, using cloud readings obtained from this 3D lidar. The major contributions of this paper are: First, we utilize a clothoid model to fit curb measurements detected using ILP features in [8]. Secondly, a RANSAC and least squares road plane fitting procedure is performed to obtain a good approximation of the road in front of the vehicle. Finally, obstacle readings are detected and clustered based on the road plane via Euclidean distance. Experiments under different urban road situations demonstrate favourable results of our proposed method.

This paper is organized as follows. Section 44.2 states some related work on obstacle detection using lidars, especially methods based on road detection.

Fig. 44.1 THIV-II and Velodyne 3D lidar

Section 44.3 describes the proposed method in detail, followed by experimental results in Sect. 44.4. The last section draws the conclusion and discusses the future work.

44.2 Related Work

A considerable amount of research has been carried out on the topic of obstacle detection using 2D or 3D lidars. Some prior approaches tried to detect obstacles by fitting models to lidar measurements, such as [9, 10]. However, these approaches are usually computationally demanding and therefore can hardly be applied in real-time applications. To overcome this problem, model-free methods that distinguish obstacles from the road are widely used. In this case, laser points are projected to an estimated road plane and lidar readings of the road and obstacles are separated according to their Euclidean distance to the estimated road plane based on the fact that obstacle readings are above the road plane to some extent. With that in mind, researchers are focused on the accurate estimation of the road surface. [11] uses fuzzy clustering method that based on maximum entropy theory to cluster lidar points and then a weight linear fitting algorithm is applied to extract road surface. A graph-based approach to segment ground and objects from 3D lidar scans using a novel unified, generic criterion based on local convexity measures is used in [12]. Road extraction by modeling the road as a dynamic system of connected planes is achieved in [13], where Kalman filter is applied to predict and monitor each plane center and its heading direction. Combined with an occupancy grid, [14–16] acquire a good description of the road surface by taking advantage of multiple heterogeneous sensors.

In comparison with prior art, our method exploits curb measurements detected in [8] with ILP features as road boundaries. Once the left and right boundaries of the road are clearly defined and appropriately modeled, laser measurements in between are mostly road surface and obstacles defined above. In most cases, road surface readings take a larger proportion than readings from obstacles, which makes RANSAC [17] a suitable method to fit plane model to the laser data. Detection of obstacles is straightforward after the road surface is accurately estimated.

44.3 Obstacle Detection Based on Road Plane Fitting

As illustrated before, our method exploits laser measurements, or readings, received from our Velodyne HDL 3D lidar. A detailed description of the lidar can be found in [18]. Here we briefly introduce components of each laser measurements. During each scan period, about 130,000 measurements are produced. Each of these measurements consists of 7 components, coordinate (x, y, z) measured in millimeter, intensity I, scanning line order c, distance to the origin d, and rotation angle θ.

The origin of the coordinate frame is the location of the 3D lidar, with x axis direction pointing right, y forward and z upward with respected to our vehicle.

In the current section, a three-stage obstacle detection approach is described in detail. First, a stable description of road curbs is presented. Then, the road surface is modeled as a plane using RANSAC and least squares. Finally, obstacle readings are distinguished based on their Euclidean distance to the road plane.

44.3.1 Curb Model with Double Validations

Curb points detected using the algorithm described in [8] may contain a fraction of false positive cases, or noise, and take laser measurements of other vehicles or pedestrians that occlude the curb as curb points. The reason for this is that vehicles and pedestrians share the same ground projection and elevational properties that are mainly used in the algorithm to detect curbs. These false positive measurements are obviously undesirable and need to be elaborately dealt with as road curbs are usually used to provide vehicle controlling parameters, especially when lane markings are invisible or terribly detected. Here we utilize a local model to eliminate the effect of measurements of obstacles far from real curbs such as cars and trucks on the road, and a global model to handle measurements reflected from pedestrians and bikes that are close to real curbs. This double-validation has the ability to handle noise and provide a stable curb description in most cases.

In this local model, we eliminate z coordinates of these detected curb points as they are not necessarily needed to fit a planar cubic curve model. As a result, a grayscale *pixel image* is created for each frame of the laser points with white pixels referring to the detected curb points and black pixels non-curbs, as illustrated in Fig. 44.2.

We split this pixel image into left and right parts resulting in two pixel images denoting each side of the curbs. The same procedure is performed in both images. For the left image, we split it into two parts: the top one and the lower one. The lower part reflects curbs that are near the vehicle while the top one further. We perform Hough transform for line segment detection in both parts and choose the one segment with the longest length as the detecting result of that part. As a result, we acquire two line segments for the two parts of left pixel image is as follows:

$$l_{l;ns} : x = a_{l;ns}y + b_{l;ns} \tag{44.1}$$

$$l_{l;fs} : x = a_{l;fs}y + b_{l;fs} \tag{44.2}$$

We assume that the curbs within a short distance are consecutive and do not change dramatically until next intersection in this local model, therefore $|a_{l;ns} - a_{l;fs}|$ and $|b_{l;ns} - b_{l;fs}|$ should be small. The local model validation fails if either of them is no smaller than predefined thresholds $T_{\text{local}} = \{T_a, T_b\}$. A global model validation is performed once these line segments passes the local model validation.

Fig. 44.2 A pixel image of a frame
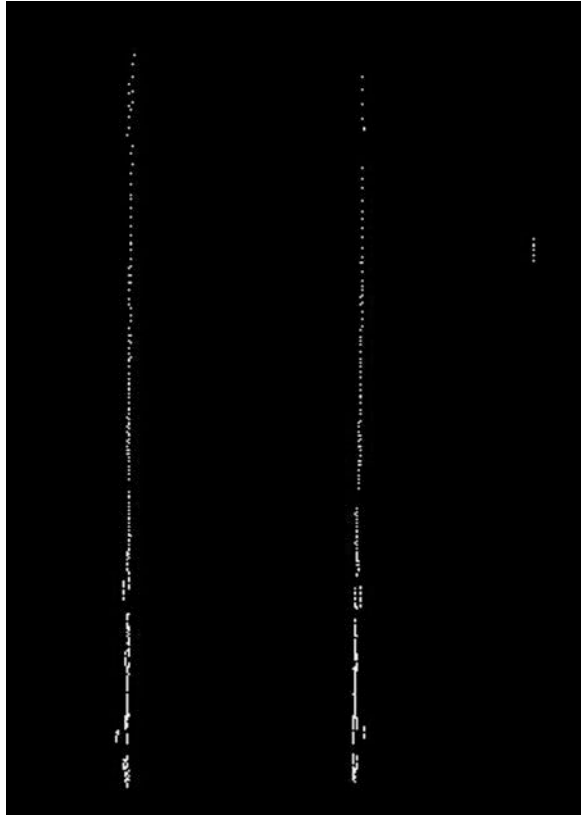
We do this as follows: First, we choose N points with some certain y-coordinates from each of the two line segments, resulting in a set of $2N$ points. Secondly, these points are transformed into a global coordinate system. We keep a queue of $K = 2N*M$ points, denoting points from the most recent M frames. These K points describe history information of the curbs, therefore can be used to check the current frame. We fit these points with a planar cubic curve model c_{hist} via least-squares method and calculate the sum of the distances between current $2N$ points and c_{hist}. The global model validation fails if the sum is no smaller than predefined threshold T_{dist}. After the double validations, we update the queue as to keep track of the curbs. If either of the validations fails, we choose $2N$ points from c_{hist} with the same y-coordinates as before and place them at the end of the queue while deleting the first $2N$ points, otherwise the current points that have passed the validations are used to update the queue. Finally, we fit the updated queue with a planar cubic curve model $c_{current}$ as the result of our curb model. However, if the validations keep failing for a certain count of frames, we may believe that the curbs have changed and a re-initialization procedure is followed.

44.3.2 Road Plan Fitting and Obstacle Detection

In this section, we present our method of obstacle detection based on the curb curve model acquired in the above section. As illustrated in the last part, we obtain both left and right curb curve models as c_l and c_r in the vehicle coordinate frame. As curbs define road boundaries, laser readings between c_l and c_r are mostly reflected by the road surface and obstacles such as trucks, cars, and pedestrians, which should be precisely detected and avoided. We assume that the road surface within a short distance does not change much and can be fitted with a 3D plane model as:

$$P : Ax + By + Cz = D \qquad (44.3)$$

We use the RANSAC algorithm and least-squares method to calculate the parameters and therefore acquire a best fit road plane as our road model. While using RANSAC, laser readings between c_l and c_r are grouped into inner points and outliers with respect to the plane. As for the outlier set, we calculate the distance of each point to the plane and points with a distance no less than a predefined threshold T_{plane} are considered as reflected from obstacles and therefore labeled as "obstacle". As there may be more than one obstacles on the road, we group "obstacle" points into different clusters according to their Euclidean distance to each other, two laser readings are considered in the same cluster if their distance is less than a fixed positive number ε. A bounding box is calculated for each of the cluster as a result of our obstacle detection for the current frame.

44.4 Experimental Results

In this section, we present some results of our obstacle detection system on real highways and urban roads. Figure 44.3 demonstrates results of curb curve model fitting. Figure 44.3a is the detection result of curb points in most cases. Figure 44.3b shows the model fitting result in a pixel image with green curves denoting each of the two sides of the curbs. Figure 44.4 shows some detection results on various road and under different road situations. Figure 44.4a is the detection result on a highway with multiple obstacles. Figure 44.4b shows results on an urban road with vehicles and bicycles. We can see that pedestrians on urban road can be detected in Fig. 44.4c. Obstacles in most cases can be detected precisely with our method. However, two obstacles can be clustered as one if they get too close to each other as shown in Fig. 44.4d.
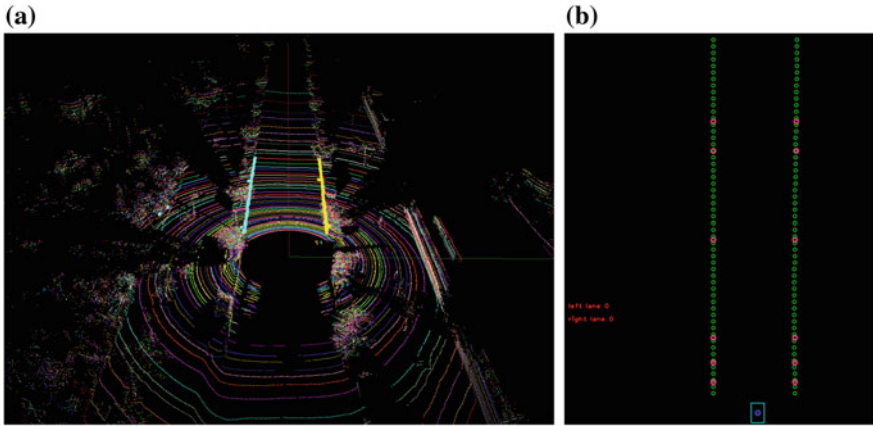
Fig. 44.3 Result of curb model fitting. **a** Detection result of curb points. **b** Fitting result of curb points
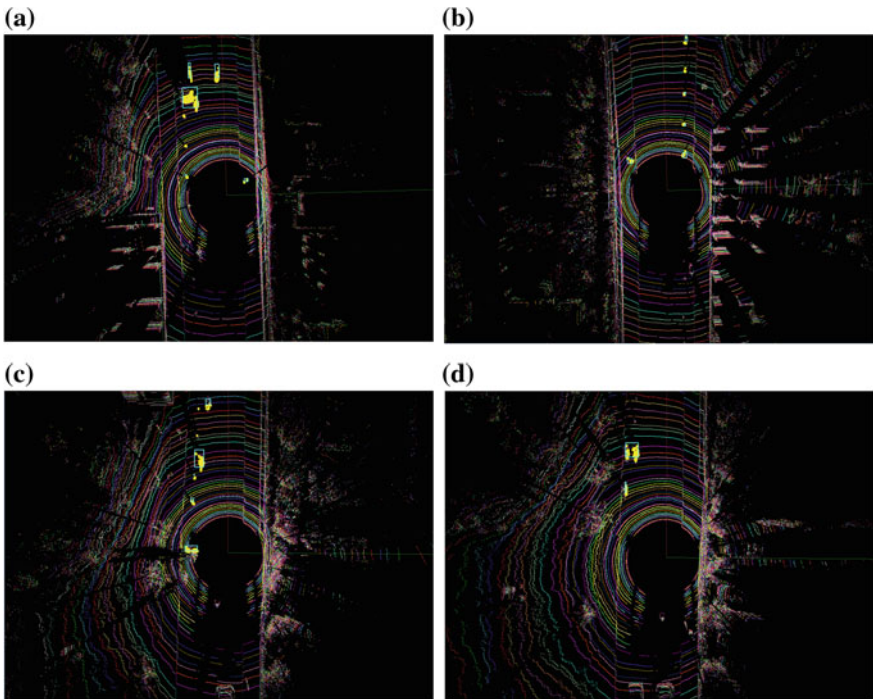
Fig. 44.4 Detection results of obstacles under different road situations. **a** Detection result on the high way. **b** Detection result on a urban road. **c** Urban roads with pedestrians. **d** Two obstacles are considered as one

44.5 Conclusions

In this paper, we present a robust and accurate road obstacle detection method using 3D lidar data. Our method is mainly based on an accurate description of road curbs, which define road boundaries, and RANSAC road plane fitting. The method is applied to our intelligent vehicle and shows good performances. However, as the road may change dramatically in a wider area, the assumption that it can be modeled as a plane may no longer be appropriate, this should be handled in the future so as to detect obstacles in the distance.

References

1. Zielke T, Brauckmann M, von Seelen W (1993) Intensity and edge-based symmetry detection with an application to carfollowing. CVGIP: Image Underst 58(2):177–190
2. Dickmanns E (1998) Vehicles capable of dynamic vision: a new breed of technical beings? Artif Intell 103(1–2):49–76
3. Dellaert F, Thorpe C (1998) Robust car tracking using Kalman filtering and Bayesian templates. In: Proceedings of SPIE, vol 3207, p 72
4. Zhao L, Thorpe C (1998). Qualitative and quantitative car tracking from a range image sequence. In 1998 IEEE computer society conference on computer vision and pattern recognition. Proceedings, pp 496–501
5. Streller D, Furstenberg K, Dietmayer K (2002) Vehicle and object models for robust tracking in traffic scenes using laser range images. In: The IEEE 5th international conference on intelligent transportation systems, 2002. Proceedings, pp 118–123)
6. Wang C, Thorpe C, Thrun S, Hebert M, Durrant-Whyte H (2007) Simultaneous localization, mapping and moving object tracking. Int J Robot Res 26:889–916
7. Wender S, Dietmayer K (2008) 3d vehicle detection using a laser scanner and a video camera. Intell Transp Syst IET 2(2):105–112
8. Yao W, Deng Z, Zhou L (2012) Road curb detection using 3D lidar and integral laser points for intelligent vehicles. In: International conference on soft computing and intelligent systems (SCIS) and 13th international symposium on advanced intelligent systems (ISIS), 2012 Joint 6th IEEE, 2012, pp 100–105
9. Rabbani T, van den Heuvel F Efficient hough transform for automatic detection of cylinders in point clouds
10. Ahn SJ, Effenberger I, Roth-Koch S, Westkamper E (2003) Geometric segmentation and object recognition in unordered and incomplete point cloud. In: DAGM-symposium, pp 450–457
11. Yuan X, Zhao CX, Zhang HF (2010) Road Detection and corner extraction using high definition lidar. Inf Technol J 9:1022–1030
12. Moosmann F, Pink O, Stiller C (2009) Segmentation of 3D lidar data in non-flat urban environment using a local convexity criterion. In: Intelligent vehicle symposium (IV) Xian
13. Lam J, Kusevic K, Mrstik P et al (2010) Urban scene extraction from mobile ground based lidar data. In: Proceedings of 3DPVT, pp 1–8
14. Douillard B, Underwood J, Melkumyan N, Singh S, Vasudevan S, Brunner C, Quadros A (2010) Hybrid Elevation Map: 3D surface models for segmentation. In: International conference on intelligent robots and systems (IROS)
15. Himmelsbach M, Hundelshausen FV, Wuensche HJ (2010) Fast segmentation of 3D point clouds for ground vehicles. In: Intelligent vehicle symposium (IV) USA, pp 560–565

16. Douillard B, Underwood J, Kuntz N, Vlaskine V, Quadros A, Morton P, Frenkel A (2011) On the segmentation of 3D LIDAR point clouds. In: IEEE international conference on robotics and automation (ICRA) Shanghai, pp 2798–2805
17. Fischler MA, Bolles RC (1981) Random sample consensus: a paradigm for model fitting with applications to image analysis and automated cartography. Commun ACM 24(6):381–395

Chapter 45
Quasi-Min-Max Model Predictive Control for Discrete-Time Singular Systems with Input-to-State Stability

Chan Gao and Xiao-Hua Liu

Abstract The paper concerns robust quasi-min-max model predictive control for a class of discrete-time singular systems with input constrains and persistent disturbance. To deal with the persistent disturbance, we introduce the notion of input-to-state stability of discrete-time singular system for the first time. The optimal control can be obtained by solving a quasi-min-max optimal problem of a finite horizon cost function. On the basis of the proposed dual-mode MPC approach, it can be proved that the closed-loop discrete-time singular system is input-to-state stability. Finally, a numerical simulation shows the feasibility and the effectiveness of the proposed method.

Keywords Model predictive control (MPC) · Discrete-time singular systems · Input-to-state stability (ISS) · Persistent disturbance · Dual-mode approach

45.1 Introduction

Due to the capacity in involving the dynamic and algebraic relationships between state variables simultaneously [1], the singular system model can describe a larger class of systems than the normal linear system model, such as power systems, economical systems, robotic systems, chemical processes, and others [2]. The study of singular systems control has attracted considerable attention in the last decades, and has achieved abundant accomplishment [3].

Model predictive control (MPC) is an effective control strategy widely applied in the industry [4], and is also an optimal control technique that deals with hard constraints and nonlinearity. With the development of model predictive control,

C. Gao (✉) · X.-H. Liu
School of Mathematics and Statistics Science, Yantai Shangdong, China
e-mail: gaochan6688@163.com

X.-H. Liu
e-mail: xhliuyt@sina.com

many MPC algorithms have been proposed for nominal systems, especially the robust MPC, which was developed to ensure the performance of systems subject to uncertainties such as parameter uncertainties, unmodeled dynamics, external disturbances, [5–7], etc. Recently, the research on robust MPC of singular systems has been carried out [8–11]. In [8], it is concerned with model predictive control of time-varying linear singular systems with norm-bounded uncertainties, and the control actions are obtained by minimizing a worst-case objective function over an infinite moving horizon. After that, some results on robust MPC of singular systems with uncertainties, decaying disturbance, state and input delays have been obtained [9–11], etc.

When some uncertainties cause a great difference between the actual models and the nominal models, such as persistent disturbance which cannot decay to zero, then the- Lyapunov stability or asymptotic stability performance of systems will not be very well guaranteed, so to this end, many robust MPC algorithms are developed to ensure the performance of MPC systems [12, 13]. In the case of persistent disturbances for nominal systems, it is clearly impossible to achieve closed-loop asymptotical stability of the origin. Recently, input-to-state stability results for min-max nonlinear MPC are presented in [14, 15] to deal with a class of systems subject to control constraint and bounded (persistent or vanishing) additive disturbance, the most utilized method is the dual-mode approach which was a local feedback controller inside the terminal constraint set and a min-max MPC controller outside the terminal constraint region. In [14], a priori sufficient condition is provided for robust stability of the resulting closed-loop system using the input-to-state stability framework and derive new conditions for guaranteeing ISS of min-max MPC closed-loop systems using a dual model approach. In [15], a robust MPC algorithm of nonlinear systems subject to input constraints and unknown but bounded disturbances, the proposed control algorithm solves a semidefinite programming problem that explicitly incorporates a finite horizon cost function and LMI-constraints. Input-to-state stable (ISS) and a dual-model approach are combined to achieve the closed-loop ISS of the controller with respect to disturbance.

However, to the best of the authors' knowledge, the problem of robust MPC for singular system with persistent disturbance has not been investigated so far.

In this paper we consider the robust MPC problem of discrete-time singular systems subject to persistent disturbance and control constraints. First, we introduce the concept of Input-to-state stability (ISS) to the design method of robust singular predictive controller; secondly, a piecewise constant control sequence is obtained by minimizing a worst-case objective function over a finite horizon outside the terminal constraint set, and a local feedback controller is used in a terminal constraint set. Finally, it is proved in that the designed dual-mode MPC approach can ensure the closed-loop discrete-time singular system to be input-to-state stability.

45.2 Problem Statement

45.2.1 System Description

Consider the following discrete-time singular system with persistent disturbance:

$$Ex(k+1) = Ax(k) + Bu(k) + Gw(k), \tag{45.1}$$

where $x(k) \in \Re^n$ is the system state vector, $u(k) \in \Re^m$ is the current input control vector, the persistent disturbance input $w(k) \in W \subset \Re^d$, and E is a real constant matrix with $\text{rank}(E) = r(r<n)$.

The control input $u(k)$ is subject to the constraint

$$u(k) \in U = \left\{ u(k) \in \Re^m : \|u(k)\| \le \bar{u}, k = 0, 1, 2 \dots \right\}, \tag{45.2}$$

where the $\bar{u}$ is a known upper bound. Moreover, the signal $w(k)$ is the persistent disturbance which cannot decay to zero, and lies in a compact set

$$w(k) \in W = \left\{ w(k) \in \Re^d : \|w(k)\| \le \bar{w}, k = 0, 1, 2 \dots \right\}, \tag{45.3}$$

where the $\bar{w}$ is a known upper bound. The disturbance $w(k)$ satisfying (45.3) will be said to be admissible.

Definition 45.1 [16]

(i) Singular system (45.1) is regular if $\det(zE - A)$ is not identically zero for $z \in C$.

(ii) Singular system (45.1) is said to be causal if $deg(det(zE - A)) = rank(E)$.

Lemma 45.1 [8] *The following items are true*

(i) *all Z satisfying $ZE^T = EZ^T$ can be parameterized as $Z = EV_1 W V_1^T + SV_2^T$, where $W \ge 0 \in \Re^{r \times r}$ and $S \in \Re^{n \times (n-r)}$. Furthermore, when z is nonsingular, $W > 0$.*

(ii) *if $EV_1 W V_1^T + SV_2^T$ is nonsingular with $W > 0$. Then there exist $\hat{W}$ such that $(EV_1 W V_1^T + SV_2^T)^{-T} = U_1 \hat{W} U_1^T E + U_2 \hat{S}$ with $\hat{W} = \sum_r^1 W^{-1} \sum_r^1$ and $\hat{S} = U_2^T (EV_1 W V_1^T + SV_1^T)^{-T}$.*

45.2.2 Input-to-State Stability

Consider the following discrete-time singular systems:

$$Ex(k+1) = F(x(k), w(k)), \tag{45.4}$$

where $x(k) \in X \subset \Re^n$ is the system state vector, $w(k) \in W \subset \Re^d$ is the disturbance inputs vector, and the function $F : \Re^n \times \Re^d$ is smooth enough and $F(0,0) = 0$. Exceptional, $E \in \Re^{n \times n}$ is singular matrix with rank$(E) = r (r < n)$, if the matrix E is nonsingular matrix, the above discrete-time singular system degenerated into normal discrete-time system. Assume that W is bounded set.

Definition 45.2 [14] We call a set $X \in \Re^n$ a robust positive invariant set of system (45.4) with respect to disturbance $w(k)$ if for all $x(k) \in X$ it holds that $F(x(k), w(k)) \in X$ for all disturbance $w(k) \in W$.

Definition 45.3 The discrete-time singular system (45.4) is said to be Input-to-state stability (ISS) in $X \subset \Re^n$ and $0 \in \text{int}(X)$ if there exist a *KL*-function and a K_∞ function γ, for each input $w(k) \in W$, and each $Ex(0) \in X$ holds that

$$|x(k, Ex(0), w(k))| \leq \beta(Ex(0), w(k)) + \gamma(\|w(k)\|), \forall k \geq 0 \tag{45.5}$$

where $x(k, Ex(0), w(k))$ is the state trajectory of system with initial condition $Ex(0) \in X$ and the disturbance $w(k) \in W$.

Theorem 45.1 *Consider discrete-time singular system* (45.4) *and suppose that the disturbance is bounded. Let* $\alpha_1(s) := as^\lambda, \alpha_2(s) := bs^\lambda, \alpha_3(s) := cs^\lambda$ *for some* $a, b, c, \lambda > 0$; *the constraint set X be an RPI set for system* (45.4) *and* $V(\cdot) : X \to \Re_+$ *be a function such that*

   (i) $V(0) = 0$
   (ii) $\alpha_1(\|Ex(k)\|) \leq V(Ex(k)) \leq \alpha_2(\|Ex(k)\|)$
   (iii) $V(F(x(k), w(k))) - V(Ex(k)) \leq -\alpha_3(\|Ex(k)\|) + \sigma(\|w(k)\|)$ *if   above inequality holds for all* $x \in X$ *and all* $w(k) \in W$, *then system* (45.4) *is ISS, and we called* $V(\cdot) : X \to R_+$ *is an ISS-Lyapunov function.*

   The aim of this paper is to design the dual-mode MPC controller which can ensure the closed-loop discrete-time singular system (45.1) input-to-state stability (ISS):

$$U^{DM}(x) = \begin{cases} u(i/k), \ x(i/k) \notin X_T & i = 1, 2 \dots N \\ K_N x(i/k), \ x(i/k) \notin X_T \end{cases}$$

where X_T is the terminal constraint region, $u(i/k)$ is the control action for time $k + i$, $x(i/k)$ denote the predicted state at time $k + i$.

45.3 Robust MPC with ISS

45.3.1 Optimization Problem Analysis

Consider the discrete-time singular system (45.1), define a sequence of control policy :

$$U^N(k) = [u(0/k), \ldots, u(N-1/k)]$$

with $u(i/k) = K(k)x(i/k)$, $i = 1, 2 \ldots N-1$. Let $x(i/k)$ denote the predicted state at time $k+i$, based on the measurements at sampling time k; $x(k/k)$ refer to the state measured at sampling time k; $u(i/k)$ is the control action for time $k+i$ obtained by an optimization problem over the finite prediction horizon.

Due to the exist singular matrix E of discrete-time singular system, we choose the following terminal cost function and performance index. At each sampling time k, consider the following finite horizon performance index:

$$J_N^* = \min_{U_0^N(k)} \max_{k=0,1\ldots N} J_N(k) \tag{45.6}$$

$$
\begin{aligned}
J_N(k) &= \sum_{i=0}^{N-1} L(x(i/k), u(i/k)) + V(x(N/k)) \\
&= \sum_{i=0}^{N-1} x(i/k)^T Q x(i/k) + u(i/k)^T R u(i/k) + x(N/k)^T E^T P E x(N/k) \\
& E^T P E \geq 0
\end{aligned}
$$

$$
\begin{aligned}
s.t.\ & Ex(i+1/k) = Ax(i/k) + Bu(i/k) + Gw(i/k), \quad i \geq 0 \\
& x(0/k) = x(k); u(i/k) \in U, \quad i = 0, 1 \ldots N-1; \\
& x(N/k) \in X_T
\end{aligned}
$$

where P, Q, R are assumed to be positive definite and symmetric matrices. X_T is the terminal state constraint set including the origin as interior and we assumed that X_T is the RPI set.

Choosing the terminal function $V(x) = x^T E^T P E x$ with a positive definite matrix P. At each sampling time k, suppose that for any disturbance, $i = 1, \ldots N$, $V(x)$ satisfies the following inequality:

$$V(x(i+1/k)) - V(x(i/k)) \leq -\|x(i/k)\|_Q^2 - \|u(i/k)\|_R^2 + \rho\|w(i/k)\|^2. \tag{45.7}$$

for some $\rho > 0$.

If there exists a suitable nonnegative variable $\gamma(k)$ satisfied $\max J_N(k) \leq \gamma(k)$, then the optimization problem (45.6) can be solved by semidefinite programming.

45.3.2 The Main Results for Optimization

Theorem 45.2 *Consider the constrained discrete-time singular system* (45.1) *and the control sequence* $U^N(k)$. *If there exist* $\gamma(k) \geq 0, \theta \geq 0, \lambda(k) > 0, W \geq 0 \in \Re^{r \times r}, S \in \Re^{n \times (n-r)}$ $Y \in \Re^{m \times n}$ *and some numbers* $\varepsilon > 0$ *and* $\rho > 0$, *with* $Z = (EV_1WV_1^T + SV_2^T) = P^{-1}$ *and* $Y = K(k)Z$, *the following optimization problem is feasible at sampling time* k:

$$\min_{\gamma(k),u(k),\theta,W,S,Y} \gamma(k)$$

$$s.t. \begin{bmatrix} -E^TZE & 0 & [AZ+BY]^T & Y^T & Z^T \\ * & -\rho I & G^T & 0 & 0 \\ * & * & -Z^T & 0 & 0 \\ * & * & * & -R^{-1} & 0 \\ * & * & * & * & -Q^{-1} \end{bmatrix} \leq 0 \qquad (45.8)$$

$$\begin{bmatrix} -\gamma_1(k) & u(k)^T & (Ax(k)+Bu(k))^T & \bar{w} \\ * & -R^{-1} & 0 & 0 \\ * & * & -\varepsilon_1^{-1}Z^T & 0 \\ * & * & * & \frac{-\varepsilon_2^{-1}\lambda^{-1}}{\sigma(G^TG)} \end{bmatrix} \leq 0 \qquad (45.9)$$

$$\begin{bmatrix} -\phi(\bar{k}-1) & u(k)^T & (Ax(k)+Bu(k))^T & \bar{w} \\ * & -R^{-1} & 0 & 0 \\ * & * & -\varepsilon_1^{-1}Z^T & 0 \\ * & * & * & \frac{-\varepsilon_2^{-1}\lambda^{-1}}{\sigma(G^TG)} \end{bmatrix} \leq 0 \qquad (45.10)$$

$$\begin{bmatrix} -\bar{u}^2 & u(k)^T \\ * & -I \end{bmatrix} \leq 0 \qquad (45.11)$$

$$\begin{bmatrix} -\bar{u}^2 E^TZE & Y^T \\ * & -\theta \end{bmatrix} \leq 0 \qquad (45.12)$$

$$\begin{bmatrix} -\gamma(k) & 1 \\ 1 & -\theta \end{bmatrix} \leq 0 \qquad (45.13)$$

where

$$\gamma_1(k) = \gamma(k) - (N-1)\rho\bar{w}^2 - x^T(k)Qx(k)$$
$$\bar{\phi}(k-1) = \Phi(k-1) - (N-1)\rho\bar{w}^2 - x^T(k)Qx(k)$$
$$\varepsilon_1 = 1 + \varepsilon; \varepsilon_2 = 1 + \varepsilon^{-1}$$

Then the following properties hold:

(a) The terminal function $V(x) = x^T E^T P E x$ with $Z = P^{-1}$ satisfies inequality (45.7) for $i = 1, \ldots N - 1$. Especially

$$V(x(i + 1/k)) - V(x(i/k)) \leq -c, \forall i = 1, \ldots N - 1$$

for any $x(i/k) \in X_f = \{x \in \Re^n : \|x(i/k)\| \geq r_1\}$ and some $c > 0$, with

$$r_1 = \sqrt{\rho \bar{w}^2 + c \Big/ \lambda_{\min}(Q)}$$

(b) It holds that inequality $\Phi(k) \leq \gamma(k)$, which yield an upper bound of the original cost function $J_N(k) \leq \gamma(k)$.

(c) The constraint (45.2) is fulfilled with respect to any admissible disturbance (45.3).

Then for the following parts, we determined a terminal region and a fixed state feedback controller.

To proceed further, we give the following Assumption 45.1.

Assumption 45.1 There exist $\lambda_{\min}(Q), \lambda_{\min}(P), \lambda_{\max}(P) > 0$ with $\lambda_{\min}(Q) \leq \lambda_{\max}(P)$, a function $h(x) = Kx(k) : \Re^n \to \Re^m$ with $h(0) = 0$, and a K-function σ such that:

(i) $X_T \subseteq X_u$ and $0 \in \text{int}(X_T)$.

(ii) X_T is an RPI set for system (45.1) in closed-loop with $u(x) = Kx(k)$.

(iii) $L(x, u) \geq x^T Q x \geq \lambda_{\min}(Q) \|x\|_2^2$ for all $x \in X$ and all $u \in U$.

(iv) $\lambda_{\min}(P) \|Ex\|_2^2 \leq x^T E^T P E x \leq \lambda_{\max}(P) \|Ex\|_2^2$ for all $x \in X_T$.

(v) $V(F(x(k), u(k), w(k))) - V(x(k)) \leq -L(x(k), u(k)) + \sigma(\|w(k)\|)$ for all $x \in X_T$ and $w(k) \in W$.

Remark 45.2 This assumption implies that the terminal cost function is a local ISS-Lyapunov function for discrete-time singular system.

Theorem 45.3 *Consider the discrete-time singular system* (45.1) *under Assumption* 45.1. *For any* $x(k) \in X_T$ *with* $X_T = \{x(k) \in \Re^n : \|x(k)\| < r_1\}$, *there exist* $\gamma \geq 0, \theta \geq 0, W_1 \geq 0$ $S_1 \in \Re^{n \times (n-r)}, Y_N \in \Re^{m \times m}$ *with* $Z_N = EV_1 W_1 V_1^T + S_1 V_2^T = \gamma P_N^{-1}$ *and* $Y_N = K_N Z_N$. *The local feedback control law* $u^*(0/k) = K_N x(k) \in U$ *for all* $x(k) \in X_T$ *and the closed-loop systems* (45.1) *with* $u(k)$ *satisfies:*

$$V(x(k+1)) - V(x(k)) \leq -\|x(k)\|_Q^2 - \|u(k)\|_R^2 + \rho \|w(k)\|^2. \qquad (45.14)$$

for all $x(k) \in X_T$ and $w(k) \in W_r$, where the terminal cost function $V(x(k)) = x^T E^T P_N E x(k)$ with $P_N = \gamma Z_N^{-1}$ such that

$$
\begin{bmatrix}
-E^T Z_N E & 0 & [AZ_N + BY_N]^T & Y_N^T & Z_N^T \\
* & -\gamma \rho I & G^T & 0 & 0 \\
* & * & -Z_N^T & 0 & 0 \\
* & * & * & -\gamma R^{-1} & 0 \\
* & * & * & * & -\gamma Q^{-1}
\end{bmatrix} \leq 0 \qquad (45.15)
$$

$$
\begin{bmatrix}
-\bar{u}^2 E^T Z_N E & Y_N^T \\
* & -\theta
\end{bmatrix} \leq 0 \qquad (45.16)
$$

$$
\begin{bmatrix}
-\gamma & 1 \\
* & -\theta
\end{bmatrix} \leq 0 \qquad (45.17)
$$

holds for some $\rho > 0, Q > 0, R > 0$ are weighing matrices in $J_N(k)$.

Then we can obtain the following dual-model control algorithm of discrete-time singular system:

Step 1. Select $Q > 0, R > 0, \rho > 0, c > 0, \varepsilon > 0, N > 0,$ and   computer $r_1 = \sqrt{\rho \bar{w}^2 + c \big/ \lambda_{\min}(Q)}$ with respect to $\bar{w}$.

Step 2. At step time $k = 0, 1, 2 \ldots$, measure the state $x(k)$;

Step 3. If $x(k) \notin X_T$, solve problem (45.8–45.13) on line; else, compute a feasible solution on LMIS (45.15–45.17) online;

Step 4. Apply the control input $u(k) = u^*(0/k)$ to discrete-time singular system (1);

Step 5. Set $k = k + 1$ and go to step 2.

45.4 The Analysis of Input-to-State Stability

Theorem 45.4 *Consider the constrained discrete-time singular system* (45.1) *under Assumption 45.1. The value function of problem 1 is an ISS-lyapunov function of the closed loop system* (45.1) *with the dual mode MPC control* $u(k) = u^*(0/k)$, *the closed loop system is regular, causal and ISS with respect to disturbance* (45.3) *in the face of input constraint* (45.2).

45.5 A Numerical Example

Consider the discrete-time singular system (45.1), whose parameter values are as follows:

$$E = \begin{bmatrix} 1 & 0 & 0 & 0 \\ 0 & 1 & 0 & 0 \\ 0 & 0 & 0 & 0 \\ 0 & 0 & 0 & 1 \end{bmatrix}, A = \begin{bmatrix} 1 & 0 & 0.1 & 0 \\ 0 & 1 & 0 & 0.1 \\ -0.02 & 0.02 & 1 & 0 \\ 0.02 & -0.02 & 0 & 1 \end{bmatrix}, B = \begin{bmatrix} 0 \\ 0 \\ 0.1 \\ 0 \end{bmatrix},$$

$$G = \begin{bmatrix} 0 \\ 0 \\ 0.1 \\ 0 \end{bmatrix}.$$

Considering the persistent disturbance $w(k) = \bar{w} \sin(k)$ with $\bar{w} = 0.5$. The aim is to design a controller with respect to persistent disturbance $|w(k)| \leq \bar{w}$ and the control constraint $|u(k)| \leq 1$ to ensure the closed-loop singular system is input-to-state stability.

In the simulation running, let $Q = I \in \Re^{n \times n}$, $R = 1$, $\varepsilon = 0.1$, $c = 0.02$, $\rho = 0.5$, $N = 3$, and computer $r_1 = 0.3808$, then the terminal constraint set is $X_T = \{x(k) \in \Re^n : \|x(k)\| < r_1\}$.

Choosing the initial state $x(0) = \begin{bmatrix} 1 & 0.5 & -0.7 & 0 \end{bmatrix}^T$ and with the sampling time 0.1 s. The dual model controller is designed on the basis of Theorems 45.2 and
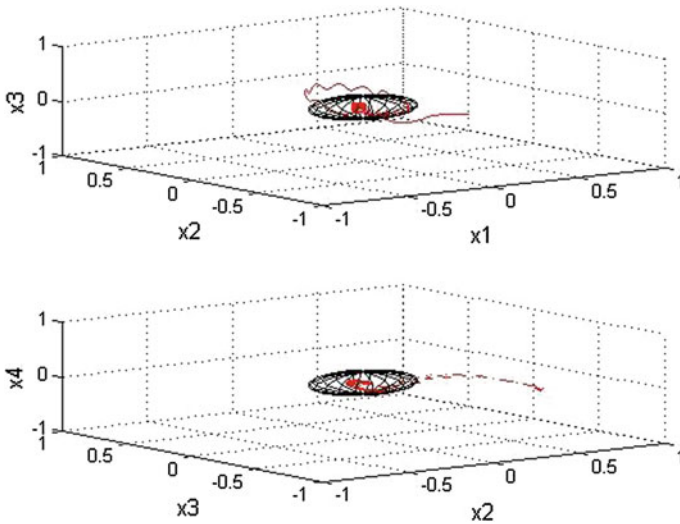
Fig. 45.1 3D section of the terminal constraint region X_T and the trajectories of closed-loop system by proposed method
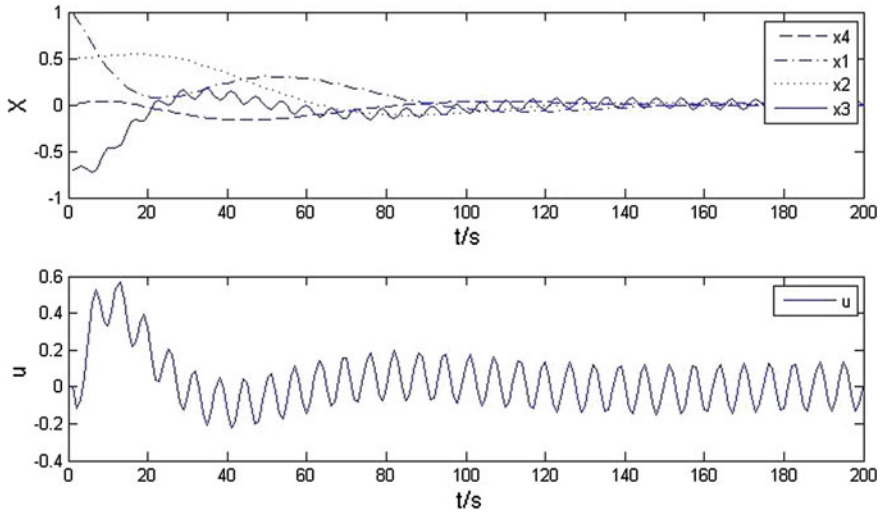
Fig. 45.2 The obtained simulation results with respect to disturbance $w(k)$

45.3, solve the LMIS by LMI Tool-box. The simulation results are shown in Figs. 45.1 and 45.2.

Above all, the simulation results show that the obtained closed-loop singular system is input-to-state stable with respect to some bounded persistent disturbance by the designed dual-mode MPC controller, moreover the closed-loop singular system is also regular and causal.

45.6 Conclusion

In this paper, the robust quasi-min-max model predictive control is studied for discrete-time singular systems with persistent disturbance and input constraints. The concept of input-to-state stability and ISS-Lyapunov function for discrete-time singular system is proposed for the first time. A robust predictive control is designed to guarantee the input-to-state stability (ISS) of closed-loop singular system. Also, the proposed optimization problem is solved.

References

1. Leweis FL (1986) A survey of linear singular systems. Circuits Syst Signal Process 5(1):3–36
2. Zhang B (2008) Parametric eigenstructure assignment by state feedback in descript or systems. IET Control Theory Appl 2:303–309

3. Duan G (2010) Analysis and design of descriptor linear systems. Springer, New York
4. Joe QS, Badgwell TA (2003) A survey of industrial model predictive control technology. Control Eng Pract 11(7):733–764
5. Magni L, De Nicolao G, Scattolini R, Allgower F (2003) Robust model predictive control for nonlinear discrete-time systems. Int J Robust Nonlinear Control 13:229–246
6. Kothare MV, Balakrishnan V, Morari M (1996) Robust constrained model predictive control using linear matrix inequalities. Automatica 32:1361–1379
7. Mayne DQ, Seron MM, Rakovic SV (2005) Robust model predictive control of constrained linear systems with bounded disturbances. Automatica 41(2):219–224
8. Zhang L, Huang B (2004) Robust model predictive control of singular systems. IEEE Trans Autom Control 49(6):1000–1006
9. Liu XH, Yang YH (2009) Robust model predictive control of singular systems with delayed-state and parameter uncertainty based on state observer. Control Decis 24(4):606–611 (in Chinese)
10. Liu XH, Wang LJ (2009) Robust model predictive control for uncertain singular systems via dynamic output feedback. Control Decis 24(9):1371–1376 (in Chinese)
11. Liu XH, Wang LJ (2010) Robust predictive control of uncertain singular system with both state and input delays. Control Theory Appl 27(4):527–531
12. Chen H, Allgpwer F (1998) A Quasi-infinite horizon nonlinear model predictive control scheme with guaranteed stability. Automatica 14:1205–1217
13. Mayne DQ, Rawlings JB, Rao CV, Scokaert POM (2000) Constrained model predictive control:stability and optimality. Automatica 36:789–814
14. Lazar M, De La Pena DM, Heemels WPMH, Alamo T (2008) On input-to-state stability of min-max nonlinear model predictive control. Syst Control Lett 57(1):39–48
15. He DF, Huang H, Chen QX (2014) Quasimin-max MPC for constrained nonlinear systems with guaranteed input-to-state stability. J Franklin Inst
16. Zhang G, Xia Y, Shi P (2008) New bounded real lemma for discrete-time singular systems. Automatica 44(3):886–890
17. Zhou Z, Yang C, Zhang Q et al (2011) Input-to-state stability for descriptor systems with nonlinear perturbations. IET Control Theory Appl 5(13):1561–1567
18. Poursafar N, Taghirad HD, Haeri M (2010) Model predictive control of nonlinear discrete-time systems: a linear matrix inequality approach. IET Control Theory Appl 4(10):1922–1932

Chapter 46
QACtools: A Quality Assessment and Quality Control Tool for Next-Generation Sequencing Data

Dandan Song, Ning Li and Lejian Liao

Abstract In recent years, next-generation sequencing technologies have been widely used, and are rapidly changing the landscape of genetics with unimaginable speed. However, the preliminary quality control regulations including trimming adaptor sequences, quality statistics, and depth and coverage statistics need to be applied to raw reads before further analysis. QACtools implements various utilities for processing raw reads in the FASTQ format and alignments in the BAM format. It analyzes some relevant properties of next-generation sequencing data such as average read length, base quality scores, and so on. Additionally, to our knowledge, none of the other tools support depth and coverage statistic that have been provided in our tool for analysis of large DNA sequencing data. It is crucial for overcoming errors in base calling and assembly. We suppose tool is useful for the quality control of NGS data to perform further analysis. This software is an open source application freely available at https://sourceforge.net/projects/qactools/.

Keywords NGS data analysis · Quality control · FASTQ format · BAM format

46.1 Introduction

Over the past three years, next-generation sequencing technologies have been widely used, and are rapidly changing the landscape of genetics with unimaginable speed [1, 2]. This wide development of massive next-generation sequencing (NGS)

D. Song · N. Li · L. Liao (✉)
Beijing Lab of Intelligent Information Technology, School of Computer Science and Technology, Beijing Engineering Research Center of High Volume Language Information Processing and Cloud Computing Applications, Beijing Institute of Technology, Beijing, China
e-mail: liaolj@bit.edu.cn

technologies has dramatically accelerated biological and biomedical research. The technologies enable the comprehensive analysis of genomes to become inexpensive and routine, rather than requiring a lot of effort.

As massive number of DNA sequence reads can be generated in a single experiment [3, 4], it is important to check the quality of reads. The preliminary quality control regulations include trimming adaptor sequences, quality statistics, and depth and coverage statistics. They need to be applied to raw reads before further analysis and may prevent undesirable outcomes in the assembly or mapping processes.

FASTQ [5] format is a common text-based file format for both a nucleotide sequence and its corresponding quality scores, for storing the output of high throughput sequencing instruments. Binary Alignment Map (BAM) [6] format is the binary representation of SAM and keeps exactly the same information as SAM. Using positional sorting and indexing, applications can perform stream-based processing on specific genomic regions, such as calculating deep sequencing and coverage, without loading the entire file into memory. Both FASTQ and BAM format files can be accepted by our tool as input.

The proposed QACtools is a quality control and quality assessment application for high throughput sequence data. It processes paired-end (PE) and single-end (SE) sequencing data in the format of FASTQ and alignments in BAM files. It provides a quick overview to tell you where there may be problems and generates summary graphs and tables to intuitively review the results of several different quality control checks. Additionally, to our knowledge, none of the other QC tools support depth and coverage statistic that have been provided in our tool, which is crucial for overcoming errors in base calling and assembly. The tool has been implemented as a standalone application on UNIX high performance computing system scheduled by SGE as well as on a single personal computer. It can either run as a standalone interactive application for the immediate analysis of small numbers of input files, or it can be run in a noninteractive mode suitable for integrating into a larger analysis pipeline for the systematic processing of large numbers of files. The source codes are available at the web address: https://sourceforge.net/projects/qactools/.

46.2 Materials and Methods

QACtools is highly configurable. The parameters of the analysis are specified and flexibly customized in an intuitive configuration file. The raw FASTQ files and the generated BAM files are taken as input. We have included multi quality control steps to check the integrity of the inputs, such as base distribution and deep and coverage of sequencing data. Different from most publicly available programs for QC of NGS data, we provide the option for adaptor contamination removal. It is able to filter the nonstandard adaptor sequences. The software is written in Perl and C++, which is driven by command-lines. Importantly, it is prepared to analyze
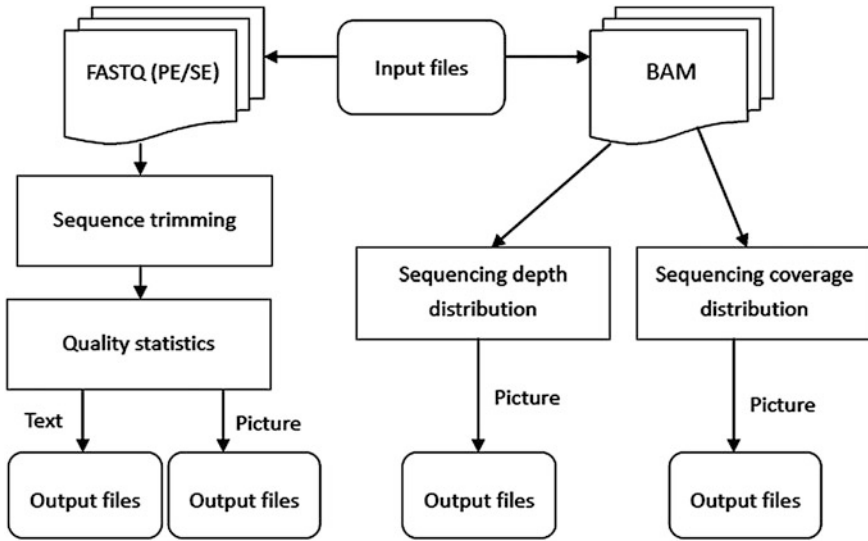
Fig. 46.1 Overview of various functions included in the QACtools

multiple samples simultaneously on a UNIX operating system, and the real execution time will be reduced a lot.

The major components of QACtools are illustrated in Fig. 46.1, where the functions and the corresponding input and out files were represented in the rectangles, the relationship between them are shown by arrows. Below we explain each major function in detail.

46.2.1 Sequence Trimming

Generally, the huge volume of data generated by NGS technologies is in the form of compressed files. Our tool takes compressed NGS data files as input and compresses the filtered data as output in the end. Thus the requirement of storage space and time for data transfer can be lowered a lot.

Both SE reads and PE reads are accepted for trimming of sequence artifacts. If the reads with high quality score pass the filter criteria, they will be conserved in the output file. While filtering of high quality reads from PE data, it is crucial to maintain the pairing information, which is important for downstream analysis. Both forward and reverse reads are processed simultaneously, and only if both of them pass the filter criteria, filtered reads are exported in a separate file. In this way, the pairing information is kept intact. In addition, we provide the function for adaptor

contamination removal. The tool can utilize the standard adaptor sequences for selected assay and remove the contaminated reads and the nonstandard adaptor sequences provided by users as well.

46.2.2 Quality Statistics

The Basic Statistics module generates a wide variety of composition statistics, including average quality score for each read, GC content, average length, and so on, for the raw data and clean data files. It generates statistics for quality control and filtering steps in the form of text files and graphs.

The statistics results in text files can be exported as formatted text or tab delimited columns, which include average read length, total bases, N50 read length, etc., for input and filtered data. The generated graphs show the average quality score at each base position, average quality distribution for input and filtered reads. In this way, user can compare and check the overall quality improvement after filtering the input of low-quality data.

46.2.3 Depth and Coverage Statistics

Depth refers to the number of times a nucleotide is read during the sequencing process. Coverage is the average number of reads representing a given nucleotide in the genome sequence. Although the sequencing accuracy for each individual nucleotide is high, the very large number of nucleotides in the genome means that if an individual genome is only sequenced once, there will be a significant number of sequencing errors. Thus, a high depth and coverage in DNA sequencing is crucial because it can overcome errors in base calling and assembly.

The depth and coverage statistics must be performed with a number of parameters. If users do not want to utilize the default parameter values, they can change the value in the configure file. We implement an R script to convert the data from text file into the intuitive png/jpeg format. Considering the BAM files are in binary format and cannot be processed directly, we use BamTools [7], which is a project that provides both a C++ API and a command-line toolkit for reading, writing, and manipulating BAM (genome alignment) files. The two modules from BamTools along with in-house developed programs have been implemented in our tool. The main function is shown in Algorithm 46.1.

**Algorithm 46.1:** Depth and coverage statistics included in the QACtools

---

INPUT: A list of BAM files X

OUTPUT: Figures of depth distribution on per-base and coverage distribution on per-chromosome generated from each BAM file

for i = 1,…,N do //N is the total number of BAM files

    //Check if the threads are all created successfully or not

    depthFlag = pthread_create(&depthThread , NULL , &depthFunction , &th_info);

    if (depthFlag != 0) {

        cerr << "Invoking depth thread failed. Please re-run this program.\n";

    }

    coverageFlag = pthread_create(&statThread , NULL , &coverageFunction , &th_info);

    if (statFlag != 0) {

        cerr << "Invoking coverage thread failed. Please re-run this program.\n";

    }

    //Add threads to the job list

    pthread_join(depthThread , &depthRet);

    pthread_join(coverageThread , &coverageRet);

    //Show the statistics results in the format of png and jpeg

    histPlot($outdir,"$outdir/depth_frequency.xls",$ylim,$ybin,$xlim,$xbin);

    cumuPlot($outdir,"$outdir/coverage_frequency.xls",24,1);

    system "qsub   -l vf=6G -q group_ name -P project_name shell_script" //Submit the job to the workstation

    job_num ++;   //The job number adds one

    if(job_num > max_job_num){

        sleep;   //The job is temporally turned into sleeping state.

    }

end for

Table 46.1 Basic statistics of the experimental DNA sequencing reads

Sample	Raw data (Mb)	Clean data (Mb)	Adapter rate (%)	Low quality rate (%)	GC content (%)	*N* rate (%)
NA12878	4217	4209	0.01	0.19	42	4.8
NA18507	4474	4473	0.01	0.01	41	1.1
NA18956	3842	3841	0.01	0.02	41	1.0
NA309293	10159	9455	0.02	0.08	53	0.1
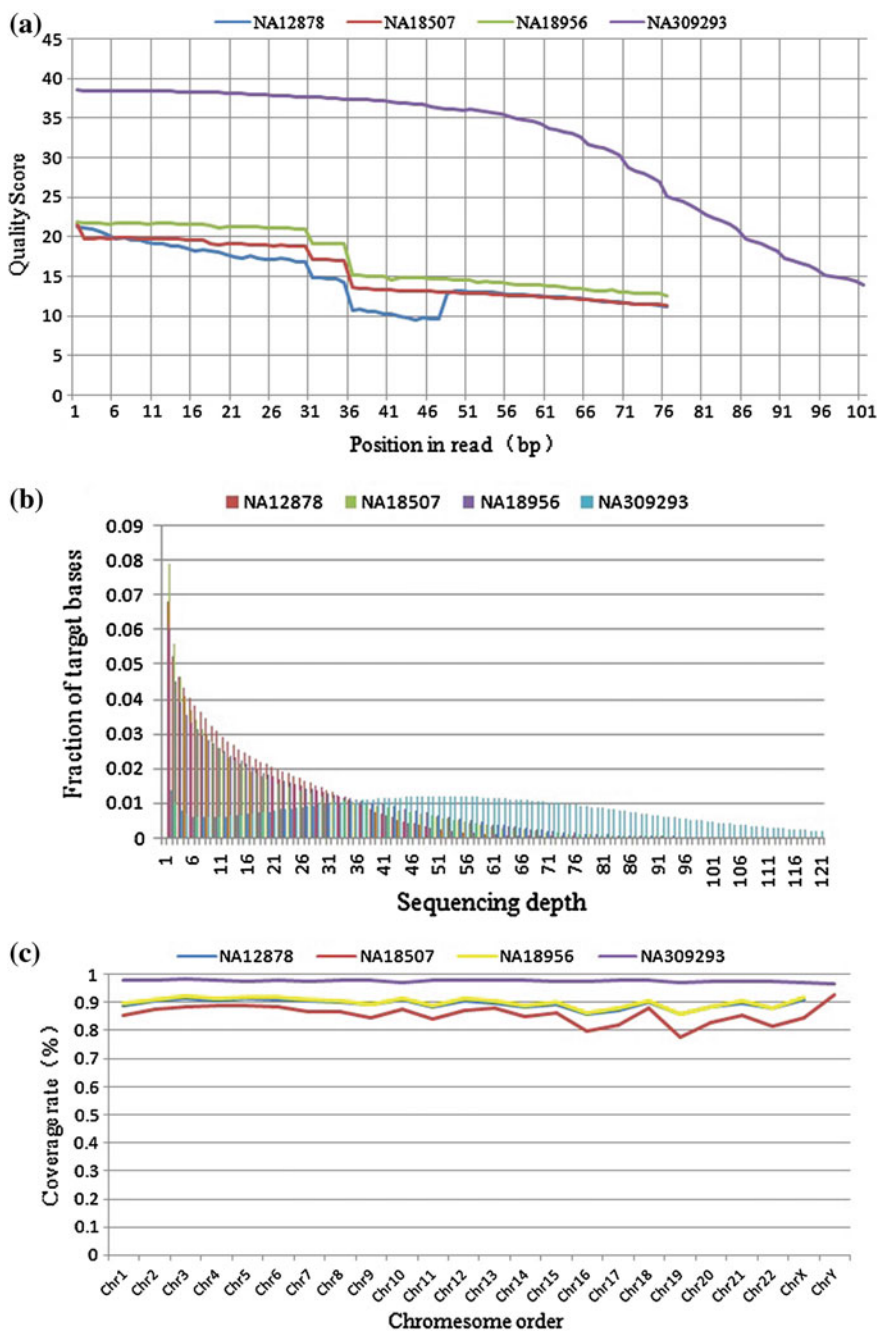
Fig. 46.2 Snapshots showing graphs of various QC statistics generated as output average quality scores at each base position. **a** Sequencing depth distribution, **b** and **c** sequencing coverage distribution

46.3 Results and Discussion

To validate the performance and efficiency of the proposed QACtools on processing DNA sequencing reads, we conduct the experiments on three Illumina paired-end and one Illumina single-end sequencing data downloaded from NCBI short read archive (SRA) public database [8]. The experiment is performed on a modern high performance computing server equipped with 2.33 GHz Intel (R) Xeon (R) CPU and 500 GB memory. The basic statistics of the experimental data is summarized in Table 46.1.

The output of quality check, trimming, and statistics tools for the above-mentioned Illumina sequencing data, contain high-quality filtered data, text file and graphs for quality statistics. The graphs generated by these tools represent various quality check (QC) statistics, including the average quality scores at each base position (Fig. 46.2a) for filtered reads to compare and check the overall quality improvement after filtering, sequencing depth distribution (Fig. 46.2b), sequencing coverage distribution (Fig. 46.2c).

A comparison of the features provided by some popular QC tools, including NGS QC Toolkit [9], FASTX Toolkit [10], FastQC [11] and QACtools (this study) is given in Table 46.2. Although there are some functions of other quality assessment tools not available in the current version of QACtools, several additional and better functions have been provided for quality check analysis. For example, to our knowledge, none of the other tools support depth and coverage statistic of large DNA sequencing data. The depth and coverage statistics in DNA sequencing is crucial because it can overcome errors in base calling and assembly.

Table 46.2 Comparison of various features of QACtools and other available QC tools

Function\tools	QACtools	FastQC	FASTX toolkit	NGS QC toolkit
Supported file format	FASTQ, BAM	FASTQ	FASTQ, FASTA	FASTQ, FASTA
Primer/adaptor removal	Yes	No	Yes	Yes
QC of paired-end reads	Yes	No	No	Yes
N filtering	Yes	No	Yes	No
Accept compressed file	Yes	Yes	No	Yes
GC content calculation	Yes	Yes	No	Yes
Output filtered reads	Yes	No	Yes	Yes
Depth calculation	Yes	No	No	No
Coverage calculation	Yes	No	No	No

46.4 Conclusion

In this study, we have developed an application, QACtools, for processing paired-end and singled-end reads in the FASTQ format and alignments in the BAM format. It analyzes some relevant properties of an ensemble of next-generation sequencing reads such as length, quality scores, and base distribution in order to prevent undesirable outcomes in the assembly or mapping processes. Importantly, to our knowledge, none of the other tools support depth and coverage statistic that have been provided in our tool for analysis of large DNA sequencing data. It is crucial for overcoming errors in base calling and assembly. The toolkit allows automatic and fast processing multiple samples simultaneously on UNIX high performance computing system scheduled by SGE, as well as on single personal computer. Given the importance of quality control of NGS data, we anticipate that this tool will be useful for the sequencing-based downstream analysis.

References

1. Shendure J, Ji H (2008) Next-generation DNA sequencing. Nat Biotechnol 26(10):1135–1145
2. Siepel A, Pollard KS, Haussler D (2006). New methods for detecting lineage-specific selection. In: Adam S, Katherine SP, David H (eds) Research in computational molecular biology, Springer, pp 190–205
3. Cock PJA, Fields CJ, Goto N, Heuer ML, Rice PM (2009) The Sanger FASTQ file format for sequences with quality scores, and the Solexa/Illumina FASTQ variants. Nucleic Acids Res 38:1767–1771
4. Meyerson M, Gabriel S, Getz G (2010) Advances in understanding cancer genomes through second-generation sequencing. Nat Rev Genet 11(10):685–696
5. Mardis ER (2008) The impact of next-generation sequencing technology on genetics. Trends Genet 24(3):133–141
6. Li H, Handsaker B, Wysoker F, Ruan J, Homer N et al (2009) The sequence alignment/map format and SAMtools. Bioinformatics 25(16):2078–2079
7. Barnett DW, Garrison EK, Quinlan AR, Strömberg MP, Marth GT (2011) BamTools: a C++ API and toolkit for analyzing and managing BAM files. Bioinformatics 27(12):1691–1692
8. Ajay SS, Parker SC, Abaan HO, Fajardo KV, Margulies EH (2011) Accurate and comprehensive sequencing of personal genomes. Genome Res 21(9):1498–1505
9. Patel RK, Jain M (2012) NGS QC Toolkit: A toolkit for quality control of next generation sequencing data. PLoS One 7(2):e30619
10. Hampton M, Melvin RG, Kendall AH, Kirkpatrick BR, Peterson N, Andrews MT (2011) Deep sequencing the transcriptome reveals seasonal adaptive mechanisms in a hibernating mammal. PLoS One 6(10)
11. FastQC A quality control tool for high throughput sequence data. Simon Andrews. http://www.bioinformatics.babraham.ac.uk/projects/fastqc/

Chapter 47
Research About the Method of Sensitivity Analysis and Quality Control Based on LS-SVM

Yiyong Yao, Hongren Chen, Liping Zhao and Guangzhou Diao

Abstract Focusing on the real-time quality control in machining process, sensitivity analysis method based on LS-SVM was proposed in this paper to control the quality of products. The relationship between machining quality and influence factors is built by LS-SVM (least squares support vector machine). Sensitivity and contribution rate are calculated in sensitivity analysis. The quality of products can be controlled by controllable factors according to the result of sensitivity analysis, and the control effect can be evaluated by quality loss function. The method verification was conducted by a simulation example. At the end of this paper, a case about globoidal cam was presented to verify the feasibility and accuracy.

Keywords LS-SVM · Machining quality · Sensitivity analysis · Quality control

47.1 Introduction

Market share and competitiveness of products are determined by processing quality directly. Quality of a product is often influenced by multiple factors and should be controlled in real time. The analysis methods of influence factors mainly include single-factor analysis of variance, correlation analysis, and sensitivity analysis.

Y. Yao (✉)
School of Mechanical Engineering, Xi'an Jiaotong University, Xi'an Jiaotong, China
e-mail: yyyao@mail.xjtu.edu.cn

H. Chen · L. Zhao · G. Diao
State Key Laboratory for Manufacturing Systems Engineering, Xi'an Jiaotong University, Xi'an Jiaotong, China
e-mail: chrjixie@stu.xjtu.edu.cn

L. Zhao
e-mail: lipingzh@mail.xjtu.edu.cn

G. Diao
e-mail: windwind110@stu.xjtu.edu.cn

Zhen [1] used single-factor analysis of variance to confirm the influence of melt temperature and holding pressure on shrinkage and warp. Liu [2] adopted the method of correlation analysis to find the parameters which have large influence on roving. Liu [3] adopted sensitivity analysis to find the primary factors that affect the quality of injection molding products. Salehi [4] used neural networks to detect the mean and variance shift. Single-factor analysis of variance and correlation analysis are statistical methods, and they need a large amount of data and complicated calculation. Simple sensitivity analysis is easy to realize, but it need to know the relationship between the machining quality and influence factors. Neural networks also need a number of sample data. So the conventional methods above are not suitable for real-time analysis and quality control.

However, machining quality of products need to be controlled in real-time. The methods above are weak in real-time quality control. Therefore, sensitivity analysis method based on LS-SVM is proposed to control the quality of products.

47.2 The Method of Sensitivity Analysis and Machining Quality Control Based on LS-SVM

Quality of a product is often influenced by many factors, and the fluctuation of quality is caused by some important factors. These fluctuations may reduce the quality of products, so sensitivity analysis must be conducted and the quality fluctuation must be controlled. The system block diagram is shown in Fig. 47.1.

47.2.1 Building Relationship Model Between Machining Quality and Influence Factors

Assume that machining quality F affected by n factors. It can be represented as $F = f(x_1, x_2, \ldots, x_n)$, where F is machining quality, and $x_1 \sim x_n$ are influence factors.

The method of sensitivity analysis and machining quality control based on LS-SVM
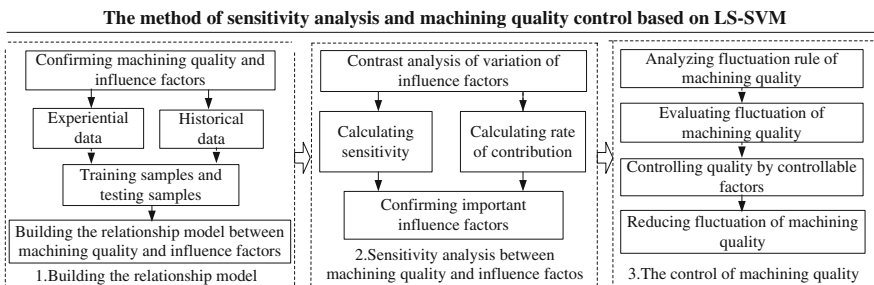
Fig. 47.1 The system block diagram of sensitivity analysis and machining quality control
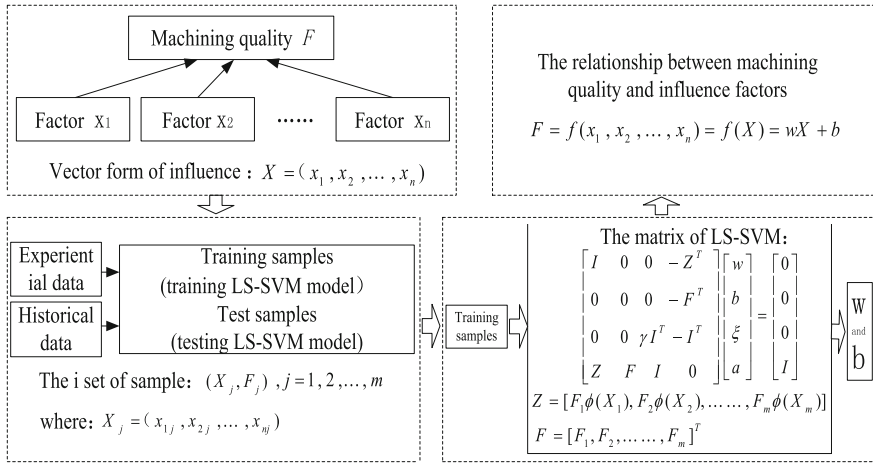
Fig. 47.2 Concrete steps of building relationship model

Training samples and test samples can be obtained by historical data, simulation data, or experiential data. The j set sample can be represented as F_j, $X_j = (x_{1j}, x_{2j}, \ldots, x_{nj})$, or the form (X_j, F_j), $j = 1, 2, \ldots, m$, where m is the number of samples. Concrete steps of building relationship model between machining quality and influence factors based on LS-SVM [5, 6] are shown in Fig. 47.2.

47.2.2 Sensitivity Analysis of Machining Quality Based on the Relationship Model

When influence factors are in the standard state $(x_1^*, x_2^*, \ldots, x_n^*)$, the balance point of machining quality could be represented as $F^* = f(x_1^*, x_2^*, \ldots, x_n^*)$. The standard values of influence factors $(x_1^*, x_2^*, \ldots, x_n^*)$ are theoretical design values or the statistical average values. Sensitivity analysis is to acquire the deviation degree between machining quality F and standard value F^* [7]. After obtaining the relationship model $F = f(x_1, x_2, \ldots, x_n) = f(X) = wX + b$, the sensitivity analysis can be conducted. Concrete steps of sensitivity analysis are shown in Fig. 47.3.

47.2.3 The Evaluation of Quality Loss and Quality Control According to the Result of Sensitivity Analysis

The fluctuation of machining quality is often associated with the sensitivity factors. Therefore, machining quality must be evaluated first.
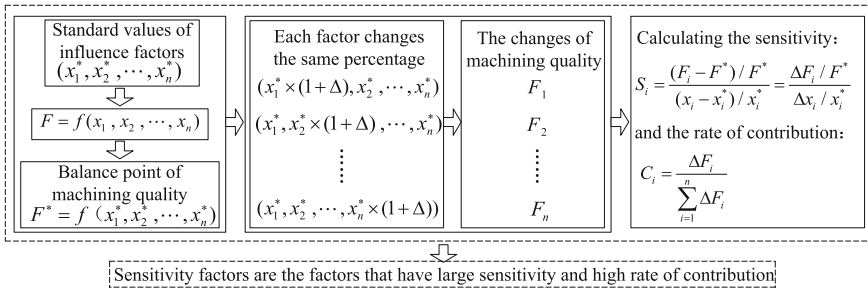
Fig. 47.3 Concrete steps of sensitivity analysis

Assume that F is the machining quality of a product, F^* is the balance point of machining quality, and K is the coefficient of quality loss. So the quality loss function [8] can be written as

$$L = K[\sigma^2 + (\mu - F^*)^2], \tag{47.1}$$

where σ^2 is the variance of F, and μ is the mean value of F. They can be calculated as: $\mu = \frac{1}{n}\sum F_i$ and $\sigma^2 = \frac{1}{n-1}\sum_{i=1}^{n}(F_i - \mu)^2$.

According to Taylor expansion, $F = f(x_1, x_2, \ldots, x_n)$ can be written as follows:

$$\Delta F = (\frac{\partial f}{\partial x_1})|_{x_1=x_1^*}\Delta x_1 + (\frac{\partial f}{\partial x_2})|_{x_2=x_2^*}\Delta x_2 + \cdots + (\frac{\partial f}{\partial x_n})|_{x_n=x_n^*}\Delta x_n. \tag{47.2}$$

It can be seen in Eq. (47.2). When one factor changes and the other factors stay the same, the change of machining quality will follow the changes of influence factors. Therefore, the fluctuation of quality can be compensated by controlling the changes of controlled factors. Concrete processes can be seen in Fig. 47.4.

Quality fluctuation can be compensated by several factors. Assume that quality fluctuation is caused by x_1. According to Eq. (47.2), the change of machining quality can be represented as $\Delta F = (\frac{\partial f}{\partial x_1})|_{x_1=x_1^*} \bullet \Delta x_1$. Quality fluctuation is compensated by $x_2 \sim x_p$. The change of x_i has the form $\Delta x_i = -(\partial f/\partial x_1)|_{x_1=x_1^*}\big/$
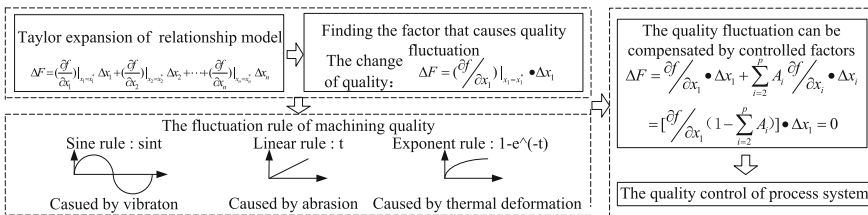

Fig. 47.4 Concrete processes of quality control

$(\partial f/\partial x_i)|_{x_i=x_i^*} \bullet A_i \bullet \Delta x_1$, where i is from 2 to p, and A_i is the proportion that x_i compensates the fluctuation, and $\sum\limits_{i=2}^{p} A_i = 1$. Δx_i is substituted into Eq. (47.2), and then quality variation is obtained

$$\Delta F = \partial f/\partial x_1 \bullet \Delta x_1 + \sum_{i=2}^{p} A_i \partial f/\partial x_i \bullet \Delta x_i = \left(\partial f/\partial x_1 - \partial f/\partial x_1 \bullet \sum_{i=2}^{p} A_i \right) \bullet \Delta x_1$$

$$= \left(\partial f/\partial x_1 - \partial f/\partial x_1 \right) \bullet \Delta x_1 = 0. \tag{47.3}$$

It can be seen that the quality fluctuation could be reduced by controlling several controlled factors.

47.3 A Simulation Example

In order to verify the feasibility of the quality control method, a simulation experiment was conducted.

47.3.1 Building Relationship Model Based on LS-SVM

Assume that machining quality and influence factors have the simulation relationship $F = 1 + \sqrt{x_1} + \frac{1}{x_2} + x_3^{-1.5}$, and $x_1 \sim N(5,1)$, $x_2 \sim N(6,1)$, $x_3 \sim N(7,1)$. The standard values of influence factors are $(x_1^*, x_2^*, x_3^*) = (5,6,7)$. 100 sets of simulation data are generated. 50 sets of data are regarded as training samples, and the other data are regarded as test samples. It can be seen in Fig. 47.5a, b that the true values are almost coincided with the predicted values, but BP-neural networks has a bigger error. Because neural networks is suitable for large sample data and has
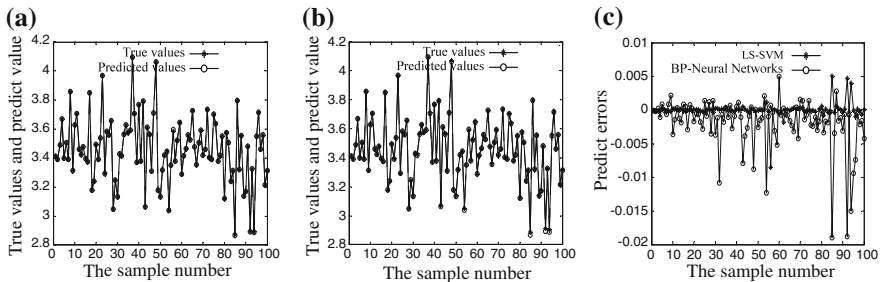
Fig. 47.5 The result of building relationship model. **a** LS-SVM, **b** BP-neural networks, **c** error comparision of BP-nn and LS-SVM

overfitting problem, LS-SVM is better than BP-neural networks in establishing a relationship model with small sample data. It can be seen in Fig. 47.5c that the errors of LS-SVM are smaller than that of neural networks. The maximal error is maximal error of LS-SVM is less than 5×10^{-3}, so LS-SVM can be used to build the relationship model in real time.

47.3.2 The Result of Sensitivity Analysis and the Effect of Quality Control

After building the relationship model, the sensitivity and rate of contribution can be calculated. It can be seen in Table 47.1. When influence factors (x_1, x_2, x_3) change $-2, -1, 1, 2$ %, respectively, x_1 has the large contribution to the change of machining quality. So the sensitivity factor is x_1. In order to reduce quality fluctuation, the change of x_1 must be controlled.

According to the analysis above, it can be seen that the sensitivity factor of $F = 1 + \sqrt{x_1} + \frac{1}{x_2} + x_3^{-1.5}$ is x_1. Assume that the change of x_1 has the form $x_1^* + 0.01x_1^* \sin t$. The fluctuation of machining quality F is caused by x_1, and x_2 is regarded as controlled factor. It can be seen in Table 47.1 that when influence factor has a variation of one percent, the sensitivities of x_1 and x_2 are $S_1 = 1.114$ and $S_2 = -0.165$, respectively. x_2 is made to change in the form $\Delta x_2 = -S_1/S_2 \bullet 0.01x_2^* \sin t = 6.75 \times 0.01x_2^* \sin t$, so x_2 could compensate the quality fluctuation caused by x_1. The result of control can be seen in Fig. 47.6a. The control of linear rule and exponential rule can be seen in Fig. 47.6b, c, respectively.

It can be seen in Fig. 47.6 that the quality fluctuation can almost be eliminated. Machining quality could not be completely stable, because Taylor expansion ignores the higher order term.

Quality loss can be calculated according to Eq. (47.1). It can be seen in Table 47.2 that the reduction of quality loss is more than 99.5 % after the control.

Table 47.1 calculated results of sensitivity and rate of contribution

	−2 %	Sensitivity	Contribution rate (%)	−1 %	Sensitivity	Contribution rate (%)
X1	−0.0224	1.122	81.6	−0.0112	1.192	82.7
X2	0.0034	−0.170	12.4	0.0017	−0.168	11.7
X3	0.0017	−0.083	6.0	0.0008	−0.082	5.6
	1 %	Sensitivity	Contribution rate (%)	2 %	Sensitivity	Contribution rate (%)
X1	0.0111	1.114	82.0	0.0222	1.110	82.1
X2	−0.0016	−0.165	11.4	−0.0033	−0.163	12.1
X3	−0.0008	−0.080	6.6	−0.0016	−0.079	5.8
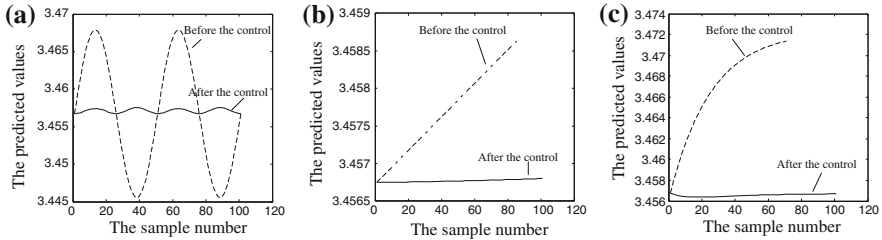
**Fig. 47.6** The result of quality control. **a** Sine rule, **b** linear rule, **c** exponential rule

Table 47.2 The comparison of quality loss

Fluctuation	Quality loss before control (K)	Quality loss after control (K)	Reduction of quality loss (%)
Sine rule	6.25×10^{-5}	2.59×10^{-7}	99.59
Linear rule	1.64×10^{-6}	6.67×10^{-10}	99.96
Exponential rule	1.53×10^{-4}	5.67×10^{-8}	99.96

47.4 A Case Study

Globoidal cam is a kind of intermittent mechanism. In order to improve the transmission accuracy, the quality of $\tan\beta$ must be controlled. $\tan\beta$ is affected by l, h, and C, where l is the distance between the roller and the center of divided plate, h is the length of rollers, and C is the center distance between the divided plate and cam. The standard values are $l^* = 44$ mm, $h^* = 10$ mm, and $C^* = 120$ mm.

100 sets of trainings samples and testing samples were acquired to establish the relationship model among $\tan\beta$ and l, h, C. It can be seen in Fig. 47.7 that the true values were in agreement with predicted values, and errors were less than 1×10^{-5}.
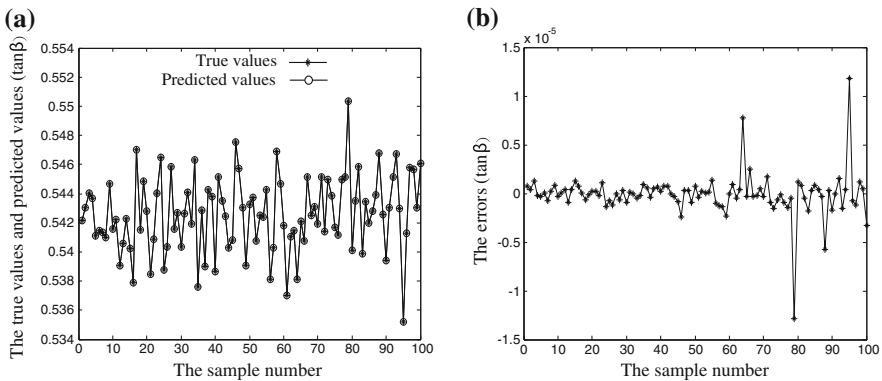
Fig. 47.7 The relationship model of globoidal cam. **a** Comparision between true values and predicted values, **b** errors between true values and predicted values

**Table 47.3** The sensitivity and rate of contribution of l, h, C

	−0.2 %	Sensitivity	Contribution rate (%)	−0.1 %	Sensitivity	Contribution rate (%)
l	-1.607×10^{-3}	0.8033	40.6	-8.040×10^{-4}	0.8040	43.0
h	-0.366×10^{-3}	0.1828	9.3	-1.828×10^{-4}	0.1829	4.4
C	1.981×10^{-3}	−0.9907	50.1	9.822×10^{-4}	−0.9839	52.6
	0.1 %	Sensitivity	Contribution rate (%)	0.2 %	Sensitivity	Contribution rate (%)
l	8.051×10^{-4}	0.8051	40.8 %	1.611×10^{-3}	0.8056	40.8
h	1.827×10^{-4}	0.1827	9.2 %	0.366×10^{-3}	0.1829	9.3
C	-9.858×10^{-4}	−0.9858	50.0 %	-1.968×10^{-3}	−0.9839	49.9

It can be seen in Table 47.3 that the rate of contribution of C is 50 %, and the rate of contribution of l was 40 %. So the sensitivity factors were C and l.

The quality fluctuation of $\tan\beta$ was caused by l. l included sine, linear and exponential rule, and had the form $l = l^* + 0.001/3 \bullet l^* \bullet \sin t + 0.001/3 \bullet l^* \bullet t +0.001/3 \bullet l^* \bullet (1 - e^{-t})$. Based on the method presented by this paper, the quality fluctuation of $\tan\beta$ could be reduced by controlling h and C. The result of quality control was shown in Fig. 47.8 and Table 47.4.

The quality fluctuation of $\tan\beta$ was almost reduced to zero by controlling h and C. It shows that the method of quality control is valid and accurate.

Fig. 47.8 Quality control ($\tan\beta$)
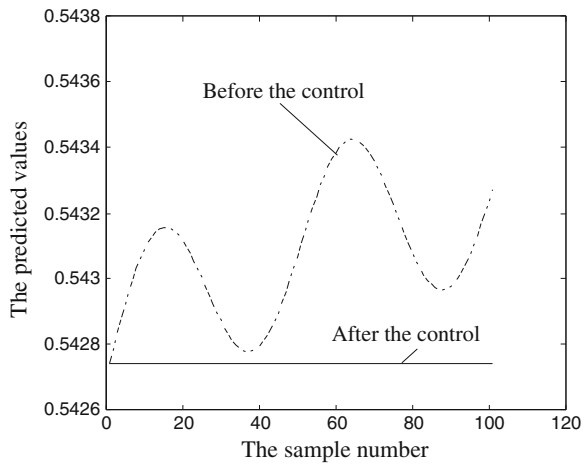
Table 47.4 The comparison of quality loss ($\tan\beta$)

Fluctuation	Quality loss before control	Quality loss after control	Reduction of quality loss
Quality loss	1.148×10^{-7}K	2.906×10^{-13}K	99.99 %

47.5 Conclusions

The present paper proposes a method of sensitivity analysis and quality control based on LS-SVM. First, the relationship model between quality and influence factors is built by LS-SVM. Then, the relationship model is used to conduct sensitivity analysis and calculate the sensitivity and rate of contribution, and the factors that have large influence on machining quality could be identified by the sensitivity and rate of contribution. Finally, controlled factors are used to reduce the fluctuation of machining quality. At the end of this paper showed an example about globoidal cam. In the example, the relationship model among $\tan\beta$ and l, h, C was established, and the sensitivity and rate of contribution were calculated. The quality fluctuation of $\tan\beta$ was almost reduced to zero by controlling h and C. The result of globoidal cam example shows that the method of sensitivity analysis and quality control based on LS-SVM is valid and accurate.

References

1. Zen SQ, Liu F et al (2011) Different effects of processing conditions on shrinkage and warpage of injection molded parts. CIESC J 62(3):33–37 (in Chinese)
2. Liu G, Yu WD (2008) Roving craft parameters' correlation analysis and BP network forecast discussion. Comput Eng Appl 44(28):233–238 (in Chinese)
3. Liu JX et al (2010) Sensitivity analysis and optimization of process parameters on sink marks of injection molding product. China Plast Ind 38(10):35–38 (in Chinese)
4. Salehi M et al (2012) On-line detection of mean and variance shift using neural networks and support vector machine in multivariate processes. Appl Soft Comput 12:2973–2984
5. Dong H et al (2007) Intelligent prediction method for small-batch producing quality based on fuzzy least square SVM. Syst Eng Theory Pract 27(3):98–104
6. Gu WP, Zhao WJ, Wu ZS (2010) Least squares support vector machine algorithm. J Tsinghua Univ (Sci Tech) 50(7):1063–1066 (in Chinese)
7. Su WB et al (2009) Research on the optimization of injection molding process parameters based on sensitivity analysis. J Plast Eng 16(3):202–206 (in Chinese)
8. Zhao Z (2008) Taguchi quality and quality of engineering. J Jianghan Petrol Inst 17(2):91–97 (in Chinese)

Chapter 48
High Order Modulation for Underwater Acoustic Communication Based on Chirp-Carrier

Fei Yuan, Wen-Cong Li, Ya-Qiong Cai and En Cheng

Abstract The advantages of Chirp Spread Spectrum make it suitable for the study of underwater acoustic communication. Binary Orthogonal Keying modulation was widely used, though, it has a low transmission rate, while QBOK may cause phase ambiguity. Therefore, the $\pi/4$-DM-DQPSK high order modulation was introduced to solve the problems. In this paper, the basic principles of $\pi/4$-DM-DQPSK communication system was presented,and the system BER performance in AWGN, pool multipath, Bellhop multipath, and ocean multipath was analyzed. It turns out $\pi/4$-DM-DQPSK system has good BER performance in the simulation experiment.

Keywords Chirp spread spectrum · High order · $\Pi/4$-DM-DQPSK · Multipath

48.1 Introduction

Underwater acoustic (UWA) channel is one of the most complex wireless communication channels because of the narrow bandwidth, high ambient noise, extensive multipath, large transmission delay, random fluctuation and Doppler frequency shift, and so on [1].

Chirp Spread Spectrum technology has the general advantages of overcoming the multipath, anti-fading, low interception rate and high secure performance. Better performance on anti-Doppler shift and anti-depth fading are its unique advantages [2]. Chirp Spread Spectrum modulation methods can be divided into two categories, which are Binary Orthogonal Keying (BOK) [3] and Direct Modulation (DM).

BOK was proposed in 1962 by M. Winkler. The Chirp signal has good matched filtering and pulse compression characteristics, which means that the matched filter will output pulse compression if signal matches. So the system has strong

F. Yuan · W.-C. Li · Y.-Q. Cai · E. Cheng (✉)
Key Laboratory of Underwater Acoustic Communication and Marine Information Technology, Ministry of Education, Xiamen University, Xiamen 361005, Fujian, China
e-mail: chengen@xmu.edu.cn

anti-interference ability and low complexity. However, BOK system can only carry 1 bit per symbol, which means it has a low data rate and a low bandwidth utilization ratio. An improved BOK modulation method is called QBOK [4, 5]. The transmitter sends 2 bits a time, mapping the bits with two kinds of frequency modulations and two additional phases. Then the receiver demodulates the data based on the polarity of the matching pulse. Two matched filters are needed for polarity discrimination, which make the whole system more complicated and probably cause phase ambiguity.

This article focuses on discussing the π/4-DM-DQPSK modulation [6, 7]. π/4-DQPSK has better power amplifier performance than DQPSK by reducing frequency hopping [8], and chirp carrier has better anti-frequency selective fading performance than sinusoidal carrier by Spread Spectrum. π/4-DM-DQPSK solves the problems of low data rate and phase ambiguity. It is especially useful for occasions that require high data rate and have no special requirements for system complexity.

48.2 π/4-DM-DQPSK Modulation System

Direct Modulation is able to combine the technologies of Chirp Spread Spectrum and conventional modulation. Instead of using sinusoidal carriers, DM system uses chirp signal as a carrier. Take BPSK as an example. Its DM waveform is shown in Fig. 48.1.

Chirp signal is used to represent the modulated symbol in BOK, while Chirp signal is only used to expand the spectrum of the modulated signal in DM. Since DM system uses one-way Chirp signal, performance degradation caused by non-orthogonal of different Chirp signals will not happen [9]. In order to fix problems like low data rate and phase ambiguity, combining DM with M-ary differential modulation is a feasible way. The following discussion focuses on π/4-DM-DQPSK. The principle block diagram is shown in Fig. 48.2.
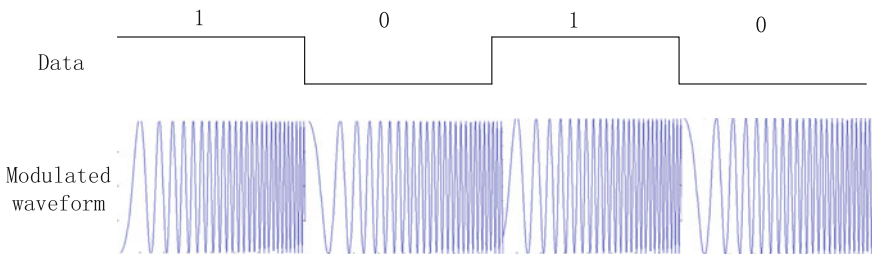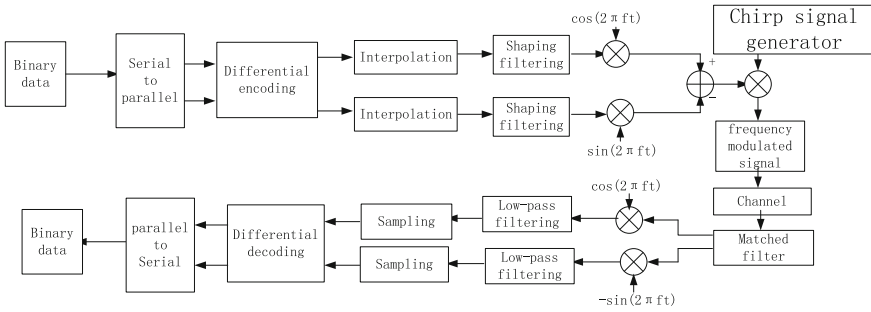

Fig. 48.1 DM-BPSK modulation waveform chart

Fig. 48.2 Principle block diagram of π/4-DM-DQPSK

Suppose the modulated signal is

$$S_k(t) = \cos(wt + \theta_k) = \cos(wt)\cos(\theta_k) - \sin(wt)\sin(\theta_k) \quad (48.1)$$

The phase of the current symbol $\theta_k = \theta_{k-1} + \Delta\theta_k$, where θ_{k-1} is the phase of the previous symbol, $\Delta\theta_k$ is the value of hopping phase of the current symbol. Thus, it can be obtained that

$$\begin{aligned}\cos(\theta_k) &= \cos(\theta_{k-1} + \Delta\theta_k) \\ &= \cos(\theta_{k-1})\cos(\Delta\theta_k) - \sin(\theta_{k-1})\sin(\Delta\theta_k)\end{aligned} \quad (48.2)$$

$$\begin{aligned}\sin(\theta_k) &= \sin(\theta_{k-1} + \Delta\theta_k) \\ &= \sin(\theta_{k-1})\cos(\Delta\theta_k) + \cos(\theta_{k-1})\sin(\Delta\theta_k)\end{aligned} \quad (48.3)$$

Define the two-way output from differential encoding as $I_k = \cos(\theta_k)$ and $Q_k = \sin(\theta_k)$. Table 48.1 illustrates the links between $\Delta\theta_k$ and them. It can be learned that π/4-DQPSK can avoid 180° phase hopping occurred by zero crossing, so that power amplifier performance of the system can be improved.

After π/4-DQPSK modulation, the modulated signal multiplies with LFM, which actualized the chirp Spread Spectrum. The modulated signal accepted all kinds of noise interference, which lead to amplitude distortion. In receiver, by passing through the match filter, signal was compressed into a pulse, and its amplitude was larger than that of the noise. Then the signal was two-way differential demodulated, low-pass filtered, sampled, differential decoded, and parallel to serial conversion,

Table 48.1 The links between the two-way output and phase variable

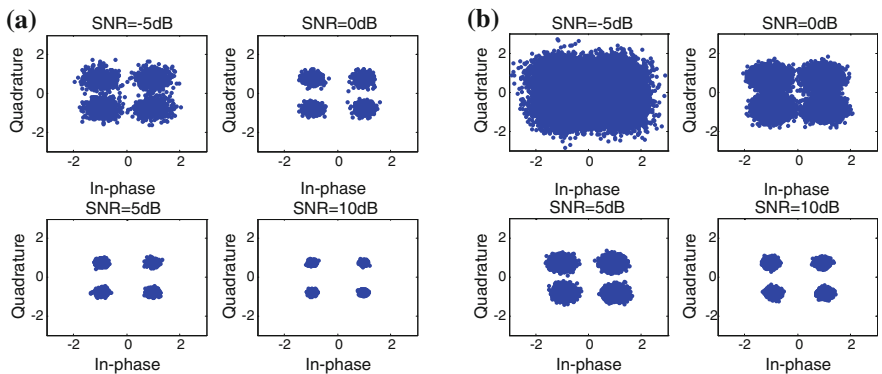| I_k	Q_k	$\Delta\theta_k$
0	0	π/4
0	1	−π/4
1	0	3π/4
1	1	3π/4
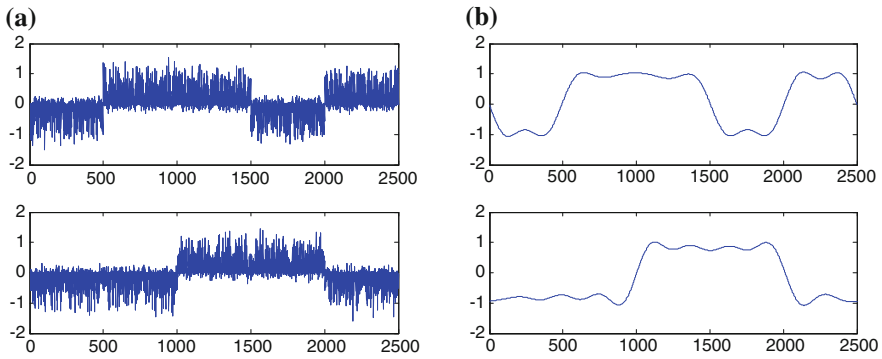
Fig. 48.3 Processing of the two-way signal. **a** After differential demodulation. **b** After low-pass filtering

the restored data was finally obtained. Figure 48.3 shows the two-way output after differential demodulation and low-pass filtering.

48.3 Simulation Analysis

48.3.1 AWGN

Figure 48.4 is a comparison of constellation of the receiver at different SNR. According to the comparison, 4 approximate circles were formed with $-1 + j$, $-1 - j$, $1 + j$, $1 - j$ as the center after adding noise. With SNR increasing, deviated points were less, the circles more concentrate, error smaller, which was consistent with the theory. Adding Bellhop multipath condition (Parameters, see Sect. 48.3.2),

Fig. 48.4 Detection scheme of pipeline leak. **a** AWGN. **b** Bellhop

a more decentralized constellation could be seen in comparison of AWGN in the same SNR, which meant there was more error in Bellhop multipath.

The following analysis focuses on the π/4-DM-DQPSK system BER performance in four kinds of channels, which are AWGN, pool multipath, Bellhop multipath, and ocean multipath, by Matlab simulation. Here are the basic parameters setting of the multipath environments.

48.3.2 Bellhop Experiment

Shallow Bellhop model: The water depth was 80 m, the speed of sound 1500 m/s, the sound source frequency 24 kHz, the number of paths 10, seabed reflection coefficient 0.9, the horizontal distance between the transmitter and the receiver 600 m, receiver depth 25 m, the depth of the sound source 20 m.

48.3.3 Pool Experiment

Pool model: L × W × H was about 22.89 × 5.18 × 1.92 m. It had tile wall, including two area of different depth. The depth of the shallow area was about 1 m, accounting for about 53 %. The depth of the deep area was about 2 m, accounting for about 47 %. In this non-anechoic pool, sound waves were effected by their reflex on the water, the wall and the bottom. So multipath effects were more apparent here than general shallow channel. Figure 48.5 is the scene of the laboratory pool.

48.3.4 Ocean Experiment

Ocean model: the model derived from the measured results of the sea in Xiamen Wuyuan Bay. The selected test sites are located on both ends of the trestle, which

Fig. 48.5 The scene of the laboratory pool

Fig. 48.6 The scene of Xiamen Wuyuan Bay

was shallow, with much clutter, and many coagulation piles under the bridge. The parameters are set as: The water depth was 20 m, the distance between transmitting transducer and the receiving transducer 220 m. The transmitter sent a Chirp signal sweeping from 10 to 20 kHz, lasting for 5 ms (Fig. 48.6).

In Matlab simulation (suppose the system has achieved the synchronization), several binary symbols were randomly generated. SNR was 0 dB, and signal duty cycle 100 %. Figure 48.7 is the waveform and spectrogram of the transmitted signal. After passing AWGN channel, the signals were then sent through shallow Bellhop multipath, pool multipath, and ocean multipath channels. Figure 48.8 illustrates the impulse response models of the four channels and waveform and spectrogram of the received signals. According to the figure, passing different kinds
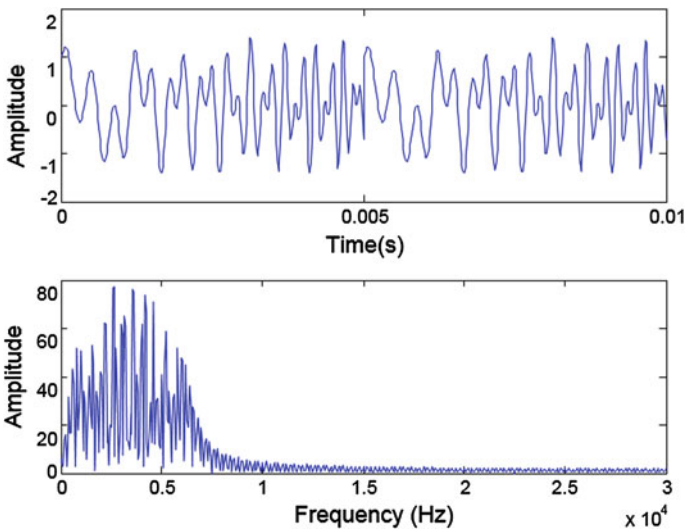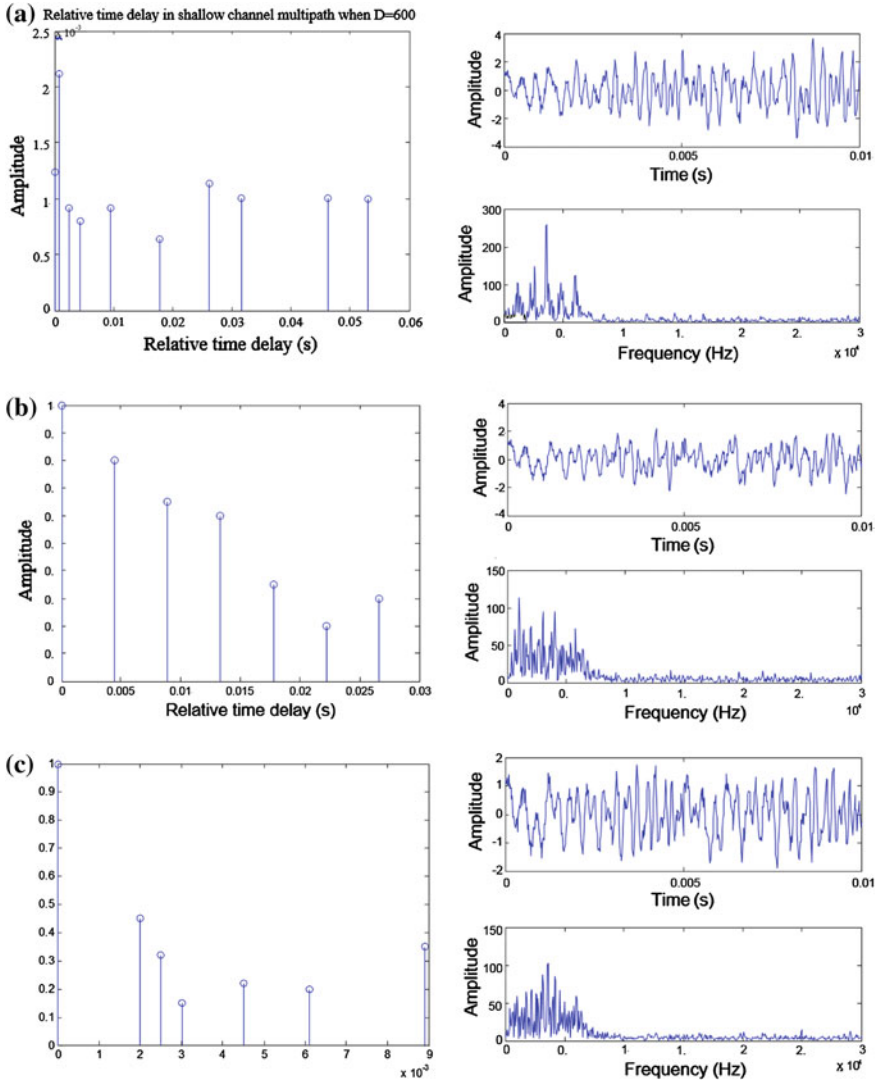

Fig. 48.7 The transmitted signal

Fig. 48.8 Impulse response models and the received signal. **a** Bellhop. **b** Pool. **c** Ocean

of channels, the signal frequency spectrums had different levels of fading. The largest fading happened in pool multipath channel where the multipath was the most intensive. Table 48.2 and Fig. 48.9 show the image transmission (black and white, 96 × 96) results of π/4-DM-DQPSK anti-multipath test. Figure 48.10 illustrates the system BER performance in AWGN, pool multipath, Bellhop multipath, and ocean multipath.

Table 48.2 Results of π/4-DM-DQPSK anti-multipath test

Multipath model	Delay-bandwidth product	Communication rate (bps)	BER (−5 dB)
Bellhop multipath	50	500	7.65×10^{-3}
Pool multipath	50	500	4.02×10^{-3}
Ocean multipath	50	500	2.85×10^{-3}
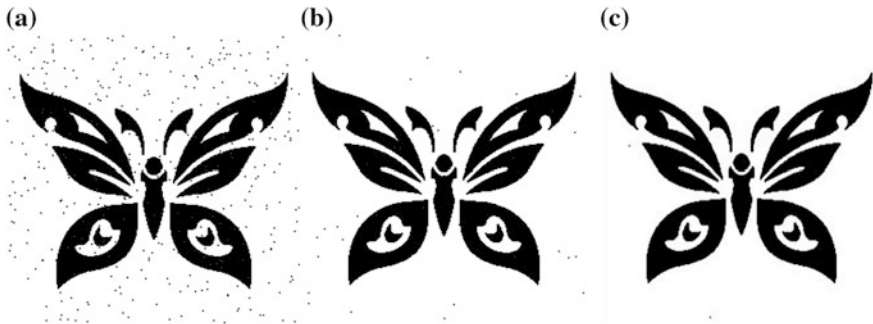
Fig. 48.9 Results of π/4-DM-DQPSK anti-multipath image transmission. **a** Bellhop multipath. **b** Pool multipath. **c** Ocean multipath

Fig. 48.10 BER *curve* of the system in four environments
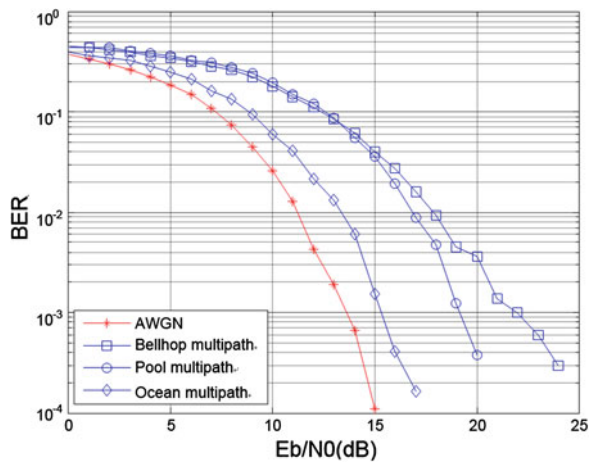
Gaussian white noise would not lead to fading, so the BER performance of π/4-DM-DQPSK was close to that of π/4-DQPSK. According to the BER curve, the BER performance of the system in multipath channel environment would decline. The shallow Bellhop multipath and pool multipath had great influence on the system, while ocean multipath had a little one.

48.4 Conclusion

π/4-DM-DQPSK modulation communication scheme is introduced in this paper, fixing the slow transmission rate and phase ambiguity in BOK system. The π/4-DM-DQPSK system has considerable advantages on power amplifier performance and anti-frequency selective fading performance. The simulation part analyzed the system BER performance in several common multipath environments. In conclusion, π/4-DM-DQPSK communication system still has good BER performance and anti-frequency selective fading performance. However, *M*-ary differential modulation brings high requirement of system complexity. On occasions that have no special requirements for system complexity, it is dependable.

References

1. Chen Y, Xu X, Zhang L, Lin M (2013) Effects of different shallow water acoustic channel models on error-correction code performance analysis. Acta Armamentarii 34(11):1404–1411 (in Chinese)
2. Zhao M, Wu W (2009) Analysis of linear frequency modulated signal. Aero Weapon (1):25–29 (in Chinese)
3. He P, Lu Y, Zhang H, Wang Y (2006) Study of ultra-wideband wireless communication system based on chirp-BOK modulation. J Nanjing Univ Posts Telecommun 26(2):21–25 (in Chinese)
4. Liu H, Sun J (2009) A modulation method for chirp ultra-wideband communication systems. Chinese Patent, Accepted on 3 July, 2009, Application number: 200810045456.4. Doctoral dissertation, University of Electronic Science and Technology, Chengdu, pp 1–93
5. Wang M, Liu H (2009) Design and FPGA implementation for a chirp UWB system based on QBOK modulation. China Integr Circ 18(7):34–39 (in Chinese)
6. Chandra A, Bose C (2012) Series solutions for pi/4-DQPSK BER with MRC. Int J Electron 99 (3):391–416
7. Meng Z, Sun H, Dong L (2009) Characteristic analysis and simulation of LFM signal. Ship Electron Eng 29(8):114–117 (in Chinese)
8. Fu F, Xue R, Zhao D-F, Zhou X-C (2013) LDPC Coded DQPSK modulation with iterative detection method for underwater acoustic communications. J Harbin Inst Technol 20(5):25–30
9. Meng F (2011) Research on chirp spread spectrum techniques in low-rate wireless personal area network. Doctoral dissertation, Harbin Institute of Technology (in Chinese)

Chapter 49
Switching Control of PWM Rectifier Based on Interconnection and Damping Assignment

Yu Gu and Haisheng Yu

Abstract To solve the limitation of single controller, the switching Hamiltonian system of Three-phase PWM Rectifier is studied in this paper. First, controller of PWM rectifier is designed by using interconnection and damping assignment (IDA-PBC) method. It has been shown that a single IDA-PBC controller cannot coordinate the contradiction between the speed of response and the overshoot of output. When the value of damper injection is small, the system starts slow. While the value of damper injection is too big, the system has output voltage overshoot. Then, two different damping matrices are assigned and a tracking-error-driven switching law is proposed to improve the dynamic and static characteristics of the rectifier. The simulation results show that the proposed switching control can overcome the limitation of a single controller based on IDA-PBC and have better performance.

49.1 Introduction

With the development of power electronic converter technology, the PWM rectifier is widely used in the power and electronics system. For it has many advanced features such as input current sinusoidal, energy bidirectional flow, and unity power factor. The port-controlled Hamiltonian (PCH) control method [1] is applied and achieved certain results [2]. In recent years, switched hybrid Hamiltonian system [3] increasingly attracts people's attention. Switching system is a special kind of hybrid system between discrete system and continuous system. Subsystem and switching law are the two important parts of switching control. In order to overcome the

Y. Gu · H. Yu (✉)
College of Automation Engineering, Qingdao University,
No. 308, NingXia Road, Qingdao 266071, People's Republic of China
e-mail: yu.hs@163.com

limitation of single controller, a plurality of controllers are switched that the advantages of each controller are combined to achieve the required system performance.

The PCH model of three-phase voltage-type PWM rectifier is established in this paper. Then the switching control method is presented that the basic idea of switching control is to assign two different damping matrices by using IDA-PBC, and make the closed-loop systems with different IDA-PBC controllers have the same Hamiltonian function to ensure stability under arbitrary switching law. At last, the switching law based on error prediction is proposed.

49.2 The PCH Model of PWM Rectifier

The PCH model of system considering the energy dissipation is [4]

$$\begin{cases} \dot{x} = [J(x) - R(x)]\frac{\partial H}{\partial x}(x) + g(x)u \\ y = g^{\mathrm{T}}(x)\frac{\partial H}{\partial x}(x) \end{cases} \tag{49.1}$$

where $x \in R^{\mathrm{n}}$, $y \in R^{\mathrm{m}}$, $J(x) = -J^{\mathrm{T}}(x)$, $J(x)$ reflects the internal interconnection. $R(x) = R^{\mathrm{T}}(x) \geq 0$, $R(x)$ reflects the additional resistive structures in port. $H(x)$ is Hamiltonian function. $g(x)$ is port input matrix, u is input voltage.

49.2.1 The Switching PCH Model of Rectifier

The switching PCH model of rectifier considering the energy dissipation is [5]

$$\begin{cases} \dot{x} = \left[J_{\lambda(t)}(x) - R_{\lambda(t)}(x)\right]\frac{\partial H_{\lambda(t)}}{\partial x}(x) + g(x)u \\ y = g^{\mathrm{T}}(x)\frac{\partial H_{\lambda(t)}}{\partial x}(x) \end{cases} \tag{49.2}$$

where $\lambda(t) : R^{+} \to \Lambda := \{1, 2, \ldots, N\}$ is switching law or switching path and $\lambda(t) = i(i \in \Lambda)$ show that the ist subsystem is working.

49.2.2 The Power PCH Model of Rectifier

The power circuit of three-phase voltage source PWM rectifier is shown in Fig. 49.1.

Assumed that the input is a balanced three-phase supply that $e_{\mathrm{a}} = U_{\mathrm{m}}\cos(\omega t)$. $VT_1 - VT_6$ are ideal IGBT. r and L are resistance and inductance of AC side. C is the DC side capacitance. R_L is the DC side load.

Fig. 49.1 Power circuit of three-phase voltage source PWM rectifier
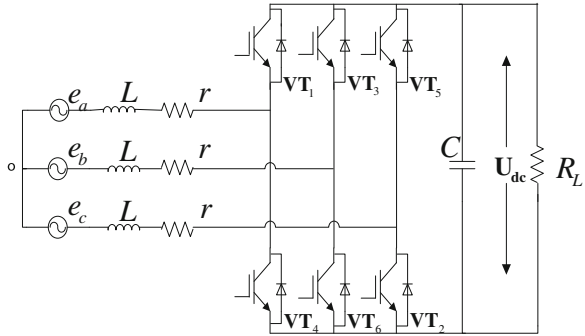
The power model of PWM rectifier in qd coordinate is given as follows [6]:

$$\begin{cases} L\dfrac{\mathrm{d}p}{\mathrm{d}t} = -rp + \omega Lq - \mu_{\mathrm{d}}e_{\mathrm{d}}u_{\mathrm{dc}} + e_{\mathrm{d}}^2 \\ L\dfrac{\mathrm{d}q}{\mathrm{d}t} = -rq - \omega Lp - \mu_{\mathrm{q}}e_{\mathrm{d}}u_{\mathrm{dc}} \\ Ce_{\mathrm{d}}\dfrac{\mathrm{d}u_{\mathrm{dc}}}{\mathrm{d}t} = \mu_{\mathrm{d}}p + \mu_{\mathrm{q}}q - e_{\mathrm{d}}\dfrac{u_{\mathrm{dc}}}{R_L} \end{cases} \tag{49.3}$$

where μ_{d}, μ_{q} is duty cycle function of rectifier in synchronous rotating qd coordinate [7], p and q are active power and reactive power of rectifier, respectively, $\boldsymbol{u} = [\,e_{\mathrm{d}} \quad e_q\,]^{\mathrm{T}} = [\,\sqrt{(3/2)}U_{\mathrm{m}} \quad 0\,]^{\mathrm{T}}$.

The state variables are shown as follows:

$$\boldsymbol{x} = [\,x_1 \quad x_2 \quad x_3\,]^{\mathrm{T}} = [\,p \quad q \quad e_{\mathrm{d}}u_{\mathrm{dc}}\,]^{\mathrm{T}} \tag{49.4}$$

The storage Hamiltonian function is given as follows:

$$\boldsymbol{H}(\boldsymbol{x}) = \frac{1}{2}\boldsymbol{x}^{\mathrm{T}}\boldsymbol{D}^{-1}\boldsymbol{x} = \frac{1}{2}\left(\mathrm{L}i_{\mathrm{d}}^2 + \mathrm{L}i_q^2 + \mathrm{C}u_{\mathrm{dc}}^2\right) \tag{49.5}$$

where $\boldsymbol{D} = e_{\mathrm{d}}^2\,\mathrm{diag}\{\,1/L \quad 1/L \quad 1/C\,\}$, (49.3) is transformed the format of (49.1), the power PCH model is established.

Where

$$\boldsymbol{J}(\boldsymbol{x}) = \begin{bmatrix} 0 & \dfrac{\omega e_{\mathrm{d}}^2}{L} & \dfrac{-\mu_{\mathrm{d}}e_{\mathrm{d}}^2}{LC} \\ \dfrac{-\omega\mu_{\mathrm{d}}^2}{L} & 0 & \dfrac{-\mu_{\mathrm{q}}e_{\mathrm{d}}^2}{LC} \\ \dfrac{\mu_{\mathrm{d}}e_{\mathrm{d}}^2}{LC} & \dfrac{\mu_{\mathrm{q}}e_{\mathrm{d}}^2}{LC} & 0 \end{bmatrix} \quad \boldsymbol{R}(\boldsymbol{x}) = \begin{bmatrix} \dfrac{e_{\mathrm{d}}^2}{L^2}r & 0 & 0 \\ 0 & \dfrac{e_{\mathrm{d}}^2}{L^2}r & 0 \\ 0 & 0 & \dfrac{e_{\mathrm{d}}^2}{C^2}\dfrac{1}{R_L} \end{bmatrix} \quad \boldsymbol{g}(\boldsymbol{x}) = \begin{bmatrix} \dfrac{e_{\mathrm{d}}}{L} & 0 \\ 0 & \dfrac{e_{\mathrm{d}}}{L} \\ 0 & 0 \end{bmatrix}$$

$$\tag{49.6}$$

49.3 The Switching Control System Design

49.3.1 The PCH Controller of PWM Rectifier

There are two control objectives for the controller of PWM rectifier. One is to make the output voltage of DC side reaches the desired value and keep constant, that $u_{dc} = V_{dc}$, V_{dc} is desired output voltage value. Another is let the power factor of rectifier stay one when the system reaches the steady state, that $p = p_0$, $q = q_0 = 0$, p_0 and q_0 are active power and reactive power when the system reaches the steady state, respectively.

According to the power conservation of grid and DC side, the active power of steady state is

$$p_0 = \frac{e_d}{2} \left[\frac{e_d}{r} - \sqrt{\frac{e_d^2}{r^2} - \frac{4V_{dc}^2}{rR_L}} \right] \tag{49.7}$$

According to PCH control principle [8], the controller $\boldsymbol{\mu} = \begin{bmatrix} \mu_d & \mu_q \end{bmatrix}^T$ is

$$\begin{cases} \mu_d = \frac{1}{e_d^2 V_{dc}} [e_d^3 - rp_0 e_d - L^2 Cj_a V_{dc} q] \\ \mu_q = \frac{1}{e_d^3 V_{dc}} [-\omega Lp_0 e_d^2 + j_a L^2 Ce_d V_{dc}(p - p_0) + r_{a2} e_d^2 q - j_a p_0 L^2 Ce_d(u_{dc} - V_{dc})] \end{cases} \tag{49.8}$$

where j_a is interconnection parameter, r_{a2} is damping parameter.

49.3.2 The Switching Law

In this paper, the switching law based on error prediction is adopted [9].

The switching law based on error prediction is as follows:

$$\lambda(t) = R(x, t, e, \dot{e}, T) = \begin{cases} R_{d1}(x), & e(e + \dot{e}T) \geq 0 \\ R_{d2}(x), & e(e + \dot{e}T) < 0 \end{cases} \tag{49.9}$$

where $R_{d1}(x)$ is big damper matrix, $R_{d2}(x)$ is small damper matrix. e is the tracking error, T is an adjustable time parameter.

The basic principle of switching law is shown in Fig. 49.2 [10]. ① represents the error curve changes with time t. ② represents the tangent of error curve at t_0. Assumed the error is e_0 at t_0, according to the current error change rate estimates the error after T moment, and then judge e_0 and $e_0 + \dot{e}_0 T$ whether the same sign. If they are same sign, indicates that the error not reach zero, which the output not reach the

Fig. 49.2 The switching law
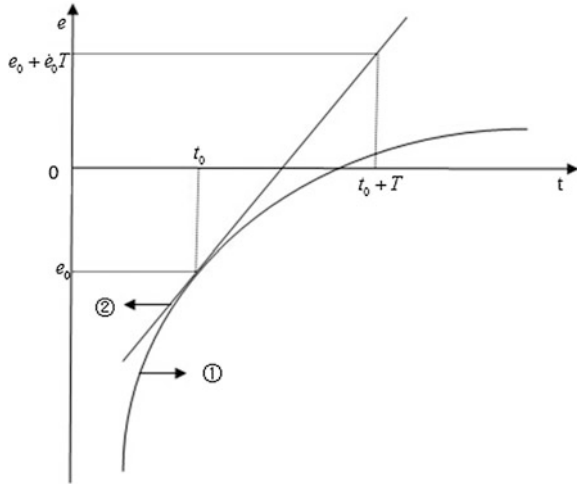
expected value. At this time the system controlled by the big damper controller, so that the system has fast response. And once when the sign of $e_0(e_0 + \dot{e}_0 T)$ changes, then the system switch to the small damper controller ensure the steady state characteristics.

49.3.3 The Switching Control System

According to (49.8), only need to change r_{a2} can change the damper matrix of system, so the controller used in switching control is given as follows:

$$\begin{cases} \mu_d = \frac{1}{e_d^2 V_{dc}} [e_d^3 - rp_0 e_d - L^2 C j_a V_{dc} q] \\ \mu_q = \frac{1}{e_d^3 V_{dc}} [-\omega L p_0 e_d^2 + j_a L^2 C e_d V_{dc}(p - p_0) + r(e, \dot{e}) e_d^2 q - j_a p_0 L^2 C e_d(u_{dc} - V_{dc})] \end{cases}$$
(49.10)

where

$$r(e, \dot{e}) = \begin{cases} r_1, & e(e + \dot{e}T) \geq 0 \\ r_2, & e(e + \dot{e}T) < 0 \end{cases}, \quad e = u_{dc} - V_{dc}$$

Set r_1 to a big damper value and r_2 to a small damper one.

According to the switching law, when $e(e + \dot{e}T) \geq 0$, indicated that the output does not reach the set value and the big damper controller works. Once $e(e + \dot{e}T) < 0$, indicated that the output reach desired value and system switch to

the small damper controller. When the load becomes small, the output voltage reduced that less than set value, the system switch the controller to get a fast response and then the small damper controller is switched to ensure the static performance. Thus, when the switched condition is reached, the system switches the controllers between big damper one and small one to ensure that the system has good performance.

49.4 Simulation Results

Parameters of the simulation system: the peak of the AC voltage $U_m = 80$ V, the inductance of AC side $L = 15$ mH, the resistance $r = 1\,\Omega$, the capacitance of DC side $C = 2200\,\mu$F, load $R_L = 80\,\Omega$, the expected value of the output voltage $V_{dc} = 200$ V.

Simulation results are shown in Figs. 49.3, 49.4 and 49.5. The response curve of different injected damper is shown in Fig. 49.3. The results in Fig. 49.4 show that the curve of DC output voltage when the load resistance changes at 0.15 s ($R_L = 80\,\Omega \rightarrow 40\,\Omega$). Seen from Fig. 49.4, changes of u_{dc} is very small and it fastly go into stable state under load disturbance when the switching control exists. The dynamic performances are better than single IDA-PBC controller works. The Fig. 49.5 shows that the power factor is equal to 1 when system to reach the stable state. Figure 49.5 shows that the voltage and current of AC side when the load resistance changes at 0.15 s ($R_L = 80\,\Omega \rightarrow 40\,\Omega$). The voltage and current of grid side are same phase when the system reaches the stable state.
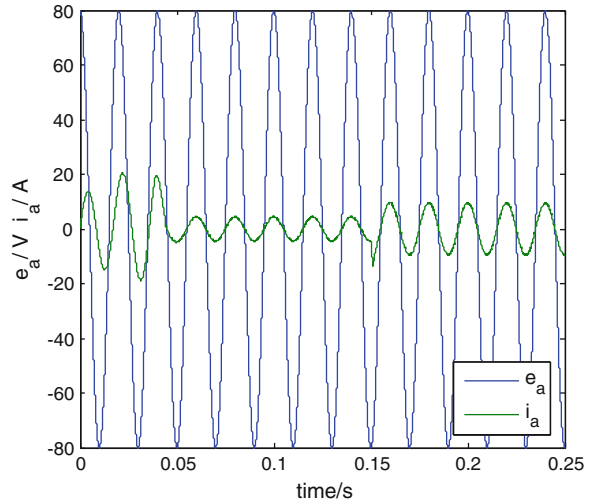
Fig. 49.3 Curves of output voltage of different damper
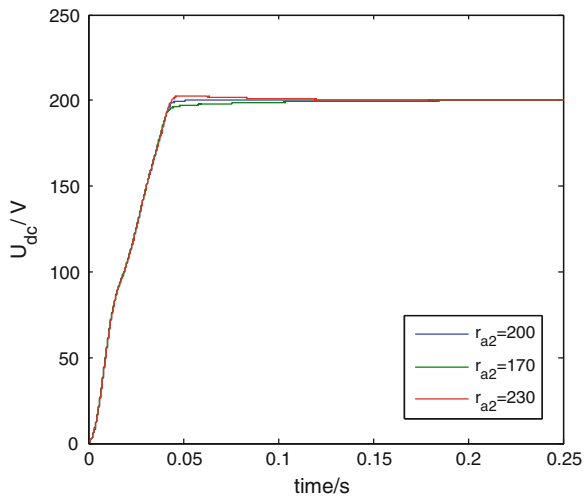
Fig. 49.4 Curves of the output voltage controlled by two methods
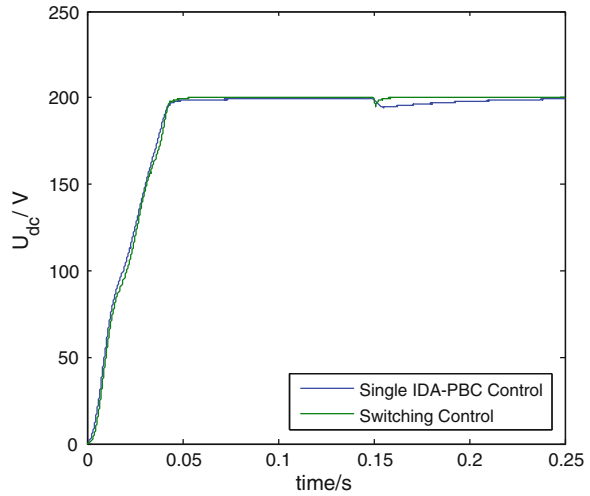
Fig. 49.5 Curves of voltage and current of grid when load change

49.5 Conclusions

The switching control method based on interconnection and damping assignment of the three-phase PWM rectifier is studied in this paper. The switching law based on error prediction is proposed to realize the switching control of PWM rectifier. Compared with single controllers, switching control has more static and dynamic performances. The simulation results also show that the method has good controllability.

References

1. Donaire A, Junco S (2009) On the addition of integral action to Port-controlled Hamiltonian systems. Automatica 45(8):1910–1916
2. Yu HS, Yu JP (2012) Output voltage control of boost converter based on port-hamiltonian systems theory. ICIC Express Lett 3(4):793–798
3. Wassim M, Sergey G (2002) Energy-based control for hybrid port-controlled hamiltonian system. In: proceedings of the 41st IEEE conference on decision and control, vol 42, issue no 12, pp 1669–1674
4. Ortega R (2002) Interconnection and damping assignment passivity-based control of port-controlled Hamiltonian systems. Automatica 38(4):585–596
5. Xu S, Guo YQ (2013) Switching control of permanent magnet synchronous motor based on interconnection damping assignment. In: Proceedings of the 32nd Chinese control conference, vol 26, issue no 1, pp 1336–1341
6. Yu HS, Teng ZB (2012) Energy-Shaping and Passivity-based Control of Three-Phase PWM Rectifiers. In: Proceedings of the 10th world congress on intelligent control and automation, vol 32, issue no 2, pp 2844–2848
7. Zhu L, Wang YZ (2006) Study on the stability of switched dissipative Hamiltonian systems. Inf Sci 49(5):578–591
8. Yu HS, Yu JP (2013) Nonlinear control of induction motors based on state error PCH and energy-shaping principle. Nonlinear Dyn 72(1–2):49–59
9. Soh YC (2003) Switched controllers and their applications in bilinear system. Automatica 39(32):517–524
10. Xu X, Antsaklis PJ (2004) Optimal control of switched systems based on parameterization of the switching instants. IEEE Trans Autom Control 49(1):2–16

Chapter 50
Ultrasonic-Assisted Extraction of Puerarin Optimized by Response Surface Methodology

Xin Zheng, Juan Chen, Xiaolong Jiang and Qing Guo

Abstract Extraction of puerarin by ultrasound, optimization requires to determine the technological parameters. In this paper, ultrasonic parameter is one of the technological parameters. The ethanol volume ratio, the intensity of cavitation ultrasonic power, and liquid–solid ratio were optimized by response surface methodology. Modeling the optimization of technological parameters by Design-expert software, thereby obtaining the global optimal parameters, three independent variables were the ethanol volume ratio (*A*: 68 %), the liquid–solid ratio (*B*: 53:1), and the intensity of cavitation power ultrasonic (5:1). Under these conditions, extraction rate of puerarin was 7.09 %. The result shows that taking ultrasonic parameters as optimized parameters, and optimizing ultrasonic-assisted extraction of puerarin by response surface methodology could get better performance.

Keywords Puerarin · Ultrasonic extraction · Response surface methodology · Technological parameters

50.1 Introduction

Radix puerariae has the active ingredients of daidzein, puerarin, etc., in which puerarin is the main component [1]. Traditional extraction methods have certain drawbacks, however, ultrasonic-assisted extraction is an efficient physical process, which has the advantage of no pollution and low energy consumption, and is suitable for the extraction of thermal sensitive material. Therefore, it has been applied in hundreds of Chinese medicine extractions such as extracting ginseng saponins, cocos nucifera, carvone, limonene, etc. [2]. Furthermore, ultrasound could sterilize, in the mean time, could avoid deterioration of extractant [3].

X. Zheng · J. Chen (✉) · X. Jiang · Q. Guo
Beijing University of Chemical Technology,
15 Beisanhuan East Road, Beijing 100029, China
e-mail: Jchen@mail.buct.edu.cn

Traditional orthogonal design methods could obtain relatively convincing result by fewer experiments. However, through response surface methodology, the extraction rate is higher. On the one hand, response surface methodology is a statistical method that could solve multivariable problems. On the other hand, it is a highly efficient methodology that is applicable to solve nonsmooth and nonlinear objective functions as well as constraint function [4]. It could undertake a comprehensive study on the selected parameters with fewer experiments in a relatively short period by seeking the best technological parameters [5].

Currently both in China and abroad, the response surface methodology had been applied in optimizing mechanical design [6]. This application could be optimized to extract botanical drug. The polysaccharides, crude polysaccharides, and pectin have been successfully extracted [7]. This article aimed at optimizing technological parameters that are used in extraction of puerarin from radix puerariae through response surface methodology Box–Behnken.

50.2 Materials and Technological Optimizing Method

Experimental materials and reagent: Radix puerariae is purchased from National Institute for the Control of Pharmaceutical and Biological. The entire reagents are analytically pure; the water was deionized water.

Equipment: double-frequency composite transducer system, which is composed of probe immersion and external slot extraction plant. UV-2102PC UV-VIS spectrophotometer: Dominique (Shanghai) Instrument Co., Ltd. Analytical balance Sartorius BP211-D: Sartorius Stedim Biotech GmbH. NV-1800 broken ultrasonic device (27 kHz, 1800 W): Nicle Ultrasonic Co. Ltd. QHW-1 power ultrasonic equipment (57 kHz, 800 W): Beijing University of Chemical Technology Plant Chemical Physics Research Institute [8]. SHB-III water circulated type multiuse vacuum pump: Zhengzhou Changcheng Co., Ltd.

50.2.1 Experimental: Ultrasonic Extracting Technological Process

The radix puerariae was dried to constant weight, stored in a dry condition. In each experiment the puerariae was accurately weighed using an analytical balance, and then a certain proportion of ethanol was added at a certain liquid–solid ratio. After a certain period, the concentration of puerarin was measured by spectrophotometry.

In this experiment, ethanol was used as extractant. Factors such as ethanol volume ratio, liquid–solid ratio, and intensity of ultrasonic power were taken into the single-factor test, in order to obtain the extraction rate.

Table 50.1 The factors and levels that affect extraction rate

Analytical factors	Coded	Levels		
	Symbols	−1	0	1
The ethanol volume ratio	A	50 %	60 %	70 %
The liquid–solid ratio	B	40	50	60
The intensity of ultrasonic power	C	80 %	83.30 %	85.70 %

Based on Box–Benkhen experimental design and the result of single-factor test, a three-level-three-factor BBD experiment was designed and analyzed by Design-expert software. The influence factors and levels were shown in Table 50.1.

50.2.2 Analysis and Determination

50.2.2.1 Preparation of Standard Curve

In the experiment, 5.4 mg dried puerariae was diluted with 95 % ethanol to 25 mL, and 216 mg/L control sample solvent was obtained. Puerarin standard has an obvious maximum absorbance at 250 nm UV light. 0.1, 0.2. 0.4, 0.6, 0.8, 1.0 ml of control samples were precisely weighed separately and diluted with 95 % ethanol to 10 ml. Absorbance was measured at 250 nm UV light. The following standard curve and regression equation were obtained, in which X-axis represents the concentration of the sample, meanwhile Y-axis represent absorbance. Related coefficient $r = 0.9998$, linear range 2.16–21.6 mg/L.

$$L = 0.0901c - 0.0025 \tag{50.1}$$

50.2.2.2 Determination of Puerarin Content

Total concentration C (mg/L) was obtained, according to formula (50.1) and the UV absorbance data. The final experimental data extraction rate $\eta(\%)$ was obtained based on the weight of material m(g) and total extractant volume v(L).
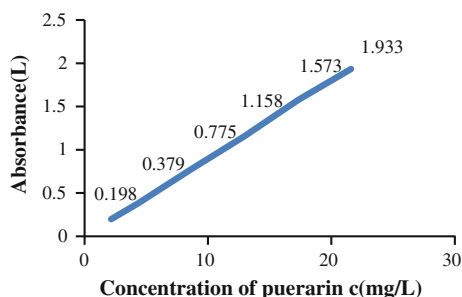
$$\eta(\%) = \left(c \times v / m \right) \times 100 \% \tag{50.2}$$

50.3 Results and Discussion

50.3.1 The Result of Single-Factor Test

Puerarin was extracted by dual frequency, in which conditions are the broken-down wall frequency $f_1 = 20$ kHz, intensity $I_1 = 895.7$ W/cm^2; ultrasonic cavitation

**Fig. 50.1** The standard curve
of the puerarin

frequency $f_2 = 28$ kHz, intensity $I_2 = 10.19$ W/cm^2. Excluded the time-invariant and ultrasonic frequency-invariant factors, single static factors were taken into consideration. Ethanol volume ratio, liquid–solid ratio, and intensity of ultrasonic power were taken as the optimizing conditions. Experiment as followed (Figs. 50.1 and 50.2).

Effect of ethanol volume ratio on extraction yield. Ultrasonic parameter conditions have remained, puerarin was extracted by different ethanol volume ratio (volume ratio is from 50 to 90 %). Figure 50.3 shows that the maximum absorbance was obtained when the volume ratio of ethanol is 70 %. According to formula (50.2), the maximal extraction rate is 0.812.

Effect of liquid–solid ratio on extraction yield. As shown in Fig. 50.2, absorbance declined with liquid–solid ratio increased (from 20:1 to 60:1). According to the relationship between absorbance and extraction rate, maximum extraction rate 0.553 was shown at 50:1 absorbance.
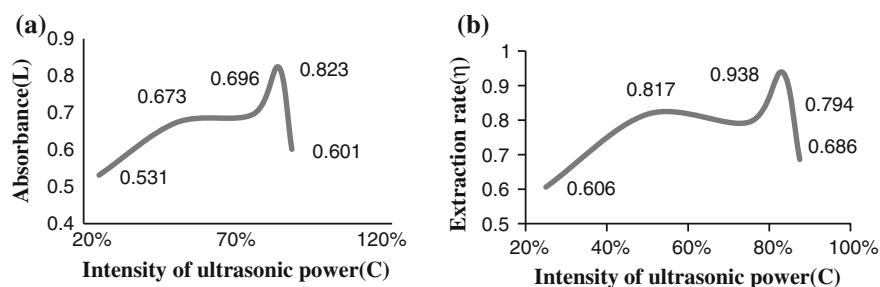
Effect of intensity of ultrasonic power on extraction yield. As shown in Fig. 50.4, the absorbance had maximum value 0.938 when the intensity of ultrasonic power is 5 s : 1 s.
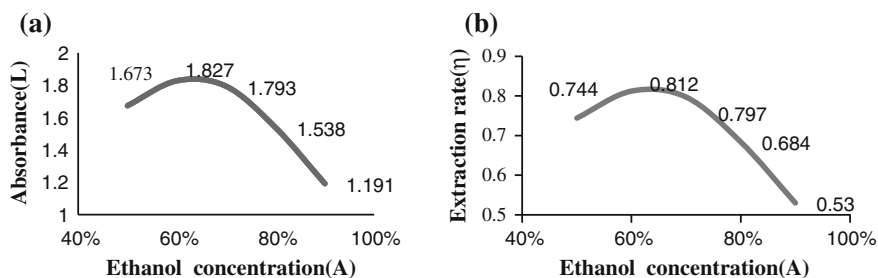
Fig. 50.2 The effect of the ethanol volume ratio on the absorbance and extraction rate. **a** Absorbance, **b** extraction rate
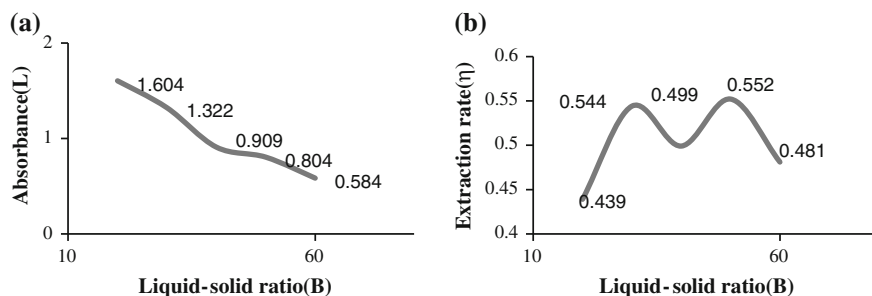
Fig. 50.3 The effect of the liquid–solid ratio on the absorbance and extraction rate. **a** Absorbance, **b** Extraction rate

Fig. 50.4 The effect of intensity of ultrasonic power on the absorbance and extraction rate. **a** Absorbance, **b** Extraction rate

50.3.2 Box–Behnken Experiment Design and Result

In order to design three-factor-three-level experiment based on single-factor test, the ethanol volume ratio, liquid–solid ratio, and intensity of ultrasonic power were chosen as the factors in orthogonal design. The result was shown in Table 50.1.

According to orthogonal table $L_9(3^4)$, different experiments had been designed, then different puerarin concentration had been obtained based on formula (50.1). The results were shown in Table 50.2. Each factor has different influence on extraction of puerarin. The best technological parameters are $A_3 \ B_1 \ C_1$, that is, liquid–solid ratio 40:1, ethanol volume ratio 70 %, intensity ultrasonic power 4:1. Under these conditions, the extraction rate is 7.02 %.

Orthogonal design was not able to predict the best parameters globally. Compared with orthogonal design, response surface methodology Box–Behnken could comprehensively studied the selected parameters by the most cost-effective way, which required a short period of time and fewer experiments. Based on the results of single-factor test, took ethanol volume ratio, liquid–solid ratio, and intensity of ultrasonic power as the factors as well. Experiment design was shown in

Table 50.2 Design and result of the orthogonal experiment

No	A	B	C	Extraction rate (%)
1	−1	−1	−1	6.29
2	−1	0	0	5.68
3	1	1	1	5.53
4	1	0	1	6.15
5	0	0	1	5.81
6	0	1	-1	6.83
7	1	−1	1	6.64
8	1	0	−1	5.97
9	1	1	0	6.25
K_1	17.5	19.08	19.09	
K_2	18.79	17.46	18.08	
K_3	18.86	18.61	17.98	
R	1.36	1.62	1.11	
The best level	A_3	B_1	C_1	

Table 50.3 Design and result of Box–Behnken

No	A	B	C	Extraction rate (%)
1	0	0	0	6.03
2	0	1	−1	6.18
3	0	0	0	6.01
4	1	−1	0	6.87
5	1	1	0	6.27
6	0	−1	−1	6.58
7	−1	−1	0	5.81
8	0	−1	1	6.33
9	1	0	1	6.24
10	−1	0	−1	5.61
11	−1	0	1	5.84
12	0	0	0	5.98
13	−1	1	0	5.92
14	1	0	−1	6.45
15	0	1	1	6.22

Table 50.1. In Table 50.3, similar to the former experiment, the three independent variables are ethanol volume ratio (A), liquid–solid ratio (B), and intensity of ultrasonic power (C).

50.3.2.1 Analysis of Response Surface

For further investigating the best technological rage, predicting the best conditions of three factors, intuitively observing the changes for extraction rate under two interacted factors, the planar projection of response surface could reflect it. On the basis of regression equation, the response surfaces figure and contour plot can analyze the influence of the three factors on extraction rate. One single factor was fixed, the others' influence on extraction rate were obtained. The response surface plots were shown as Figs. 50.5, 50.6, and 50.7. In Figs. 50.5a, 50.6a, and 50.7a, the more response surface curves, the more obvious the interaction are; in Figs. 50.5b, 50.6b, and 50.7b, the more contour plots lines curve, the more they looked like oval, the more obvious interaction are. The round shapes are exact contrary.

As shown in Figs. 50.5, 50.6, 50.7 and Table 50.4, the obvious influence order (gradually reduced) of single factors are ethanol volume ratio, liquid–solid ratio, intensity of ultrasonic power. The interaction order (gradually reduced) is ethanol volume ratio and liquid–solid ratio, intensity of ultrasonic power and liquid–solid ratio, ethanol volume ratio, and intensity of ultrasonic power. Comparatively
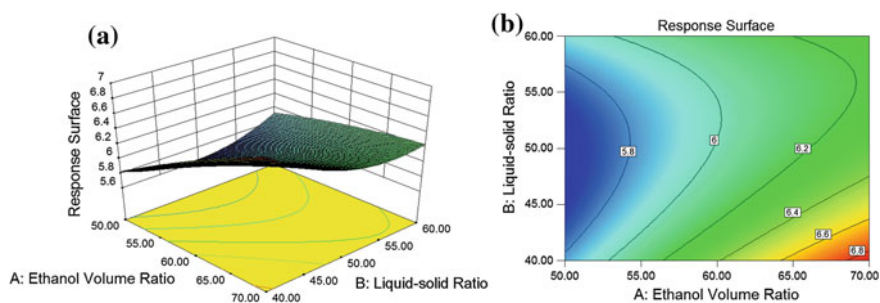
Fig. 50.5 Ethanol volume ratio and liquid–solid ratio on extraction rate. **a** Response surface, **b** Plane projection $Y = f(A, B)$
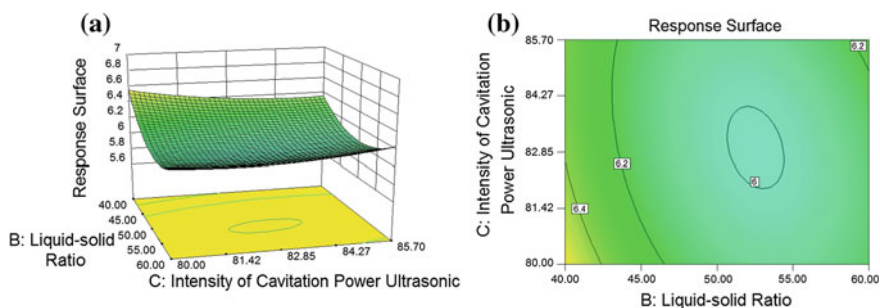
Fig. 50.6 Liquid–solid ratio and intensity of ultrasonic power on extraction rate. **a** Response surface, **b** plane projection $Y = f(B, C)$
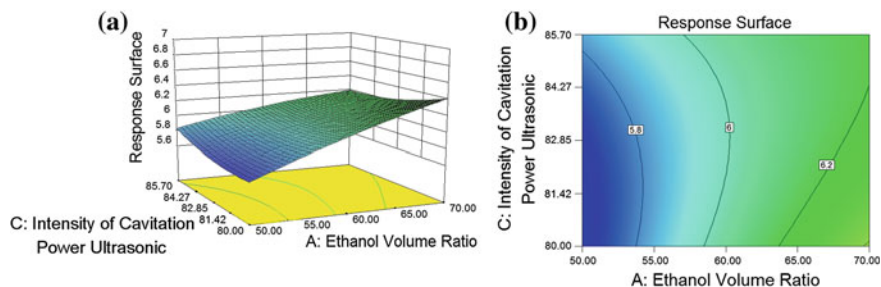
Fig. 50.7 Ethanol volume ratio and intensity of ultrasonic power on extraction rate. **a** Response surface, **b** Plane projection $Y = f(A, C)$

Table 50.4 Analysis of variance

Source	Sum of squares	df	Mean square	F value	P value	Significance
Model	1.46	9	0.16	53.83	0.0002	**
A	0.090	1	0.090	29.75	0.0028	**
B	0.055	1	0.055	18.25	0.0079	**
C	0.014	1	0.014	4.49	0.0875	
AB	0.13	1	0.13	41.89	0.0013	**
BC	0.021	1	0.021	6.98	0.0459	*
AC	0.045	1	0.045	14.91	0.0118	
A^2	0.006	1	0.006	2.05	0.2120	
B^2	0.23	1	0.23	77.74	0.0003	**
C^2	0.016	1	0.016	5.19	0.0717	
Residual error	0.015	5	0.003			
Lack of fit	0.014	3	0.004	7.25	0.12	Not
Pure error	0.001	2	0.006			
Cor total	1.47	14				
Regression coefficient of decision 0.9898						
Adjusted determination coefficient		0.9714				

Note ** Extremely significance level ($P < 0.01$); * significance level ($P < 0.05$)

speaking, the intensity of ultrasonic power has remained 82.85 % (4.8 s :1 s), the interaction between ethanol volume ratio and liquid–solid ratio's had the most obvious influence on extraction rate. So did the liquid–solid rate was 5:1 and the ethanol volume ratio was 60 %.

50.3.2.2 Determine the Optimal Value and Regression Model Validation Test

Based on the extraction conditions of response surface methodology, as shown in Tables 50.3 and 50.4. The best result was obtained, when solved the partial derivatives of three factors separately, in the meantime, the regression equation equaled zero. The results were $A = 0.8246$, $B = 0.3419$, $C = 0.9599$.

The results could be converted to the best technological parameters: the ethanol volume ratio was 68 %, the liquid–solid ratio was 53:1, and the intensity of ultrasonic power was 5:1. In such circumstances, the extraction rate of puerarin was experimentally tested and the average puerarin extraction rate was 7.09 %, approaching the prediction of Design-expert software 7.13 %. The relative error was less than 0.9 %, meaning that the actual application is suitable for response surface. Compared with orthogonal design, which had the result of ethanol volume ratio: 70 %, liquid–solid ratio: 40:1, and intensity of ultrasonic power: 4:1, extraction rate: 7.02 %. It is obviously that response surface methodology has better extraction rate.

50.4 Conclusions

The best optimizing parameters of puerarin extraction had been confirmed by ultrasonic-assisted based on response surface methodology and single-factor test. Taking ultrasonic factors as technological parameters were proposed, the influence of intensity of ultrasonic power on extraction rate had been researched. The regression model of extraction rate and parameters were built, by adopted surface methodology optimizing technological parameters. The optimized parameters: ethanol volume ratio was 68 %, liquid–solid ratio was 53:1, and intensity of ultrasonic power was 5:1. The ethanol volume ratio has the maximal influence, liquid–solid ratio came second, and the intensity of ultrasonic power had the minimum influence. Experimented by these parameters, the extraction rate from response surface methodology Box–Behken was 7.09 % and it had increased by 0.07 %, compared with that obtained from orthogonal design.

References

1. Yao D, Ding X (2008) Discussions in pharmacological action and the development in clinical application of puerarin. Chin J Clin Pharmacol Therap 13(4):468–474 (in Chinese)
2. Chemat S, Lagha A, AitAmar H et al (2004) Comparison of conventional and ultrasound-assisted extraction of carvone and limonene from caraway seeds. Flavour Fragr J 19(3):188–195

3. Babić S, Petrović M, Kaštelan-Macan M (1998) Ultrasonic solvent extraction of pesticides from soil. J Chromatogr A 823(1):3–9
4. Guo Q, Zhang Q, Fei Q(2005) Response surface method and its experimental design for deterministic computer simulation. Acta Aeronaut Astronaut Sin 27(1):55–61
5. Sheng Z, Li JC, Li YH (2011) Optimization of forsythoside extraction from Forsythia suspensa by Box-Behnken design. Afr J Biotechnol 10(55):11728–11737
6. Jun HUANG, Zhe WU (2000) Recent developments in conceptual/preliminary design optimization of aircraft. Acta Aeronaut Astronaut Sin 21(6):481–487 (in Chinese)
7. Zhong K, Wang Q (2010) Optimization of ultrasonic extraction of polysaccharides from dried longan pulp using response surface methodology. Carbohydr Polym 80(1):19–25
8. Chen J, Huang X, Qi Y et al (2014) Process optimization of ultrasonic extraction of puerarin based on support vector machine. Chin J Chem Eng 22(7):735–741

Chapter 51
An Intelligent Active Defense Method Against Trojan Based on Behavior Sequence

Linbo Tao, Jianjing Shen and Peng Hu

Abstract For the question of lacking Trojans structure analyzing and relationship research of behavior sequence combination in current plan of active defense, the paper studies principles of traditional anti-virus and active defense, then it modularizes the commonality of Trojans by analyzing their structure, generalizes breakthrough methods and proposes two analyzing tactics. With the help of the two tactics and module belonging of Trojan behavior sequence analyzing, the relevance of message sequence and typical Trojans behavior sequences are studied. At last we can effectively improve the ability of the active defense to identify Trojans through experiments.

Keywords Active defense · Breakthrough method · Module · Behavior sequence

51.1 Introduction

The development of Internet brings convenience to users, it reduces our daily official cost and communication cost, with these conveniences, the user's privacy data, government and commercial important data are greatly threatened. The only thing we can do is to rely on anti-virus software and firewall which can help us to resist malware [1] attack and illegal access. But sometimes the anti-virus software and firewall cannot do correct judgment at every choice, many operating or access seem like legal behaviors, these malware usually simulate normal execution of legal software, which makes it difficult to distinguish between legal procedures and illegal procedures. In all types of threatens, maybe Trojan virus is the most harmful one, and the Trojans increase its weight in malware year by year. Most anti-virus software identify them depending on signature before, so we must

L. Tao (✉) · J. Shen · P. Hu
The Sixth Faculty of the PLA Information Engineering, University,
Zhengzhou 450001, China
e-mail: taotlb@126.com

enlarge our signature library all the time, until the active defense system [2] was invented, so current anti-virus software identify malware by signature [3] together with active defense system, this method solve the hysteresis quality of anti-virus software to some extent, so the active defense system really reverse the passive situation of traditional anti-virus software in some ways, as the old saying goes "While the priest climb a post, the devil climb ten," attackers also find many ways to bypass anti-virus software. Here we will do some works to summarize the methods that attackers bypass anti-virus software, especially the active defense system, so the first thing we must do is to introduce the working principles and structure changes of the anti-virus software and Trojans, then we will propose a behavior sequence analyzing method to help the anti-virus software work more currently and intelligent.

51.2 The Working Principles of Anti-virus Software and Their Breakthrough Methods

51.2.1 The Working Principles of Anti-virus Software

Early anti-virus software adopt the method to analyze virus is the mode scanner + virus signature library, its principle is to analyze samples of virus, and then extract their characteristics as virus signatures, add them to virus library. This method is of so low efficiency, so it had been eliminated. In order to improve the analyzing efficiency, engineers build to a simulation execution area [4] which can simulate the analyzing procedure of security engineers, we call it virtual machine module, and add it to the anti-virus software, it can extract virus signature automatically and improve the anti-virus ability of the anti-virus software effectively. The advantage of this method is obviously that it is of—fast speed and efficient, but its shortage is also obvious that it cannot identify new virus whose virus signature is not in the virus signature library, so this method does not solve the problem of hysteresis quality either. How to make machines more clever like human, AI gives us many good ideas, enlightened ideas [5] are imported to anti-virus analyzing, it can help the anti-virus software identify new virus whose virus signature is not in the signature library.

Until now the anti-virus software is more and more like an expert system and to some extent it has been an expert system. But it is not intelligent enough, it cannot distinguish some behavior's legality, so it has to ask user to judge the behavior, but most users do not know how to judge, with the inquiry times increasing, many users will be bored by the inquiries. So more AI techniques are imported to anti-virus analyzing and the anti-virus software becoming more and more clever. But the AI techniques maybe kill by mistake or leak kill some legal programs. All these methods mainly help the anti-virus software build the signature library more quickly, less identify new virus actively, so we call them passive defense. In order to identify unknown Trojans more efficiently, security engineers find out that it

must depend more on behaviors produced by program. After that more focus is brought to behavior judgment, engineers build a rule set to tell anti-virus software how to judge messages produced by API hook from Ring0, this improves the ability of anti-virus software to identify unknown Trojans greatly. At the same time, AI algorithms are applied in it which makes anti-virus software more humane. The advantage of this method is that it can cope with unknown virus at most time, the disadvantage is it is difficult to make the rule set. But it really helps us to deal with virus from passive to active, so we call it active defense. Although the active defense is not accurate enough now, it is really a milepost on our way to anti-virus. In the following part we will discuss the methods to deal with Trojans, because it is the most dangerous malware and we find out its principle of structure, so we have the confidence to improve our active defense system.

51.2.2 Breakthrough Methods of Active Defense

According to the principle changes of the anti-virus software, especially the applying of active defense system, old Trojan attacking mode has no chance to live. In order to survive their Trojans, attackers have to change their Trojans form to bypass the active defense system, and they really find some, and we summarize them as the following five ways:

(1) Decomposition method
A complex Trojan is decomposed into small parts, each part execute some certain functions. A main program is built to manage these functional parts, and it does not produce dangerous behavior or these parts can call each other, if one part is killed by anti-virus software, the other parts are still alive, so we cannot kill them completely.

(2) Masquerading method
Sometimes a Trojan will masquerade itself as a legal file by legitimate signature or adding itself to the white list, or masquerade its icon as a frequently used program, so user will usually ignore the dangerous warning and run the program.

(3) The underlying method
A Trojan will be designed or compiled more underlying than anti-virus software. So anti-virus software cannot discover it or kill it.

(4) The replacing method
A Trojan replaces its sensitive functions by some insensitive functions which can escape the monitoring of active defense system, or replaces them with some similar functions, or programs the functions by themselves.

(5) Customized version method
Different anti-virus software have different rules, in the case of finding out conditions of targets, attackers can configure different versions of Trojans against the special targets. So it can control the target chronically and steadily.

51.2.3 The Commonness of Trojans

The development of anti-virus software makes changes of Trojans, from the early structure of C/S, structure of B/S, and C/S or B/S with transfer. Trojans develop their communication way from socket, Raw socket, even IOCP [6] technique which can increase control scale greatly. The data transmission forms are from the early TCP packets, developing into UDP, ICMP packets, or even HTTP packets who can effectively hide socket link or data transfer, in favor of breaking through firewalls and hiding connection. In order to break through the firewall's examination to external links, most Trojans actively connect the control computer from the internal network which we call it rebound Ports Trojan or even they use the technique port reuse to bypass the firewall's examination, the control end will bind a certain domain, so the Trojans can easily connect them when the IP is changed. Despite there are so many changes have been taken place on Trojans, their connection, their data packets and so on, but the core structure of Trojans have not changed. It must be a Trojan end to control target, a control end to send commands and receive data. A complete Trojans usually consist of several modules, including with communication module, function module, self-running module, supplementary module.

Communication module is responsible for establishing connection channels for instructions and data transmission; function module is responsible for file management, remote shell, screen capturing, system modification functions; self-running module is responsible for writing the registry or registered the Trojan as a service which can achieve the automatic start-up; auxiliary module includes keyboard recording, download executable files backstage, and other functions. A Trojan usually consists of all these modules or parts of them, each module corresponds to its corresponding functions, function implementation can be seen as a series of attributes of a module, i.e., a Trojan behavior [7] always corresponds to a series produced by functions which are the realization of constitution behavior sequence. As shown in Fig. 51.1.

51.3 Active Defense Method Based on Behavior Sequence

51.3.1 Behavioral Analysis Based on the Modular

The Fig. 51.1 shows that every Trojan attack is actually a series of corresponding function module running, each function is often associated with the previous or next function, they often have certain relatedness. Their steps are usually start-up first, then the communication module will be called, a covert channel will be established when information feedback to the controller, the Trojan will wait for the next instruction, by parsing the control instruction, the Trojan will execute further control, the specific call as shown in Fig. 51.2.
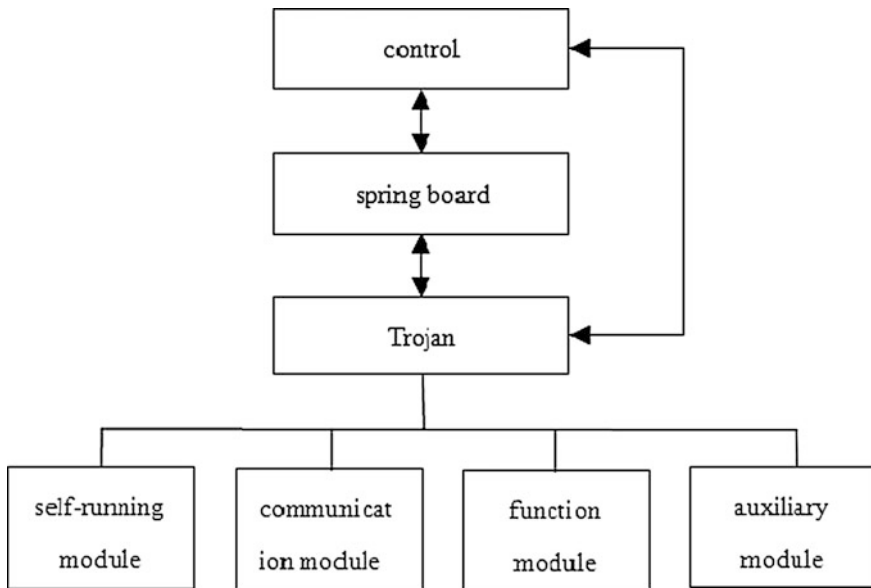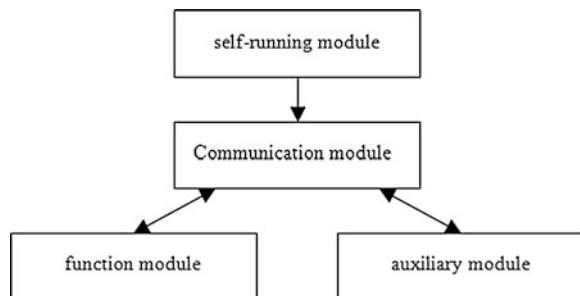
Fig. 51.1 The modular structure of Trojan

Fig. 51.2 Module calling graph

Let us analyze the four modules of a Trojan, we set the Trojan as *T*, it is composed by the four modules or parts of them, but the communication module and function module are the essential modules. Then we set the attribute set of self-running module as *A* (activation), the attribute set of communication module as *C* (communication), the attribute set of function module as *F* (function), the attribute set of supplementary module as *S* (supplementary), each set has a number of elements, that is, the module execution mode sum. An element of set *A* will be expressed as *a*, the other three elements of the sets are expressed as *c*, *f*, *s*, each implementation of the Trojan, in fact is the calling for a series of API, which corresponds to the corresponding elements in the four sets, these elements constitute a behavioral sequence.

The elements in set A only will be used in the first execution or system restarting. Because its sensitivity is high, so they are the focus of the anti-virus software monitoring. But most of the Trojans start-up successfully for its social engineering, most attackers get through some form of camouflage to obtain the trust of users, then users will add them into a white list [8] or cheat users execute their program actively, that is, the main way attackers realize their self-running module, regardless of the manner in which the implementation of a Trojan start-up, the majority are still elements of set A, they will provide help to our analysis on dangerous behavior.

After the successful start-up, a Trojan can simulate legal procedures in a variety of forms, which makes anti-virus software difficult to discern its legitimacy. But with the combination of their inherent characteristics of Trojans, we can find out high asymmetry in their communication module, sent data will be much more than received data, because Trojans' purpose are to steal confidential data and achieve long-term control, so most Trojans receive commands with short characters, after their receiving the instructions, some Trojans will immediately send data, some will send a small amount of data, then sleep a period of time and then continue to send data, when we calculate the cumulative amount of sent data, we will find out its much more than the cumulative amount of received data, although sometimes IP address of the control ends will change often, their link is relatively fixed. Any Trojan wants to control a target it must establish a channel of communication, through this channel it can send and receive data, so communication module is the base of Trojans. Another part, function module is the core part of Trojans, its purpose is to search sensitive data, modify system settings, so these behaviors will call some sensitive API function, these functions integration are more sensitive, the more sensitive API functions called the more easily discovered. System APIs have no positive and negative differentiation, the key is to see the caller's purpose, the order of execution of these API functions and combination mode can greatly reflect the intention of the caller. Auxiliary module usually be added according to attackers' need, there are large individual difference, but the running form is similar to the function module, by receiving instructions, then executing function, so we can put the module as a weight adjustment reference. Through the above analysis we can find, the communication module and the function module are the core modules of Trojans, they are also the weak sessions of anti-virus software defense, because of their flexible structure, wide function range, great crossing with normal procedures. If the anti-virus software monitors every sensitive API call strictly, it must bring low efficiency of the operation system and poor user experience. So anti-virus software in this respect usually chooses some kind of strategy selection based on a compromise.

51.3.2 Two Complementary Strategies

Based on the above analysis, two complementary strategies are proposed in this paper.

Strategy one: In view of the asymmetry of sending and receiving data about Trojans, we establish data statistics on monitoring procedures about their sending and receiving data, and randomly extract sample on the sending and receiving of packets, if there are a lot of the same address in the sending and receiving packets address, and the ratio of sending amount with receiving amount increases gradually, we will raise the risk weights of the procedure.

Here we may set sending amount as set d_s, receiving amount as set d_r, their ratio as formula (51.1).

$$p = d_s/d_r \tag{51.1}$$

Strategy Two: When a process triggered a sensitive API function, and element in set A and set C or only element in set C before the process is called, then record the order and frequency of these elements appearing sequence and find the file location corresponding to the process, if the process or other process calls these sensitive functions, and these corresponding files are stored in the same folder, then rise the risk weights. After this, if the communication module and the functional module alternately emerge, then rise the risk weights again.

According to the feature of windows system, any program will be files in the system, so Trojans is also no exception, it will be a executing file or composed by some types of files, the modules of Trojans will exist in these files, these modules will execute as independent process or insert other process, but all these modules will still obey the message passing mechanism, so the mutual calling of these modules must have some relationship. Especially their calling sequence. Based on the two strategies above, we can analyze the suspicious behavior sequence as following.

First we start-up the message monitoring, if some behaviors are writing registry or registered as service, then this behavior will regard as an element of set A, then label the process who produce the message, and find the file who produce the process, and then build a behavior sequence table which can record the behavior sequences. If the elements of set C and set F constantly and alternately appear, we will add up the values of d_s and d_r, and then calculate the value P, if there is no element of set A, just elements of set C and set F appear constantly and alternately, we also record them, because the communication module and function module are the core of Trojans. Then we unify the dangerous weights calculating formula for these two conditions as formula (51.2)

$$q = e_1 n_1 + e_2 n_2 + e_3 n_3 + e_4 n_4 \tag{51.2}$$

the e_1, e_2, e_3, e_4 are weighting coefficient. n_1, n_2, n_3, n_4 are the appeared times of elements in set A, set C, set F and set S, and $0 < e_1, e_2, e_3, e_4 < 1$, $e_4 < e_1 < e_2 < e_3$, it allows $n_1 = 0$, $n_4 = 0$ but it must be $n_2 \geq 2$, $n_3 \geq 1$, it means the elements of core modules must appear, and value q increase as elements appearing times increasing.

The process satisfied with the above conditions will be tagged as the intensive monitored program, combined with strategy one, we unify the calculating formula of risk weights as formula (51.3)

$$q = e_1 n_1 + e_2 n_2 + e_3 n_3 + e_4 n_4 + e^{\frac{1}{p}} \qquad (51.3)$$

The value of n_1, n_2, n_3, n_4 are calculated on the basis of the appearance times of messages according to set A, C, F, and S, the values of e_1, e_2, e_3, e_4 adjusted by the experiment dynamically. The value of q is calculated according to the lower limit of some typical Trojans behaviors corresponding to set A, C, F, and S, and calculated by formula (51.3). In order to reduce the interception to normal procedures, we can take $\frac{q}{2}$ as the lower limit of risk weights. If the value of risk weights is greater than q, then we mark it as dangerous procedure and monitor it all the way. And then we build a matrix Z which encoded by message sequences from our Trojan library

$$Z = \begin{bmatrix} z_{11} & . & . & . & z_{1n} \\ . & . & & & \\ . & & . & & \\ . & & & . & \\ z_{m1} & . & . & . & z_{mn} \end{bmatrix} \qquad (51.4)$$

Each column vector of matrix Z is signed as Z_{ij} $1 \leq j \leq n$, they are message sequences generated by our Trojan library, these message sequences are corresponding to a certain behavior sequences of Trojan, so these behavior sequences construct a sequence space, each column represents a complete Trojan behavior, then calculate the matrix rank of Z, we sign it as r, encode the message sequence of the process whose risk weights is greater than q, add these message code as a column vector to the last column of matrix Z, we call this new matrix Z_1.

$$Z = \begin{bmatrix} z_{11} & . & . & . & z_{1n} & z_{1n+1} \\ . & . & & & . & \\ . & & . & & . & \\ . & & & . & . & \\ z_{m1} & & & & z_{mn} & z_{mn+1} \end{bmatrix} \qquad (51.5)$$

Then we calculate the matrix rank of Z_1, and sign it as r_1, if

$$r_1 = r \qquad (51.6)$$

It shows that the newly added sequences belong to the original sequence space, so we can determine the behavior sequence should be a Trojan behavior. In order to
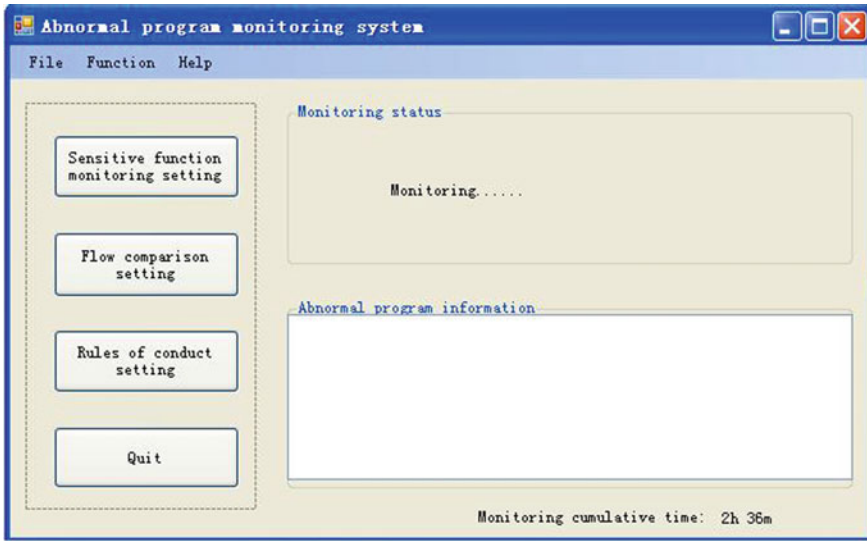
Fig. 51.3 The renderings before opening the data exception monitoring

enhance the robustness of the algorithm, swap any two elements of matrix Z_1 in its last column vector $z_{1n+1}z_{2n+1}\ldots z_{nm+1}$, according to the previous conditions $n_2 \geq 2$, $n_3 \geq 1$, Holding the position of the previous three elements of the vector, then swap two elements randomly in the remaining part of the vector, we name the new matrix Z'_1, calculate the matrix rank of Z'_1, and sign it as r'_1, if

$$r'_1 = r_1 = r \tag{51.7}$$

We can regard the behavior of the sequence as a dangerous behavior sequence, then stop the processes that trigger the behavior sequence, and gives warning tips.

51.3.3 Experiments and Results Analysis

Operating System: Windows XP SP3 Professional; Development Tools: vs2008; development language: c++; Trojan being tested: SEU_Peeper Remote Control Version 1.2.

Avoidance strategies: using signature tool to signature the Trojan program into the QQ program.

The contrast of test results before and after opening the data exception monitoring as Figs. 51.3 and 51.4.
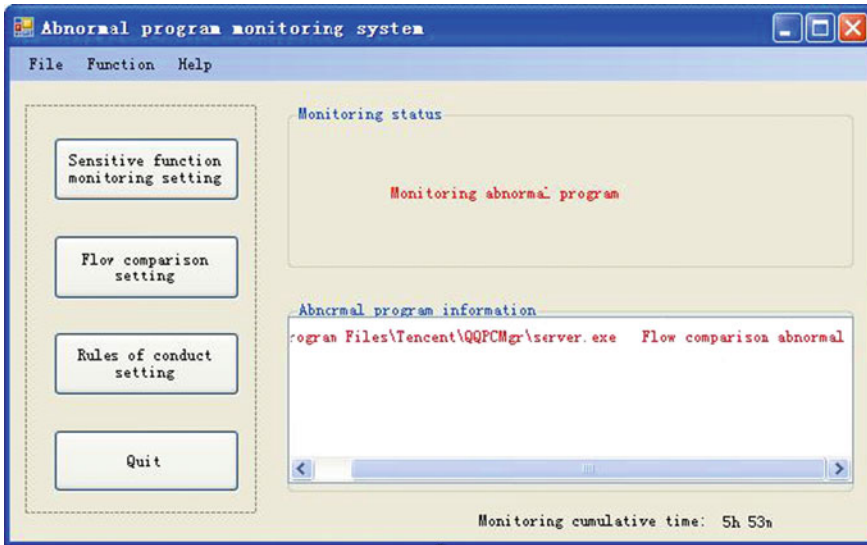
Fig. 51.4 The renderings after opening the data exception monitoring

51.4 Conclusion

Trojans are regarded as one of major threats to computers, attackers have done a lot of work to bypass the detection of active defense, but the core mechanism of Trojans have not changed. Based on the analysis of the structure changing and the avoidance methods of Trojans, we propose two complementary strategies and an analytical method based on behavior sequence which build a message matrix, then we prove it through experiments that it really works efficiently in certain aspects to discover new Trojan

References

1. Elisan CC (2012) Malware, rootkit and botnets a beginner's guide. McGraw-Hill/Osborne Media, NewYork
2. Jiang X (2010) Research on open source project feature code anti-virus and active defense avoiding. Shanghai Jiao Tong University, Shanghai
3. Liu H, Wang Z, Guo Y (2012) An IPv6 proactive network defense model based on multi-homing hopping. J Electron Inf Technol 34(7):1715–1720
4. Xun K, Liao X (2012) Research on proactive defense model based on virtualization technology. Microelectron comput 29(12):189–192
5. Fang S, Chen S, Tang F (2010) Applied research of active defense technology in access control. Comput Technol Dev 20(11):150–154

6. Lin M (2013) Based on Windows7 Trojan connection technology and viability studies, Master's thesis, Xi'an University of Electronic Science and Technology
7. Luo X, Wang K, Lianghua X (2009) On active defence technology based on behaviour analyzing and its vulnerabilities. Comput Appl Softw 26(7):269–271
8. Wang F, Zhou D (2011) Design and implementation of active defense system based on white list. Comput Eng Des 32(7):2241–2245

Chapter 52
Modeling for Two-Cart Mass-Spring-Damper System with Uncertainties Based on Mixed μ-Synthesis

Ya Wang, Baoyong Zhao and Yixin Yin

Abstract This paper provides a tutorial introduction and overview of design techniques for a system with both parametric uncertainty and unmodeled uncertainty, using mixed μ-synthesis. This paper also includes LFTs representation for modeling and an example of two-cart mass-spring-damper system (MSDs) is used to analyze its robust stability and performance, based on mixed μ-synthesis.

Keywords LFTs · Parametric uncertainty · Unmodeled uncertainty · Mixed μ-synthesis

52.1 Introduction

In order to improve the robust stability of a system with both unmodeled and parametric uncertainties. The mixed μ-synthesis was suggested by Doyle [1] who proposed 'D-G-K iteration' procedures, and it was further developed by Fan et al., who considered the development of upper bound for uncertainties. Their research led to the release of the μ-Tools toolbox [2] by Balas et al. in 1991. Subsequently, a large body of work concentrated on the properties of the mixed μ problems [3] and robust controller synthesis [4].

The purpose of this paper is to use mixed μ-synthesis for designing a controller, and to offer a necessary analysis for robust stability of MSDs by comparing its disturbance rejection response with the results of a conventional method. The two-cart mass-spring-damper system [5] is used to illustrate robust analysis issues. A different topology of the two-cart system is also presented in the reference [6].

Y. Wang (✉) · B. Zhao · Y. Yin
School of Automation and Engineering, University of Science and Technology, Beijing, China
e-mail: s20130918@xs.ustb.edu

52.2 Notation

There are two main categories of uncertainties, namely unstructured uncertainties and parametric uncertainties. Both uncertainties play an important role in stability and performance of a system. This section describes in detail how certainties can be represented in LFTs.

52.2.1 Structured Uncertainty

Consider using a single block Δ to represent unstructured uncertainties such as unmodeled, high frequence dynamics. In the case of the two-cart mass-spring-damper system, the unmodeled dynamic is referred to constant time-delay τ. Regularly, the block Δ can be described by an unknown transfer function matrix in the linear, time-invariant system.

In the μ-synthesis, a weighing function $W_{un}(s)$ is needed to cover the gain of $e^{-\tau s} - 1$. Figure 52.1 shows how a system with time-delay can be transformed into LFTs. The time-delay $W_{un}(s)$ is represented by multiplicative error associated with $W_{un}(s)$ and $\Delta(s)$ which must satisfy that $W_{un}(s)$ is chosen to have magnitude higher than $\|e^{-\tau s} - 1\|_\infty$ and $\|\Delta(s)\|_\infty \leq 1$.

52.2.2 Parametric Uncertainty

Parametric uncertainty is related to inaccurate description of parameters (complex or real) of a system. This means such uncertainties can be represented by variations of certain system parameters within some legal ranges.

Suppose three uncertain parameters m, c, k, m are represented by $m_0 + \delta_m$ where m_0 is a nominal parameter value and δ_m is a possible variation over a certain range, so does c and k. As a result, Δ is used to indicate a set of parametric uncertainties.
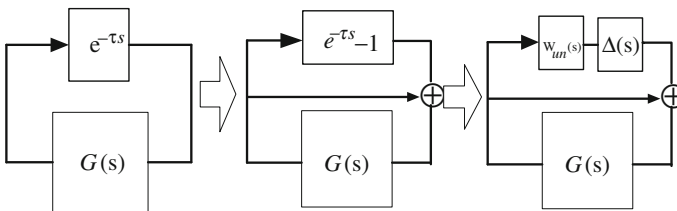

Fig. 52.1 Representation of constant time-delay in LFTs

$$\Delta = \mathrm{diag}(\delta_m, \delta_c, \delta_k) = \begin{bmatrix} \delta_m & 0 & 0 \\ 0 & \delta_c & 0 \\ 0 & 0 & \delta_k \end{bmatrix} \tag{52.1}$$

52.2.3 Linear Fractional Transformations (LFTs)

Linear fractional transformations are a powerful and useful method to represent model uncertainties and to use μ-synthesis for analyzing uncertain systems in involving interconnections of constant matrix block and feedback blocks with uncertain parameters and unmodeled dynamics.

Consider a matrix M with one input u and one output y, obviously

$$y = Mu \tag{52.2}$$

If there are two inputs u_1, u_2, and two outputs y_1, y_1 to M, the relationship between u_1, u_2 and y_1, y_1 is

$$\begin{cases} \mathrm{y1} = M_{11}u1 + M_{12}u2 \\ \mathrm{y2} = M_{21}u1 + M_{22}u2 \end{cases} \tag{52.3}$$

The representation of M in LFTs form is as followed in Fig. 52.2.
Relationship left between u_1, y_1 and Δ below

$$v_1 = \left[M_{11} + M_{12}\Delta(I - M_{22}\Delta)^{-1}M_{21} \right] r_1 \tag{52.4}$$

In addition, a cascade connection of LFTs is shown below Fig. 52.3.
Assume a new box P around M and G is drawn. Apparently, P is made up of variables $(u, w_{\Delta 1}, z_{\Delta 1})$ from M and variables $(y, w_{\Delta 2}, z_{\Delta 2})$ from G.
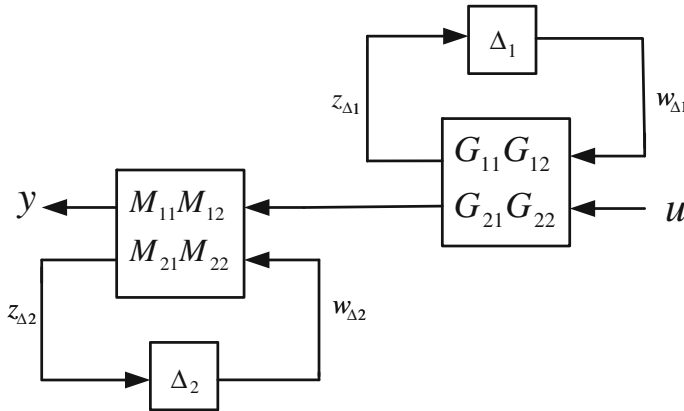
Fig. 52.2 LFTs representation of M
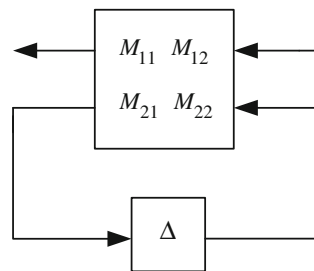
Fig. 52.3 A cascade connection of LFTs

The relationship between inputs and outputs can be easily calculated as

$$
\begin{bmatrix} y \\ z_{\Delta 2} \\ z_{\Delta 1} \end{bmatrix} = \begin{bmatrix} M_{11}G_{22} & M_{12} & M_{11}G_{21} \\ M_{21}G_{22} & M_{22} & M_{21}G_{21} \\ G_{12} & 0 & G_{11} \end{bmatrix} \begin{bmatrix} u \\ w_{\Delta 2} \\ w_{\Delta 1} \end{bmatrix} \tag{52.5}
$$

52.3 Modeling

In this section, $z_1(t)$ and $z_2(t)$ are adopted to define the displacement of the mass m_1 and the mass m_2 respectively. The displacement of the mass m_2 mixed with the continuous-time white noise is as an input of the compensator and the output of the compensator is as a control force with time delay applied to the mass m_1, which in return minimizes the displacement of the mass m_2, while the stiffness k_1 varying within a certain range. The system includes a disturbance force $f_2(t)$ which is a stationary colored stochastic signal acting on the mass m_1 Fig. 52.4.

The state-space representation of the MSD system can be represented as below

$$
\begin{cases} \dot{z}(t) = Az(t) + Bf_1(t) + Lf_2(t) \\ y(t) = Cz(t) + \theta(t) \end{cases} \tag{52.6}
$$

The state vector is defined as

$$
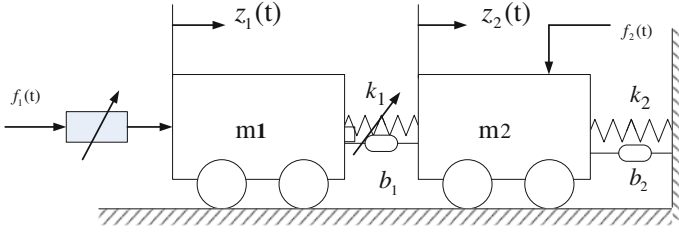z^T(t) = [z_1(t)z_2(t)\dot{z}_1(t)\dot{z}_2(t)] \tag{52.7}
$$

Fig. 52.4 Two-cart mass-spring-damper system (MSDs)

Thus

$$
\begin{cases}
\dfrac{\mathrm{d}}{\mathrm{d}t}\dot{z}_1(t) = \dfrac{k_1}{m_1}z_2(t) - \dfrac{k_1}{m_1}z_1(t) + \dfrac{b_1}{m_1}\dot{z}_2(t) - \dfrac{b_1}{m_1}\dot{z}_1(t) + \dfrac{1}{m_1}f_1(t) \\[3mm]
\dfrac{\mathrm{d}}{\mathrm{d}t}\dot{z}_2(t) = -\dfrac{(k_1+k_2)}{m_2}z_2(t) + \dfrac{k_1}{m_2}z_1(t) - \dfrac{(b_1+b_2)}{m_2}\dot{z}_2(t) + \dfrac{b_1}{m_2}\dot{z}_1(t) + \dfrac{1}{m_2}f_2(t)
\end{cases}
$$

$$(52.8)$$

Assuming the uncertain spring constant k_1 varies between 0.25 and 1.75, k_1 can be represented using the equation $k_1 = \bar{k}_1 + \tilde{k}_1\delta_k$ where $\bar{k}_1$ is a nominal value and the absolute value of δ_k is varying within one unit. Here $\bar{k}_1 = 1$ and $\tilde{k} = 0.75$.

The basic idea of modeling in LFTs is to separate inputs and outputs and indentify the relationship among them, according to Sect. 52.2.

Replace k_1 in Eq. (52.8) with $\bar{k}_1 + \tilde{k}_1\delta_k$

$$
\begin{cases}
\dfrac{\mathrm{d}}{\mathrm{d}t}\dot{z}_1(t) = \dfrac{\bar{k}_1}{m_1}(z_2(t) - z_1(t)) + \dfrac{\tilde{k}_1}{m_1}\delta_k(z_2(t) - z_1(t)) + \dfrac{b_1}{m_1}\dot{z}_2(t) - \dfrac{b_1}{m_1}\dot{z}_1(t) + \dfrac{1}{m_1}f_1(t) \\[3mm]
\dfrac{\mathrm{d}}{\mathrm{d}t}\dot{z}_2(t) = -\dfrac{\bar{k}_1}{m_2}(z_2(t) - z_1(t)) - \dfrac{\tilde{k}_1}{m_2}\delta_k(z_2(t) - z_1(t)) - \dfrac{k_2}{m_2} + \dfrac{b_1}{m_2}\dot{z}_1(t) - \dfrac{(b_1+b_2)}{m_2}\dot{z}_2(t) + \dfrac{1}{m_2}f_2(t)
\end{cases}
$$

$$(52.9)$$

w_Δ and z_Δ are used to represent $\delta_k(z_2(t) - z_1(t))$ and $z_2(t) - z_1(t)$ respectively. Thus, the MSD system is defined as follows:

$$
\begin{bmatrix}
\dot{z}_1(t) \\
\dot{z}_2(t) \\
\frac{\mathrm{d}}{\mathrm{d}t}\dot{z}_1(t) \\
\frac{\mathrm{d}}{\mathrm{d}t}\dot{z}_1(t) \\
z_\Delta \\
z_2(t) \\
z_1(t)
\end{bmatrix}
=
\begin{bmatrix}
0 & 0 & 1 & 0 & 0 & 0 & 0 \\
0 & 0 & 0 & 1 & 0 & 0 & 0 \\
-\frac{\bar{k}_1}{m_1} & \frac{\bar{k}_1}{m_1} & -\frac{b_1}{m_1} & \frac{b_1}{m_1} & \frac{\tilde{k}_1}{m_1} & 0 & \frac{1}{m_1} \\
\frac{\bar{k}_1}{m_2} & -\frac{\bar{k}_1+k_2}{m_2} & \frac{b_1}{m_2} & -\frac{b_1+b_2}{m_2} & -\frac{\tilde{k}_1}{m_2} & \frac{1}{m_2} & 0 \\
-1 & 1 & 0 & 0 & 0 & 0 & 0 \\
0 & 1 & 0 & 0 & 0 & 0 & 0 \\
1 & 0 & 0 & 0 & 0 & 0 & 0
\end{bmatrix}
\begin{bmatrix}
z_1(t) \\
z_2(t) \\
\dot{z}_1(t) \\
\dot{z}_2(t) \\
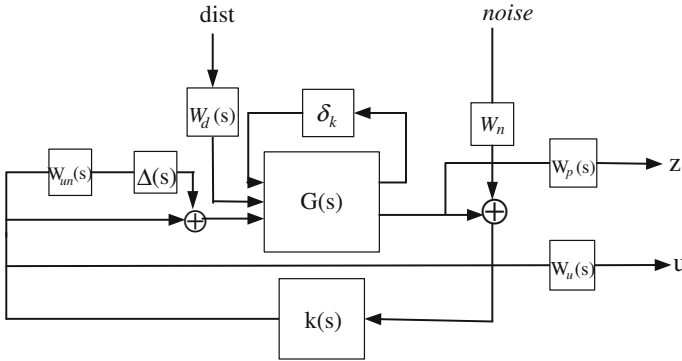w_\Delta \\
f_2(t) \\
f_1(t)
\end{bmatrix}
\quad (52.10)
$$

Fig. 52.5 The MSD system with weighting functions for mixed μ- synthesis

The following parameters are fixed and known as in Fig. 52.5.

$$m_1 = m_2 = 1, \, k_2 = 0.15, \, b_1 = b_2 = 0.1, \alpha = 0.1 \tag{52.11}$$

It is known that there is a delay-time τ for the control force $f_1(t)$ to reach the mass m_1. In the μ-synthesis, the time-delay τ whose maximum of 0.05 s is treated as an unmodeled dynamic. $W_{un}(s)$ is set as

$$W_{un}(s) = \frac{2.5\,s}{s + 40} \tag{52.12}$$

We define the control disturbance force $f_2(t)$ as a stationary colored stochastic process and $\xi(t)$ as a continuous-time white noise with zero mean and unit intensity.

$$f_2(s) = \frac{0.1}{s + 0.1}\xi(s) \tag{52.13}$$

In addition, we put the following weighing functions on the control force, measurement noise, and $z_2(t)$

$$\text{Control weight: } W_u(s) = \frac{10(s + 10)}{s + 10^3} \tag{52.14}$$

$$\text{Measurement noise weight: } W_n = 10^{-3} \tag{52.15}$$

$$\text{Performance weight: } W_p(s) = A_p\left(\frac{0.1}{s + 0.1}\right) \tag{52.16}$$

$W_u(s)$ is used to penalize the system that has large signals with high frequencies and limits the bandwidth together with the unmodeled dynamic weight. In the μ-synthesis, the nonnegative μ should be guaranteed under one unit and the larger μ is, the system has better performance in robustness. Thus one should try to maximize A_p in Eq. (52.16) until the largest μ is just under one unit.

52.4 Simulation

Based on the conception, we examined the condition of $\|W_{\mathrm{un}}(s)\|_\infty \geq \|e^{-\tau s} - 1\|_\infty$ Fig. 52.6.

Apparently, the $W_{\mathrm{un}}(s)$ is chosen legally.

From Fig. 52.7, the displacement of the mass m_1 fluctuates obviously with the uncertain parameter k_1 varying within a range, in other words, the parametric uncertainty cannot be ignored. Next, by using the command dksyn to synthesize a robust controller for open-loop interconnection and injecting the white noise into filter, a comparison for the disturbance rejection performance between mixed μ controller and conventional controller can be acquired. After 5 to 6 time D-G-K iterations, the result of closed-loop robust performance is about 0.95, which means that the uncertain system achieves desired performance. A comparison for disturbance rejection response in the worst case can be seen from Fig. 52.8. Obviously, mixed μ controller performed better than that designed by the conventional method.

Fig. 52.6 Bode plots of $W_{\mathrm{un}}(s)$ (*green line*) and $e^{-\tau s} - 1$ (*blue line*)
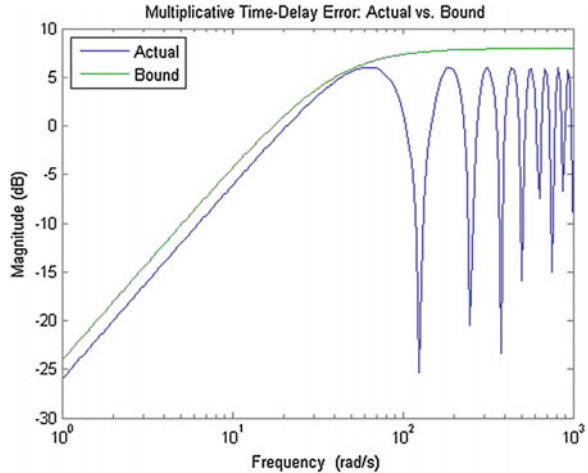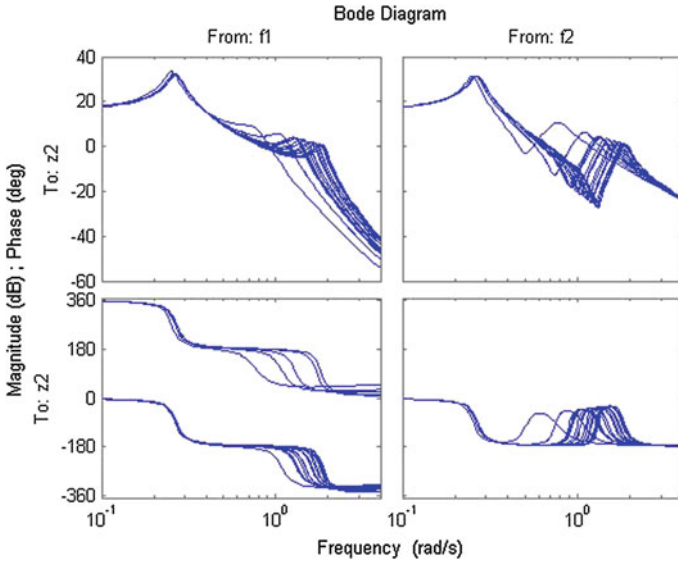
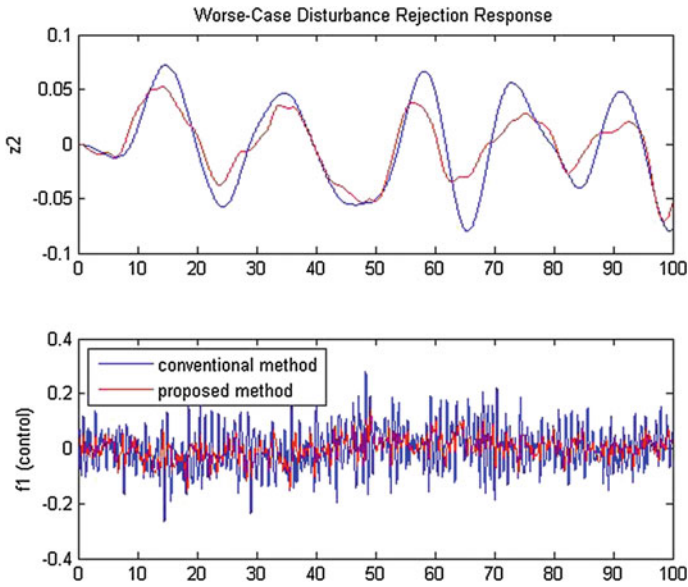**Fig. 52.7** Plot of respective bode response from $f_1(t)$ and $f_2(t)$ to $z_2(t)$

Fig. 52.8 Disturbance rejection response

52.5 Conclusions

This paper is aimed at introducing linear fractional transformations (LFTs) to model uncertain system subjected to both unmodeled and parametric uncertainties. With the help of μ-tool of Matlab box, the results indicate that mixed μ controller performed better than controller designed by conventional method. So our future work is planning to combine multiple model adaptive control with mixed μ method.

References

1. Doyle JC (1985) Structured uncertainty in control system design. In: Proceedings of the 24th conference on decision and control, IEEE, pp 260–265
2. Balas GJ, Packard A, Doyle JC, Glover K, Smith R (1991) Development of advanced control design software for researchers and engineers. In: Proceedings of the American control conference, pp 996–1001
3. Young PM (1996) Controller design with real parametric uncertainty. Int J Control 65:469–509
4. Young PM, Doyle JC (1996) Properties of the mixed-μ problem and its bounds. In: IEEE transactions on automatic control, vol AC-4, pp 155–159
5. Hamamoto K, Sugie T (1996) Controller design of 2 mass-spring system via LMI. In: Proceedings of the 35th conference on decision and control, pp 1140–1145
6. Fekri S, Athans M, Pascoal A (2004) A novel robust adaptive control: performance evaluation. In: Proceedings of the IEEE conference on decision and control, pp 1140–1145

Chapter 53
The Design of Quality and Measurement Control-Execution System Based on IOT Bus

Qiaoshun Wu, Shenghui Kuang and Haibo Peng

Abstract This paper analyzes the critical factors of the process of manufacture on the basis of four aspects: the material purchase, product sale, piecewise process, and the unit of single product equipment. Furthermore, it gives a general analysis and design of quality and measurement Control-Execution system based on the Internet of things bus, and the business process model of quality and measurement, as well as the model for system control and trace based on the Internet of things are mainly discussed. The study of the system also supplies a beneficial reference for the construction of similar information system of large-scale iron and steel enterprise.

Keyword Internet of things · Quality · Measurement · Control

53.1 Introduction

The iron and steel enterprise is a typical process production enterprise. It has a feature of wide production area, complicit process, large product coverage, etc. [1]. The production process involves different kinds of raw materials, auxiliary materials, different grade and quality, various intermediate products and product; and it has strong and interlocking continuity production technology whose production activities include quality testing and measurement statistics of ore into the factory, material resources, metallurgical processing products into finished products. There are numerous measurement sites for inspection which have complex working conditions, geographical dispersion. To significantly improve product quality and reduce logistics cost, strictly quality and measurement control is necessary in the production of each link and each working procedure. Therefore, it is a vital problem to meet the needs of the market, customer's order, and product design requirement while manufacturing and timely inspection of product quality, real-time record of

Q. Wu · S. Kuang (✉) · H. Peng
Information Center of Kun Steel Holding Co., Ltd. WISCO Group, Kunming 650302, China
e-mail: ksh6193@ynkg.com

logistics supply and material consumption, deep development and utilization of quality and measurement information resources, improving the level of comprehensive analysis, on the basis of material purchase, product sale, piecewise process, and the unit of single product equipment in implementing the strategy of energy conservation and emissions reduction. This paper, taking Kunming iron and steel as an example, mainly discusses the key business elements of quality and measurement control-execution system for large-scale iron and steel enterprise based on the Internet of things. At the same time, the author gives an overall design of the system.

53.2 System Requirements Analysis

The goal of design and development for quality and measurement control-execution system based on Internet of things is to establish a controllable, reliable, and scalable network system which can deeply fuse computing, communication, and control while integrating statistics of materials and resources, as well as goods "in process and products" quality inspection data.

Generally speaking, the characteristic of steel industry production process is maximization, continuum, and automation [2]. On the basis of the corresponding analysis of the control status of the enterprise, the technical basis, equipment conditions, network environment, staff environment and software application, etc., this paper concludes that the system for the quality, measuring information processing has the following distinctive features:

(1) The environment of production is extremely harsh, while production process contains extremely complex processes of physics and chemistry. Materials and intermediate products or the products in process mostly show flowing or high temperature state, involving all kinds of mutations and uncertainty factors.

(2) The system scheduling function needs to provide the best control strategy to quality of materials and measurement not just to improve the production efficiency, improve product quality, and reduce production cost as the goal, but also to save energy, reduce pollution, realize the goal of optimizing control, and so on.

(3) In order to conduct a comprehensive control on the production process, material measurement, and product quality, the model of quality and measurement analysis and control must be fused into the various control models in the main continuous production process on physical and chemical changes.

(4) It is difficult to dynamically change the established product path because of many variable factors in each production unit. Meanwhile, the information processing becomes difficult to handle for tremor of various factors in production process, mutual influence between before and after processes, difficulties in determining production time and random variation of material supply, and product quality of each production unit. Therefore, the system

requires a continuous online execution in the quality and measurement process.

(5) The process in the iron and steel industry is from less to more. For example, a furnace can be cast into many billets and a billet can be rolled into multiple materials. Material keeps adding together in the process of smelting, so information processing is on the rise.

53.2.1 Requirement Analysis of Quality Control and Execution

The function of quality management and control for iron and steel enterprise is explained from the perspective of total quality management. In the process of implementation, due to the hierarchy and distribution of smelting as well as manufacturing, quality inspection function also has a layered and distributed feature. The system of quality management consists of six main functions: technology standard database, quality design, quality inspection and process parameter acquisition, quality judgment, quality analysis and optimization, and quality control. The quality control system mainly consists of the following functions:

(1) The process standard database, used to store production technology standard data.
(2) Quality design, conducting quality design, based on the product quality standards and contract while conducting technology parameters design based on production process standards and adjusting quality design based on the results of quality analysis and optimization.
(3) Quality inspection and process parameter acquisition.
(4) Quality judgment. Give a verdict according to the quality inspection results combined with the technology standard and qualified parameters appointed in contract.
(5) The quality analysis and optimization. Find out the harmful effects on product quality according to the actual parameter analysis in production process combination of experiences of the experts when quality problems arise.
(6) Quality control. Conducting quality adjustment and optimization in production process and organization according to the analysis of influencing factors as well as key quality characteristics.

53.2.2 Requirement Analysis of Measurement Control and Execution

Measurement management is an important part of Manufacturing Execution System (MES). The concentration measurement system combines with various kinds of

metering station and measurement monitoring centre organically. Different kinds of production data can be timely communicated and shared through the measurement management system which runs in a private network, as well as business processing and cooperation between multiple departments becomes more efficient, and also the information system improves the measurement capacity and service level significantly. To establish a remote centralized measurement system not only standardizes metering process, prevents artificial error and cheat, reduces production costs, improves working efficiency, but also realizes unattended centralized metering and controlling, without interruption measurement, multiple measurement model, balance load work of weighing instruments, rapid analysis of measurement data, the disposition of objection in metering, data mining and business tracing, reasonable allocation of material resources, optimization of production organization, enterprise quality strategy, production quality assurance. The centralized measurement system mainly contains the following functions:

(1) Remote centralized measuring: the remote measurement system involves business of material purchasing plan, material allocation plan, energy consumption, verification for the materials coming in and out of the plant and so on, it improves the logistics efficiency by using the perdition information of the trucks or trains coming in and out of the plant, therefore, the logistics cycle time becomes shorter than before.

(2) Measurement data acquisition: the remote unattended measurement system has the function of automatic weight discrimination, it acquires and saves data automatically when the instrument data become stable, which avoids artificial error, prevents manual data input as well as copying or pasting, ensures the safety, accuracy and reliability of measurement data and its transmission.

(3) Query measurement information statistics: Users obtain the integrated information which contains original measurement data and computed data, these data can provide convenience for production preparation, process control, logistics scheduling. Such approach is in good for integration of purchase, storage, production, quality inspection, sales, and financial settlement.

(4) Measurement information synchronization: the system has realized the synchronous transmission in real time between metering data and production process data, which has improved the control and execution efficiency in production activities.

(5) The measurement process monitoring: the system provides whole process supervision, which makes it easy to trace the measurement process when dissent raised.

(6) Using IC card to realize closed-loop control of measurement process, it runs through the entire logistics course which contains materials coming in the plant, the first weighting, discharge cargo, the second weighting and the truck coming out of the plant, and also it prevents repeated weighing.

(7) Storage Management: It achieves data acquiring automatically by using the bar code and two-dimensional code technology in the process of product

storage, transfer, warehousing, inventory, and improves the logistics efficiency, realizes the consistency of logistics flow, and information flow.

53.3 Business Process Model of Quality and Measurement

The quality monitoring model assures that products that customers received meets all quality items in the contract through the whole process of comprehensive quality inspection and measurement data statistics of raw materials, semi products, finished products, and ensures that each phase quality can be controlled in the technology requirements range of manufacturing process through the online test inspection of manufacturing technology, equipment, material, energy, and manual operation. In order to control the bad influences and improve the weak stage in producing, it is important to find quality problems in working and make full use of the feedback information of product quality parameter, trace back to the product defect problems. The model provides the solutions and means to further improve the overall quality of products through the analysis of various quality factors to reveal the main contradiction; it also ensures the stability and improvement of product quality through a series of quality assurance measures [3].

53.3.1 Core Businesses Flow of Quality Control

Workflow of quality control mainly includes the following functions: synthesis of raw materials, semi-finished products, finished products, and commodity quality inspection in manufacturing process; synthesis of the testing of the equipment and energy consumption online in manufacturing process; comprehensive quality tracking; analysis of factors for the quality of products; development and implement of quality control measures.

In the above aspects, testing and inspection in the manufacturing process on raw materials, semi products, finished products, and commodity is the most direct measure of quality control. The collected data from testing and inspection directly reflects the quality status in the product manufacturing process. However, this is a kind of post and passive quality control mode; it plays a role of stuck effect. The online detection in the manufacturing process immediately reflects quality problems and realizes prompt control because of its online dynamic testing, although it is a kind of indirect quality control methods; on the other hand, even if indirectly, if it indeed captured the effect of product quality of key parameters, it can control parameters of industry technology, equipment, material, and energy consumption. Therefore, it is the most effective means of implementing quality control. Quality tracking has important significance for finding quality problems while it is an "after to track", especially when quality is not usually an important factor of the original
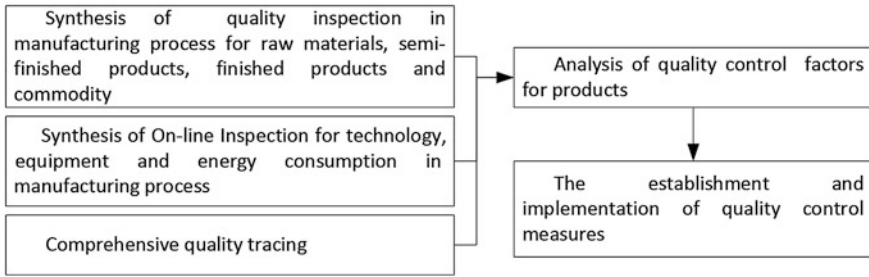
Fig. 53.1 The work flow of quality control

investigation. The two parts of the implementation of the overall situation from the perspective of quality products to develop and factors of quality of product analysis and quality control measures, further analyzes the main factors affecting the product quality, develops and implements a series of quality control measures to stabilize, improves and enhances the overall quality level of the product. The quality control process model is shown in Fig. 53.1.

53.3.2 Core Businesses Flow of Measurement Control

The metering control workflow mainly includes the following functions: synthesis of raw materials, auxiliary materials, materials resources, energy metering; remote concentration measurement in manufacturing process; comprehensive measurement information and production process; measurement data tracing back; the guidance of the measurement controlling on the phases of production, sales, production scheduling, supply, warehousing and other logistics links.

The measuring and monitoring models connects the metering and monitoring centre and various kinds of material measurement points by remote concentrated metering management system. It makes various measurement information between different departments and business processing data sharing and communicating timely, and improve the overall efficiency and service level in the material measurement stage, and forms a new measurement and management system with modern, intelligence, unmanned. The remote concentrated measurement model standardizes the metering flow, prevents human error, and reduces the cost for enterprise, achieves unattended and centralized management without interruption measurement, as well as variety of measurement model, well balanced work of weigher, and has the feature of traceability and rapid analysis. The metering control process model is shown in Fig. 53.2.
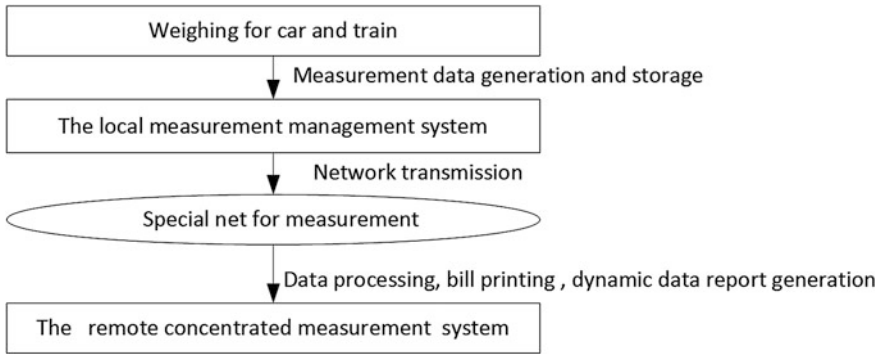
Fig. 53.2 The work flow of measure control

53.4 Model Design of Quality Control and Trace

In the process of quality control, the material tracing is often carried out by collecting quality data from quality inspection station under the normal production process and using Statistical Process, Control (SPC) method, while combining with the enterprise's production standards to establish a series of control standard through the analysis of quality data. These standards are dynamic and progressive because incoming materials and products in every stage of production process may be different. The initial data that is used to establish SPC criteria in the system from quality is from historical data of measurement system, but the renewal and increase of these standards is completed in the system quality determination [4]. After the establishment of SPC standard, the same process state can be effectively monitored to achieve the purpose of quality control and traceability.

In this system, there are different types of data of products or final products in the production process before or after the steel production such as chemical test date of steel products, mechanical test date and the field test data, and so on. The method of mathematical statistics to analyze these quality data mostly uses normal distribution.

For the random variables X deferred to normal distribution: $X \sim N(\mu, \sigma^2)$, its probability density function is:

$$f(x) = \frac{1}{\sqrt{2\pi}\sigma} e^{-\frac{(x-\mu)^2}{2\sigma^2}}, \quad -\infty < x < +\infty \tag{53.1}$$

In the above mathematics formula, μ is the mean value of X as well as σ is standard deviation of X, while the random variables X is related to the quality data to be analyzed [5].

For the test data obeying the normal distribution, we can analyze it by using normal distribution formula and the corresponding chart, and the results can backtrack to the control of production process of Manufacturing Executive System.
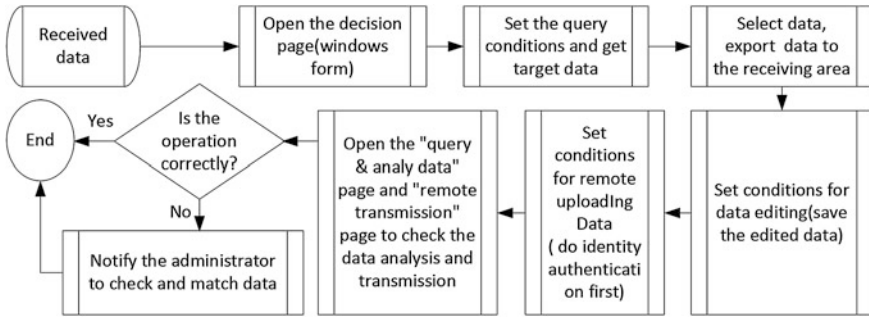
Fig. 53.3 The quality control and trace model

Combined with the design target of this system, we can see that this process is finished online to achieve the most rapid information feedback on MES level or PCS level. Quality control process model is shown in Fig. 53.3.

53.5 Model Design of Measurement Control and Trace

In the process of measurement and control, the material tracing comes from measurement data which is collected under normal production process from the metering station. Statistical Process Control is an integration of modern production techniques and management science [6]. In general, SPC is mainly used to control quality in the production process, but in this system, due to the continuity of the steel production process (for example: from smelting to rolling, hot delivery, and hot charging process) as well as the features of the technological process, measurement control should coordinate with quality control to ensure product quality and certain yield in the production process. Based on the principle and method of SPC, combining with the production of the enterprise standards and the analysis of quality date, a series of control standard is established. This analysis phase is finished under the constraints of measurement data.

The system, according to the established SPC standards, combines the yield with quality and implements different scheduling. Then it realizes online monitoring of production status of quality standard according to the measurement data in each process section. In this process, the schedule of next batch products can be adjusted while backtracking and quality and measurement data of incoming can be provided for the next process section forward to realize the measurement control and traceability. The measurement control process model is shown in Fig. 53.4.
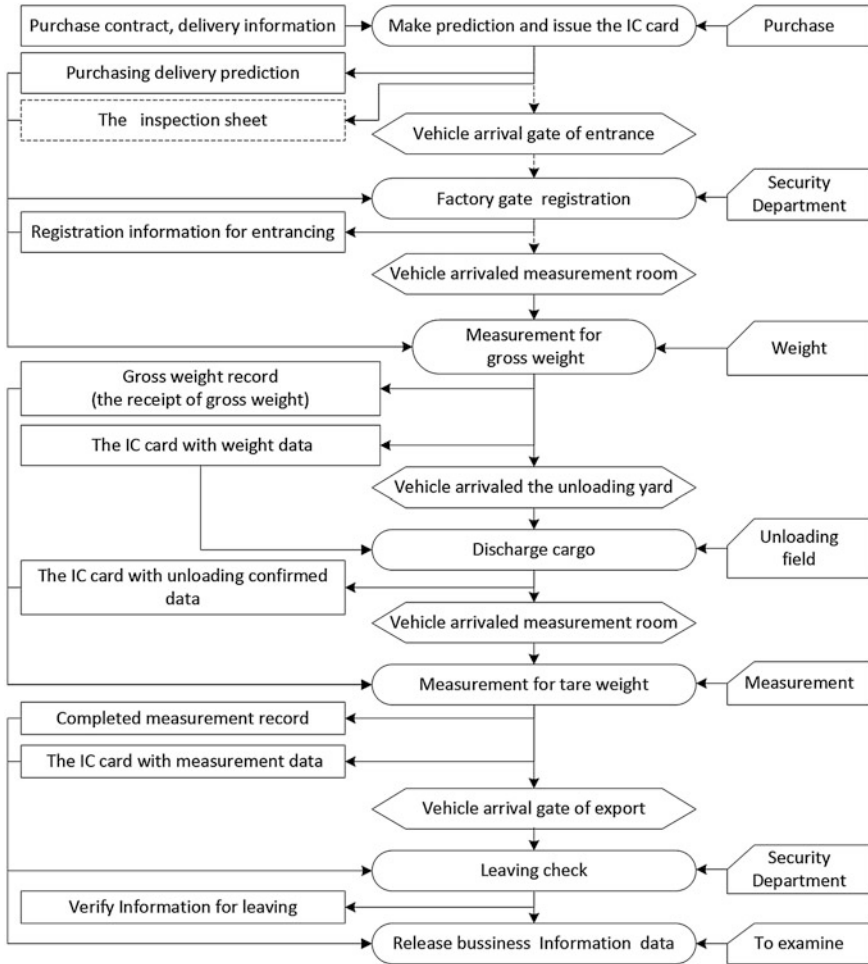
Fig. 53.4 The measurement control and trace model

53.6 Summary

The system, based on the enterprise information backbone network, the production process industrial ethernet, and wireless sensor network to establish the Internet things, which connects measuring, testing, testing equipment, integrates all the key test and measuring parts into a network platform; it also establishes a control system which integrates process control layer and the integration of Enterprise Resource Planning (ERP) layer, sets all the quality testing station and metering station with related technology and business of all the quality measurement management department and production unit as well as takes the real-time database and relational

database as the core on the base of quality monitoring model and statistical model of measurement. In the process of production control and implementation, the system can realize real-time acquisition and statistical analysis of inspection, measurement data, and measuring equipment running status parameters. It can also realize dynamic centralized and unified management of logistics scheduling and product quality control, metering production equipment unit with PLC and DCS data collection and integration control to upload data and receive instruction from management system quality control system automatically while automatically sending data to the production control system, and automatically receiving online data from control system. Therefore, it achieves the synchronization of production flow, logistics, information flow, which provides beneficial reference for the construction of large-scale integrated iron and steel enterprise's quality control execution system.

References

1. Jiang S (2004) The study of production plan based on CIMS of iron and steel enterprises. Graduate of Institute of Automation Chinese Academy of Sciences, Beijing, pp 1–13 (in Chinese)
2. Xiao H (2014) Analysis of the new technology on continuous casting and steel rolling. Architect Eng Technol Des (11):33 (in Chinese)
3. Song J, Zhong C (2011) The development and application for cost and quality monitoring system on big pipe steel billet of steelmaking plant of Hengyang steel tube group. In: The 2011 annual meeting of special steel branch of chinese society for metals. Metallurgical Industry Press, pp 147–154 (in Chinese)
4. Huang Z (2012) Quality monitoring and analysis of steel products based on real-time data. Graduate school of Wuhan University of Science and Technology, Wuhan, pp 23–31 (in Chinese)
5. Kou L (2014) Normal distribution and its application of probability theory and mathematical statistics. Education digest, vol 113, pp 13 (in Chinese)
6. Li X, Wang M, He J et al (2011) Application of statistical process control in preparing flavor and spices. The Food industry, vol (3), pp 27 (in Chinese)

Chapter 54
Network Time-Delay Prediction Based on Non-gaussian FARIMA Model

Chunyan Hu, Yang Song, Jie Yang and Xiaohua Wang

Abstract Large time delay often occurs unexpectedly in data transmission via Internet. As a kind of typical non-Gaussian stochastic process cannot be described by traditional prediction models with Gaussian innovation. In this paper, FARIMA model with standard symmetrical α stable distribution is adopted to model the transmission time-delay in Internet, and the method for estimating the model parameters is presented. Numerical results show that the approach proposed in this paper is more accurate than the general FARIMA model with Gaussian innovation in modeling Internet time-delay.

Keywords Symmetrical α stable distribution · Burst · Delay prediction

54.1 Introduction

Network control systems (NCSs) are feedback control systems wherein the control loops are closed through a real-time network, which entail advantages of sharing resource, remote operation, ease of system diagnosis and maintenance, increasing system flexibility and reliability and so on [1]. Consequently, NCSs have been applied in board areas such as industrial control, remote surgery and unmanned aerial vehicles [2]. However, network time-delay can greatly degrade the performance of NCSs, such as increasing the rise time and adjustment time, reducing stable region of the control system and even destabilizing the control system.

C. Hu · Y. Song (✉) · J. Yang · X. Wang
School of Mechatronical Engineering and Automation, Shanghai University,
Shanghai, China
e-mail: y_song@shu.edu.cn

Y. Song
Shanghai Key Laboratory of Power Station Automation Technology,
Shanghai 200072, China

On the research of Internet time-delay, the early employed models are Bernoulli model [3], Markov chain model [4] and Auto Regressive moving Average model [5]. These models are relatively mature and widely used in optimal control and stability analysis, and they are of short-range dependence. However, abundant literatures indicate that Internet delay has the features of self-similarity, long-range dependence and burst [6–8], which means that the aforementioned models are not suitable for modeling Internet time-delay. Furthermore, for modelling and calculation complexity, Support Vector Machine [9] and Neural Network Model [10] are also not suitable for time-delay estimation of real-time network. Noting that FARIMA (Fractional Autoregressive Integrated Moving Average) model has the ability to describe short-range dependence and long-range dependence simultaneously, and recently it has been introduced to model Internet delay [11]. However, the innovation of FARIMA model is Gaussian with no ability to describe non-Gaussian characteristic, so Internet time-delay prediction based on FARIMA model cannot reflect the burst of delay.

In this paper FARIMA model and α stable distribution are combined into the Internet time-delay model, for α stable distribution can describe the non-Gaussian distribution with heavy tail. Numerical results show that the approach proposed in this paper is more accurate than the general FARIMA model with Gaussian innovation in modeling Internet time-delay.

54.2 FARIMA Model Based on Symmetric α Stable Distribution

FARIMA model with Gaussian innovation is generally written as FARIMA (p, d, q), where d is the level of differencing, p is the autoregression order, q is the moving average order. By the following formula:

$$\Phi(z^{-1})(1 - z^{-1})^d X_t = \Theta(z^{-1})\varepsilon_t \qquad (54.1)$$

where $d \in (-0.5, 0.5)$, ε_t is white Gaussian noise with zero mean and variance σ^2. $\Phi(z^{-1}) = 1 - \phi_1 z^{-1} - \cdots - \phi_p z^{-p}$, $\Theta(z^{-1}) = 1 - \theta_1 z^{-1} - \cdots - \theta_q z^{-q}$

The fractional differencing operator $(1 - z^{-1})^d = \sum_{k=0}^{\infty} g(d, k)(-z^{-1})^k$ where $g(d, k) = \Gamma(d + 1)/\Gamma(k + 1)\Gamma(d - k + 1)$, $\Gamma(\cdot)$ is the Gamma function.

Noting that for time-delay sequence with a long-range dependence, its Hurst parameter: $0.5 < H < 1$ [12]. For FARIMA (p, d, q) model, $d = H - 0.5$, so $0 < d < 0.5$.

α stable distribution is used to describe the non-Gaussian distribution with heavy tail characteristics. It is generally represented by the characteristic function:

$$\varphi(t) = \exp\{ju(t) - \gamma|t|^a[1 + j\beta\mathrm{sgn}(t)\omega(t,a)]\} \tag{54.2}$$

where j is an imaginary unit, u is the real value, $\gamma \geq 0$, $-1 \leq \beta \leq 1$,

$$\omega(t,a) = \begin{cases} \tan\frac{a\pi}{2}, & a \neq 1 \\ \frac{2}{\pi}\log|t|, & a = 1 \end{cases}, \mathrm{sgn}\begin{cases} 1, & t > 0 \\ 0, & t = 0 \\ -1 & t < 0 \end{cases} \text{ and } 0 \leq a \leq 2.$$

Four parameters a, β, γ, u can completely determine the characteristic function of the stable distribution. The parameters have the following meanings:

Characteristic exponent a can measure the thickness of tail of PDF with the stable distribution. a is smaller, the tail of the PDF is thicker, the burst of random variables is stronger. $a = 2$ corresponds to a Gaussian distribution. u is the location parameter, which means the coordinate position of stable distribution. β, which affects the skewness of distribution, is a symmetry parameter. When $\beta = 0$, the distribution is symmetrical to u. Dispersion coefficient γ indicates the dispersion degree of stable distribution, which is similar to the variance of the Gaussian distribution.

α stable distribution with $\beta = 0$, $\gamma = 1$, $u = 0$, which is called the standard symmetrical α stable distribution, has only one parameter α.

FARIMA model based on standard symmetric α stable distribution regard standard SαS distribution instead of white Gaussian noise as the model innovation, which is written as FARIMA (α, p, d, q).

The level of differencing $d = H - 1/a$, $0 < d < 1 - 1/a$, so $1 < a < 2$.

FARIMA (α, p, d, q) model can be expressed as:

$$\Phi_p(B)(1 - B)^d X_t = \Theta_q(B)\xi_t \tag{54.3}$$

where B is the backshift operator, ξ_t is a sequence of i.i.d. SαS random variables. $\Phi_p(B) = 1 - \phi_1 B - \cdots - \phi_P B^P$, $\Theta_q(B) = 1 - \theta_1 B - \cdots - \theta_q B^q$.

Time sequence X_t can be written as: $X_t = \sum_{j=0}^{\infty} c_j \xi_{t-j}$, where the coefficient c_j satisfies: $\sum_{j=0}^{\infty} c_j z^j = \Theta(z)(1 - z)^{-d}/\Phi(z)$

For FARIMA (α, 0, d, 0), the coefficient $c_j = b(j)$ can be obtained by the Gamma function [12]:

$$b(0) = 1, \; b(j) = \Gamma(j + d)/\Gamma(d)\Gamma(j + 1), \quad j = 1, 2, \ldots \tag{54.4}$$

54.3 Parameter Estimation of FARIMA (α, *p*, *d*, *q*) Model

Stable parameter α is obtained by calculating reference estimators v_a and v_β. If known estimators v_a and v_β, do look-up table to determine the stable parameter $\hat{a}$ of the FARIMA (α, *p*, *d*, *q*) model, referring to table detailed in [13]. Estimators v_a and v_β are obtained through fractiles of the random sequence:

$$\hat{v}_a = \left(\widehat{X}_{0.95} - \widehat{X}_{0.05}\right) \Big/ \left(\widehat{X}_{0.75} - \widehat{X}_{0.05}\right) \tag{54.5}$$

$$\hat{v}_\beta = \left(\widehat{X}_{0.95} + \widehat{X}_{0.05} - 2\widehat{X}_{0.5}\right) \Big/ \left(\widehat{X}_{0.95} - \widehat{X}_{0.05}\right) \tag{54.6}$$

where $\widehat{X}_f$ is the fractile estimation of a random sequence. Therefore, to calculate v_a and v_β, do solve $\widehat{X}_f$ firstly:

Commanding that $F(\cdot)$ is a distribution function, its f fractile X_f satisfies $F(X_f) = f$, where $0 < f < 1$.

For a random sample $X_1, X_2, \ldots, X_n$, its order statistics are the sample values placed in ascending order, represented by $X_1, X_2, \ldots, X_n$.

Let $X_{(1)}, X_{(2)}, \ldots, X_{(n)}$ are a random sample which obey $F(x)$ distribution, its order statistics are $X_{(1)}, X_{(2)}, \ldots, X_{(n)}$. Assuming that $0 \leq i \leq N$ and $(2i-1)/2N \leq f \leq (2i+1)/2N$, so $\widehat{X}_f = X_{(i)} + \left(X_{(i+1)} - X_{(i)}\right)\frac{f-q(i)}{q(i+1)-q(i)}$, where $q(i) = (2i-1)/(2N)$. when $i = 0$ and $i = N$, $\widehat{X}_f$ respectively equals $X_{(1)}$ and $X_{(N)}$.

For FARIMA (α, *p*, *d*, *q*) model, its level of differencing $d = H - 1/a$, where H is the Hurst parameter of the delay sequence. There are many approaches to estimate Hurst parameter, such as R/S analysis, periodogram, variance clustering method, wavelet analysis method. The simulation part of this paper uses periodogram to estimate the Hurst parameter of the delay data.

For FARIMA (α, *p*, *d*, *q*), after getting fractional differential data, one don't directly use ARMA model to predict data, because the innovation is the *SαS* distribution, not a Gaussian distribution. And ARMA model with *SαS* distribution is presented in [14], but fixed-order and parameters estimation of which are complex. And in many references, one likes AR process with infinite variance and non-Gaussian distribution instead of ARMA model with *SαS* distribution. The principle is that any ARMA or MA process can be represented by high-order AR process, and the parameter estimation of AR model is relatively simple and especially it satisfys the high real-time requirement of network control system [15]. Parameter estimation of Non-Gaussian AR model consists of two parts: the order identification and coefficients fitting.

The order of non-Gaussian AR model is determined by the rank of third-order cumulant matrix which is converted by order identification of non-Gaussian AR model [16]. Firstly construct a third-order cumulant matrix sample, the method shows in [17]. Then do singular value decomposition [SVD] of the third-order cumulant matrix. Finally, by comparing two adjacent singular values, select the

largest singular value by the comparison with the next singular value, and the corresponding order of the singular value is the order of non-Gaussian AR model. The normalized ratio method and normalized singular value method are also used to calculate the effective rank of the cumulative matrix.

Non-Gaussian AR model coefficients can be obtained by the generalized Yule-Walker (GYW) equation. The general form of Yule-Walker equation is as follows:

$$C \times \partial = P \tag{54.7}$$

where $\partial = [\partial_1 \partial_2 \cdots \partial_P]^T$ are the known parameters,

$$P = [\lambda(1)\lambda(2)\cdots\lambda(p)]^T \tag{54.8}$$

$$P = \begin{bmatrix} \lambda(0) & \lambda(-1) & \dots & \lambda(1-p) \\ \lambda(1) & \lambda(0) & \dots & \lambda(2-p) \\ \vdots & \vdots & \ddots & \vdots \\ \lambda(p-1) & \lambda(p-2) & \dots & \lambda(0) \end{bmatrix} \tag{54.9}$$

The elements $\lambda(k)$ $(k = 1 - p, 2 - p, \ldots p)$ of covariance matrix C and vector P are the coefficient of the sequence $X(n + i)$ and $X(n)$, and $\lambda(0) = 1$. If C has full rank, solve (54.9) to obtain value of parameter ∂. To construct C and P, firstly estimate the coefficient of covariance $\lambda(k)$ according to data observed.

The coefficients of covariance of two joint $S\alpha S$ distributed random variables X and $Y(\alpha > 1)$ are:

$$\lambda_{xy} = E\big(XY^{p-1}\big)/E(|Y|^p), \quad 1 \leq p < \alpha \tag{54.10}$$

This paper uses fractional lower order moment (FLOM) estimation method. For an ergodic process X, the coefficient of covariance of the sequence $X(n + i)$ and $X(n)$ can be solved by the following formula:

$$\hat{\lambda}_{\text{FLOM}}(k) = \sum_{i=1}^{N} (X_i \, \text{sgn}(X_{i+k})) \bigg/ \sum_{i=1}^{N} |X_{i+k}| \tag{54.11}$$

By (54.11), get the covariance matrix C and the elements $\lambda(k)$ of vector P.

54.4 Internet Delay Prediction Based on FARIMA (α, *p*, *d*, *q*) Model

54.4.1 Parameters Estimation

All algorithms are programmed in MATLAB. Experimental data is a set of network delay sequence collected through the program. The length of the delay sequence is 2100; the former 2000 data are used for FARIMA (α, *p*, *d*, *q*) model to predict and the latter 100 data are used to compare with the predicted results.

The stable parameter and the level of differencing estimation: the delay data are written as *X*, its histogram is shown in Fig. 54.1. Calculate $\hat{v}_a$ and $\hat{v}_\beta$ of *X* and then get the stable parameter $a = 1.924$. Use periodogram to calculate Hurst parameter $H_1 = 0.973$. $d = H_1 - 1/a = 0.453$. After *X* finishing the difference scores, get a new sequence *Y*, which *H* is 0.563. It is obvious that the long-range dependence of delay data has significant attenuation through the score difference.

Parameters estimation of Non-Gaussian AR model: according to the afore-mentioned method, the order of the non-Gaussian AR model $p = 16$. AR modeling function in MATLAB toolbox is based on Gaussian process, so in this paper, firstly solve the GYW equation to get the coefficients of non-Gaussian AR model, then directly calculate the predicted value via the model formula. Finally, do d-order anti- score difference of *Y* to get final predicted results (Table 54.1).

54.4.2 The Results of Time-Delay Prediction

To prove the effect of FARIMA (α, *p*, *d*, *q*) model, use FARIMA (*p*, *d*, *q*) model to predict with the same set of data. Predicted results of two models and the original
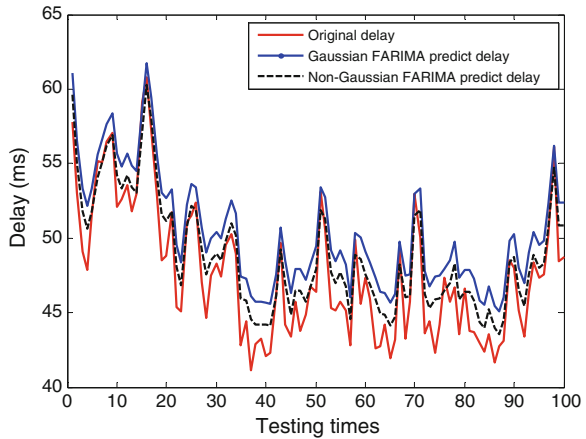

Fig. 54.1 The histogram of time-delay data
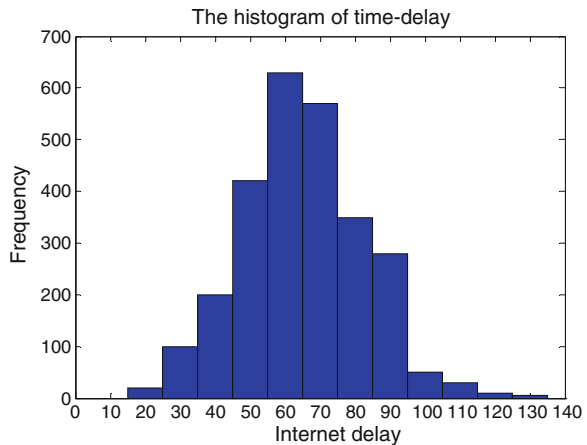
Table 54.1 The Simulation experiments data

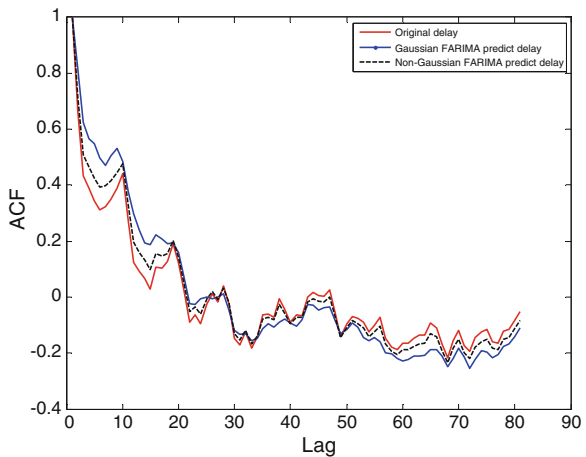| Stable parameters a	H before differential	Differential order d	H after differential	Non-Gaussian AR model order p
1.924	0.973	0.453	0.563	16

Fig. 54.2 Time-delay prediction

delay X are shown in Fig. 54.2. Simulation results show that FARIMA (α, p, d, q) model is more exact to reflect the fluctuations and burst of network delay than FARIMA (p, d, q) model with Gaussian white noise.

The auto-correlation function (ACF) can reflect the basic characteristics of time series, it is used to reflect the prediction accuracy of two models, shown in Fig. 54.3. It can be seen that ACF of predicted sequence of FARIMA (α, p, d, q) model is closer to ACF of original delay than that of FARIMA (p, d, q) model.

Fig. 54.3 ACF of the predicted delay

Table 54.2 The contrast of simulation experiment data

Serial number	Model Excitation	Stable parameters α	Differential order d	Mean of prediction error/ raw data average (%)	Mean of ACF difference	Variance of ACF difference
1	G	–	0.108	41.3	0.112	0.006
	SαS	1.943	0.094	19.1	0.042	0.004
2	G	–	0.274	13.9	1.180	0.054
	SαS	1.821	0.226	11.3	0.064	0.008
3	G	–	0.269	34.2	0.267	0.105
	SαS	1.543	0.121	31.9	0.051	0.006
4	G	–	0.212	22.5	0.119	0.020
	SαS	1.623	0.096	22.3	0.059	0.009

In order to further proof that FARIMA (α, p, d, q) model has more accurate prediction. Table 54.2 shows 4 groups of experimental data, each experimental data respectively use FARIMA (α, p, d, q) model and FARIMA (p, d, q) model to forecast. Comparing the each set of experimental data, the predicted error, the mean and variance of ACF difference of FARIMA (α, p, d, q) model is smaller than that of the Gaussian FARIMA (p, d, q) model. The result demonstrates that FARIMA (α, p, d, q) has better prediction.

54.5 Conclusions

In order to overcome the burst and self-similarity of Internet delay, this paper presents FARIMA (α, p, d, q) for Internet delay prediction. The model can reflect heavy tail characteristics of the network delay. This paper separately establish FARIMA (p, d, q) model and FARIMA (α, p, d, q) model to predict the delay via delay data measured, the results show that the prediction of FARIMA (α, p, d, q) model are more exact than that of FARIMA (p, d, q) model. The research method provides a new perspective for the Internet network predictive control.

References

1. Zhang W, Branicky MS, Phillips SM (2001) Stability of networked control systems. Control Syst IEEE 21(1):84–99
2. Hespanha JP, Naghshtabrizi P, Xu Y (2007) A survey of recent results in networked control systems. Proc IEEE 95(1):138

 3. Yang F, Wang Z, Hung YS et al (2006) H_∞ control for networked systems with random communication delays. Autom Control IEEE Trans 51(3):511–518
 4. Nilsson J, Bernhardsson B, Wittenmark B (1998) Stochastic analysis and control of real-time systems with random time delays. Automatica 34(1):57–64
 5. Bitsoris G, Athanasopoulos N, Dritsas L (2009) Feedback stabilization of networked control systems. Control Applications and Intelligent Control, IEEE. IEEE 2009, pp 1–6
 6. Li Q, Mills DL (1998) On the long-range dependence of packet round-trip delays in Internet. Int Conf IEEE 2:1185–1191
 7. Fujimoto K, Shingo ATA, Murata M (2001) Statistical analysis of packet delays in the Internet and its application to playout control for streaming applications. IEICE Trans Commun 84 (6):1504–1512
 8. Qingyun W, Aleksandra M, Matjaž P et al (2011) Taming desynchronized bursting with delays in the Macaque cortical network. Chin Phys B 20(4):040504
 9. Li J, Zhang Y, Pan H (2008) Chattering-free ls-svm sliding mode control for a class of uncertain discrete time-delay systems with input saturation. Intell Comput Technol Autom IEEE 1:322–326
10. Wu YY, Wu YQ (2009) Stability analysis for recurrent neural networks with time-varying delay. Int J Autom Comput 6(3):223–227
11. Yang S, Xiaomin T, Minrui F (2012) Internet time-delay prediction based on FARIMA model. Chin J Sci Instr 33(4):757–762 (in Chinese)
12. Stacy EW (1962) A generalization of the gamma distribution. Ann Math Stat 33 (3):1187–1192
13. McCulloch JH (1986) Simple consistent estimators of stable distribution parameters. Commun Stat Simul Comput 15(4):1109–1136
14. Harmantzis HF, Hatzinakos D (2005) Heavy network traffic modeling and simulation using stable FARIMA processes. In: Stevens institute of technology. Castle point on the Hudson, Hoboken
15. Hongyan L, Hong W, Chao G (2006) Internet time-delay prediction based on autoregressive and neural network model. Int Conf IEEE 3:1758–1761
16. Al-Smadi AM (2007) AR model identification using higher order statistics. In: ACS international conference on IEEE, pp 588–591
17. Georgiosb G, Jerrym M (1990) Cumulant-based order determination of non-gaussian AMAR models. Trans Acoust Speech Signal Process IEEE 38(8):1411–1423

Chapter 55
Leak Detection Research of Water Supply Pipeline Based on HHT

Fei Yuan, Zhangting Zhong, Yaqiong Cai and En Cheng

Abstract In this paper, the leak detection problem of water supply pipeline, the main sound source and its generating mechanism were studied. The authors use the power spectrum and the Hilbert Huang transform analysis of the vibration frequency characteristics of acoustic signal, and use them for leak detection. Design a set of water supply pipeline leak detection and alarm system based on MATLAB GUI and sensor, acquisition card and other peripheral equipment combined with the hardware and software, and realize the water supply pipeline leak detection. Validate and analyze the proposed scheme by collecting a large number of acoustic signals of different leakages through the experiment. The system is verified with more than 96 % accurate rate, and has a certain practical application value.

Keywords Pipeline leakage · Feature extraction · Leak detection

55.1 Introduction

As we all known, water is the source of life while fresh water resources which can be utilized by the human is more precious. Water shortage degree of China has been on the world's top 15, which may lead to the fresh water resources crisis [1]. The breakage of the drinking water pipeline makes this phenomenon more serious.

In a foreign country, relatively advanced pipeline leak detection instrument integrated signal detection, processing, transmission, application of microcomputer technology and other related to the leak detection system was widely used [2]. This kind of leak detection equipment was used by the water companies with actual strength in China though, it is expensive and issues such as maintenance support are difficult to handle.

F. Yuan · Z. Zhong · Y. Cai · E. Cheng (✉)
Key Laboratory of Underwater Acoustic Communication and Marine Information
Technology, Ministry of Education, Xiamen University, Fujian Xiamen 361005, China
e-mail: chengen@xmu.edu.cn

In the domestic, Changchun University of Science and Technology [3] studied the velocity, attenuation and frequency characteristics of acoustic signal were analyzed in detail; Jilin University [4] designed a communication prototype based on DSP and used for leak detection; Harbin Industrial University [5] had put forward a leakage point positioning system based on acoustic wave; Due to water pipeline leak detection and location system technology now is still in research stage, the leak detection method combined traditional artificial listening inspection method with abroad related leak detection positioning instrument was widely used in Chinese water company [6]. This method was poor anti-interference. Generally, the method was implemented at night in order to achieve a good detection effect which will result in costing a lot of manpower and material resources.

In this paper, a complete set of pipeline leak detection and alarm system based on MATLAB GUI monitoring system were puts forward. The authors use the Hilbert-Huang transform to obtain the frequency characteristic of leakage acoustic signal, which can be used to detect leaking, and then send leakage alarm.

55.2 Leaking Sound and Its Generating Mechanism

Leakage signal is one of the acoustic emission signals, which is a kind of phenomenon on the state of pressure. Because pressure difference exists between pipeline inside and outside, when the high pressure water sprayed outward from leakage point, spewing water, leakage point as well as surrounding soil would have friction, which will cause different frequencies of vibration. In Fig. 55.1, because of the different conditions of vibration, it usually contains three kinds of sound source: (1) the vibration sound [7]; (2) the rushing sound [8]; (3) the friction sound.

The above analysis shows that water pipeline leakage signal is a mixture of a variety of different voices and frequencies, which can use Eq. (55.1) to indicate:

$$s(t) = \sum_{i=1}^{n} a_i \cos(w_i t) \tag{55.1}$$

a_i is the amplitude of the ith frequency components w_i. n is the number of frequency components.

Fig. 55.1 Main sound source of pipeline leak
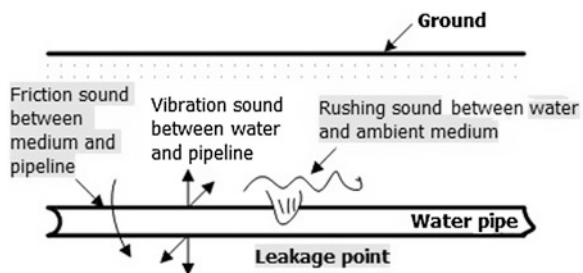
Leakage signal $s(t)$ would spread from the leak point to the surrounding media at a certain speed V, which could calculate the spread time τ to any given point A, that is: $\tau = r_A/V$, where r_A is the distance from leakage point to point A. Then the leakage signal spread to the arbitrary point A of the medium is:

$$s_A(t, r_A) = \sum_{i=1}^{n} a_i \cos\left(w_i\left(t - \frac{r_A}{V}\right)\right) \tag{55.2}$$

Leakage signal would be affected by the absorption or decay, and the decay is associated with propagation distance r_A. So Eq. (55.2) can be changed:

$$s_A(t, r_A) = \sum_{i=1}^{n} a_i e^{-\alpha r_A} \cos\left(w_i\left(t - \frac{r_A}{V}\right)\right) \tag{55.3}$$

α is attenuation factor of the surrounding medium for the leakage signal.

In practical applications, the signals received by sensor included leakage signal and random interference noise. So the vibration signal model of point A can be written as follow:

$$x_A(t) = s_A(t, r_A) + n_A(t) \tag{55.4}$$

$x_A(t)$ is the signal received by the sensor of point A; $s_A(t, r_A)$ is the leakage signal defined in Eq. (55.2); $n_A(t)$ is the random interference noise signal of point A.

55.3 Scheme Design and Experiment Scenario

A design scheme of the pipeline leakage detection and alarm system was presented in: frame diagram of overall scheme, introduction of each module.

In Fig. 55.2, the scheme could be divided into four parts: sensor, signal conditioner, collection unit and upper monitor unit.

In this experiment, a signal produced by adjustable tap was regarded as leakage signal. The pipe diameter was 20 mm. The pressure is regular pressure. LC0155

Fig. 55.2 Detection scheme of pipeline leak
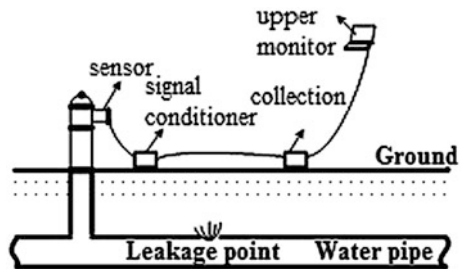
Table 55.1 Statistical table of experimental equipment used

Device name	Function
LC0155 piezoelectric acceleration sensor	Converts vibration into electrical signals
LC0201-5 signal conditioner	Provide constant current source
MCC USB-1608GX-2AO acquisition card	Collect signal, A/D transform
The oscilloscope	Signal display, debug equipment
Personal computer	Receive, display, process, analyze the collecting signal
Cable	Connect device, transmit data

sensors were placed far from leaking 10 cm. The close tap signal was first collected as noise, and was adjusted in three sizes as leakage signals. Each state collected 120 groups, sampling rate was 10 kHz, and single sampling time was 2 s (Table 55.1).

55.3.1 Time-Frequency Characteristics of Leakage Acoustic Signal

Plenty of studies showed that frequency of plastic leakage pipeline is mainly in 5–100 Hz while in metal pipeline is in 200–2500 Hz [9]. And as shown by Eqs. (55.2, 55.1), Eq. (55.4), leakage signal is combined many signals, so it belongs to time-varying non-stationary random signal. In this paper, Hilbert-Huang Transform (HHT) was used in time and frequency domain analysis for the collecting signals.

Empirical Mode Decomposition (EMD) and Hilbert transform were included in HHT. The EMD decomposed nonlinear and non-stationary signal from high frequency to low frequency into multiple IMF (Eq. (55.5)):

$$X(t) = \sum_{i=1}^{n} c_i(t) + r_n(t) \tag{55.5}$$

r_n is residual function shown the average trend of signal. IMF $c_1, c_2, \ldots c_n$ contains different elements of signal from high frequency to low frequency.

The Hilbert transform for each component IMF in Eq. (55.5) is obtained by:

$$\overset{\Lambda}{c_i}(t) = \frac{1}{\pi} \int\limits_{-\infty}^{+\infty} \frac{c_i(\tau)}{t - \tau} \mathrm{d}\tau \tag{55.6}$$

Construct analytic function $z_i(t) = c_i(t) + j \overset{\wedge}{c_i}(t) = a_i(t)e^{j\varphi_i(t)}$, hence the amplitude function $a_i(t)$ and phase function $\varphi_i(t)$ were obtained, and then the instantaneous frequency $f_i(t) = \frac{1}{2\pi}w_i(t) = \frac{1}{2\pi}\frac{d\varphi_i(t)}{dt}$ was found. Thus,

$$X(t) = \mathrm{Re}\left[\sum_{i=1}^{n} a_i(t)e^{j\varphi_i(t)}\right] = \mathrm{Re}\left[\sum_{i=1}^{n} a_i(t)e^{j\int w_i(t)dt}\right] \tag{55.7}$$

$r_n(t)$ was ignored. "Re" meant real component. Signal amplitude was expressed as a function of time and frequency in Eq. (55.7). This kind of signal amplitude function shown in time domain is called as the Hilbert time domain spectrum, short for Hilbert spectrum, shown as $H(w, t)$. Its mathematical expression is:

$$H(w, t) = \mathrm{Re}\left[\sum_{i=1}^{n} a_i(t)e^{j\int w_i(t)dt}\right] \tag{55.8}$$

Thus Hilbert marginal spectrum was defined as:

$$H(w) = \int_{0}^{T} H(w, t)dt \tag{55.9}$$

T is the period of signal. The Hilbert marginal spectrum is a measure of contribution of amplitude of each frequency within the scope of entire time.

55.4 Result Analysis

Tap state was divided into four kinds, corresponding to four kinds of leaks. The authors regard closed tap state as the background noise, a small amount of leakage as leaked 1, medium leak as leakage 2, a large number of leaks as leakage 3.

55.4.1 Test Standard Analysis

Figures 55.3, 55.4, 55.5 and 55.6, 4 kinds of leakages in time domain compared. The amplitude and energy of the noise are feeble. The amplitude and energy depend on the opening size. That means the larger of the leakage sizes are, the greater of signals' strength are.

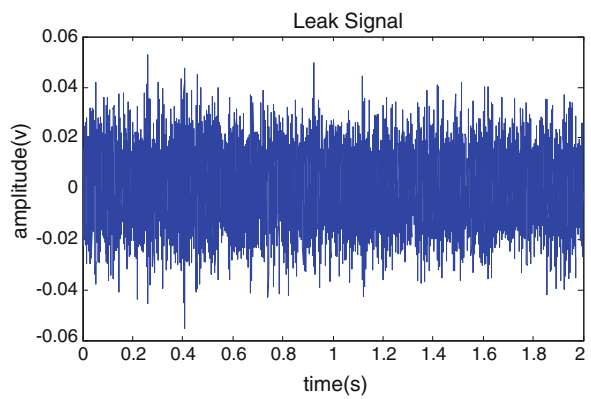Power density spectrum curve of the signals are shown below (Fig. 55.7):
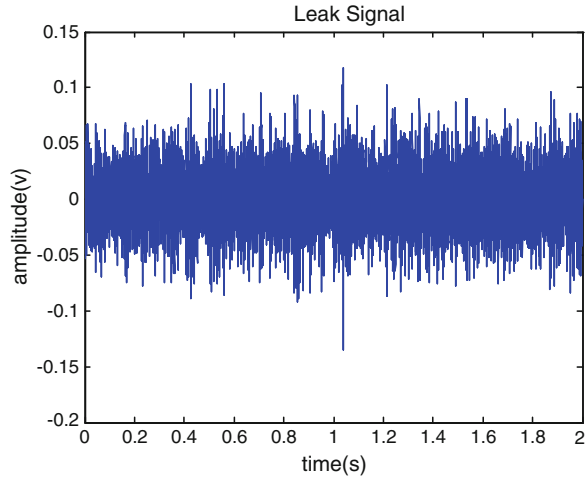
Fig. 55.3 Time domain
waveform of noise
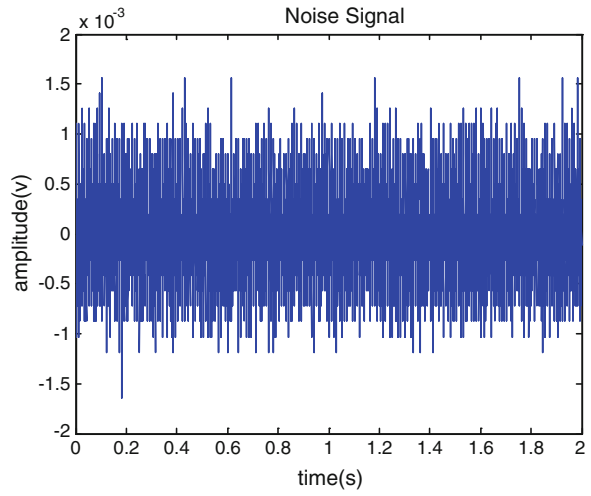
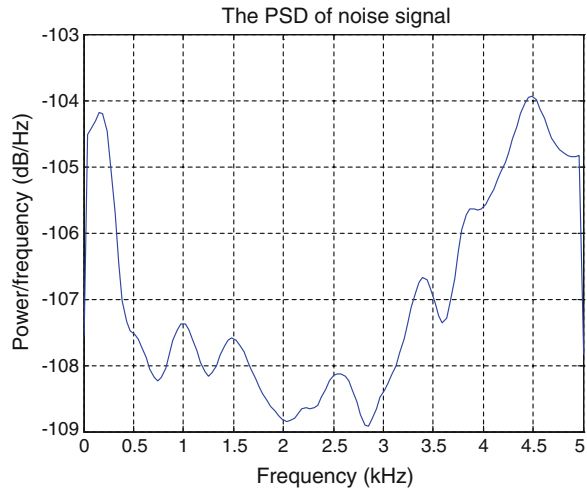**Fig. 55.4** Time domain
waveform of leakage 1
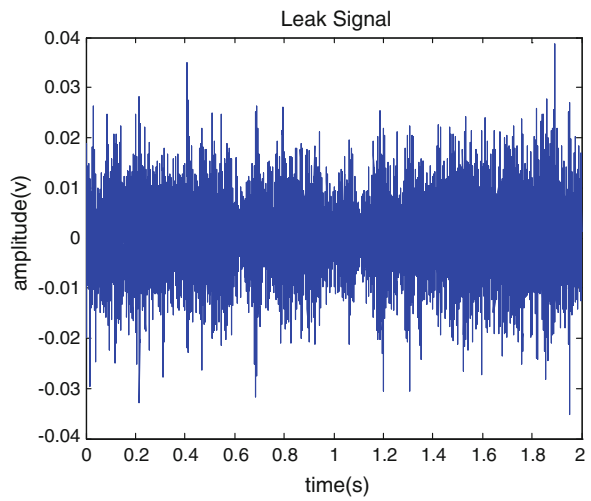
Fig. 55.5 Time domain
waveform of leakage 2

Fig. 55.6 Time domain waveform of leakage 3

Leak Signal

amplitude(v) / time(s)

Fig. 55.7 Power spectrum of background noise

The PSD of noise signal

Power/frequency (dB/Hz) / Frequency (kHz)

(1) Frequency's peak of background noise appears around 200 Hz, which is caused by vibrations of pipeline mainly while high pressure water flows in tube.

(2) Comparing Figs. 55.8, 55.9 and 55.10, leak size has little impact on the frequency component of leakage signal. The main frequency components are focused on the range of 500 Hz–1.1 kHz. But it has a great influence on the energy.

While use HHT introduced in the third chapter to analyze, signals were decomposed into IMF by using EMD in Eq. (55.5), then got signal marginal

Fig. 55.8 Power spectrum of leakage 1
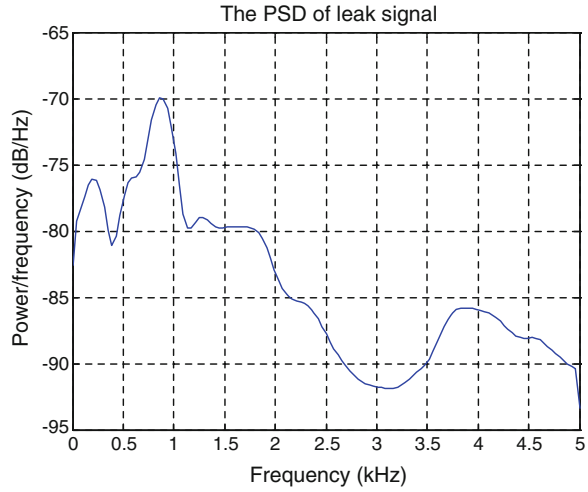
Fig. 55.9 Power spectrum of leakage 2
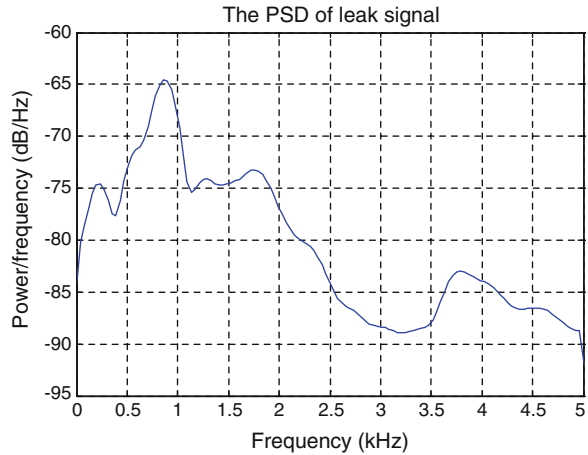
spectrum using Eq. (55.9). The frequency features of the signals could be observed below (Fig. 55.11).

(1) The frequency resolution of the marginal spectrum was much better than power spectrum (Figs. 55.7, 55.8, 55.9 and 55.10). But peak was close to 0 Hz in the marginal spectrum, which was caused by the end effect of the EMD decomposition. This is one of the limitations of the EMD decomposition;

(2) From the marginal spectrum (Figs. 55.12, 55.13 and 55.14) of leakage signals, the signal frequency components were similar, the larger peak all appeared around 500 Hz–1 kHz. But the energy of different frequency components were distinct;

Fig. 55.10 Power spectrum
of leakage 3
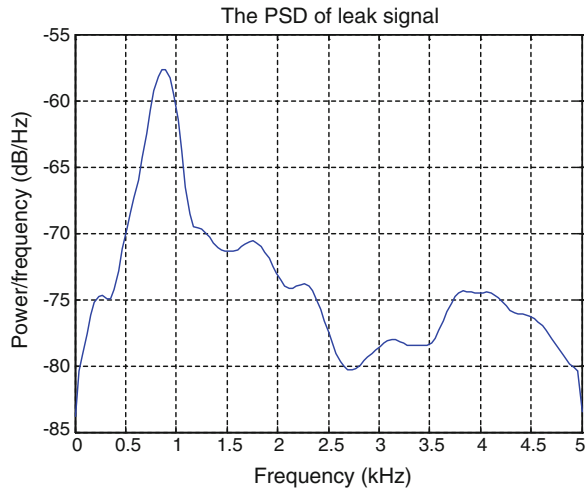
Fig. 55.11 Marginal
spectrum of background
noise
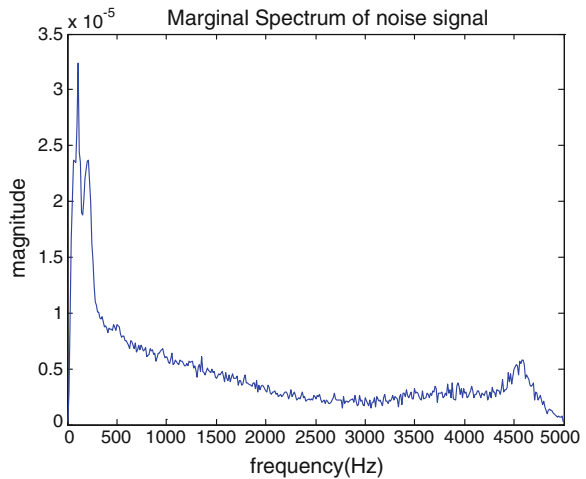
The amplitude of leakage signal in 500 Hz–1 kHz was greater than 10^{-5} while
the amplitude of the background noise in this frequency band was below 10^{-5}.

55.4.2 Scheme Performance Analysis

MATLAB GUI was used as development tool for monitoring unit. The scheme
includes the following three modules: (1) signal acquisition module; (2) signal
analysis module; (3) leakage identification module.

The monitor unit based on MATLAB GUI was showed in the Fig. 55.15.

Fig. 55.12 Marginal spectrum of leakage 1
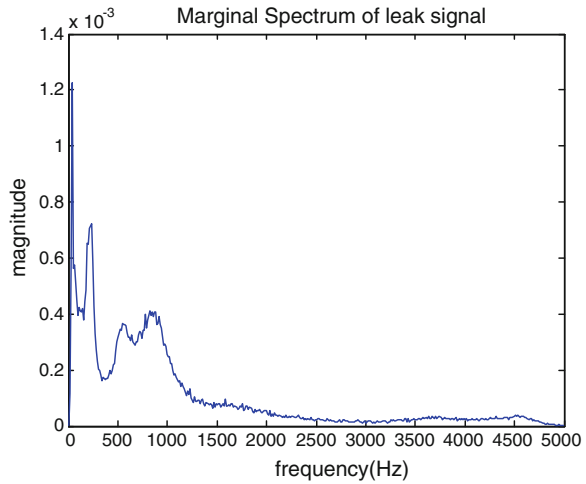
Fig. 55.13 Marginal spectrum of leakage 2
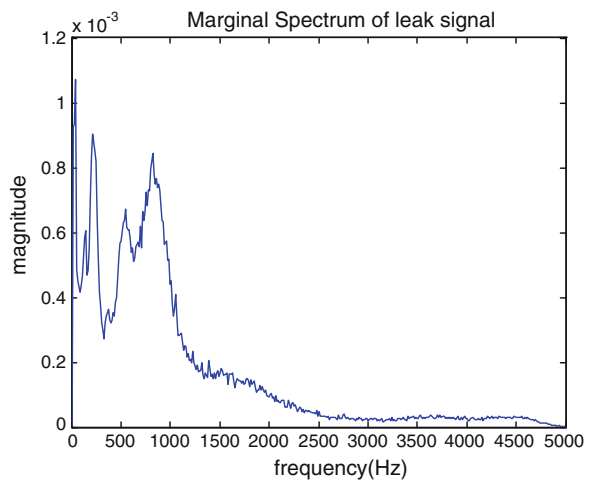
Data collected by the acquisition card could be sent into this system for analyzing. In the monitor screen, the time domain waveform of signal and HHT marginal spectrum can be shown.

Through the time-frequency analysis of 4 kinds of signals above, it was known that leak signals' frequency focused on 500 Hz–1 kHz, and amplitude was greater than 10^{-5} within this frequency band. So the leak detection standards could be made: setting the range of 500 Hz–1 kHz as detecting frequency band, and 10^{-5} as amplitude detection threshold. When the frequency was within this band range and the amplitude of the signal was greater than the threshold, the pipe was regarded as leaking, and the system would alarm.
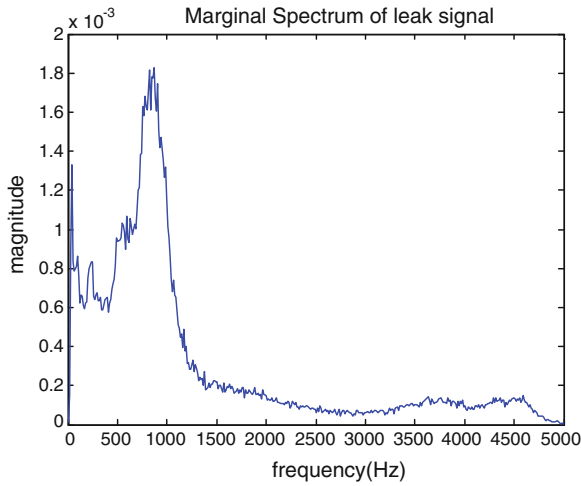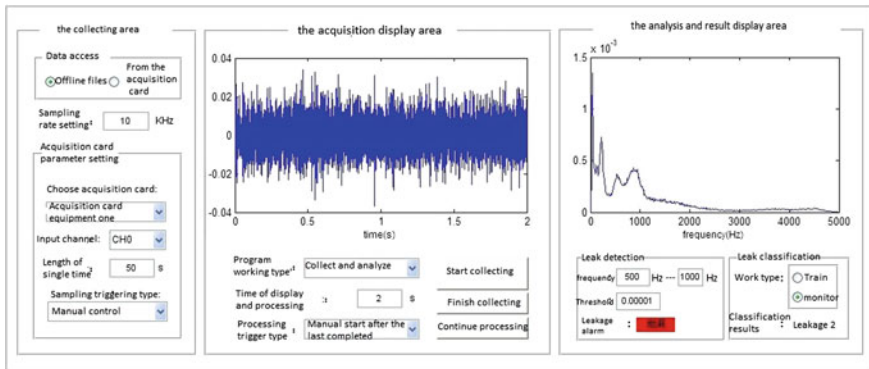
Fig. 55.14 Marginal spectrum of leakage 3

Fig. 55.15 Interface of monitoring

According to the above testing standards, the performance of leak detection and alarm scheme rose in this paper were validated by collecting pipeline signals in experiment. The authors collected 120 samples of noise and leakage 1 respectively, and the test results are shown in Table 55.2.

The performance in Table 55.1 confirmed: the system had a good availability; the leakage detection according to the leakage acoustic signal spectrum and frequency amplitude characteristics had very high leakage detection accuracy.

Table 55.2 Testing results of performance of leak detection

Pipe state	Amount of sample	Amount of error testing	Accuracy rate (%)
Normal	120	0	100
Leak	120	4	96.67

55.5 Summary and Prospect

Water supply pipeline leakage always has been very serious problems, causing large economic loss and severe waste of resources. It is of great significance to improve the water supply pipeline monitoring by advanced detection methods. In this paper, analyzed the time domain and frequency domain characteristics of 4 kinds of signals; The pipeline leak detection and alarm platform based on MATLAB GUI was set up, and the water pipeline leak detection system was realized. After many experiments, it was confirmed with accuracy more than 96 %.

References

1. Chen B (2001) The study of urban water supply pipe network leakage issue, Harbin Institute of Technology (in Chinese)
2. International Water Association (2000) Manual of best practice: performance indicators for water supply services. Int Water Assoc
3. Yan H (1999) The analysis of characteristics of underground water pipe leak signal. Changchun Univ Sci Technol (in Chinese)
4. Zhang T (2006) The improvement of the portable related leakage detection device based on DSP. Jilin University (in Chinese)
5. Xia K (2004) Applied research of relevant measuring and weak signal detection in pipe network leakage positioning system. Harbin Institute of Technology (in Chinese)
6. Ji-ming W, Chang-bin Y (2002) Introduction to water leakage listening principle and its application in practice. Undergr Pip Manage 3:38–39 (in Chinese)
7. Toshitaka S, Akira M (2007) Leak detection using the pattern of sound signals in water supply systems. In: Proceedings of SPIE sensors and smart structures technologies for civil, mechanical, and aerospace systems 2007, vol 6529
8. Hunaidi O, Chu W, Wang A, Guan W (2000) Detecting leaks in plastic pipes. J Am Water Works Assoc 92(2):82–94
9. Matin T, Chapman CJ, Howison SD, Ockendon JR (2001) Noise generation by water pipe leaks. In: 40th European study group with industry, Keele2001

Chapter 56
Mechanism Design of Virtual Power Plant for the Future Smart Grid

Weihui Shao, Weisheng Xu, Zhiyu Xu and Ning Wang

Abstract Virtual power plant (VPP) can respond to the real-time electricity price and implement management of controllable power plants and the distributed energy resource (DER) coordinately in future Smart Grid. Thus the mechanism of virtual power plant in future Smart Grid is designed in this paper. The model formulations are presented and the MS-VND algorithm is used to optimize the objects of both commercial VPP (CVPP) and technical VPP (TVPP). Simulations are conducted on IEEE-30 standard test system and the performance of the solutions is computationally compared and analyzed.

Keywords Smart grid · Virtual power plant · Mechanism design · Multi-objective

56.1 Introduction

Distributed energy resources (DERs) including distributed generation (DG), energy storage systems, and electric vehicles are widely used to cope with the increasingly prominent energy shortage and environmental pollution problems. DERs are reliable, economical, flexible, and environmental friendly. Despite the advantages, there are still many unsolved problems [1]. First, DERs are usually small capacity, large quantities, and unevenly distributed which makes it difficult for the independent system operator (ISO) to manage. Second, arbitrarily connecting to the Grid brings a lot of security risks such as power flow changing, line blocking, and voltage flicker.

Virtual power plant was proposed to solve all these problems. The concept of virtual power plant was first proposed by Dr. Shimon Awerbuch in 1997 which can be divided into commercial VPP and technical VPP according to different

W. Shao · W. Xu (✉) · Z. Xu · N. Wang
School of Electronics and Information Engineering, Tongji University,
Cao'an Highway. 4800, Shanghai 201804, China
e-mail: xuweisheng@tongji.edu.cn

emphases [2]. The purpose of VVP is to achieve the optimal operation of DERs through advanced control, metering, and communication technologies [3]. In [4–6], it is pointed out that DERs of the VPP must contain at least one controlled power plant and the proposed models are built to describe the mechanism of the VPP. The difference is that [4, 5] used the linear programming method while the accelerated particle swarm optimization is proposed in [6].

In the future Smart Grid, both sides of the generation and demand participate in the real-time electricity market, and their activities are responsive to the electricity price. In this scenario, a flexible mechanism based on the existing ones is imperatively needed for VPP to respond to the electricity price and manage the DERs, which is designed and modeled in this paper.

56.2 The Proposed Model

At t^k, ISO predicts the demand PL_i^k during the period of T based on historical load demand and calculates the output x_j^k when only the controllable power plants work. Assume j is a thermal power plant, the cost of j is presented as

$$\pi_j^k = a_j \cdot \left(x_j^k \cdot T \right)^2 + b_j \cdot \left(x_j^k \cdot T \right) + c_j \tag{56.1}$$

According to π_j^k, the reference price is

$$\theta^k = \sum_j \pi_j^k \Big/ \sum_j \left(x_j^k \cdot T \right) \tag{56.2}$$

DER i predicts the generating capacity during the period of T as $\left[\mathrm{PG}_{i\min}^k, \mathrm{PG}_{i\max}^k \right]$ based on the forecasted renewable energy, formulates a bidding strategy according to θ^k and responses to ISO. The bidding strategy is expressed in the form of linear function. The gains of contribution are presented as

$$\varphi_i^k \left(\mathrm{PG}_i^k \cdot T \right) = m_i^k \cdot \left(\mathrm{PG}_i^k \cdot T \right) + n_i^k \tag{56.3}$$

The average bidding price of DER i is

$$\lambda_i^k \left(\mathrm{PG}_i^k \cdot T \right) = m_i^k + n_i^k \Big/ \left(\mathrm{PG}_i^k \cdot T \right) \tag{56.4}$$

In the formula above, m_i^k, n_i^k are the bidding parameters of DER i. The bidding strategy can be divided into four categories because of the monotonicity of λ_i^k:

$$\alpha \cdot \theta^k \leq \lambda_i^k \left(\mathrm{PG}_{i\max}^k \cdot T \right) \leq \theta^k \leq \lambda_i^k \left(\mathrm{PG}_{i\min}^k \cdot T \right) \leq \beta \cdot \theta^k \tag{56.5}$$

$$\alpha \cdot \theta^k \leq \lambda_i^k \left(PG_{i\max}^k \cdot T \right) \leq \theta^k, \alpha \cdot \theta^k \leq \lambda_i^k \left(PG_{i\min}^k \cdot T \right) \leq \theta^k \tag{56.6}$$

$$\theta^k \leq \lambda_i^k \left(PG_{i\max}^k \cdot T \right) \leq \beta \cdot \theta^k, \theta^k \leq \lambda_i^k \left(PG_{i\min}^k \cdot T \right) \leq \beta \cdot \theta^k \tag{56.7}$$

$$\alpha \cdot \theta^k \leq \lambda_i^k \left(PG_{i\min}^k \cdot T \right) \leq \theta^k \leq \lambda_i^k \left(PG_{i\max}^k \cdot T \right) \leq \beta \cdot \theta^k \tag{56.8}$$

α, β are scale factors and $0 < \alpha \leq 1, \beta \geq 1$. In (56.5) is shown that the average bidding price decreases as the output power increases. (56.6) represents the strategy that the average bidding price is always lower than the reference price, while (56.7) represents the opposite situation. Equation (56.8) shows that the average bidding price increases as the output power decreases.

ISO determines the optimization goals and sends the bidding results to DERs. Controllable power plants supply power in collaboration with DERs. A commercial VPP (CVPP) is only concerned with the business benefits. In this paper, the optimization goals of a CVPP is the composition of the controllable generation marginal cost and the bidding cost which is presented as $Cost_{CVPP}$.

$$Cost_{CVPP} = \sum_j \pi_j^k + \sum_i \varphi_i^k \left(PG_i^k \cdot T \right) \tag{56.9}$$

A technical VPP (TVPP) concerns the management of the power system such as the security, reliability and the energy efficiency. The optimization objective of a TVPP in this paper is simply expressed as the active power loss which can reflect the energy efficiency of the power system.

$$Cost_{TVPP} = \frac{1}{2} \sum (U_i - U_{i'})^2 \Big/ R_{ii'} \tag{56.10}$$

The multi-objective optimization base on $Cost_{CVPP}$ and $Cost_{TVPP}$ is also considered. Multi-objective analysis is based on the fuzzy theory. Design the fuzzy membership degree as

$$F(Cost_i) = \frac{Cost_i - (Cost_i)_{\min}}{(Cost_i)_{\max} - (Cost_i)_{\min}}, \quad i = CVPP/TVPP \tag{56.11}$$

$Cost_i$ can infinitely approach the optimal value when $F(Cost_i)$ is approaching to 0. The multi-objective cost function is presented in two forms

$$Cost_{multi1} = (F(Cost_{CVPP}), \ F(Cost_{TVPP}))_{\max} \tag{56.12}$$

$$Cost_{multi2} = \omega_1 \cdot F(Cost_{CVPP}) + \omega_2 \cdot F(Cost_{TVPP}) \tag{56.13}$$

Equation (56.12) ensures both objects have better performance. In (56.13), ω_1, ω_2 are weight parameters which can set the priority of the objects.

56.3 The MS-VND Algorithms

The Multi Start Variable Neighborhood Descent algorithm (MS-VND) is used in this paper based on the proposed model. The flowchart of the algorithm is shown in Fig. 56.1. Integer coding is used to characterize the percentage of the output power of DERs. $N_{startpoint}$ groups of initial solutions are randomly generated. Variable Neighborhood Descent (VND) is the core of the algorithm. It is a kind of Variable
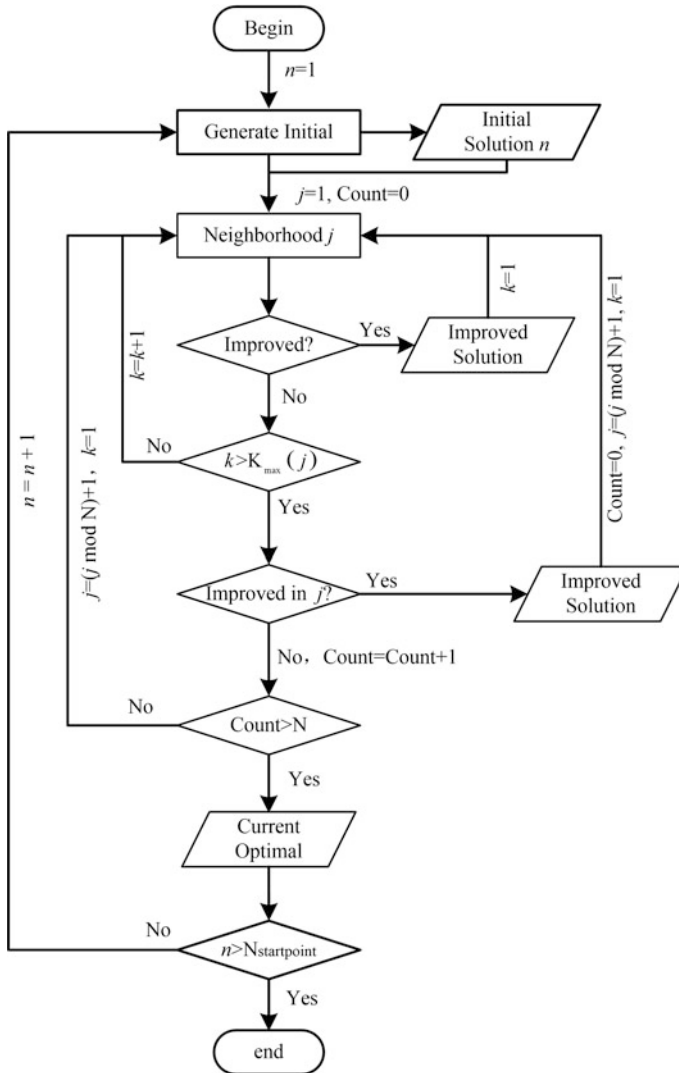

Fig. 56.1 Flowchart of the MS-VND algorithm

Neighborhood Search (VNS), originally proposed by Mladenovic and Hansen [7]. The major task is to design a series of neighborhood search operators with different radius and optimize the descending order. All the neighborhood searches belong to greedy search mode.

In Fig. 56.1, k is presented the maximum search number in each neighborhood. The termination condition of neighborhood j is that the current solution cannot be improved after $K_{max}(j)$ times search. $K_{max}(j)$ changes adaptively with the radius of neighborhood j. It steps to the next neighborhood after finishing the search in j until looping through all neighborhoods. It includes translation operator, increment (minus) operator, and mutation operator in this paper. The descending order is determined by the radii of the neighborhoods to ensure the depth and breadth of the search.

56.4 Simulation and Analysis

The IEEE-30 standard test system is used to simulate the power system of a residential region (Fig. 56.2).

Set the period T as 1 h. Assume that the balance node of test system (node 1) is a 500 MW controllable power plant. The generation cost parameters set as
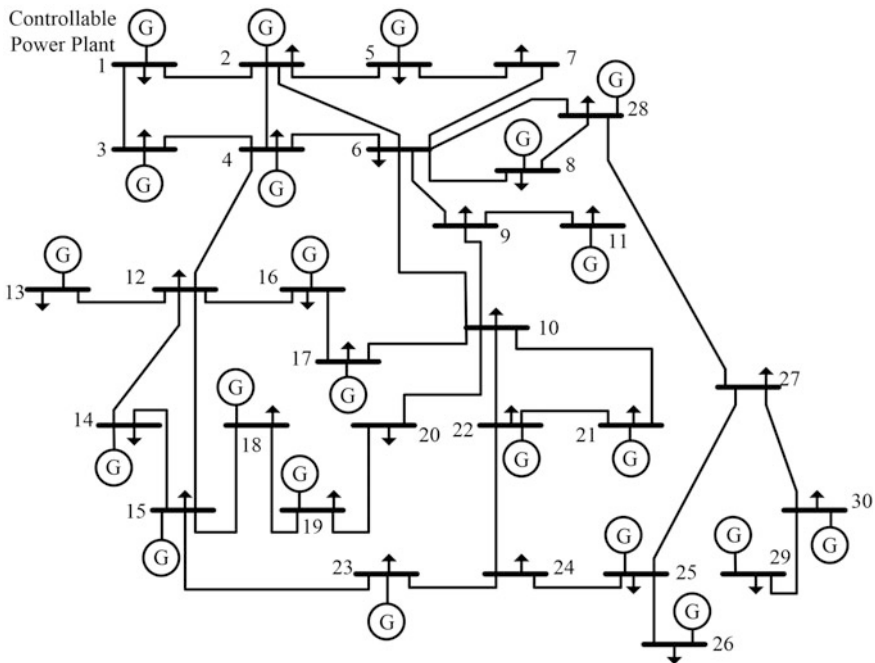

Fig. 56.2 IEEE-30 standard test system

Table 56.1 Active and reactive power of 30 loads

Load	PL/MW	QL/Mvar	Load	PL/MW	QL/Mvar	Load	PL/MW	QL/Mvar
1	10.87	1.82	11	10.36	2.00	21	13.6	3.23
2	8.99	0.40	12	12.53	1.07	22	9.77	2.40
3	10.20	1.75	13	9.50	2.93	23	9.36	2.22
4	12.39	2.12	14	9.59	2.63	24	11.64	2.45
5	10.24	2.03	15	5.60	2.13	25	10.98	1.92
6	7.93	1.48	16	8.45	1.96	26	11.53	1.21
7	8.29	0.97	17	7.21	3.18	27	11.56	2.29
8	9.66	1.67	18	9.23	2.46	28	7.04	0.70
9	9.62	3.76	19	11.05	2.00	29	11.08	1.44
10	8.27	1.26	20	13.05	2.11	30	9.82	2.85

$a = 0.03$ \$ $(MW\ h)^{-2}$, $b = 3$ \$ $(MW\ h)^{-1}$, $c = 10$ [8]. 21 of the 30 nodes are DER nodes while the others are just loads. The active power loads PL shown in Table 56.1 subject to normal distribution with the parameters of $\mu = 10$, $\sigma = 2$. Power factor of the residential load is always close to 1, as a result the reactive power loads QL is relatively small.

The generating capacity of DERs subject to normal distribution with the parameters of $\mu_{min} = 3$, $\mu_{max} = 6$, $\sigma_{min} = 0.5$, $\sigma_{max} = 1$. By power flow calculation, it requires 325.279 MW of output power when the controllable power plant is the only supplying. The cost is 4160 \$ and the reference price is 12.79 3 \$ $(MW\ h)^{-1}$. The generating capacity and the bidding strategy of each DER are shown in Table 56.2.

10 groups of startpoints and 8 neighborhood search operators are setted in the MS-VND algorithm in this paper.

**Table 56.2** Capacity of generating and bidding strategy of DERs

DER	Capacity/MW	$m/\$(MW\ h)^{-1}$	n/\$	DER	Capacity/MW	$m/\$(MW\ h)^{-1}$	n/\$
2	[2.93, 7.03]	17.21	−17.67	18	[2.46, 6.03]	15.47	−8.96
3	[2.91, 6.18]	20.01	−27.18	19	[3.12, 5.38]	8.70	22.24
4	[2.75,5.81]	4.65	30.31	21	[3.00, 4.34]	30.14	−61.56
5	[2.57, 5.43]	14.24	−3.10	22	[3.41,5.83]	8.47	25.45
8	[2.24, 5.64]	16.41	−13.28	23	[2.70, 6.87]	15.65	−15.31
11	[2.19, 6.03]	11.39	9.78	25	[3.93, 7.81]	16.57	−17.16
13	[3.39, 6.30]	22.33	−41.25	26	[3.54, 6.52]	9.43	20.59
14	[1.95, 5.30]	15.82	−11.62	28	[3.09, 6.34]	13.39	−2.71
15	[3.15, 5.00]	17.92	−26.03	29	[3.01, 6.46]	8.54	20.37
16	[3.03, 6.04]	14.09	−7.32	30	[2.53, 6.11]	12.38	6.45
17	[3.23, 6.16]	8.84	14.29				

Table 56.3 Results of the simulations

DER	SL1/MW	SL2/MW	SL3/MW	SL4/MW	DER	SL1/MW	SL2/MW	SL3/MW	SL4/MW
2	2.93	7.03	6.01	4.78	18	6.03	6.03	6.03	6.03
3	2.91	6.18	5.23	2.91	19	5.38	5.38	5.38	5.38
4	5.81	5.81	5.81	5.81	21	3.00	4.34	3.00	3.00
5	5.43	5.43	5.43	5.43	22	5.83	5.83	5.83	5.83
8	2.24	5.64	5.57	5.64	23	6.87	6.87	6.87	6.87
11	6.03	6.03	6.03	6.03	25	7.81	7.81	7.81	7.81
13	3.39	6.30	3.83	3.39	26	6.52	6.52	6.52	6.52
14	5.30	5.30	5.30	5.30	28	6.34	6.34	6.34	6.34
15	3.15	5.00	4.70	5.00	29	6.46	6.46	6.46	6.46
16	6.04	6.04	6.04	6.04	30	6.11	6.11	6.11	6.11
17	6.16	6.16	6.16	6.16					

Five simulations have been conducted, respectively, on the single objective and multi-objective situations. The results of all the simulations are shown in Table 56.3.

Simulation 0 (SL0) is the situation that DERs are offline. In this case, $Cost_{CVPP}$ is 4160 \$ and $Cost_{TVPP}$ equals 25.869 MW. Simulation 1 (SL1) individually optimized $Cost_{CVPP}$. In this case, $Cost_{CVPP}$ is 3153 \$, which is 24.20 % less than SL0. Simulation 2 (SL2) individually optimized $Cost_{TVPP}$. In this case, $Cost_{TVPP}$ is 8.912 MW, which is 65.55 % less than SL0.
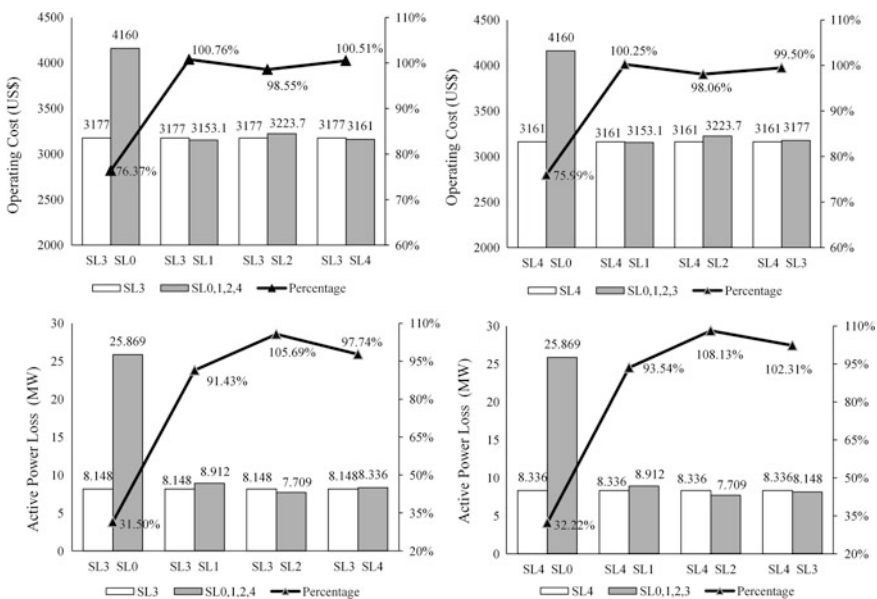
Fig. 56.3 Comparison of simulations 3 and 4

Simulation 3 (SL3) and Simulation 4 (SL4) are the multi-objective simulations. SL3 optimized $Cost_{multi1}$ and SL4 optimized $Cost_{multi\,2}$. The comparison of SL3 and SL4 is shown in Fig. 56.3. It is obvious that SL3 and SL4 both have better performance than SL0. The operating costs of SL3 and SL4 are similar to SL1 while the active power losses are much less. The operating costs of SL3 and SL4 are less compared to SL2. The results of SL3 and SL4 are almost the same. SL3 ensures both objects have good performance while the result of SL4 is more polarized.

56.5 Conclusion

This paper designs the mechanism of virtual power plant in the future Smart Grid. The model formulations of the mechanism are presented and the MS-VND algorithm is used to optimize the objects of the model. The result of simulations shows that both the operating costs and the active power losses can be reduced by rationally planning of VPP. A satisfactory solution can be found between the objects of businesses benefits and system management using the proposed model and algorithm.

References

1. Wei Z, Yu S, Sun G et al (2013) Concept and development of virtual power plant. Autom Electr Power Syst 37(13):1–9 (in Chinese)
2. FENIX (2012) Flexible electricity network to integrate expected "energy solution". http://www.fenix-project.org/
3. Asmus P (2010) Microgrids, virtual power plants and our distributed energy future. Electricity J 23(10):72–82
4. Kuzle I, Zdrilic M, Pandzic H (2011) Virtual power plant dispatch optimization using linear programming. In: The 10th international conference on environment and electrical engineering Rome, Italy, pp 1–4
5. Zdrilic M, Pandzic H, Kuzle I (2011) The mixed-integer linear optimization model of virtual power plant optimization. In: The 8th international conference on the European energy market Zagreb, Croatia, pp 467–471
6. Hropko D, Ivanecky J, Turcek J (2012) Optimal dispatch of renewable energy sources included in virtual power plant using accelerated particle swarm optimization. ELEKTRO Rajeck Teplice, Slovakia, pp 196–200
7. Mladenovi´c N, Hansen P (1997) Variable neighborhood search. Comput Oper Res 24 (11):1097–1100
8. Syothert A, Macleod I (2000) Competitive bidding as a control problem. IEEE Trans Power Syst 15(1):88–94

Chapter 57
Study on Improved DC Bus Series-Connection of Microconverter System

Hong Li, Jun Wang, Zhang Sun, Ming Li and Chaorun Feng

Abstract The research on improved series-connection DC bus of microconverter system is explained in this paper. The disturbance observer is used for maximum power point tracking in each individual microconverter. And the Z-source boost converter topology is used in the paper, the overall output efficiency of the system is improved effectively. In this paper, the algorithm of the series-connection micro-converter is improved. First of all, the ripple voltage compensation link is joined to reduce the harmonics of DC bus. Next, the PI control and the compensation of repetitive controller for quasi PR control technology are, respectively, used for voltage outer loop and current loop. Both the frequency gain of the system can be improved, and the repetitive distortion of the system can be eliminated, and the accuracy is improved. Finally, Matlab/Simulink software is used for building a simulation model in the system, and the relevant simulation is progressed, the results indicate that the improved control algorithm can be used to achieve good control effect.

Keywords DC bus · Series-connection · Z-source · Microconverter · The compensation of quasi PR control of repetitive controller

57.1 Introduction

In the twenty-first century, tightening of the global energy situation, solar photovoltaic power generation with huge development of prospects has become one of the new energy technologies of the large-scale development. Currently, how to improve the utilizing efficiency of solar energy, and maximize the output efficiency of photovoltaic power generation system must be considered during the design.

H. Li (✉) · J. Wang · Z. Sun · M. Li · C. Feng
School of Electrical and Information Engineering, Xihua University,
No. 999 Jinzhou Road, Chengdu, Sichuan, China
e-mail: 465037115@qq.com

The functions of PV modules are combined by traditional and centralized photovoltaic inverter and the output power is realized by the converter and the inverter [1].

Because of the large distribution of photovoltaic modules, the factor of illumination and temperature are different in each module, the maximum power point voltage differ, making it impossible to track the maximum power point [2]. In order to track the maximum power point of PV systems and improve output efficiency, microconverter of DC bus series-connection has become the best solution at present to solve these two problems [3, 4]. The DC bus voltage is obtained by multiple microconverter modules in series, the withstand voltage of each microconverter is low. The required breakdown voltage capability of devices is not high. The cost of system device is reduced and the flexibility of the design is improved. At present, the study of microinverter is developed rapidly in countries [5], the research of microconverter of DC bus series-connection is still relatively small.
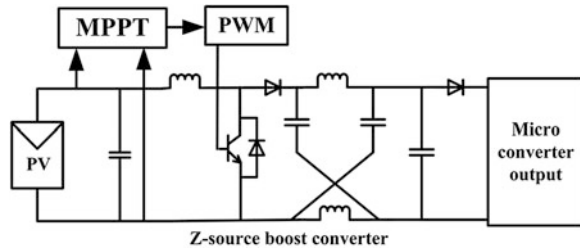
57.2 System Topology

57.2.1 DC Bus Topologies Series System

The system topology of series-connection DC bus of microconverter is shown in Fig. 57.1, the DC bus series-connection structure not only has many advantages of parallel DC bus structure, but also has the following distinct advantages: the ratio of input and output of the converter can be reduced. Both nonisolated topology and isolated topology can be used. The system can be optimized easily and the output efficiency can also be improved. The level of output voltage is low, so you can use the switch device with low voltage. The accuracy of system can be improved easily by synchronous rectification technology, and the system cost can be reduced greatly while it is easy to constitute a high-capacity system.

Fig. 57.1 The topology structure of series-connection DC bus
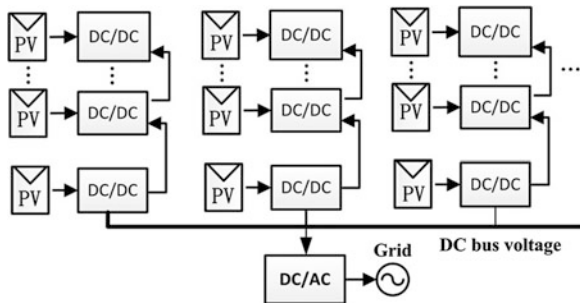
Fig. 57.2 Topology of single microinverter system

57.2.2 Topology of Signal Microconverter System

The Z-source boost converter is used in this system of microconverter [6], the topology of single microinverter system is shown in Fig. 57.2. The advantages of Z-source boost converter output voltage is greatly improved compared to Boost, and the efficiency of circuit is higher. In this system, the disturbance observer method is used to the track of MPPT [7], and the adjusting of duty cycle D is the most critical. The working voltage of photovoltaic cells and the completion of the maximum power tracking can be indirectly regulated by changing D in the situations of power balance. Due to the introduction of the Z-source boost converter circuit, MPPT loop, DC voltage loop, and net current loop can be controlled independently, making the system more stable.

57.3 Algorithm

57.3.1 The Algorithm of the Compensation of Repetitive Controller for Quasi PR Control

The advantages of quasi PR control [8] algorithm and repetitive control algorithm [9] are combined, an algorithm of the compensation of repetitive controller for quasi PR control is proposed in this paper. The quasi PR control and repetitive control algorithms in parallel are presented in this system. The frequency gain of the system can be increased, while the repetitive distortion of the system can be eliminated. The structure of the system of the compensation of quasi PR control of repetitive controller is shown in Fig. 57.3. The dotted line shown in Fig. 57.3, respectively, are the repetitive controller and quasi PR controller.

The error of output voltage as the input of the compensation of repetitive controller for quasi PR control. The output of the repetitive controller is a correction amount. The command control signal after correction is acquired by adding the correction amount to the command voltages. The relationship among repetitive control deviation, the amount of disturbance, and the quantification inferred from Fig. 57.3 can be elaborated by formula (57.1). Transfer function of the quasi-control
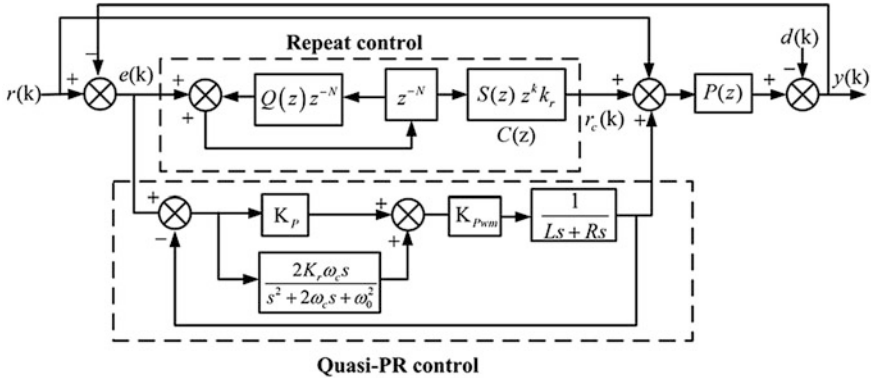
Fig. 57.3 The structure of the quasi PR compensation control of repetitive controller

compensation PR can be elaborated by formula (57.2). The simulation models of the compensation of repetitive controller for quasi PR control can be built by formulas (57.1) and (57.2).

$$E(z) = \frac{(1 - P(z))(z^N - Q(z))}{z^N - (Q(z) - z^k k_r S(z))} R(z) + \frac{Q(z) - z^N}{z^N - (Q(z) - z^k k_r S(z) P(z))} D(z) \quad (57.1)$$

$$G_{PR}(s) = K_P + \frac{2K_r \omega_c s}{s^2 + 2\omega_c s + \omega_0^2} \quad (57.2)$$

57.4 The Control Strategy of Series-Connection DC Bus of Microconverter

The topology of the DC bus in series is expressed in this paper, and the control strategy is shown in Fig. 57.4. The system consists of four photovoltaic modules in series, and each photovoltaic modules power is 250 W. The modules are used MPPT algorithm and Z-source boost converter to achieve the trace of the maximum power point. And a diode and resistor are added to the output terminal of each module to prevent heat spot effect. When any submodule fails, other modules can still work normally. When the four PV modules in series, the total power of the system is 1 kW, then through the rectifier and inverter to become single-phase AC power for grid connected. In this paper, closed double-loop control method of outer voltage loop and inner current loop are utilized. The PI control strategy is applied to the outer voltage loop, and ensured the DC bus voltage stabilized at 400 V by adding ripple voltage compensation. PLL control and quasi PR control strategy are applied to the current loop. The decoupling transfer of energy is realized from DC to AC by phase-shifted SPWM controlling inverter.
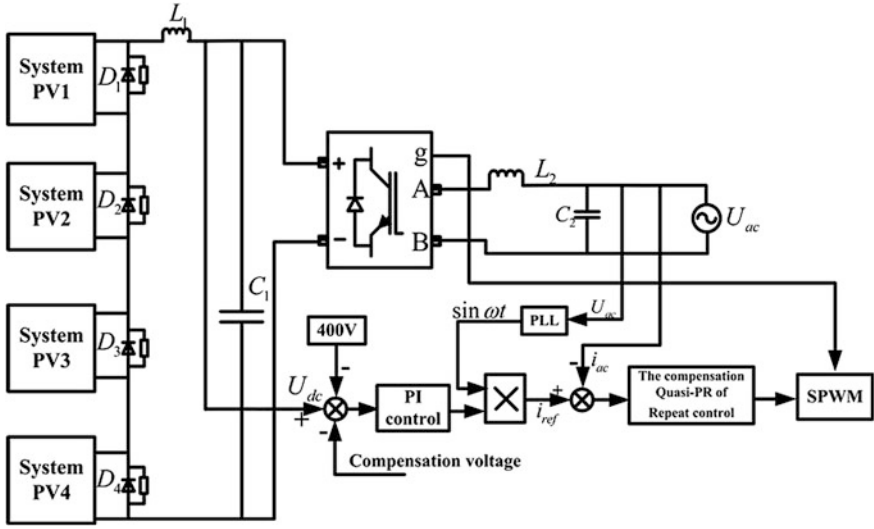
Fig. 57.4 DC bus series-connection control strategy block diagram of microinverter

Assuming the photovoltaic system inverters before the total power is P_{in}, inverter output power is P_o, grid voltage is V_{ac}, grid current is I_{ac}, according to this structure can be obtained:

$$P_{in} = P_1 + P_2 + P_3 + P_4 \tag{57.3}$$

$$P_o = \frac{1 - \cos2\theta}{2} \cdot V_{ac} \cdot I_{ac} \tag{57.4}$$

57.5 Simulation Result Analysis

The topology structure and control strategy of the system simulation model is built by Matlab/Simulink software; the simulation parameters and technical indicators are shown in Table 57.1.

The process of experiment: first of all, the photovoltaic power generation module is simulated, setting hair 250 W active power of each system, in order to simulate illumination changes, the maximum frequency tracking performance test systems. When 0.05, 0.1, 1 s were sent 205, 106, 205 W active, in 0.15 s stabilized hair 250 W active power system simulation results shown in Figs. 57.5, 57.6, 57.7, 57.8, 57.9, 57.10, and 57.11.

Figure 57.5 shows that the output power of single module photovoltaic and the output power is stable at 250 W, which is consistent with the theory, and are waveforms with low harmonic, high accuracy. The result verifies the excellent

Table 57.1 Microconverter of DC bus series-connection of parameters and technical indicators

Circuit parameters	Parameter values
Input DC voltage	37.3 V
Output AC voltage	Uo = 220 V
DC bus voltage	400 V
Output rating	Po = 1000 W
Grid filter inductor	4 mH
Output efficiency	93.9 %
Grid frequency	50 ± 0.2 Hz
THD	<5 %
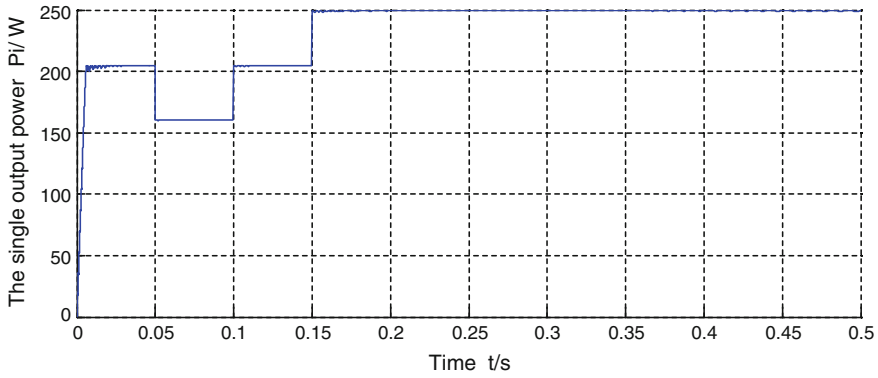
Fig. 57.5 Single PV module output power
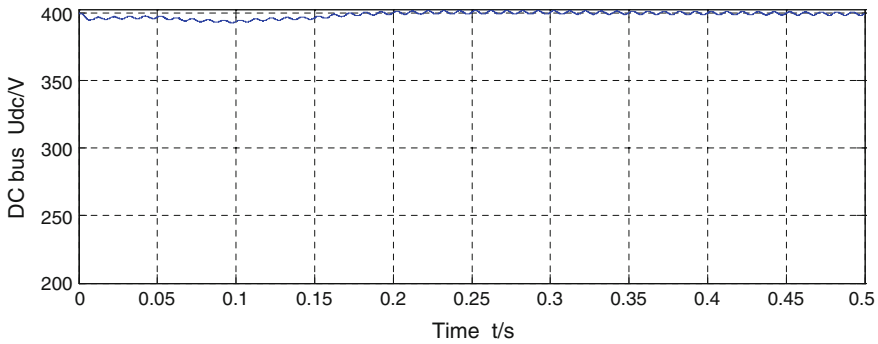
Fig. 57.6 DC bus voltage

performance of the source Z boost converter. Figure 57.6 is the DC bus voltage and the figure shows that the voltage is modulated after the simulated illumination changing, eventually stabilize at 400 V, the DC bus voltage with high accuracy, which verifies the excellent performance of the compensation of quasi PR control of repetitive controller.
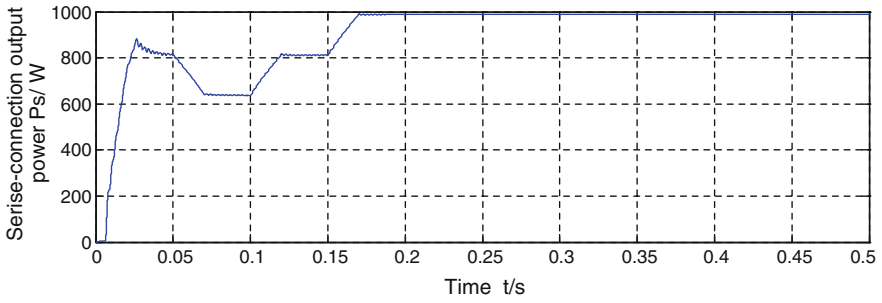
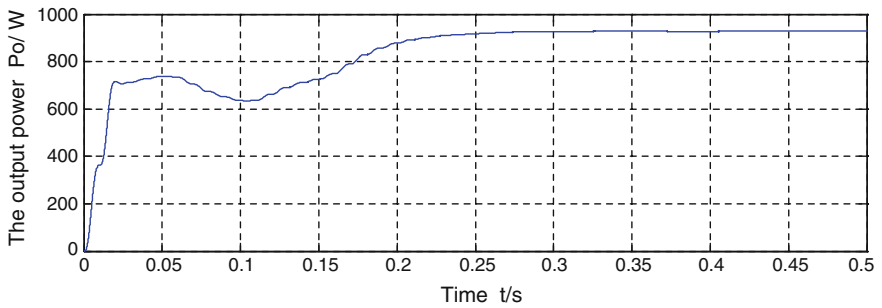**Fig. 57.7** Series-connection PV module before inverter output power

Fig. 57.8 Series-connection PV module after inverter output power
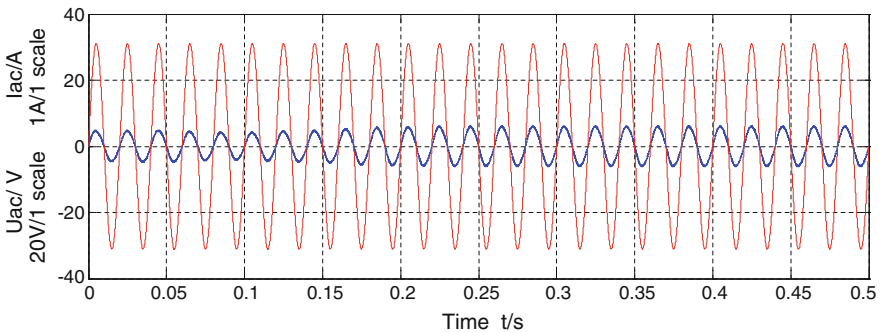

Fig. 57.9 Grid voltage and current

Figure 57.7 is the output power of four photovoltaic modules DC bus in series before inverter, after the modulation of the simulation of illumination changing, the power eventually stabilized at 1 kW, and the harmonic content is less, the series-connection DC bus is proved to achieve the real-time series of the power, and the effect is remarkable. Figure 57.8 is the final output power of the inverter in series to
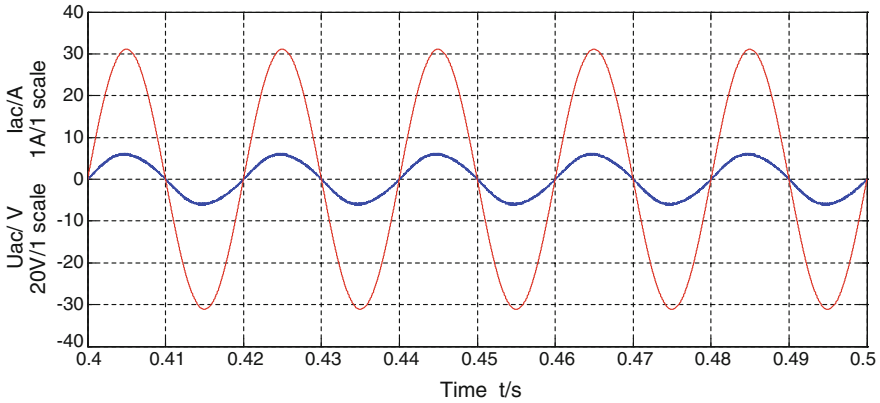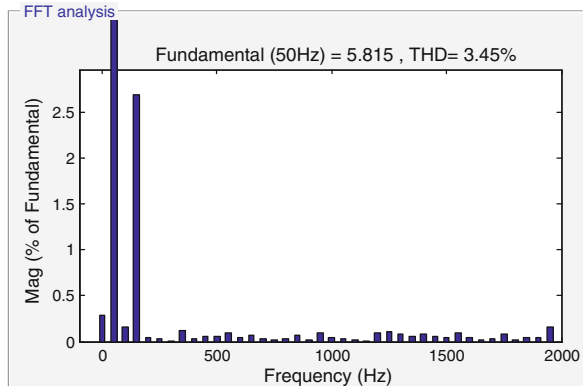
Fig. 57.10 Grid voltage and current local amplification

Fig. 57.11 Grid current harmonic analysis

the system. By comparison of the two figures shows that the prior inverter power is 1 kW and the later inverter power is 939 W, and the entire inverter efficiency is very high. Figure 57.9 is the grid current waveform and the reduced 20-fold of the grid voltage waveform, figure can be analyzed by the grid voltage and current to get the same frequency and phase to achieve control, voltage, and current size are consistent with the theoretical value and the grid current can be real-time illumination changed according to real-time tracking, and the harmonic content is less, and the system can realize effective grid. Figure 57.10 is the grid voltage and current local amplification waveform. Figure 57.11 is the analysis of the grid current harmonics, from the THD of grid current figure is 3.45 %, and reached the requirements of grid current THD <5 % in the national standard, and achieved the excellent grid of overall system.

57.6 Conclusions

An improved control strategy of the series-connection DC bus of microconverter is presented in this paper, the feasibility and efficient of the control strategy is verified by the test result. The algorithm of quasi PR control compensation repetitive controller is proposed in this paper. Both the frequency gain of the system can be improved, and the repetitive distortion of the system can be eliminated by two algorithms in parallel complementary; the accuracy and stability of the improved algorithm is verified by the test result. The inverter efficiency of this system is 93.9 %, the DC bus voltage stability in 400 V, the grid current THD is 3.45 %, the grid operation of unity power factor is realized, and be able to track the maximum power point rapidly. The system of the series DC bus of microconverter has stability, high efficiency, high precision, and strong practicability.

References

1. Yu Y (2008) The research of single-phase photovoltaic grid-connected inverter. Zhejiang University, Zhenkiang, pp 1–80 (In Chinese)
2. Zhang S, Jun W, Quan L, Li L, Huiling W (2013) Research on an improved maximum power point tracking algorithm for photovoltaic systems. ICIC Express Lett 7(3B):1061–1066 (ISSN 1881-803X) (in Chinese)
3. Hua H, Yao L, Yao S, Mei S, Guerrero JM (2014) An improved droop control strategy for reactive power sharing in islanded microgrid. IEEE Trans Power Electron, pp 1–9 (in Chinese)
4. Scholten DM, Ertugrul N, Soong WL (2013) Micro-inverters in small scale PV systems: a review and future directions. In: Australasian universities power engineering conference, pp 1–6
5. Sher HA, Addoweesh KE (2012) Micro-inverters promising solutions in solar photovoltaics. Energy Sustainable Dev 389–400
6. Wang L, Qian Z, Peng F (2007) Z-source DC converter. Electr Appl 2(24):28–32 (in Chinese)
7. Petreus D, Daraban S, Ciocan I, Patarau T, Morel C, Machmoum M (2013) Low cost single stage micro-inverter with MPPT for grid connected applications. Sol Energy 92:241–255
8. Zhao Q, Guo X, Weiyang W (2007) Research on control strategy for single-phase grid-connected inverter. Proc CSEE 27(16):60–64 (in Chinese)
9. Dou Wei X, Zhengguo PY, Jing L, Honghua X (2010) Current controller optimum design for three-phase photovoltaic grid-connected inverter. Trans China Electrotechnical Soc 25(8):85–90

Chapter 58
Operational Reliability Analysis for the Rolling Bearing of Bogie in Urban Rail Train

Ting Yun, Yong Qin, Limin Jia, Jianlong Ding and Shaohuang Pang

Abstract Rolling bearings of bogie in city rail train play an important role in operation safety. The operation reliability PHM for rolling bearings of bogie is designed, based on a general idea including data acquisition, covariate selection and calculation, model hypothesis testing and parameter estimation. Aiming at the problem of complexity and difficulty of parameter estimation of multi-parameter WPHM, constriction factor PSO algorithm is modified to realize faster convergence of the parameter estimation. Finally the numerical example shows that this method is reasonable and efficient.

Keywords Rolling bearings · Operation reliability · PHM · PSO · Parameter estimation

58.1 Introduction

Reliability of rolling bearings of bogie directly affects the overall performance of the train and its immediate failure will bring huge losses of life and property. Traditional reliability research did not consider the influence of the running state on reliability, and also ignored the difference between the individual and overall reliability [1]. Therefore, it has important theoretical and practical significance to explore the relationship between running status and reliability and realize real-time reliability evaluation of rolling bearings.

Proportional Hazards Model (PHM) [2] establishes the connection between the equipment running status covariates and reliability statistics, so as to continuously update reliability index, and provide the basis for the decision-making of preventive maintenance. Accordingly, the main aim of this thesis is to design the PHM for

T. Yun · Y. Qin (✉) · L. Jia · J. Ding · S. Pang
State Key Laboratory of Rail Traffic Control and Safety, Beijing Jiaotong University, Beijing 100044, China
e-mail: qinyong2146@126.com

rolling bearings of bogie based on a general idea including data acquisition, covariate selection and calculation, model hypothesis testing and parameter estimation according to PHM theory.

58.2 Rolling Operational Reliability Assessment Model

58.2.1 Proportional Hazard Models

According to Cox PHM theory, considering the stress in operation process of equipment such as temperature, pressure. The relationship between failure rate [3] and operating status is built. The model is defined as follows:

$$h(t, X) = h_0(t)e^{\gamma X} \tag{58.1}$$

where: $h(t, X)$—failure rate; $h_0(t)$—the basic failure rate relate to time; X—Covariate, reflect the running status of equipment; γ—The regression parameters, said the covariate X's effects on the equipment failure rate. According to the relationship between the reliability and failure rate, reliability function $R(t; X)$ with time t is expressed as follow:

$$R(t; X) = e^{-\int_0^t h(t, X)dt} \tag{58.2}$$

58.2.2 Rolling Operational Reliability Model Based on PHM

The commonly used reliability distribution including exponential distribution, weibull distribution, binomial distribution, normal distribution, lognormal distribution and poisson distribution, etc. [4]. Rolling bearing life obeys the Weibull distribution of two parameters [5], its failure density function is:

$$f(t) = m/\eta(t/\eta)^{m-1} \exp[-(t/\eta)^m] \tag{58.3}$$

where: m—Shape parameter; η—Scale parameter, or features of life; Let $Z = (Z_1 \ldots Z_p)$ denote the covariate of bearing, running state, $h_0(t)$ said the Weibull failure rate function, then the Weibull proportional hazards model (WPHM) of rolling bearing reliability can be expressed as:

$$h(t, Z) = m/\eta(t/\eta)^{m-1}\exp(\gamma Z) \tag{58.4}$$

Operation reliability of rolling bearing at the time t can be expressed as:

$$R(t; Z) = \exp\left[- \int_0^t m/\eta(t/\eta)^{m-1} \exp(\gamma Z) \mathrm{d}t\right] \quad (58.5)$$

58.3 Parameter Estimation

58.3.1 MLE Method

The PHM is more suitable for larger sample size, and MLE has good statistical properties and better approximate distribution, thus with censored data in the sample case, by the MLE method is used to estimate the parameters in the model

In order to accurate estimation of parameters in the PHM model, the characteristic data of rolling bearing should be collected in specific operation condition. These data include the bearing life time, censored or not, failure characteristics, let $(t_1, t_2, \ldots t_n)$ and (m, η, γ) be time data be parameters separately, then we can get the MLE function:

$$L(\theta) = \prod_{i \in N} f(t_i, \theta)^{\delta_i} R(t_i, \theta)^{1-\delta_i} = \prod_{i=1}^{D} h(t_i, \theta) \prod_{j=1}^{N} R(t_j, \theta) \quad (58.6)$$

where $f(t_i, \theta)$—fault probability function; $R(t_i, \theta)$—reliability function; $h(t_i, \theta)$—failure rate function; D, N—Failure set and sample se, D is the number of failure, $N - D$ is censored data set; δ_i—failure or not, $\delta_i = 1$ indicates failure.

58.3.2 Parameter Estimation Based on PSO

The calculation efficiency of operation reliability of rolling bearings of bogie of urban rail train is needed to satisfy real-time and rapid, and high accuracy and stability of the model results is also required to provide the scientific basis for the maintenance decision-making. But in the process of MLE parameter estimation, the computation speed is slow because of the general requirements of transcendental equations, especially for the PHM with more parameters. In order to make this research more practical, this section proposes a modified constriction factor particle swarm optimization algorithm (MCFPSO) to estimate parameter of PHM [6].
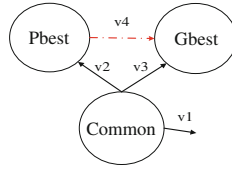
Fig. 58.1 Particle velocity updating of MCFPSO algorithm

58.3.2.1 MCFPSO

The standard PSO algorithm (SPSO) is a new evolutionary algorithm based on colony [7]. Because of the poor convergence of standard particle swarm algorithm, Clerc uses constriction factor to establishes a connection among the coefficients, to ensure the convergence of algorithm from algorithm mathematical angle, thus the constriction particle swarm optimization (CPSO) algorithm is put forward [8].

Because the speed update formula of SPSO and CFPSO is composed of particle-self speed (V1 in Fig. 58.1), speed to Pbest (V2 in Fig. 58.1) and speed to Gbest (V3 in Fig. 58.1). Based on the SPSO algorithm, the random speed operator (V4 in Fig. 58.1) from local optima to global optima is added into speed update formula of CFPSO, V4 will allow the particles to converge to the optimal solution faster, so as to realize faster convergence of the algorithm.

The speed update formulas of MCFPSO algorithm can be described as follows:

$$v_{in}(k+1) = \chi(v_{in}(k) + c_1 \mathrm{rand}_1(p_{bestin}(k) - x_{in}(k)) + c_2 \mathrm{rand}_2(G_{bestin}(k) - x_{in}(k))$$
$$+ \mathrm{rand}_3(G_{bestin}(k) - p_{bestin}(k))$$

$$(58.7)$$

rand_3—random numbers in [0, 1];

58.3.2.2 Parameter Estimation Algorithm Based on PSO

As the rolling bearing life data acquisition is difficult, and the quantity is limited, the gap between the fitting function and the true value of should not be used as the objective function [9], the MLE function can be adopted as the object function. PHM parameters estimation with PSO algorithm can be attributed to the following optimization problems:

$$\min f(\beta, \eta, \gamma_1, \gamma_2) = -\ln \mathrm{L}(t, z, \beta, \eta, \gamma_1, \gamma_2)$$
$$\mathrm{s.t.} \begin{cases} \beta > 0; \\ \eta > 0; \end{cases}$$

$$(58.8)$$

The initial position of the particle can be described as:

$$X^1 = \left[\beta^T, \eta^T, \gamma_1^T, \gamma_2^T\right] \tag{58.9}$$

where:

$$\beta = [\beta_1, \beta_2, \beta_3, \ldots \beta_N]; \quad \eta = [\eta_1, \eta_2, \eta_3, \ldots \eta_N];$$
$$\gamma_1 = [\gamma_{11}, \gamma_{12}, \gamma_{13}, \ldots \gamma_{1N}]; \quad \gamma_2 = [\gamma_{21}, \gamma_{22}, \gamma_{23}, \ldots \gamma_{2N}]$$

N is the number of particles. The initial velocity of particles is described as:

$$V^1 = \left[V_\beta^T, V_\eta^T, V_{r_1}^T, V_{r_2}^T\right] \tag{58.10}$$

(1) $k = 1$: calculate the objective function with the randomly generated initial position $X^1, f_1 = \left[f_1^1, f_1^2, \ldots f_1^N\right]^T$. let $Pbest^1 = X^1$, search $Pbest_j^1$ meeting $f_j^1 = \min\left(f_1^1, f_2^1, \ldots f_N^1\right)$, and $Pbest_j^1 = Gbest_j^1$.

(2) $K = 2$: update the velocity of particles according to three kinds of velocity update formula above respectively

$$\begin{cases} v_j^{k+1} = w\left(v_j^k + c_1 \text{rand}_1\left(Pbest_j^k - x_j^k\right) + c_2\text{rand}_2\left(Gbest_j^k - x_j^k\right)\right) \\ v_j^{k+1} = \chi\left(v_j^k + c_1\text{rand}_1\left(Pbest_j^k - x_j^k\right) + c_2\text{rand}_2\left(Gbest_j^k - x_j^k\right)\right) \\ v_j^{k+1} = \chi\left(v_j^k + c_1\text{rand}_1\left(Pbest_j^k - x_j^k\right) + c_2\text{rand}_2\left(Gbest_j^k - x_j^k\right) + \text{rand}_3\left(Gbest_j^k - Pbest_j^k\right)\right) \end{cases} \tag{58.11}$$

Calculate V^2, update the position of particles according to $x_j^{k+1} = x_j^k + v_j^{k+1}$, then we get X^2, judge:

$$\sum\left(f^k - f^{k-1}\right)^2 < \varepsilon \text{ and } \text{Count}\left(\sum\left(f^k - f^{k-1}\right)^2 < \varepsilon\right) \geq N_c \quad (\varepsilon \text{ is accuracy of}$$

convergence; N_c is the minimum test iterations) or $K \geq N_{\max}$. If the answer is yes, $Gbest_j^1$ is got

(3) If the answer is no, $K = K+1$, according to the formula:

$$Pbest_j^k = \begin{cases} Pbest_j^{k-1}, & f\left(Pbest_j^{k-1}\right) < f\left(X_j^k\right) \\ X_j^k, & f\left(Pbest_j^{k-1}\right) \geq f\left(X_j^k\right) \end{cases} \tag{58.12}$$

Search $P\mathrm{best}_j^k$ (the local optima of particle j in iteration k), calculate:

$$G\mathrm{best}^k = \left\{ P\mathrm{best}_j^k \Big| f\left(P\mathrm{best}_j^k\right) = \min\left[f\left(P\mathrm{best}_j^k\right)\right]\right\}$$

$G\mathrm{best}^k$ is the global optima in iteration k, do not stop the iteration until $G\mathrm{best}^k$ meets the following condition:

$$\sum \left(f^k - f^{k-1}\right)^2 < \varepsilon \text{ and } \mathrm{Count}\left(\sum \left(f^k - f^{k-1}\right)^2 < \varepsilon\right) \geq N_c \text{ or } K \geq N_{\max}.$$

58.4 Numerical Example

In this paper, failure life data and censored data is collected on the same type of bearing test-bed, and take vibration test on each rolling bearing at its failure time or at the end of the observation period. In engineering practice, the various failure modes of bearing can be reflected by the vibration signal, and characteristic components is often accompanied in the vibration signal, bearing vibration time domain statistical indicators such as kurtosis, square root, the peak factor and so on is widely applied in the condition monitoring and fault diagnosis based on vibration. Based on literature research, kurtosis and square root are selected as covariate in PHM; the WPHM of rolling bearings of bogie is expressed as:

$$h(t; Z) = \beta/\eta(t/\eta)^{\beta-1}\exp(\gamma_1 Z_1 + \gamma_2 Z_2) \tag{58.13}$$

where: β and η are the shape and scale parameters of Weibull respectively; Z_1- Kurtosis; Z_2-root-mean-square value; γ_1, γ_2- the regression coefficient vector, said kurtosis and root-mean-square value impact on the rolling bearing failure rate.

58.4.1 Parameter Estimation Using MLE

MLE is used to estimate parameters in this paper. According to the lifetime vibration data of rolling bearing and MLE, and use Nelder-Mead simplex of Matlab to search with 0 point as the initial, the number of iteration is 446 times in total and the optimizing performance trajectory is shown in Fig. 58.2. The parameter of WPHM is shown in Table 58.1.
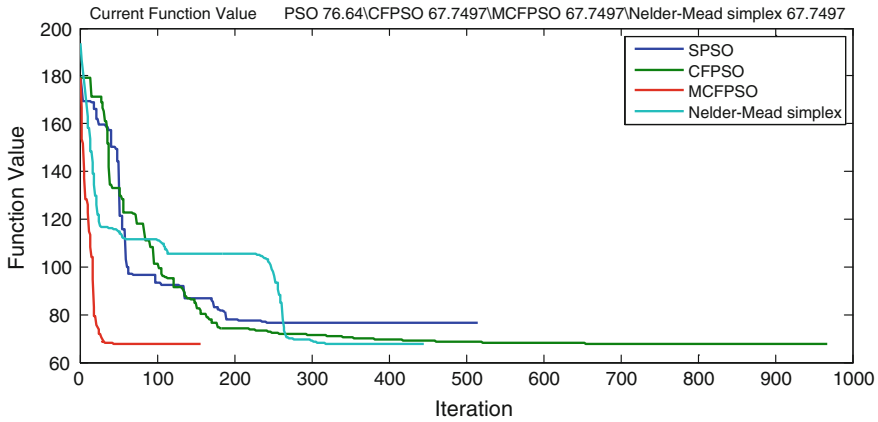
Fig. 58.2 Optimizing performance trajectory of three kinds of PSO algorithm

Table 58.1 Parameter estimation results of PHM using Nelder-Mead simplex algorithm

Parameter	β	η	γ_1	γ_2	Min
Estimates	3.67	221.87	0.062	3.8	67.7497

58.4.2 Compare Parameter Estimation Results of PSO Algorithm

The calculation efficiency of algorithm is mean to obtain right solution by less iteration number, PSO, CFPSO and MCFPSO are used for parameter estimation. Parameter settings is shown in Table 58.2:

Where N_{max} is maximum number of iterations, N_c is the minimum test iterations, ε is convergence error; c_1, c_2, ω is coefficient of velocity updating formula, *popsize* is population size, dim *size* is dimension or the number of independent variables. In order to assess the superiority of three algorithms, the same initial population position and speed is selected. In this paper, Compile PSO algorithm using Matlab software and the estimation results of parameters is shown in Table 58.3.

Table 58.3 shows: In terms of the solution quality, MCFPSO, CFPSO and the maximum likelihood can get the optimal solution, better than the results of SPSO algorithm; in terms of the number of iterations, MCFPSO is better than the other three algorithms, the number of iterations accounted for 30.3, 16.12 and 34.98 % of the other three algorithms; respectively, CFPSO algorithm has the largest number of

Table 58.2 Parameter settings of three kinds of PSO algorithm

Parameter	N_{max}	N_c	ε	c_1	c_2	ω	*popsize*	dim *size*
Settings	5000	200	1E-10	2.05	2.05	0.1	20	4

Table 58.3 Parameter estimation result, optimal value and iteration of three kinds of PSO algorithm

Parameter	β	η	γ_1	γ_2	Min	Iteration($-N_c$)
SPSO	1.82	65.3	−0.09	−3.4	76.64	515
CFPSO	3.699	221.87	0.062	3.8	67.7497	968
MCFPSO	3.699	221.87	0.062	3.8	67.7497	156
Nelder-Mead simplex	3.699	221.87	0.062	3.8	67.7497	446
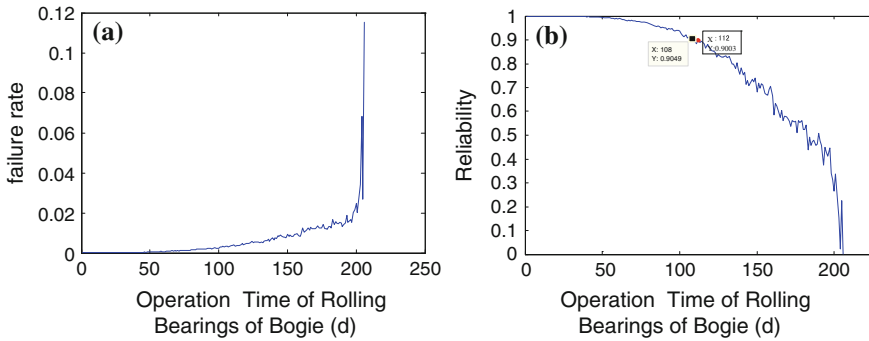
Fig. 58.3 Operation failure rate *curve* (**a**) and operation reliability *curve* (**b**) of rolling bearing

iteration. The comparison of optimization performance of three kinds of PSO algorithm and Nelder Mead—simplex algorithm is shown in Fig. 1.4:

From Fig. 58.2, it can be concluded that MCFPSO has fewer iteration times, faster convergence speed,and higher calculation accuracy than the other three algorithms. According to the parameter estimated, the WPHM of rolling bearings of bogie of urban rail train is:

$$h(t; Z) = 3.67/221.87(t/221.87)^{2.67} \exp(0.062\, Z_1 + 3.8\, Z_2) \qquad (58.14)$$

According to WPHM, the operating reliability curve and failure rate curve of the rolling bearing are drawn as follows.

As shown in Fig. 58.3a, the failure rate showed an increasing trend along with the running time of rolling bearing going. Much more break points appears in operation reliability curve of rolling bearing in Fig. 58.3b, The reason for this is that Kurtosis and Root-Mean-Square is not dependent on time, their increasing or decreasing both will bring the reliability rise and fall.

58.5 Conclusion

This paper studies the reliability modeling method based on equipment condition and realizes reliability evaluation of rolling bearing of bogie based on vibration signal feature, and therefore reliability evaluation can be updated based on condition monitoring data of rolling bearing. The detailed analysis of the maximum likelihood parameters on PHM is conducted and CFPSO algorithm which has higher accuracy, higher computation efficiency for the parameter estimation of PHM is put forward. This research shows that if continuous degradation data can be obtained, the reliability curve of the whole life cycle of rolling bearings will be got by using this method, and the technical support and maintenance decision can be provided for CBM.

References

1. Liao H, Zhao W, Guo H (2006) Predicting remaining useful life of an individual unit using proportional hazards model and logistic regression model. In: IEEE proceedings annual reliability and maintainability symposium, pp 127–132
2. Maoxiang HAH, Luqun YAO (2002) The probability distribution and reliability analysis of the life of air-engine's main axle bearings Nanjing. J Nanjing Univ Sci Technol 26(5):552–556
3. Chinnam RB (1999) On-line reliability estimation of individual components using degradation signal models. IEEE Trans Reliab 48:403–412
4. Cox DR (1972) Regression models and life tables (with discussion). J Roy Stat Soc B 34:187–220
5. Zhaojiang DAN (2013) Life and reliability evaluation of rolling bearings for no-failure data. China Institute of Metrology, Beijing
6. Dexin ZHU, Hongzhao LIU (2013) Reliability evaluation of high-speed train bearing with minimum sample. J Central S Univ 44(3):963–969
7. Zio E (2009) Reliability engineering: old problems and new challenges. Reliab Eng Syst Saf 94(2):125–141
8. Sun Y, Cheng L, Liu H (2005) Power system operational reliability evaluation based on real-time operating state. In: Power engineering conference, 2005, issue 2, pp 722–727
9. Lu H, Kolarik WJ, Lu SS (2001) Real-time performance reliability prediction. IEEE Trans Reliab 50:353–357

Chapter 59
Design of Quadrotor's Autonomous Flight Control System Based on BeagleBone Black

Pei-pei Ni, Qiang Lyu, Guo-sheng Wang, Kui-feng Su and Feng Guo

Abstract A problem of quadrotor's autonomous flight control system based on BeagleBone Black (BBB) high-performance embedded computer is investigated in this paper. BBB is chosen as the main control computer equipped with Wi-Fi receiver, GPS, and camera, while STMS320F28335 is used as the attitude control processer equipped with IMU, optical flow sensor, and infrared range finder. The software system is made up of a cascaded (inner-outer loop) attitude control based on optical flow sensor and ground station control system based on robot operating system (ROS) network. This system enhances quadrotor's ability of performing complex tasks and enables it autonomy. Indoor hovering tests prove that attitude control algorithm has a stable performance.

Keywords Quadrotor · Autonomous flight · BeagleBone black (BBB) · Robot operating system ROS

59.1 Introduction

Quadrotors are vertical take-off and landing (VTOL) four rotor helicopters with small size, light weight. Because of these characteristics, the quadrotor can operate in military and civilian fields, for instance, search and rescue, inspection, and exploration [1]. Many scholars keep studying on it and have made a lot of outstanding academic achievement. Research hotspots about quadrotor include attitude control algorithm [2], outdoor waypoints setting and route planning [3], indoor simultaneous localization and mapping (SLAM) [4], and Multi-UAV cooperative flight.

P. Ni (✉) · Q. Lyu · G. Wang · K. Su · F. Guo
Department of Control Engineering, Academy of Armored Force Engineering,
No. 21, Dujiakan, Fengtai District, Beijing City, China
e-mail: answer9@126.com

In order to realize quadrotor's autonomous flight, it should be equipped with a low-cost, light weight, and high-performance onboard microcomputer. BeagleBone Black, with the advantage of rich peripherals, low power consumption, and small size, can process data with strong capability. In this paper, BBB is chosen as the main control computer, while STMS320F28335 is adopted as the attitude processer. Flight data packaged in MAVLink protocol are transferred between attitude processer and main processer via serial ports. Image is captured by the front camera and sent to Ground control PC through ROS network. PC processes image to figure out the control instructions and then operates quadrotor.

59.2 System Hardware

BeagleBone Black, a true open hardware, has 1G Hz high-speed processing capability with the Sitara™ ARM® Cortex-A8 processor. Users can quickly develop this community-supported embedded computer with just a single USB cable. Besides, the USB port improves its versatility, compatibility, and data transmission rate. The USB devices, like Camera, GPS, and Wi-Fi receiver, can be fixed in the BBB via the USB hub. As the main control computer, it is responsible for building ROS network which contains topics.

As the attitude processor, STMS320F28335 collects attitude information from MTI-G high accuracy IMU [5], translational velocity from PX4FLOW optical flow sensor, and altitude from SHARP GP2Y0A02YK0F infrared range finder so as to figure out PWM to drive the four brushless motors according to the control algorithms. Attitude processor connects main control computer via serial port. All messages are packaged in MAVLink protocol (Table 59.1).

MTI-G contains three-axis gyroscope, three-axis accelerometer, and magnetometer. Its angular resolution is 0.05°. The max update rate can reach 120 Hz. MTI-G is connected to serial communications interface B (SCI-B). Pitch, roll, yaw, and their angular rate are chosen as input data.

SHARP GP2Y0A02YK0F consists of position sensitive detector, infrared emitting diode, and signal processing circuit. Its measurement range is 10–150 cm and accuracy is 0.3 mm. It is connected to A/D converter (ADC).

PX4FLOW [6] is an optical flow smart camera. It can detect quadrotor's translational velocity and send data in MAVLink protocol via SCI-A. Optical flow is estimated on an ARM Cortex M4 microcontroller in real-time at 250 Hz update rate. Angular rate compensation with a gyroscope and distance scaling using an ultrasonic sensor are performed onboard.

Wireless Router sets up a wireless network and assigns IP address to BBB and PC. BBB runs ROS core to construct the ROS network. Topics containing flight

Table 59.1 MAVLink protocol

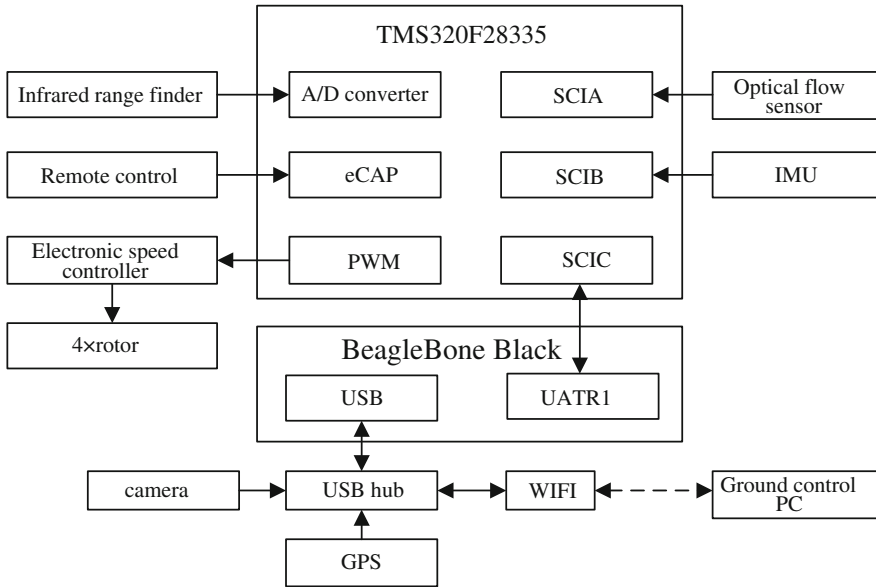| Packet start sign	Payload length	Packet sequence	System ID	Component ID	Message ID	Data	Checksum

Fig. 59.1 Description of the control system hardware construction

data or image will be published in the ROS network. Ground station PC subscribes these topics and sends control command to BBB. The whole hardware construction is shown as Fig. 59.1.

59.3 Attitude Control Algorithm

Attitude estimation based on the Inertial Measurement Unit usually makes certain errors. Besides, GPS has disadvantages as low accuracy and environment limitation. So the quadrotor drifts a lot while hovering. A method based on optical flow sensor for hovering calibration is provided. The optical flow sensor is mounted in the bottom of the quadrotor aircraft. Attitude estimation is compensated to correct hovering with the horizontal velocity, which is detected by the optical flow information. A cascaded (inner-outer loop) structure is often adopted [7]. Figure 59.2 is the controller structure for quadrotor hovering control with the controller parameters, which is roughly tuned in the experiments.

v_x and v_y are horizontal velocity in x-direction and y-direction, measured by optical flow sensor, respectively. v_x is proportional to pitch error $base_x$ and v_y to roll error $base_y$, besides, $v_x, v_y \in (-1.0, 1.0)$ m/s. The expected horizontal velocity is 0 m/s. PI controller is chosen as the out loop controller. v_x and v_y are input, $base_x$ and $base_y$ are output, then the real attitude angular are
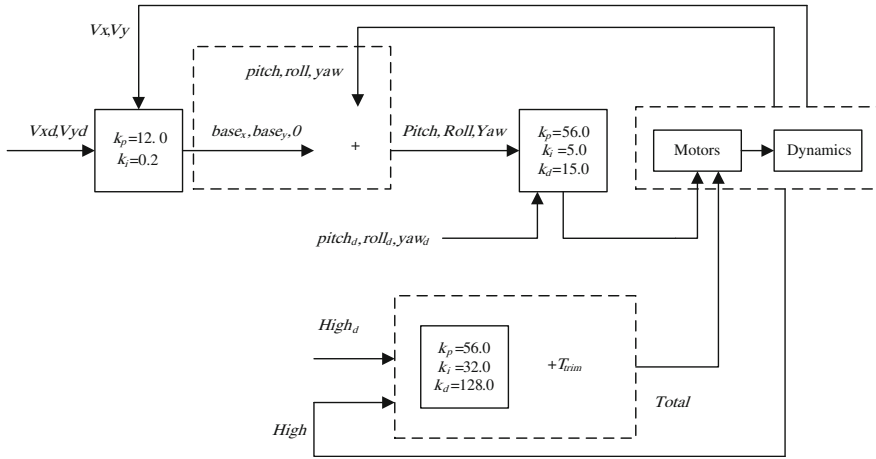
Fig. 59.2 Controller structure for hovering control

$$
\begin{cases}
\text{Pitch} = \text{pitch} + \text{base}_x \\
\text{Roll} = \text{roll} + \text{base}_y \quad , \\
\text{Yaw} = \text{yaw} + 0
\end{cases}
\tag{59.1}
$$

where pitch, roll, and yaw are measured by magnetometer.

Since the expected attitude angular are all 0°, we take the calibrated pitch, roll, and yaw as input and use PID controller as the inner loop controller. The control output can be drawn as

$$
\begin{cases}
u_x = kp_x \cdot \text{Pitch} + ki_x \cdot \sum_0^n \text{Pitch} + kd_x P \\
u_y = kp_y \cdot \text{Roll} + ki_y \cdot \sum_0^n \text{Roll} + kd_y \cdot v_R \quad , \\
u_z = kp_z \cdot \text{Yaw} + ki_z \cdot \sum_0^n \text{Yaw} + kd_z \cdot v_Y
\end{cases}
\tag{59.2}
$$

where v_P, v_R and v_Y are the angular rate measured by MTI-G.

Altitude control also uses PID controller, the altitude control output is

$$
u_h = kp_h \cdot \text{High} + ki_h \cdot \sum_0^n \text{High} + kd_h \cdot (\text{High}_n - \text{High}_{n-1}),
\tag{59.3}
$$

where High is the altitude measured by infrared range finder. Then the four duty cycles are

$$\begin{cases} \text{CMPA1} = 4000 + u_x - u_z + u_h \\ \text{CMPA2} = 4000 + u_y + u_z + u_h \\ \text{CMPA3} = 4000 - u_x - u_z + u_h \\ \text{CMPA4} = 4000 - u_x - u_z + u_h \end{cases}, \qquad (59.4)$$

where 4000 is the trim value T_{trim} during hovering.

59.4 Ground Station Control System

Ground station PC uses the ROS network to perform the control, because topics and nodes are good tools to have a discrete control. The nodes are processes that execute a special task [8]. The running nodes in BBB package different message into topics. Topics are published in the ROS network and subscribed by PC. PC analyses attitude information, GPS information and image, then gives orders to control quadrotor. Nodes are as follows:

(a) "/linker"
    This node is design for realizing the connection between attitude processer and main control computer. Its function contains serial port activation, messages packaging and parsing in MAVLink protocol (including heartbeat, attitude, optical flow and control order), and message transmission to ROS network.
(b) "/cam_cap"
    This node is used to capture images from front camera and convert video from YUYV format to ROS format.
(c) "/GPS_cap"
    In outdoor environment, this node reads GPS information from USB GPS device. The GPS information can be used for outdoor waypoints setting and route planning or moving vehicle tracking.
(d) "/flight"
    The three nodes above are run by BBB, while this node is executed by PC. It accomplishes indoor environment recognition and flight control. Indoor environment can be divided into three parts; corridors, stairways, and rooms. Image processing algorithms can extract and analyze environmental features. Canny edge detection algorithm is good for environment outline extraction. For example, ordinary corridor's outline consists of four straight lines. Their extension lines intersect at one point called vanish point. This vanish point can guide quadrotor to fly along the corridor.

Figure 59.3 is the description of the ground station control system. The circles represent nodes and blocks represent topics
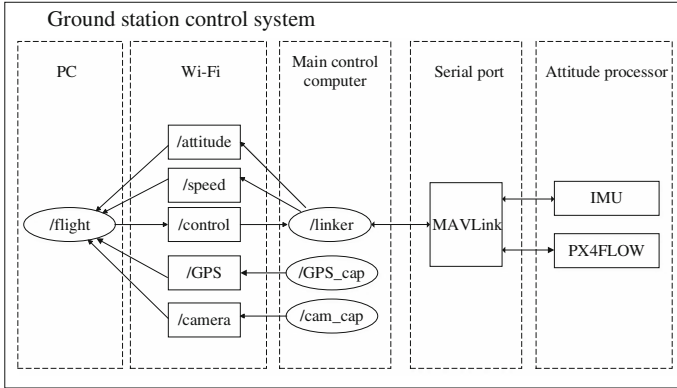
Fig. 59.3 Description of the ground station control system

59.5 Hovering Control Test

Figure 59.4 is the description of quadrotor's hovering track. We can conclude that quadrotor can hover within a circular area with a radius of 12 cm. Figures 59.5, 59.6 and 59.7 are pitch, roll, and yaw control effects, respectively. We can conclude that attitude can be stable within $\pm 5°$ and quadrotor can hover stably. Figure 8 is altitude curve. In the take-off stage, about 8 cm overshoot happened when it reaches the maximum altitude; altitude stables at 50 cm or so, the maximum error is less than 10 cm; from take-off to landing, the altitude control had a good performance (Figs. 59.8 and 59.9).

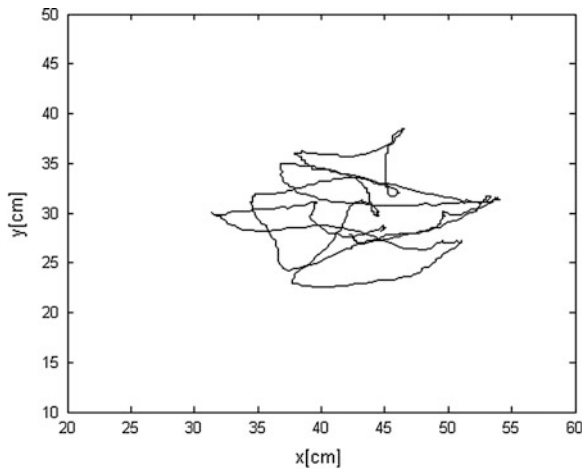**Fig. 59.4** Description of quadrotor's hovering track
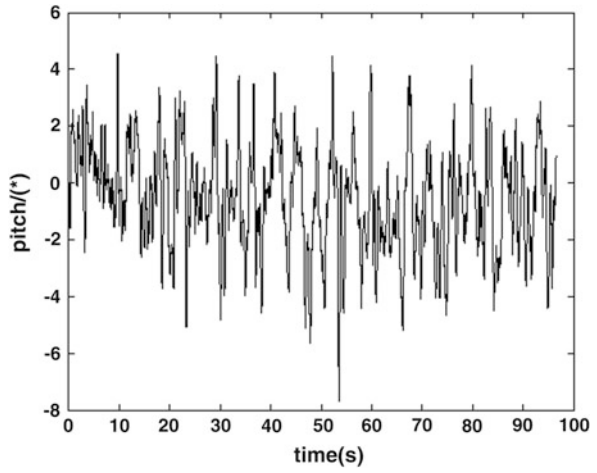
Fig. 59.5 Pitch control curve

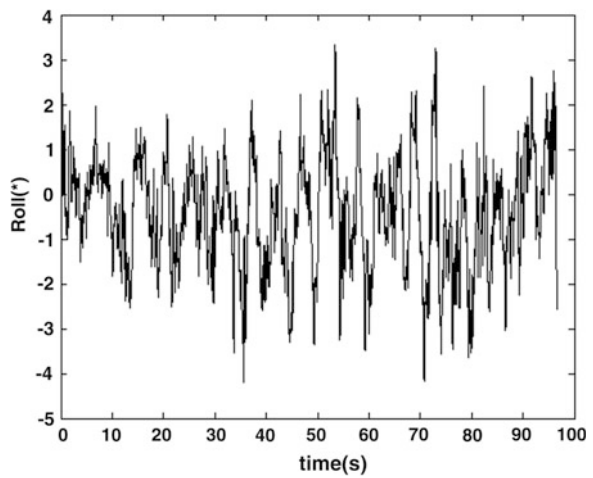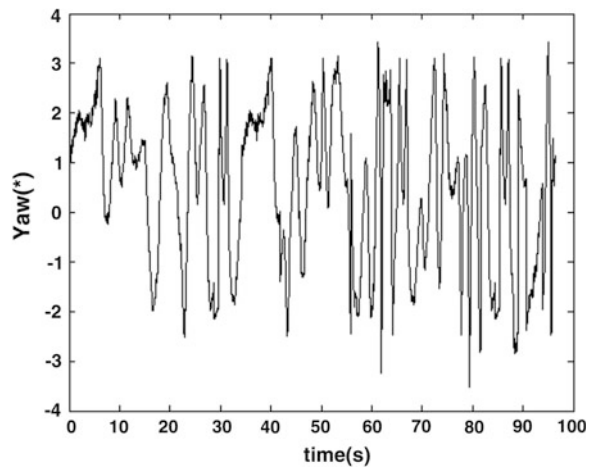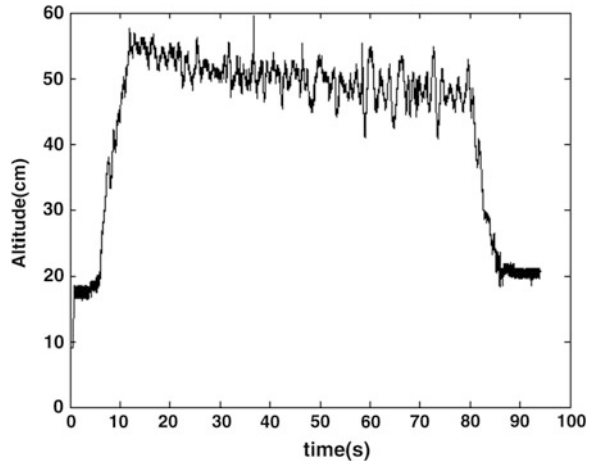**Fig. 59.6** Roll control curve

Fig. 59.7 Yaw control curve

Fig. 59.8 Altitude control
curve

Fig. 59.9 Picture of
quadrotor indoor flying

59.6 Conclusion

In this paper, we combine BeagleBone Black with STMS320F28335, and select
MTI-G IMU, PX4FLOW optical flow sensor, and SHARP GP2Y0A02YK0F
infrared range finder to design quadrotors' autonomous flight control system. This
system consists of a cascaded (inner-outer loop) attitude control based on optical
flow sensor and ground station control system based on ROS network. This system
enhances quadrotor's ability of performing complex tasks and enables it autonomy.
Indoor hovering experiment shows that the attitude control algorithm is very
effective in eliminating the long-term drift.

References

1. Hong-rui B (2012) Control system design for a quadrotor aircraft. Master thesis, Academy of Armored Forces Engineering, Beijing (in Chinese)
2. Dong-lai W (2012) Research on the miniature quadrotor attitude control strategy. PhD thesis, Academy of Armored Forces Engineering, Beijing (in Chinese)
3. Bouktir Y, Haddad M, Chettibi T (2008) Trajectory planning for a quadrotor helicopter. In: 2008 16th mediterranean conference on control and automation. IEEE, pp 1258–1263
4. Xiao-huan Y, Bo H, Yu Z et al (2014) Binocular stereo vision based 3D mapping for micro aerial vehicles in an indoor environment. Inf Control 43(4):392–397 (in Chinese)
5. Wei-quan H, Han-zeng M (2010) Program design on data access and display from micro AHRS of the MTi based on VC. High Sci Pap (Online) 3(6):530–535 (in Chinese)
6. Honegger D, Meier L, Tanskanen P et al (2013) An open source and open hardware embedded metric optical flow CMOS camera for indoor and outdoor applications. In: International conference robotics and automation
7. Qiang L, Pei-pei N, Guo-sheng W, Feng L (2014) Design of quadrotor's control system based on DSP. Adv Mater Res 989:3216–3219
8. Ivan M (2013) Developing a ROS enabled full autonomous quadrotor. Master thesis, Luleå University of Technology, Sweden